UNIVERSITY OF GRANADA

FACULTY OF SCIENCES

DEPARTMENT OF MINERALOGY AND PETROLOGY

Doctoral Thesis

METAMORPHIC AND MAGMATIC CONSEQUENCES OF SUBDUCTION OF YOUNG OCEANIC LITHOSPHERE AND EXHUMATION IN A SERPENTINITE SUBDUCTION CHANNEL. EASTERN CUBA.

IDAEL FRANCISCO BLANCO QUINTERO

SEPTEMBER, 2010

Editor: Editorial de la Universidad de Granada
Autor: Idael Francisco Blanco Quintero
D.L.: GR 4266-2010
ISBN: 978-84-693-6702-5

UNIVERSITY OF GRANADA

FACULTY OF SCIENCES

DEPARTMENT OF MINERALOGY AND PETROLOGY

Doctoral Thesis

Tesis Doctoral

METAMORPHIC AND MAGMATIC CONSEQUENCES OF SUBDUCTION OF YOUNG OCEANIC LITHOSPHERE AND EXHUMATION IN A SERPENTINITE SUBDUCTION CHANNEL. EASTERN CUBA.

Tesis que presenta IDAEL FRANCISCO BLANCO QUINTERO para optar al grado de Doctor por la Universidad de Granada

Fdo. Idael Francisco Blanco Quintero

VºBº del Director

Antonio García Casco

VºBº del Director

Joaquín Proenza Fernández

Granada, 1 de Septiembre de 2010

AGRADECIMIENTOS

Deseo lleguen mis más sinceros agradecimientos a todas las personas que de una forma u otra contribuyeron en el desarrollo de la presente investigación:

En primer lugar, quiero agradecer a mis directores de Tesis, Antonio García Casco y Joaquín A. Proenza Fernández. Antonio, gracias por haber confiado en mí y darme esta oportunidad única, por la amistad de estos años y el tiempo tan largo que has dedicado a instruirme en conceptos y métodos novedosos para mi, y sobre todo por la paciencia con el inglés. Joa, gracias por haberme demostrado que con tesón todo se puede lograr. Por el apoyo brindado cuando parecía que todo se perdía e indicarme que las rocas ultramáficas también son muy importante en las mélanges.

A Yamirka Rojas Agramonte, quien ha contribuido de forma sustancial en esta investigación, así como por el tiempo dedicado a las correcciones de inglés. Taras Gerya por haberme acogido en el ETH-Zurich y enseñarme que las matemáticas son muy importantes dentro de la geología. Alfred Kroner por la ayuda en aquellos primeros viajes de campo y en las dataciones. Al profesor Antonio Rodríguez Vega quien me inicio en la investigación en Cuba y me mostró la mélange de La Corea por primera vez. Al Departamento de Mineralogía y Petrología, a todos los profesores, técnicos e investigadores, a su director Miguel Ortega. Al igual que a los técnicos del Centro de Instrumentación Científica por su ayuda incondicional.

A José María por haberme recibido en el aeropuerto y enseñarme la España autentica, compartir conmigo los mejores y también los más difíciles momentos y además su ayuda en la adaptación a este nuevo (para mi) país y su cultura.

Un saludo a todos mis compañeros de oficina y colegas becarios con los que he compartido buenos y malos momentos: Concha, Sandra, Juan, Iñaki, J. Alberto, Aratz, Cristina, Claudio, Farida, J. Antonio, C. Tome, Antonio, Maja, Anna, Ana, Verónica, Marta,…

A mis colegas cubanos, que como yo se han aventurado en la investigación y tomado importantes decisiones, por su apoyo y los consejos mutuos: Israel, Leomaris, Yaniel e Ismael, así como Yordán, Aliuska, Yuri, Adrián, Amparo,…

En especial a mi familia cubana, mis padres por haber comprendido y apoyado en el paso tan importante que he dado, mis hermanos y demás familiares. A mi nueva familia española por haberme acogido, en especial a ti, Celeste, por apoyarme en esta dura tarea.

A todos los que han confiado en mí

Muchas gracias

ABSTRACT

Ophiolitic rocks associated with high pressure blocks occur in serpentinite matrix mélanges in the north-western Antilles (northern part of Cuba and Hispaniola). These mélanges represent fragments of a well preserved oceanic subduction channel related to subduction of the Protocaribbean (Atlantic) lithosphere below the Caribbean plate during the Cretaceous. The mélanges occur in three tectonic domains of the north-western Antilles: western and central Cuba occupying the western portion, eastern Cuba (east of the Nipe-Guacanayabo fault) in the center, and Hispaniola representing the eastern portion.

The high pressure blocks from mélanges of the western and eastern portions of the north-western Antilles indicate cold subduction represented by eclogite, blueschist as well as lawsonite-eclogite/blueschist as the main lithologies. On the other hand, the high pressure blocks from mélanges of the central portion (eastern Cuba) indicate hot and cold subduction, with epidote-amphibolite rocks containing the tonalitic-trondhjemitic products of partial melting of the slab, and blueschists. The Sierra del Convento and La Corea mélanges, being located in the central portion, are geologically similar and provide a good example for studying hot subduction processes and, in particular, partial melting of the slab. Partial melting of a subducted young oceanic lithosphere in eastern Cuba is unique in the Caribbean realm (and probably in the world). This scenario can only be compared with the Catalina schist (a fragment of the Franciscan mélange) in south western USA and has significant consequences for the plate tectonic interpretation of the region. This is the focus of this PhD thesis in the La Corea mélange.

The La Corea mélange is located in the Sierra del Cristal mountain range. It occurs as a tectonic window between the Mayarí-Cristal ophiolite massif, on top, and the Cretaceous Santo Domingo volcanic arc formation, below. Exotic blocks, mainly of garnet-amphibolite, blueschist and greenschist, occur in the mélange within a serpentinite-matrix. The metamorphism is related to subduction processes and evolved under medium to high-pressure and high- to low-temperature. A unique characteristic of the mélange, shared by the Sierra del Convento mélange, is the presence of dikes and veins of intermediate to acid (tonalitic-trondhjemitic-granitic) composition which occur intimately associated with the amphibolites.

The integrated field, petrological, and geochemical study of the amphibolite blocks and the associated tonalitic-trondhjemitic materials indicate that the latter formed by partial melting of the former under water-saturated conditions. The main (peak) mineral assemblage of the amphibolite blocks is pargasitic amphibole + epidote + quartz + rutile + titanite ± garnet ± phengite, lacking primary (peak) plagioclase. The amphibolites have variable grain size and degree of deformation. The magmatic mineral assemblage of the tonalite-trondhjemite rocks is plagioclase + quartz + phengite ± epidote ± paragonite ± pargasite. These rocks show variable grain size and a mild deformation. The leucocratic bodies appear associated with the amphibolites and do not crosscut other types of exotic blocks or the serpentinitic matrix.

Major and trace element geochemistry of the amphibolites show a basaltic composition within the subalkaline series and a tholeiitic low-K affinity. The REE patterns indicate N-MORB composition. N-MORB signatures are locally modified

by infiltrating fluids evolved from dehydration of the subducting Protocaribbean lithosphere. Therefore the mafic protoliths (amphibolites) represent subducted Protocaribbean lithosphere exhumed in the subduction channel. The tonalitic-trondhjemitic-granitic rocks are of andesitic to rhyolitic composition in the TAS diagram, have a peraluminous character, and display distinctive REE patterns with a negative slopes and positive Eu anomalies. The positive Eu anomalies suggest an important contribution of plagioclase to the partial melting processes, consistent with the lack of peak plagioclase in the amphibolites.

Thermobarometric determinations by means of the multiequilibrium and pseudosection approaches indicate that partial melting of the amphibolites took place at. 700ºC and 14-16 kbar during subduction and accretion to the upper plate mantle, while crystallization of the tonalitic-trondhjemitic melts occurred within the blocks at similar depths but during cooling in the upper plate (ca. 680-700ºC and 13-15 kbar). At these conditions (ca. 50 km depth; > 600 ºC), antigorite is not stable, preventing the formation of the serpentinitic subduction channel.

Upon further cooling of the subduction system due to continued subduction, antigoritite formed due to hydration of the upper plate peridotite, allowing the formation of the subduction channel and, henceforth, the blocks started exhumation. The retrograde overprints in the amphibolites and trondhjemites are made of combinations of actinolite + glaucophane + tremolite + paragonite + lawsonite + albite + clino-zoisite + chlorite + phengite, formed during retrograde blueschist/greenschist facies conditions. Calculated P-T conditions indicate counterclockwise P-T paths (i.e., “hot Franciscan type” exhumation). Occasionally, the blocks indicate large-scale convective circulation in the channel, which is consistent with predictions of thermo-mechanical models. This finding constitutes the first report of large-scale convective circulation of tectonic blocks in a subduction channel in the literature.

Formation of amphibolite-trondhjemite rocks at high pressure - high temperature conditions documents high thermal gradient at the slab-wedge interface. The counterclockwise P-T paths followed by these rocks indicate, in turn, cooling of the subduction system upon continued subduction. This thermal history suggests onset of subduction of a young oceanic lithosphere, consistent with predictions of thermo-mechanical models. However, a similar thermal evolution is possible after subduction of young lithosphere followed by subduction of older lithosphere, whether or not onset of subduction is involved, during oblique subduction of a ridge. The thermo-mechanical models permit also considered the partial melting process in eastern Cuba as a cold plume aborted and crystallized in the slab-mantle wedge interface.

Ba-rich phengite-bearing rocks, including amphibolite, trondhjemite, pegmatite and Qtz+Ms rocks, have major and trace elements composition that indicates circulation of Ba-rich fluids and melts in the subduction channel. Fluid infiltration at high temperature of Ba-rich fluids, likely evolved from subducting sediments, transformed subducted/accreted MORB material (amphibolites). This process led to the formation of Ba-rich trondhjemites with adakitic signature during fluid-fluxed melting of amphibolite. The partial melts represent pristine slab melts that did not react with the upper mantle. The pegmatites are interpreted as magmatic products after differentiation of trondhjemitic melts, while Qtz-Ms rocks probably represent

material crystallized from a primary sediment-derived fluid. The chemistry of phengite is primarily governed by the celadonite (tschermak) ($(Mg,Fe)Si(^{VI}Al^{IV}Al)_{-1}$) and celsian ($AlBa(SiK)_{-1}$) exchange vectors. The preservation of zoning in phengite indicates sluggish diffusion. This finding is important because crystallization of phengite at depth makes the behaviour of Ba (and K and other LILE) compatible, preventing the transfer of these elements to the mantle wedge and reinforcing the importance of phengite stability in the subduction channel for the transference of elements from the slab to the arc environment.

Two main groups of ultramafic material appear in the mélange associated with the high pressure blocks: antigorite- and antigorite-lizardite-serpentinites. The strong alteration (i.e., serpentinization, Cr-spinel transformation) of ultramafic protholiths indicate pervasive fluid flow, best explained if the rocks experienced hydration during infiltration of fluids evolved from the subducted slab. Antigorite serpentinites have harzburgitic protolith and most likely formed at depth after hydration of the mantle wedge (Caribbean lithosphere) by fluids derived from the SW-dipping subducted slab (Protocaribbean lithosphere). Antigorite-lizardite serpentinites are of harzburgitic-lherzolitic composition and are best explained as abyssal (meta)peridotites (Protocaribbean lithosphere) accreted to the subduction channel developed in the Caribbean-Protocaribbean plate interface. Antigorite-serpentinites document large-scale hydration of the Caribbean plate mantle wedge and the formation of a thick subduction channel which allowed exhumation of accreted subducted material during Cretaceous times.

U-Pb SHRIMP and Ar-Ar dating constrain the evolution of the subduction zone. Zircon from trondhjemitic rocks provided U-Pb crystallization ages ranging 105-110 Ma. Ar-Ar phengite data from the same trondhjemitic samples yielded cooling ages of 83-86 Ma (interpreted as the closure-cooling temperature of phengite). These data, combined with the calculated counterclockwise P-T paths indicate a very slow syn-subduction exhumation history in the channel (~1mm/yr). The leucocratic rocks and the host amphibolite slowly cooled and exhumed from 700 ºC and 15 kbar to 350 ºC and 8 kbar during 25 My. Final exhumation in the mélange occurred during the late Cretaceous (70-65 Ma) obduction of the supra-subduction ophiolitic and volcanic arc rocks as determined by the presence of syn-tectonic deposits.

RESUMEN

Rocas ofiolíticas asociadas con bloques de alta presión aparecen en las mélanges de matriz serpentinítica del noroeste de las Antillas (parte norte de Cuba y La Española). Estas mélanges representan un ejemplo bien preservado de un canal de subducción oceánico. El canal se formó con la subducción durante el Cretácico de la litósfera del Protocaribe (Atlántica) bajo la Placa del Caribe. Las mélanges se encuentran en los bloques tectónicos del noroeste de las Antillas: Cuba occidental y central ocupando la porción oeste, Cuba oriental (al este de la falla de Nipe-Guacanayabo) en el centro y La Española ocupando la porción oriental.

Los bloques de alta presión (eclogitas y esquistos azules con epidota, eclogitas y esquistos azules con lawsonita) de las mélanges de los dominios occidental y oriental indican una subducción fría. Por otro lado, los bloques de alta presión de las mélanges de Cuba Oriental indican una subducción caliente y fría, con rocas de la facies de anfibolitas con epidota que contienen productos de fusión parcial formados durante la subducción/accreción (tonalitas-trondhjemitas), y esquistos azules. Las mélanges de La Sierra del Convento y La Corea, situadas en el dominio central (Cuba oriental), son muy similares geológicamente y proporcionan un buen ejemplo para estudiar los procesos de subducción calientes relacionados con la fusión parcial de la placa subduccente. La fusión parcial de una litosfera oceánica joven subducida en Cuba oriental es única en el área del Caribe (y probablemente en el mundo). Este escenario se puede comparar solamente con el esquisto de Catalina (un fragmento de la mélange Franciscana) en la costa suroeste de los E.E.U.U. y tiene consecuencias significativas para la interpretación tectónica de las placas en la región. El núcleo principal de esta tesis doctoral es la mélange de La Corea.

La mélange de La Corea se encuentra en el sistema montañoso de la Sierra del Cristal. Esta mélange aparece como una ventana tectónica por debajo del macizo ofiolítico de Mayarí-Cristal y encima de la formación volcánica Santo Domingo del Cretácico. Los bloques exóticos (principalmente anfibolitas con granate, esquistos azules y esquistos verdes) aparecen dentro de una mélange de matriz serpentinítica. El metamorfismo se relaciona con procesos de subducción y se desarrolla bajo unas condiciones de presión de media a alta y temperatura de alta a baja. Una característica única de esta mélange, compartida con La Sierra del Convento, es la presencia de diques y de venas de composición intermedia a ácida (tonalítica-trondhjemítica-granítica) que aparecen íntimamente asociadas a las anfibolitas.

El estudio integrado de campo, petrológico y geoquímico de los bloques de anfibolitas y de los materiales tonalíticos-trondhjemíticos asociados indican que estos últimas se formaron por la fusión parcial de las anfibolitas en condiciones de saturación en agua. La asociación mineral principal de pico de los bloques anfibolíticos es: anfíbol pargasítico + epidota + cuarzo + rutilo + titanita ± granate ± fengita, con plagioclasa primaria (de pico metamórfico) ausente. Las anfibolitas tienen variable tamaño de grano y grado de deformación. La asociación mineral magmática de las rocas tonalíticas-trondhjemíticas es plagioclasa + cuarzo + fengita ± epidota ± paragonita ± pargasita. Estas rocas muestran tamaño de grano variable y una leve deformación. Los cuerpos leucocráticos aparecen asociados con las anfibolitas y no cortan otros tipos de bloques exóticos ni la matriz serpentinítica.

La geoquímica de los elementos mayores y trazas de los bloques anfibolíticos indican una composición basáltica dentro de la serie subalcalina y de afinidad toleítica baja en potasio. Los patrones de tierras raras indican una composición N-MORB. La signatura N-MORB esta localmente modificada por la infiltración de fluidos producidos por la deshidratación de la litosfera del Protocaribe. Por lo tanto los protolitos máficos (anfibolitas) representa parte de la litosfera Protocaribeña exhumada en el canal de subducción. Las rocas leucocráticas tienen una composición en el rango de andesita hasta riolita, con carácter peraluminoso, y exhiben patrones distintivos de tierras raras con pendientes negativas y anomalías positivas de Eu. Las anomalías positivas de Eu sugieren una contribución importante de plagioclasa a los procesos de fusión parcial, consistente con la ausencia de plagioclasa primaria en las anfibolitas.

Los cálculos termobarométricos usando los métodos del multiequilibrio y seudosecciones indican que la fusión parcial de las anfibolitas ocurrió a 700ºC y 14-16 kbar durante la subducción y acreción al manto de la placa suprayacente, mientras la cristalización de las trondhjemitas ocurrió dentro de estos mismos bloques a profundidades similares pero durante el enfriamiento en la placa superior (ca. 680-700ºC y 13-15 kbar). En estas condiciones (ca. 50 km de profundidad; > 600 ºC) la antigorita no es estable, imposibilitando la formación del canal de subducción serpentinítico.

Al continuar el enfriamiento del sistema de la subducción debido a la subducción continua, se forma antigorita por la hidratación de la peridotita de la placa superior, permitiendo la formación del canal de la subducción y, subsiguientemente, la exhumación de los bloques. El metamorfismo sobreimpuesto en las anfibolitas y las trondhjemitas se representa por la combinación de: actinolita + glaucofana + tremolita + paragonita + lawsonita + albita + clino-zoisita + clorita + fengita, formados durante condiciones retrógradas de la facies de esquistos azules y esquistos verdes. Las condiciones de presión y temperatura calculadas indican trayectorias antihorarias (exhumación caliente de “tipo Franciscana”). Ocasionalmente, algunos bloques denotan circulación convectiva en el canal que confirma la predicción de los modelos termo-mecánicos. Esto constituye el primer reporte en la literatura de circulación convectiva a gran escala de bloques en un canal de subducción.

La formación de rocas anfibolíticas-trondhjemíticas en condiciones de alta presión y alta temperatura documentan altos gradientes térmicos en la interfase de la placa subducente y la placa suprayacente. Las trayectorias antihorarias seguidas por estas rocas indican que el enfriamiento del sistema ocurrió durante la subducción. Esta historia térmica sugiere el inicio de la subducción de una litosfera oceánica joven, que confirma las predicciones de modelos termo-mecánicos. Sin embargo, una evolución térmica similar es posible después de la subducción de una litosfera joven seguida por la subducción de una litosfera vieja, no necesariamente implicando el inicio de la subducción, durante la subducción oblicua de una dorsal. Los modelos termo-mecánicos permiten también considerar los procesos de función parcial en Cuba oriental como una pluma fría abortada y cristalizada en la interfase de la placa subducente y suprayacente.

Rocas con fengita rica en Ba (incluyendo anfibolitas, trondhjemitas, pegmatitas y rocas de Qtz+Ms) tienen composiciones de elementos mayores y trazas que indican

circulación de fundidos y fluidos ricos en Ba en el canal de subducción. La infiltración de fluidos ricos en Ba a alta temperatura indica que se formaron probablemente a partir de los sedimentos subducidos, transformando el material MORB subducido y acrecionado (anfibolitas). Este proceso llevó a la formación de trondhjemitas ricas en Ba con signatura adakítica durante la fusión de las anfibolitas. Los fundidos parciales representan fundidos primarios de la placa subducente que no reaccionaron con el manto superior. Las pegmatitas se interpretan como productos magmáticos diferenciados de los fundidos trondhjemíticos, mientras que las rocas de Qtz-Ms representan probablemente materiales cristalizados de un fluido primario derivado de los sedimentos subducidos. La química mineral de las fengitas esta gobernada sobre todo por los vectores de intercambio celadonita (tschermak; $((Mg,Fe)Si(^{VI}Al^{IV}Al)_{-1}$) y celsiana ($AlBa(SiK)_{-1}$). La preservación de zonación en la fengita indica una difusión lenta. Esto es un punto importante porque la cristalización de la fengita en profundidad hace que el Ba (K y otros LILE) sean compatibles, previniendo la transferencia de estos elementos al manto superior; reforzando la importancia de la estabilidad de la fengita en el canal de subducción para la transferencia de elementos de la placa subducente al contexto del arco.

Dos grupos principales de material ultramáfico aparecen en la mélange asociados a los bloques de alta presión: serpentinitas con antigorita y antigorita-lizardita. La fuerte alteración de los protolitos ultramáficos (dada por la serpentinización y transformación de las Cr-espinelas) indican un alto flujo de fluidos, que puede explicarse si las rocas experimentaron la hidratación durante la infiltración de los líquidos producidos por la placa subducente. Las serpentinitas con antigorita tienen protolitos harzburgíticos y se formaron muy probablemente en profundidad por la hidratación del manto superior (litosfera del Caribe) a partir de la infiltracion de fluidos derivados de la placa subducente. Las serpentinitas con antigorita-lizardita son de composición harzburgítica-lherzolítica y sus protolitos pueden explicarse como peridotitas abisales (litosfera del Protocaribe) acrecionados al canal de subducción desarrollado en la interfase de las Placas Caribe y Protocaribe. Las serpentinitas con antigorita documentan la hidratación a gran escala del manto superior de la placa del Caribe y la formación de un grueso canal de subducción que permitió la exhumación del material subducido y acrecionado durante el Cretácico.

Dataciones de SHRIMP U-Pb y Ar/Ar permiten perfilar la evolución temporal de la zona de subducción. Zircones de las rocas trondhjemíticas proporcionan edades U-Pb de cristalización de 105-110 Ma. Las edades de Ar/Ar de las fengitas en las mismas rocas trondhjemíticas brindan edades de enfriamiento de 83-86 Ma (interpretado como la temperatura de bloqueo-enfriamiento de las fengitas). Estos datos, combinados con las trayectorias antihorarias sugieren una historia de exhumación sin-subducción muy lenta para la región (~1mm/a). Las rocas leucocráticas y las rocas de caja anfibolíticas se enfriaron y exhumaron lentamente a partir de 700 ºC y 15 kbar hasta 350 ºC y 8 kbar durante 25 millones de años. La exhumación final de la mélange ocurrió durante el final del Cretácico (70-65 Ma) con la obdución de las ofiolitas de supra-subducción y las rocas del arco volcánico determinado por la presencia de depósitos sin-tectónicos.

INDEX

INTRODUCTION

The subduction channel concept was first defined by Shreve and Cloos (1986) and Cloos and Shreve (1988a, b) to describe complex rock assemblies developed in the interface between the subducting and the hanging wall plates in a convergent margin. Cloos and Shreve developed the concept to model actual subduction environments (e.g., Japan, Mariana, Lesser Antilles, etc.). The subduction channel model provides a mechanism for the exhumation of subducted high pressure rocks accreted as blocks to the overlying accretionary prism formed, mostly, by sediments. The subduction channel concept has been extended to much deeper near-sub-arc depths by means of thermo-mechanical (Fig. 1; Gerya et al., 2002) and conceptual models (Fig. 2; Guillot et al., 2000; 2001; 2009). In this context the subduction channel is formed by the mantle wedge peridotite hydrated in the antigorite stability field (i.e., below ca. 650 ºC).

The fluids necessary for this serpentinization process are thought to be provided by prograde metamorphism of the subducted slab (oceanic plate, including its sedimentary cover). According to Iwamori (1998) the oceanic crust contains about 6 wt % water in chlorite, lawsonite and amphibole. This amount is reduced to less than 3 wt % at 50 km depth, providing the necessary free-water for the hydration of mantle wedge and the exhumation of high pressure blocks in the mélanges. Also, the fluids play an important role within the subduction system because they influence the progress of the metamorphic reactions, magma generation in the mantle wedge and the generation of seismicity (double Benioff plane) due to the progress of dehydration reactions within the slab (Brudzinski et al., 2007).

The exposed materials exhumed from the plate interface (i.e. mélange) contain information about processes taking place during long periods of time, making the mélanges the best laboratory for the study of processes occurring in the plate interface to ca. 100-150 km depth (Ernst, 1999). The occurrence of a well preserved

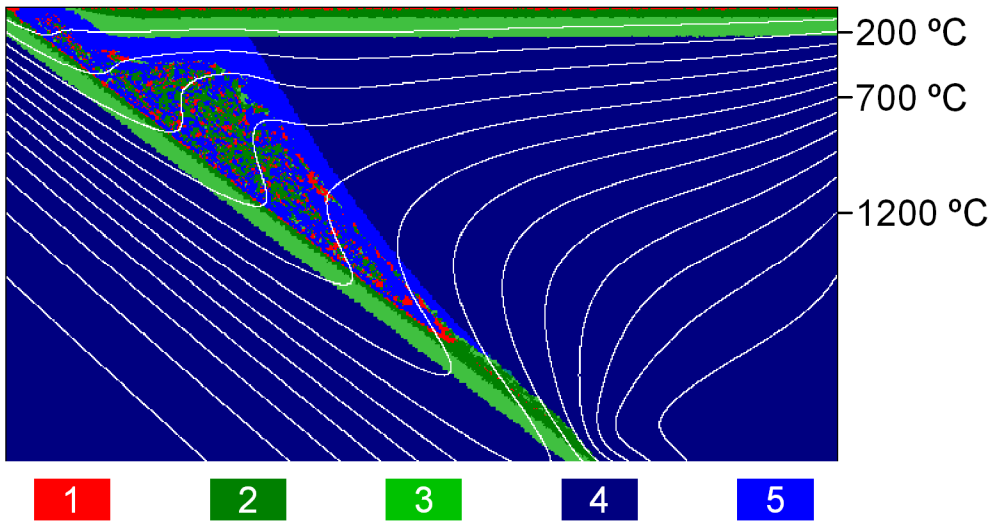

Fig. 1 Thermo-mechanical model of oceanic subduction 1 = sedimentary rocks; 2 = basaltic upper oceanic crust; 3 = gabbroic lower oceanic crust; 4 = unhydrated mantle; 5 = serpentinized mantle. Isotherms labeled in the right each 100 ºC.

Cretaceous subduction channel in eastern Cuba makes this region an appropriated area to study the evolution of subduction channels during tens of millions of years, from onset of subduction to final exhumation.

Summary of Cuban Geology

The Cuban orogenic belt was formed during the Cretaceous-Tertiary convergence of the Caribbean oceanic plate and the North American margin (Iturralde-Vinent, 1998). Cretaceous S-SW dipping subduction of the Proto-Caribbean (i.e., Atlantic) oceanic lithosphere below the Caribbean plate formed an intraoceanic arc system that collided with the Jurassic-Cretaceous passive margin-like intra-Protocaribbean terrane of Caribeana (in Cuba represented by the Cangre, Pinos, Escambray and Asunción terrenes), the margin of the continental Maya block (i.e., the Guaniguanico terrane of western Cuba) and the Bahamas platform (i.e., the Cayo Coco, Remedios, Camajuaní and Placetas belts of Central Cuba) during latest Cretaceous-Tertiary times (Fig. 4). The collision involved tectonic emplacement of

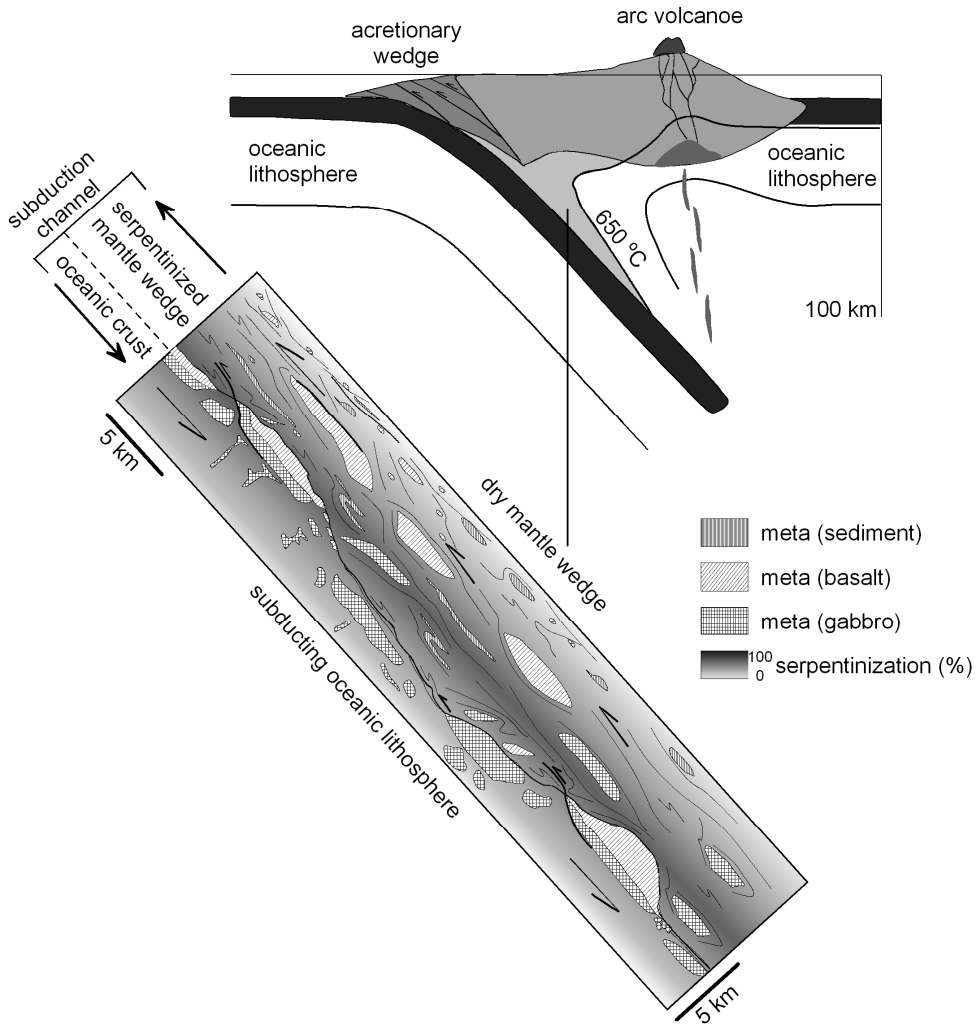

Fig. 2 Conceptual model of subduction channel, after Guillot et al. (2009).

oceanic units, including Cretaceous-Tertiary volcanic arc sections, ophiolites, subduction mélanges (subduction channel), as well as subducted and non-subducted continental margin rocks, and syntectonic basin sequences (Iturralde-Vinent et al. 2008; García-Casco et al. 2008a).

The volcanic arc units are made of volcanic, volcano-sedimentary and plutonic arc rocks (e.g., Iturralde-Vinent, 1996). The magmatic rocks are basic to acid in composition, and document an early Cretaceous (late Neocomian?-Aptian) oceanic island arc of tholeiitic affinity which evolved to a voluminous calc-alkaline and high-K arc in Albian to Campanian times (Kerr et al., 1999; Iturralde-Vinent et al., 2006). Similar sequences have been identified all along the Caribbean realm, from Guatemala through the Antilles, Trinidad-Tobago, the Netherlands Antilles, and the northern part of Venezuela to north and northwestern Colombia. All these sequences have been collectively termed as the "Great Arc of the Caribbean" (Burke, 1988), which resumed in the Late Campanian all along its northern edge (including Cuba) but was re-stablished the Tertiary in several parts of the Greater Antilles. During the Paleogene (upper Danian-lower Eocene), a well developed volcanic arc of tholeiític to calc-alkaline affinity formed in eastern Cuba (Sierra Maestra; e.g., Cazañas et al., 1998; Rojas-Agramonte et al., 2006). Other occurrences of Tertiary volcanism in the region include Jamaica, Hispaniola, and Puerto Rico (Lewis and Draper, 1990), but not western and central Cuba. The actual equivalents of the larger Cretaceous-Tertiary Caribbean subduction zone and volcanic arc are the Lesser Antilles trench and volcanic arc, respectively.

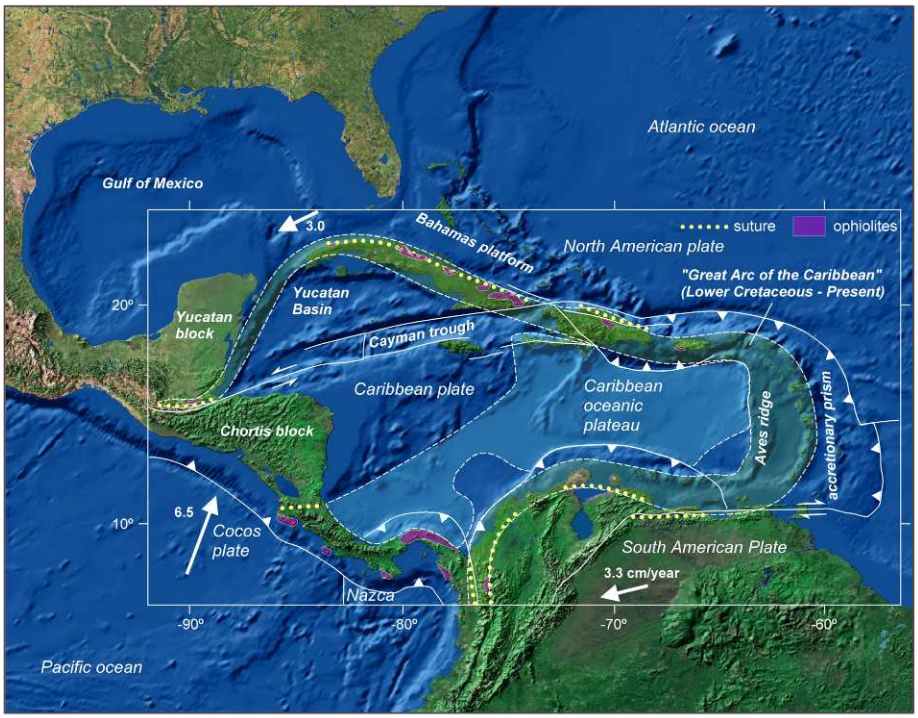

Fig. 3 Plate tectonic configuration of the Caribbean region, with important geological features including ophiolitic bodies and Cretaceous- Tertiary suture zones (compiled after Draper et al., 1994; Meschede and Frisch, 1998; and Mann, 1999).

The ophiolitic material in Cuba appears as a discontinuous belt of more than 1000 km in length composed of discrete, variously sized bodies exposed in the north of the island. From west to east this ophiolite belt includes the Cajálbana, Mariel-La Habana-Matanzas, Las Villas, Camagüey, Holguín, Mayarí-Cristal, Moa-Baracoa bodies (Fig. 4). The bodies are made of fragments of typical ophiolites (serpentinitic harzburgite tectonites, gabbroids, basalts and oceanic sedimentary rocks). Dispersed within these bodies occur tectonic mélanges composed of serpentinitic matrix and exotic blocks of ophiolite, volcanic arc material, sediments of the Bahamian-Maya borderlands, and subduction-related high pressure metamorphic rocks. All these bodies have been widely considered to represent a single geologic element formed within the same paleogeographic/paleotectonic setting during the Mesozoic and was named “Northern Ophiolite Belt” (Iturralde-Vinent, 1989). However, Iturralde-Vinent et al. (2006) argued that eastern Cuba bodies (i.e. Mayarí-Cristal and Moa-Baracoa) should not be included as part of this belt, and proposed the term "Eastern Ophiolite Belt". Proenza et al. (2006) and Marchesi et al. (2006) used the term Mayarí-Baracoa Ophiolitic Belt.

According to García-Casco et al. (2008a) Caribeana is a conceptual paleogeographic domain characterized by Mesozoic sedimentary piles that formed off the Maya Block and occupied a portion of the Proto-Caribbean oceanic domain. The principal outcrops in Cuba belt are the Cangre, Pinos, Escambray and Asunción terrenes (Fig. 4), all metamorphosed in a subduction environment during the latest Cretaceous. The Guaniguanico terrane, located in western Cuba (Fig. 4), is characterized by north-verging thrust sheets and partially superimposed belts of Jurassic-Cretaceous sedimentary sequences and syntectonic Paleogene foreland sediments. The Guaniguanico terrene is considered to have formed part of the Maya block (Iturralde-Vinent, 1994; Pszczółkowski, 1999). The Bahamas platform is subdivided in the (from northeast to southwest, proximal-distal) belts of Cayo Coco, Remedios,

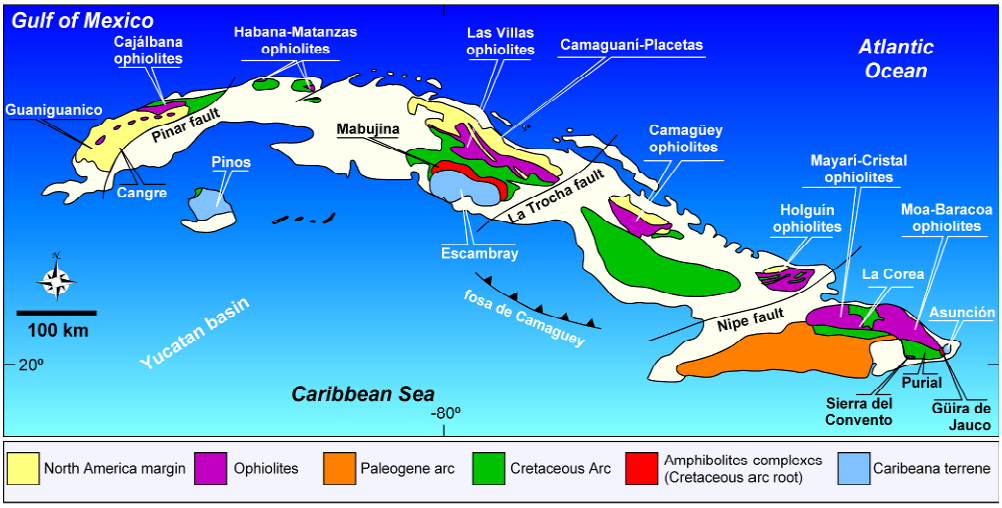

Fig. 4 Geological sketch map of Cuba (modified after Iturralde-Vinent, 1996) showing location of the principal geological elements.

Camajuaní, and Placetas, the latter of deep water oceanic affinity (Fig. 4). The deformation of the rocks decreased to the North. All these rocks form part of discrete N-NE directed tectonic units of the Cuban fold and nappe belt. The stacks are covered by Paleocene-Eocene syn-orogenic deposits typically of turbiditic and olistostromic character which are also overridden by the allochtonous units (Iturralde-Vinent, 1996, 1998).

Cuba was divided into three major blocks (Meyerhoff & Hatten, 1968); (1) Western Cuba, (2) Central Cuba and (3) Eastern Cuba. In Western and Central Cuba blocks, the basic architecture of the belt is defined by a stack of units made of (top to bottom in the pile) volcanic-arc, fore-arc ophiolites and sedimentary units of the Bahamian-Mayan borderlands, covered by Paleocene-Eocene syn-orogenic deposits (Iturralde-Vinent, 1996, 1998). At divergence with respect to Western and Central Cuba blocks, the ophiolitic sheets in Eastern Cuba are emplaced on top of the Cretaceous volcanic arc units (Figure 5b).

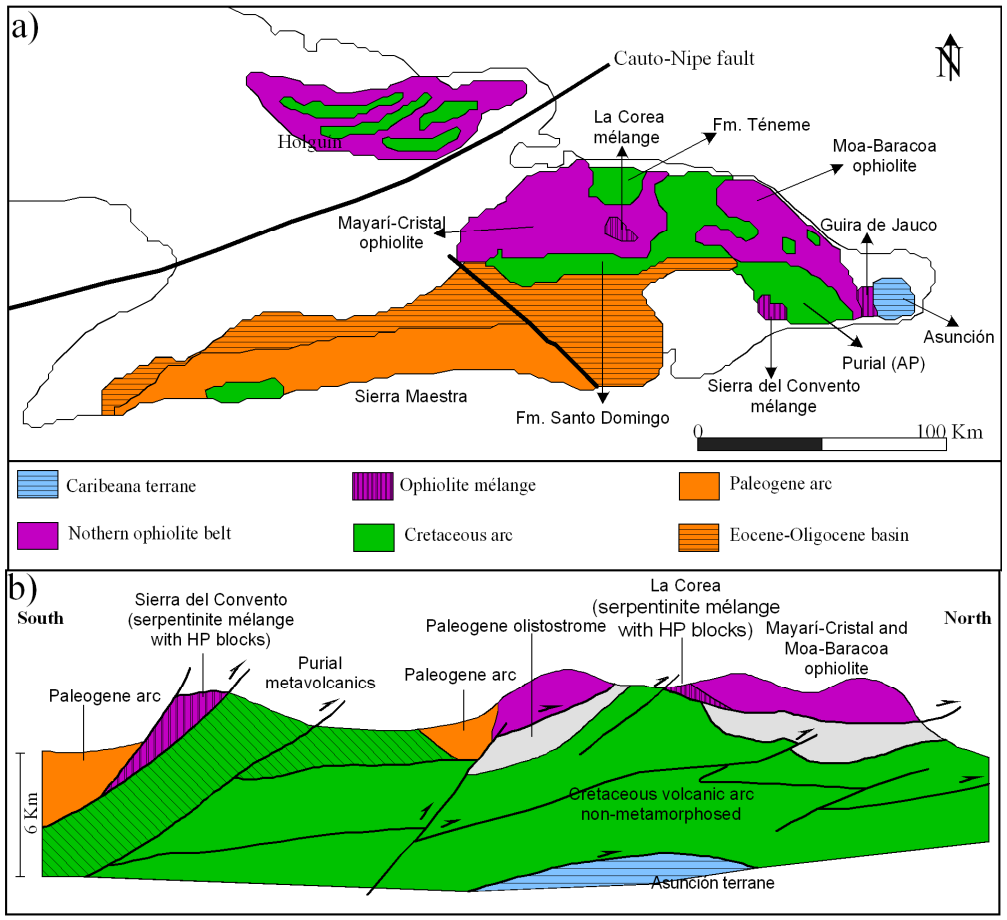

Fig. 5 a) Geological sketch map of Eastern Cuba showing the principal geological units. b) Generalized sketch cross-section of eastern Cuba (after Iturralde-Vinent, 1998) showing the relations among major geological complexes in the region.

The Eastern Cuba block is perhaps the worst known geological region of Cuba, as a result of geographic factors (steep slopes, tropical vegetation, and poor surface communication system). The literature is scarce and hardly available (most of it is made of unpublished reports or papers published in Cuban journals in Spanish). The block is located between the Nipe and the Oriente faults (Fig. 5a). The most important tectonic units in the northeastern part of the area are the Cretaceous volcanic arc and the Mayarí-Baracoa Ophiolitic Belt. The arc displays several volcanic sections with mafic to felsic composition and tholeiitic, boninitic and calc-alkaline signatures (Proenza et al., 2006). Based on paleontological data, the Cretaceous arc formed during early (Aptian-Albian) to late Cretaceous (Mid Campanian) times (Iturralde-Vinent et al. 2006). The volcanic arc complex of El Purial, located in the southeastern part of the region, was metamorphosed to greenschist and blueschist facies conditions (Boiteau et al., 1972; Cobiella et al., 1977; Somin and Millán 1981; Millán et al., 1985), probably during latest Cretaceous times (ca. 70 Ma; Iturralde-Vinent et al., 2006; García-Casco et al., 2006; Lázaro et al., 2009).

The Mayarí-Baracoa Ophiolitic Belt includes mafic and ultramafic rocks with supra-subduction geochemical signatures (Proenza et al., 1999; 2006; Iturralde-Vinent et al. 2006; Marchesi et al. 2007). The Mayarí-Baracoa Ophiolitic Belt includes two massifs: the Mayarí-Cristal massif to the west and the Moa-Baracoa massif to the east. According to Marchesi et al. (2006) the Mayarí-Baracoa Ophiolitic Belt is represented by highly depleted peridotites and cumulate gabbroic rocks formed in a back-arc spreading center environment. An important feature of the Mayarí-Baracoa Ophiolitic Belt peridotites is that they are highly altered (serpentinized) as a consequence of seawater circulation during the oceanic stage in the suprasubduction environment (Proenza et al., 2003).

The largest serpentinite-matrix mélanges in eastern Cuba are located in the La Corea and the Sierra del Convento (Fig. 5a), located 100 km apart from one each other. The La Corea mélange is tectonically below the Mayarí-Cristal Massif and over the Santo Domingo arc formation (Fig. 5b) while the Sierra del Convento mélange overrides the El Purial complex (Fig. 5b). These mélanges contain exotic blocks of various origin, size and composition within a serpentinite-matrix. Metamorphic blocks attained high- to medium-pressure and low- to high-temperature (mainly garnet-amphibolite, blueschist and greenschist facies; Somin and Millán 1981; Millán 1996, Garcia-Casco et al. 2006; 2008a; Lázaro et al., 2009; Blanco-Quintero et al. 2010a). Metamorphism occurred in a subduction environment during the Cretaceous (120-75 Ma) subduction of oceanic lithosphere and latest-Cretaceous (70-75 Ma) subduction erosion of the volcanic arc. The most common rock type, however, is MORB-derived amphibolite formed in the earliest stages of oceanic subduction during the Aptian (ca. 120 Ma). These epidote±garnet±plagioclase amphibolites appear as m-sized blocks. They are massive to banded and fine to medium grained, within coarse grained varieties. Peak P-T conditions of formation were 700-750 ºC and ca. 15 kbar (García-Casco et al. 2006, 2008b; Lázaro et al. 2009; Blanco-Quintero et al., 2010a).

An exceptional characteristic of both mélange complexes is the presence of leucocratic bodies, dikes and veins of intermediate to acid composition (tonalitic-trondhjemitic) intimately associated with the amphibolites and formed by partial

melting of the latter. The structures show crosscutting to concordant relations, indicating syn-metamorphic partial melting of amphibolite. García-Casco (2007), García-Casco et al. (2008b) and Lázaro et al. (2009) estimated melt crystallization at pressures of 12-15 kbar. SHRIMP, Ar/Ar, and K/Ar data (Adamovich and Chejovich 1964; Somin and Millán 1981; Lázaro et al. 2009) and interpretation of P-T paths indicate that all these types of rock formed during the Early Cretaceous (115-120 Ma), likely during the onset of subduction of a young oceanic lithosphere (even a ridge), and slowly exhumed in the subduction channel environment during the Late Cretaceous until they finally exhumed rapidly during the latest Cretaceous (70-75 Ma) collision stage. The serpentinitic matrix is essentially made of antigorite serpentinite, but massive antigoritite is also common as blocks within sheared serpentinite matrix (Blanco-Quintero et al., 2010b).

This work is focused to the magmatic and metamorphic characteristics of amphibolite blocks, associated tonalite-trondhjemite bodies and the ultramafic blocks and matrix from these mélanges, especially in the La Corea mélange.

Aim and Structure of the Thesis

This PhD Thesis is entitled "Metamorphic and magmatic consequences of subduction of young oceanic lithosphere and exhumation in a serpentinite subduction channel. Eastern Cuba". The manuscript is the result of a four-year FPU grant in the Department of Mineralogy and Petrology of University of Granada. The work has been supervised by Dr. Antonio García Casco (Department of Mineralogy and Petrology, University of Granada) and Dr. Joaquín Proenza Fernández (Department of Crystallography, Mineralogy and Mineral Deposits, University of Barcelona). Although the aim of this PhD thesis is the petrology of the La Corea mélange, the similarities and the genetic relationships with the Sierra del Convento mélange allowed considering both complexes during the investigation (e.g. Chapter 5).

The PhD manuscript includes Abstract (English and Spanish), Introduction, Conclusions (English and Spanish), and seven chapters in paper format. Three of the papers are in press, one has been submitted and other three are to be submitted soon. Because the papers treat the same complexes certain degree of repetition was unavoidable, especially in the geological sections. Several collaborators appear as co-authors (listed below) of these papers. These collaborators helped with data acquisition in the field, assistance during laboratory work and interpretation of the results. However, most of the work has been performed by myself. In addition, two papers are included as appendixes, also related with the eastern Cuba mélanges, in which I collaborated during the investigations.

Chapter 1 "Metamorphic evolution of subducted hot oceanic crust (La Corea mélange, Cuba)". In press in **American Journal of Science**. This study presents the petrology and geochemistry of amphibolite blocks using field occurrence, mineral assemblages and textures, and major element compositions of rocks and minerals, as well as P-T paths using the average P-T method and isochemical PT projections calculated with software THERMOCALC (Powell-Holland). A petrogenetic model of formation of the mélange is present.

Chapter 2 "Tectonic blocks in serpentinite mélange (eastern Cuba) reveal large-scale convective flow of the subduction channel". In press in **Geology**. Although

most of the amphibolite blocks have similar metamorphic evolutions, some blocks have particularities, like coarse garnet porphyroblasts with different stages of growths. The chemical composition of garnet, mineral inclusions and P-T calculations were used to interpret the concentric zonation in garnets in the context of the subduction channel concept. This result was compared with thermo-mechanical models, making this paper very innovative in term of the subduction channel concept.

Chapter 3 "Timing of onset of subduction and rates of exhumation in a subduction channel: evidence from slab melts from La Corea mélange (E Cuba)". To be submitted. In this work, whole rock and mineral compositions, SHRIMP zircon and Ar/Ar phengite ages of tonalite-trondhjemite rocks are presented. These data are used to construct the P-T-t evolution of the mélange. The origin and crystallization of tonalitic-trondhjemitic-granitic partial melts is discussed. Also was discussed is the onset of subduction in the North Caribbean and the exhumation rate of the mélange.

Chapter 4 "The imprint of sediment-derived fluid on melting of MORB amphibolite in a subduction setting (Sierra del Convento mélange, Cuba)". To be submitted. Major and trace element geochemical signatures and Sr–Nd isotope data of MORB-like Ms-amphibolite blocks and associated leucocratic Ms-trondhjemitic rocks from the Sierra del Convento indicate a variety of process and fluids evolved in the subduction environment. The origin of these rocks and the implication of sediment-derived fluid in the subduction channel environment and in the volcanic arc activity are discussed.

Chapter 5 "Barium-rich fluids and melts in the subduction environment (La Corea and Sierra del Convento mélanges, eastern Cuba)". Submitted to **Contributions to Mineralogy and Petrology**. Although most of the amphibolite rocks in La Corea and the Sierra del Convento mélanges have N-MORB affinity, some blocks show enrichment in mobile elements, especially in Barium. Major and minor elements compositions in whole rocks and minerals are presented. The chemical variation in the phengite grains and the importance of exchange vector in the grains diffusivity are discussed. The importance of phengite stability in the slab and the fluids evolved from subducting sediments in term of mass transfer in the subduction factory are also discussed.

Chapter 6 "Serpentinites and serpentinites within a fossil subduction channel: La Corea mélange, eastern Cuba". In press in **Geologica Acta**. An important group of rocks within the mélange is composed of the serpentinite rocks. In the La Corea mélange two groups of serpentinite rocks appear: antigorite and antigorite-lazardite serpentinites. The chemical compositions, textural relation, mineral structure and P-T calculations are used to discriminate between abyssal and mantle wedge origin. The importance of hydration of mantle wedge rocks in the formation of subduction channel and exhumation of HP blocks are discussed.

Chapter 7 "Subduction of a young oceanic plate: a numerical study". To be submitted. Thermo-mechanical modelling was used to study subduction initiation for intra-oceanic lithospheres. Experiments were carried out varying the age of the lithosphere (10, 12.5, 15, 17.5, 20, 25 and 30 Ma) and rate of convergence (2, 4 and 5 cm/a). Also the rock that formed the weak zone, responsible of the subduction

initiation was varied. The results were analyzed and compared with a natural example (i.e., Caribbean Cretaceous subduction zone).

Appendix 1 "Partial melting and counterclockwise P-T path of subducted oceanic crust (Sierra del Convento, E Cuba)". Published in **Journal of Petrology** 49, 129-161. Detail descriptions of mineral assemblages and textures, and major element compositions of rocks and minerals, as well as P-T estimates for the evolution of amphibolites and their trondhjemitic-tonalitic melt products. These data are used to derive a petrogenetic model based on phase relations and a tectonic model of formation of the mélange was proposed.

Appendix 2 "A new jadeitite jade locality (Sierra del Convento, Cuba): First report and some petrological and archaeological implications". Published in **Contributions to Mineralogy and Petrology** 158, 1-26. New report of jadeitite jade in Cuba is present, with the field occurrence, minerals chemistry and the PT evolution. A petrogenetic model of jade veins is discussed. The archaeological significance of this deposit in the Caribbean region is also discussed.

REFERENCES

Adamovich, A., Chejovich, V., 1964. Principales características de la geología y de los minerales útiles de la región nordeste de la Provincia de Oriente. Revista Tecnológica 2, 14-20.

Blanco-Quintero, I.F., García-Casco, A., Rojas-Agramonte, Y., Rodríguez-Vega, A., Lázaro, C., Iturralde-Vinent, M.A., 2010a. Metamorphic evolution of subducted hot oceanic crust (La Corea mélange, Cuba). American Journal of Science (in press).

Blanco-Quintero, I.F., Proenza, J.A., García-Casco, A., Tauler, E., Galí, S., 2010b. Serpentinites and serpentinites within a fossil subdution channel: La Corea mélange, eastern Cuba. Geologica Acta (in press).

Boiteau, A., Michard, A., Saliot, P., 1972. Métamporphisme de haute pression dans le complexe ophiolitique du Purial (Oriente, Cuba). Comptes Rendus de l'Académie des Sciences, Série D 274, 2137–2140.

Brudzinski, M.R., Thurber, C.H., Hacker, B.R., Engdahl, E.R., 2007. Global Prevalence of double Benioff zones. Science 316, 1472-1474.

Burke, K., 1988. Tectonic evolution of the Caribbean. Annual Reviews of Earth and Planetary Sciences 16, 201-230.

Cazañas, X., Proenza, J.A., Mattietti-kysar, G., Lewis, J., Melgarejo J.C., 1998. Rocas volcánicas de las series Inferior y Media del Grupo El Cobre en la Sierra Maestra (Cuba Oriental): volcanismo generado en un arco de islas toleítico Acta geológica hispánica 33(1-4), 57-74.

Cloos, M., Shreve, R.L., 1988a. Subduction-channel model of prism accretion, melange formation, sediment subduction, and subduction erosion at convergent plate margins, 1, Background and description. Pure and Applied Geophysics 128, 455 – 500.

Cloos, M., Shreve, R.L., 1988b. Subduction-channel model of prism accretion, melange formation, sediment subduction, and subduction erosion at convergent plate margins, 2, Implications and discussion. Pure and Applied Geophysics 128, 501 – 545.

Cobiella, J., Campos M., Boiteau, A., Quintas, F., 1977. Geología del flanco sur de la Sierra del Purial. Revista La Minería de Cuba 3, 54-62.

Draper, G., Jackson, T.A. Donovan, S.K., 1994. Geologic provinces of the Caribbean Region. In: Donovan, S.K., Jackson, T.A., eds., Caribbean Geology: An Introduction, 3-12, U.W.I. Publishers' Association, Kingston (Jamaica).

Ernst, W.G., 1999. Metamorphism, partial preservation, and exhumation of ultrahigh-pressure belts. Island Arc 8, 125-153.

García-Casco A., 2007. Magmatic paragonite in trondhjemites from the Sierra del Convento mélange, Cuba. American Mineralogist 92, 1232–1237.

García-Casco, A., Torres-Roldán, R.L., Iturralde-Vinent M.A., Millán, G., Núñez Cambra, K., Lázaro, C., Rodríguez Vega, A., 2006. High pressure metamorphism of ophiolites in Cuba. Geologica Acta 4, 63–88.

García-Casco, A., Iturralde-Vinent, M.A. Pindell, J., 2008a. Latest Cretaceous collision/accretion between the Caribbean Plate and Caribeana: Origin of metamorphic terranes in the Greater Antilles. International Geology Review 50, 781-809.

García-Casco, A., Lázaro, C., Torres-Roldán, R.L., Núñez Cambra, K., Rojas Agramonte, Y., Kröner, A., Neubauer, F., Millán, G., Blanco-Quintero, I.F., 2008b. Partial melting and counterclockwise P-T path of subducted oceanic crust (Sierra del Convento mélange, Cuba). Journal of Petrology 49, 129-161.

Gerya, T.V., Stoeckhert, B., Perchuk, A.L., 2002. Exhumation of high-pressure metamorphic rocks in a subduction channel-a numerical simulation. Tectonics 21, 6-1–6-19.

Guillot, S., Hattori, K., Sigoyer de, J., 2000. Mantle wedge serpentinization and exhumation of eclogites: insights from eastern Ladakh, northwest Himalaya. Geology 28, 199-202.

Guillot, S., Hattori, K., Sigoyer de, J., Nägler, T., Auzende, A.L., 2001. Evidence of hydration of the mantle wedge and its role in the exhumation of eclogites. Earth and Planet Science Letters 193, 115-127.

Guillot, S., Hattori, K., Agard, P., Schwartz, S., Vidal, O., 2009. Exhumation processes in oceanic and continental subduction contexts: a review. In: Lallemand, S., Funiciello, F., eds., Subduction Zone Dynamics, 175-204, doi 10.1007/978-3-540-87974-9, Springer-Verlag Berlin Heidelberg.

Iturralde-Vinent, M.A., Díaz Otero, C., Rodríguez-Vega, A., Díaz-Martínez, R., 2006. Tectonic implications of paleontologic dating of Cretaceous–Danian sections of Eastern Cuba. Geologica Acta 4, 89–102.

Iturralde-Vinent, M.A., Díaz Otero, C., García-Casco, A., Van Hinsbergen, D.J.J., 2008. Paleogene Foredeep Basin Deposits of North-Central Cuba: A Record of Arc-Continent Collision between the Caribbean and North American Plates. International Geology Review 50, 863–884.

Iturralde-Vinent, M.A., 1989. Role of ophiolites in the geological constitution of Cuba. Geotectonics 4, 63-74.

Iturralde-Vinent, M.A., 1994. Cuban geology: A new plate tectonic synthesis. Journal of Petroleum Geology 17, 39-70.

Iturralde-Vinent, M.A., 1996. Cuba: El arco de islas volcánicas del Cretácico. In: Iturralde-Vinent, M.A. ed., Cuban ophiolites and volcanic arcs. Miami, IGCP-364, 179–189.

Iturralde-Vinent, M.A., 1998, Sinopsis de la Constitución Geológica de Cuba. Acta Geológica Hispánica 33, 9-56.

Iwamori, H., 1998. Transportation of H2O and melting in subduction zones. Earth and Planetary Science Letters 160 (1-2), 65-80.

Kerr, A.C.; Iturralde-Vinent, M.A.; Saunders, A.D.; Babbs, T.L.; Tarney, J., 1999. A new plate tectonic model of the Caribbean: implications from a geochemical reconnaissance of Cuban Mesozoic volcanic rocks. Geological Society of America Bulletin 111, 1581–1599.

Lázaro, C., García-Casco, A., Neubaurer, F., Rojas-Agramonte, Y., Kröner, A., Iturralde-Vinent, M.A., 2009. Fifty-five-million-year history of oceanic subduction and

exhumation at the northern edge of the Caribbean plate (Sierra del Convento mélange, Cuba). Journal of Metamorphic Geology 27, 19–40.

Lewis, J.F.; Draper, G., 1990. Geological and tectonic evolution of the northern Caribbean margin. In: Dengo, G., Case, J.E., eds., The Geology of North America, The Caribbean Region. The Geological Society of America, Colorado, 77–140.

Mann, P., 1999. Caribbean sedimentary basins: Classification and tectonic setting. In: Mann, P., ed., Caribbean Basins. Sedimentary Basins of the World 4, 3-31, Elsevier Science B.V., Amsterdam.

Marchesi, C., Garrido, C.J., Godard, M., Proenza, J.A., Gervilla, F., Blanco-Moreno, J., 2006. Petrogenesis of highly depleted peridotites and gabbroic rocks from the Mayarí-Baracoa Ophiolitic Belt (eastern Cuba). Contributions to Mineralogy and Petrology 151, 717-736.

Marchesi, C., Garrido, C.J., Bosch, D., Proenza, J.A., Gervilla, F., Monié, P., Rodríguez-Vega, A., 2007, Geochemistry of Cretaceous magmatism in eastern Cuba: recycling of North American continental sediments and implications for subduction polarity in the Greater Antilles Paleo-arc. Journal of Petrology 48, 1813–1840.

Meschede, M., Frisch, W., 1998. A plate tectonic model for the Mesozoic and Early Cenozoic history of the Caribbean plate. Tectonophysics 296, 269-291.

Millán, G., 1996. Metamorfitas de la asociación ofiolítica de Cuba. In: Iturralde-Vinent, M.A., ed., Ofiolitas y Arcos Volcánicos de Cuba. IGCP-364 Special Contribution 1, p. 131–146.

Millán, G., Somin, M.L., Díaz, C., 1985. Nuevos datos sobre la geología del macizo montañoso de la Sierra del Purial, Cuba Oriental. Reporte de Investigación del Instituto de Geología y Paleontología 2, 52–74.

Proenza, J.A., Díaz-Martínez, R., Iriondo, A., Marchesi, C., Melgarejo, J.C., Gervilla, F., Garrido, C.J., Rodríguez-Vega, A., Lozano-Santacruz, R., Blanco-Moreno, J.A., 2006. Primitive Cretaceous island-arc volcanic rocks in eastern Cuba: the Téneme Formation. Geologica Acta 4, 103–121.

Proenza, J., Gervilla, F., Melgarejo, J.C., Bodinier, J.L., 1999. Al- and Cr rich chromitites from the Mayarí-Baracoa Ophiolitic Belt (eastern Cuba): consequence of interaction between volatile-rich melts and peridotite in suprasubduction mantle. Economic Geology 94, 547–566.

Proenza, J.A., Melgarejo, J.C., Gervilla, F., Rodríguez-Vega, A., Díaz-Martínez, R., Ruiz-Sánchez, R., Lavaut, W., 2003. Coexistence of Cr- and Al-rich ophiolitic chromitites in a small area: the Sagua de Tánamo district, Eastern Cuba. In: Eliopoulos et al., eds., Mineral Exploration and Sustainable Development. Rotterdam Netherlands, Millpress 1, 631-634.

Pszczolkowski, A., 1999, The exposed passive margin of North America in western Cuba. In Mann, P., ed., Caribbean Basins, Sedimentary Basins of the World 4, 93-121, Elsevier Science B.V., Amsterdam.

Rojas-Agramonte, Y., Neubauer, F., Bojar, A.V., Hejl, E., Handler, R., García-Delgado, D.E., 2006. Geology, age and tectonic evolution of the Sierra Maestra Mountains, southeastern Cuba. In: Itturalde-Vinent, M., Lidiak, E.G., eds., Caribbean Plate Tectonics: Stratigraphic, magmatic, metamorphic and tectonics events. Geologica Acta 4, 123–150.

Shreve, R.L., Cloos, M., 1986. Dynamics of Sediment Subduction, Melange Formation, and Prism Accretion. Journal of Geophysical Research 91, 10229-10245.

Somin, M.L., Millán, G., 1981. Geology of the Metamorphic Complexes of Cuba: Nauka, Moscow, 219 (in Russian).

1- METAMORPHIC EVOLUTION OF SUBDUCTED HOT OCEANIC CRUST (LA COREA MÉLANGE, CUBA).

I.F. Blanco-Quintero[(1)], A. García-Casco[(1,2)], Y. Rojas-Agramonte[(3)], A. Rodríguez-Vega[(4)], C. Lázaro[(1)], and M.A. Iturralde-Vinent[(5)].

(1) Departamento de Mineralogía y Petrología, Universidad de Granada, Fuentenueva s/n, 18002-Granada, Spain

(2) Instituto Andaluz de Ciencias de la Tierra (CSIC-UGR), Fuentenueva s/n, 18002-Granada, Spain

(3) Institut für Geowissenschaften, Universität Mainz, D-55099 Mainz, Germany

(4) Departamento de Geología, Instituto Superior Minero-Metalúrgico, Las Coloradas s/n, 83329-Moa, Cuba

(5) Museo Nacional de Historia Natural, Obispo no. 61, Plaza de Armas, La Habana 10100, Cuba

ABSTRACT

Thermobarometric estimates and predictions of theoretical and experimental isochemical P-T phase diagrams for epidote±garnet amphibolite blocks from the serpentinite mélange of La Corea (eastern Cuba) indicate partial melting of subducted oceanic lithosphere occurred at peak metamorphic conditions of ca. 700 ºC and 14-15 kbar. These anomalously high geothermal conditions suggest onset of subduction of young oceanic lithosphere of the Proto-Caribbean. The amphibolites have basaltic composition and MORB affinity. Partial melting produced tonalitic-trondhjemitic-granitic melts that crystallized at depth associated with the amphibolites. Calculated retrograde conditions for the amphibolites (450 ºC and 8-10 kbar) indicate counterclockwise P-T paths during exhumation in the subduction channel, in agreement with published predictions on thermo-mechanical modelling of onset of subduction of young lithosphere. These findings have important consequences for the plate tectonic configuration of the Caribbean realm since they corroborate the existence of fragments of early subducted young oceanic lithosphere in the eastern Cuba mélanges that indicate subduction of an oceanic ridge during mid-Cretaceous times.

Keywords: Amphibolite; partial melting; subduction channel; Caribbean plate.

INTRODUCTION

Subduction zones are dynamic regions that represent one of the most important structural features of the lithosphere, with more than 55 000 km of integrated length of trenches (Lallemand, 1999). Their thermal and geodynamic conditions depend on plate velocity, direction and angle of convergence, thickness and age of the lithosphere, convection in the overlying mantle wedge, fluids and melts migrating through the subduction zones and time (Kirby and others, 1991; Peacock, 1996). Subduction products, including subduction mélanges representing deep subduction channels, are generally exhumed within accretionary wedges. Examinations of these rocks offer insight into the geothermal gradients and the geodynamics of deep parts of the subduction system. However, this information normally pertains only to the late stage of the subduction history (e.g., Agard and others, 2009). Knowledge of the early history of subduction zones is constrained by the few known cases that attest to the general recycling of early subducted lithosphere into the mantle, such as in Chile (Willner and others, 2004; Glodny and others, 2005), the Franciscan complex (e.g., Cloos, 1985; Oh and Liou, 1990; Wakabayashi, 1990; Krogh and others, 1994; Anczkiewicz and others, 2004) and the Caribbean (García-Casco and others, 2006, 2008a; Krebs and others, 2008; Lázaro and others, 2009). Available information from these complexes indicates that onset of subduction generally takes place under relatively high geothermal gradients, as predicted by numerical models (Peacock, 1990; Guinchi and Richard, 1999; Gerya and others, 2002). Also, low geothermal gradients are found in cold and old subducted lithosphere (e.g. ~5 ºC/km; NE Japan) while high geothermal gradients are found in young and hot subducted lithosphere (e.g. ~ 10 ºC/km; SW Japan; Peacock and Wang, 1999; Stern, 2002).

High geothermal gradients in the subduction scenario produce amphibolites and eclogites at > 700 ºC and pressures ranging from 10-20 kbar, locally showing evidence for partial melting of subducted oceanic crust (Sorensen and Barton, 1987; Sorensen, 1988; García-Casco, 2007; García-Casco and others, 2008a; Lázaro and García-Casco, 2008). These rock assemblages are only possible if the associated geothermal environment is hot enough to avoid production of blueschist-facies in the dowgoing slab, as is typical of mature subduction zones. In addition, the P-T paths related to exhumation in these hot subduction scenarios are generally counterclockwise, indicating exhumation during ongoing cooling of the subduction system (Perchuk and others, 1999; Gerya and others, 2002; Wakabayashi, 2004; Willner and others, 2004; Krebs and others, 2008; García-Casco and others, 2008a; Lázaro and others, 2009).

Rocks formed during the earliest stages of subduction have recently been identified in the Sierra del Convento mélange, eastern Cuba (García-Casco and others, 2006, 2008a; Lázaro and García-Casco, 2008; Lázaro and others, 2009). This mélange is related to onset of SWard subduction of the proto-Caribbean lithosphere during Aptian times (ca. 120 Ma). Partial melting of MORB-derived amphibolite at ca. 750 and 15 kbar formed peraluminous tonalitic-trondhjemitic melts that crystallized at depth. These rocks were slowly exhumed within the subduction channel during ca. 55 Ma (Lázaro and others, 2009).

In this paper, we present a new locality that documents the early stages of subduction in the Caribbean region. (i.e., La Corea mélange, eastern Cuba; Fig. 1B).

This complex records the subduction of very young oceanic lithosphere. La Corea mélange is located ca. 100 km NW of the Sierra del Convento mélange. Its geographic situation (steep slopes, tropical vegetation, and poor surface communication system) makes the region poorly known from the geological point of view. The literature is scarce and hardly available (most of it are unpublished reports). A survey of crystal rock quartz for electrical application was the principal investigation carried out in the region (Leyva, 1996, and references therein), and only few petrographic descriptions and K/Ar dating of rocks from the complex are available (Adamovich and Chejovich, 1964; Somin and Millán, 1981; Somin and others, 1992; Millán, 1996a). Here we give for the first time detailed petrologic descriptions and interpretations of the earliest products of subduction found in this mélange (i.e., garnet amphibolites), and analyze the geodynamic implications of their thermal history.

GEOLOGICAL SETTING

The geology of Cuba relates to the evolution of the Caribbean orogen (Fig. 1A), which developed in the southern margin of the North American plate during the latest Cretaceous to mid-Eocene times (García-Casco and others, 2008b; Iturralde-Vinent and others, 2008, and references therein). During the Mesozoic to latest Cretaceous times, the back-bone of Cuba (a Cretaceous volcanic arc) was part of the leading edge of the oceanic Caribbean plate (Fig. 1A). After collision of this arc and the associated fore-arc oceanic lithosphere with the Bahamas margin of the North American plate during the middle Eocene, the Cuban segment of the orogenic belt was separated from the remaining Caribbean Plate (Pindell and Dewey, 1982; Iturralde-Vinent and others, 2008 and references therein), along the Swan-Cayman-Oriente transform fault (Mann and others, 1995; Rojas-Agramonte and others, 2005; Fig. 1A). The Caribbean orogenic belt in Cuba includes several tectonic units that are complexly imbricated as tectonic slices, consisting mainly of Caribeana terrane metamorphic complexes, the Bahamas platform, two different volcanic arc complexes of Cretaceous and Paleogene ages, ophiolite bodies forming the northern and eastern ophiolite belts, subduction mélanges, and syn- and post-orogenic sedimentary basins (Iturralde-Vinent, 1998; Iturralde-Vinent and others, 2006, 2008; García-Casco and others, 2008b). In northeastern Cuba the most important units are the Mayarí-Baracoa ophiolite belt and the Cretaceous volcanic arc (Santo Domingo and El Purial complexes). The ophiolites were thrust over the Cretaceous volcanic arc during Maastrichtian times (ca. 65 Ma; Cobiella and others, 1984; Iturralde-Vinent and others, 2006) in a NNE direction (Nuñez-Cambra and others, 2004).

The Cretaceous volcanic arc units contain several formations with mafic to felsic composition and distinct island arc tholeiitic, boninitic and calc-alkaline signatures (Proenza and others, 2006). These signatures indicate different stages of arc evolution from the early Cretaceous (Aptian-Albian) to the late Cretaceous (mid-Campanian), according to paleontological data (Iturralde-Vinent and others, 2006). The Purial volcanic complex constitutes the main unit containing Cretaceous volcanic arc rocks in eastern Cuba and is located to the south of the Moa-Baracoa ophiolite massif (Fig 1B). As opposed to other volcanic arc units in eastern, central and western Cuba, the El Purial complex contains arc rocks metamorphosed to high pressure blueschist facies (Boiteau and others, 1972; Cobiella and others, 1977; Somin and Millán, 1981; Millán and others, 1985; Millán, 1996b), suggesting

complex tectonic processes in the region including subduction erosion of upper-plate fragments during latest Cretaceous times (García-Casco and others, 2006; García-Casco and others, 2008b).

The Mayarí-Baracoa Ophiolitic Belt (MBOB), which includes the Mayarí-Cristal massif to the west and the Moa-Baracoa massif to the east (Fig. 1B), is a pseudotabular, strongly faulted mafic-ultramafic massif over-riding the volcanic arc. Mafic rocks in the massif show supra-subduction geochemical signatures (Proenza and others, 2006; Marchesi and others, 2007). The MBOB is composed of highly depleted peridotites and cumulate gabbroic rocks formed at a back-arc spreading centre (Marchesi and others, 2006). A general feature of the MBOB peridotites is that they are highly altered (serpentinized), mainly because of seawater alteration during the suprasubduction oceanic stage (Proenza and others, 2003).

The La Corea mélange, which contains high pressure tectonic blocks and fragments of ophiolite, is located at the base of the Mayarí-Cristal massif. A similar structural arrangement occurs in the Sierra del Convento mélange, though the latter is not associated with large ophiolitic bodies.

THE LA COREA MÉLANGE

The La Corea mélange occurs tectonically between the Cretaceous Volcanic Arc (Santo Domingo Fm.; Fig. 1C) and the Mayari-Cristal ophiolitic massif. The regional geologic configuration indicates that this metamorphic complex, together with the ophiolites, overrides the volcanic arc units, but details of the structure are unknown. The mélange extends for about 72 km2 and is made up of tectonic blocks of amphibolite, garnet-amphibolite, greenschist, quarzite, blueschist, antigoritite, pegmatite and trondhjemite, all set in a serpentinite-matrix. Masses of tremolite-actinolite rock and other products of metasomatism of mafic and ultramafic rocks are also present. The tectonic blocks are concentrated in two regions separated by serpentinized peridotites of the Mayarí-Cristal ophiolite massif (Fig. 1C).

The most common lithology of blocks within the mélange is epidote±garnet amphibolite. These blocks are of m-size, massive to banded and fine- to medium-grained amphibolite, and occur associated with coarse-grained varieties of amphibole-rich rocks. The amphibolitic blocks are foliated and normally contain garnet porphyroblasts. Veins of igneous rocks of intermediate to felsic composition (tonalitic-trondhjemitic-granitic) and with peraluminous character are intimately associated with the amphibolites (Fig. 2A, B). The veins show concordant to cross-cutting relationships relative to the main metamorphic foliation of the amphibolite blocks (Fig. 2B). The leucocratic bodies generally consist of m-sized pods of pegmatite made of albitic plagioclase, muscovite and quartz. Pegmatitic rocks also occur as discrete blocks. All types of blocks are cut by quartz-rich veins.

K/Ar dating of pegmatites (125±5, 119±10 and 96±4 Ma; Adamovich and Chejovich, 1964; Somin and Millán, 1981) and SHRIMP zircon ages (ca. 110 Ma; Blanco-Quintero and others, 2008) of tonalitic-trondhjemitic-granitic rocks indicate an early Cretaceous age of crystallization. Similar zircon ages have been documented in the Sierra del Convento mélange (112.8±1.1 Ma) and were interpreted as the age of onset of cooling after accretion and partial melting of amphibolite shortly after onset of subduction and before formation of a subduction channel (i.e., mélange; Lázaro and others, 2009). Blocks of blueschist indicate that

the subduction channel incorporated fragments of oceanic crust subducted late in the tectonic history of the Proto-Caribbean lithosphere. Regional geological arguments suggest final exhumation of the mélange during the initial stages of thrusting over the volcanic arc units in the late Campanian-Maastrichtian (Iturralde-Vinent and others, 2006).

ANALYTICAL TECHNIQUES

Whole-rock analyses of major and trace elements were carried out at the (Centro de Instrumentación Científica, CIC) in the University of Granada. Major element and Zr compositions were determined in PHILIPS Magix Pro (PW-2440) X-ray fluorescence (XRF) equipment using a glass beads, made of 0.6g of powdered sample diluted in 6g of $Li_2B_4O_7$. Trace elements, except Zr, were determined by ICP-MS after HNO_3 + HF digestion of 0.1000 g of sample powder in a Teflon-lined vessel at ~180ºC and ~200 p.s.i. for 30 min, evaporation to dryness, and subsequent dissolution in 100 ml of 4 vol % HNO_3. All major (wt %) and trace (ppm) elements data are shown in Table 1. The analyses plotted in the figures were recalculated to an anhydrous 100 wt % basis.

The SEM images were obtained by a LEO 1430-VPSEM instrument with a 3.5 nm spatial resolution and operating at an accelerating voltage of 20 kV, using BSE imaging, (CIC, Granada University). Mineral compositions were obtained by WDS with a CAMECA SX-100 microprobe (University of Granada) (Tables 2-7) operated at 15 kV and 15 nA, beam size of 5 µm. Amphibole compositions were normalized following the schemes of Leake and others, (1997), and Fe^{3+} was estimated after the method of Schumacher (in Leake and others, 1997). Garnet composition was normalized to 8 cations and 12 oxygens, and Fe^{3+} was estimated by stoichiometry. Epidote and feldspar were normalized to 12.5 and 8 oxygens, respectively, and $Fe_{total}=Fe^{3+}$. White mica and chlorite were normalized to 22 and 28 oxygen, respectively, and $Fe_{total} = Fe^{2+}$. Rutile, titanite and apatite were normalized to 2, 5 and 5 oxygens respectively. Mineral and end member abbreviations are after Kretz (1983), except for amphibole (Amp). The atomic concentration of elements per formula units is abbreviated apfu. The Mg number of minerals (Mg#) is expressed as $Mg/(Mg+Fe^{2+})$. Software CSpace (Torres-Roldán and others, 2000) was used to calculate ternary phase diagrams.

Elemental X-ray images were obtained with the same CAMECA SX-100 microprobe operated at 20 kV, 150 nA beam current, with step (pixel) size of 5-7 µm, and counting time of 30 ms. The images were processed with software DWImager (Torres-Roldán and García-Casco, unpublished) and consist of the X-ray signals of Kα lines of the elements (colour coded; expressed in counts/nA/s) corrected for 3.5 µs deadtime. A "Z" image calculated by the sum of the products of the counts by atomic number (Si, Ti, Al, Fe, Mn, Mg, Ca, Na, Ba, K, P, F and Cl) was used as a gray scale base layer of the colored images to show the basic textural relations of the scanned areas.

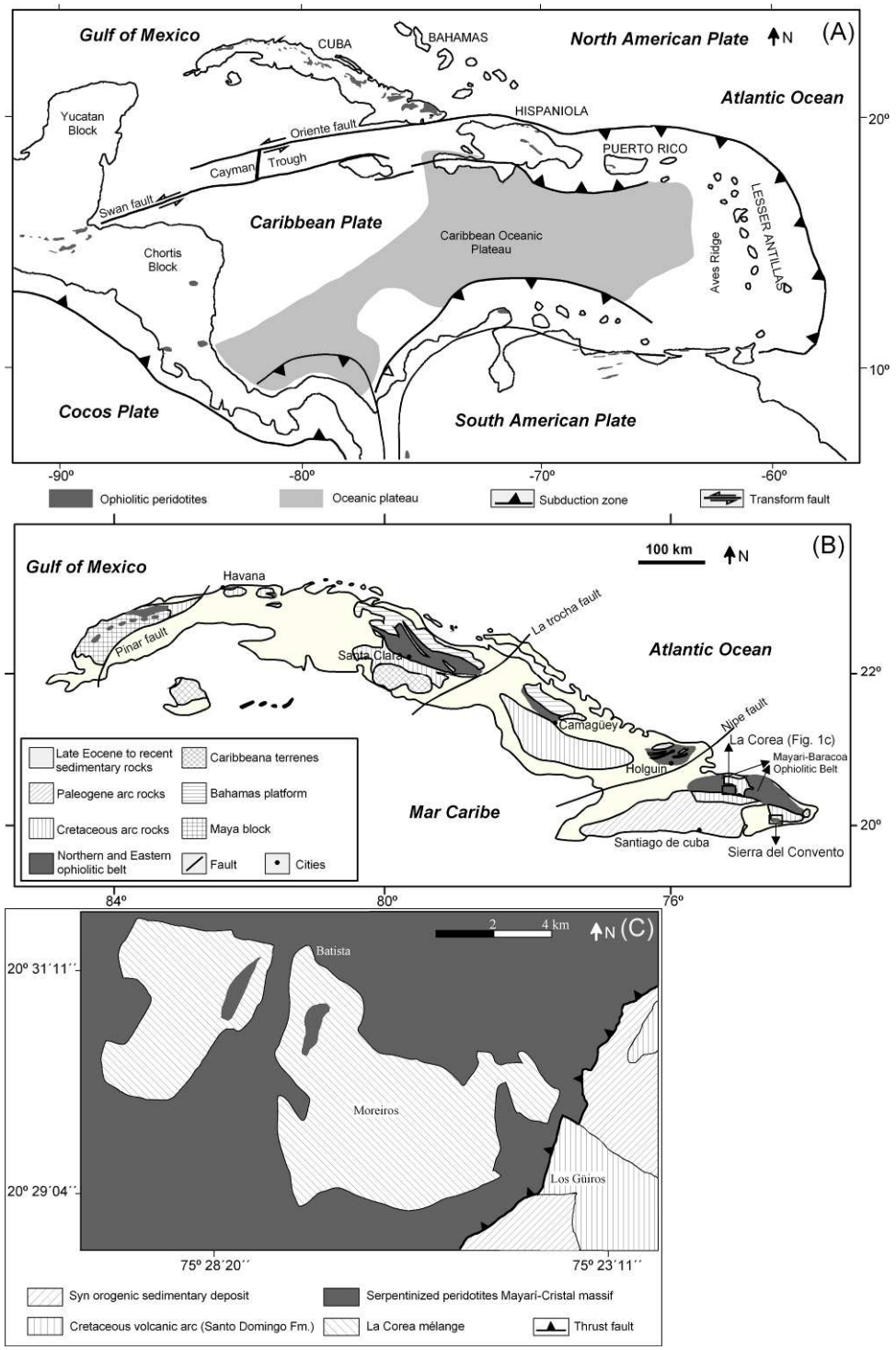

Fig. 1. (A) Plate tectonic configuration of the Caribbean region, including ophiolitic bodies. (B) General geologic map of Cuba (after Iturralde-Vinent, 1998) showing the main geological units. (C) Geologic map of the La Corea mélange (after Leyva, 1996).

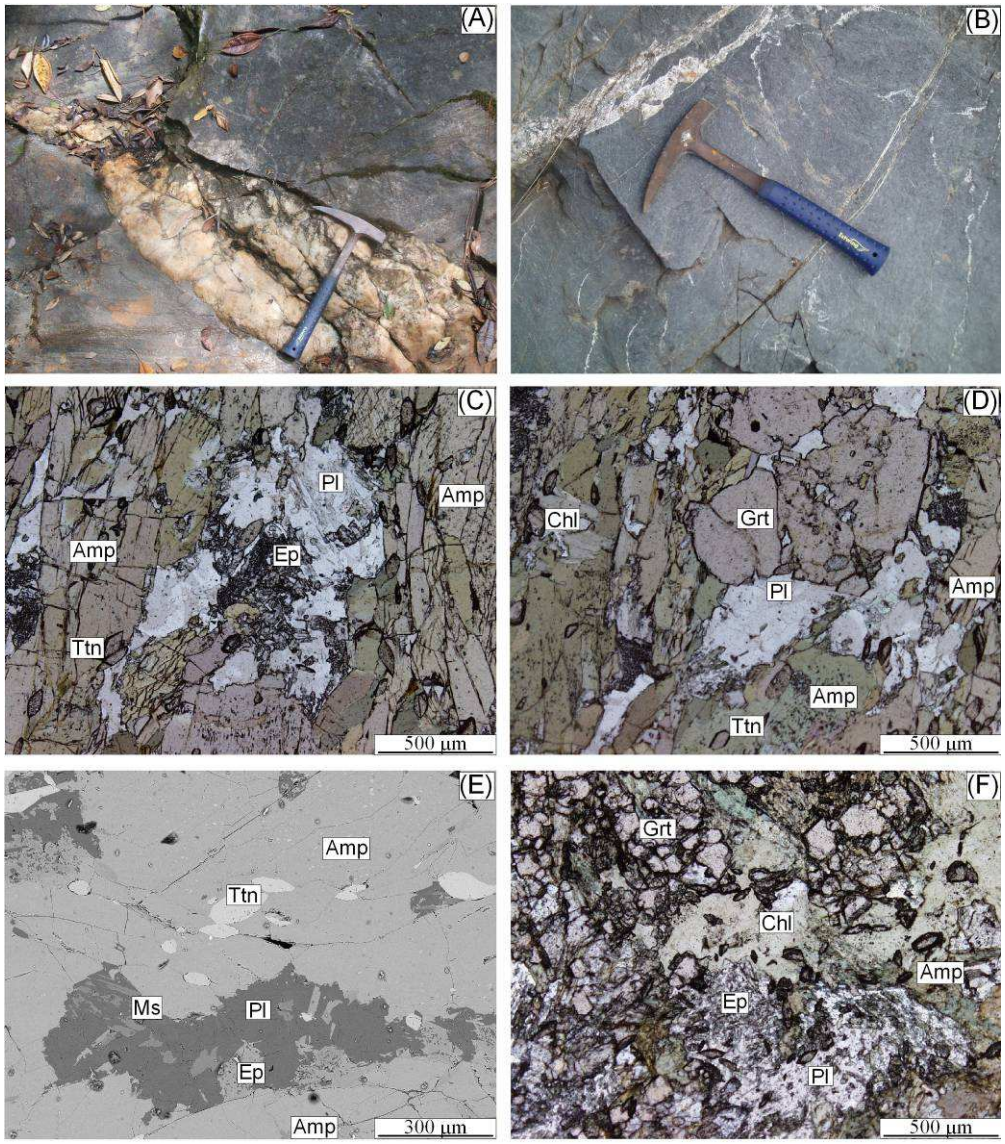

Fig. 2. (A) Garnet-amphibolite with trondhjemite layers. (B) amphibolite with crosscutting trondhjemite veins. Optical images of (C) amphibolite with retrograde epidote, plagioclase and white mica, (D) garnet amphibolite showing peak amphibole, and retrograde chlorite and plagioclase, (E) BSE image showing a pocket of epidote, plagioclase and muscovite surrounded by amphibole, and (F) Optical image of garnet-amphibolite showing garnet aggregate and amphibole, and retrograde chlorite, epidote and plagioclase.

MINERAL ASSEMBLAGES AND TEXTURES

The peak mineral assemblages in amphibolitic rocks consist of amphibole – epidote – titanite – rutile ±quartz ± garnet ± phengite ± plagioclase, and apatite as accessory phase. The abundance of amphibole and epidote (around 80 % of modal proportion in most samples) and the low abundance of peak plagioclase (absent to up to 5 % modal proportion) make these rocks bizarre. Amphibole is medium- to coarse-grained, with grains up to 3 mm, oriented parallel to the foliation (Fig. 2C, D and

3E). Epidote is very common and occurs as euhedral, patchy zoned crystals of 0.1-0.5 mm size defining and cross-cutting the fabric. Garnet porphyroblasts range in size from 1 to 6 mm and contain inclusions of rutile, titanite, apatite, epidote, plagioclase, quartz and amphibole (Figs. 3A, C). The grains are euhedral or partly replaced by chlorite and epidote at the rims and along fractures (Fig. 3C). Although garnet is common (up to 15-20 modal %), it is not present in all samples. Quartz appears as small dispersed grains in the matrix (e.g. LC-GU-8). Apatite and rutile are present in small concentrations in the matrix. Rutile and titanite are dispersed in the matrix and occur in apparent textural equilibrium at peak metamorphic conditions, though titanite locally replaces rutile.

The lack of primary plagioclase in most samples is interpreted as the result of (low degree of) partial melting of amphibolite (García-Casco and others, 2008a; Lázaro and García-Casco, 2008). Peak and relict plagioclase is present in some of the studied samples (Fig. 3F) within small pockets together with epidote and quartz (sample LC-GU-6; Fig. 2E) and as inclusions within garnet, respectively. These pockets probably represent unextracted liquid, and the composition of plagioclase is taken as that of (near) peak equilibrium with the amphibolite assemblage.

Retrograde overprints are composed of combinations of actinolite, albite, clinozoisite, chlorite, phengite and paragonite (Figs. 2C, D, F and 3D). These retrograde minerals are fine-grained and form reaction rims around peak metamorphic minerals, are dispersed in the matrix, or located along fractures. Retrograde albite, occurs in aggregates with epidote, titanite, and white micas (Figs. 2C and F). Retrograde chlorite replaces pargasitic amphibole and garnet and is also present with actinolite + albite + epidote aggregates in the matrix (Fig. 2F). Chlorite is green to colourless in pleochroism, depending on the primary minerals being replaced and their Mg# contents. Typically, chlorite replacements after garnet are greener (Fe-richer) than replacements after amphibole. Retrograde phengitic mica commonly appears associated with retrograde actinolite, epidote and chlorite in fractures and replacing other minerals. Paragonite is very rare and has been identified in one sample (LC-GU-8), where it appears dispersed in the matrix.

GEOCHEMISTRY

The studied amphibolite samples have SiO_2 (48.37 – 51.76 wt %) and $Na_2O + K_2O$ (1.52 – 3.50 wt %) contents which correspond to basaltic composition within the subalkaline series in the TAS diagram (Le Maitre and others, 1989; Fig. 4A). They have high Al_2O_3 (13.73 – 18.16 wt %), TiO_2 (1.59 – 2.71 wt.%), FeO_{tot} (10.41 – 13.20 wt.%), MgO (4.99 – 6.74 wt.%) and CaO content (10.24 – 11.62 wt %), and are poor in Na_2O (1.23 – 3.12 wt.%) and K_2O (0.29 – 0.42 wt.%) (Table 1), indicative of low-K affinity (Peccerillo and Teylor, 1976; Fig. 4B). The Mg# is relatively low (0.30 – 0.34). REE contents and other geochemical features (Fig. 4C) also indicate a MORB composition. The Th/Yb versus Ta/Yb diagram (Wood and others, 1979) clearly shows a MORB affinity of these amphibolites, but with variable composition indicating a heterogeneous subducting oceanic crust.

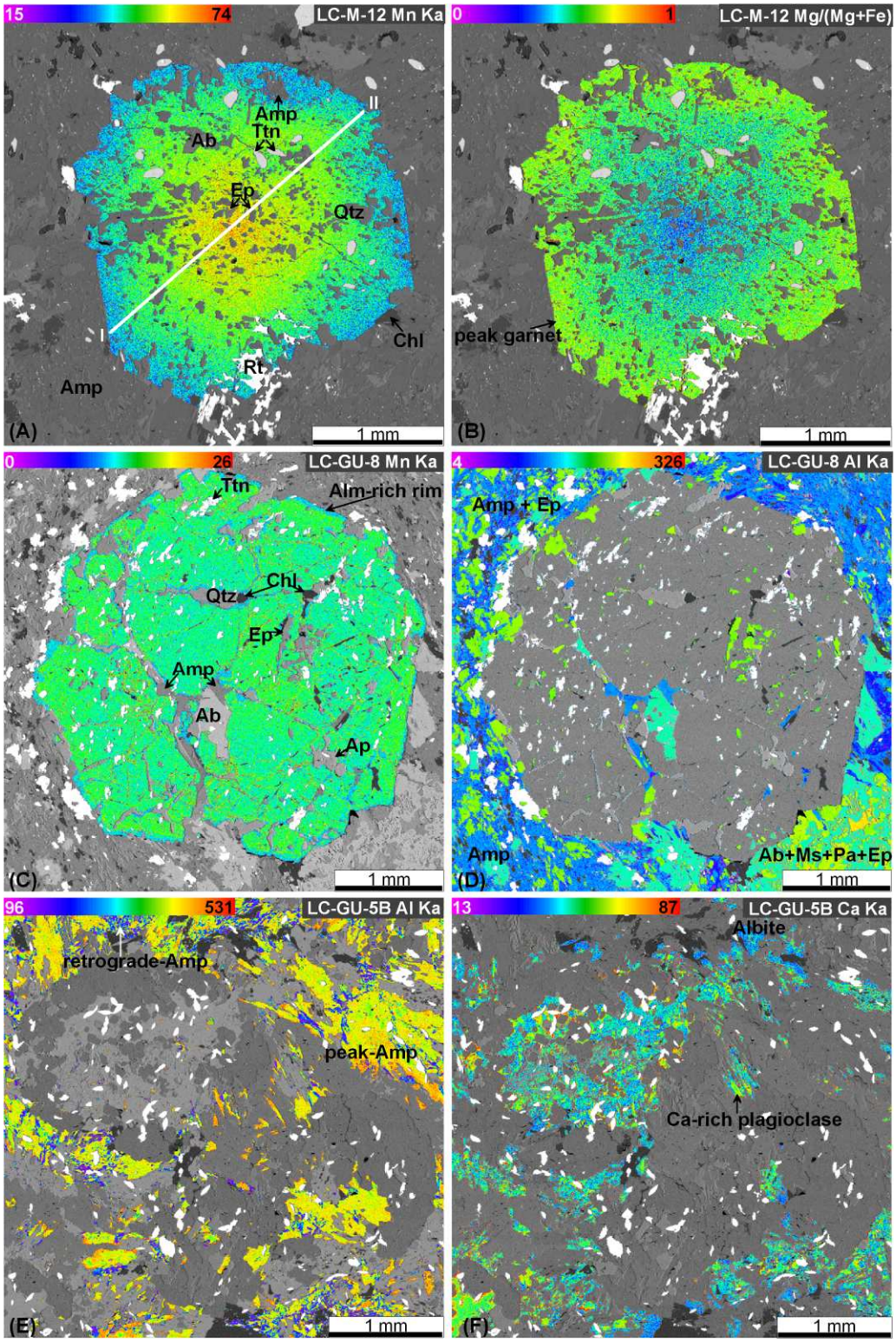
15
74
LC-M-12 Mn Ka
II
Amp
Ttn
Ab
Ep
Qtz
I
Chl
Rt
Amp
(A)
1 mm
0
1
LC-M-12 Mg/(Mg+Fe)
peak garnet
(B)
1 mm
0
26
LC-GU-8 Mn Ka
Ttn
Alm-rich rim
Chl
Qtz
Ep
Amp
Ab
Ap
(C)
1 mm
4
326
LC-GU-8 Al Ka
Amp + Ep
Amp
Ab+Ms+Pa+Ep
(D)
1 mm
96
531
LC-GU-5B Al Ka
retrograde-Amp
peak-Amp
(E)
1 mm
13
87
LC-GU-5B Ca Ka
Albite
Ca-rich plagioclase
(F)
1 mm

Fig.3. XR images showing textures and composition of La Corea amphibolites. (A) Mn image of concentric zoned garnet, showing Mn-richer core (orange) and Mn-poorer rim (blue); note inclusions of plagioclase, epidote, quartz, titanite and amphibole. (B) Mg# image denoting peak garnet composition in the rim (yellow). (C) Mn image of garnet showing homogeneous composition with a Mn-poorer discrete rim. (D) Al image showing matrix phases: amphibole (blue), epidote (green), albite (yellow) and muscovite-paragonite (orange). (E) Al image showing peak pargasite (yellow) and retrograde magnesiohornblende-actinolitice (purple). (F) Ca image showing Ca-richer composition of plagioclase cores (green-yellow) and retrograde albite (blue). Colour scale bar: counts/nA per second.

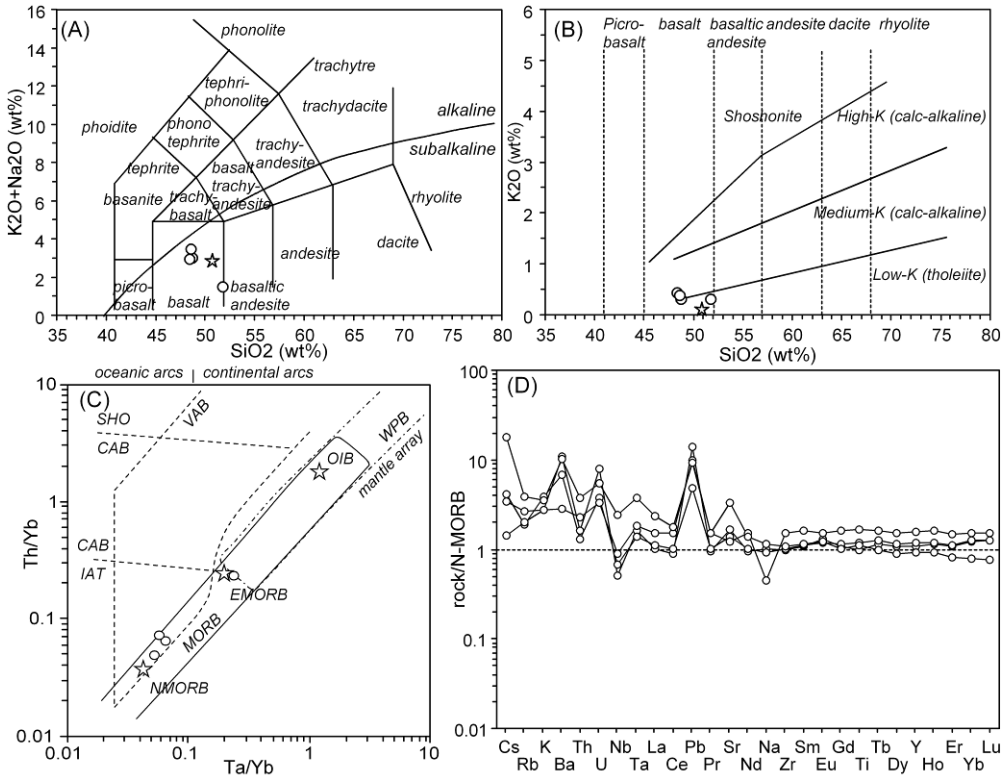

Fig. 4 Composition of studied samples in the (A) TAS classification of volcanic rocks from Le Maitre and others (1989), (B) K2O vs. SiO2 diagram (Peccerillo and Taylor, 1976), (C) Th-Ta discrimination diagram (Wood and others, 1979) using Yb as normalization factor, showing the fields of shoshonite (SHO), calc-alkaline basalt (CAB), island-arc tholeiite (IAT), volcanic arc basalt (VAB) and within plate basalt (WPB), and (D) N-MORB (Sun and MCDonough, 1989) normalized spider diagram. In (A) and (B) the MORB composition is projected as a star. In (C) ocean island basalt (OIB), enriched-MORB, and N-MORB (Sun and MCDonough, 1989) have been projected for comparison.

The N-MORB normalized trace element patterns (Sun and McDonough, 1989) are characterized by fractionated LILE patterns with enrichment in Cs, Rb, K, Ba, U and Pb (Fig. 4D), and patterns relatively flat for high field strength elements (HFSE). The enrichments of LILE are a likely consequence of interaction of metabasite and fluids in the slab/subduction channel, as clearly indicated by the mobile elements (e.g. Cs, Rb, Ba). Fluid flux into metabasite triggered partial melting at peak metamorphic conditions.

Table1: Major (wt %) and trace (ppm) elements composition of studies samples.

	LC-M-12	LC-GU-8	LC-GU-5B	LC-GU-6
SiO_2	49.38	47.16	47.47	47.11
TiO_2	2.59	1.76	1.55	1.88
Al_2O_3	13.10	17.63	17.57	14.50
FeO	12.23	10.10	11.36	12.86
MnO	0.22	0.26	0.37	0.26
MgO	6.43	5.20	4.87	6.45
CaO	9.77	11.09	11.13	11.32
Na_2O	1.17	3.03	2.63	2.46
K_2O	0.28	0.37	0.29	0.41
P_2O_5	0.24	0.48	0.28	0.14
LOI	2.57	1.19	0.69	0.61
Sum	97.97	98.27	98.20	98.00
Mg#	0.34	0.34	0.30	0.33
Rb	2.55	4.89	3.38	2.42
Cs	0.02	0.25	0.05	0.06
Be	1.28	0.52	0.35	0.69
Sr	140.11	381.60	190.12	159.40
Ba	39.25	140.45	149.49	95.42
Sc	46.58	36.47	31.65	44.73
V	477.52	267.78	292.82	380.12
Cr	110.70	251.71	118.89	147.74
Co	72.36	51.38	53.48	58.46
Ni	79.40	137.60	51.66	85.47
Cu	133.86	19.58	7.13	10.20
Y	56.73	32.81	38.81	42.94
Nb	3.12	8.65	1.81	2.39
Ta	0.35	0.72	0.31	0.26
Ta	0.18	0.49	0.10	0.14
Zr	158.80	111.40	103.30	105.40
Hf	0.96	0.38	0.98	1.25
Mo	2.73	1.50	2.85	1.70
Sn	2.53	1.20	1.68	1.50
Tl	0.04	0.07	0.03	0.02
Pb	4.86	4.54	6.78	2.38
U	0.24	0.39	0.57	0.27
Th	0.43	0.71	0.31	0.24
La	5.94	9.15	3.98	4.30
Ce	18.44	21.63	10.85	12.06
Pr	3.20	3.16	1.97	2.10
Nd	17.11	15.49	10.66	11.36
Sm	6.03	4.27	4.05	4.24
Eu	2.03	1.62	1.72	1.56
Gd	8.15	5.19	5.56	5.82
Tb	1.44	0.88	1.01	1.11
Dy	9.54	5.73	6.89	7.30
Ho	2.17	1.26	1.53	1.62
Er	6.12	3.43	4.47	4.66
Tm	0.93	0.52	0.71	0.74
Yb	5.10	3.04	4.76	4.93
Lu	0.90	0.45	0.74	0.74

MINERAL COMPOSITION

Amphibole

Amphibole is predominantly calcic, with variation in (Na+K)A between 0.51-0.61 apfu for edenite-pargasite and 0.06-0.49 apfu for actinolite-magnesiohornblende compositions (Fig. 5A; Table 2). The pargasitic-edenite compositions correspond to grains formed at the metamorphic peak. They are rich in Na-in-A (max. 0.53 apfu),

total Al (max. 3.17 apfu), Mg# (max. 0.58) and Ca (max. 1.72 apfu), and poor in Si (min. 5.93 apfu).

The actinolite-magnesiohornblende compositions correspond to retrograde overprints (Fig. 5A). Magnesiohornblende compositions (Si 6.5-7.5 apfu) are most abundant, being poorer in Na(A) (between 0.04-0.44 apfu) and total Al (max. 2.35 apfu), and richer in Mg# (Max. 0.69; Fig. 5A) than peak amphibole. The actinolite compositions (Si > 7.5 apfu) have still lower Na(A) and total Al contents. A few analyses contain Na(B) corresponding to sodic-calcic composition (barroisite) with relatively high total Al (max 2.29 apfu) and Na(A) (max. 0.50 apfu) contents.

Epidote Group Minerals

Clinozoisite is the most common composition of the epidote group minerals with very low pistacite contents (Xps = Fe3+/[(Al+Fe3+)] ranging from 0.04 to 0.16 (Table 3). Zoning is generally faint or not present. However, some grains may show zoning with lower Xps at the rims, probably reflecting retrograde readjustments/growth, whereas irregular areas with higher Xps contents in the interior of the grains probably represent formation at higher temperature.

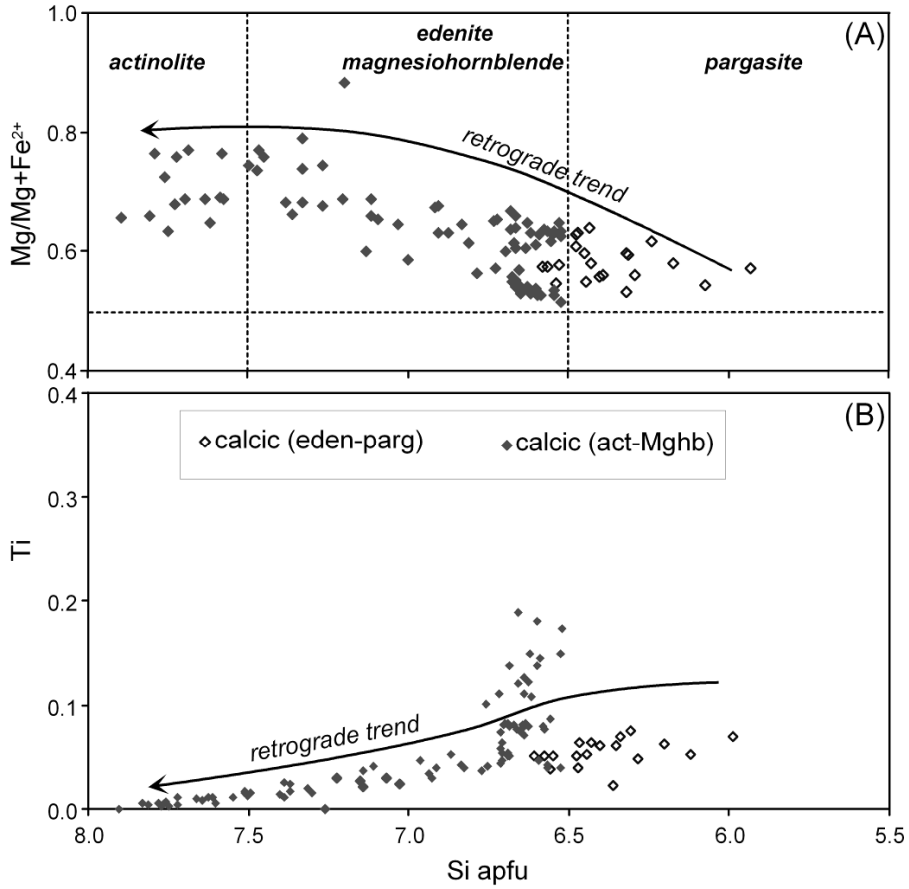

Fig. 5. Composition of calcic amphibole with indication of retrograde trends. (A) Si versus Mg(Mg+Fe2+). (B) Ti versus Si.

Garnet

Garnet is relatively rich in almandine (Xalm max. 0.62) and, to some extent, grossular (0.23-0.45), but poor in pyrope (0.02-0.10) and spessartine (0.03-0.16, Table 4). The composition of garnet is related to bulk-rock composition with lower almandine contents in garnet from Fe-poorer bulk-rock compositions. Zoning is faint and concentric. In most samples the cores are homogeneous, and the spessartine component decreases to the rim (Figs. 3A and 6). The lack of low temperature phases included in garnet (e.g., chlorite) and the faint prograde zoning suggest a relatively late stage of garnet growth, as otherwise indicated by pseudosection calculations (see below).

Plagioclase

The compositions of plagioclase from pods in samples LC-GU-5B and LC-M-12 show maximum Xan of 0.17 (Table 5), though Ca-poorer values are common. We interpret the Ca-richer compositions as representative of near-peak conditions (e.g., St-Onge, 1987) and Ca-poorer compositions produced by retrograde readjustments/growth. Retrograde grains dispersed in the matrix or associated with retrograde chlorite and magnesiohornblende-actinolite are of almost pure albite composition (Xab > 0.92, with most analyses reaching Xab > 0.99).

Phengite

Phengitic mica is rich in celadonite content (Table 6), with Mg# (0.62-0.71 apfu), Si (6.34-6.97 apfu), Mg (0.38-0.72 apfu), Fe^{2+}total (0.21-0.39 apfu), and Na (0.04-0.36 apfu). Si is negatively correlated with Al, Ba, and Na, and positively with Fe, Mg and K (Fig. 7). Ba contents are low in most grains, but some grains show a discernible enrichment in the core (max. 0.16 apfu). Based on these relations and the fact that high Na contents of up to 0.36 atoms pfu are consistent with relative high temperature during crystal growth, we conclude that peak metamorphic phengite is characterized by Al-, Ba-, and Na-rich compositions.

Paragonite

Retrograde paragonite (sample LC-GU-8) is relatively rich in muscovite component (Table 6), with K (0.11-0.19 apfu), and poor in Ti (< 0.01 apfu) and Fe2++Mg (< 0.09 apfu). The crystals may display zoning, with lower K-contents at the rims, suggesting late readjustments during retrogression and interaction with the minerals which are in contact (albite, epidote and muscovite). The relictic high-K compositions, however, suggest relatively high temperature of paragonite formation.

Chlorite

Chlorite is heterogeneous in composition with Si = 5.44-5.71 apfu, Al = 4.68-5.22 apfu, Mn = 0.01-0.07 apfu, and Mg# = 0.41-0.61 apfu (Table 7). This compositional variability may relate to continuous growth/readjustment during retrograde chlorite growth, but much of it is due to the effect of the mineral being replaced, because Fe-richer chlorite relates to garnet replacements (max. 5.65 Fe apfu, corresponding to 3.98 Mg apfu), whereas Mg-richer chlorite relates to amphibole replacement (max. 5.82 Mg apfu, corresponding to 3.73 Fe apfu).

Table2: Representative analyses of amphibole (normalized to 22 O and 2 OH).

Sample	LC-M-12			LC-GU-8			LC-GU-5B		LC-GU-6	
Type	pre-peak	peak	retro	peak	retro	Na-Ca	peak	retro	peak	retro
SiO_2	44.81	42.66	45.78	45.36	51.21	45.92	42.71	53.38	44.41	45.87
TiO_2	0.46	0.68	0.42	0.39	0.16	0.35	0.62	0.04	0.68	0.35
Al_2O_3	13.90	16.29	12.79	14.02	6.75	13.30	15.52	2.71	12.15	11.30
FeO	14.08	14.22	13.61	15.32	13.58	15.22	15.52	13.48	16.65	16.30
MnO	0.09	0.06	0.06	0.12	0.15	0.16	0.11	0.08	0.17	0.19
MgO	10.36	9.44	11.02	9.59	13.78	9.86	9.13	15.09	9.60	10.18
CaO	10.98	10.73	10.93	9.43	10.56	9.07	10.83	11.74	10.52	10.54
Na_2O	2.61	2.67	2.49	3.19	1.66	3.18	2.53	0.79	1.93	1.78
K_2O	0.37	0.46	0.31	0.40	0.20	0.32	0.64	0.09	0.57	0.48
Sum	97.66	97.21	97.41	97.82	98.05	97.38	97.61	97.40	96.68	96.99
Si	6.57	6.29	6.70	6.62	7.33	6.71	6.32	7.70	6.63	6.78
Ti	0.05	0.08	0.05	0.04	0.02	0.04	0.07	0.00	0.08	0.04
Al	2.40	2.83	2.20	2.41	1.14	2.29	2.71	0.46	2.14	1.97
Fe^{3+}	0.06	0.12	0.08	0.20	0.26	0.25	0.14	0.16	0.26	0.28
Fe^{2+}	1.66	1.63	1.59	1.67	1.36	1.61	1.78	1.47	1.81	1.74
Mn	0.01	0.01	0.01	0.01	0.02	0.02	0.01	0.01	0.02	0.02
Mg	2.26	2.08	2.40	2.09	2.94	2.15	2.01	3.24	2.14	2.25
Ca	1.72	1.70	1.71	1.48	1.62	1.42	1.72	1.81	1.68	1.67
Na	0.74	0.76	0.71	0.90	0.46	0.90	0.73	0.22	0.56	0.51
K	0.07	0.09	0.06	0.07	0.04	0.06	0.12	0.02	0.11	0.09
Mg#	0.58	0.56	0.60	0.56	0.68	0.57	0.53	0.69	0.54	0.56

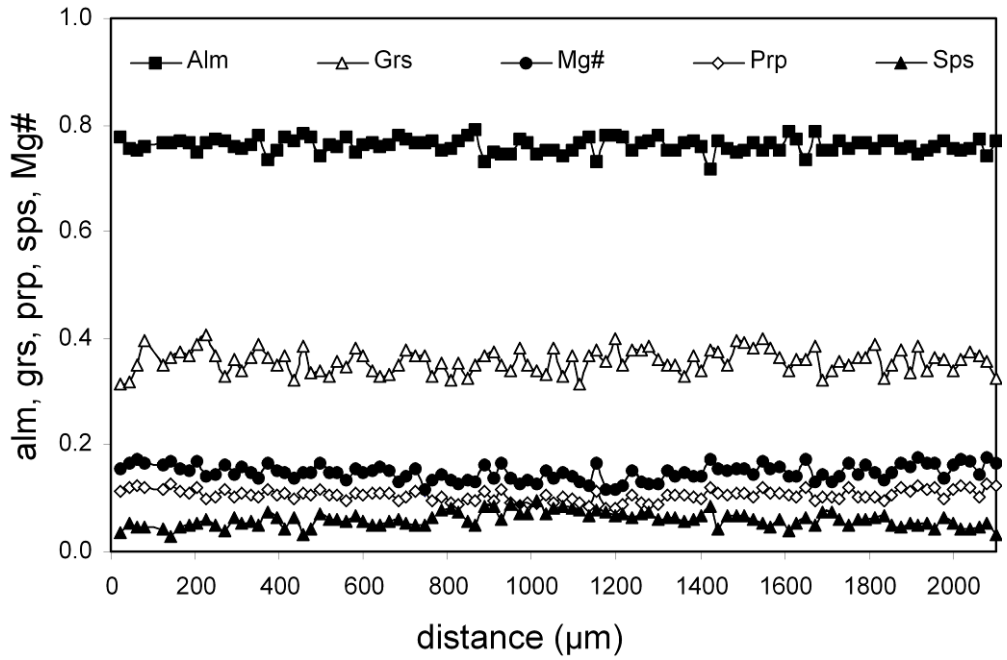

Fig. 6. Profile of garnet from sample LC-M-12 showing a flat zoning pattern (see Fig. 3A for location).

P-T CONDITIONS AND PATHS

The calculated peak P-T conditions are based on the peak assemblages Grt+Amp+Ep+Ms+Qtz (LC-GU-8), Grt+Amp+Ep+Pl+Qtz (samples LC-GU-5B and LC-M-12) and Grt+Amp+Ep+Qtz (sample LC-GU-6). For the Pl-bearing samples, plagioclase with the highest Ca-content was used for the calculation of peak conditions. The assemblages used for P-T calculations are shown in the ACF and

AFN phase diagrams of Fig. 8. These diagrams are projected from coexisting phases and appropriate exchange vectors which allow condensation of the composition space. Plagioclase-lacking samples are plotted in the ACF diagram (Fig. 8A and B, for samples LC-GU-8 and LC-GU-6 respectively), whereas plagioclase-bearing samples are plotted in the AFN diagram (Fig. 8C and D, for samples LC-M-12 and LC-GU-5B respectively), because the former do not allow evaluation of plagioclase solid solution (albite and anorthite are colinear in the ACF diagram).

Pre-peak conditions were calculated using the composition of inclusions within garnet for the assemblages Grt+Ep+Ms+Chl+Qtz (sample LC-GU-8) and Grt+Ep+Pl+Ms+Amp+Qtz (LC-M-12). Retrograde conditions were calculated using actinolite+Chl+Ep+Ms+Ab+Qtz (LC-GU-8), actinolite+Chl+Ep+Ms+Qtz (LC-G-5B) and actinolite+Chl+Ms+Ab+Qtz (LC-M-12 and LC-GU-6).

Table 3: Representative analyses of epidote (normalized to 12 O and 1 OH).

Sample	LC-M-12		LC-GU-8			LC-GU-5B		LC-GU-6
Type	pre-peak	peak	pre-peak	peak	retro	peak	retro	peak
SiO_2	38.56	38.82	38.85	38.8	39.38	38.48	38.67	38.51
TiO_2	0.12	0.22	0.14	0.11	0.02	0.11	0.63	0.12
Al_2O_3	27.90	30.13	29.61	28.60	31.40	27.25	28.98	28.09
FeO	7.50	4.04	4.80	5.80	2.36	7.56	4.41	7.04
MnO	0.42	0.05	0.23	0.11	0.03	0.14	0.25	0.24
MgO	0.04	0.10	0.06	0.05	0.03	0.03	0.10	0.05
CaO	23.34	23.46	23.68	23.60	24.24	23.43	23.58	23.45
Sum	97.88	96.82	97.37	97.15	97.46	97.00	96.62	97.5
Si	2.98	3.00	3.00	3.01	3.01	3.00	3.01	2.99
Ti	0.01	0.01	0.01	0.01	0.00	0.01	0.04	0.01
Al	2.55	2.75	2.69	2.62	2.83	2.51	2.65	2.57
$Fe3^+$	0.49	0.26	0.31	0.38	0.15	0.49	0.29	0.46
Mn	0.03	0.00	0.02	0.01	0.00	0.01	0.02	0.02
Mg	0.00	0.01	0.01	0.01	0.00	0.00	0.01	0.01
Ca	1.94	1.94	1.96	1.96	1.99	1.96	1.96	1.95
Xps	0.16	0.09	0.10	0.13	0.05	0.16	0.10	0.15

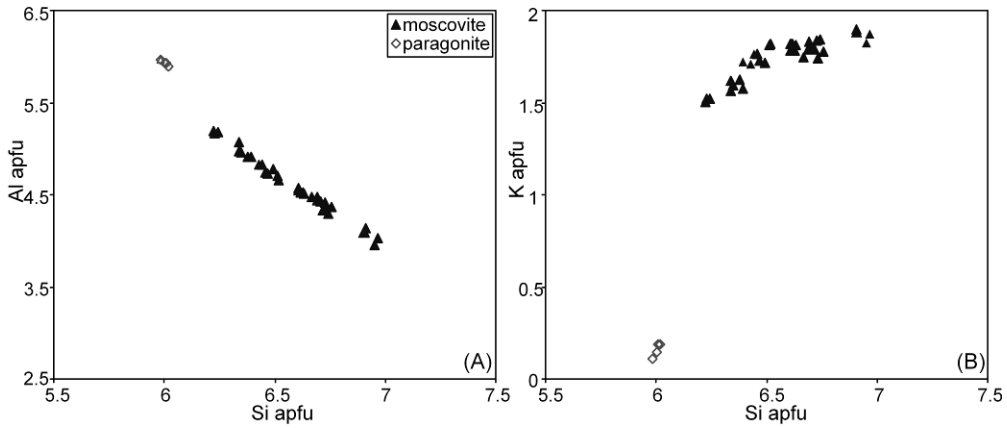

Fig. 7. Composition of white micas. (A) Si versus Al. (B) Si versus K.

Table 4: Representative analyses of garnet (normalized to 12 O).

Sample	LC-M-12		LC-GU-8		LC-GU-5B	LC-GU-6
Type	pre-peak	peak	pre-peak	peak	peak	peak
SiO_2	37.44	37.92	37.68	37.77	38.05	37.82
TiO_2	0.20	0.05	0.10	0.12	0.07	0.07
Al_2O_3	20.89	21.31	21.07	21.16	21.18	21.31
FeO	26.37	27.8	23.77	27.27	24.53	25.50
MnO	4.99	1.24	4.45	2.39	1.19	3.41
MgO	1.50	3.24	1.47	2.03	2.48	2.72
CaO	9.67	9.28	12.00	10.38	13.32	9.01
Sum	101.06	100.84	100.54	101.12	100.82	99.84
Si	2.98	2.98	2.98	2.98	2.98	3.00
Ti	0.01	0.00	0.01	0.01	0.00	0.00
Al	1.96	1.97	1.97	1.97	1.96	1.99
Fe^{3+}	0.00	0.00	0.00	0.00	0.00	0.00
Fe^{2+}	1.75	1.83	1.57	1.80	1.61	1.69
Mn	0.34	0.08	0.30	0.16	0.08	0.23
Mg	0.18	0.38	0.17	0.24	0.29	0.32
Ca	0.82	0.78	1.02	0.88	1.12	0.77
Mg#	0.09	0.17	0.10	0.12	0.15	0.16

Average P-T Calculations

P-T conditions were calculated using the average P-T method and software THERMOCALC version 3.31 and dataset 5.5 (Holland and Powell, 1998; Powell and Holland, 1994). The calculations were performed for the lower variance mineral assemblages containing garnet, because these produce a larger number of linearly independent reactions. An H2O-fluid was included in all assemblages. The activities and activity uncertainties of each end-member included in the calculations were obtained with software AX (Holland and Powell, unpublished). In order to reduce the error, phase components with low activities (i.e. ferroceladonite in phengite) were occasionally excluded from the calculations (cf. Powell and Holland, 1994). The results, including the correlations, sigfit values, and uncertainty ellipses, are given below and in Fig. 9, and were calculated following Powell and Holland (1994).

The calculated peak conditions are 697±52 ºC, 14.5±2.1 kbar (corr 0.90, sigfit 1.56), 622±35 ºC, 14.2±1.6 kbar (0.41, 0.59), 696±37 ºC, 14.3±1.4 kbar (0.85, 0.53) and 708±75 ºC, 13.8±2.8 kbar (0.18, 1.19) in samples LC-M-12, LC-GU-8, LC-GU-5B and LC-GU-6, respectively. These results suggest that most blocks underwent similar peak P-T conditions ranging from 690 to 710 ºC and 14-15 kbar, which correspond to conditions above the wet-saturated solidus of MORB composition. This indicates that the rocks experienced wet partial melting processes that consumed peak plagioclase produced the associated trondhjemitic-tonalitic segregations (cf. García-Casco and others, 2008). Sample LC-GU-8, however, yielded lower peak temperature conditions below the wet solidus of MORB, in agreement with the presence of peak plagioclase.

Table 5 Representative analyses of plagioclase (normalized to 8 O).

Sample	LC-M-12		LC-GU-8	LC-GU-5B		LC-GU-6
Type	peak	retro	retro	peak	retro	retro
SiO_2	64.29	69.3	68.93	64.19	68.68	68.93
Al_2O_3	22.41	19.38	19.68	22.57	19.51	20.43
FeO	0.60	0.17	0.21	0.42	0.22	0.04
MnO	0.08	0.03	0.00	0.01	0.00	0.01
CaO	3.52	0.03	0.28	3.53	0.14	0.18
BaO	0.03	0.00	0.00	0.05	0.03	0.00
Na_2O	9.69	11.88	11.84	9.81	11.99	11.71
K_2O	0.09	0.02	0.06	0.06	0.05	0.04
Sum	100.71	100.81	101.00	100.64	100.62	101.34
Si	2.83	3.00	2.99	2.82	2.99	2.97
Al	1.16	0.99	1.00	1.17	1.00	1.04
Fe^{3+}	0.02	0.01	0.01	0.01	0.01	0.00
Mn	0.00	0.00	0.00	0.00	0.00	0.00
Ca	0.17	0.00	0.01	0.17	0.01	0.01
Ba	0.00	0.00	0.00	0.00	0.00	0.00
Na	0.83	1.00	0.99	0.84	1.01	0.98
K	0.01	0.00	0.00	0.00	0.00	0.00
Xab	0.83	1.00	0.99	0.83	0.99	0.99

The calculated pre-peak conditions are 586±44 °C, 10.1±1.5 kbar (0.86, 1.34) for sample LC-M-12, and 517±16 ºC, 11.1±1.2 kbar (-0.27, 0.73) for sample LC-GU-8. The calculated retrograde conditions are 357±55 ºC, 6.5±1.6 kbar (0.69, 2.16), 433±23 ºC, 11.8±1.3 kbar (-0.02, 0.83), 417±39 ºC, 8.1±1.9 kbar (0.36, 1.33) and 517±35 ºC, 9.0±1.6 kbar (0.78, 1.51) in samples LC-M-12, LC-GU-8, LC-GU-5B and LC-GU-6, respectively

The P-T calculations are consistent with counterclockwise PT paths for all studied blocks. The pre-peak prograde path cut across the epidote-amphibolite-facies, peak conditions are within the epidote-amphibolite-facies generally above the wet solidus of meta-MORB, and retrogression occurred within the greenschist/blueschists-facies (Fig. 9). Counterclockwise P-T paths indicate that retrogression occurred upon exhumation within the subduction channel when subduction was active (e.g., Gerya and others, 2002).

The isochemical P-T projection calculated for sample LC-GU-8 (Fig. 10) is used as a proxy of processes taking place in blocks during peak conditions above the MORB solidus. The results are consistent with observed mineral assemblages. In particular, the calculated relations predict that the studied rocks would undergo wet melting at 650-700 ºC between 12-16 kbar (Fig. 10). Prograde melting at intermediate conditions within the plagioclase stability field would be dominated by consumption of plagioclase and quartz. At ca. 13 kbar, the field of coexistence of plagioclase and melt is very restricted to conditions close to the solidus (Fig. 10), in agreement with the observed lack of plagioclase in most amphibolite samples and with independent mass-balance calculations for similar rocks from the Sierra del Convento mélange (García-Casco and others, 2008a).

Table5: Representative analyses of micas (normalized to 22 O and 4 OH)

Phase	Phengite								Paragonite	
Sample	LC-M-12		LC-GU-8			LC-GU-5B		LC-GU-6	LC-GU-8	
Type	pre-peak	retro	pre-peak	peak	retro	peak	retro	retro	peak	retro
SiO_2	52.14	50.18	48.9	46.68	49.77	45.15	50.68	50.51	47.05	46.84
TiO_2	0.01	0.10	0.31	0.57	0.34	0.45	0.07	0.22	0.07	0.05
Al_2O_3	25.55	27.94	28.70	30.45	28.24	29.94	25.43	28.76	39.41	39.67
FeO	2.98	2.61	2.45	2.10	2.34	1.97	3.30	3.18	0.45	0.40
MnO	0.05	0.00	0.06	0.05	0.04	0.02	0.03	0.03	0.00	0.00
MgO	3.60	3.10	2.76	2.09	2.76	2.08	3.28	3.02	0.18	0.16
CaO	0.01	0.02	0.02	0.02	0.04	0.01	0.00	0.00	0.16	0.15
BaO	0.08	0.13	0.56	1.60	0.71	2.91	0.45	0.90	0.12	0.00
Na_2O	0.16	0.45	0.63	1.17	0.48	1.01	0.17	0.27	7.03	7.36
K_2O	10.98	10.75	10.33	9.03	10.5	8.89	10.9	10.37	1.17	0.68
Sum	95.56	95.28	94.72	93.76	95.22	92.43	94.31	97.25	95.64	95.31
Si	6.97	6.73	6.60	6.39	6.69	6.34	6.91	6.67	6.01	5.98
Ti	0.00	0.01	0.03	0.06	0.03	0.05	0.01	0.02	0.01	0.00
Al	4.02	4.41	4.57	4.91	4.48	4.96	4.08	4.47	5.93	5.97
Fe^{2+}	0.33	0.29	0.24	0.22	0.26	0.21	0.37	0.34	0.05	0.04
Mn	0.01	0.00	0.01	0.01	0.00	0.00	0.00	0.00	0.00	0.00
Mg	0.72	0.62	0.56	0.43	0.55	0.44	0.67	0.59	0.03	0.03
Ca	0.00	0.00	0.00	0.00	0.01	0.00	0.00	0.00	0.02	0.02
Ba	0.00	0.01	0.03	0.09	0.04	0.16	0.02	0.05	0.01	0.00
Na	0.04	0.12	0.16	0.31	0.13	0.28	0.04	0.07	1.74	1.82
K	1.87	1.84	1.78	1.58	1.80	1.59	1.89	1.75	0.19	0.11
Mg#	0.69	0.68	0.70	0.66	0.68	0.67	0.64	0.63	0.42	0.42

Table7: Representative analyses of chlorite (Normalized to 20 O and 16 OH))

Sample	LC-M-12		LC-GU-8		LC-GU-5B		LC-GU-6
SiO_2	26.39	26.18	26.82	26.50	25.83	26.38	26.40
Al_2O_3	19.40	20.44	18.96	21.05	18.23	20.46	21.41
FeO	25.23	21.47	28.24	22.67	31.07	22.51	23.52
MnO	0.12	0.06	0.26	0.09	0.27	0.11	0.14
MgO	15.92	18.77	13.56	17.41	12.26	17.54	16.57
Sum	87.06	86.92	87.84	87.72	87.66	87.00	88.03
Si	5.57	5.44	5.71	5.48	5.63	5.49	5.46
Al	4.83	5.01	4.76	5.13	4.68	5.02	5.22
Fe^{2+}	4.44	3.73	5.03	3.90	5.65	3.91	4.06
Mn	0.02	0.01	0.05	0.02	0.05	0.02	0.02
Mg	5.01	5.82	4.31	5.36	3.98	5.44	5.11
Mg#	0.53	0.61	0.46	0.58	0.41	0.58	0.56

Isopleths of mineral chemistry and abundance are presented in Fig. 11. The distribution of isopleths of garnet and amphibole are similar in slope but opposite in trend: garnet production implies amphibole consumption (Fig. 11A, 11B). Isopleths of modal abundance of garnet indicate late growth during the prograde evolution. Mg# increases smoothly along the subsolidus prograde path and more abruptly above the solidus (Fig. 11C). These predictions are in agreement with the observed faint prograde zoning of garnet and its mineral inclusions (Fig. 3C). Similarly, the amount of Na in plagioclase increases slowly along the subsolidus path, because the slopes of Xab isopleths are positive and similar to that of the P-T path, whereas at higher temperature above the solidus it decreases sharply until plagioclase exhaustion close to the solidus (Fig. 11D). High values of XAb (0.9), similar to those of plagioclase from pods in samples LC-GU-5B and LC-M-12, are predicted upon cooling at ca. 650 ºC and 13 kbar.

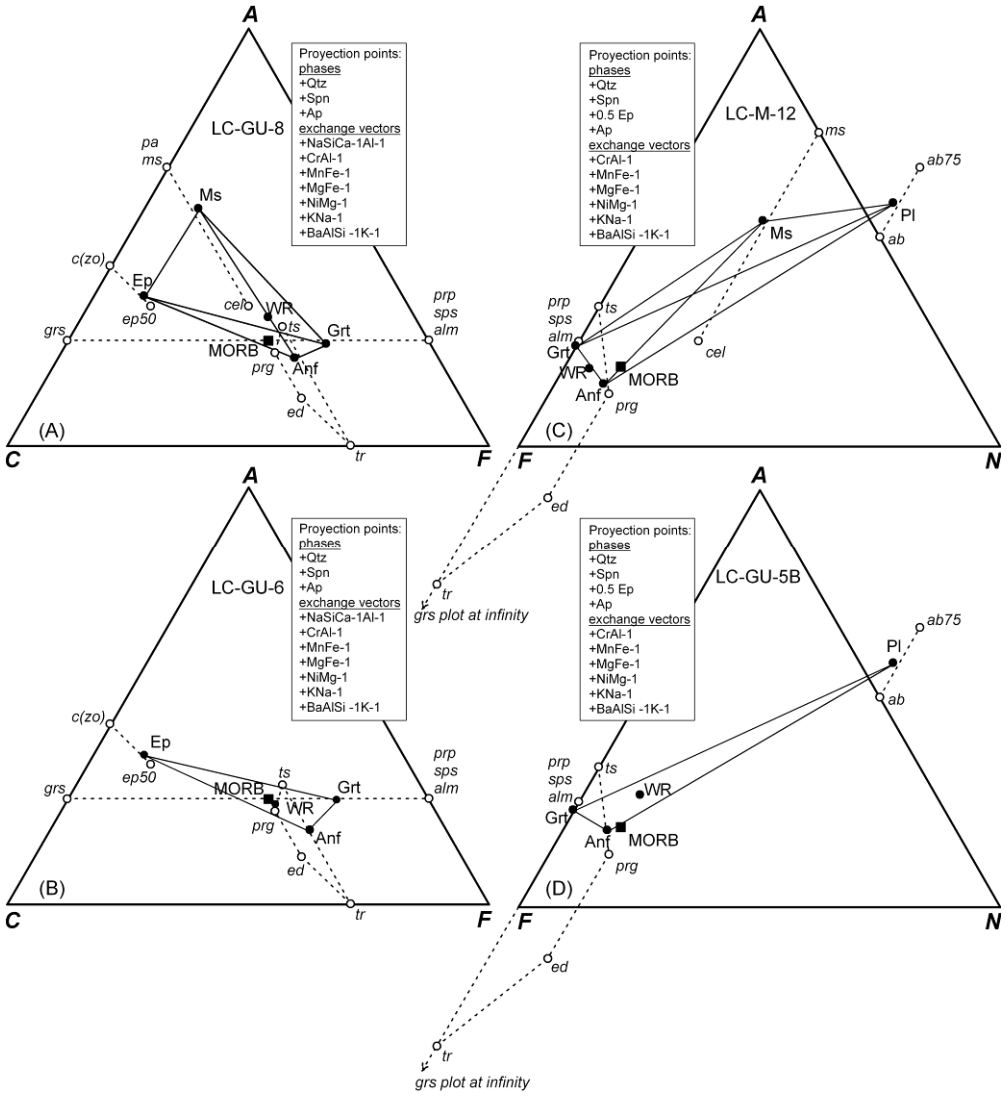

Fig. 8. (A) and (C) ACF, and (B) and (D) AFN phase diagrams showing peak metamorphic assemblages of amphibolites (bold circles joined by solid tie-lines) and whole-rock compositions (WR). Average MORB (filled squares, Sun and McDonough, 1989) has been plotted for comparison. End-members (labels in italic) of the solid solutions on interest are indicated by empty circles joined by dashed lines.

DISCUSSION

Thermal Evolution

The peak conditions within the epidote amphibolite facies, partial melting, and relatively high temperature/depth relation (14-16 ºC/km) indicate that metabasite rocks of La Corea mélange experienced intermediate P/T metamorphic gradient during subduction. A normal metamorphic gradient during subduction (ca. 10 ºC/km) produces eclogites at similar depth (e.g., Peacock and Wang, 1999).

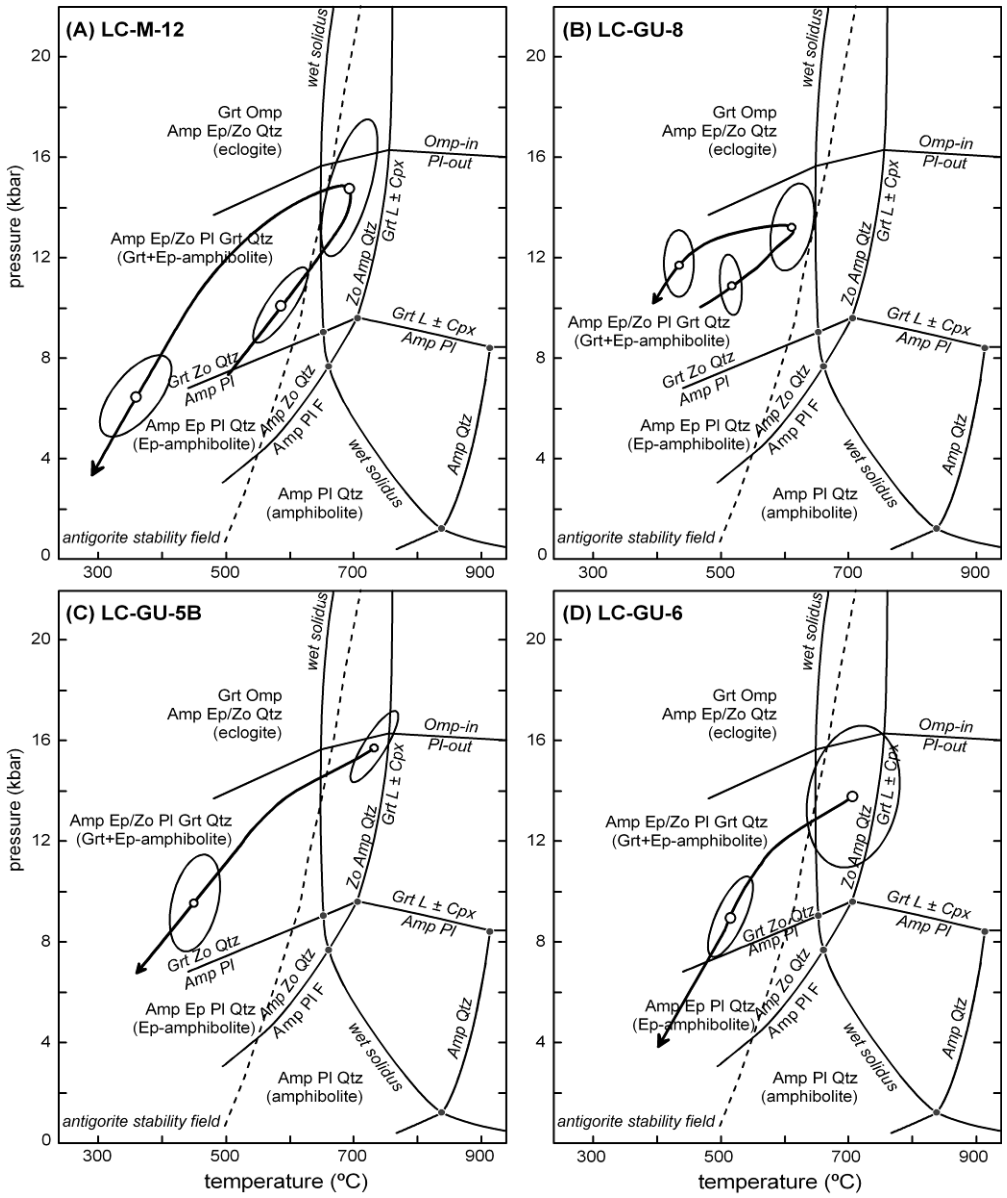

Fig. 9. P-T diagrams showing paths for garnet-bearing amphibolite samples calculated with THERMOCALC. The grid for the basaltic system is after Vielzeuf and Schmidt, (2001). The broken line is the antigorite stability limit of Ulmer and Trommsdorff (1995).

Anomalously high geothermal conditions (>14 ºC/km) can be produced within two main tectonic scenarios: a) onset of subduction, because heat must be rapidly withdrawn from the hanging wall and conducted into the descending slab, and b) subduction of young oceanic lithosphere (including a ridge), because of the high geothermal state of the subducted lithosphere. Both cases may generate moderate P-T gradients in the descending slab, though the combination of both would produce anomalously high P-T gradients. The peak P-T conditions and the counter-clockwise P-T paths followed by the amphibolite blocks are consistent with the combination of

both scenarios, in agreement with geodynamic models for the Caribbean region.These models postulate initiation of a SW-dipping subduction zone of young oceanic lithosphere during the Aptian (ca., 120 Ma; Pindell and others, 2005; Fig. 12). Similar counter-clockwise P-T paths have been deduced by Krebs and others, (2008) from contemporaneous (ca. 103 Ma) eclogite blocks in the Rio San Juan complex (Dominican Republic), and amphibolite blocks from the Sierra del Convento mélange (115 Ma; García-Casco and others, 2008a; Lázaro and others, 2009).

In the numerical modelling of subduction zones presented by Gerya and others, (2002), the wet solidus of MORB is reached at more than 20 kbar in a subducting lithosphere of 40 Myr age. The model of Pindell and others, (2005, 2006) shows the possibility of subduction of still younger lithosphere, including a ridge (i.e. 5 MA), in the Caribbean realm, because ocean spreading took place along the Proto-Caribbean ridge nearly orthogonal to the Caribbean trench (Fig. 12A). This scenario would allow a shallower location of subducted isotherms in the subducting ridge relative to more distal sections of the slab and, henceforth, the intersection of the MORB wet solidus at relatively shallow depth (Fig. 12B).

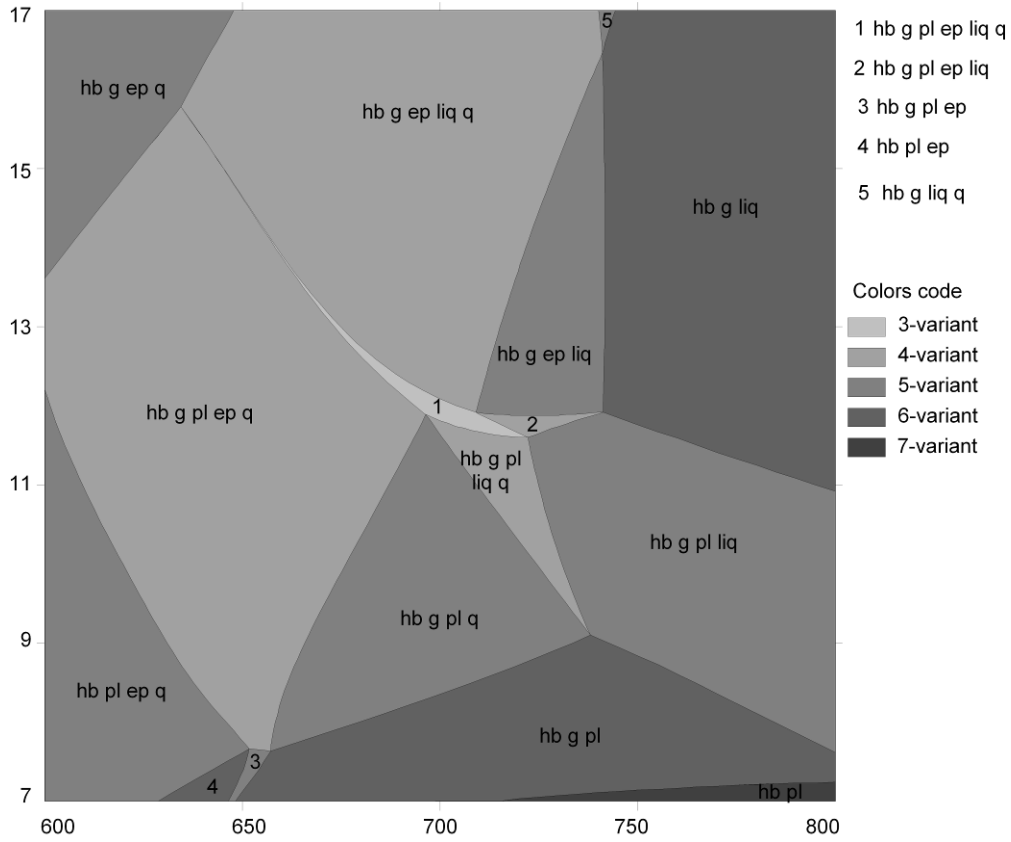

Fig. 10. Isochemical P-T equilibrium phase diagram for sample LC-GU-8 calculated with THERMOCALC. Mineral code is hb (hornblende), g (garnet), ep (epidote), liq (melt), pl (plagioclase), q (quartz).

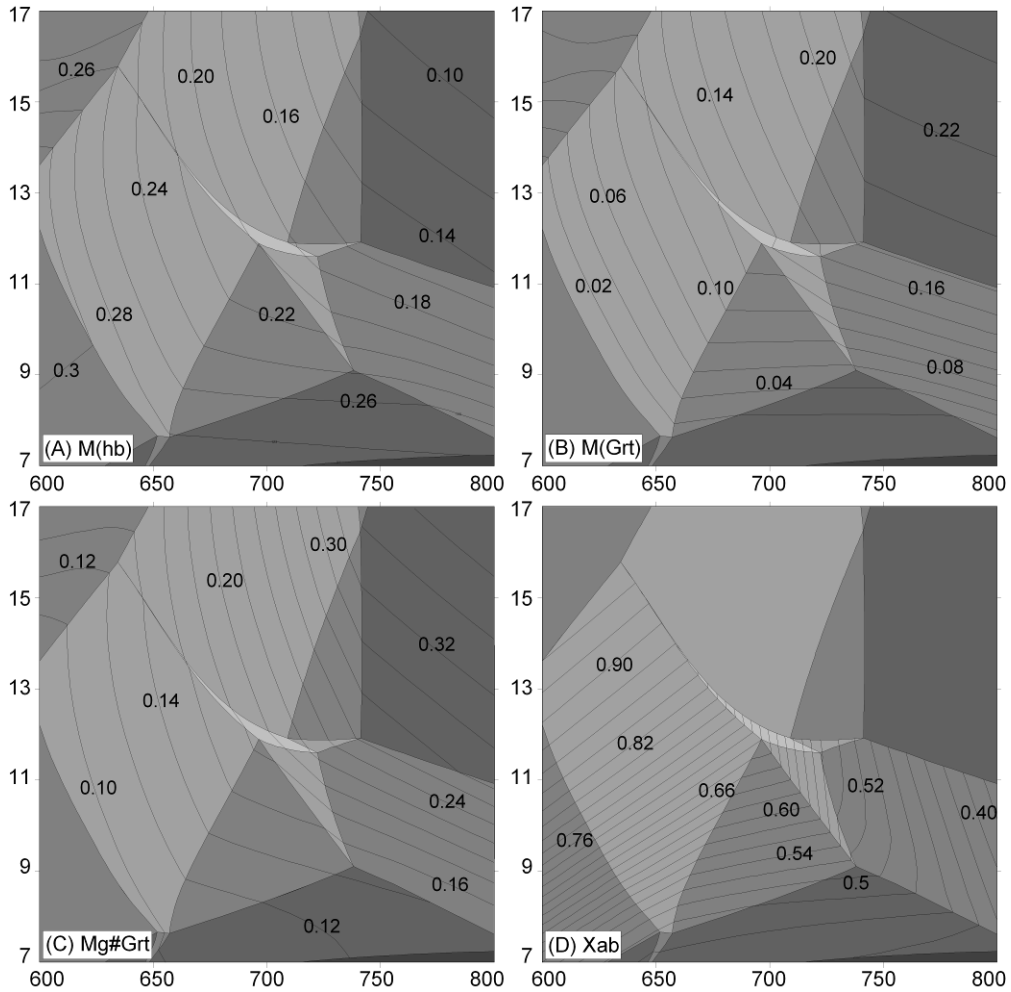

Fig. 11. Mineral abundance and composition isopleths for sample LC-GU-8 calculated with THERMOCALC (see Fig. 8B for mineral assemblages). (A) Modal proportion of hornblende. (B) Modal proportion of garnet (C) Mg# (Mg/(Mg+Fe2+) in garnet. (D) XAb in plagioclase. Colour scale as in Fig. 10.

Partial Melting

Amphibolite blocks of La Corea mélange constitute one of the rare cases where partial melting of subducted oceanic crusts can be observed. For partial melting to take place at ca. 15 kbar at 700-750 ºC in a subduction scenario, water is needed in the system. Free water can be produced by the decomposition of hydrated assemblages in the lower subducted oceanic lithosphere, including subducted oceanic crustal metabasite and mantle serpentinite. The upper thermal stability limit of antigorite is approximately isothermal at the conditions experienced in La Corea mélange (Fig. 9), between 600-700 ºC above 8 kbar (Ulmer and Trommsdorff, 1995). Dehydration of subducted peridotite is potentially a major source of water for partial melting of metabasite in La Corea mélange.

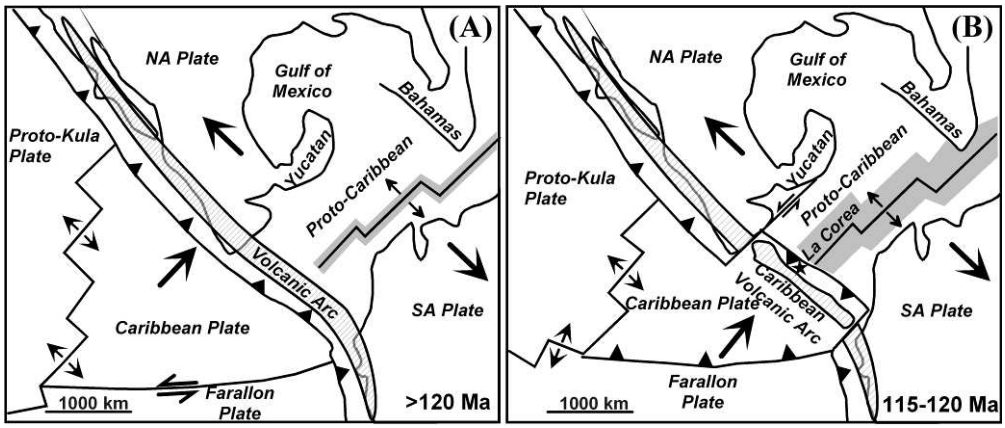

Fig. 12. Evolutionary model for the Caribbean region with indication of the polarity flip of subduction based on Pindell and others (2005). (A) Pre-Aptian (>120 Ma). (B) Aptian (115-120 Ma).

At the wet solidus of metabasalt, amphibole is stable at low pressure, zoisite and amphibole are present at intermediate pressure, whereas a single hydrous phase, zoisite, occurs at still higher pressures (Vielzeuf and Schmidt, 2001). The coexistence of zoisite and amphibole at peak conditions in the studied samples confirm an intermediate pressure (ca. 14-16 kbar) during partial melting. Fig. 9 shows that plagioclase is consumed approximately at 13 kbar, explaining the general absence of this phase in the studied amphibolites.

The pockets and veins with tonalitic-trondhjemitic composition (composed mostly of plagioclase, quartz and epidote) demonstrate that partial melting contributed to extraction of incompatible elements from the subducted lithosphere. These elements were incorporated primarily in the partial melts, but were later concentrated in pegmatitic rocks present in the mélange. Percolation of these melts and fluids should contribute, in turn, to partial melting of the upper plate and the generation of arc magmas.

Counterclockwise P-T Paths

Retrograde P-T paths of rocks formed during onset of subduction scenarios have been modelled by geophysical (Gerya and others, 2002) and geochemical (Perchuk and others, 1999) methods. These results indicate that, as subduction proceeds, downward migration of isotherms occurs as a result of material transport of ocean lithosphere, producing the continuous cooling of the subduction interface. However, the process is characterized by two stages, with a first stage of near isobaric cooling at high pressure, followed by a second stage of exhumation characterized by decreasing pressure and temperature. Following the results of these models, the first stage is developed once the blocks are accreted to the (H_2O-bearing, antigorite-lacking) upper plate mantle, while the second stage is developed once a serpentinitic subduction channel is formed upon reaction of H2O with the upper plate mantle at conditions within the antigorite stability field, allowing upward flow of the blocks. Increasing evidence of counterclockwise P-T paths within this type of geotectonic regime have become available in locally restricted occurrences. Such examples were recorded from relatively small-scale tectonic blocks (Wakabayashi, 1990; Oh and Liou, 1990; Krogh and others, 1994; Perchuk and others, 1999; Smith and others,

1999; García-Casco and others, 2008a; Lázaro and others, 2009), indicating that subduction channel (mélange) formation in onset of subduction scenarios is a requisite of this type of P-T paths.

At the pressure conditions experienced by amphibolites of La Corea mélange (i.e., ca 15 kbar), serpentinization of the upper plate mantle can only take place below 650 ºC (Fig. 9). This is consistent with the calculated retrograde P-T paths and inferred processes. Once the fragments of subducted amphibolite were accreted to the hanging wall at 700-750 ºC, the infiltrating H_2O could not be consumed in serpentinization of the hanging wall peridotite, but only in partial melting of accreted amphibolite. Moreover, as cooling proceeded, the wet solidus of segregated trondhjemite was intersected. This should have released H_2O-bearing fluids at 650-700 ºC that may have contributed to onset of retrogression of amphibolite, but not peridotite. However, percolation of these fluids and additional fluids released from the downgoing slab in a continuously cooling scenario triggered the formation of serpentinite at <650 ºC during the essentially isobaric stage, allowing upward flow and further cooling of the blocks.

Tectonic Implications

As indicated above, the counterclockwise P-T paths followed by amphibolites blocks are consistent with an onset of subduction scenario of young oceanic lithosphere (Perchuk and others, 1999; Gerya and others, 2002; Wakabayashi, 2004; Willner and others, 2004; Vignaroli and others, 2005; Krebs and others, 2008; García-Casco and others, 2008a; Lázaro and others, 2009), as predicted by geodynamic models for the Caribbean region during the Aptian (Pindell and Dewey, Fig. 6, 1982; Pindell and others, 2005).

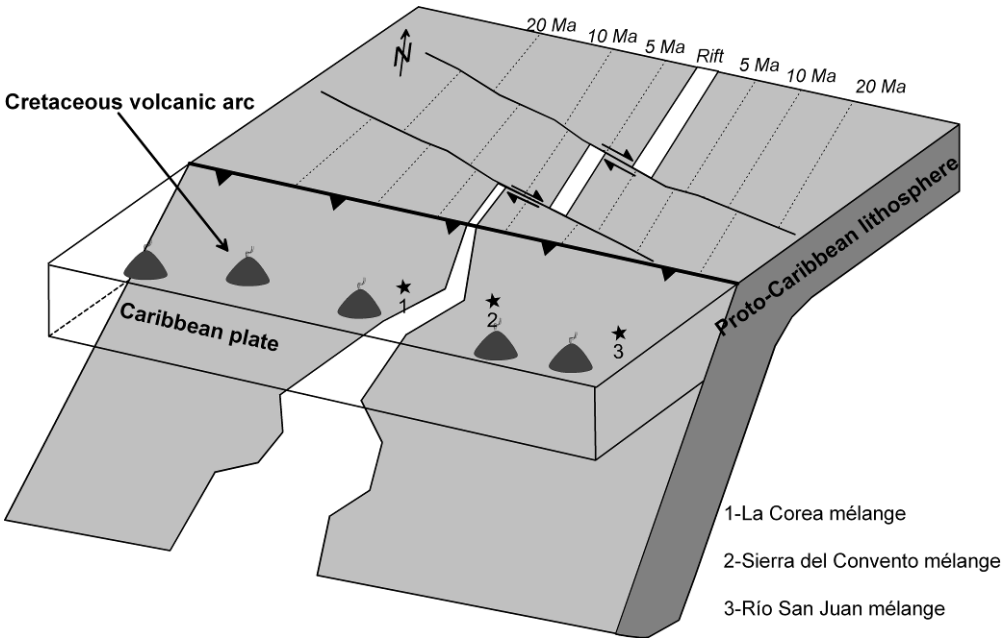

Fig. 13. Cartoon showing subduction of the Proto-Caribbean ridge during Aptian time. Dashed lines depict the age of the subducting lithosphere. Filled stars show the positions of the eastern Cuba and Dominican Republic mélanges.

Amphibolites of La Corea mélange indicate high geothermal gradient, similar to Sierra del Convento. García-Casco and others (2008a) suggested that the earlier products of subduction of the Sierra del Convento mélange, located to the NNW of Hispaniola during Aptian times (Pindell and others, 2005), represents younger subducted lithosphere than that of the Rio San Juan mélange (Dominican Republic, Krebs and others, 2008) and, consequently, that the Proto-Caribbean ridge should have been located close to eastern Cuba in that time. The new findings in La Corea mélange, located to the WNW of these complexes, reinforces this view, for the early products of subduction that appear in this mélange underwent similar but somewhat hotter conditions to those of the Sierra del Convento mélange. Tentatively, we suggest that La Corea and the Sierra del Convento mélange were located above the two flanking sides of the subducting ridge (Fig. 13), for colder conditions are recorded in HP rocks of mélanges located to the west of La Corea (i.e., the Holguín and central Cuba regions, cf. García-Casco and others, 2002, 2006, and references therein).

The Purial complex is geologically related to the Sierra del Convento mélange rather than La Corea. Nevertheless, the Purial is a peace of the Cretaceous volcanic arc that subducted due to subduction erosion. Preliminary results indicate that subduction erosion took place during the late Cretaceous, probably related with the subduction of Caribeana terrane (Garcia-Casco and others, 2008b). As consequence of subduction/accretion of continental margin material (Caribeana) during the latest Cretaceous, collision tectonics and, possibly, ensuing extension, produced finally exhumation of the La Corea other deep complexes in eastern Cuba.

CONCLUSIONS

Amphibolite blocks of La Corea mélange, eastern Cuba, have MORB affinity and heterogeneous compositions. These amphibolite blocks record an early stage of subduction of very young oceanic lithosphere during the Aptian. Peak metamorphic conditions attained of 690-710 ºC and 14-15 kbar were appropriate for wet melting of metabasite. Infiltration of H_2O likely occurred once the blocks were accreted to the hanging wall, triggering partial melting of the metabasites and the formation of trondhjemitic-tonalitic melts extracted out or precipitated inside the rocks as pockets. Formation of the subduction channel (mélange) took place upon cooling during continuous subduction and fluid migration to the upper plate mantle, allowing the blocks to start exhumation and further cooling following counterclockwise P-T paths during retrogression. The La Corea and Sierra del Convento mélanges share similarities in terms of structural position, lithology, age, P-T paths, and petrological processes, suggesting that they formed synchronously in the same subduction system close to a subducting oceanic ridge.

ACKNOWLEDMENTS

We are grateful for Alfred Kröner's utter dedication to Geology and inspiration and friendly advice to students and collaborators in all aspects of the evolution of orogenic belts. He also kindly revised an earlier version of this paper. Comments by Jim Pindell, Dave Moecher and Zeb Page and editor Peter Cawood greatly improved this paper. We appreciate financial support from Spanish MICINN projects CGL2006-08527/BTE and CGL2009-12446. This is a contribution to IGCP-546 'Subduction zones of the Caribbean' and is Mainz Geocycles contribution. Blanco-

Quintero is supported by grant AP2005-5258 from the ‘‘Programa de Formación del Profesorado Universitario’’ of the Spanish Ministry of Education and Science.

REFERENCES

Adamovich, A., and Chejovich, V., 1964, Principales características de la geología y de los minerales útiles de la región nordeste de la Provincia de Oriente: Revista Tecnológica, v. 2, p. 14-20.

Agard, P., Yamato, P., Jolivet, L., and Burov, E., 2009, Exhumation of oceanic blueschists and eclogites in subduction zones: Timing and mechanisms: Earth Science Reviews, v. 92, p. 53-79.

Anczkiewicz, R., Platt, J. P., Thirlwall, M. F., and Wakabayashi, J., 2004, Franciscan subduction off to a slow start: evidence from high-precision Lu–Hf garnet ages on high grade-blocks: Earth and Planetary Science Letters, v. 225, p. 147-161.

Blanco-Quintero, I.F., García-Casco, A., Proenza, J., Rojas-Agramonte, Y., Kröener, A., Lázaro, C., Iturralde-Vinent, M., Rodríguez-Vega, A., and Millán, G., 2008, Geochemistry and age of a partially melted subducted slab. La Corea mélange (eastern Cuba, 18th Caribbean Geological Conference. Santo Domingo, Dominican Republic 24–29 March.

Boiteau, A., Michard, A., and Saliot, P., 1972, Métamporphisme de haute pression dans le complexe ophiolitique du Purial (Oriente, Cuba, Comptes Rendus de l’Académie des Sciences, Série D 274, p. 2137–2140.

Cloos, M., 1985, Thermal evolution of convergent plate margins: Thermal modeling and re-evaluation of isotopic Ar-ages for blueschists in the Franciscan complex of California: Tectonics, v. 4, p. 421-433.

Cobiella, J., Campos M., Boiteau, A., and Quintas, F., 1977, Geología del flanco sur de la Sierra del Purial: Revista La Minería de Cuba, v. 3, p. 54-62.

Cobiella, J., Quintas, F., Campos, M., and Hernández, M., 1984, Geología de la Región Central y Suroriental de la Provincia de Guantánamo. Santiago de Cuba. Santiago de Cuba: Editorial Oriente, 125 p.

Diener, J.F.A., Powell, R. White, R.W., and Holland, T.J.B., 2007, A new thermo-dynamic model for clino- and orthoamphiboles in Na2O-CaO-FeO-MgO-Al2O3-SiO2-H2O-O: Journal of Metamorphic Geology, v. 25, p. 631-656.

García-Casco A., 2007, Magmatic paragonite in trondhjemites from the Sierra del Convento mélange, Cuba: American Mineralogist, v. 92, p. 1232–1237.

García-Casco, A., Torres-Roldán, R. L., Millán, G., Monié, P., and Schneider, J., 2002, Oscillatory zoning in eclogitic garnet and amphibole, Northern Serpentinite Melange, Cuba: a record of tectonic instability during subduction?: Journal of Metamorphic Geology, v. 20, p. 581-598.

García-Casco, A., Torres-Roldán, R.L., Iturralde-Vinent M.A., Millán, G., Núñez Cambra, K., Lázaro, C., and Rodríguez Vega, A., 2006, High pressure metamorphism of ophiolites in Cuba: Geologica Acta, v. 4, p. 63–88.

García-Casco, A., Lázaro, C., Torres-Roldán, R. L., Núñez Cambra, K., Rojas Agramonte, Y., Kröner, A., Neubauer, F., Millán, G., and Blanco Quintero, I., 2008a, Partial melting and counterclockwise P-T path of subducted oceanic crust (Sierra del Convento mélange, Cuba): Journal of Petrology, v. 49, p. 129-161.

García-Casco, A., Iturralde-Vinent, M.A., and Pindell, J., 2008b, Latest Cretaceous collision/accretion between the Caribbean Plate and Caribeana: Origin of metamorphic terranes in the Greater Antilles: International Geology Review, v. 50, p. 781-809.

Gerya, T.V., Stoeckhert, B., and Perchuk, A.L., 2002, Exhumation of high-pressure metamorphic rocks in a subduction channel—a numerical simulation: Tectonics, v. 21, p. 6-1–6-19.

Glodny, J., Lohrmann, J., Echtler, H., Grafe, K., Seifert, W., Collao, S., and Figueroa, O., 2005, Internal dynamics of a paleoaccretionary wedge: insights from combined isotope tectonochronology and sandbox modelling of the south-central Chilean forearc: Earth and Planetary Science Letters, v. 231, p. 23-39.

Guinchi, C., and Ricard, Y., 1999, High-pressure/low-temperature metamorphism and the dynamic of an accretionary wedge: Geophysical Journal International, v. 136, p. 620–628.

Holland, T.J.B., and Powell, R., 1998, An internally consistent thermodynamic data set for phases of petrological interest: Journal of Metamorphic Geology, v. 16, p. 309–343.

Holland, T.J.B., and Powell, R., 2001, Calculation of phase relations involving haplogranitic melts using an internally consistent thermodynamic data set: Journal of Petrology, v. 42, p. 673-683.

Holland, T.J.B., and Powell, R., 2003, Activity-composition relations for phases in petrological calculations: an asymmetric multicomponent formulation: Contributions to Mineralogy and Petrology, v. 145, p. 492-501.

Holland, T.J.B., Baker, J.M., and Powell, R., 1998, Mixing properties and activity-composition relationships of chlorites in the system MgO-FeO-Al2O3-SiO2-H2O: European Journal of Mineralogy, v. 10, p. 395-406.

Iturralde-Vinent, M. A., 1998, Sinopsis de la Constitución Geológica de Cuba: Acta Geológica Hispánica, v. 33, p. 9-56.

Iturralde-Vinent, M.A., Díaz Otero, C., Rodríguez-Vega, A., and Díaz-Martínez, R., 2006, Tectonic implications of paleontologic dating of Cretaceous–Danian sections of Eastern Cuba: Geologica Acta , v. 4, p. 89–102.

Iturralde-Vinent, M.A., Díaz Otero, C., García-Casco, A., and Van Hinsbergen, D.J.J., 2008, Paleogene Foredeep Basin Deposits of North-Central Cuba: A Record of Arc-Continent Collision between the Caribbean and North American Plates: International Geology Review, v. 50, p. 863–884.

Kirby, S. H., Durham, W. B., and Stern, L. A., 1991, Mantle phase changes and deep-earthquake faulting in subducting lithosphere: Science, v. 252, p. 216–225.

Krebs, M., Maresch, W.V., Schertl, H.P., Baumann, A., Draper, G., Idleman, B., and Münker, C., 2008, The dynamics of intra-oceanic subduction zones: A direct comparison between fossil petrological evidence (Rio San Juan Complex, Dominican Republic) and numerical simulation: Lithos, v. 103, p. 106-137.

Kretz, R., 1983, Symbols for rock-forming minerals: American Mineralogist, v. 68, p. 277–279.

Krogh, E.I., Oh, C.W., and Liou, J.G., 1994, Polyphase and anticlockwise P–T evolution for Franciscan eclogites and blueschists from Jenner, California, USA: Journal of Metamorphic Geology, v. 12, p. 121–134.

Lallemand, S., 1999, La Subduction Oceanique. Gordon and Breach, Newark, N. J.

Lázaro, C., and García-Casco, A., 2008, Geochemical and Sr-Nd isotope signatures of pristine slab melts and their residues (Sierra del Convento mélange, eastern Cuba: Chemical Geology, v. 255, p. 120-133.

Lázaro, C., García-Casco, A., Neubaurer, F., Rojas-Agramonte, Y., Kröner, A., and Iturralde-Vinent, M.A., 2009, Fifty-five-million-year history of oceanic subduction and exhumation at the northern edge of the Caribbean plate (Sierra del Convento mélange, Cuba: Journal of Metamorphic Geology, v. 27, p. 19-40.

Leake, B. E., Woolley, A. R., Arps, C. E. S., Birch, W. D., Gilbert, M. C., Grice, J. D., Hawthorne, F .C., Kato, A., Kisch, H. J., Krivovichev, V. G., Linthout, K., Laird, J., Mandarino, J. A., Maresch, W. V., Nickel, E. H., Rock, N. M. S., Schumacher, J. C., Smith, D. C., Stephenson, N. C. N., Ungaretti, L., Whittaker, E. J. W., and Touzhi, G., 1997, Nomenclature of amphiboles: Report of the Subcommittee on Amphiboles of the International Mineralogical Association, Commission on New Minerals and Mineral Names: American Mineralogist v. 82, p. 1019-1037.

Le Maitre, R.W., Bateman, P., Dudek, A., Keller, J., Lameyre Le Bas, M.J., Sabine, P.A., Schmid, R., Sorensen, H., Streckeisen, A., Woolley, A.R., and Zanettin, B., 1989. A classification of igneous rocks and glossary of terms: Blackwell, Oxford, 196 p.

Leyva R. C., 1996, Características geológicas, regularidades de distribución y perspectivas de utilización del cuarzo filoniano de la región oriental de Cuba: Unpublished report of the Instituto Superior Minero-Metalúrgico de Moa (Cuba), 90 p.

Mann, P., Taylor, F.W., Lawrence Edwards, R., and Ku., T-L., 1995, Actively evolving microplate formation by oblique collision and sideways motion along strike slip faults: An example from the northeastern Caribbean plate margin: Tectonophysics, v. 246, p. 1-69.

Marchesi, C., Garrido, C. J., Godard, M., Proenza, J. A., Gervilla, F., and Blanco-Moreno, J., 2006, Petrogenesis of highly depleted peridotites and gabbroic rocks from the Mayarí-Baracoa Ophiolitic Belt (eastern Cuba): Contributions to Mineralogy and Petrology, v. 151, p. 717-736.

Marchesi, C., Garrido, C.J., Bosch, D., Proenza, J.A., Gervilla, F., Monié, P., and Rodríguez-Vega, A., 2007, Geochemistry of Cretaceous magmatism in eastern Cuba: recycling of North American continental sediments and implications for subduction polarity in the Greater Antilles Paleo-arc: Journal of Petrology, v. 48, p. 1813–1840.

Millán G., 1996a, Metamorfitas de la asociación ofiolítica de Cuba, in: Iturralde-Vinent, M.A., editor, Ofiolitas y Arcos Volcánicos de Cuba. IGCP Project 364 Special Contribution 1, p. 131–146.

Millán G., 1996b, Metavulcanitas del Purial, in: Iturralde-Vinent, M.A., editor, Ofiolitas y Arcos Volcánicos de Cuba. IGCP Project 364 Special Contribution 1, p. 131–146.

Millán, G., Somin, M.L., and Díaz, C., 1985, Nuevos datos sobre la geología del macizo montañoso de la Sierra del Purial, Cuba Oriental. Reporte de Investigación del Instituto de Geología y Paleontología 2, p. 52–74.

Nuñez Cambra, K.E., García-Casco, A., Iturralde-Vinent, M.A., and Millán, G., 2004, Emplacement of the ophiolite complex in Eastern Cuba. Proceedings of the 32nd International Geological Congress, Florencia. Session: G20.11 Caribbean Plate Tectonics.

Oh, C.-W., and Liou, J.G., 1990, Metamorphic evolution of two different eclogites in the Franciscan Complex, California, USA: Lithos, v. 25, p. 41-53.

Peacock, S. M., 1990, Numerical simulation of metamorphic pressure–temperature –time paths and fluid production in subduction slabs: Tectonics, v. 9, p. 1197– 1211.

Peacock, S. M., 1996, Thermal and petrologic structure of subduction zones, in: Bebout, G.E., School, D., and Kirby, S., editors, Subduction: Top to Bottom: American Geophysical Union Geophysical Monograph 96, p. 119-133.

Peccerillo, A., Taylor, S.R., 1976. Geochemistry of Eocene calc-alkaline volcanic-rocks from Kastamonu Area, Northern Turkey: Contributions to Mineralogy and Petrology, v. 58, p. 63–81.

Perchuk, A. L., Philippot, P., Erdmer, P., and Fialin, M., 1999, Rates of thermal equilibration at the onset of subduction deduced from diffusion modeling of eclogitic garnets, Yukon-Tanana terrane: Geology, v. 27, p. 531-534.

Pindell, J. L., and Dewey, J. F., 1982, Permo-Triassic reconstruction of western Pangea and the evolution of the Gulf of Mexico/ Caribbean region: Tectonics, v. 1, p. 179-211.

Pindell, J.L., Kennan, L., Maresch, W.V., Stanek, K.P., Draper, G., and Higgs, R., 2005, Plate-kinematics and crustal dynamics of circum-Caribbean arc–continent interactions: Tectonic controls on basin development in Proto-Caribbean margins, in: Avé Lallemant, H.G., and Sisson, V.B., editors, Caribbean–South American Plate Interactions, Venezuela: Geological Society of America, Special Papers 394, p. 7–52.

Pindell, J. L, Kennan, L., Stanek, K. P., Maresch,W. V., and Draper, G., 2006, Foundations of Gulf of Mexico and Caribbean evolution: eight controversies resolved: Geologica Acta, v. 4, p. 303-341.

Powell, R., and Holland, T.J.B., 1994, Optimal geothermometry and geobarometry: American Mineralogist, v. 79, p. 120–133.

Proenza, J.A., Melgarejo, J.C., Gervilla, F., Rodríguez-Vega, A., Díaz-Martínez, R., Ruiz-Sánchez, R., and Lavaut, W., 2003, Coexistence of Cr- and Al-rich ophiolitic chromitites in a small area: the Sagua de Tánamo district, Eastern Cuba. In: Eliopoulos et al., eds., Mineral Exploration and Sustainable Development. Rotterdam Netherlands, Millpress, v. 1, p. 631-634.

Proenza, J.A., Díaz-Martínez, R., Iriondo, A., Marchesi, C., Melgarejo, J.C., Gervilla, F., Garrido, C.J., Rodríguez-Vega, A., Lozano-Santacruz, R., and Blanco-Moreno, J.A., 2006, Primitive Cretaceous island-arc volcanic rocks in eastern Cuba: the Téneme Formation: Geologica Acta , v. 4, p. 103–121.

Rojas-Agramonte, Y., Neubauer, F., Handler, R., García-Delgado, D.E., Friedl, G., and Delgado-Damas, R., 2005, Variation of paleostress patterns along the Oriente Transform Fault, Cuba: Significance for Neogene–Quaternary tectonics of the Caribbean realm: Tectonophysics, v. 396, p. 161–180.

Smith, C.A., Sisson, V.B., Ave´ Lallemant, H.G., and Copeland, P., 1999, Two contrasting pressure – temperature – time paths in the Villa de Cura blueschist belt, Venezuela: possible evidence for Late Cretaceous initiation of subduction in the Caribbean: Geological Society of America Bulletin, v. 111, p. 831–848.

St-Onge, M.R., 1987, Zoned poiltiloblastic garnets: P-T paths and syn-metamorphic uplift through 30 km of structural depth, Wopmay Orogen, Canada: Journal of Petrology v. 28, p. 1-21.

Somin, M.L., and Millán, G., 1981, Geology of the Metamorphic Complexes of Cuba. Nauka: Moscow, 219 p., (in Russian).

Somin, M. L., Arakelyants, M. M., and Kolesnikov, E. M., 1992, Age and tectonic significance of high-pressure metamorphic rocks in Cuba: International Geology Review, v. 34, p. 105-118.

Sorensen, S. S., 1988, Petrology of amphibolite-facies mafic and ultramafic rocks from the Catalina Schist, Southern California: metasomatism and migmatization in a subduction zone metamorphic setting: Journal of Metamorphic Geology, v. 6, p. 405–435.

Sorensen, S. S., and Barton, M. D., 1987, Metasomatism and partial melting in a subduction complex: Catalina Schist, southern California: Geology, v. 15, p. 115–118.

Stern, R.J., 2002, Subduction zones: Reviews of Geophysics, v. 40, 1012, doi: 10.1029/2001RG000108.

Sun, S.S., and McDonough, W.F., 1989, Chemical and isotopic systematics of oceanic basalts; implications for mantle composition and processes, in: Saunders, A.D. and

Norry, M.J., editors, Magmatism in the Ocean Basins Geological Society Special Publications, Geological Society of London, London, United Kingdom, p. 313–345.

Torres-Roldán, R. L., García-Casco, A., and García-Sánchez, P. A., 2000, CSpace: An integrated workplace for the graphical and algebraic analysis of phase assemblages on 32-bit Wintel platforms: Computers and Geosciences, v. 26, p. 779-793.

Ulmer, P., and Trommsdorff, V., 1995, Serpentine stability to mantle depths and subduction-related magmatism: Science, v. 268, p. 858–861.

Vielzeuf, D., and Schmidt, M.W., 2001, Melting reactions in hydrous systems revisited: applications to metapelites, metagreywackes and metabasalts: Contributions to Mineralogy and Petrology, v. 141, p. 251–267.

Vignaroli, G., Rossetti, F., Bouybaouene, M., Massonne, H.-J., Theye, T., Faccenna, C., and Funiciello, R., 2005, A counter-clockwise P-T path for the Voltri Massif eclogites (Ligurian Alps, Italy): Journal of Metamorphic Geology, v. 23, p. 533-555.

Wakabayashi, J., 1990, Counterclockwise PTt paths from amphibolites, Franciscan Complex, California: relics from the early stages of subduction zone metamorphism: Journal of Geology, v. 98, p. 657– 680.

Wakabayashi, J., 2004, Tectonic mechanisms associated with P–T paths of regional metamorphism: Alternatives to single-cycle thrusting and heating: Tectonophysics, v. 392, p. 193-218.

White, R.W., Powell, R., and Holland, T.J.B., 2007, Progress relating to calculation of partial melting equilibria for metapelites: Journal of Metamorphic Geology, v. 25, p. 511-527.

Willner, A.P., Glodny, J., Gerya, T.V., Godoy, E., and Massonne, H.-J., 2004, A counterclockwise PTt path of high-pressure/low-temperature rocks from the Coastal Cordillera accretionary complex of southcentral Chile: constraints for the earliest stage of subduction mass flow: Lithos, v. 75, p. 283-310.

Wood, D.A., Joron, J.L., Treuil, M., 1979. Re-Appraisal of the Use of Trace-Elements to Classify and Discriminate between Magma Series Erupted in Different Tectonic Settings: Earth and Planetary Science Letters, v. 45, p. 326-336.

Worley, B., and Powell, R., 1998, Singularities in NCKFMASH (Na2O-CaO-K2OFeO-MgO-Al2O3-SiO2-H2O: Journal of Metamorphic Geology, v. 16, p. 169-188.

2- TECTONIC BLOCKS IN SERPENTINITE MÉLANGE (EASTERN CUBA) REVEAL LARGE-SCALE CONVECTIVE FLOW OF THE SUBDUCTION CHANNEL

I.F. Blanco-Quintero[(1)]; A. García-Casco[(1,2)]; T. V. Gerya[(3,4)]

(1) Departamento de Mineralogía y Petrología, Universidad de Granada, Fuentenueva s/n, 18002-Granada, Spain

(2) Instituto Andaluz de Ciencias de la Tierra (CSIC-UGR), Fuentenueva s/n, 18002-Granada, Spain

(3) Department of Geosciences, Swiss Federal Institute of Technology, 8093 Zurich, Switzerland

(4) Department of Geology, Moscow State University, 119899 Moscow, Russia

ABSTRACT

Detailed petrological study of MORB-derived high pressure amphibolite blocks from a fragment of the Caribbean subduction channel (La Corea serpentinite-matrix mélange, E Cuba) has revealed contrasted zoning patterns of garnet porphyroblasts, including well defined complex oscillatory prograde-retrograde concentric zoning in one sample. Calculated P-T conditions for this sample using mineral inclusion assemblages and isochemical P-T projections reveal large P-T recurrences best explained by large-scale convective movement of the tectonic block in a serpentinitic subduction channel. P-T conditions attending garnet growth followed an overall counter-clockwise path as a consequence of continued refrigeration of the subduction channel during ongoing underflow after its onset at ca. 120 Ma. These findings constitute the first report of large scale convective circulation of deeply subducted material in the subduction channel, and are consistent with the thermo-mechanical behavior of the channel predicted by numerical models.

Keywords: subduction channel; garnet; convective circulation; numerical modeling

INTRODUCTION

Subduction channels (or flow channels) are complex rock assemblies developed along the interface between the subducting and the hanging wall plates in convergent margins. Shreve and Cloos (1986) and Cloos and Shreve (1988a, b) first developed the concept to model the dynamics of convergent plate margins (prism accretion, sediment subduction, mélange formation, subduction erosion…). These authors identified the subduction channel as a relatively shallow, thin layer of poorly consolidated sediment, dragged by the descending plate beneath the overriding plate/accretionary prism, where most of the subduction-driven deformation is concentrated and accretion of subducted material takes place. The concept can be applied to modern and ancient subduction complexes such as the Franciscan (e.g., Ernst, 1970), where the P-T history of tectonic blocks in sediment-matrix melánges document subduction of accreted materials down to 30 km depth. Cloos and Shreve (1988b) indicated that flow in the channel can be downward, upward (providing a mechanism of exhumation of accreted blocks) and convective.

Following the seminal work by these authors, the subduction channel concept has been extended to much deeper near-sub-arc depths (e.g., Guillot et al., 2000; 2001; 2009; Gerya et al., 2002). At these depths, characterized by mantle rocks in the hanging wall, dehydration reactions in the subducting sediments, mafic crust and ultramafic materials trigger the release of H_2O-rich fluids. Upward flow of these fluids triggers the transformation of upper plate peridotite into serpentinite (at temperature below ca. 650 ºC; Ulmer and Trommsdorff, 1995), causing the formation of a ductile layer of serpentinite in between the subducting and overriding plates where much of the subduction-driven deformation concentrates. Thermo-mechanical models also predict downward, upward and convective flow in this serpentinitic subduction channel (Gerya et al., 2002).

Petrological studies have shown that HP blocks accreted within the channels –i.e., metasedimentary/serpentinitic-matrix mélanges- undergo hairpin P-T paths (Ernst, 1988), indicating syn-subduction exhumation in the channel. Syn-subduction exhumation in the channel is also confirmed by blocks subducted/accreted during the early stages of subduction, for these blocks follow counter-clockwise P-T paths documenting the progressive refrigeration of the nascent subduction system upon continued subduction of lithosphere (e.g., Wakabayashi, 1990). Although much petrological work has been presented to demonstrate up-and-down circulation, little work has been yet provide to demonstrated large-scale convective flow in subduction channels.

Garnet composition is very sensitive to changes in pressure and temperature, and cation diffusion in garnet is sufficiently slow to preserve zoning at low to moderate temperature (e.g., Konrad-Schmolke et al., 2005). Oscillatory zoning of Mn in HP garnet was described in Franciscan rocks by Dudley (1969). While Ghent (1988) indicated a potential kinetic control (reaction-diffusion problems) and disequilibrium growth, other possibilities for oscillatory zoning in Ca-Fe-Mn-Mg garnets include equilibrium processes during episodic inflections of P–T paths (e.g., Enami, 1998; Schumacher et al., 1999; García-Casco et al., 2002). Such inflections can only be related to complex material/heat flow in the lithosphere and, when identified in tectonic blocks of subduction mélanges, offer important clues for understanding the

mechanics of subduction systems. In this paper, we give petrological evidence for the first time that supports large-scale convective flow in serpentinitic channels.

GEOLOGICAL AND PETROLOGICAL SETTINGS

The Caribbean plate is fringed from Guatemala through the Greater Antilles to northern South America by subduction-related high pressure (HP) complexes, most of which formed after the onset of subduction (at ca. 120 Ma) of the Protocaribbean (i.e., Atlantic) lithosphere below the Caribbean plate (Pindell et al., 2005; García-Casco et al., 2008a). Many of these HP complexes constitute serpentinite mélanges bearing exotic tectonic blocks of diverse nature (subducted oceanic lithosphere, fore-arc/arc and continental platform materials) and variable metamorphic grade (high-grade eclogite, garnet amphibolite and blueschist, and low grade blueschist). In Cuba, serpentinitic mélanges are exposed all along the >1000 km length of the island (Fig. 1A; Somin and Millán, 1981) and have been interpreted as fragments of Antillean subduction channel (García-Casco et al., 2006).

In eastern Cuba, the Sierra del Convento and La Corea serpentinite-matrix mélanges represent fragments of this subduction channel (Fig. 1B, C; see García-Casco et al., 2006, 2008b; Lázaro et al., 2009; Blanco-Quintero et al., 2010a and b, for details of the following descriptions and for references on the geology of the region). These mélanges contain blocks of subducted high-grade garnet-amphibolite (Fig. 1D) and blueschist surrounded by sheared and massive antigoritite interpreted as the matrix of the subduction channel (Fig. 1E). Metamorphic conditions of garnet-amphibolite blocks (700–750 ºC; 15 kbar; ca. 50 km) indicate a very hot subduction zone environment that caused partial melting of subducted MORB and the formation of tonalite-trondhjemite melts crystallized at a similar depth. Most amphibolite blocks provide evidence for rather simple counter-clockwise P-T paths characterized by high-T during accretion to the upper plate and low-T blueschist facies overprint during exhumation. Hot and ensuing cold conditions relate to onset of subduction of young oceanic Protocaribbean lithosphere at ca. 120 Ma and to very slow syn-subduction exhumation in the subduction channel (115–70 Ma), respectively. Final fast exhumation of the subduction channel occurred after an arc-platform-like terrane collision at 70–65 Ma.

A few blocks from these mélanges, however, show evidences for more complex P-T evolutions in the channel. In this paper we give detailed information for a singular block of epidote-garnet amphibolite from the La Corea mélange (Fig. 1C; sample LC-G-1B) which has provided a rather complex P-T evolution.

ANALYTICAL TECHNIQUES AND METHODS

Whole-rock major element compositions were determined with a PHILIPS Magix Pro (PW-2440) X-ray fluorescence equipment (University of Granada) using a glass beads, made of 0.6g of powdered sample diluted in 6g of $Li_2B_4O_7$.

Mineral compositions were obtained using WDS with a CAMECA SX-100 microprobe (University of Granada) operated at 15 kV and 15 nA. Amphibole composition was normalized following the procedure of Leake et al. (1997), and Fe^{3+} was estimated after the method of Schumacher (in Leake et al., 1997). Garnet composition was normalized to 12 oxygens and 8 cations, with Fe^{3+} estimated by stoichiometry. Epidote and plagioclase were normalized to 12.5 and 8 oxygens,

respectively, and $Fe_{total}=Fe^{3+}$. White mica and chlorite were normalized to 22 and 28 oxygens, respectively, and $Fe_{total} = Fe^{2+}$.

Elemental X-ray images were obtained with the same machine operated at 20 kV, 150 nA beam current, step (pixel) size of 7 µm and counting time of 30 ms. The images were processed with Imager software (Torres-Roldán and García-Casco, unpublished) to obtain quantitative images of garnet composition (expressed in atoms per 12 oxygen formula unit). The procedure of Bence and Albee (1968) was followed for matrix correction by using the composition of an internal garnet standard analyzed with the electron microprobe. In the images the other minerals are masked out, and the resulting images are overlain onto a gray-scale "Z" image calculated by the sum of the products of the counts by atomic number (Si, Ti, Al, Fe, Mn, Mg, Ca, Na, Ba, K, P, F and Cl). The profile was extracted from the quantified X-ray images of Si, Al, Fe, Mn, Mg, and Ca with a resolution of 7 µm/point (total number of points plotted: 518) and transformed to continuous lines by regression. The atomic concentration of elements per formula units is abbreviated apfu, the Mg number of minerals (Mg#) is expressed as $Mg/(Mg+Fe^{2+})$.

Solution models used in the thermodynamic calculations for amphibole, chlorite, epidote, plagioclase and muscovite are from Diener et al. (2007), Holland et al. (1998), Holland and Powell (1998), Holland and Powell (2003) and Coggon and Holland (2002) respectively, and for garnet and ilmenite from White et al. (2005).

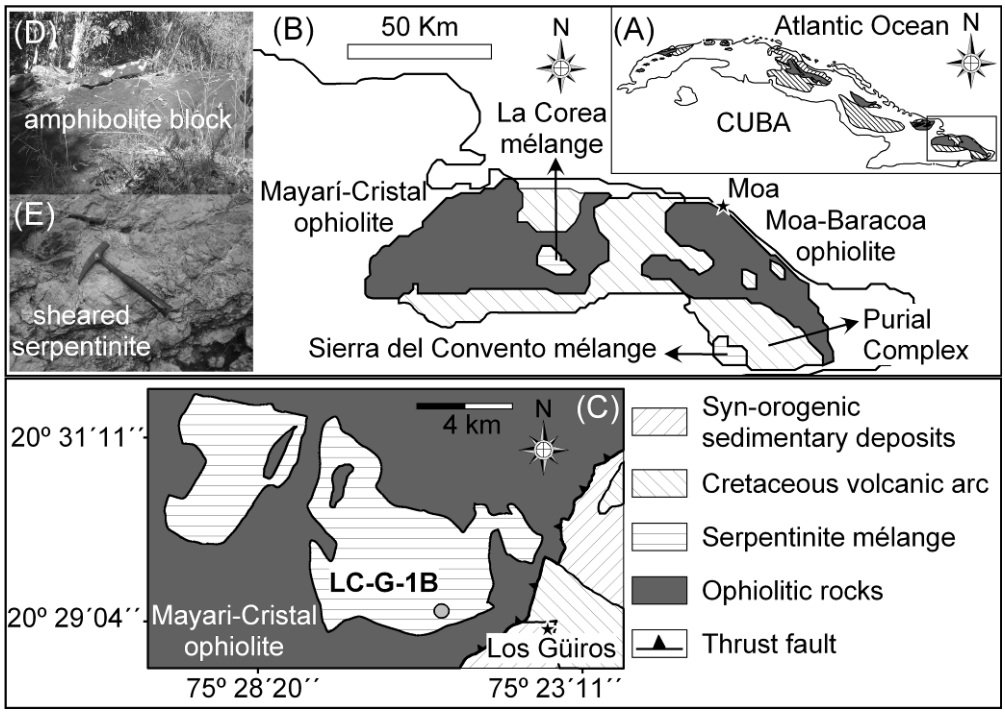

Figure 1. A: Geological maps of A: Cuba, B: eastern Cuba, and C: La Corea mélange with indication of main geological complexes. Photographs of outcrops showing D: amphibolite block and E: serpentinite matrix in La Corea mélange. Legend is for all maps.

PETROGRAPHY

The mineral assemblage of amphibolite sample LC-G-1B consists of calcic (pargasitic) amphibole – epidote – garnet – titanite – rutile – quartz – phengite, and apatite. Amphibole is medium- to coarse-grained, with grains up to 4 mm in length, oriented parallel to the foliation. Garnet porphyroblasts are up to 6 mm in diameter (Fig. 2) and are anhedral. The porphyroblasts contain inclusions of rutile, titanite, apatite, epidote, plagioclase, quartz, calcic amphibole, phengite and chlorite, and their xenoblastic rims penetrate into the amphibolitic matrix and/or appear replaced by retrograde amphibole ± chlorite (Fig. 2B). Epidote is abundant and occurs as euhedral patchy zoned crystals of 0.1–0.5 mm long. Phengite is scarce and appears as medium-size flakes.

Retrograde overprints are composed of combinations of actinolite, glaucophane, albite, clinozoisite, chlorite and phengite. These retrograde minerals are fine-grained and form reaction rims around peak metamorphic minerals and locally fill fractures. Retrograde albite is scarce and appears aggregated with epidote, titanite and phengite. Chlorite replaces garnet and pargasitic amphibole. Glaucophane appears as small patches replacing pargasitic amphibole and indicates a high pressure/low temperature trajectory during exhumation.

MINERAL COMPOSITION

Amphibole is calcic, with (Na+K)A = 0.51 – 0.61 apfu (atom per formula unit) for peak edenite-pargasite and 0.04 – 0.48 apfu for retrograde actinolite-magnesiohornblende compositions. The peak compositions are rich in NaA (max. 0.52 apfu), total Al (max. 3.16 apfu) and Mg# (max. 0.64), and poor in Si (min. 6.07 apfu). Retrograde compositions have higher Si (max. 7.90 apfu) and Mg# (max. 0.79) and lower NaA (min. 0.02 apfu) and total Al (min. 0.35 apfu) contents. Retrograde glaucophane is near pure end-member glaucophane with Si = 7.97, Al = 1.58, NaB = 1.87, NaA = 0.07 and Ca = 0.07 apfu and intermediate Mg# (0.57).

Garnet is relatively rich in almandine (Xalm max. 0.64) and, to some extent, grossular (0.20–0.30), and is poor in pyrope and spessartine (0.15–0.20 and 0.02–0.10, respectively). It is concentrically zoned. In the case illustrated in the quantitative images of Figure 2A-C and in the profile of Figure 2D, four zones can be identified: 1) a low-T core having low Mg# and high Mn, with inclusions of chlorite, albite, epidote and quartz, overgrown by 2) a prograde high Mg# zone (peak-1), with inclusion of rutile, quartz, pargasite and phengite, 3) a retrogressive xenomorphic zone likely generated after garnet dissolution characterized by high Mn and low Mg# (retro-1) associated with inclusions of chlorite, titanite and actinolitic amphibole confirming its retrogressive nature, and 4) an outer rim of prograde high Mg# zone (peak-2). Large compositional variations characterize the internal retrogressive event retro-1 (Fig. 2D).

Epidote grains have pistacite (Fe3+/([Al-2]+Fe3+) contents of 0.10–0.30. Phengitic mica exhibits a range in celadonite contents (Si = 6.23–6.97 apfu), with Mg# = 0.62–0.71; the cores of the matrix flakes have lower celadonite and higher Na contents (max. 0.35 apfu), indicating higher temperature of formation. Plagioclase is

Table 1. Whole rock and mineral compositions.

Mineral		Grt	Grt	Grt	Grt	Amp	Amp	Amp	Amp	Amp	Ep	Ep	Ep	Pl	Chl	Chl	Chl	Ms	Ms	Ms
Zone	WR	pre-peak	Peak-1	Retro-1	Peak-2	Peak-1	Retro-1	Peak-2	Retro-2	Retro-2	Peak-2	pre-peak	Retro-2	pre-peak	pre-peak	Retro-1	Retro-2	Retro-2	Peak-1	Peak-2
SiO_2	44.05	37.71	38.00	37.71	37.82	45.88	54.47	41.29	57.21	51.29	38.77	38.12	38.75	68.72	25.30	26.26	26.47	50.29	49.92	46.56
TiO_2	2.30	0.24	0.12	0.12	0.14	1.00	0.07	0.47	0.21	0.23	0.11	0.16	0.18	0.00	0.04	0.03	0.06	0.15	0.15	0.59
Al_2O_3	13.22	21.05	21.43	21.00	21.28	11.97	2.52	18.24	9.65	6.41	28.74	28.77	28.79	19.61	17.91	19.75	20.64	27.55	27.92	29.63
Cr_2O_3		0.02	0.05	0.01	0.00	0.01	0.01	0.02	0.02	0.00	0.04	0.00	0.06	0.00	0.04	0.06	0.00	0.04	0.05	0.01
FeO	14.39	27.44	28.46	21.18	28.36	13.00	11.30	15.52	14.09	11.60	5.88	5.74	5.69	0.36	32.44	25.32	21.72	3.16	3.10	2.09
MnO	0.25	3.83	1.69	6.95	1.71	0.20	0.22	0.24	0.11	0.14	0.23	0.25	0.23	0.02	0.98	0.54	0.21	0.02	0.03	0.02
MgO	10.29	2.47	4.32	0.91	3.31	12.11	16.91	8.53	8.83	15.16	0.05	0.10	0.05	0.00	10.22	15.84	18.47	2.97	2.99	2.45
NiO		0.00	0.02	0.00	0.04	0.01	0.02	0.00	0.02	0.03	0.00	0.01	0.00	0.01	0.00	0.00	0.03	0.04	0.04	0.00
CaO	9.78	8.63	7.14	12.92	8.78	10.33	11.52	9.73	0.48	11.02	23.77	22.38	23.65	0.10	0.10	0.03	0.01	0.07	0.07	0.01
BaO		0.00	0.00	0.01	0.00	0.02	0.00	0.01	0.00	0.00	0.00	0.00	0.00	0.00	0.00	0.00	0.01	0.05	0.07	1.79
Na_2O	1.81					2.36	0.75	3.12	7.20	1.50	0.00	0.00	0.00	12.01	0.08	0.02	0.01	0.33	0.34	0.64
K_2O	0.34					0.25	0.05	0.44	0.02	0.14	0.01	0.01	0.01	0.04	0.05	0.03	0.01	10.36	10.45	9.72
P_2O_5	0.18																			
Total	96.61	101.39	101.23	100.81	101.44	97.30	97.99	97.78	98.02	97.66	97.75	95.66	97.56	100.97	87.44	88.05	87.81	95.15	95.30	93.64
Si		2.97	2.97	2.99	2.96	6.68	7.73	6.07	7.96	7.33	3.00	3.00	3.00	2.98	5.63	5.53	5.47	6.76	6.71	6.43
Ti		0.01	0.01	0.01	0.01	0.11	0.01	0.05	0.02	0.02	0.01	0.01	0.01	0.00	0.01	0.00	0.01	0.02	0.02	0.06
Al		1.96	1.97	1.96	1.97	2.05	0.42	3.16	1.58	1.08	2.62	2.67	2.63	1.00	4.70	4.91	5.03	4.36	4.42	4.82
Cr		0.00	0.00	0.00	0.00	0.00	0.00	0.00	0.00	0.00	0.00	0.00	0.00	0.00	0.01	0.01	0.00	0.00	0.01	0.00
Fe^{3+}		0.00	0.00	0.00	0.01	0.27	0.18	0.35	0.23	0.24	0.38	0.38	0.37	0.01						
Fe^{2+}		1.81	1.86	1.40	1.85	1.31	1.16	1.56	1.41	1.14					6.04	4.46	3.75	0.36	0.35	0.24
Mn		0.26	0.11	0.47	0.11	0.02	0.03	0.03	0.01	0.02	0.02	0.02	0.02	0.00	0.18	0.10	0.04	0.00	0.00	0.00
Mg		0.29	0.50	0.11	0.39	2.63	3.58	1.87	1.83	3.23	0.01	0.01	0.01	0.00	3.39	4.98	5.69	0.60	0.60	0.51
Ni		0.00	0.00	0.00	0.01	0.00	0.00	0.00	0.00	0.01	0.00	0.00	0.00	0.00	0.00	0.00	0.02	0.02	0.02	0.00
Ca		0.73	0.60	1.10	0.74	1.61	1.75	1.53	0.07	1.69	1.97	1.89	1.96	0.00	0.02	0.01	0.00	0.01	0.01	0.00
Ba		0.00	0.00	0.00	0.00	0.00	0.00	0.00	0.00	0.00	0.00	0.00	0.00	0.00	0.00	0.00	0.00	0.00	0.00	0.10
Na						0.67	0.21	0.89	1.94	0.42	0.00	0.00	0.00	1.01	0.03	0.01	0.00	0.09	0.09	0.17
K						0.05	0.01	0.08	0.00	0.03	0.00	0.00	0.00	0.00	0.01	0.01	0.00	1.78	1.79	1.71
#Mg		0.14	0.21	0.07	0.17	0.67	0.76	0.54	0.56	0.74					0.36	0.53	0.60	0.63	0.63	0.68

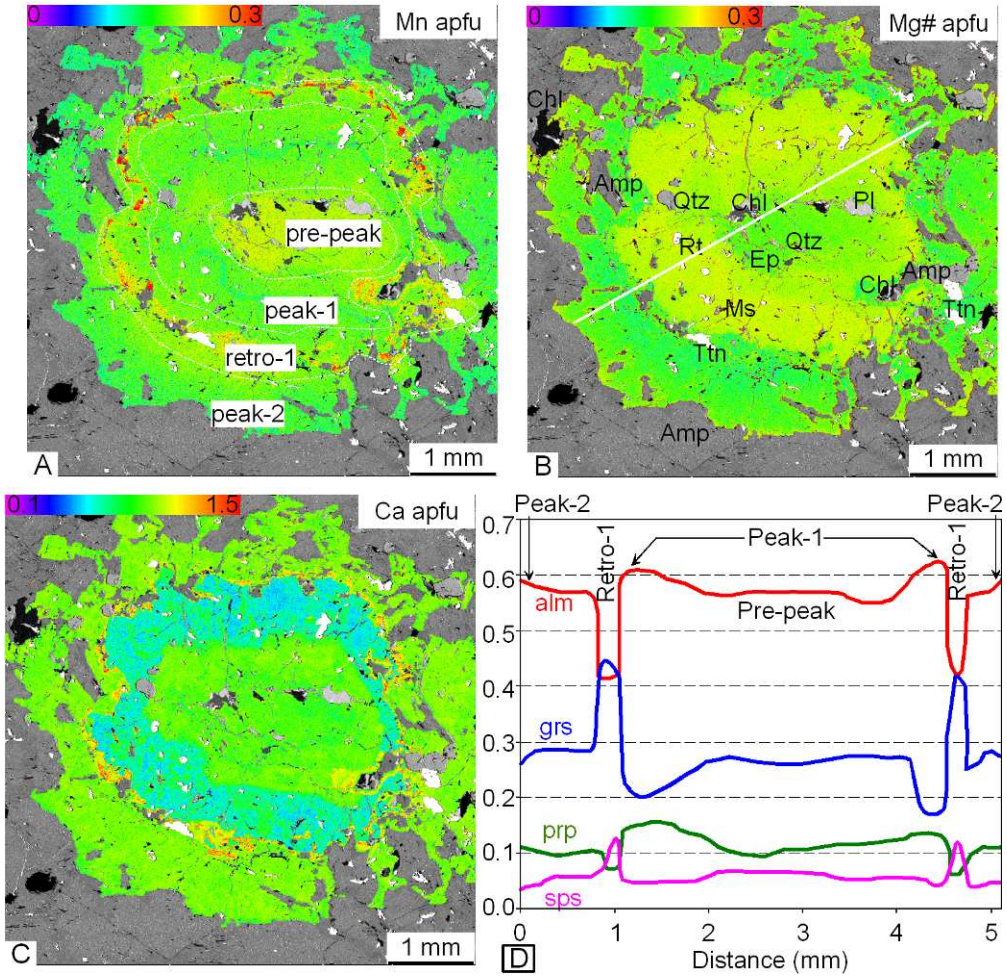

Figure 2. Quantitative X-ray images showing textures and garnet composition (color code, cations per 12 oxygens; see Appendix 1 for details of calculations) of sample LC-G-1B. A: Mn, B: Mg# and C: Ca. D: Profile across garnet showing oscillations in composition.

almost pure albite in composition (Xab > 0.99). Chlorite (inclusions and late retrograde replacements in the matrix) displays a large compositional variation denoting variable P-T of formation and diffusion problems during retrogression.

P-T CALCULATIONS

P-T conditions were calculated using the average P-T method (Powell and Holland, 1994) and software THERMOCALC (Holland and Powell, 1998; version 3.31 and data set 5.5). The activities and activity uncertainties of end-members were obtained with software AX (Holland and Powell, unpublished). The pre-peak P-T conditions were determined for the assemblage Grt+Ep+Ab+Chl+Qtz+H2O using the composition of garnet cores and associated inclusions. The conditions for peak-1 garnet were calculated using the compositions of associated inclusions of Amp and Ms (+H2O). The conditions for peak-2 garnet were calculated with the same assemblage using the composition of matrix pargasite and the cores of matrix

muscovite. Retrograde conditions were calculated using actinolitic Amp+Grt+Chl+Qtz+H2O (retro-1) and actinolitic Amp+Chl+Ep+Ms+Qtz+Ab+H2O (retro 2), using the composition of included and matrix phases, respectively.

The calculated physical conditions indicate a complex P-T path characterized by first an increase in P-T from the garnet core (536 ± 22 ºC, 10.6 ± 1.6 kbar) to the internal peak-1 zone (634 ± 71 ºC, 15.9 ± 2.0 kbar), a strong decrease in P-T for the internal retro-1 zone (446 ± 19 ºC, 11.4 ± 2.0 kbar), a second increase for the peak-2 stage (590 ± 54ºC, 16.4 ± 2.1 kbar), and a decrease for the final retro-2 stage (471 ± 62 ºC, 11.1 ± 1.6 kbar). Note that the highest P-T condition correspond to the internal peak-1 zone rather than the external final overgrowth (peak-2).

An isochemical P-T phase-diagram (pseudosection) was calculated for sample LC-G-1B using THERMOCALC (same version as above). The physical conditions predicted for the different zones of garnet using mineral isopleths and mineral assemblages (Fig. 3A) are in agreement with P-T conditions calculated by the average P-T method. The distribution of isopleths of chemical composition and abundance of garnet (Fig. 3B) indicates that garnet was consumed during formation of retro-1 zone. This conclusion reveals that fluid infiltration occurred during the retrograde steps of the P-T path.

DISCUSSION

Major element abundances of the studied sample indicate a protolith of MORB composition similar to other metabasite blocks from the La Corea mélange (Blanco-Quintero et al., 2010a). The P-T path followed by the amphibolite block was counter-clockwise for the initial stages of prograde-retrograde metamorphism (core > peak-1 > retro-1) and is consistent with the paths of other amphibolite blocks of eastern Cuba mélanges (García-Casco et al., 2008b; Lázaro et al., 2009; Blanco-Quintero et al., 2010a). These authors indicated that the thermal history of these blocks document onset of subduction of young oceanic lithosphere followed by exhumation in the subduction channel. Colder conditions during exhumation relates to cooling of the subduction system as subduction proceeded, involving development of the serpentinite subduction channel after hydration of the upper plate peridotite at <650 ºC by fluids released from the downgoing slab. Similar counter-clockwise P-T-t evolutions are predicted by thermal-mechanical models of nascent subduction systems followed by continued subduction and development of subduction channels (Gerya et al., 2002).

The second part of the P-T path (retro-1 > peak-2 > retro-2) is critical for understanding the geodynamic scenario. A key aspect is that the prograde growth of garnet (peak-2) indicates substantial reburial (ΔP = 6 kbar; Δdepth = 20 km) to depths similar to those that characterize peak-1 stage (i.e., accretion stage). Such a reburial excursion experienced by the studied block is possible due to a) collision, b) subduction erosion, or c) large-scale convective circulation of the subduction channel. The recurrent prograde-retrograde evolution described above contrasts with the simple prograde-retrograde P-T evolution of most blocks from eastern Cuba mélanges. This contrast invalidates collision and subduction erosion, for these scenarios would have produced similar complex P-T paths in most, if not all, blocks

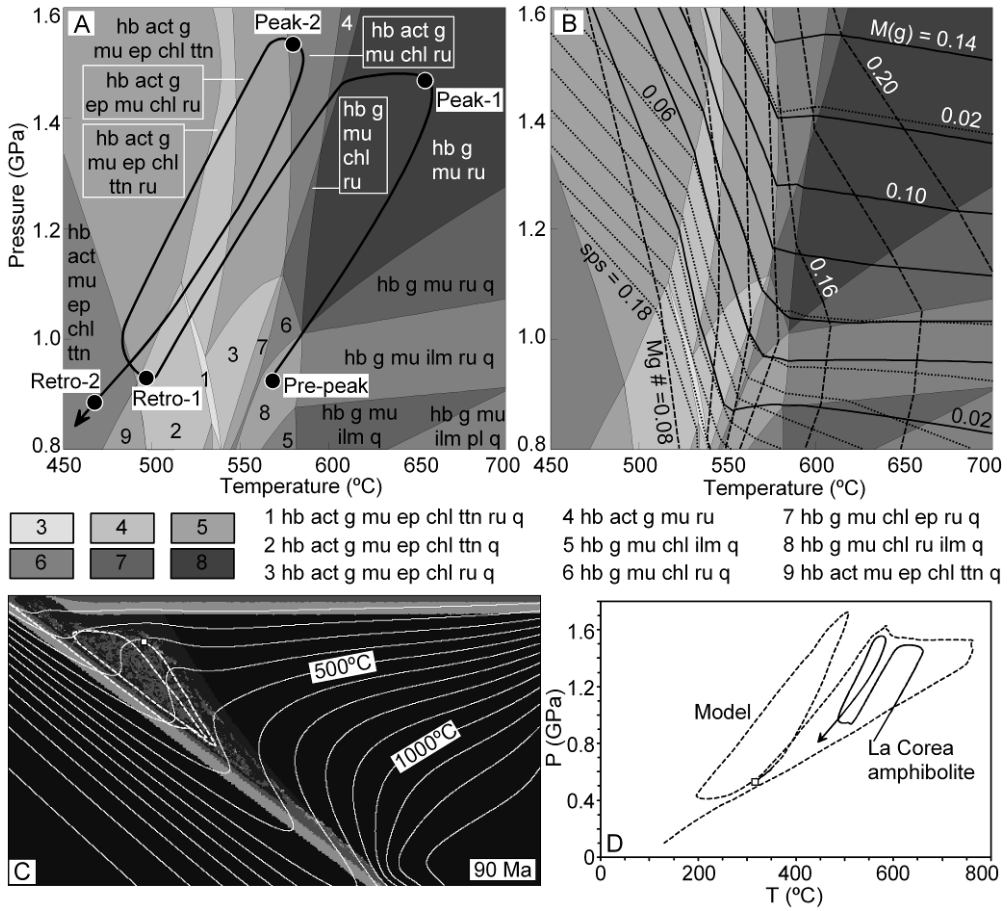

Figure 3. A: Isochemical P-T equilibrium phase diagram for the studied sample in the KNCFMMnASTHO system (SiO_2 = 47.06, Al_2O_3 = 8.32, TiO_2 = 1.85, Fe_2O_3 = 1.54, FeO = 11.32, MgO = 16.39, MnO = 0.23, CaO = 11.19, Na_2O = 1.88, K_2O = 0.23, percent molar units; excess H_2O is assumed). Mineral abbreviations are hb (hornblende), act (actinolite), g (garnet), ep (epidote), mu (muscovite), chl (chlorite), ru (rutile), ttn (titanite), ilm (ilmenite), pl (plagioclase), q (quartz). Color code indicates thermodynamic variance. The P-T trajectory calculated using mineral assemblages, garnet composition isopleths, and average P-T data is indicated. B: Isopleths of Mg# (dashed lines), spessartine (dotted lines) and modal abundance of garnet (solid lines). C: Thermo-mechanical model for subduction of young (20 m.y.) lithosphere with the geometry and the thermal structure of the subduction zone after 900 km of convergence at a subduction rate of 3 cm/y (i.e., 30 m.y. after onset of subduction). The sketch represents 110 X 100 km areas. For details of numerical model see table 1, model G; in Gerya et al. (2002). White marker shows the trajectory of a representative accreted oceanic crust fragment subjected to large-scale circulation in the channel. D: P-T path calculated for the representative oceanic crust fragment shown in C vs paths of amphibolite from La Corea mélange.

of the mélanges. Contrasted P-T histories, however, are expected for individual blocks flowing in a viscous dynamic medium of the channel (Cloos and Shreve, 1988a; Schwartz et al., 2001; Gerya et al., 2002; Gorzyck et al., 2007).

A second important aspect is that the temperature of peak-2 stage was lower than that of peak-1 stage, consistent with cooling of the subduction system with time. This process would permit the development of serpentinite after hydration of the upper plate mantle, expanding the channel in width and depth. Such expansion of ductile material makes feasible the convective flow of the channel and, hence, the

re-burial of circulating blocks to depths greater than those attained at the earlier accretion stage. Note that a total 100–150 °C cooling of the subduction channel suggested by the geometry of the P-T path (Fig. 3A) is at the lower limit of results of numerical experiments (Gerya et al., 2002) predicting 125–300 °C cooling of channel rocks in a few tens of Myrs after the onset of subduction (Fig. 3D).

Complex fluxes of material in the channel, including large-scale convective flow, are predicted by thermo-mechanical models of subduction zones (Gerya et al., 2002; Gorzyck et al., 2007). However, the expected petrological consequences of convective flow of blocks from subduction mélanges have not been previously documented. Oscillatory zoning of garnet reflecting possible prograde-retrograde fluctuations in the subduction environment was described by Dudley (1969) for the Franciscan Complex, García-Casco et al. (2002, 2006) for serpentinite mélanges from central and western Cuba, and Tsujimori et al. (2006) for serpentinite mélanges from Guatemala. Only García-Casco et al. (2002) interpreted these features, suggesting subtle P-T fluctuations related to tectonic forcing during subduction of oceanic material rather than to processes in the subduction channel. However, these and other similar examples, if properly identified as the result of complex flow in the channel, will provide further evidence for this important aspect of the dynamics of subduction systems.

ACKNOWLEDGMENTS

The authors thank the constructive reviews of W.G. Ernst and two anonymous reviewers and the comments of editor W. Collins. IFBQ and AGC were supported from Spanish MCINN project CGL2009-12446 and grant AP2005-5258 from the FPU Program of Spanish MEC, and TVG from Swiss NSF research grants 200020_129487, 200020_126832 and ETH research grants ETH-06 09-2, ETH-08 07-2. This is a contribution to IGCP-546 “Subduction zones of the Caribbean”.

REFERENCES

Bence, A.E., and Albee, A.L., 1968, Empirical correction factors for the electron microanalysis of silicate and oxides: The Journal of Geology, v. 76, p. 382–403, doi:10.1086/627339.

Blanco-Quintero, I.F., García-Casco, A., Rojas-Agramonte, Y., Rodríguez-Vega, A., Lázaro, C., and Iturralde-Vinent, M.A., 2010a, Metamorphic evolution of subducted hot oceanic crust (La Corea mélange, Cuba): American Journal of Science, In press.

Blanco-Quintero, I.F., Proenza, J.A., García-Casco, A., Tauler, E., and Galí, S., 2010b, Serpentinites and serpentinites within a fossil subdution channel: La Corea mélange, eastern Cuba: Geologica Acta. In press.

Cloos, M., and Shreve, R.L., 1988a, Subduction-channel model of prism accretion, melange formation, sediment subduction, and subduction erosion at convergent plate margins, 1, Background and description: Pure and Applied Geophysics, v. 128, p. 455–500, doi:10.1007/BF00874548.

Cloos, M., and Shreve, R.L., 1988b, Subduction-channel model of prism accretion, melange formation, sediment subduction, and subduction erosion at convergent plate margins, 2, Implications and discussion: Pure and Applied Geophysics, v. 128, p. 501–545, doi:10.1007/BF00874549.

Coggon, R., and Holland, T.J.B., 2002, Mixing properties of phengitic micas and revised garnet-phengite thermobarometers: Journal of Metamorphic Geology, v. 20, p. 683–696, doi:10.1046/j.1525-1314.2002.00395.x.

Diener, J.F.A., Powell, R., White, R.W., and Holland, T.J.B., 2007, A new thermo-dynamic model for clino- and orthoamphiboles in Na2O-CaO-FeO-MgO-Al2O3-SiO2–H2O-O: Journal of Metamorphic Geology, v. 25, p. 631–656, doi:10.1111/j.1525-1314.2007.00720.x.

Dudley, P.P., 1969, Electron microprobe analyses of garnet in glaucophane schists and associated eclogites: The American Mineralogist, v. 54, p. 1139–1150.

Enami, M., 1998, Pressure-temperature path of Sanbagawa prograde metamorphism deduced from grossular zoning of garnet: Journal of Metamorphic Geology, v. 16, p. 97–106, doi:10.1111/j.1525-1314.1998.00058.x.

Ernst, W.G., 1970, Tectonic contact between the Franciscan mélange and the Great Valley sequence-Crustal expression of a late Mesozoic Benioff zone: Journal of Geophysical Research, v. 75, p. 886–901, doi:10.1029/JB075i005p00886.

Ernst, W.G., 1988, Tectonic history of subduction zones inferred from retrograde blueschist P-T paths: Geology, v. 16, p. 1081–1084, doi:10.1130/0091-7613(1988)016<1081:THOSZI>2.3.CO;2.

García-Casco, A., Torres-Roldán, R.L., Millán, G., Monié, P., and Schneider, J., 2002, Oscillatory zoning in eclogitic garnet and amphibole, Northern Serpentinite Melange, Cuba: a record of tectonic instability during subduction?: Journal of Metamorphic Geology, v. 20, p. 581–598, doi:10.1046/j.1525-1314.2002.00390.x.

García-Casco, A., Torres-Roldán, R.L., Iturralde-Vinent, M.A., Millán, G., Núñez Cambra, K., Lázaro, C., and Rodríguez Vega, A., 2006, High pressure metamorphism of ophiolites in Cuba: Geologica Acta, v. 4, p. 63–88.

García-Casco, A., Iturralde-Vinent, M.A., and Pindell, J., 2008a, Latest Cretaceous collision/accretion between the Caribbean Plate and Caribeana: Origin of metamorphic terranes in the Greater Antilles: International Geology Review, v. 50, p. 781–809, doi:10.2747/0020-6814.50.9.781.

García-Casco, A., Lázaro, C., Torres-Roldán, R.L., Núñez Cambra, K., Rojas Agramonte, Y., Kröner, A., Neubauer, F., Millán, G., and Blanco-Quintero, I., 2008b, Partial melting and counterclockwise P-T path of subducted oceanic crust (Sierra del Convento mélange, Cuba): Journal of Petrology, v. 49, p. 129–161, doi:10.1093/petrology/egm074.

Gerya, T.V., Stoeckhert, B., and Perchuk, A.L., 2002, Exhumation of high-pressure metamorphic rocks in a subduction channel-a numerical simulation: Tectonics, v. 21, p. 6–1–6–19.

Ghent, E.D., 1988, A review of chemical zoning in eclogite garnets, in: Smith, D.C., ed., Eclogite and Eclogite-Facies Rocks, Developments in Petrology, 12, p. 207–236, Elsevier, Amsterdam.

Gorczyk, W., Guillot, S., Gerya, T.V., and Hattori, K., 2007, Asthenospheric upwelling, oceanic slab retreat and exhumation of UHP mantle rocks: insights from Greater Antilles: Geophysical Research Letters, v. 34, L211309, doi:10.1029/2007GL031059.

Guillot, S., Hattori, K., and Sigoyer de, J., 2000, Mantle wedge serpentinization and exhumation of eclogites: insights from eastern Ladakh, northwest Himalaya: Geology, v. 28, p. 199-202.

Guillot, S., Hattori, K., Sigoyer de, J., Nägler, T., and Auzende, A.L., 2001, Evidence of hydration of the mantle wedge and its role in the exhumation of eclogites: Earth and Planetary Science Letters, v. 193, p. 115-127.

Guillot, S., Hattori, K., Agard, P., Schwartz, S., and Vidal, O., 2009, Exhumation processes in oceanic and continental subduction contexts: a review, in: Lallemand, S., and Funiciello, F., eds., Subduction Zone Dynamics, p. 175–204, doi 10.1007/978-3-540-87974-9, Springer-Verlag Berlin Heidelberg.

Holland, T.J.B., and Powell, R., 1998, An internally consistent thermodynamic data set for phases of petrological interest: Journal of Metamorphic Geology, v. 16, p. 309–343.

Holland, T.J.B., and Powell, R., 2003, Activity-composition relations for phases in petrological calculations: an asymmetric multicomponent formulation: Contributions to Mineralogy and Petrology, v. 145, p. 492–501, doi:10.1007/s00410-003-0464-z.

Holland, T.J.B., Baker, J.M., and Powell, R., 1998, Mixing properties and activity-composition relationships of chlorites in the system MgO-FeO-Al2O3-SiO2–H2O: European Journal of Mineralogy, v. 10, p. 395–406.

Konrad-Schmolke, M., Handy, M.R., Babist, J., and O'Brien, P.J., 2005, Thermodynamic modelling of diffusion-controlled garnet growth: Contributions to Mineralogy and Petrology, v. 149, p. 181–195, doi:10.1007/s00410-004-0643-6.

Lázaro, C., García-Casco, A., Neubaurer, F., Rojas-Agramonte, Y., Kröner, A., and Iturralde-Vinent, M.A., 2009, Fifty-five-million-year history of oceanic subduction and exhumation at the northern edge of the Caribbean plate (Sierra del Convento mélange, Cuba): Journal of Metamorphic Geology, v. 27, p. 19–40, doi:10.1111/j.1525-1314.2008.00800.x.

Leake, B.E., Woolley, A.R., Arps, C.E.S., Birch, W.D., Gilbert, M.C., Grice, J.D., Hawthorne, F.C., Kato, A., Kisch, H.J., Krivovichev, V.G., Linthout, K., Laird, J., Mandarino, J.A., Maresch, W.V., Nickel, E.H., Rock, N.M.S., Schumacher, J.C., Smith, D.C., Stephenson, N.C.N., Ungaretti, L., Whittaker, E.J.W., and Touzhi, G., 1997. Nomenclature of amphiboles: Report of the Subcommittee on Amphiboles of the International Mineralogical Association, Commission on New Minerals and Mineral Names: American Mineralogist, v. 82, p. 1019-1037.

Pindell, J.L., Kennan, L., Maresch, W.V., Stanek, K.P., Draper, G., and Higgs, R., 2005, Plate-kinematics and crustal dynamics of circum-Caribbean arc–continent interactions: Tectonic controls on basin development in Protocaribbean margins, in: Avé Lallemant, H.G., and Sisson, V.B., eds, Caribbean–South American Plate Interactions, Venezuela: Geological Society of America, Special Papers 394, p. 7–52.

Powell, R., and Holland, T.J.B., 1994, Optimal geothermometry and geobarometry: The American Mineralogist, v. 79, p. 120–133.

Schumacher, R., Rötzler, K., and Maresch, W.V., 1999, Subtle oscillatory zoning in garnet from regional metamorphic phyllites and mica schists, western Erzgebirge, Germany: Canadian Mineralogist, v. 37, p. 381–402.

Schwartz, S., Allemand, P., and Guillot, S., 2001, Numerical model of the effect of serpentinites on the exhumation of eclogitic rocks: insights from the Monviso ophiolitic massif (Western Alps): Tectonophysics, v. 42, p. 193-206.

Shreve, R.L., and Cloos, M., 1986, Dynamics of Sediment Subduction, Melange Formation, and Prism Accretion: Journal of Geophysical Research, v. 91, p.10229-10245.

Somin, M.L., and Millán, G., 1981, Geology of the Metamorphic Complexes of Cuba: Nauka, Moscow, 219 p., (in Russian).

Tsujimori, T., Sisson, V.B., Liou, J.G., Harlow, G.E., and Sorensen, S., 2006, Petrologic characterization of Guatemalan lawsonite eclogite: Eclogitization of subducted oceanic crust in a cold subduction zone, in: Hacker, B., ed., Geological Society of America Special Paper, v. 403, p. 147–168.

Ulmer, P., and Trommsdorff, V., 1995, Serpentine stability to mantle depths and subduction-related magmatism: Science, v. 268, p. 858–861.

Wakabayashi, J., 1990, Counterclockwise P–T–t paths from amphibolites, Franciscan complex, California: relics from the early stages of subduction zone metamorphism: The Journal of Geology, v. 98, p. 657–680, doi:10.1086/629432.

White, R.W., Pomroy, N.E., and Powell, R., 2005, An in-situ metatexite-diatexite transition in upper amphibolite facies rocks from Broken Hill, Australia: Journal of Metamorphic Geology, v. 23, p. 579–602, doi:10.1111/j.1525-1314.2005.00597.x.

3- TIMING OF ONSET OF SUBDUCTION AND RATES OF EXHUMATION IN A SUBDUCTION CHANNEL: EVIDENCE FROM SLAB MELTS FROM LA COREA MÉLANGE (EASTERN CUBA)

I.F. Blanco-Quintero[(1)], Y. Rojas-Agramonte[(2)], A. García-Casco[(1,3)], A. Kroner[(2)], D.F. Mertz[(2)], C. Lázaro[(1)], J. Blanco-Moreno[(4)]

(1) Departamento de Mineralogía y Petrología, Universidad de Granada, Fuentenueva s/n, 18002-Granada, Spain

(2) Institut für Geowissenschaften, Universität Mainz, D-55099 Mainz, Germany

(3) Instituto Andaluz de Ciencias de la Tierra (CSIC-UGR), Fuentenueva s/n, 18002-Granada, Spain

(4) Departamento de Geología, Instituto Superior Minero-Metalúrgico, Las Coloradas s/n, 83329-Moa, Cuba

ABSTRACT

High pressure igneous rocks (tonalites and trondhjemites) formed after partial melting of subducted MORB occur in the serpentinite-matrix La Corea mélange (eastern Cuba) as m- to cm-sized blocks and concordant to crosscutting veins within high-P amphibolite blocks. The slab melts have adakitic signatures, in agreement with formation after partial melting of metabasite. Thermobarometric calculations indicate 620-680 ºC and 13-15 kbar during crystallization of magmatic rocks and down to 250-300 ºC, 6 kbar during retrogression, indicating counter-clockwise P-T paths. Free water needed for melting of amphibolite at moderate temperature (700-750 ºC) close to the wet basaltic solidus is inferred to have been provided after dehydration of sediments, altered basaltic crust and serpentinite of the subducting Proto-Caribbean lithosphere. Single zircon (SHRIMP) and phengite Ar-Ar geochronologic data constrain the P-T-t evolution of the mélange from the timing of crystallization of melts at ~110-105 Ma to cooling at ~83-86 Ma, ca. 350 ºC, ca. 9 kbar. These figures are in agreement with previous data and proposals for onset of subduction of young oceanic lithosphere shortly before 115 Ma. However, the data are also consistent with subduction of an oblique ridge, irrespective of the timing of onset of subduction in the Caribbean region. Furthermore, our data indicate very slow exhumation (ca. 1 mm/yr) in the subduction channel during the oceanic convergence stage (120-70 Ma) until final fast exhumation to the surface took place at 70-65 Ma during a regional arc-platform collision event.

Keywords: SHRIMP age, slow exhumation, onset of subduction, Caribbean plate

INTRODUCTION

The evolution of subduction zones can be conceptualized by means of three main phases: onset of subduction, mature stage and demise of subduction. Ancient and recent structures and rock complexes allow a good characterization and recognition of the mature (i.e., volcanic arc development, formation of eclogites and blueschists) and demise (by means of arc-continent, arc-arc, or arc-ocean collision, with termination of volcanic arc activity and emplacement of ophiolites) stages. However, the onset of subduction stage is, by far, less well known because of the intrinsic complexities of this transient stage. It is unclear how subduction zones are initiated (cf. Stern, 2002, 2004).but also, rocks and structures formed during the earliest stage of subduction will normally disappear in the subduction channel and therefore not commonly preserved in the surface.

According to Stern (2004) the onset of subduction is generated either by convergence of lithospheric plates and blocking of a subduction zone by incoming buoyant continental or oceanic crust (induced onset of subduction) or by gravitational collapse of oceanic lithosphere (spontaneous onset of subduction). Transference or polarity reversal of subduction characterizes the induced type, while the spontaneous type occur at a passive margin or at a transform/fracture zone normally if the downgoing plate is old (i.e., cold and dense). Distinguishing these types and sub-types of onset of subduction is difficult. Compression (and uplift) and extension (and rifting) in the upper plate characterize the induced and spontaneous types, respectively. Compression in the induced type may generate metamorphism and ductile deformation of the incoming buoyant continental/oceanic crust, the pre-existent volcanic arc and its continental/oceanic basement and the fore-arc. On the other hand, in the spontaneous type, extension and rifting in the upper plate generates tholeiitic and boninitic rocks in the arc/fore-arc by means of sea-floor spreading triggered by the rise of asthenosphere predating plate convergence (i.e., mature stage). Both types of onset of subduction are characterized by warm-hot geothermal gradients (relative to mature subduction) along the subduction interface, but spontaneous initiation of subduction of old lithosphere should be characterized by relatively colder conditions. In both types, however, subducted rocks accreted to the upper plate during the early stages of subduction show counter-clockwise PT paths during exhumation due to the effects of continued refrigeration of the subduction system during the mature stage, while subducted rocks accreted during the mature stage follow hairpin P-T paths (Ernst, 1988; Wakabayashi, 2004, Gerya et al., 2002).

During the onset of subduction stage, the fluids that evolved from subducted sediments, altered basaltic crust and serpentinitic abyssal peridotite start fluxing the upper plate. Much of the upper plate mantle is characterized at this stage by hydrous peridotite, for temperature at relatively shallow depth is above the stability field of antigorite (> 650 ºC; Ulmer and Trommsdorff, 1995), but antigorite serpentinite forms in the upper plate mantle down to ca. 100 km depth upon continued subduction and refrigeration during the mature stage. This process triggers the formation of a buoyant serpentinitic subduction channel at the plate interface which provides the medium for syn-subduction exhumation of high-pressure accreted rocks (Guillot et al., 2000; 2001; Gerya et al., 2002). Hence, exhumation of high-pressure rocks accreted to the upper mantle during the onset of subduction is delayed until the

mature stage when the subduction channel is formed. This has important consequences, for early accreted rocks undergo near-isobaric cooling at the upper plate before exhumation in the channel starts (i.e., counter-clockwise PT paths).

Serpentinitic mélanges bearing high-pressure blocks are commonly considered exhumed fragments of subduction channels (Guillot et al., 2000; 2001; Agard et al., 2009). In these melanges, the timing of exhumation of subducted mafic oceanic crust relative to the onset of subduction is highly variable, ranging from early to late and from slow to fast, though it appears that in most cases the exhumation is episodic (Agard et al., 2009). In the northern Caribbean (Fig. 1a), high-pressure blocks from serpentinitic melanges record a protracted history of subduction and continued exhumation enduring ca. 60 Myrs, from onset of subduction until final exhumation to the Earth's surface (Krebs et al., 2008; Lázaro et al., 2009). Early subducted rocks record high geothermal gradient along the plate interface during the onset of subduction stage. I In eastern Cuba, the Sierra del Convento and the La Corea melanges (Fig. 1b), record the uncommon case of partial melting of the subducted basaltic crust at relatively shallow depth (ca. 50 km), documenting very hot conditions related to subduction of very young lithosphere or even a ridge (García-Casco et al., 2008a; Lázaro and García-Casco, 2008; Blanco-Quintero et al., 2010a and b). Such a young age of the subducting lithosphere would indicate induced rather than spontaneous onset of subduction. Lázaro et al. (2009) dated blocks of high-pressure amphibolite and associated tonalitic-trondhjemitic rocks formed after partial melting of the latter and offered a comprehensive P-T-t path for one of these melanges (the Sierra del Convento mélange). These data indicate that onset of exhumation was delayed ca. 10 myr. since accretion of subducted crust took place, and that syn-subduction exhumation in the channel was continued during ca. 40 Ma and very slow (0.7 mm/yr). In this paper, we report new petrological, geochemical and geochronological (SHRIMP zircon and phengite $^{40}Ar/^{39}Ar$) data of tonalite-trondhjemite rocks of the La Corea mélange (eastern Cuba) in order to provide clues for deciphering the nature and age of hot, deep-seated processes that occurred during onset of subduction of oceanic lithosphere in the Caribbean realm.

GEOLOGICAL SETTING

The Greater Antilles fold and thrust belt accreted to the southern margin of the North American plate in the Tertiary (Fig. 1a). It evolved during the Mesozoic-Tertiary along the northern edge of the Caribbean plate margin, where Proto-Caribbean (i.e., Atlantic) lithosphere was consumed and a complex intraoceanic volcanic arc (or arcs) evolved. Onset of subduction of the Proto-Caribbean has been inferred to have occurred as a consequence of polarity reversal (implying induced onset of subduction), but the timing of this process remains unclear. Pindell et al. (2005, 2006), Pindell and Kennan (2009), Krebbs et al. (2008), Lázaro et al. (2009), among others, suggested an Albian age (ca. 120 Ma), while Duncan and Hargraves (1984), Burke (1988) and Kerr et al. (2003), among others suggest an Upper Cretaceous age (ca. 85 Ma).

The eastern Cuba block (Meyerhoff and Hatten, 1968), between the Nipe-Guacanayabo and the Oriente faults, is representative of the Greater Antilles geology. It includes several tectonic units of different paleogeographic and paleotectonic environments like including fragments of the Caribeana terrane

(Asunción terrene), the Mayarí-Baracoa ophiolitic belt (MBOB), subduction-related metamorphic complexes (La Corea and the Sierra del Convento mélanges), two different volcanic arcs complexes of Cretaceous and Paleogene age, respectively, and syn- and post-orogenic sedimentary deposits (Cobiella et al., 1977, 1984; Iturralde-Vinent, 1998; García-Casco et al., 2006, 2008b). The rocks and the geological evolution of the eastern Cuba block have been correlated with northern Hispaniola (e.g., Iturralde-Vinent and MacPhee, 1999).

Island arc Cretaceous arc units occur in the area with tholeiitic and calc-alkaline mafic to felsic chemical compositions (Iturralde-Vinent et al., 2006; Proenza et al., 2006). The Purial volcanic complex, located to the south and tectonically below the Moa-Baracoa ophiolitic massif (Cobiella et al., 1984; Millán, 1996; Fig 1b), contains rocks with tholeiitic and calc-alkaline signatures metamorphosed to high pressure/low temperature (Boiteau et al., 1972; Cobiella et al., 1977; Somin and Millán, 1981; Millán et al., 1985), suggesting subduction erosion processes in the region. From the stratighraphic point of view the age of the arc was estimated from early (Aptian-Albian) to late (Campanian) Cretaceous (Iturralde-Vinent et al., 2006), while the age of high-pressure metamorphism is latest Cretaceous (García-Casco et al., 2006, 2008b and references therein).

The Mayarí-Baracoa ophiolitic belt is formed by two massifs, the Mayarí-Cristal to the west and the Moa-Baracoa to the east (Fig. 1b). It includes volcanic, cumulate gabbroic and highly depleted ultramafic rocks with supra-subduction geochemical signatures (Proenza et al., 2006; Marchesi et al., 2007) that formed at a back-arc spreading centre (Marchesi et al., 2006). The ultramafic rocks are highly serpentinized by seawater alteration during the oceanic stage (Proenza et al. 2003). Thrusting of the ohiolitic bodies over the volcanic arc units occurred in the Late Campanian-Maastrichtian (Iturralde-Vinent et al., 2006). This collision process is marked by the age of syn-tectonic sediments (La Picota and Micara Formations) deposited during the emplacement of the ophiolites on top of the Cretaceous volcanic arc.

Serpentinite-matrix mélanges containing subduction-related metamorphic blocks (La Corea and Sierra del Convento mélanges) appear at the bottom of the ophiolite sheets. The La Corea mélange is related to the Mayarí-Cristal ophiolite massif and is tectonically located between the latter (top) and the Cretaceous Santo Domingo volcanic arc formation (bottom). The mélange represents a section of the Caribbean Cretaceous subduction channel which experienced partial melting in the subducted slab (Blanco-Quintero et al., 2010a). Exotic blocks of various origins and compositions (garnet-amphibolite, blueschist and greenschist) occur within a serpentinite-matrix. Foliated fine to medium grained epidote±garnet amphibolite is the predominant rock type within the mélange (Fig. 2a). Geochemical data indicate N-MORB signature of the amphibolites (Blanco-Quintero et al., 2010a). The serpentinitic matrix of the mélange is mainly composed of antigorite (94 %) formed after hydration of the mantle wedge by fluids released from the slab (Blanco-Quintero et al., 2010b). Blocks of serpentinite bearing antigorite-lizardite and clinopyroxene (relictic and deformed) represent abyssal rocks incorporated from the incoming plate into the subduction channel at shallow depths (Blanco-Quintero et al., 2010b).

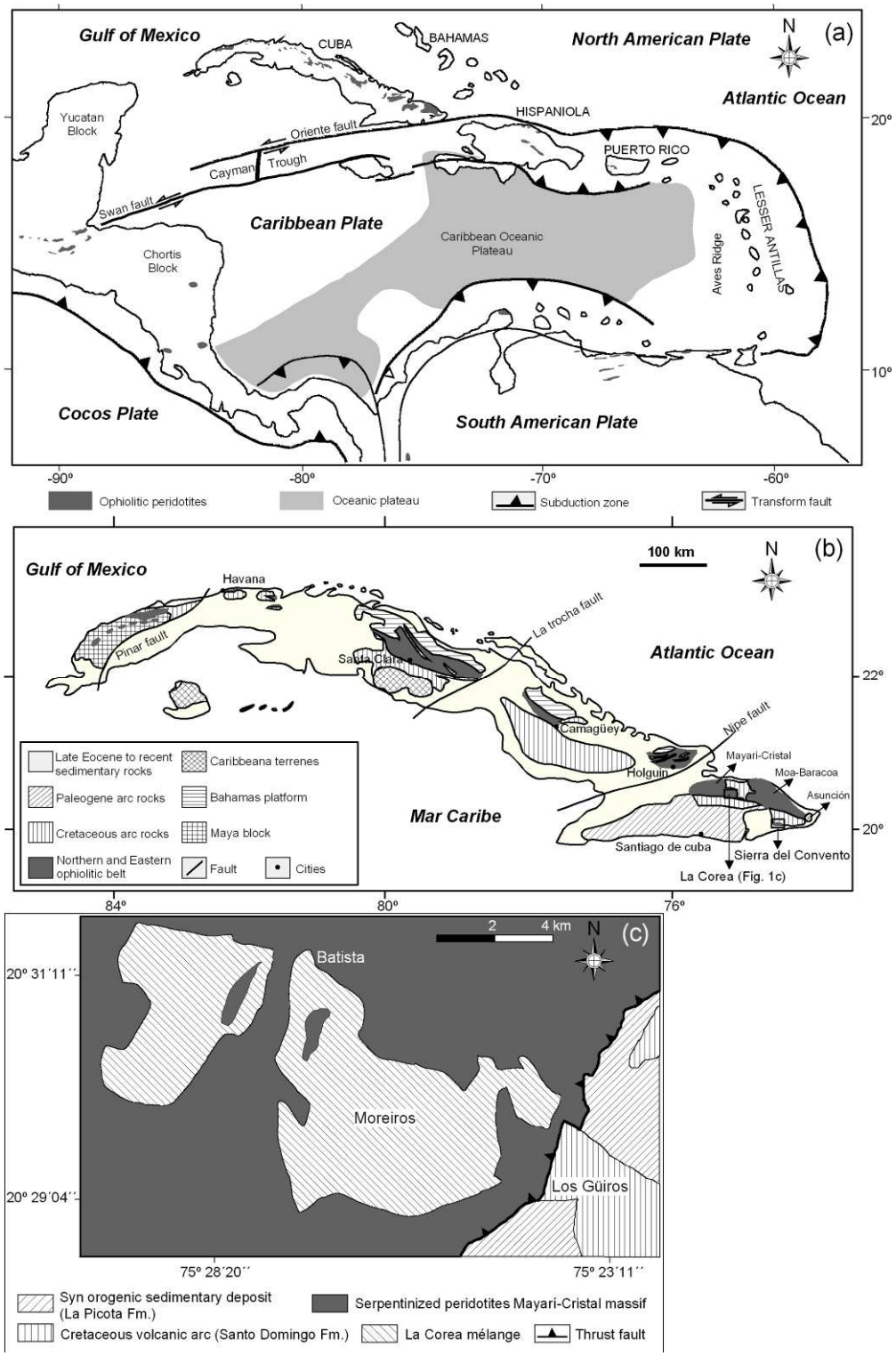

Figure 1. a) Plate tectonic configuration of the Caribbean region, including ophiolitic bodies. b) General geologic map of Cuba (after Iturralde-Vinent, 1998) showing the main geological units. c) Geologic map of the La Corea mélange (after Leyva, 1996).

Dikes and veins of intermediate to acid (tonalitic-trondhjemitic-granitic) composition occur intimately associated with the amphibolites showing concordant to crosscutting relationships relative to the main foliation of the amphibolites (Fig. 2a-d). The leucocratic rocks can be separated in two groups: 1) Medium grained tonalitic-trondhjemitic rocks, bearing the primary (magmatic) assemblage Pl+Qtz+Ep+Ms±Amp and overprinted by retrograde Chl+Ms+Czo+Ab±Lws, and 2) Granitic rocks, commonly pegmatitic, composed by magmatic Pl+Qtz+Ms crosscut by quartz-veins.

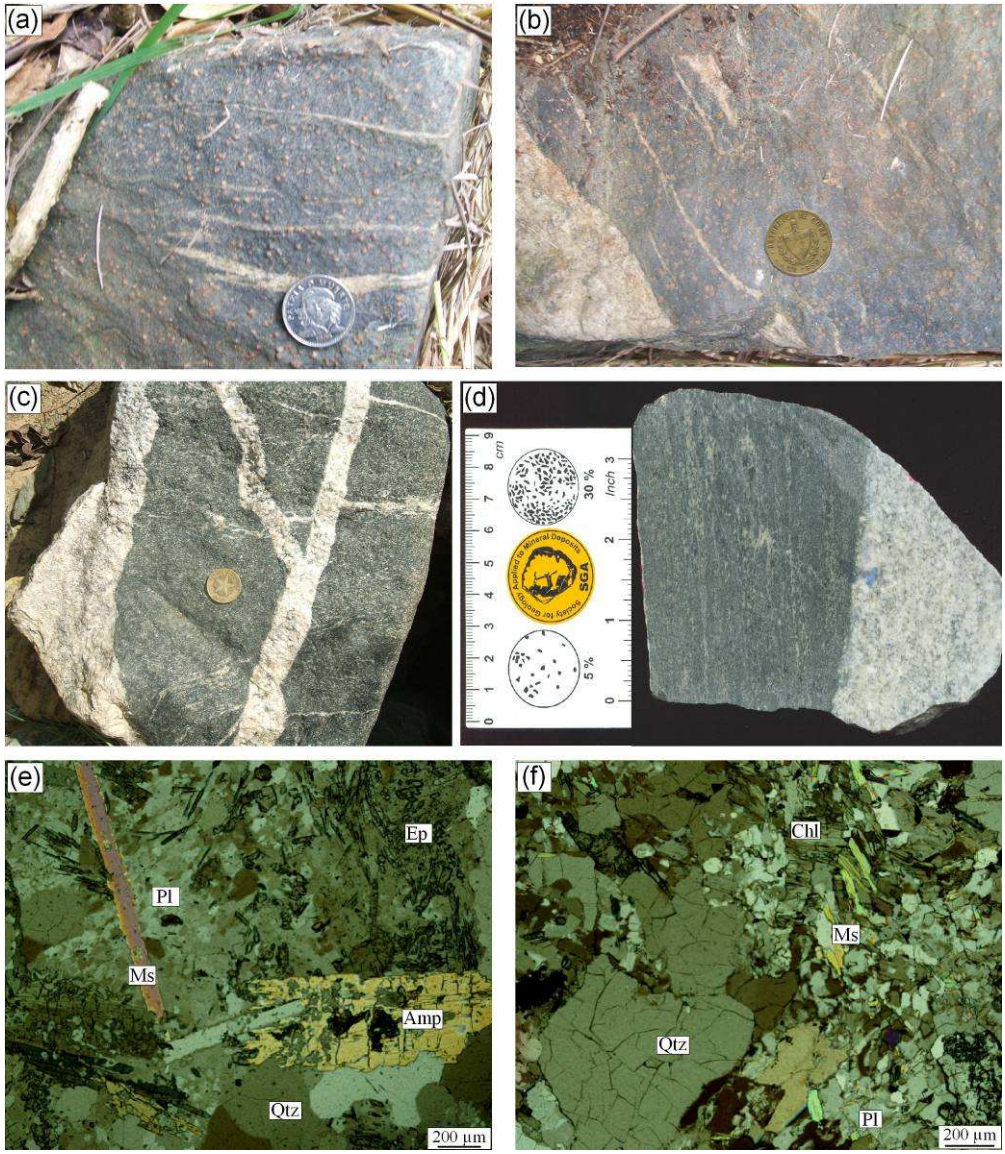

Figure 2. Field relations and textures of studied rocks. a) Trondhjemite veins parallel to foliation crosscutting garnet amphibolite. b) Trondhjemite dike crosscutting amphibolite. c) Different generations of trondhjemite dikes crosscutting amphibolite. d) Sheared trondhjemite and amphibolite. e) Microphotograph showing trondhjemite with magmatic amphibole, quartz and muscovite, and retrograde fine-grained epidote and albite formed after plagioclase, f) Trondhjemite with magmatic quartz and retrograde muscovite and chlorite.

Geochronologic data from the La Corea mélange are scarce and imprecise. Somin and Millán (1981) reported K-Ar ages of 104±12 and 67±7 Ma on blocks of metacherty material and Adamovich and Chejovich (1964) and Somin and Millán (1981) reported K-Ar ages on pegmatites of 125±5 and 119±10 Ma, and an age of unknown rock type of 96±4 Ma. These ages were interpreted as the age of metamorphism.

ANALYTICAL TECHNIQUES

Microprobe analyses

Mineral compositions (Tables 1-5) were obtained by WDS with a CAMECA SX-100 microprobe (University of Granada) operated at 15 kV and 15 nA. Amphibole compositions were normalized following the procedures of Leake et al. (1997), and Fe^{3+} was estimated after the method of Schumacher (in Leake et al., 1997). Epidote, lawsonite and feldspar were normalized to 12.5, 8 and 8 oxygens, respectively, and $Fe_{total}=Fe^{3+}$. White mica and chlorite were normalized to 22 and 28 oxygen, respectively, and $Fe_{total} = Fe^{2+}$. Mineral and end member abbreviations are after Kretz (1983), except for amphibole (Amp). The atomic concentration of elements per formula units is abbreviated apfu. The Mg-number of minerals (Mg#) is expressed as $Mg/(Mg+Fe^{2+})$. Software CSpace (Torres-Roldán et al., 2000) was used to calculate ternary phase diagrams.

Elemental X-ray images were obtained with the same CAMECA SX-100 microprobe of Granada University operated at 20 kV, 150 nA beam current, with step (pixel) size of 4-5 µm and counting time of 30 ms. The images were processed with Imager software (Torres-Roldán and García-Casco unpublished) and consist of the X-ray signals of Kα lines of the elements (colour coded; expressed in counts) and corrected for 3.5 µs deadtime. The X-ray spectra of these images were clipped to show the mineral of interest and set on top of a black and white "Z" image calculated by the sum of the products of the counts/nA/s by atomic number (Si, Ti, Al, Fe, Mn, Mg, Ca, Na, Ba, K, P, F and Cl) to show the basic textural relations of the scanned areas.

Major and trace element analysis

Major and trace elements were carried out at the Centro de Instrumentación Científica (CIC) of the University of Granada. Major elements and Zr compositions were determined in a PHILIPS Magix Pro (PW-2440) X-ray fluorescence (XRF) equipment using a glass beads, made of 0.6 g of powdered sample diluted in 6 g of $Li_2B_4O_7$. Trace elements, except Zr, were determined by ICP-MS after HNO_3 + HF digestion of 100 mg of sample powder in a Teflon-lined vessel at ~180ºC and ~200 p.s.i. for 30 min, evaporation to dryness, and subsequent dissolution in 100 ml of 4 vol % HNO_3. All major (wt %) and trace (ppm) elements analysis are shown in Table 6. The major element analyses were recalculated to an anhydrous 100 wt % basis, and these new results are used in the text and figures.

SHRIMP analytical procedure and cathodoluminescence imaging

Zircons were obtained from fresh samples (~ 5 kg) that were processed in the Institüt für Geowissenschaften at Mainz University. The samples were crushed and

zircons were separated after using the Franz magnetic separator and heavy liquid separation techniques.

Cathodoluminescence (CL) images of the dated zircons were obtained prior to SHRIMP analysis to distinguish between different zircon domains. Reconnaissance CL imaging of zircon crystals was undertaken in the Center for Microscopy and Microanalyis at the University of Western Australia, Perth, on a JEOL 6400 scanning electron microscope (SEM), operating at 15 kV accelerating voltage and 5 nA beam current.

The U–Pb ion microprobe data for the analyzed samples were obtained on the SHRIMP II (B), of the John de Laeter Center of Mass Spectrometry at Curtin University, Australia (De Laeter and Kennedy 1998). Clear euhedral zircons some 100 to 250 µm in length were handpicked and mounted in epoxy resin together with chips of the Perth zircon standard CZ3. For data collection, six scans through the critical mass range were made, and counting times on individual masses at both instruments were $^{196}Zr_2O$ = 2s, ^{204}Pb = 10s, background = 10s, ^{206}Pb = 20s, ^{207}Pb = 30s, ^{208}Pb = 10s, ^{238}U = 10s, ^{248}ThO = 5s and ^{254}UO = 2s. Further details on technique can be found in Compston et al. (1992), Stern (1997), Nelson (1997) and Williams (1998).

Precise dating of young zircons by ion-microprobe is best achieved by using $^{206}Pb/^{238}U$-ages because they are more precise than $^{207}Pb/^{235}U$-ages due to the extreme depletion of ^{235}U compared to 238U. Also $^{207}Pb/^{206}Pb$-ages are quite imprecise because the concordia curve is nearly parallel to a line through the origin (also see Black et al. 2003, for more explanation). The reduced $^{206}Pb/^{238}U$ ratios were normalized to CZ3 ($^{206}Pb/^{238}U$ = 0.09432, age: 564 Ma). Primary beam intensity was about 2.8 nA and a Köhler aperture of 100 µm diameter was used, giving a slightly elliptical spot size of about 25 µm. Peak resolution was between 5100 and 5500, enabling clear separation of the 208Pb-peak from the nearby HfO_2-peak. Sensitivity was about 26 cps/ppm/nA Pb on the standard CZ3. Analyses of samples and standards were alternated to allow assessment of Pb+/U+ discrimination. Raw data reduction followed the method of Nelson (1997). Common-Pb corrections were applied using the ^{204}Pb-correction method. Errors on individual analyses are given at the 1-sigma level and are based on counting statistics and include the uncertainty in the standard U/Pb age (Nelson 1997). Errors for pooled analyses are at the 2-sigma or 95% confidence interval. The data are graphically presented on conventional concordia plots (Fig. 9) and Table 7.

40Ar/39Ar analytical procedure

Three hand-picked white mica separates (grain size fraction 355 to 250 µm) were analyzed using the $^{40}Ar/^{39}Ar$ dating technique. The separates wrapped in copper foil were loaded in wells in aluminium discs and irradiated in the cadmium shielded port (CLICIT) at the Oregon State University TRIGA (OSTR) reactor and analyzed at the Berkeley Geochronology Center. Values of J (a measure of fast neutron fluence) were determined from single-crystal laser fusion analyses of co-irradiated Fish Canyon sanidines (n = 10) based on an age of 28.02 Ma for the sanidine (Renne et al. 1998). Corrections for interfering nucleogenic isotopes of Ar from Ca, K and Cl were made using the values given by Renne et al. (2005, 2008) for the OSTR CLICIT. The separates were baked out at ca. 200 °C for about 15 hours prior to

analysis and heated incrementally with a CO_2 laser with an integrator lens by 16 temperature steps. After removing reactive components as H_2O or CO_2 by Zr-Al getters, the purified gas was analyzed using a Mass Analyser Products 215-50 mass spectrometer, configured for a mass resolution of 450. Mass discrimination was determined from repeated analyses of air Ar using an on-line pipette, yielding a mean value of 1.0075 ± 0.0019/atomic mass unit (n = 16) during the measuring period. Mass discrimination was determined using a power-law relationship (e.g., Renne et al. 2009) with reference to atmospheric $^{40}Ar/^{36}Ar$ = 295.5 (Steiger and Jäger 1977). A more recent determination of atmospheric $^{40}Ar/^{36}Ar$ by Lee et al. (2006) is considered more accurate, but was not used in this study because (i) it has not yet been formally adopted by the geochronology community and (ii) the effects are negligible in the present cases because the effects of changes in mass discrimination and air correction are almost entirely cancelled (Renne et al. 2009). Blank corrections were applied as described by Sharp et al. (1996). The decay constants and isotopic ratios used are those given by Steiger and Jäger (1977). Uncertainties for ages are given at the 1σ level and include errors arising from Ar isotope abundances and corrections for blanks, radioactive decay and interfering nuclear reactions but do not include errors in ^{40}K decay constants, the age of the standard, or isotopic abundances of K. The data are presented in Table 8 and Fig. 10.

PETROGRAPHY AND MINERALOGY

Petrography

The studied samples are trondhjemitic in composition composed by medium-grained plagioclase and quartz with magmatic textures (Fig. 2e, f). These minerals make more than 75% of the modal mineralogy of the samples. In general, they are not deformed, though sample LCG-2 has a strong foliation. Subordinate epidote, muscovite and amphibole are present (Fig. 2e, f). Apatite, titanite and rutile are present in small amounts. Magmatic (clino)zoisite is idiomorphic with faint zonation. Magmatic muscovite crystals reach sizes of more than 1 mm (Fig. 2e).

Retrograde overprints on plagioclase consist of combinations of epidote/(clino)zoisite, lawsonite, albite, K-feldspar, and phengite (Fig. 2f). Small retrograde crystals of (clino)zoisite and phengitic mica are dispersed in the matrix, associated with retrograde albite. Chlorite replaces amphibole, being colourless (high Mg contents, see below). Titanite replaces rutile forming discrete rims around the latter.

Mineral Chemistry

Amphibole

Amphiboles are calcic in composition, with (Na+K)A ranging between 0.04-0.44 apfu, typical of actinolite-magnesiohornblende series (Fig. 4a). Magnesiohornblende compositions typically occur in the relictic magmatic cores of the crystals. As would

Figure 3. X-ray images showing textures and mineral composition of La Corea trondhjemites. a) Si and b) Al in amphibole showing from core to rim retrograde zoning. c) Al and d) Ca in plagioclase and epidote group minerals showing the very low contents of Ca in the plagioclase (purple) and the intimately relations between these phases. e) Mg and f) Si in phengite showing zoning in celadonite component. Color code scale bar represent counts.

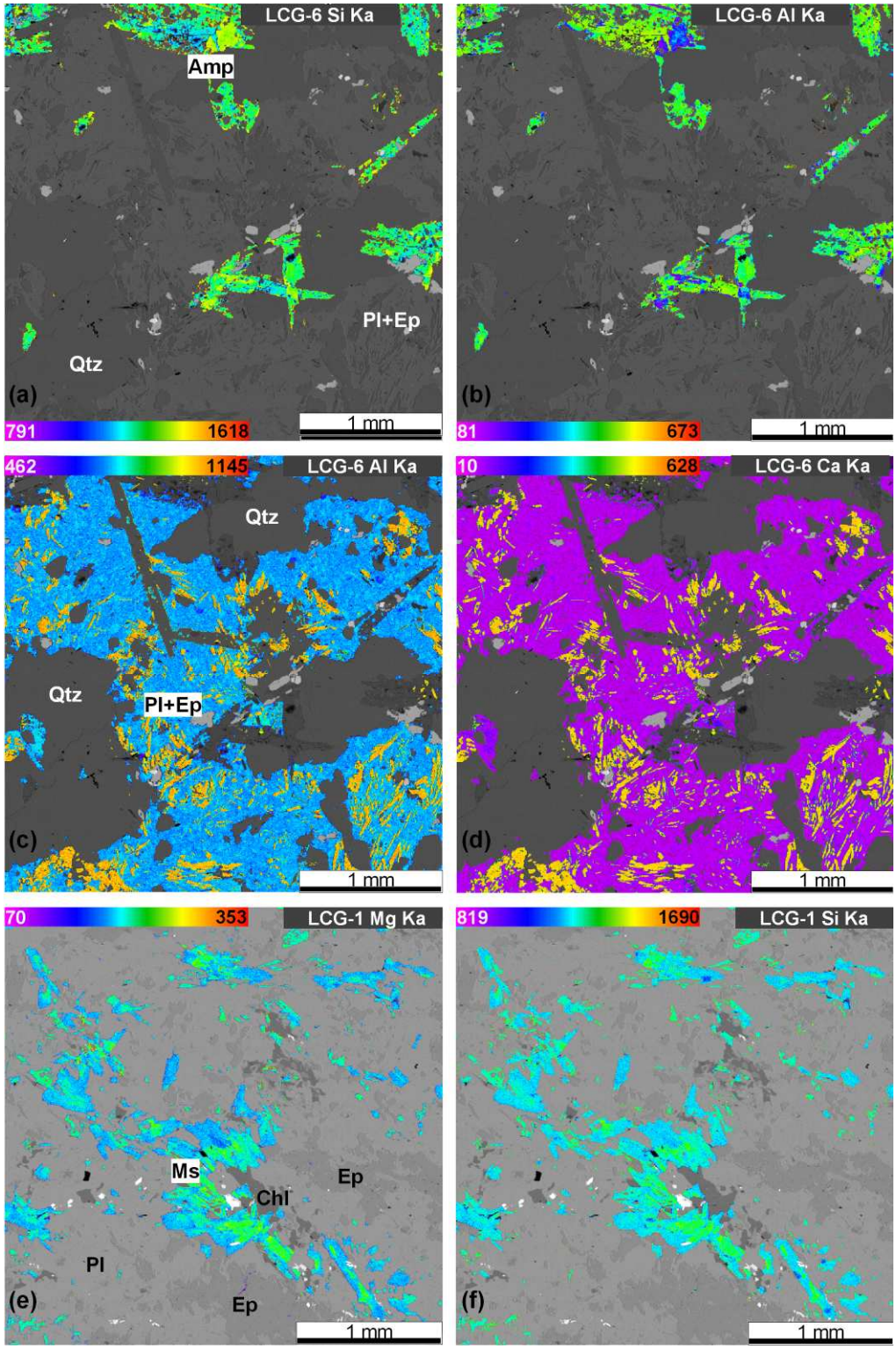
LCG-6 Si Ka
Amp
Pl+Ep
Qtz
(a)
791
1618
1 mm
LCG-6 Al Ka
(b)
81
673
1 mm
462
1145
LCG-6 Al Ka
Qtz
Qtz
Pl+Ep
(c)
1 mm
10
628
LCG-6 Ca Ka
(d)
1 mm
70
353
LCG-1 Mg Ka
Ms
Ep
Chl
Pl
(e)
Ep
1 mm
819
1690
LCG-1 Si Ka
(f)
1 mm

be expected Ti shows negative correlation with Si, while Mg# shows positive correlation (Fig. 4). The composition of magmatic magnesiohornblende is characterized by Si and Mg# down to 6.63 apfu and 0.66, respectively, while NaA, Al, and Ti reach up to 0.31, 2.35 and 0.07 apfu, respectively (Table 1). The actinolitic compositions reach Si and Mg# up to 7.83 apfu and 0.77, respectively, while Al reach down to 0.29 apfu.

Epidote

(Clino)Zoisite is the most common mineral, composed with very low pistacite contents (Xps = Fe3+/[(Al+Fe3+)] ranging from 0.01 to 0.06 (Table 2) with some samples with values above 0.12. (Clino)Zoisite zoning is faint, and no characteristic zoning was detected.

Feldspar

The major proportion of plagioclase is albitic, (Xab > 0.86), with most analyses reaching Xab > 0.99 (Table 3) as a result of retrogression of magmatic plagioclase. In sample LCG-12, relicts of magmatic plagioclase within albite-(clino)zoisite-phengite replacements show high calcium contents (XAn = 0.46).

The chemical composition of fine-grained disseminated crystals of K-feldspar overprinting plagioclase corresponds to orthoclase Xor > 0.99 (Table 3).

White mica

Potassic white mica, termed here phengite, is muscovite-phengite in composition, with Si ranging 6.24-6.99 apfu (Table 4). The relictic magmatic cores have higher Ti (up to 0.07 apfu) and Na (up to 0.49 apfu) contents indicating high temperature and pressure during crystallization (Fig. 3e, f, Fig. 5). Ba-contents are low, but locally the cores show enrichments (max. 0.06 apfu). The chemical variations are the result of the tschermak $(Mg,Fe)Si(^{VI}Al^{VI}Al)_{-1}$; and celsian $(BaAl)(SiK)_{-1}$ exchange vectors (cf. Blanco-Quintero et al., 2010c).

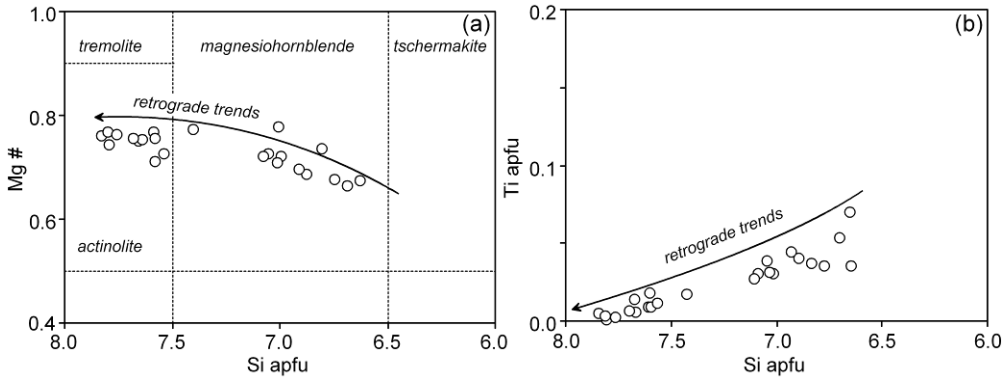

Figure 4. Composition of calcic amphibole with indication of retrograde trends. a) Si versus Mg#. b) Ti versus Si. Classification scheme from Leake et al. (1997).

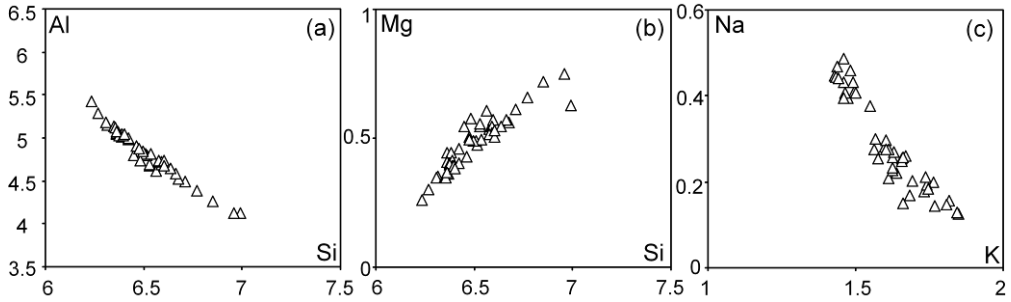

Figure 5. Composition of muscovite-phengite. a) Si versus Al. b) Si versus Mg. c) K versus Na.

Other minerals

Chlorite is magnesian (Mg# = 0.62-0.76), with Si and Al ranging 5.50-6.11 and 4.60-5.11 apfu; respectively (Table 5). Lawsonite is almost pure and does not display chemical variation (Table 2).

P-T PATHS

Two different methods were used to determine P-T conditions, namely the average P-T method (for samples LCG-1, LCG-6 and LCG-12) and an isochemical P-T projection for a representative bulk rock composition (sample LCG-3) using software THERMOCALC, version 3.31 and dataset 5.5 (Holland and Powell, 1998. The average P-T method was used on the principal assemblages for peak crystallization and retrograde conditions during exhumation. The peak assemblage used was Amp+Ep+Pl+Ms+Qtz. For retrograde conditions the assemblage used was

Table 1: Representative analyses of amphibole (normalized to 22 O and 2 OH).

Mineral	Amp	Amp	Amp	Amp	Amp	Amp	Amp	Amp
Type	Mhb	Mhb	Mhb	Mhb	Tr	Tr	Tr	Tr
SiO_2	45.92	47.41	48.65	46.54	55.43	53.86	52.89	53.71
TiO_2	0.64	0.37	0.29	0.32	0.05	0.13	0.17	0.05
Al_2O_3	13.79	10.76	9.63	12.49	1.72	3.67	4.53	3.50
Cr_2O_3	0.03	0.01	0.03	0.00	0.01	0.01	0.03	0.00
FeO_{tot}	11.58	11.51	11.20	12.17	10.49	10.56	11.94	11.04
MnO	0.16	0.19	0.16	0.25	0.16	0.19	0.18	0.15
MgO	11.98	13.18	13.87	12.23	17.42	16.36	15.04	16.43
CaO	10.45	11.45	11.56	10.71	12.35	11.99	11.47	11.83
Na_2O	2.33	1.91	1.58	2.14	0.40	0.77	1.03	0.78
K_2O	0.66	0.34	0.41	0.28	0.05	0.09	0.10	0.08
Sum	97.74	97.38	97.58	97.41	98.28	97.79	97.57	97.78
Si	6.63	6.88	7.01	6.74	7.83	7.66	7.58	7.64
Ti	0.07	0.04	0.03	0.03	0.01	0.01	0.02	0.01
Al	2.35	1.84	1.64	2.13	0.29	0.61	0.77	0.59
Cr	0.00	0.00	0.00	0.00	0.00	0.00	0.00	0.00
Fe^{3+}	0.16	0.10	0.12	0.20	0.09	0.11	0.12	0.17
Fe^{2+}	1.24	1.30	1.23	1.27	1.15	1.15	1.31	1.14
Mn	0.02	0.02	0.02	0.03	0.02	0.02	0.02	0.02
Mg	2.58	2.85	2.98	2.64	3.67	3.47	3.21	3.48
Ca	1.62	1.78	1.79	1.66	1.87	1.83	1.76	1.80
Na	0.65	0.54	0.44	0.60	0.11	0.21	0.29	0.22
K	0.12	0.06	0.08	0.05	0.01	0.02	0.02	0.01
#Mg	0.68	0.69	0.71	0.68	0.76	0.75	0.71	0.75

Table 2: Representative analyses of (clino)zoisite and lawsonite (normalized to 12 O and 1 OH, and 8 O, respectively).

Mineral	(C)Zo	(C)Zo	(C)Zo	(C)Zo	Lws	Lws
SiO_2	39.35	39.42	37.10	39.27	38.89	38.59
TiO_2	0.03	0.05	0.48	0.08	0.03	0.04
Al_2O_3	32.22	32.54	29.49	31.83	31.81	31.19
FeO_{tot}	1.46	0.92	5.71	1.70	0.25	0.65
MnO	0.08	0.02	0.07	0.00	0.00	0.04
MgO	0.04	0.03	0.07	0.03	0.03	0.52
CaO	24.51	24.49	22.34	23.91	16.56	17.45
Na_2O	0.01	0.01	0.03	0.02	0.01	0.03
K_2O	0.02	0.03	0.04	0.02	0.01	0.01
Sum	97.85	97.59	95.52	96.99	87.60	88.53
Si	3.00	3.01	2.93	3.02	2.05	2.02
Ti	0.00	0.00	0.03	0.00	0.00	0.00
Al	2.89	2.92	2.74	2.88	1.97	1.93
Cr	0.00	0.00	0.00	0.00	0.00	0.00
Fe^{3+}	0.09	0.06	0.38	0.11	0.01	0.03
Mn	0.01	0.00	0.00	0.00	0.00	0.00
Mg	0.00	0.00	0.01	0.00	0.00	0.04
Ca	2.00	2.00	1.89	1.97	0.93	0.98
Na	0.00	0.00	0.00	0.00	0.00	0.00
K	0.00	0.00	0.00	0.00	0.00	0.00
Xpist	0.03	0.02	0.12	0.04		

actinolitic Amp+Cz+Ab+Ms+Chl+Qtz. An H_2O-fluid was included in both assemblages. The activities and activity uncertainties of each end-member included in the calculations were obtained with the software AX (Holland and Powell, unpublished). The results, including correlations, sigfit values, and uncertainty ellipses, are given below and in Fig. 6a and were calculated following Powell and Holland (1994).

The calculated peak conditions are 626±90 ºC, 15.6±3.6 kbar (corr 0.98, sigfit 0.83), 617±94 ºC, 13.4±3.4 kbar (corr 0.90, sigfit 1.56), 675±89 ºC, 15.6±3.4 kbar (0.74, 0.71), in samples LCG-1, LCG-6 and LCG-12, respectively. The calculated retrograde conditions are 314±49 ºC, 6.1±1.4 kbar (0.90, 0.98), 255±21 ºC, 5.8±0.8 (0.61, 0.62) and 257±21 ºC, 5.9±0.8 kbar (0.61, 0.60) in samples LCG-1, LCG-6 and LCG-12, respectively. The P-T calculations are similar in all rocks and indicate counterclockwise P-T paths, consistent with the P-T paths of associated amphibolites (Blanco-Quintero et al., 2010a).

The isochemical P-T projection (pseudosection) for sample LCG-3 was calculated in the KNCFMSH system. A fluid phase, assumed to be pure H_2O, is considered to be in excess. The solution models used for silicate melt, plagioclase, white mica, amphibole, pyroxene and chlorite are from White et al. (2007), Holland and Powell (2003), Coggon and Holland (2002), Diener et al. (2007), Green et al. (2007) and Holland et al. (1998), respectively. The results of the calculations (Fig. 6b) are used as a proxy of processes occurring during and after melt crystallization. The results are consistent with observed mineral assemblages. The predicted stability of hornblende+epidote is consistent with a counter-clockwise P-T path during exhumation.

Figure 6. a) P-T diagrams showing conditions calculated with THERMOCALC. The grid of reactions in the simple NASH system is from Spear(1993). b) Isochemical P-T projection for sample LCG-3. Mineral abbreviations are hb (hornblende), jd (jadeite), liq (melt), pl (plagioclase), cz (clinozoisite), mu (muscovite), chl (chlorite), q (quartz).

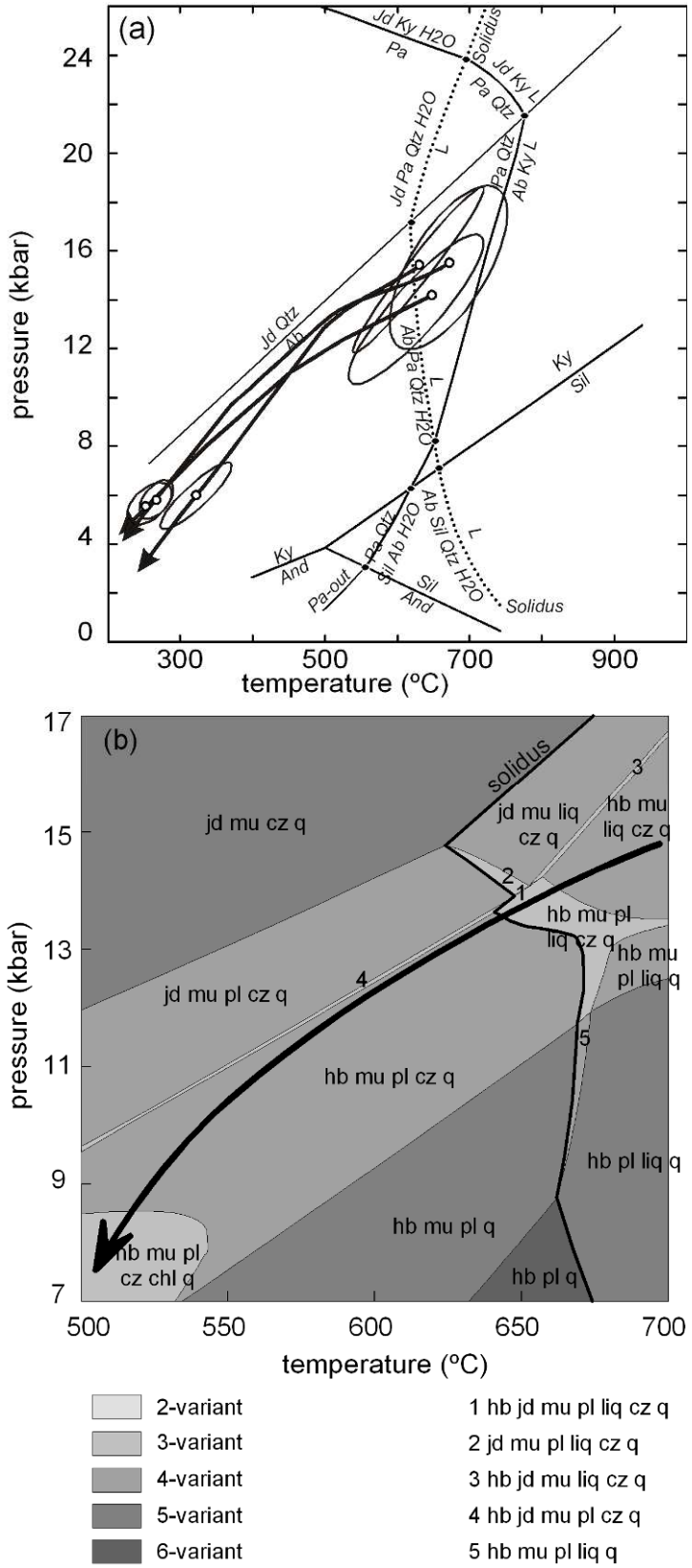
(a)
pressure (kbar)
temperature (ºC)
Jd Ky H2O
Pa
Solidus
Jd Ky L
Pa Qtz
Jd Pa Qtz H2O
L
Ab Ky L
Jd Qtz
Ab
Ab Pa Qtz H2O
Ky
Sil
Ab Sil Qtz H2O
Ky
And
Pa Qtz
Sil Ab H2O
Pa-out
Sil
And
Solidus
(b)
pressure (kbar)
temperature (ºC)
solidus
jd mu cz q
jd mu liq cz q
hb mu liq cz q
hb mu pl liq cz q
hb mu pl liq q
jd mu pl cz q
hb mu pl cz q
hb pl liq q
hb mu pl q
hb mu pl cz chl q
hb pl q
1
2
3
4
5
2-variant
3-variant
4-variant
5-variant
6-variant
1 hb jd mu pl liq cz q
2 jd mu pl liq cz q
3 hb jd mu liq cz q
4 hb jd mu pl cz q
5 hb mu pl liq q

Table 3 Representative analyses of plagioclase and K-feldspar (normalized to 8 O).

Mineral	Pl	Pl	Pl	Pl	Pl	Kfs	Kfs
SiO_2	66.65	68.32	56.23	68.24	68.85	63.57	64.68
TiO_2	0.00	0.00	0.05	0.00	0.00	0.00	0.01
Al_2O_3	20.89	19.45	24.35	19.36	19.25	18.22	19.06
FeO_{tot}	0.04	0.03	0.83	0.52	0.02	0.57	0.11
MnO	0.00	0.00	0.00	0.04	0.00	0.02	0.01
MgO	0.00	0.00	0.02	0.02	0.00	0.39	0.00
CaO	1.60	0.26	10.10	0.35	0.31	0.01	0.01
BaO	0.04	0.00	0.00	0.00	0.00	0.00	0.26
Na_2O	10.92	11.77	6.63	10.87	11.51	0.03	0.06
K_2O	0.04	0.04	0.18	0.61	0.04	16.50	16.29
Sum	100.28	99.98	98.51	100.09	100.12	99.42	100.63
Si	2.92	2.99	2.59	2.99	3.00	2.97	2.98
Ti	0.00	0.00	0.00	0.00	0.00	0.00	0.00
Al	1.08	1.00	1.32	1.00	0.99	1.00	1.03
Fe^{3+}	0.00	0.00	0.03	0.02	0.00	0.02	0.00
Mn	0.00	0.00	0.00	0.00	0.00	0.00	0.00
Mg	0.00	0.00	0.00	0.00	0.00	0.03	0.00
Ca	0.08	0.01	0.50	0.02	0.01	0.00	0.00
Ba	0.00	0.00	0.00	0.00	0.00	0.00	0.00
Na	0.93	1.00	0.59	0.92	0.97	0.00	0.01
K	0.00	0.00	0.01	0.03	0.00	0.98	0.96
Ab	0.93	0.99	0.54	0.98	0.99		
An	0.07	0.01	0.46	0.02	0.01		
Or						1.00	0.99

WHOLE-ROCK GEOCHEMISTRY

The trondhjemitic rocks exhibit a range of SiO_2 contents from 58.82 to 75.66 wt % corresponding to andesite and rhyolite compositions within the subalkaline field in the TAS diagram (Fig. 7a, Table 6). The high-silica samples have low Al_2O_3 (14.17 wt %), CaO (4.29 wt %) and Na_2O (3.3 wt %). These chemical characteristics correspond to high proportion of quartz and low plagioclase. Similarly, the low-silica samples are rich in CaO (7.42 wt %) in agreement with the larger abundance of epidote. The low K_2O (0.22 – 0.63 wt %) contents correspond to tholeiitic composition (Fig. 7b). The FeO and MgO contents are low, and the Mg # is relatively homogenous, ranging from 0.42 to 0.45.

Based on the O'Connor (1965) diagram, the studied leucocratic rocks are classified as tonalitic (Fig. 7c). However, the rocks are leucocratic, being of tonalitic composition due to the abundance of epidote. For this reason, they are characterized as trondhjemitic. They are slightly peraluminous (Fig. 7d), in agreement with the presence of magmatic muscovite.

The chondrite-normalized REE patterns (Fig. 8a, Table 6) are characterized by a negative slope, with depletion in HREE elements and enrichment in LREE [(La/Yb)N = 9.12-17-02] and positive Eu anomalies (Eu/Eu* = 1.26–1.74). These chemical characteristics indicate that garnet was a stable phase during partial melting of the source, preventing HREE fractionation into the melt. The positive Eu

Figure 7. Composition of studied samples in the a) TAS classification of volcanic rocks from Le Maitre et al. (1989), b) K2O vs. SiO2 diagram (Peccerillo and Taylor, 1976), c) molecular normative (CIPW) diagram (O´Connor, 1965), with fields after Barker (1979), d) ACF phase diagrams showing magmatic assemblages and whole rock composition (WR); end-members of solid solutions on interest are indicated by empty circles joined by dashed lines. The leucocratic rocks from Sierra del Convento mélange (Lázaro and García-Casco, 2008) are plotted for comparison (grey fields).

Table 4: Representative analyses of muscovite (normalized to 22 O and 4 OH)

SiO_2	47.25	48.11	48.31	47.67	46.31	51.83
TiO_2	0.40	0.40	0.15	0.23	0.49	0.14
Al_2O_3	31.85	31.69	30.23	30.43	33.21	26.08
FeO_{tot}	1.57	1.61	1.43	1.79	0.95	1.49
MnO	0.03	0.01	0.00	0.02	0.00	0.01
MgO	2.22	2.30	2.45	2.44	1.48	3.75
NiO	0.05	0.05	0.00	0.02	0.00	0.00
CaO	0.03	0.05	0.01	0.00	0.02	0.00
BaO	0.85	0.67	0.87	0.75	0.82	0.57
Na_2O	0.98	0.81	0.95	0.98	1.85	0.87
K_2O	9.47	9.47	9.59	9.58	8.45	9.50
Sum	94.84	95.24	94.17	94.04	93.65	94.38
Si	6.36	6.42	6.54	6.47	6.27	6.96
Ti	0.04	0.04	0.02	0.02	0.05	0.01
Al	5.05	4.98	4.82	4.87	5.30	4.12
Fe^{2+}	0.18	0.18	0.16	0.20	0.11	0.17
Mn	0.00	0.00	0.00	0.00	0.00	0.00
Mg	0.45	0.46	0.49	0.49	0.30	0.75
Ni	0.02	0.02	0.00	0.01	0.00	0.00
Ca	0.00	0.01	0.00	0.00	0.00	0.00
Ba	0.04	0.04	0.05	0.04	0.04	0.03
Na	0.26	0.21	0.25	0.26	0.49	0.23
K	1.63	1.61	1.66	1.66	1.46	1.63
Mg#	0.72	0.72	0.75	0.71	0.74	0.82

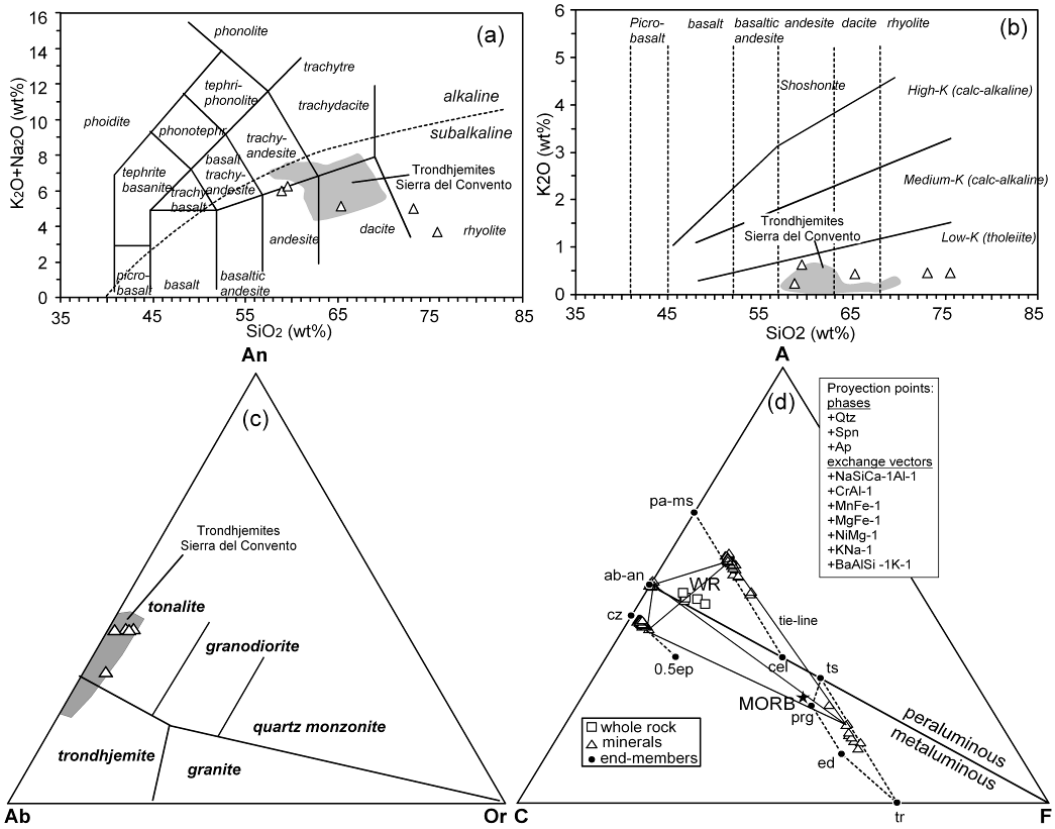

anomalies suggest that a significant relative amount of plagioclase participated in the partial melting process.

Trace element patterns normalized to N-MORB are similar, with negative slopes, and enrichment in LILE and depletion in HFSE compared to N-MORB (Fig. 8b). Strong positive anomalies in Ba, Pb and Sr are discernible. Zr also shows a positive anomaly in line with the presence of abundant zircon in the samples. The strong enrichment in Ba (up to 70 times N-MORB values) may be the result of the flux of Ba-rich fluids evolved from the subducting crust during partial melting (Blanco-Quintero et al. 2010c).

GEOCHRONOLOGY

SHRIMP zircon age

The zircons of trondhjemite sample LCG-1 are clear, long-prismatic and display well developed oscillatory magmatic zoning under cathodo-luminenscence (Fig. 9a) with no older cores. Six grains were analyzed on SHRIMP II, and the concordant data are well grouped, providing a precise mean $^{206}Pb/^{238}U$ age of 109.7 ± 1.7 Ma (Fig. 9a, Table 7). Zircons of sample LCG-3 (Fig. 9b), are clear, mostly euhedral and long-prismatic with oscillatory magmatic zoning. Five grains provided consistent and concordant results with a precise mean $^{206}Pb/^{238}U$ age of 104.6 ± 1.0 Ma (Fig. 9b, Table 7). The zircons of trondhjemite sample LCG-6 (Fig. 9c) define a homogeneous population of mostly clear and stubby grains with developed oscillatory zoning. Five grains were analyzed and provided concordant data points with a precise mean $^{206}Pb/^{238}U$ age of 109.2 ± 0.9 Ma (Fig. 9c, Table 7). Trondhjemite sample LCG-12 also contains a population of clear, long-prismatic and idiomorphic zircons of magmatic origin (Fig. 9d). Five grains were analyzed and provided identical and concordant $^{206}Pb/^{238}U$ ratios with a mean age of 109.4 ± 1.5 Ma (Fig. 9d, Table 7). We interpret all ages as reflecting the time of magmatic crystallization at ca. 15 kbar.

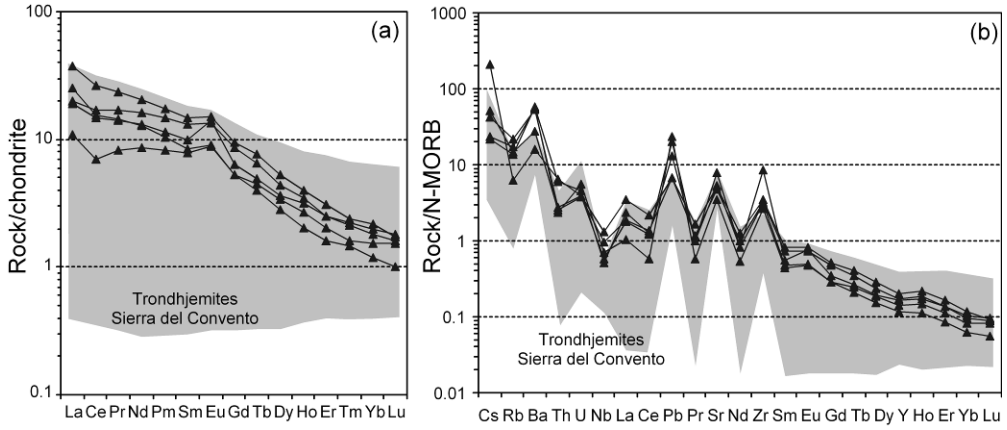

Figure 8. a) Chondrite (C1, McDonough and Sun, 1995) normalized REE patterns and b) N-MORB (Sun and McDonough, 1989) normalized spider diagram. The leucocratic rocks from Sierra del Convento mélange (Lázaro and García-Casco, 2008) are plotted for comparison (grey fields).

Table 4: Representative analyses of muscovite (normalized to 22 O and 4 OH)

SiO_2	47.25	48.11	48.31	47.67	46.31	51.83
TiO_2	0.40	0.40	0.15	0.23	0.49	0.14
Al_2O_3	31.85	31.69	30.23	30.43	33.21	26.08
FeO_{tot}	1.57	1.61	1.43	1.79	0.95	1.49
MnO	0.03	0.01	0.00	0.02	0.00	0.01
MgO	2.22	2.30	2.45	2.44	1.48	3.75
NiO	0.05	0.05	0.00	0.02	0.00	0.00
CaO	0.03	0.05	0.01	0.00	0.02	0.00
BaO	0.85	0.67	0.87	0.75	0.82	0.57
Na_2O	0.98	0.81	0.95	0.98	1.85	0.87
K_2O	9.47	9.47	9.59	9.58	8.45	9.50
Sum	94.84	95.24	94.17	94.04	93.65	94.38
Si	6.36	6.42	6.54	6.47	6.27	6.96
Ti	0.04	0.04	0.02	0.02	0.05	0.01
Al	5.05	4.98	4.82	4.87	5.30	4.12
Fe^{2+}	0.18	0.18	0.16	0.20	0.11	0.17
Mn	0.00	0.00	0.00	0.00	0.00	0.00
Mg	0.45	0.46	0.49	0.49	0.30	0.75
Ni	0.02	0.02	0.00	0.01	0.00	0.00
Ca	0.00	0.01	0.00	0.00	0.00	0.00
Ba	0.04	0.04	0.05	0.04	0.04	0.03
Na	0.26	0.21	0.25	0.26	0.49	0.23
K	1.63	1.61	1.66	1.66	1.46	1.63
Mg#	0.72	0.72	0.75	0.71	0.74	0.82

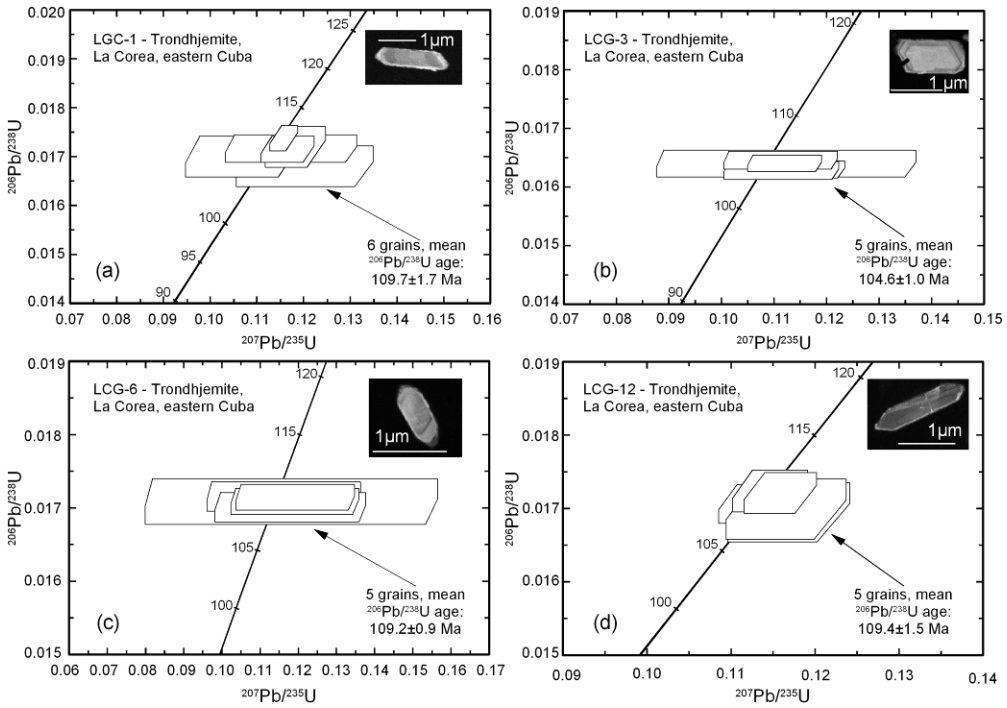

Figure 9. Concordia diagrams showing SHRIMP analyses of zircons from La Corea mélange: a) LCG-1, b) LCG-3, c) LCG-6, d) LCG-12. Data boxes for each analysis are defined by standard errors in $^{207}Pb/^{235}U$, $^{206}Pb/^{238}U$ and $^{207}Pb/^{206}Pb$. Inset images correspond to cathodoluminescence (CL) images of zircon grains from each trondhjemite sample.

Table 5: Representative analyses of chlorite (normalized to 20 O and 16 OH)

SiO_2	29.30	28.25	27.49	29.17
Al_2O_3	19.96	21.10	21.29	19.49
FeO_{tot}	19.26	19.34	16.48	13.66
MnO	0.19	0.21	0.13	0.14
MgO	18.17	18.05	20.68	23.70
NiO	0.00	0.00	0.01	0.00
CaO	0.10	0.05	0.02	0.11
Na_2O	0.02	0.18	0.00	0.01
K_2O	0.14	0.04	0.03	0.02
Sum	87.20	87.33	86.32	86.50
Si	5.97	5.76	5.60	5.84
Al	4.79	5.07	5.11	4.60
Fe^{2+}	3.28	3.30	2.81	2.29
Mn	0.03	0.04	0.02	0.02
Mg	5.52	5.49	6.28	7.07
Ni	0.00	0.00	0.01	0.00
Ca	0.02	0.01	0.00	0.02
Na	0.01	0.07	0.00	0.00
K	0.04	0.01	0.01	0.01
Mg#	0.63	0.62	0.69	0.76

Ar/Ar phengite dating

The summary of the $^{40}Ar/^{39}Ar$ age and isochron calculation results are presented in Table 8. A forced plateau of LCG-1 comprising low- and medium-temperature Ar degassing (steps B to I, Figure 10a; Table 8) yield an age of 86.2 ± 0.2 Ma. In this case, “forced“ means that the plateau does not comprise > 50% of the totally degassed 39Ar as required on the basis of the plateau definition by Fleck et al. (1977), but only ca. 46%. This discrepancy is of only subordinate relevance and considered to be insignificant for the geological discussion. The isochron age calculated from the forced plateau degassing steps is 86.1 ± 0.4 Ma and identical to the forced plateau age within 1sigma analytical errors. The $^{40}Ar/^{36}Ar$ intercept of 301 ± 8 is atmospheric and indicates that there is no excess Ar. In contrast, isochron and inverse isochron calculation using the high-temperature Ar degassing steps J to P yields sub-atmospheric $^{40}Ar/^{36}Ar$ intercepts of 20 ± 80 and 100 ± 80, respectively (not shown in Table 8). Although the corresponding isochron calculation does not provide statistically meaningful ages, the $^{40}Ar/^{36}Ar$ intercepts substantially lower than atmospheric most likely indicate disturbances of the K-Ar isotopic system related to the high-temperature degassing steps.

Age spectra of micas from samples LCG-2, LCG-3 are disturbed and show more or less developed saddle-shaped or stair case-type spectra, respectively. Isochron age calculations yield no statistically significant results (Table 8). The integrated ages of 86.3 ± 0.2 and 83.1 ± 0.2 (Figure 10b and c, respectively), to a certain extent show some consistency in so far as a) they form a relatively small age range of < ca. 4 Ma and b) this age range overlaps with the forced plateau age of sample LCG-1. Despite the disturbed age spectra, this consistency could imply geological significance.

Table 6 Major(wt%) and trace (ppm) element composition of rocks.

Sample	LCG-1	LCG-2	LCG-3	LCG-6	LCG-12
SiO_2	57.99	64.19	57.05	71.70	74.77
TiO_2	0.65	0.72	0.71	0.50	0.42
Al_2O_3	22.18	18.60	21.51	14.52	14.00
FeO_{tot}	1.76	2.05	2.52	1.36	1.11
MnO	0.02	0.02	0.03	0.02	0.02
MgO	1.34	1.41	2.16	0.92	0.70
CaO	7.35	6.16	7.20	4.13	4.24
Na_2O	5.51	4.65	5.61	4.52	3.28
K_2O	0.61	0.42	0.21	0.44	0.44
P_2O_5	0.13	0.18	0.22	0.06	0.05
LOI	1.43	1.83	1.89	0.93	0.94
Total	99.05	100.33	99.14	99.13	99.86
Rb	12.20	8.20	3.49	9.65	7.79
Cs	0.29	0.37	1.45	0.16	0.16
Be	0.88	0.81	0.62	0.84	0.50
Sr	708.99	429.24	458.59	308.67	487.07
Ba	335.96	173.46	101.98	348.68	371.27
Sc	3.89	4.27	6.99	2.88	1.72
V	33.27	45.42	62.23	31.17	19.72
Cr	17.04	30.76	32.71	46.37	40.18
Co	19.47	33.99	30.39	36.74	37.39
Ni	3.51	4.69	12.14	3.92	20.97
Y	4.73	4.79	5.69	3.29	4.03
Nb	1.37	2.27	3.03	1.66	1.19
Zr	634.70	238.90	261.40	193.10	233.80
Hf	0.14	0.12	0.12	0.12	0.02
Pb	5.98	2.02	2.03	6.99	3.97
U	0.18	0.18	0.18	0.26	0.21
Th	0.33	0.31	0.77	0.29	0.72
La	4.48	4.73	8.87	2.58	5.95
Ce	8.97	10.35	16.11	4.33	9.48
Pr	1.32	1.57	2.20	0.76	1.34
Nd	5.97	7.37	9.39	3.93	5.91
Sm	1.48	1.95	2.20	1.17	1.23
Eu	0.78	0.76	0.85	0.49	0.51
Gd	1.28	1.73	1.90	1.05	1.05
Tb	0.18	0.23	0.28	0.14	0.16
Dy	0.90	1.08	1.30	0.70	0.84
Ho	0.17	0.19	0.22	0.11	0.15
Er	0.41	0.41	0.50	0.26	0.33
Tm	0.06	0.05	0.06	0.04	0.04
Yb	0.32	0.29	0.35	0.19	0.25
Lu	0.04	0.04	0.04	0.03	0.04

DISCUSSION

Petrogenesis of leucocratic rocks

Lázaro and García-Casco (2008) concluded that the leucocratic rocks that occur in the Sierra del Convento mélange (similar to the ones in La Corea mélange) formed after partial melting of amphibolites. The leucocratic rocks in La Corea mélange have distinct REE patterns with a negative slope and positive Eu anomalies (Fig. 8) indicating an adakitic affinity. The Y and HREE depletion, typical of adakites, is explained by the presence of residual garnet in the source, whereas the Sr enrichment and negative Nb anomaly are thought to be due to the absence of plagioclase and the presence of amphibole in the melt residue, therefore we conclude that the tonalitic-trondhjemitic rocks of La Corea most likely represent slab melts (c.f. Lázaro and García-Casco, 2008). The relative low MgO (0.71-2.23

wt %), Cr (17.04-46.37 ppm) and Ni (3.51-20.97 ppm) in the trondhjemitic rocks indicated that the melt did not interact with the ultramafic rocks of the mantle wedge (or subduction channel matrix).

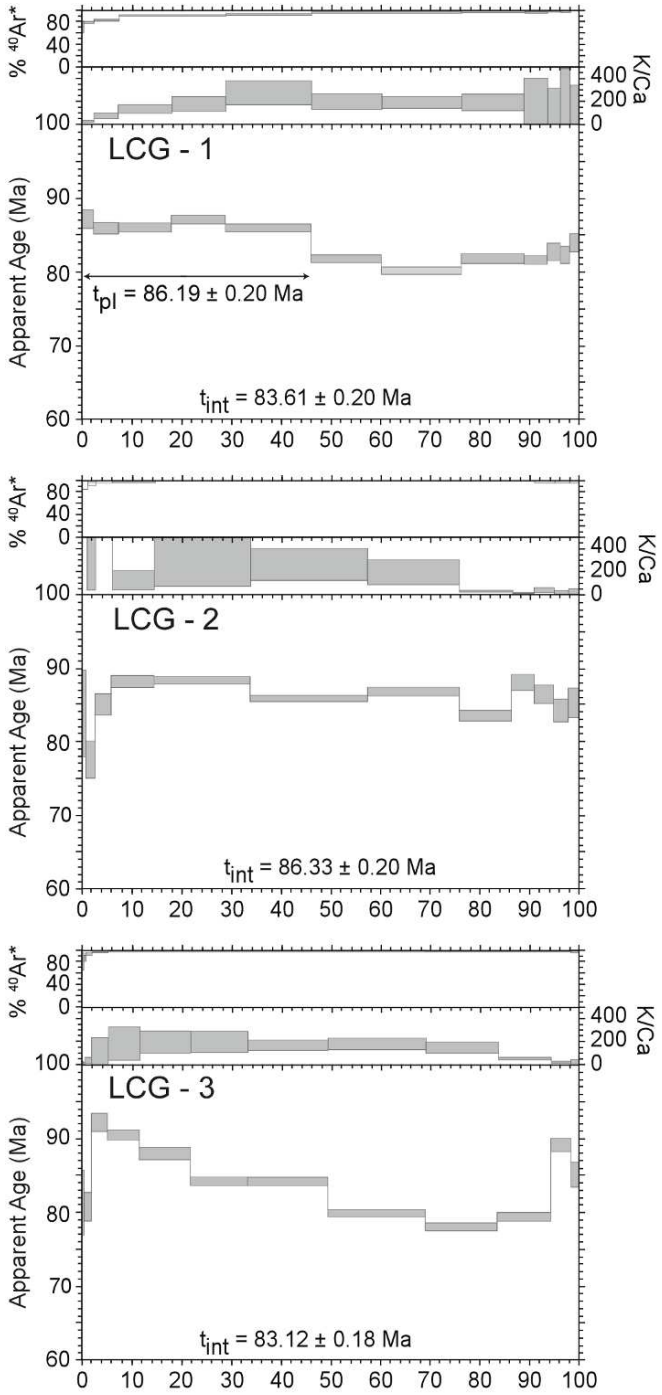

Figure 10. $^{40}Ar/^{39}Ar$ age spectra muscovite from trondhjemite samples a) LCG-1, b) LCG-2, c) LCG-3.

Table 7. SHRIMP II analytical data for spot analyses of single zircons from studied samples.

Sample	U	Th	$^{206}Pb/^{204}Pb$	$^{208}Pb/^{206}Pb$	$^{207}Pb/^{206}Pb$	$^{206}Pb/^{238}U$	$^{207}Pb/^{235}U$	$^{206}Pb/^{238}U$ age ± 1
LCG1								
LGC1-1	958	166	1000000	0.0580±12	0.0484±7	0.0174±3	0.1161±25	111±2
LGC1-2	208	94	7501	0.1567±134	0.0497±56	0.0172±3	0.1176±138	110±2
LGC1-3	224	117	41533	0.1968±56	0.0494±17	0.0172±3	0.1169±48	110±2
LGC1-4	186	64	959	0.1498±151	0.0520±61	0.0168±4	0.1206±148	107±3
LGC1-5	298	116	1132	0.1179±118	0.0455±47	0.0170±4	0.1066±118	109±3
LGC1-6	391	151	3433	0.1318±58	0.0500±23	0.0172±4	0.1186±65	110±3
LCG3								
LCG3-1	185	70	5570	0.1252±254	0.0498±109	0.0164±2	0.113±25	105±1
LCG3-2	189	86	5374	0.1539±117	0.0497±48	0.0163±2	0.112±11	104±1
LCG3-3	225	111	6507	0.2228±123	0.0499±50	0.0163±2	0.112±11	104±1
LCG3-4	204	91	15839	0.1512±76	0.0496±30	0.0164±1	0.112±7	105±1
LCG3-5	360	105	13041	0.0932±109	0.0491±47	0.0165±2	0.112±11	105±1
LCG6								
LCG6-1	128	60	2700	0.1620±198	0.0491±83	0.0171±2	0.116±20	110±1
LCG6-2	130	57	3528	0.1355±371	0.0502±160	0.0171±3	0.118±38	109±2
LCG6-3	149	58	3547	0.1438±152	0.0505±64	0.0171±2	0.119±15	109±1
LCG6-4	122	34	6418	0.0881±191	0.0503±82	0.0170±2	0.118±20	109±1
LCG6-5	131	47	6932	0.1316±164	0.0506±70	0.0171±2	0.119±17	109±1
LCG12								
LGC12-1	207	79	424820	0.0864±35	0.0488±15	0.0172±3	0.1159±43	110±2
LGC12-2	495	191	12596	0.1238±69	0.0492±29	0.0171±3	0.1158±73	109±2
LGC12-3	159	60	5000000	0.1293±45	0.0482±16	0.0172±3	0.1146±45	110±2
LGC12-4	464	206	2214	0.1598±67	0.0498±26	0.0170±4	0.1166±71	109±3
LGC12-5	217	104	4585	0.2176±74	0.0500±27	0.0170±4	0.1168±73	108±3

Table 8. Summary of Ar-Ar age and isochron calculation results on white mica separates from studied samples.

Sample	Plateau age* [Ma] ± 1sigma	Integrated age [Ma] ± 1sigma	Isochron age [Ma] ± 1sigma	$^{40}Ar/^{36}Ar$ intercept ± 1sigma	MSWD*	P**
LCG-1	86.2 ± 0.2	83.6 ± 0.2	86.1 ± 0.4	301 ± 8	0.43	0.86
LCG-2		86.3 ± 0.2	86.6 ± 0.5	110 ± 50	5.5	0.00
LCG-3		83.1 ± 0.2	87.0 ± 0.8	100 ± 55	24	0.00

MSWD = Mean Square Weighted Deviate, representing a measure of the observed scatter of the points from the best-fit line to the expected scatter based on the assigned errors and error correlations. P = Probability of isochron calculation yielding a statistically meaningful age.

Melting of amphibolites (700-750 ºC, 15 kbar) and formation of trondhjemitic melt in the La Corea and Sierra del Convento mélanges involved the influx of H2O-fluids derived from the slab (García-Casco et al., 2008a, Blanco Quintero et al., 2010a). Lázaro and García-Casco (2008) inferred the influx of primitive fluids evolved from dehydration of subducting serpentinite during the formation of K-Ba-poor trondhjemites. However, Blanco-Quintero et al. (2010c) and Lázaro et al. (in preparation), have identified a group of K-Ba-rich trondhjemites for which the influx of sediment derived fluid is inferred. The rocks studied here are relatively poor in K, but display enrichment in Ba and other LILE. This suggest that fluids evolved from subducting oceanic sediments, altered basaltic crust and serpentinized ultramafic rocks mixed in variable proportions during devolatilization of the slab at ca. 50 km depth to yield mixed fluids of variable composition that interacted with accreted amphibolites at conditions above the wet basaltic solidus to yield trondjemitic rocks of variable composition.

Age of onset of subduction

The zircon ages of our dated samples range between 105 and 110 Ma. A similar zircon age of 112.8 ± 1.1 Ma was determined for a trondhjemite sample from the Sierra del Convento and was interpreted as the crystallization age (Lazaro et al., 2009). Furthermore, eclogites from the Río San Juan mélange of Hispaniola, which can be correlated with the eastern Cuba melanges, have a Lu-Hf age of 103.6 ± 2.7 Ma indicating formation during the early Cretaceous (Krebs et al., 2008). Thermodynamic calculations yielded counter-clockwise trajectories for HP rocks (see García-Casco et al., 2008b and Lázaro et al., 2009, for the Sierra del Convento mélange and Krebs et al., 2008, for the Río San Juan mélange). These results enable us to compare these three complexes from the geological point of view. In all cases the counter-clockwise trajectories are interpreted as reflecting the onset of subduction, in correspondence with numerical modelling (i.e., Gerya et al., 2002).

Subduction of the MOR basaltic protolith of the amphibolites can be calculated following the procedures by Krebs et al. (2008) and Lázaro et al. (2009) and the data presented here, which indicate crystallization (cooling) of the trondhjemitic melts at ca. 50 km depth in the range 105-110 Ma. The results of calculations, assuming a convergence rate of 10 km/Ma yield 117 Ma, similar to the other estimations of ca. 120 Ma for Sierra del Convento (Lázaro et al., 2009) and Río San Juan (Krebs et al., 2008). This age is considered as the time of onset of subduction of the Proto-Caribbean lithosphere below the Pacific-derived Caribbean plate. Counter-clockwise P-T paths and hot geothermal conditions are typical of onset of subduction scenarios. These ages and inferences can hardly be reconciled with onset of subduction of the Proto-Caribbean at ca. 85 Ma, as proposed by Duncan and Hargraves (1984), Burke (1988) and Kerr et al. (2003), among others.

Recently, however, Rojas-Agramonte et al. (submitted) have indicated that onset of subduction of the Proto-Caribbean may have started earlier, at 135-140 Ma, based on age evidence from volcanic arc rocks in Central Cuba. Reconciling both proposals is difficult. Pindell and Kennan (2009; note added in proof) suggested that onset of subduction at ca. 130 Ma may have occurred along a transform/fracture zone rather than polarity reversal. We do not consider spontaneous subduction feasible because the thermal evolution of the rocks subducted by ca. 120 Ma in

eastern Cuba and Dominican Republic indicates young to very young oceanic Proto-Caribbean lithosphere. Induced subduction of the Proto-Caribbean along a transform/fracture zone boundary may have occurred at 130-140 Ma if plate convergence took place at this stage, in a similar way that Pindell and Kennan (2009) suggested for their 125-120 Ma stage. These authors indicated that the older, thicker and stronger Farallon plate wound resist compression while the younger and weaker Proto-Caribbean lithosphere buckled and imbricated below the former. Evidence for compression and uplift during 130-140 Ma is, however, scarce or non-existent. Baumgartner et al. (2008) reported a phengite Ar-Ar cooling age of 139 Ma from a high-pressure block from the Siuna serpentinite mélange, of the Mesquito/Siuna terrane (Nicaragua), thought to be a composite terrane with fragments of the Caribbean arc system, and Brueckner (2009) obtained Sm-Nd mineral isochrons of 144-126 Ma in high pressure blocks within the serpentinite melanges of Guatemala, north and south of the Motagua fault, suggesting Neocomian transpressional tectonics. Although these ages can hardly relate to subduction of the Proto-Caribbean and most probably represent subduction of the Pacific (Farallon) lithosphere, they indicate tectonic processes (uplift) that may relate to induced (forced) onset of subduction of the Proto-Caribbean during Neocomian times.

If the Proto-Caribbean, indeed, began subducting at ca. 135-140 Ma, it is still possible to explain the P-T conditions and counter-clockwise paths of eastern Cuba and Rio San Juan mélanges developed ca. 20 Ma later. García-Casco et al. (2008a) and Blanco-Quintero et al. (2010a) point out that the incoming Proto-Caribbean plate should have been very young (hot) in order to explain partial melting of amphibolites at shallow depths (50 km), and that the thermal state of the incoming plate was different along strike, with hottest conditions in eastern Cuba and somewhat colder conditions in Rio San Juan. This inference obviously explains the hot conditions of amphibolites and eclogites from these mélanges by itself, and therefore no need for additional constraints, such as onset of subduction. Subduction of an oblique mid-ocean ridge would also lead to counter-clockwise P-T paths of young subducted MORB (amphibolites and eclogites) because continued subduction would involve continuously older (colder) lithosphere. Consequently, the characteristic hot counter-clockwise P-T paths of amphibolites and eclogites, the partial melting of the former, and the crystallization of trondhjemitic melts at depth, as identified in eastern Cuba and the Rio San Juan mélanges, can be explained by subduction of an oblique ridge and should not be the necessary products of onset of subduction. More geochronological work on subduction-related metamorphic and magmatic rocks in the Caribbean region is needed to solve the timing and tectonic causes of onset-of-subduction of the Proto-Caribbean.

Exhumation history and rates

The Ar-Ar phengite cooling ages for the leucocratic rocks (83-86 Ma) indicate exhumation rates in the subduction channel of ca. 1 mm/yr, assuming linear exhumation from ca. 50 (zircon crystallization at 15 kbar, 700 ºC, 105 Ma) to 30 km and 350 ºC for the blocking temperature of the K-Ar system in muscovite (Purdy and Jäger, 1976; Kirschner et al., 1996). This exhumation rate is very slow, but comparable to other rates of exhumation during convergence in subduction channels (1-5 mm/yr, Agard et al. 2009, Guillot et al., 2009).

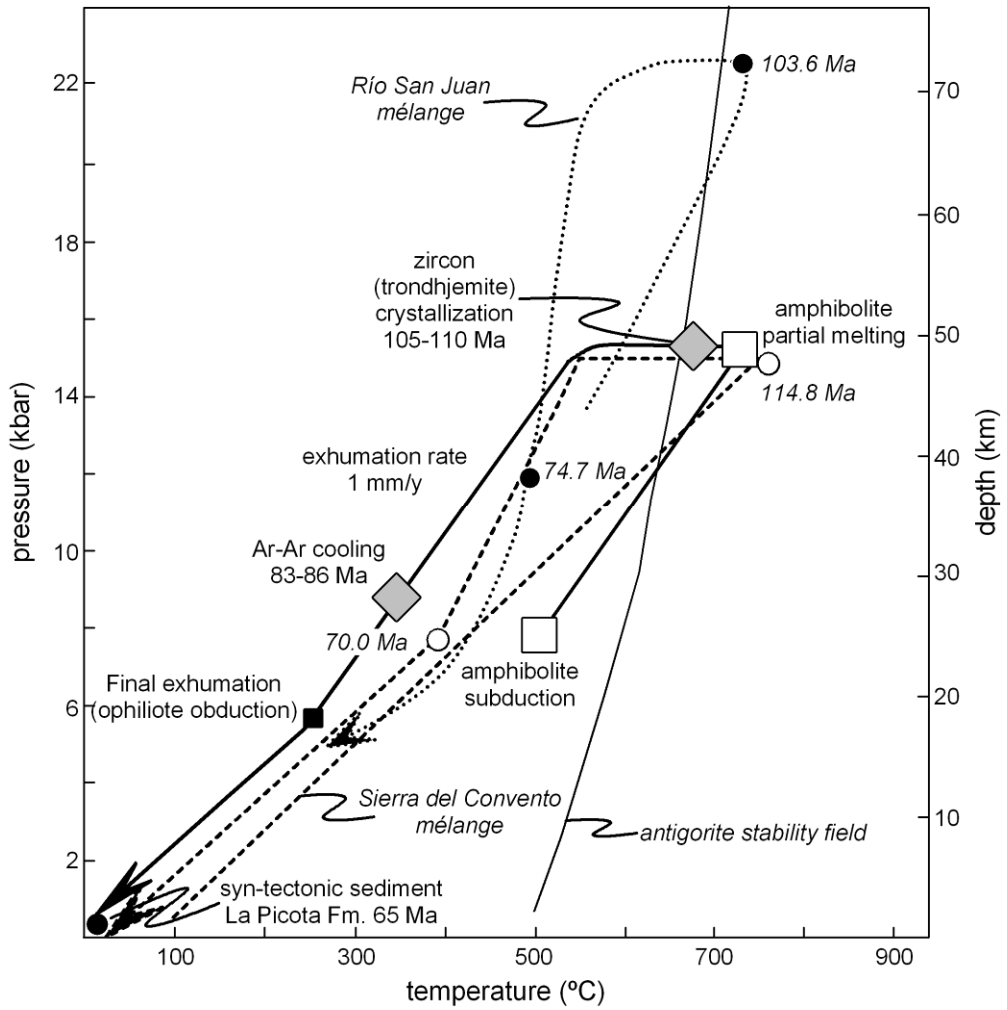

Figure 11. Model P-T-t path for the mélange (amphibolite and trondhjemites) including the subduction, cooling in the upper plate, exhumation in the channel and final collision-related exhumation stages. White squares correspond with data of amphibolite blocks (Blanco-Quintero et al., 2010a) and grey diamonds data from this work. The dashed line indicated the PT trajectory and of Sierra del Convento mélange and the empty circles data of this complex (Lázaro et al., 2009). The dotted line is the trajectory of Río San Juan mélange and the black circles data of this complex (Krebs et al., 2008). The antigorite stability limit is after Ulmer and Trommsdorff (1995).

The Ar-Ar phengite cooling ages for the studied leucocratic rocks are similar to the ages of growth/cooling at 465 ºC and 11 kbar of retrograde calcic amphibole in Sierra del Convento mélange (85.6 Ma in average; Lázaro et al., 2009). However, since these P-T conditions of retrograde amphibole growth/cooling are higher than the 350 ºC (ca. 9 kbar) closure temperature of Ar-Ar in phengite, it appears that the blocks in the La Corea mélange experienced faster cooling and exhumation than in the Sierra del Convento mélange. In fact, Lázaro et al. (2009) calculated an average linear exhumation rate of 0.7 mm/yr in the range 107-70 Ma (15-8 kbar). Furthermore, Krebs et al. (2008) estimated 1.2 and 4.8 mm/yr (depending on assumptions) for early subducted eclogites from the Rio San Juan mélange. Because all these mélanges were closely spatially related and their blocks may have formed

at depth simultaneously, such variations in the exhumation rates would indicate variations along strike in the flux rate within subduction channels.

Near steady state upward movement of blocks probably characterize subduction channels during the near-steady state oceanic convergence stage (Gerya et al., 2002). However, numerical models for intra-oceanic environments show that exhumation do not proceed to the Earth's surface, but stops at about 15-20 km depth (e.g., Goczyk et al., 2007). The blocks are stored (probably at the base of the crust) until significant variations in the subduction factors take place, for example, by means of collision. In the La Corea mélange, this stage took place at 70-65 Ma, as documented by the ages of the syn-tectonic La Picota Formation (Fig. 1c), formed as the result of collision and exhumation of the forearc/arc/backarc units and the platform terrane Caribeana (Iturralde-Vinent et al., 2006, García-Casco et al., 2008b, and reference therein). This stage would involved a faster exhumation rate in the mélanges of ca. 5 mm/yr (cf. Lázaro et al., 2009).

CONCLUSIONS

Field, petrologic and whole-rock chemical data indicate that tonalitic-trondhjemitic rocks from the La Corea mélange in eastern Cuba represent melts formed during partial melting of subducted amphibolites. SHRIMP zircon ages of the trondhjemites provide crystallization ages ranging from 105 to 110 Ma, dating partial melting processes in the subduction environment. The process implied accretion of subducting amphibolites to the upper plate and ensuing infiltration of fluids evolved from downgoing serpentintes, altered basaltic crust and sediments. Partial melting of the amphibolite in the subduction environment indicates a very hot subduction environment caused by subduction of a very young oceanic lithosphere (oblique ridge) and, perhaps, onset of subduction (at ca. 120 Ma). Continued subduction during the Late Cretaceous (of older -colder- lithosphere) allowed cooling of the subduction system and serpentinization of the upper plate mantle wedge, forming a serpentinite matrix subduction channel with HP blocks. ^{40}Ar-^{39}Ar cooling ages of phengite of 83-86 Ma indicate very slow exhumation rates of ca. 1 mm/yr during the oceanic convergence stage. Data from related serpentinte-matrix mélanges of eastern Cuba and Dominican Republic suggest variations along strike in the upward flux rate from 0.7 to 4.8 mm/yr. Regional data indicate final exhumation of the mélange at 70-65 Ma as a result of arc-platform terrane collision in the region.

ACKNOWLEDGMENTS

We appreciate financial support from Spanish MICINN projects CGL2006-08527/BTE and CGL2009-08527/BTE. This is a contribution to IGCP-546 ‘Subduction zones of the Caribbean’ and is Mainz Geocycles contribution. Rojas-Agramonte acknowledges a Humboldt-Foundation Georg Forster Fellowship. Blanco-Quintero is supported by grant AP2005-5258 from the ‘‘Programa de Formación del Profesorado Universitario’’ of the Spanish Ministry of Education and Science.

REFERENCES

Adamovich, A., Chejovich, V., 1964. Principales características de la geología y de los minerales útiles de la región nordeste de la Provincia de Oriente. Revista Tecnológica 2, 14-20.

Agard P., Yamato P., Jolivet L., Burov E., 2009. Exhumation of oceanic blueschists and eclogites in subduction zones: timing and mechanisms. Earth Science Reviews 92, 53-79.

Barker, F., 1979. Trondhjemite: Definition, environment and hypotheses of origin. In: F. Barker (Ed.). Trondhjemites, dacites and related rocks. Elsevier, Amsterdam, pp. 1-12.

Baumgartner, P.O., Flores, K., Bandini, A.N., Girault, F., Cruz, D., 2008, Upper Triassic to Cretaceous radiolaria from Nicaragua and northern Costa Rica – The Mesquito composite oceanic terrane: Ofioliti, 33, 1-19.

Black, L.P., Kamo, S.L., Allen, C.M., Aleinikoff, J.N., Davis, D.W., Korsch, R.J., Foudoulis, C., 2003. TEMORA 1: A quality zircon standard for Phanerozoic U-Pb geochronology. Chemical Geology 200, 155-170.

Blanco-Quintero, I.F., García-Casco, A., Rojas-Agramonte, Y., Rodríguez-Vega, A., Lázaro, C., Iturralde-Vinent, M.A., 2010a. Metamorphic evolution of subducted hot oceanic crust, La Corea mélange, Cuba. American Journal of Science (in press).

Blanco-Quintero, I.F., Proenza, J.A., García-Casco, A., Tauler, E., Galí, S., 2010b. Serpentinites and serpentinites within a fossil subdution channel: La Corea mélange, eastern Cuba. Geologica Acta (in press).

Blanco-Quintero, I.F., Lázaro, C., García-Casco, A., Proenza, J.A., Rojas-Agramonte, Y., 2010c. Barium-rich fluids and melts in the subduction environment (La Corea and Sierra del Convento mélanges, eastern Cuba). Submitted to Contributions to Mineralogy and Petrology.

Boiteau, A., Michard, A., Saliot, P., 1972. Métamporphisme de haute pression dans le complexe ophiolitique du Purial (Oriente, Cuba). Comptes Rendus de l'Académie des Sciences, Série D 274, 2137–2140.

Brueckner H.K., Avé Lallemant H.G., Sisson V.B., Harlow G.E., Hemming S.R., Martens U., Tsujimori T., Sorensen S.S. (2009) Metamorphic reworking of a high pressure–low temperature mélange along the Motagua fault, Guatemala: A record of Neocomian and Maastrichtian transpressional tectonics. Earth and Planetary Science Letters 284 (2009) 228–235.

Burke, K., 1988. Tectonic evolution of the Caribbean. Annual Reviews of Earth and Planetary Sciences, 16, 201-230.

Cobiella, J., Campos M., Boiteau, A., Quintas, F., 1977. Geología del flanco sur de la Sierra del Purial. Revista La Minería de Cuba 3, 54-62.

Cobiella, J., Quintas, F., Campos M., Hernández, M., 1984. Geología de la Región Central y Suroriental de la Provincia de Guantánamo. Santiago de Cuba: Editorial Oriente, Santiago de Cuba, 125 pp.

Coggon, R., Holland, T.J.B., 2002. Mixing properties of phengitic micas and revised garnet-phengite thermobarometers. Journal of Metamorphic Geology 20, 683-696.

Compston, W., Williams, I.S., Kirschvink, J.L., Zhang, Z., Ma, G., 1992. Zircon U-Pb ages for the Early Cambrian time scale. Journal Geological Society London 149, 171-184.

De Laeter, J.R., Kennedy, A.K., 1998. A double focusing mass spectrometer for geochronology. International Journal of Mass Spectrometry 178, 43- 50.

Defant, M.J., Drummond, M.S., 1990. Derivation of some modern arc magmas by melting of young subducted lithosphere. Nature 347 (6294), 662–665.

Diener, J.F.A., Powell, R., White, R.W., Holland, T.J.B., 2007. A new thermo-dynamic model for clino- and orthoamphiboles in Na2O-CaO-FeO-MgO-Al2O3-SiO2-H2O-O. Journal of Metamorphic Geology 25, 631-656.

Duncan, R.A., Hargraves, R.B., 1984. Plate tectonic evolution of the Caribbean region in the mantle reference frame. In: Bonini, W., Hargraves, R.B., Shagam, R. (eds.) The

Caribbean-South American Plate Boundary and Regional Tectonics. Boulder, Colorado, Geological Society of America, Memoir 162, 81-93.

Ernst, W.G., 1988. Tectonic history of subduction zones inferred from retrograde blueschist P–T paths. Geology 16, 1081–1084.

Escuder-Viruete JE. , Contreras F. , Stein G., Urien P ., Joubert M ., Perez Estaun A., Friedman R ., Ullrich T . Magmatic relationships and ages between adakites, magnesian andesites and Nb-enriched basalt-andesites from Hispaniola: Record of a major change in the Caribbean island arc magma sources. LITHOS, 99, 3-4, 151-177, 2007

Fleck, R.J., Sutter, J.F., Elliot, D.H., 1977. Interpretation of discordant 40Ar/39Ar spectra of Mesozoic tholeiites from Antarctica. Geochimica et Cosmochimica Acta 41, 15-32.

García-Casco, A., Torres-Roldán, R.L., Iturralde-Vinent, M.A., Millán, G., Núñez Cambra, K., Lázaro, C., Rodríguez Vega, A., 2006. High pressure metamorphism of ophiolites in Cuba. Geologica Acta 4, 63–88.

García-Casco, A., Lázaro, C., Rojas-Agramonte, Y., Kröner, A., Torres-Roldán, R.L., Núñez, K., Millán, G., Neubauer, F., Blanco-Quintero, I., 2008a. Partial melting and counterclockwise P-T path of subducted oceanic crust (Sierra del Convento mélange, Cuba). Journal of Petrology 49, 129-161.

García-Casco, A., Iturralde-Vinent, M.A., Pindell, J., 2008b. Latest Cretaceous collision/accretion between the Caribbean Plate and Caribeana: Origin of metamorphic terranes in the Greater Antilles. International Geology Review 50, 781-809.

Gerya, T.V., Stoeckhert, B., Perchuk, A.L., 2002. Exhumation of high-pressure metamorphic rocks in a subduction channel - a numerical simulation. Tectonics 21(6), 6-1 - 6-19.

Gorczyk, W., Guillot, S., Gerya, T.V., Hattori, K., 2007. Asthenospheric upwelling, oceanic slab retreat and exhumation of UHP mantle rocks: insights fromGreater Antilles. Geophysical Research Letters 34 (21), doi:10.1029/2007GL031059.

Green, E.C.R., Holland, T.J.B., Powell, R., 2007. An order-disorder model for omphacitic pyroxenes in the system jadeite-diopside-hedenbergite-acmite, with applications to eclogite rocks. American Mineralogist 92, 1181-1189.

Gutscher, M.A., Maury, R., Eissen, J.P., Bourdon, E., 2000. Can slab melting be caused by flat subduction?. Geology 28(6), 535-538.

Guillot, S., Hattori, K., Sigoyer de, J., 2000. Mantle wedge serpentinization and exhumation of eclogites: insights from eastern Ladakh, northwest Himalaya. Geology 28, 199-202.

Guillot, S., Hattori, K., Sigoyer de, J., Nägler, T., Auzende, A.L., 2001. Evidence of hydration of the mantle wedge and its role in the exhumation of eclogites. Earth and Planet Science Letters 193, 115-127.

Guillot, S., Hattori, K., Agard, P., Schwartz, S., Vidal, O., 2009. Exhumation processes in oceanic and continental subduction contexts: a review In: Lallemand, S., Funiciello, F., eds., Subduction Zone Dynamics, p. 175–204, doi 10.1007/978-3-540-87974-9, Springer-Verlag Berlin Heidelberg.

Holland, T.J.B., Powell, R., 1998. An internally consistent thermodynamic data set for phases of petrological interest. Journal of Metamorphic Geology 16, 309–343.

Holland, T.J.B., Powell, R., 2003. Activity-composition relations for phases in petrological calculations: an asymmetric multicomponent formulation. Contributions to Mineralogy and Petrology 145, 492-501.

Holland, T.J.B., Baker, J.M., Powell, R., 1998. Mixing properties and activity-composition relationships of chlorites in the system MgO-FeO-Al2O3-SiO2-H2O. European Journal of Mineralogy 10, 395-406.

Iturralde-Vinent, M.A., 1995. Meeting Reports: Caribbean ophiolites and volcanic arcs: Jamaica, October 1994. Journal of Petroleum Geology, 18. 234-235.

Iturralde-Vinent, M.A., 1998. Sinopsis de la Constitución Geológica de Cuba. Acta Geológica Hispánica 33, 9-56.

Iturralde-Vinent, M., MacPhee, R., 1999. Paleogeography of the Caribbean region, implications for Cenozoic biogeography. Bull. Amer. Mus. Nat. Hist. (238):1-95

Iturralde-Vinent, M.A., Díaz Otero, C., Rodríguez Vega, A., Díaz Martínez, R., 2006. Tectonic implications of paleontologic dating of Cretaceous-Danian sections of Eastern Cuba. Geologica Acta 4, 89-102.

Kerr A.C., White, R.V., Thompson, P.M.E., Tarney, J. & Saunders, A.D. 2003. No oceanic plateau - No Caribbean Plate? The seminal role of an oceanic plateau in Caribbean plate evolution. In: Bartolini, C., Buffler, R.T. & Blickwede, J. (eds) The Circum Gulf of Mexico and Caribbean: Hydrocarbon Habitats Basin Formation and Plate Tectonics. American Association of Petroleum Geology Memoir, 79, 126-268

Kirschner, D. L., Cosca, M. A., Masson, H., Hunziker, J. C., 1996. Staircase 40Ar⁄39Ar spectra of fine grained white mica: timing and duration of deformation and empirical constraints on argon diffusion. Geology, 24, 747-750.

Krebs, M., Maresch, W.V., Schertl, H.P., Baumann, A., Draper, G., Idleman, B., Münker, C., 2008. The dynamics of intra-oceanic subduction zones: A direct comparison between fossil petrological evidence (Rio San Juan Complex, Dominican Republic) and numerical simulation. Lithos 103, 106-137.

Kretz, R., 1983. Symbols for rock-forming minerals. American Mineralogist 68, 277–279.

Lambert, I.B., Wyllie, P.J., 1972. Melting of gabbro (quartz eclogite) with excess water to 35 kilobars, with geological applications. Journal of Geology 80, 693–708.

Lázaro, C., García-Casco, A., 2008. Geochemical and Sr-Nd isotope signatures of pristine slab melts and their residues (Sierra del Convento mélange, eastern Cuba). Chemical Geology 255, 120-133.

Lázaro, C., García-Casco, A., Neubaurer, F., Rojas-Agramonte, Y., Kröner, A., Iturralde-Vinent, M.A., 2009. Fifty-five-million-year history of oceanic subduction and exhumation at the northern edge of the Caribbean plate (Sierra del Convento mélange, Cuba). Journal of Metamorphic Geology 27, 19-40.

Leake, B.E., Woolley, A.R., Arps, C.E.S., Birch, W.D., Gilbert, M.C., Grice, J.D., Hawthorne, F.C., Kato, A., Kisch, H.J., Krivovichev, V.G., Linthout, K., Laird, J., Mandarino, J.A., Maresch, W.V., Nickel, E.H., Rock, N.M.S., Schumacher, J.C., Smith, D.C., Stephenson, N.C.N., Ungaretti, L., Whittaker, E.J.W., Touzhi, G., 1997. Nomenclature of amphiboles: Report of the Subcommittee on Amphiboles of the International Mineralogical Association, Commission on New Minerals and Mineral Names. American Mineralogist 82, 1019-1037.

Lee, J.-Y., Marti, K., Severinghaus, J.P., Kawamura, K., Yoo, H.-S., Lee, J.B., Kim, J.S., 2006. A redetermination of the isotopic abundances of atmospheric Ar. Geochimica et Cosmochimica Acta 70, 4507-4512.

Le Maitre, R.W., Bateman, P., Dudek, A., Keller, J., Lameyre Le Bas, M.J., Sabine, P.A., Schmid, R., Sorensen, H., Streckeisen, A., Woolley, A.R., Zanettin, B., 1989. A classification of igneous rocks and glossary of terms: Blackwell, Oxford, 196 p.

Leyva, R.C., 1996. Características geológicas, regularidades de distribución y perspectivas de utilización del cuarzo filoniano de la región oriental de Cuba. Unpublished report of the Instituto Superior Minero-Metalúrgico de Moa (Cuba), 90 pp.

Marchesi, C., Garrido, C.J., Godard, M., Proenza, J.A., Gervilla, F., Blanco-Moreno, J., 2006. Petrogenesis of highly depleted peridotites and gabbroic rocks from the Mayarí-Baracoa Ophiolitic Belt (eastern Cuba). Contributions to Mineralogy and Petrology 151, 717-736.

Marchesi, C., Garrido, C.J., Bosch, D., Proenza, J.A., Gervilla, F., Monié, P., Rodríguez-Vega, A., 2007. Geochemistry of Cretaceous magmatism in eastern Cuba: recycling of North American continental sediments and implications for subduction polarity in the Greater Antilles Paleo-arc. Journal of Petrology 48, 1813–1840.

Martin, H., 1999. The adakitic magmas: modern analogues of Archaean granitoids. Lithos 46(3), 411–429.

McDonough, W.F., Sun, S.S., 1995. The Composition of the Earth. Chemical Geology 120(3-4), 223-253.

Meyerhoff, A.A., Hatten, C.W., 1968. Diapiric structure in Central Cuba. Memoir of the American Association of Petroleum Geologists 8, 315–357.

Millán, G., 1996. Metamorfitas de la asociación ofiolítica de Cuba. In: Iturralde-Vinent, M.A. (Ed.). Ofiolitas y Arcos Volcánicos de Cuba. IGCP Project 364 Special Contribution 1, 131–146.

Millán, G., Somin, M.L., Díaz, C., 1985. Nuevos datos sobre la geología del macizo montañoso de la Sierra del Purial, Cuba Oriental. Reporte de Investigación del Instituto de Geología y Paleontología 2, 52–74.

Nelson, D.R., 1997. Compilation of SHRIMP U-Pb zircon geochronology data, 1996. In: Geological Survey Western Australia, pp. 189.

O´Connor, J.T., 1965. A classification of quartz-rich igneous rocks based on feldspar ratios., 525B. U. S. Geological Survey Professional Paper, B79-B84 pp.

Peccerillo, A., Taylor, S.R., 1976. Geochemistry of Eocene calc-alkaline volcanic-rocks from Kastamonu Area, Northern Turkey. Contributions to Mineralogy and Petrology 58, 63–81.

Pindell, J., Kennan, L., 2009. Tectonic evolution of the Gulf of Mexico, Caribbean and northern South America in the mantle reference frame: an update. In: James, K.H., Lorente, M.A. Pindell, J. L., eds., The Origin and Evolution of the Caribbean Plate. Geological Society of London, Special Publications 328, 1–55.

Pindell, J.L., Kennan, L., Maresch, W.V., Stanek, K.P., Draper, G., Higgs, R., 2005, Plate-kinematics and crustal dynamics of circum-Caribbean arc–continent interactions: Tectonic controls on basin development in Proto-Caribbean margins. In: Avé Lallemant, H.G., Sisson, V.B., eds., Caribbean–South American Plate Interactions, Venezuela. Geological Society of America, Special Papers 394, 7–52.

Pindell, J. L, Kennan, L., Stanek, K. P., Maresch,W. V., Draper, G., 2006. Foundations of Gulf of Mexico and Caribbean evolution: eight controversies resolved. Geologica Acta 4, 303-341.

Powell, R., Holland, T.J.B., 1994. Optimal geothermometry and geobarometry. American Mineralogist 79, 120–133.

Proenza, J.A., Melgarejo, J.C., Gervilla, F., Rodríguez-Vega, A., Díaz-Martínez, R., Ruiz-Sánchez, R., Lavaut, W., 2003. Coexistence of Cr- and Al-rich ophiolitic chromitites in a small area: the Sagua de Tánamo district, Eastern Cuba. In: Eliopoulos et al. (Eds.). Mineral Exploration and Sustainable Development. Rotterdam Netherlands, Millpress 1, 631-634.

Proenza, J.A., Díaz-Martínez, R., Iriondo, A., Marchesi, C., Melgarejo, J.C., Gervilla, F., Garrido, C.J., Rodríguez-Vega, A., Lozano-Santacruz, R., Blanco-Moreno, J.A., 2006. Primitive Cretaceous island-arc volcanic rocks in eastern Cuba: the Téneme Formation. Geologica Acta 4, 103–121.

Prouteau, G., Scaillet, B., Pichavant, M., Maury, R., 2001. Evidence for mantle metasomatism by hydrous silicic melts derived from subducted oceanic crust. Nature 410(6825), 197-200.

Purdy, J.W., Jäger, E., 1976. K-Ar ages on rock-forming minerals from the Central Alps. Mere Ist Geol Mineral University of Padova 30,1-32.

Renne, P.R., Swisher, C.C., Deino, Al.L., Karner, D.B., Owens, T.L., DePaolo, D.J., 1998. Intercalibration of standars, bsolute ages and uncertainties in 40Ar/39Ar dating. Chemical Geology 145, 117-152.

Renne, P.R., Knight, K.B., Nomade, S., Leung, K.-N., Lou, T.-P., 2005. Application of deuteron-deuteron (D-D) fusion neutrons to 40Ar/39Ar geochronology. Applied Radiation and Isotopes 62, 25-32.

Renne, P.R., Sharp, Z.D., Heizler, M.T., 2008. Cl-derived argon isotope production in the CLICIT facility of OSTR reactor and the effects of the Cl-correction in 40Ar/39Ar geochronology. Chemical Geology 255, 463-466.

Renne, P.R., Cassata, W.S., Morgan, L.E., 2009. The isotopic composition of atmospheric argon and 40Ar/39Ar geochronology: time for a change? Quaternary Geochronology, in press, doi: 10.1016/j.quageo.2009.02.015.

Sharp,Turrin, B.D., Renne, P.R., Lanphere, M.A., 1996. 40Ar/39Ar and K-Ar dating of lavas from the Hilo 1-km corehole Hawaii. Geochemestry, Geophisics, Geosystems 6 (4), doi: 10.1029/2004GC000846.

Somin, M., Millán, G., 1981. Geology of the Metamorphic Complexes of Cuba (in russian). Nauka, Moscow.

Spear, F.S., 1993. Metamorphic Phase Equilibria and Pressure-Temperature-Time Paths. Mineralogical Society of America, Monograph 1, 799 p.

Steiger, R.H., Jäger, E., 1977. Subcommission on geochronology: convention on the use of decay constants in geo- and cosmochronology. Earth and Planetary Science Letters 36, 359-362.

Stern, R.A., 1997. The GSC sensitive high resolution ion microprobe (SHRIMP): Analytical techniques of zircon U-Th-Pb age determinations and performance evaluation. In: Radiogenic age and isotope studies, pp. F1-31, Geological Survey Canada.

Stern, R.J., 2002. Subduction Zones Reviews of Geophysics, 40, DOI: 10.1029/2001RG000108

Stern, R.J. 2004. Subduction Initiation: Spontaneous and Induced. Earth Planet. Sci. Lett. 226, 275-292)

Sun, S.S., McDonough, W.F., 1989. Chemical and isotopic systematics of oceanic basalts; implications for mantle composition and processes, in: Saunders, A.D. and Norry, M.J. (Eds), Magmatism in the Ocean Basins Geological Society Special Publications, Geological Society of London, London, United Kingdom, p. 313–345.

Torres-Roldán, R.L., García-Casco, A., García-Sánchez, P.A., 2000. CSpace: An integrated workplace for the graphical and algebraic analysis of phase assemblages on 32-bit Wintel platforms. Computers and Geosciences 26, 779-793.

Ulmer, P., Trommsdorff, V., 1995. Serpentine stability to mantle depths and subduction-related magmatism. Science 268, 858–861.

Wakabayashi, J., 2004. Tectonic mechanisms associated with P–T paths of regional metamorphism: Alternatives to single-cycle thrusting and heating: Tectonophysics 392, 193-218.

White, R.W., Powell, R., Holland, T.J.B., 2007. Progress relating to calculation of partial melting equilibria for metapelites. Journal of Metamorphic Geology 25, 511-527.

Williams, I.S., 1998. U-Th-Pb geochronology by ion microprobe. In: McKibben, M. A., Shanks III, W.C., Ridley, W.I. (Eds.), Applications of microanalytical techniques to understanding mineralizing processes: Society of Economic Geologists, review, pp. 1-35.

Wolf, M.B., Wyllie, P.J., 1994. Dehydration-melting of amphibolite at 10 kbar: the effects of temperature and time. Contributions to Mineralogy and Petrology 115, 369-383.

Yogodzinski, G.M., Kay, R.W., Volynets, O.N., Koloskov, A.V., Kay, S.M., 1995. Magnesian Andesite in the Western Aleutian Komandorsky Region – Implications for Slab Melting and Processes in the Mantle Wedge. Geological Society of America Bulletin 107(5), 505- 519.

Yogodzinski, G.M., Lees, J.M., Churikova, T.G., Dorendorf, F., Woerner, G., Volynets, O.N., 2001. Geochemical evidence for the melting of subducting oceanic lithosphere at plate edges. Nature 409(6819), 500-504.

4- THE IMPRINT OF SEDIMENT-DERIVED FLUIDS ON MELTING OF MORB AMPHIBOLITE IN A SUBDUCTION SETTING (SIERRA DEL CONVENTO MÉLANGE, CUBA)

C. Lázaro[(1)], I.F. Blanco-Quintero[(1)], C. Marchesi[(2)], D. Bosch[(2)], A. García-Casco[(1,3)]

(1) Departamento de Mineralogía y Petrología, Universidad de Granada, Avda. Fuentenueva s/n, 18002 Granada, Spain.

(2) Geosciences Montpellier, Equipe Manteau-Noyau, UMR 5243, CNRS-Universite Montpellier II, 34095, Montpellier, France.

(3) Instituto Andaluz de Ciencias de la Tierra, CSIC-Universidad de Granada, Avda. Fuentenueva s/n, 18002 Granada, Spain.

ABSTRACT

Major and trace element geochemical signatures and Sr–Nd isotope data of muscovite (Ms)-bearing amphibolite blocks and associated muscovite-bearing trondhjemitic and quartz-muscovite rocks from the Sierra del Convento mélange (eastern Cuba) indicate that oceanic crust underwent partial melting processes during subduction and accretion to the upper plate triggered by the infiltration of fluids evolved from the subducting sediments. REE patterns of the Ms-trondhjemites are fractionated ($2<(La/Yb)n<62$), with LREE enrichment and HREE depletion. These patterns are similar to adakitic melts formed by partial melting of mafic material at moderate to high pressure. Indeed, Ms-trondhjemites from Sierra del Convento mélange exhibit geochemical features considered distinctive of adakites, including SiO_2>56 wt %, high Na_2O contents (4.5-9 wt.%), (K_2O/Na_2O)≈0.42, Mg#≈50, LREE enrichment, HREE depletion, and high La/Yb and Sr/Y. We consider that these rocks represent an end-member of the volcanic arcs series formed at depth in the subduction environment that did not react with the mantle wedge before eruption. Furthermore, we have identified the crystallization products (Qtz-Ms rocks, highly enriched in LILE, K and Ba) of the primary fluids evolved from subducted sediments that infiltrated the accreted blocks of MORB amphibolite and promoted their partial melting under water-saturated conditions.

Keywords: Slab melt, Adakite, Fluid composition, sedimentary imprint, Sr–Nd isotopes

INTRODUCTION

Different conditions may trigger partial melting of the slab and/or the overlying mantle wedge in subduction settings. In cold subduction zones the geothermal conditions of the slab may not allow attaining P–T conditions for melting at sub-arc depths (ca. 150 km), but triggers dehydration of the slab and the release of large ion lithophile element (LILE)-enriched hydrous fluids that metasomatize the overlying mantle wedge and instigate its melting (e.g. Gill,1981; Kushiro,1990; Tatsumi and Kogiso, 1997). Partial melting of the slab is however inferred to occur at sub-arc depths in many warm and hot subduction zones (Bebout, 2007). These melts may eventually reach shallow depths in the volcanic arc after infiltration through the mantle wedge (and triggering its melting, Rapp et al., 1999) or after formation of underplated mantle wedge plumes (Gerya and Yuen, 2003; Gorczyk et al., 2007; Castro and Gerya, 2008; Castro et al., 2010). However, direct observation of processes taking place at sub-arc depths is hampered by the scarcity of rocks that escaped burial into the mantle.

Examples of pristine slab-derived melts that reached the Earth's surface are scarce. Only in rare cases of oceanic subduction complexes, such as the Catalina Schist mélange (California) and the Sierra del Convento and La Corea mélanges (eastern Cuba), partial melting of metabasite and metasomatic mass-transfer processes in the slab have been described (Sorensen, 1988; Sorensen and Grossman, 1989; Bebout and Barton, 1993; Grove and Bebout, 1995; García-Casco, 2007; García-Casco et al., 2008a; Lázaro and García-Casco, 2008; Blanco-Quintero et al., 2010a). The tonalitic–trondhjemitic rocks produced after melting of amphibolite in the Catalina Schist were considered as primary adakitic liquids by Martin (1999). The geochemical characteristics of K-poor tonalitic-trondhjemitic rocks of the Sierra del Convento mélange indicate that they constitute pristine partial melts formed after fluid-fluxed melting of subducted N-MORB garnet-epidote amphibolite in response to a very hot subduction scenario likely caused by subduction of a young hot slab (García-Casco et al,. 2008a; Lázaro and García-Casco, 2008). The depth of melting was ca. 50 km, shallower than typical sub-arc depths where slab melts segregate from garnet+clinopyroxene-rich residues. Elemental and isotopic features of the K-poor tonalitic-trondhjemitic rocks of the Sierra del Convento exclude a sediment source for the infiltrating fluid and suggest, in turn a fluid evolved from a depleted source such as dehydrating serpentinite from the downgoing slab (Lázaro and García-Casco, 2008).

Recently, however, we have identified K-rich trondhjemitic rocks in the Sierra del Convento and La Corea mélanges (eastern Cuba). These rocks formed after partial melting of MORB-derived amphibolite and crystallized at depth in the subduction environment, same as the K-poor trondhjemites described so far (references above), but are strongly enriched in LIL elements such as K, Ba, Rb, suggesting a different source for the infiltrating fluid. In this paper, we characterize the major, trace element and Sr–Nd isotope geochemistry of K-rich primary melts, residual rocks, and hydrothermal rocks produced in the hot subduction scenario of the Sierra del Convento mélange.

GEOLOGICAL SETTING

The Greater Antilles constitute an orogenic belt located at the northern margin of the Caribbean plate that documents the collision of a Mesozoic–Tertiary volcanic arc with buoyant parts of the North American plate during the Late Mesozoic and Tertiary. The orogenic belt is mainly composed of oceanic material, including ophiolites and intra-oceanic volcanic arc complexes, as well as continental material represented by fragments of the southern borderlands of North America (Bahamas platform and the Maya block) and the Caribeana terrane (García-Casco et al., 2008b). All these terrains are well exposed in Cuba (Fig. 1a), where the oceanic material includes the northern and eastern ophiolite belts and the Cretaceous and Palaeogene volcanic arcs (Iturralde-Vinent, 1998 and references therein).

In eastern Cuba, the ophiolitic belt is formed by two large bodies named Mayarí-Cristal and Moa-Baracoa. The elemental and isotopic composition of these complexes indicates a supra-subduction environment (Marchesi et al., 2006, 2007; Proenza et al., 2006). The ophiolitic bodies form the highest structural complexes in the region, overriding the volcanic-arc complexes. The latter, formed by the Santo Domingo (to the NW) and the Purial (tom the S-SE) complexes, have been classically considered the eastern continuation of the western and central Cuban Cretaceous volcanic arc complex (Fig. 2a; Iturralde-Vinent et al., 1996, 2006). They are composed of tholeiitic and calcalkaline volcanic arc sequences (Gyarmati et al., 1997), and the Purial complex was metamorphosed to greenschist and blueschist facies (Boiteau et al., 1972; Somin and Millán, 1981; Cobiella et al., 1984; Millán and Somin, 1985; Millán, 1996) during latest Cretaceous (70-75 Ma) times (Somin et al., 1992; Iturralde-Vinent et al., 2006).

Mélange complexes made of serpentinitic matrix enclosing high pressure metamorphic exotic blocks crop out below the ophiolitic bodies and above the volcanic arc complexes The most significant serpentinite mélanges are the Sierra del Convento and La Corea mélanges, both sharing similar lithological assemblages (Somin and Millán, 1981; Kulachkov and Leyva, 1990; Hernández and Canedo, 1995; Leyva, 1996; Millán, 1996; Blanco-Quintero, 2003; García-Casco et al., 2006, 2008a). The Sierra del Convento mélange, located in the south, overrides the Purial complex (Fig. 1a,b). The La Corea mélange is located in the Sierra de Cristal, and is associated with the Mayarí-Cristal ophiolitic body (Fig. 1a). The serpentinitic matrix is made of antigoritite and formed deep in the subduction environment after hydration of upper plate harzburgitic rocks (Blanco-Quintero et al., 2010b). These mélanges have been interpreted as fragments of the subduction channel related to south-westward-directed subduction on the leading edge of the Caribbean plate during the Cretaceous (García-Casco et al., 2006, 2008a,b; Blanco-Quintero et al., 2010a, b).

The main type of block in these melanges is epidote ± garnet amphibolite and associated leucocratic trondhjemite-tonalite rocks. The amphibolites show variable grain size and extent of deformation and recrystallization (García-Casco et al, 2008a). They are foliated and mainly composed of amphibole+epidote±quartz±garnet and have major and trace element geochemistry indicative of N-MORB signature (Lázaro and García-Casco, 2008). Leucocratic rocks of trondhjemitic–tonalitic composition are commonly associated with the amphibolites and constitute their partial melting product at 700-750 ºC ca. 15 kbar

(García-Casco et al, 2008a; Lázaro and García-Casco, 2008; Blanco-Quintero et al., 2010a). They are formed by primary (magmatic) plagioclase+quartz+epidote±paragonite±pargasite, have variable grain size, and show minor deformation.

Muscovite-bearing amphibolites and trondhjemites constitute rock varieties associated with Ms-lacking lithologies. This paper examines the geochemistry of these muscovite-bearing rocks in order to get insight into the source and role of slab-derived fluids in the generation of slab magmas. The rocks examined are muscovite-bearing amphibolites (samples CV139a, CV140a, CV230a, CV230c), trondhjemites (SC-20, CV230e, CU-72-I, CU-72), locally with pegmatitic texture (CV201a, CV201g, CV201h), and Qtz-Ms hydrothermal rocks (CV201d, CV201f, CV53e-I, CV53e-II) that crosscut other types of rock or form discrete bodies.

ANALYTICAL TECHNIQUES

Bulk-rock chemistry

Powered whole-rock samples were obtained by grinding in a tungsten carbide mill. Major element and Zr compositions were determined on glass beads, made of 0.6 g of powered sample diluted in 6 g of $Li_2B_4O_7$, by a PHILIPS Magix Pro (PW-2440)

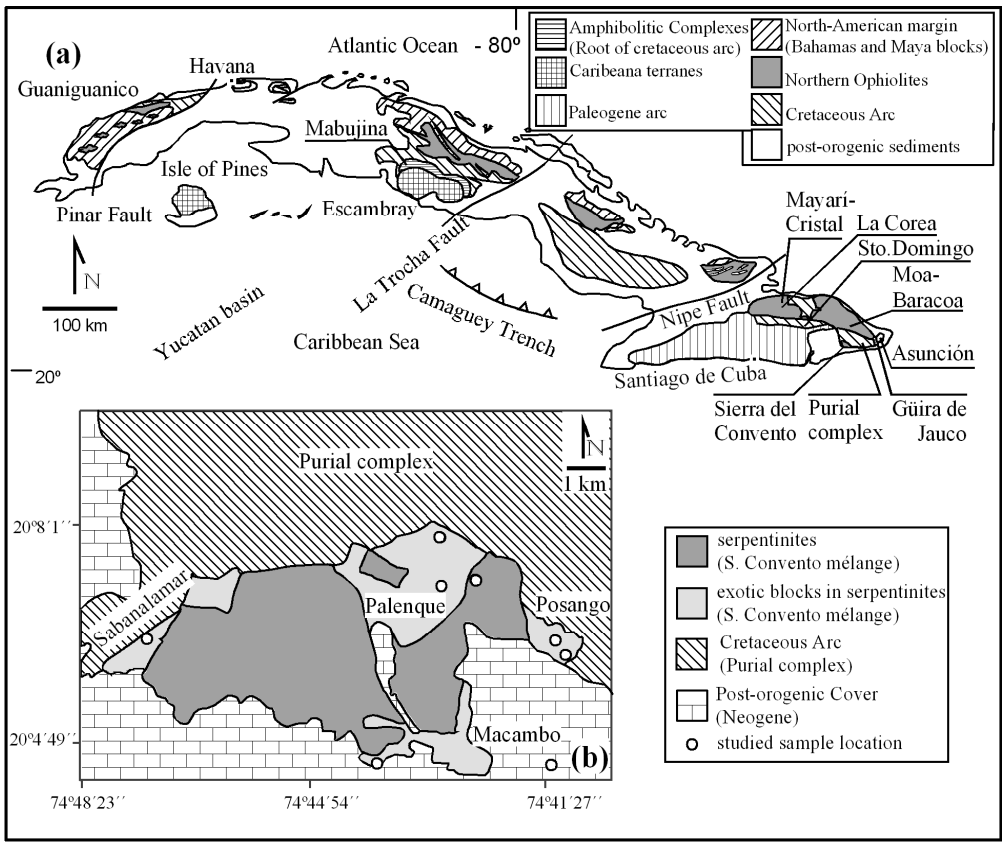

Fig. 1. (a) General geological map of Cuba (Iturralde-Vinent, 1998) showing the main geological units, (b) Geological map of Sierra del Convento (Kulachkov and Leyva, 1990) with location of sample sites.

X-ray fluorescence (XRF) equipment at the University of Granada (Centro de Instrumentación Científica, CIC). Precision was better than ±1.5% for an analyte concentration of 10 wt.%. Precision for Zr and LOI is better than ±4% at 100 ppm concentration. The analyses were recalculated to an anhydrous 100 wt % basis compositions, and these new data are used in the text and figures. The Mg number (Mg#) is expressed (100*molar MgO/(MgO+FeOtot)).

Trace element, except Zr, were determined at the University of Granada (CIC) by ICP-Mass Spectrometry (ICP-MS) after HNO_3+HF digestion of 0.1000 g of sample powder in a Teflon-lined vessel at ~180 °C and ~200 p.s.i. for 30 min, evaporation to dryness, and subsequent dissolution in 100 ml of 4 vol % HNO_3. Blanks and international standards PMS, WSE, UBN, BEN, BR, and AGV (Govindaraju, 1994) were run as unknowns during analytical sessions. Precision was better than ±2% and ±5% for analyte concentrations of 50 and 5 ppm.

Isotope analysis

Isotope analyses were carried out at the University of Granada (CIC). Whole rock samples for Sr and Nd isotope analyses were digested in the same way as for ICP-MS analysis, using ultra-clean reagents and analyzed by thermal ionization mass spectrometry (TIMS) in a Finnigan Mat 262 spectrometer after chromatographic separation with ion exchange resins. Normalization values were 86Sr/88Sr=0.1194 and 146Nd/144Nd=0.7219. Blanks were 0.6 and 0.09 ng for Sr and Nd, respectively. The external precision (2σ), estimated by analysing 10 replicates of the standard WSE (Govindaraju, 1994), was better than 0.003% for $^{87}Sr/^{86}Sr$ and 0.0015% for $^{143}Nd/^{144}Nd$. The $^{87}Sr/^{86}Sr$ measured value in the laboratory for NBS 987 international standard was 0.710250±0.0000044 (2σ, n=106). Measurements of La Jolla Nd international standard on this mass spectrometer yield a $^{143}Nd/^{144}Nd$ ratio of 0.511844±0.0000067 (2σ, n=49).

PETROGRAPHY

Peak metamorphic mineral assemblage of the studied Ms-amphibolite samples consists of pargasitic amphibole, epidote, garnet, phengite, rutile, titanite, and accessory apatite and quartz (Fig. 2a; Table 1). These assemblages define a crude foliation mainly marked by phengite and pargasite crystals. Quartz appears as small dispersed grains in the matrix, but quartz-absent samples are common. Garnet has been observed in all the studied samples (Table 2). It forms large porphyroblasts containing inclusions of amphibole and epidote (Fig. 2a). Phengitic mica appears as idiomorphic and medium grained crystals. Titanite forms idiomorphic crystals elongated along the foliation, but it also replaces rutile. Retrograde overprints consist of association of glaucophane, actinolite, (clino)zoisite, chlorite, pumpellyite, and, less abundantly, albite and paragonite. All these retrograde minerals are fine-grained and corrode the peak-metamorphic minerals, but they are also dispersed in the matrix or located in fractures. Retrograde glaucophane is typically aggregated with actinolite, chlorite and albite, and commonly overprints peak amphibole (Fig. 2a). Chlorite and pumpellyite replace garnet and pargasite. Retrograded crystals of pargasite commonly contain small needles of exsolved rutile or titanite.

The magmatic mineral assemblage of the Ms-trondhjemites (including the pegmatitic varieties) is composed of medium-grained plagioclase, quartz and phengite, with subordinate epidote, plus accessory apatite, titanite, and rutile (Fig. 2b; Table 2). Garnet is occasionally present. Epidote and garnet are idiomorphic and medium grained. Phengite is idiomorphic and has medium grain size. Retrograde mineral assemblages overprint the magmatic assemblages. Magmatic plagioclase appears generally transformed to retrograde albite plus fine-grained (clino)zoisite, paragonite, phengite, and, locally, lawsonite. Magmatic epidote is overprinted by fine grained overgrowths of (clino)zoisite. Glaucophane is absent. Titanite replaces rutile. Very small amounts of retrograde K-feldspar, celsian and cymrite have been observed in some samples.

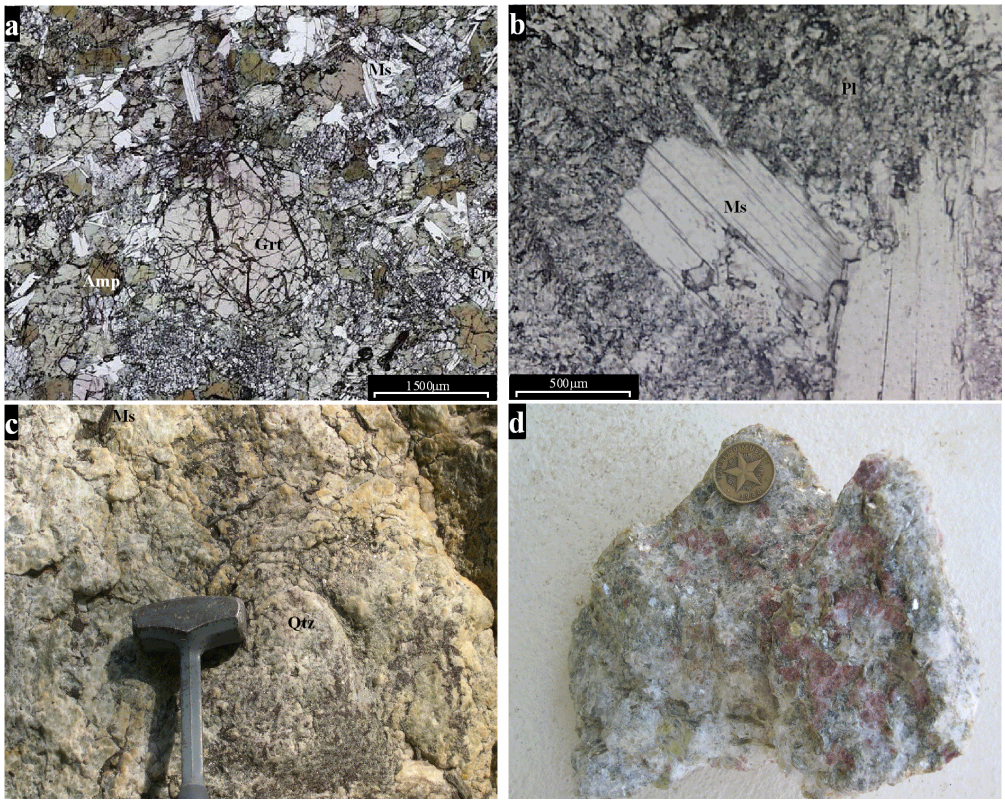

Fig. 2. (a) Photomicrograph of Ms-amphibolite composed of amphibole, epidote, garnet, mica (phengite) and titanite. (b) Photomicrograph of a Ms-trondhjemite bearing plagioclase, muscovite, quartz and clinozoisite-epidote. (c) Qtz-Ms block. (d) Garnet-bearing Qtz-Ms rock. The scale bar is 1500 µm in (a) and 500 µm in (b). Mineral abbreviations after Kretz (1983).

Table 1 Mineral abundance in the studied samples (visual estimates).

	peak metamorphic / magmatic										retrograde									
	Amp	Ep	Grt	Phe	Qtz	Pl	Pa	Rt	Ttn	Ap	CaAmp	Gl	Chl	Pmp	Ab	Lws	Pa	Czo	Kfs
Ms-amphibolites																				
CV139a	45	20	20	10	5				x			x	x	x	x	x				
CV140a	55	15	10	15	5			x				x	x	x	x					
CV230c	74	10	10	5					1			x	x	x	x			x	x	
CV230a	55	25	15						5			x	x	x	x				x	
Ms-trondhjemites																				
CV201a	x		20	30	40				x				x			x		10	x	
CV201g		x	20	20	50														x	
SC-20	8	x	x	20	55	x							x			3	10	4		
CV201h			20	15	55										x	1	4	5		
CV230e			5	35	55													5	x	
CU-72-I		2	10	30	45								x			5	x	3		
CU-72		1	10	30	45								x			5	x	4		
Qtz-Ms rocks																				
CV201d			55	45	x														x	
CV201f			35	65															x	
CV278a-I			10	35	55														x	
CV53e-I			45	55																
CV53e-II			45	55																

The Qtz-Ms rocks present a mineralogy essentially composed of medium to coarse size crystals of quartz and phengite (Fig. 2c). Sample CV278a-I also has coarse garnet crystals (Fig. 2d). Scarce fine-grained of K-feldspar is also present in all the samples.

GEOCHEMISTRY

Major elements

Ms-amphibolites

The SiO_2 contents of Ms- bearing amphibolite range from 42.1 to 46.5 wt % (Table 2), varying from picro-basaltic to basaltic compositions in the TAS diagram (Le Maitre et al., 1989), lying on the sub-alkaline-alkaline field (Fig. 3a). They have medium-K to high-K calc-alkaline affinity in the SiO_2-K_2O diagram (Fig. 3b; Peccerillo and Taylor, 1976) but, as discussed below, K_2O (and Na_2O) contents do not represent primary (magmatic) abundances. In general, the samples have higher contents in K_2O (Fig. 3b), Al_2O_3, and BaO, and significantly lower contents in MgO (Fig. 4) than the Ms-lacking amphibolites of Sierra del Convento mélange (Lázaro and García-Casco, 2008).

Notably, the samples show quite variable Na_2O contents (1.17-4.17 wt %), so that two samples have high inverse agpaitic index as compared to MORB and other amphibolites from the Sierra del Convento while another two samples present a similar inverse agpaitc index as MORB (Fig. 5).

Ms-trondhjemites

Ms-trondhjemites in the TAS diagram have rhyolite composition, except one sample which has trachyte composition (Fig. 3a), with SiO_2 contents ranging from 65.6 to 75.6 wt %. They have low-K tholeiitic to medium-K calc-alkaline affinity (Fig. 3b). They have Na_2O and K_2O contents ranging from 5.4 to 9 wt % and from 0.77 to 1.74 wt %, respectively. The Mg# values, from 14 to 60, are lower than or similar to those of Ms-lacking trondhjemites (Fig. 4).

Considering amphibolites and trondhjemites in Harker diagrams, they show similar trends to those of Ms-lacking amphibolite-trondhjemite rocks (Lázaro and García-Casco, 2008) and acid rocks from the Catalina Schist (Fig. 4), except for higher SiO_2, K_2O and BaO contents (Fig. 3b and Fig. 4). A gap in silica content ranging from 47 to 66 wt.% SiO2 is consistent with derivation of the trondhjemitic rocks from partial melting of amphibolites and melt extraction (cf., Lázaro and García-Casco, 2008).

Importantly, the Ms-trondhjemites are Al-saturated (i.e. peraluminous; ASI = 1.108-1.289; Fig. 5) and plot close to the alkali feldspar-white mica mixing line delineated in Fig. 5. In the CIPW normative An-Ab-Or diagram of O´Connor (1965), with the classification of acid and intermediate rocks modified by Barker (1979), these samples mainly plot in the trondhjemitic field (Fig. 6).

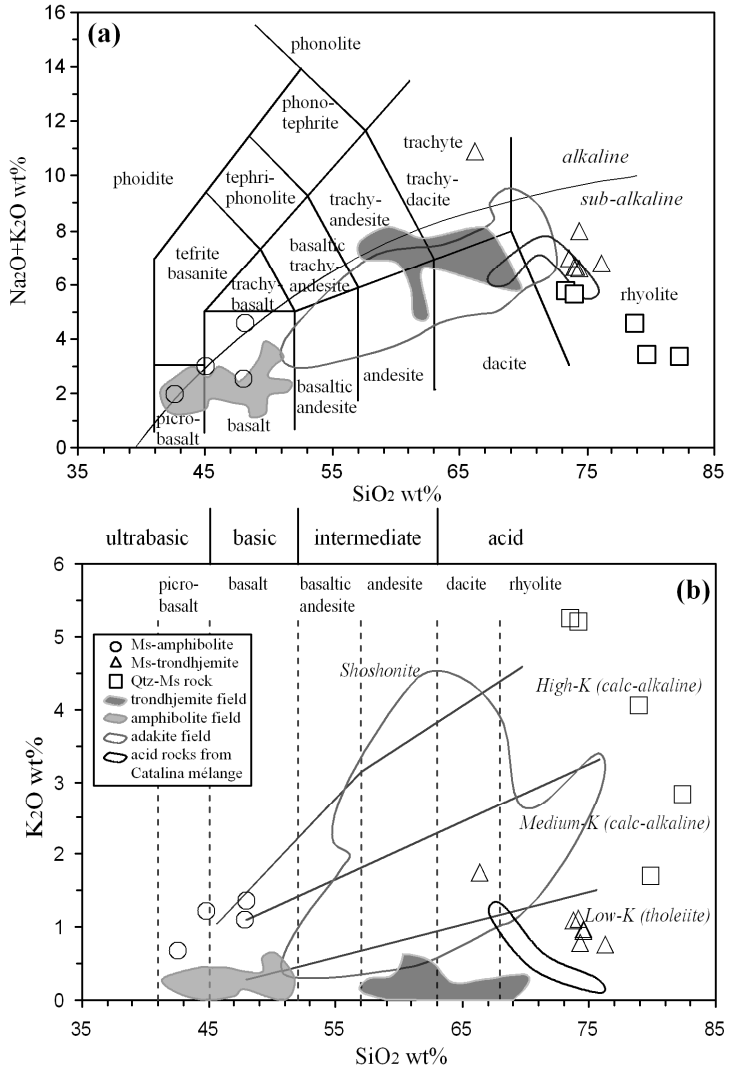

Fig. 3. (a) TAS diagram of classification of volcanic rocks from Le Maitre et al. (1989) and (b) K_2O vs. SiO_2 diagram (Peccerillo and Taylor, 1976) with subdivision of volcanic series and TAS based names of rocks of the subalkaline series. The diagrams contain the studied Ms-amphibolites, Ms-trondhjemites, Qtz-Ms rocks and, for comparison, the K-poor amphibolites and trondhemites from the Sierra del Convento mélange (Lázaro and García-Casco, 2008), acid rocks from the Catalina mélange, California (pegmatites and leucocratic segregates, Sorensen and Grossman, 1989); Cenozoic adakites from the Aleutians (Yogodzinski et al., 1995), Argentina (Benoit et al., 2002), Chile (Stern and Kilian, 1996), Ecuador (Beate et al., 2001; Bourdon et al., 2002; 2003; Samaniego et al., 2005), Philippines (Sajona et al., 1996; 2000), Japan (Morris, 1995), Panama-Costa Rica (Defant et al., 1992), USA (Smith and Leeman, 1987); and average adakite values (Martin, 1999; Smithies, 2000). All analyses normalized to 100 wt% anhydrous.

Qtz-Ms rocks

Qtz-Ms rocks are hydrothermal and are not suitable of classification in geochemical diagrams devised for igneous rocks. However, for comparison, they have been plotted in the same diagrams. Their SiO_2 contents range from 71.5 to 81.2 wt % (Fig. 3). Contents of K_2O are higher than 1.7 wt %, reaching 5.1 wt %. These rocks

have lower Na_2O contents (<1.66 wt %) than the Ms-trondhjemites, while the Al_2O_3 contents are similar (12.3-18.3 wt %). They are depleted in CaO, with contents lower than 0.2 wt %. These Qtz-Ms veins show significant contents in BaO, reaching values of 1.35 wt % (Fig. 4).

Similar to the Ms-trondhjemites, and due to the impoverishment in CaO, these rocks lie on the albite/Kfeldspar-paragonite/muscovite line in the IAI vs. ASI diagram (Fig 5). Therefore, Qtz-Ms rocks are peraluminous, with ASI values considerably high due to the scarcity of feldspar (2.63-3.11; Fig. 5).

Trace elements

Ms-amphibolites

The general pattern of element distribution indicates important deviations from MORB composition, with enrichments in Ba, La, Pb, Sr, and Eu, and variable enrichment/depletion in Th and Zr (Fig. 7a), with homogeneous values from Sm to Ni (Fig. 7a).

The abundances of LREE and HREE range from 28 to 120 and from 12 to 25 the chondrite values, respectively (Fig. 8a). The chondrite-normalized REE diagrams are characterized by enriched LREE patterns showing basaltic affinity. The REE compositions of these Ms-amphibolites show different values to the Ms-lacking amphibolites from the mélange (Lázaro and García-Casco, 2008) indicating a heterogeneous subducting oceanic crust or a MOR-basaltic rock modified before, during, or after subduction. The (La/Yb)n ratio (normalized to chondrite, McDonough and Sun, 1995) varies from 2.1 to 5.1, showing fractionated patterns. The samples have no or positive Eu anomaly (Eu/Eu* = 0.98-1.45).

Ms-trondhjemites

The Ms-trondhjemites show fractionated patterns (Fig. 7b) similar to those of Ms-lacking trondhjemites of the Sierra del Convento mélange (grey field in Fig. 7b). Relative to the latter (Lázaro and García-Casco, 2008), the Ms-trondhjemites are enriched in Ba and Pb, depleted in Sr, and have similar contents in other element (Table 4, Fig. 7b).

LREE and HREE range from 3 to 24 and from 0.1 to 4.5 the chondrite values, respectively (Fig. 8b). The (La/Yb)n ratio ranges from 2 to 62, showing slightly to strongly fractionated patterns. The general low REE contents and (La/Yb)n ratios of the Ms-bearing trondhjemites can be explained in terms of a minor contribution of REE-bearing phases during melting of the amphibolites. The samples display positive Eu anomalies, with Eu/Eu* values higher than 1.1, reaching 10. This, in turn, suggests the important participation of plagioclase in the melting process, in agreement with the lack of peak plagioclase in the amphibolites (cf. García-Casco et al., 2008a).

The Nb–Y and Rb–(Y+Nb) diagrams (Fig. 9) of Pearce et al. (1984) indicates that the samples correspond to the volcanic arc setting, precluding ocean ridge, within-plate, and syn-collision settings. In these diagrams, adakites from a number of localities worldwide and Ms-lacking trondhjemites from the Sierra del Convento mélange compare well with the studied Ms-trondhjemitic rocks.

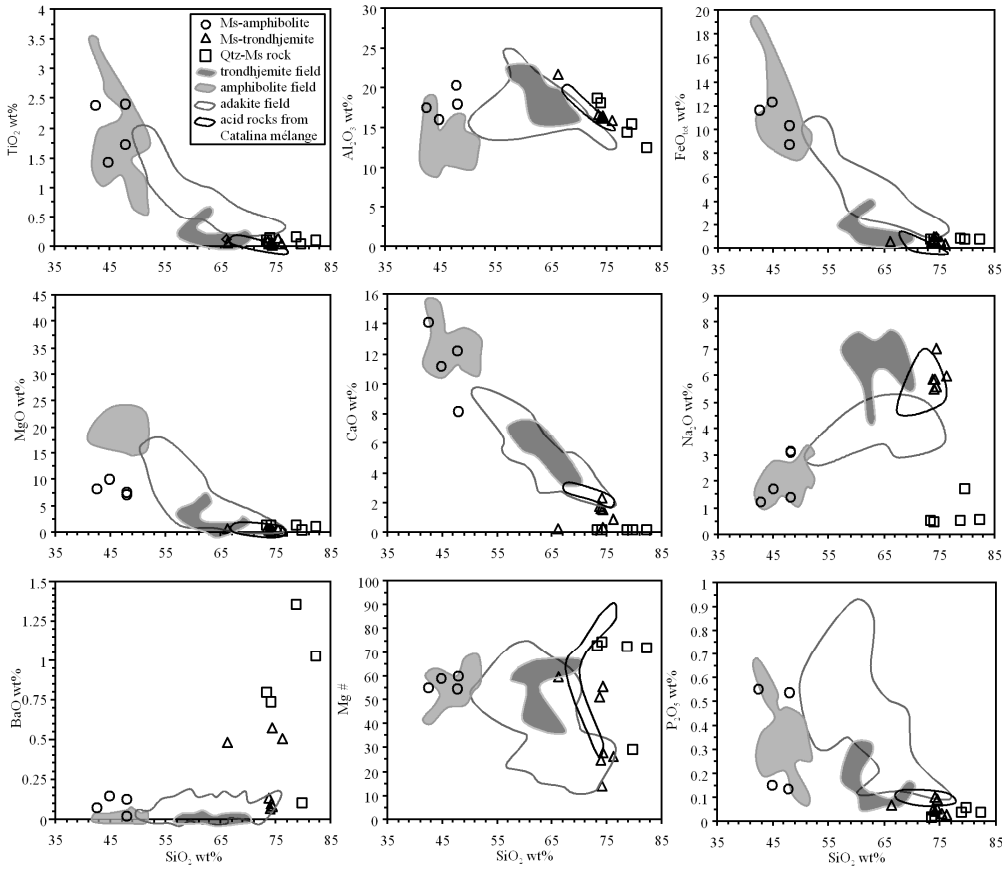

Fig. 4. Harker variation diagrams showing the composition of Ms-amphibolites, Ms-trondhjemites and Qtz-Ms rocks from the Sierra del Convento and, for comparison, N-MORB (Hofmann, 1988; Kelemen et al., 2003), altered MORB (Staudigel et al., 1996), amphibolites and trondhemites from the Sierra del Convento mélange (Lázaro and García-Casco, 2008), Cenozoic adakites (references as in Fig. 3), and acid rocks from the Catalina mélange, California (Sorensen and Grossman, 1989).

The Sr contents are high (from 86 to 410 ppm) and the Y contents are low (<10.7 ppm) (Table 4). This is clearly appreciated in the Sr/Y vs. Y diagram of Defant and Drummond (1990), where the Ms-trondhjemites mostly plot in the adakite field although they do not reach the high values of Ms-lacking trondhjemites of the mélange (Fig. 10a). However, in the (La/Yb)n vs. (Yb)n diagram (Martin, 1986) two different patterns can be observed; one group of Ms-trondhjemite samples plots outside the typical field of adakites, with low (La/Yb)n values (same as Ms-lacking trondhjemites from the Sierra del Convento and the acid rocks from the Catalina Schist mélanges), while other group of samples has distinctively higher (La/Yb)n values (Fig. 9b).

Qtz-Ms rocks

Given the mineral assemblage of these rocks, their geochemical characteristics are largely controlled by the chemistry of muscovite. They are slightly enriched in LILE compared to Ms-trondhjemites (Fig. 7c). Qtz-Ms rocks display fractionated chondrite-normalized REE patterns. The (La/Yb)n ratio ranges from 4 to 25 (except

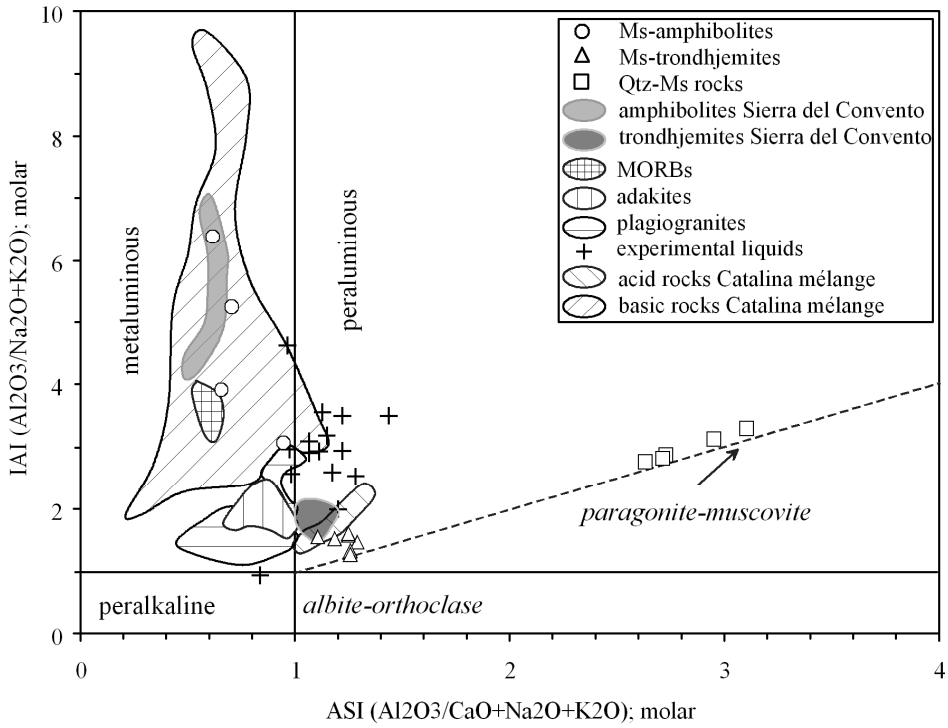

Fig. 5. IAI (inverse agpaitic index)-ASI (alumina saturation index) diagram with indication of the projection of alkali-feldspar and white micas for reference.

sample CV278a-I due to the presence of garnet, see Fig 2d) and the Eu anomaly is in general positive (Eu/Eu* = 1.8-3.5). These rocks present LREE values similar to the most enriched samples of Ms-trondhjemite, while their HREE values are similar to the medium HREE Ms-trondhjemite samples. The REE patterns for Qtz-Ms rocks are more fractionated than those of Ms-trondhjemites, as can be also appreciated from their larger (La/Yb)n ratios (Fig. 10b).

The Sr (<187 ppm) and Y contents are low (<5.4 ppm, in general) and similar to Ms-trondhjemites (Table 4). However, this rock type has very low Sr/Y, (La/Yb)n and (Yb)n (Figs. 9a and b).

Sr and Nd isotopes

The measured $^{87}Sr/^{86}Sr$ ratio of Ms-amphibolites ranges from 0.703745 to 0.705905, similarly to the isotopic ratio of the analyzed Ms-trondhjemite (0.705817). The measured $^{87}Sr/^{86}Sr$ ratios of Qtz-Ms rocks are higher (0.706729 and 0.708927). Values measured of 143Nd/144Nd range from 0.5122921 to 0.512997 (Ms-amphibolites), 0.512745 (Ms-trondhjemite) and 0.512550 and 0.512709 (Qtz-Ms rocks).

Following Lázaro and García-Casco (2008) and Lázaro et al. (2009) all isotopic measured data were corrected at 114 Ma (Table 3, Fig. 11). This age was established by SHRIMP zircon ages of trondhjemites of the Sierra del Convento mélange (Lázaro et al., 2009). The εNd(114 Ma) value of the analyzed Ms-trondhjemite (+1.94) deviates from that depleted mantle rocks and points to significant input of a

Table 2. Major (wt%) element (ppm) composition of Ms-amphibolites, Ms-trondhjemites, Ms-pegmatites and Average trondhjemite from the Sierra del Convento mélange.

Rock	Ms-amphibolites				Ms-trondhjemites							Qtz-Ms rocks				
Sample	CV139a	CV140a	CV230c	CV230a	CV201a	CV201g	SC-20	CV201h	CV230e	CU-72-I	CU-72	CV201d	CV201f	CV278a-I	CV53e-I	CV53e-II
SiO_2	46.27	46.54	42.08	44.24	75.55	73.80	73.09	65.63	72.72	73.37	73.18	81.15	77.11	77.90	71.47	71.82
TiO_2	1.66	2.31	2.34	1.39	0.03	0.05	0.04	0.06	0.07	0.02	0.03	0.08	0.13	0.02	0.08	0.12
$Al2O_3$	17.54	19.69	17.34	15.78	15.69	16.40	15.99	21.47	16.37	15.94	16.22	12.31	14.12	15.12	18.26	17.58
Fe_2O_{3tot}	11.11	9.39	12.75	13.45	0.28	0.40	0.61	0.51	0.59	0.98	1.03	0.73	0.84	0.76	0.78	0.72
MnO	0.21	0.22	0.19	0.11	0.03	0.05	0.04	0.01	0.01	0.04	0.03	0.01	0.01	0.29	0.02	0.01
MgO	6.71	7.08	7.90	9.70	0.05	0.25	0.05	0.38	0.31	0.19	0.17	0.93	1.11	0.16	1.05	1.06
CaO	11.84	7.95	13.99	11.01	0.87	0.34	2.28	0.21	1.73	1.49	1.60	0.14	0.15	0.17	0.19	0.16
Na_2O	1.32	3.02	1.21	1.65	5.93	6.92	5.74	9.01	5.77	5.50	5.40	0.54	0.48	1.66	0.48	0.43
K_2O	1.08	1.33	0.67	1.21	0.77	0.95	0.78	1.74	1.08	0.97	1.12	2.80	3.98	1.69	5.14	5.07
P_2O_5	0.13	0.52	0.54	0.15	0.03	0.05	0.04	0.07	0.05	0.09	0.10	0.03	0.03	0.06	0.01	0.02
LOI	1.68	2.15	0.77	1.14	0.50	0.67	1.73	0.85	1.22	1.19	0.94	1.38	1.83	1.61	2.37	2.89
Total	99.55	100.20	99.79	99.83	99.73	99.88	100.38	99.94	99.92	99.78	99.82	100.10	99.79	99.43	99.85	99.88
Mg #	54.47	59.90	55.11	58.83	26.13	55.32	13.73	59.61	51.00	27.75	24.64	71.62	72.36	29.43	72.73	74.47

Table 3 Rb/Sr and Sm/Nd isotope data of Ms-amphibolites, Ms-trondhjemites and Qtz-Ms rocks from Sierra del Convento mélange.

Rock Type	Sample	Rb	Sr	$^{87}Rb/^{86}Sr$	$^{87}Sr/^{86}Sr$	±2σ	Sm	Nd	$^{147}Sm/^{144}Nd$	$^{143}Nd/^{144}Nd$	±2σ
Ms-amphibolite	CV139a	15.6	504	0.089244	0.705481	0.002	4.1	13.9	0.177980	0.512921	0.002
Ms-amphibolite	CV140a	19.2	458	0.121178	0.703745	0.006	5.2	22	0.141026	0.512931	0.002
Ms-amphibolite	CV230a	22	273	0.232118	0.705905	0.002	2.5	7.6	0.200739	0.512997	0.002
Ms-trondhjemite	CV201a	11.5	182	0.182579	0.705817	0.002	0.88	2.6	0.206801	0.512745	0.006
Qtz-Ms rock	CV278a	40	181	0.639976	0.706729	0.004	1.02	1.89	0.326092	0.512709	0.004
Qtz-Ms rock	CV53e	85	98	2.507765	0.708927	0.002	0.87	2.4	0.220551	0.512550	0.002

Table 4. Trace element (ppm) composition of Ms-amphibolites, Ms-trondhjemites and Ms-pegmatitesfrom the Sierra del Convento mélange

Rock	Ms-amphibolites				Ms-trondhjemites					Qtz-Ms rocks						
Sample	CV139a	CV140a	CV230c	CV230a	CV201a	CV201g	SC-20	CV201h	CV230e	CU-72-I	CU-72	CV201d	CV201f	CV278a-I	CV53e-I	CV53e-II
Zr	98.50	211.50	201.80	62.40	17.80	13.80	24.60	70.50	47.00	21.20	22.60	42.50	19.30	25.70	42.00	31.70
Li	7.42	49.43	7.44	9.99	0.42	2.51	0.00	4.62	0.64	1.06	0.64	6.94	6.31	2.68	4.72	4.62
Rb	15.83	20.07	10.41	22.01	12.25	16.06	15.10	30.91	20.40	15.73	15.08	57.49	78.80	40.82	88.00	85.29
Cs	0.17	0.43	0.11	0.17	0.10	0.23	0.63	0.16	0.30	0.00	0.02	0.30	0.45	1.18	0.32	0.33
Be	0.71	1.77	1.19	1.29	1.00	7.87	0.77	1.02	0.50	0.93	0.89	1.96	2.38	3.65	2.36	2.20
Sr	509.69	458.03	530.77	258.87	191.50	86.00	388.83	97.49	409.93	149.65	132.17	21.01	24.21	186.81	99.61	99.01
Ba	1021.76	157.03	573.85	1266.63	4459.62	5063.09	758.73	4220.04	1095.06	647.36	504.31	9039.87	11810.00	833.17	6882.23	6328.76
Sc	37.64	27.12	44.94	50.73	0.70	7.68	0.36	0.37	0.00	0.00	0.00	1.56	4.56	3.72	5.65	4.77
V	279.55	184.86	321.94	350.22	3.70	20.17	2.99	14.95	5.86	2.56	3.13	37.61	51.66	5.26	20.41	18.22
Cr	332.74	292.51	405.24	544.63	39.38	34.21	129.25	118.63	164.89	27.74	136.17	40.34	35.37	26.19	53.97	40.14
Co	48.80	48.48	53.25	62.69	36.36	28.99	0.00	0.99	0.87	29.17	118.30	45.31	36.91	22.95	25.44	30.84
Ni	77.65	191.56	146.38	154.25	2.77	3.81	1.33	12.91	18.69	0.00	10.92	13.36	18.43	1.66	23.00	18.83
Zn	108.58	72.76	146.41	159.39	7.30	3.52	20.49	12.40	9.18	22.52	19.25	18.92	21.80	29.09	8.00	7.94
Y	28.53	31.84	44.71	22.67	10.67	5.36	0.74	3.27	0.64	1.32	1.47	1.80	4.08	17.37	5.33	5.41
Nb	7.60	21.36	30.35	4.94	2.46	12.15	0.55	1.95	0.29	1.22	2.70	4.24	8.18	7.41	5.60	4.50
Ta	0.74	1.64	2.29	0.32	0.56	1.30	0.02	0.26	0.03	0.10	0.45	0.99	0.65	0.86	0.45	0.47
Hf	0.96	0.37	1.27	0.86	0.37	0.27	0.20	2.63	0.14	0.05	0.08	0.20	0.36	0.44	0.95	0.50
Tl	0.11	0.04	0.10	0.22	0.12	0.12	0.18	0.28	0.21	0.15	0.14	0.47	0.64	0.24	0.60	0.57
Pb	11.34	1.55	6.59	5.41	20.01	13.89	3.12	6.67	4.83	9.03	8.21	2.31	2.99	10.18	5.43	4.98
U	0.40	0.78	1.06	0.61	0.63	1.54	0.12	3.09	0.06	0.23	0.52	0.90	2.56	10.41	0.77	1.01
Th	0.63	3.12	3.25	0.84	0.93	1.57	0.22	2.55	0.04	0.27	0.46	1.55	6.44	2.33	4.30	3.57
La	8.34	21.75	28.06	6.60	3.13	1.31	0.77	1.80	0.72	4.18	5.74	3.72	10.70	1.26	2.96	3.19
Ce	19.80	47.58	54.27	12.79	4.38	2.43	1.13	2.60	0.54	9.04	12.01	4.50	15.05	2.56	5.83	6.05
Pr	3.05	5.55	7.06	1.92	0.65	0.35	0.18	0.34	0.10	1.25	1.64	0.74	2.14	0.45	0.65	0.68
Nd	14.18	22.68	30.26	8.66	2.56	1.63	0.72	1.37	0.38	4.99	6.86	2.58	8.41	2.23	2.79	2.77
Sm	4.39	5.42	7.36	2.61	0.95	0.58	0.17	0.50	0.09	1.25	1.59	0.66	1.95	0.99	0.79	0.76
Eu	2.15	1.71	2.89	1.35	0.63	0.40	0.09	1.13	0.32	0.51	0.51	0.72	1.08	0.23	0.65	0.65
Gd	4.86	5.23	7.21	3.09	1.32	0.81	0.16	0.56	0.10	0.89	1.17	0.60	1.81	1.72	0.83	0.99
Tb	0.85	0.90	1.25	0.57	0.23	0.14	0.03	0.09	0.02	0.10	0.10	0.08	0.23	0.36	0.13	0.15
Dy	5.16	5.53	7.80	4.03	1.53	0.88	0.16	0.58	0.10	0.30	0.30	0.37	1.06	2.53	0.89	0.94
Ho	1.11	1.15	1.63	0.88	0.29	0.17	0.03	0.11	0.02	0.03	0.04	0.06	0.16	0.58	0.18	0.18
Er	3.07	3.06	4.50	2.40	0.77	0.48	0.08	0.23	0.05	0.06	0.07	0.14	0.36	1.62	0.53	0.47
Tm	0.45	0.46	0.66	0.35	0.11	0.07	0.01	0.03	0.01	0.00	0.01	0.02	0.05	0.26	0.08	0.07
Yb	2.64	2.91	4.14	2.01	0.73	0.44	0.10	0.16	0.05	0.06	0.06	0.13	0.29	1.90	0.54	0.39
Lu	0.37	0.43	0.63	0.30	0.11	0.08	0.01	0.02	0.01	0.01	0.00	0.02	0.04	0.28	0.09	0.05

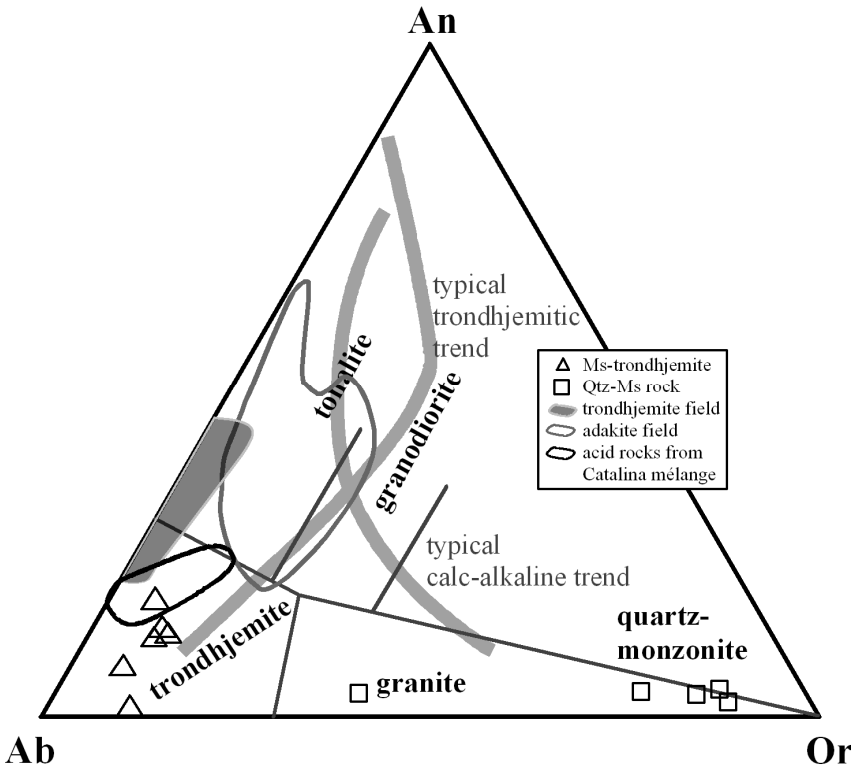

Fig. 6. Molecular normative (CIPW) diagram (O'Connor, 1965), with fields after Barker (1979) and typical calc-alkaline and trondhjemitic trends, of Ms-trondhjemites and Qtz-Ms rocks from Sierra del Convento mélange and, for comparison, K-poor trondhjemites from the Sierra del Convento, pegmatites and leucocratic segregates from the Californian Catalina Schist mélange (grey triangles) and Cenozoic adakites (sources as in Fig. 3).

continental crust/sediment component. The εNd (114 Ma) of Ms-amphibolites (from +5.8 to +6.9) do not overlap the Ms-trondhjemite value, and these rocks show the contribution of fluids derived from a sedimentary source to the oceanic crust component (i,e., Ms-lacking amphibolites; Lázaro and García-Casco, 2008). This indicates that the partial melting process involved fluid-present conditions, likely caused by the influx of external fluids into the amphibolites (García-Casco et al., 2008a), and that the external fluid had an isotopic composition typical of a source influenced by seawater or subducted (meta)sediments, as suggested by isotope composition of the Qtz-Ms rocks, the Atlantic Cretaceous Pelagic Sediment (AKPS, Jolly et al., 2006), which may be used as a proxy of potential subducted sediments, and sediment columns subducting at several trenches (Fig. 11).

In terms of Sr–Nd systematics, the Ms-trondhjemite is comparable to adakitic rocks from different localities. However, the Sr isotopic signature of the Ms-trondhjemite shows a significant sedimentary component in the origin of this type of rocks compared to adakites, which normally reflect a significant contribution of the mantle wedge in their isotopic signatures (Fig. 11). Moreover, both Ms-amphibolites and Ms-trondhjemites are also comparable to IAB field determined by Aleutians, Antilles, and Mariana Arcs rocks (GEOROC database http://georoc.mpch-

mainz.gwdg.de/georoc/Entry.html). This does not imply a common source and process of formation since the depleted source of adakites must be interpreted in terms of partial melting of MORB followed by interaction with a depleted supra-subduction mantle wedge. Notably, the Ms-trondhjemites studied here were trapped within their parental amphibolites and did not interact with the mantle wedge.

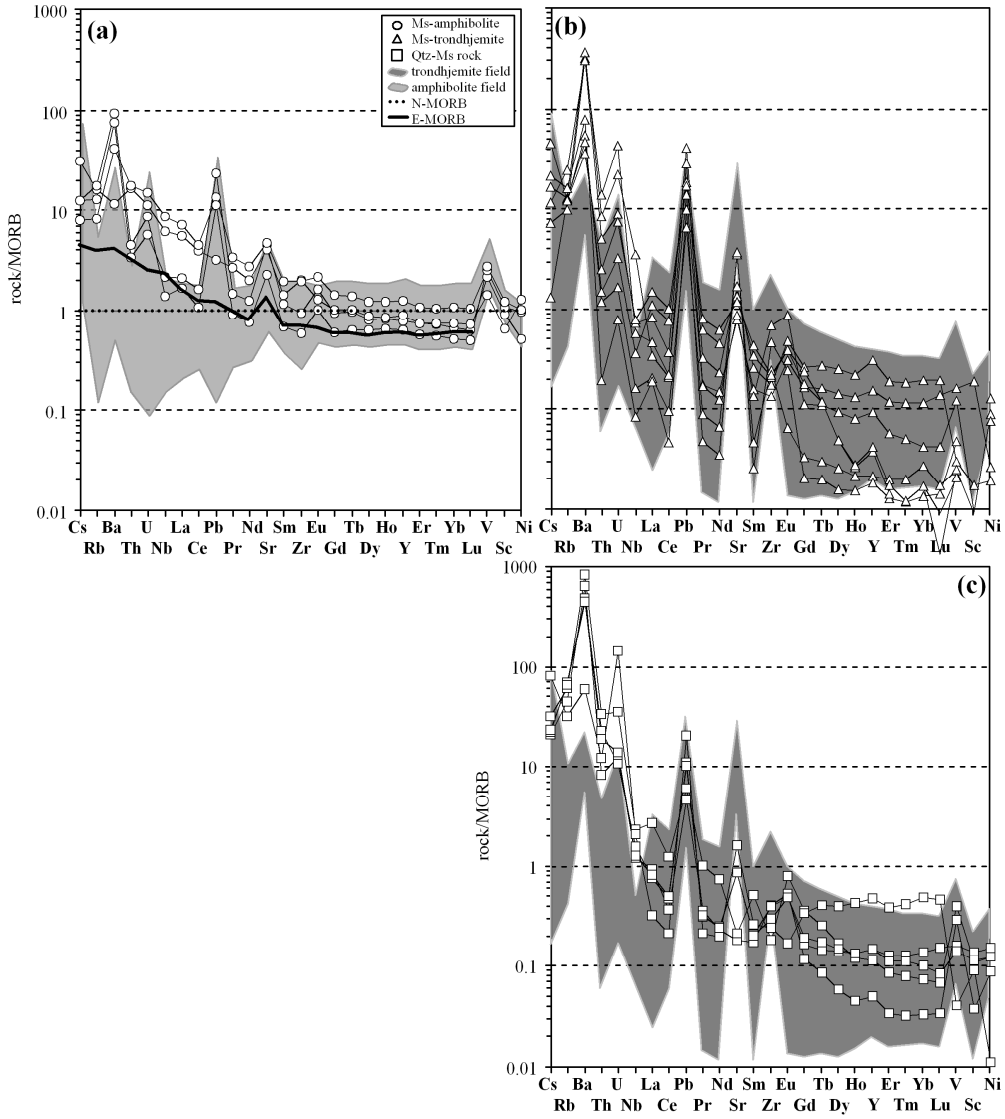

Fig. 7. N-MORB (Hofmann, 1988) normalized spider diagrams for: (a) Ms-amphibolites, (b) Ms-trondhjemites and (c) Qtz-Ms rocks from Sierra del Convento mélange. The fields of K-poor amphibolites and trondhjemites from the Sierra del Convento mélange (Lázaro and García-Casco, 2008) have been included for comparison.

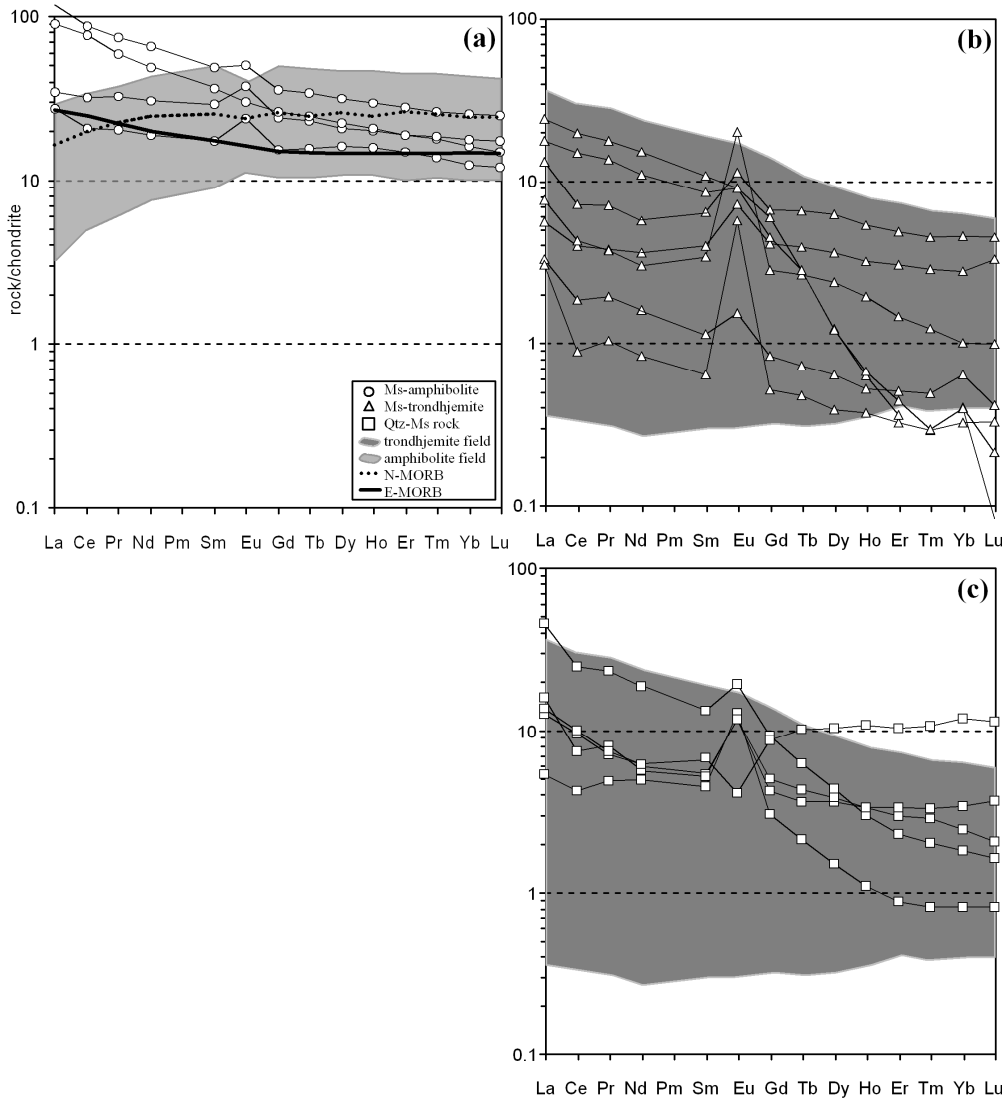

Fig. 8. Chondrite (McDonough and Sun, 1995) normalized REE patterns for: (a) Ms-amphibolites, (b) Ms-trondhjemites and (c) Qtz-Ms rocks from Sierra del Convento mélange. The fields of K-poor amphibolites and trondhjemites from the Sierra del Convento mélange (Lázaro and García-Casco, 2008) have been included for comparison.

DISCUSSION

The origin of Ms-protoliths

Lázaro and García-Casco (2008) demonstrated that the protoliths of the amphibolites from the Sierra del Convento mélange are basaltic rocks of N-MORB composition that evolved from a depleted mantle source, and did not identify LILE- and LREE-enriched island-arc, within-plate basalts and/or ocean plateau-like protoliths. These amphibolites are best explained as slightly modified residues of MORB protoliths, while the K-poor tonalites-trondhjemites constitute pristine slab melts formed during the initial stage of subduction of young oceanic crust.

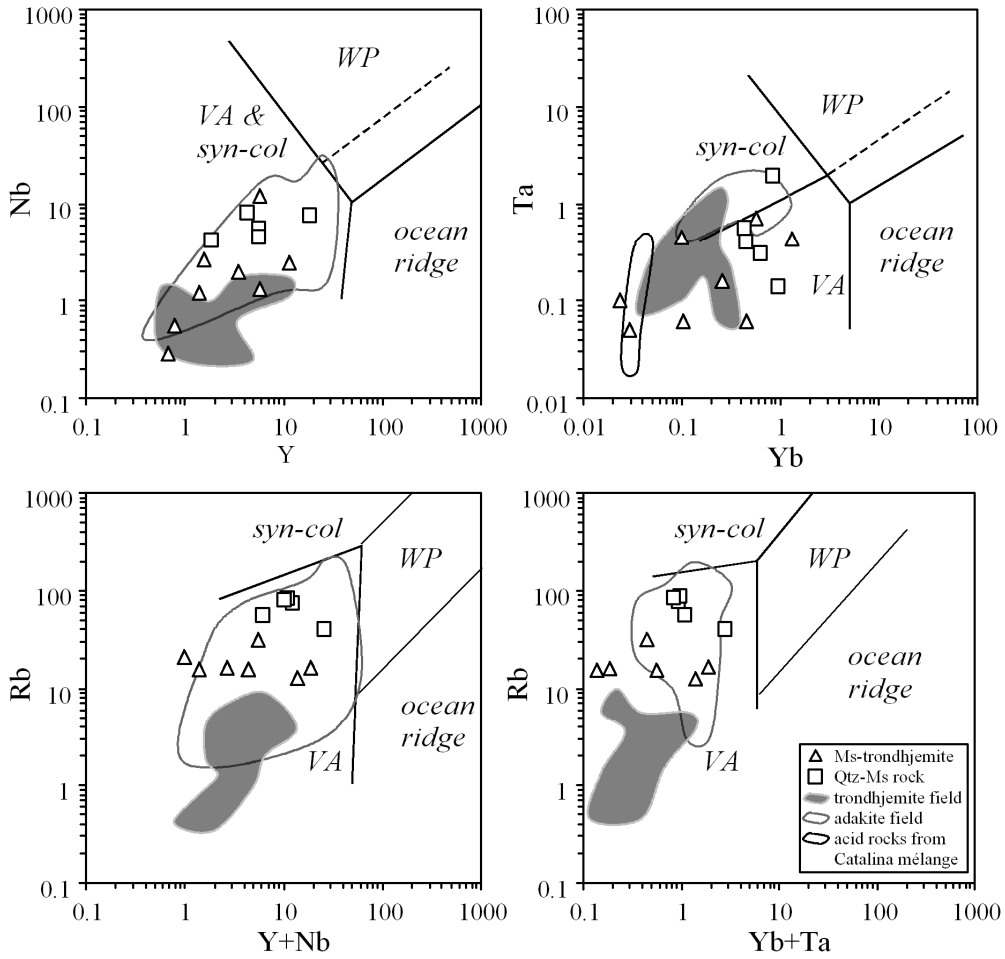

Fig. 9. Ms-trondhjemites and Qtz-Ms rocks plotted in discrimination diagrams for granitic rocks (Pearce et al., 1984) showing the fields of ocean ridge, volcanic arc (VA), syn-collisional, and within-plate (WP) granitic rocks. Grey fields correspond to trondhjemites from the Sierra del Convento mélange and white fields, to Cenozoic adakite compositions (references as in Fig. 3). Acid rocks from the Catalina mélange are plotted in the Ta-Yb diagram.

Petrological and geochemical resemblances can be established between the K-poor and Ms-bearing amphibolite blocks studied in this work. However, detailed petrological, elemental and isotopic geochemical data of the Ms-amphibolites indicate that these rocks suffered modifications before or during subduction/accretion involving the influence of seawater or sediment-derived fluids, respectively, that allowed the formation of muscovite and the concentration in K, Ba, La, U, and Pb. This fact can be observed in the isotopic signatures that appear modified by seawater influence or subducted sediment sources (Fig. 11).. In our view, the process perhaps involved seawater alteration of MORB at a sea-floor environment, but most of the geochemical characteristics of these rocks were acquired during high grade metamorphism and partial melting triggered by the infiltration of fluids derived from subducting sediments. This inference is based on

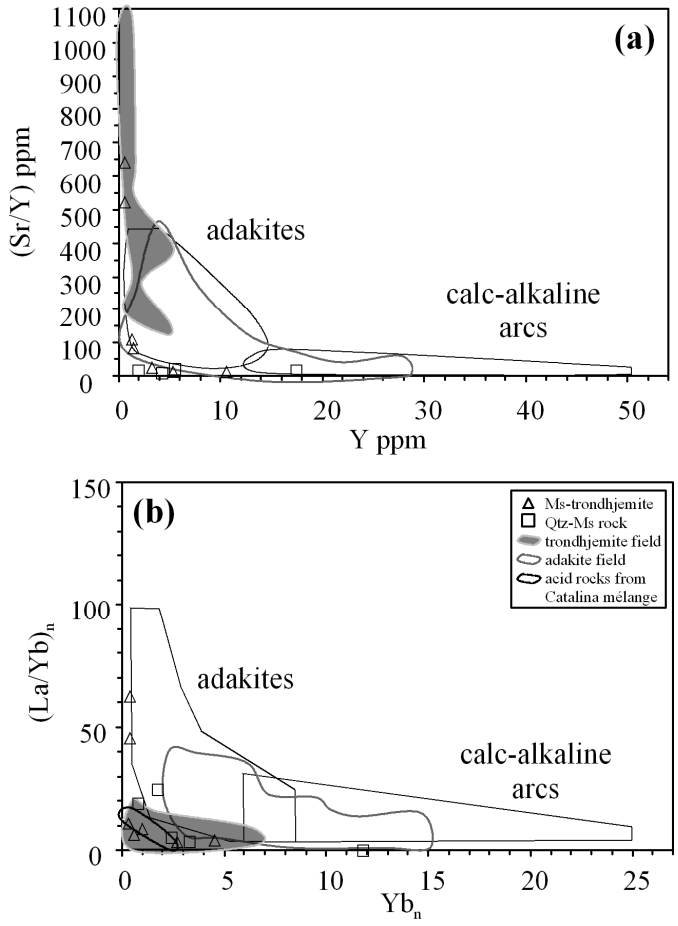

Fig. 10. Ms-trondhjemites and Qtz-Ms rocks plotted in (a) (Sr/Y) vs. Y and (b) $(La/Yb)_n$ vs. Yb_n diagrams with adakite and calc-alkaline arcs fields as defined by Defant and Drummond (1990) and Martin (1986), respectively. Grey fields correspond to K-poor trondhjemites from the Sierra del Convento mélange, and white fields to Cenozoic adakite compositions (references as in Fig. 3). Acid rocks from the Catalina mélange have been plotted in b).

the presence of Qtz+Ms rocks formed at depth after precipitation from a sediment-derived fluid and evidences provided by chemical zoning of muscovite (Blanco-Quintero et al., submitted).

The petrological and geochemical characteristics of the Ms-trondhjemites indicate a similar origin as that of the K-poor trondhjemites from the Sierra del Convento mélange. Field relations, petrological analysis, and elemental geochemistry allow us to infer that these rocks generated by partial melting of a Ms-bearing amphibolitic protolith or, most likely, a K-poor amphibolitic protolith invaded by a sediment-derived fluid enriched in LILE (Cs, Rb, Ba, U, and Pb). Conditions of melting were ca. 15 kbar and 750 °C (P-T conditions for sample CV139a; Lázaro et al., 2009). Isotopic data strengthen this view. The mixing curves between MORB and the isotopic composition of the sediment-derived fluid (i.e., Qtz+Ms rocks), explain the

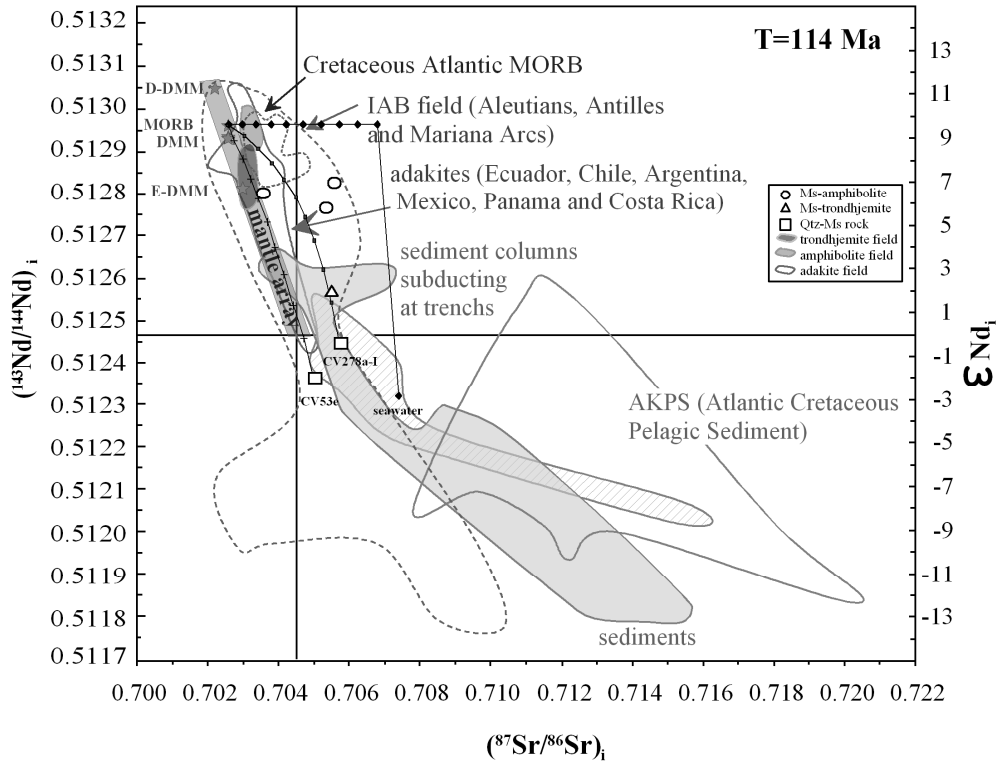

Fig. 11. $(^{87}Sr/^{86}Sr)_i$ vs. $(^{144}Nd/^{143}Nd)_i$ and εNd_i diagram. $\varepsilon Nd=((^{143}Nd/^{144}Nd_{sample}/^{143}Nd/^{144}Nd_{CHUR})-1)x10^4$, where CHUR=chondrite uniform reservoir (De Paolo, 1988). εNd and initial values calculated using $^{(143Nd/144Nd)}CHUR=0.512638$, $^{(147Sm/144Nd)}CHUR=0.1967$ (Wasserburg et al.,1981). Composition of seawater is from McCulloch et al. (1981) and Sm/Nd data is from Piepgras and Wasserburg (1980). Samples were corrected for T=114 Ma (see Lázaro et al., 2009). Data for depleted MORB mantle (DMM), depleted DMM (D-DMM), and enriched DMM (E-DMM) are from Workman and Hart (2005); N-MORB data are from Hart et al. (1999) and Kelemen et al. (2003); and Cretaceous Atlantic MORB data are from Jahn et al. (1980). The adakite field (grey colour line) includes data from Ecuador (Samaniego et al., 2005), Chile (Stern and Kilian, 1996), Argentina (Kay et al.,1993), Mexico (Aguillón-Robles et al., 2001), and Panama–Costa Rica (Defant et al., 1992); Marianas, Aleutians, and Antilles arc volcanic rocks field (dashed line), sediments and sediment columns subducting at trenches from the GEOROC database (http://georoc.mpch-mainz.gwdg.de/ georoc/Entry.html); and the Atlantic Cretaceous Pelagic Sediment (AKPS) field constructed after data from Jolly et al. (2006). Data from Ms-lacking amphibolites and trondhjemites from the Sierra del Convento (Lázaro and García-Casco, 2008) have been included. Mixing curves calculated between MORB and seawater and Qtz-Ms rocks are indicated.

distribution of Ms-bearing amphibolites and trondhjemites (Fig. 11). Similarly, the peraluminous character of the trondhjemites is best explained by infiltration of a peraluminous fluid during partial melting (Fig. 5).

Metasomatism and melting processes in subduction zones environments: melts in situ vs. melts in volcanic arcs

In arc magmas, elevated concentrations of large-ion-lithophile elements (LILE; e.g., Ba, K, Rb, Cs, Ca, Sr), U, and Pb relative to high-field-strength elements (e.g., Ti, Th, Hf, Nb, Zr) are considered key indicators of fluid addition to arc magma source regions. These fluids are released by dehydration of subducting altered MORB and

sediments of the slab. Transfer of LILE-, U-, and Pb-enriched fluids to the mantle wedge at sub-arc depths can trigger partial melting of peridotite and generate basaltic magmas with elevated Ba/Th, Sr/Th, Pb/Th, and U/Th, as well as radiogenic Sr (e.g., Breeding et al., 2004). However, these enriched fluids can also react with the subducted oceanic crust triggering partial melting upon appropriate conditions, forming melts derived from MORB source having a sedimentary imprint (e.g., Gao et al., 2007; Castro et al., 2010).

The experiments of Johnson and Plank (1999) in red clay at 700 ºC and 2.0 GPa allowed analyzing the type of sediment contribution from the subducting slab to the source of arc magmas and the magmas themselves. These authors determined that Rb, Sr, Ba and Pb are incompatible and Th is compatible below the solidus of metasediment. Hence, the addition of Th to arc magmas requires partial melting of the subducting sediment. The implied relations allow using the Ba/Th and Th/Nb ratios as monitors of effect of addition of fluids and melts derived from subducted sediment to arc magmas. Both Ms-amphibolites and Ms-trondhjemites have variable enrichment in Ba/Th and are poor in Th/Nb, suggesting the influence of sediment derived fluid (Fig. 12). The Qtz-Ms rocks have higher Th/Nd and relatively low Ba/Th ratio, suggesting a mixed component influence of a sediment-derived fluid and melt. The compositions of the Ms-trondhjemite and Qtz-Ms rocks indicate contrasted processes of sedimentary input in the subduction environment, though a

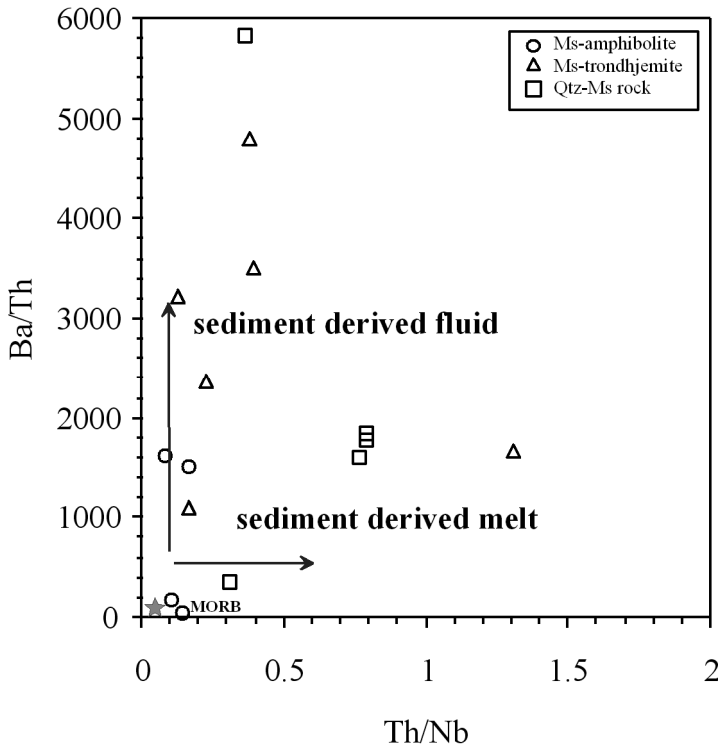

Fig. 12. Ba/Th versus Th/Nb of rocks showing the effect of addition of fluids and melts derived from subducted sediment to arc magmas (after Fretzdorff et al., 2002). N-MORB composition after Hoffman (1988).

sediment-derived fluid seems to be the agent that explains the formation of the studied trondhjemitic and Qtz-Ms rocks (cf. Fretzdorff et al. 2002); while the Qtz-Ms rocks may represent the result of the crystallization of this fluid or melt evolved from the sediments.

CONCLUSIONS

Major, trace element and isotopic compositions of the Ms-amphibolite from Sierra del Convento mélange indicate a MORB affinity altered by seawater and fluids evolved from subducted sediments. Fluid availability was the key controlling factor in the melting process. This process and the P-T conditions reached during subduction/acretion triggered partial melting and formation of K-rich trondhjemitic melt having an adakitic geochemical affinity. This melt did not escape and react with the upper plate peridotite, representing an end-member (pristine slab melts) of the volcanic arc series. The hydrothermal Qtz-Ms rocks have a strong sedimentary imprint, with the higher concentrations of mobile elements (K, Ba, etc.) and more evolved Sr-Nd isotopic composition. These rocks represent the crystallization products of fluids produced by dehydration of sedimentary source in the slab and involved in the partial melting process that generated the Ms-trondhjemitic melts.

ACKNOWLEDGMENTS

The authors thank financial support from Spanish MEC and MICINN projects CGL2006-08527/BTE and CGL2009-12446. This is a contribution to IGCP-546 “Subduction zones of the Caribbean”.

REFERENCES

Aguillón-Robles, A., Calmus, T., Benoit, M., Bellon, H., Maury, R.O., Cotten, J., Bourgois, J., Michaud, F., 2001. Late Miocene adakites and Nb-enriched basalts from Vizcaino Peninsula, Mexico: indicators of East Pacific Rise subduction below Southern Baja California? Geology 29 (6), 531–534.

Barker, F.,1979. Trondhjemite:definition, environment and hypotheses of origin. In: Barker, F. (Ed.), Trondhjemites, dacites and related rocks. Elsevier, Amsterdam, pp. 1–12.

Beate, B., Monzier, M., Spikings, R., Cotten, J., Silva, J., Bourdon, E., Eissen, J.P., 2001. Mio-Pliocene adakite generation related to flat subduction in southern Ecuador: the Quimsacocha volcanic center. Earth and Planetary Science Letters 192 (4), 561–570.

Bebout, G.E., Barton, M.D., 1993. Metasomatism during subduction — products and possible paths in the Catalina schist, California. Chemical Geology 108 (1–4), 61–92.

Bebout, G. E., Barton, M. D., 2002. Tectonic and metasomatic mixing in a subduction-zone melange: insights into the geochemical evolution of the slab-mantle interface, Chemical Geology 187, 79-106.

Bebout, G.E., 2007. Metamorphic chemical geodynamics of subduction zones. Earth and Planetary Science Letters 260, 373–393.

Benoit, M., Aguillón-Robles, A., Calmus, T., Maury, R.C., Bellon, H., Cotten, J., Bourgois, J., Michaud, F., 2002. Geochemical diversity of Late Miocene volcanism in southern Baja California, Mexico: implication of mantle and crustal sources during the opening of an asthenospheric window. Journal of Geology 110 (6), 627–648.

Blanco Quintero, I.F., 2003. Nuevos datos petroquímicos y petrográficos de las migmatitas y metamorfitas de algunos sectores del bloque oriental cubano (sectores Moa-Baracoa y Sierra del Convento). Master's Thesis, University of Moa, Moa (Cuba), 77 pp.

Blanco-Quintero, I.F., García-Casco, A., Rojas-Agramonte, Y., Rodríguez-Vega, A., Lázaro, C., Iturralde-Vinent, M.A., 2010a. Metamorphic evolution of subducted hot oceanic crust, La Corea mélange, Cuba. American Journal of Science (in press).

Blanco-Quintero, I.F., Proenza, J.A., García-Casco, A., Tauler, E., Galí, S., 2010b. Serpentinites and serpentinites within a fossil subdution channel: La Corea melange, eastern Cuba. Geologica Acta (in press).

Boiteau, A., Saliot, P., Michard, A., 1972. High-pressure metamorphism in ophiolite complex of purial (Oriente, Cuba). Comptes Rendus Hebdomadaires Des Seances De L Academie Des Sciences Serie D 274 (15), 2137–2140.

Bourdon, E., Eissen, J.P., Gutscher, M.A., Monzier, M., Samaniego, P., Robin, C., Bollinger, C., Cotten, J., 2002. Slab melting and slab melt metasomatism in the Northern Andean Volcanic Zone: adakites and high-Mg andesites from Pichincha volcano (Ecuador). Bulletin De La Societe Geologique De France 173 (3), 195–206.

Bourdon, E., Eissen, J.P., Gutscher, M.A., Monzier, M., Hall, M.L., Cotten, J., 2003. Magmatic response to early aseismic ridge subduction: the Ecuadorian margin case (South America). Earth and Planetary Science Letters 205 (3–4), 123–138.

Breeding, C.M., Ague, J.J., Bröcker, M., 2004. Fluid-metasedimentary rock interactions in subduction-zone melange: Implications for the chemical composition of arc magmas. Geology 32, 1041–1044.

Castro, A., Gerya, T., García-Casco, A., Fernández, C., Díaz-Alvarado, J., Moreno-Ventas, I., Löw, I., 2010. Melting Relations of MORB–Sediment Mélanges in Underplated Mantle Wedge Plumes; Implications for the Origin of Cordilleran-type Batholiths. Journal of Petrology 51, 1267-1295.

Castro, A., Gerya, T.V., 2008. Magmatic implications of mantle wedge plumes: Experimental study. Lithos 103 (1-2), 138-148.

Cobiella, J., Quintas, F., Campos, M., Hernández, M., 1984. Geología de la Región Central y Suroriental de la Provincia de Guantánamo. Editorial Oriente, Santiago de Cuba, Santiago de Cuba, 125 p.

Defant, M.J., Drummond, M.S., 1990. Derivation of some modern arc magmas by melting of young subducted lithosphere. Nature 347 (6294), 662–665.

Defant, M.J., Jackson, T.E., Drummond, M.S., Deboer, J.Z., Bellon, H., Feigenson, M.D., Maury, R.C., Stewart, R.H., 1992. The geochemistry of young volcanism throughout Western Panama and Southeastern Costa-Rica—an overview. Journal of the Geological Society 149, 569–579.

Fretzdorff, S., Livermore, R. A., Devey, C. W., Leat, P. T., Stoffers, P., 2002. Petrogenesis of the back-arc East Scotia Ridge, South Atlantic Ocean. Journal of Petrology, 43, 1435– 1467.

Gao, Y., Hou, Z., Kamber, B.S., Wei, R., Meng, X., Zhao, R., 2007. Adakite-like porphyries from the southern Tibetan continental collision zones: evidence for slab melt metasomatism. Contributions to Mineralogy and Petrology 153, 105–120.

García-Casco, A., Torres-Roldán, R.L., Iturralde-Vinent, M.A., Millán, G., Núñez Cambra, K., Lázaro, C., Rodríguez Vega, A., 2006. High pressure metamorphism of ophiolites in Cuba. Geologica Acta 4, 63–88.

García-Casco, A., Lázaro, C., Rojas-Agramonte, Y., Kröner, A., Torres-Roldán, R.L., Núñez, K., Millán, G., Neubauer, F., Blanco-Quintero, I., 2008a. Partial melting and counterclockwise P-T path of subducted oceanic crust (Sierra del Convento mélange, Cuba). Journal of Petrology 49, 128–161.

García-Casco, A., Iturralde-Vinent, M. A., Pindell, J., 2008b. Latest Cretaceous collision ⁄ accretion between the Caribbean Plate and Caribeana: origin of metamorphic terranes in the Greater Antilles. International Geology Review 50, 781– 809.

Gerya, T. V., Yuen, D. A., 2003. Rayleigh–Taylor instabilities from hydration and melting propel 'cold plumes' at subduction zones. Earth and Planetary Science Letters 212 (1-2), 47-62.

Gill, J.B., 1981. Orogenic Andesites and Plate Tectonics. Springer-Verlag, Berlin. 390 pp.

Gorczyk, W., Gerya, T.V., Connolly, J.A.D., Yuen, D.A., 2007. Growth and mixing dynamics of mantle wedge plumes. Geology 35, 587–590.

Govindaraju, K., 1994. Compilation of working values and sample description for 383 geostandards. Geostandards Newsletter 18, 1–158.

Grove, M., Bebout, G.E., 1995. Cretaceous tectonic evolution of coastal southern California: insights from the Catalina Schist. Tectonics 14 (6), 1290–1308.

Gyarmati, P., Méndez, I., Lay, M., 1997. Caracterización de las rocas del arco de islas Cretácico en la Zona Estructuro-Facial Nipe-Cristal-Baracoa. In: Furrazola, G.F., Núñez-Cambra K.E., eds., Estudios sobre Geología de Cuba, Ciudad de la Habana, Instituto de Geología y Paleontología, 357-364.

Hart, S.R., Blusztajn, J., Dick, H.J.B., Meyer, P.S., Muehlenbachs, K.,1999. The fingerprint of seawater circulation in a 500-meter section of ocean crust gabbros. Geochimica Et Cosmochimica Acta 63 (23–24), 4059–4080.

Hernández, M., Canedo, Z., 1995. Geoquímica de las ofiolitas meridionales de Cuba oriental. Minería y Geología 3, 3–9.

Hofmann, A.W., 1988. Chemical differentiation of the Earth — the relationship between mantle, continental-crust, and oceanic-crust. Earth and Planetary Science Letters 90 (3), 297–314.

Iturralde-Vinent, M.A., 1998. Sinopsis de la Constitución Geológica de Cuba. Acta Geológica Hispánica 33, 9–56.

Iturralde-Vinent, M. A., Millán, G., Korkas, L., Nagy, E., Palón, J., 1996. Geological interpretation of the Cuban K-Ar data base. In: Ofiolitas Y Arcos Volcánicos de Cuba (ed. Iturralde-Vinent, M. A.), pp. 48–69, IGCP Project 364, Miami, FL.

Iturralde-Vinent, M. A., Díaz Otero, C., Rodríguez Vega, A., Díaz Martínez, R., 2006. Tectonic implications of paleontologic dating of Cretaceous-Danian sections of Eastern Cuba. Geologica Acta, 4, 89–102.

Jahn, B.M., Bernardgriffiths, J., Charlot, R., Cornichet, J., Vidal, F., 1980. Nd and Sr isotopic compositions and REE abundances of cretaceous MORB (Holes 417d and 418a, Legs 51, 52 and 53). Earth and Planetary Science Letters 48 (1), 171–184.

Johnson, M.C., Plank, T., 1999. Dehydration and melting experiments constrain the fate of subducted sediments: Geochemistry Geophysics and Geosystems 1, p. 1999GC000014.

Jolly, W.T., Lidiak, E.G., Dickin, A.P., 2006. Cretaceous to mid-Eocene pelagic sediment budget in Puerto Rico and the Virgin Islands (northeast Antilles Island arc). Geologica Acta 4 (1–2), 35–62.

Kay, S.M., Ramos, V.A., Marquez, M., 1993. Evidence in Cerro-Pampa volcanic-rocks for slab-melting prior to ridge-trench collision in southern South-America. Journal of Geology 101 (6), 703–714.

Kelemen, P.B., Hanghøj, K., Green, A.R., 2003. One viewof the geochemistry of subductionrelated magmatic arcs, with an emphasis on primitive andesite and lower crust. In: Rudnick, R. (Ed.), Geochemistry of the Crust: Treatise of Geochemistry. Elsevier, Amsterdam, pp. 593–659.

Kretz, R., 1983. Symbols for rock-forming minerals. American Mineralogist, 68, 277–279.

Kulachkov, L.V., Leyva, R.C., 1990. Informe sobre los resultados de los trabajos de reconocimiento geolo´gico para cuarzo filoniano en la parte oriental de Cuba. Instituto Superior Minero-Metalúrgico, Moa, Cuba.

Kushiro, I., 1990. Partial melting of mantle wedge and evolution of island-arc crust. Journal of Geophysical Research-Solid Earth and Planets 95 (B10), 15929–15939.

Lázaro, C., García-Casco, A., 2008. Geochemical and Sr-Nd isotope signatures of pristine slab melts and their residues (Sierra del Convento mélange, eastern Cuba). Chemical Geology 255:120–133.

Lázaro, C., García-Casco, A., Neubauer, F., Rojas-Agramonte, Y., Kröner, A., Iturralde-Vinent, M.A., 2009. Fifty five-million-year history of oceanic subduction and exhumation in the northern edge of the Caribbean plate (Sierra del Convento mélange, Cuba). Journal of Metamorphic Geology, 27, 19-40.

Le Maitre, R.W., Bateman, P., Dudek, A., Keller, J., Lameyre Le Bas, M.J., Sabine, P.A., Schmid, R., Sorensen, H., Streckeisen, A., Woolley, A.R., Zanettin, B., 1989. A Classification of Igneous Rocks and Glossary of Terms. Blackwell, Oxford. 196 pp.

Leyva, R. C., 1996. Características geológicas, regularidades de distribución y perspectivas de utilización del cuarzo filoniano de la región oriental de Cuba. Masters Thesis, University of Moa, Moa, Cuba.

Marchesi, C., Garrido, C.J., Godard, M., Proenza, J.A., Gervilla, F., Blanco-Moreno, J., 2006. Petrogenesis of highly depleted peridotites and gabbroic rocks from the Mayarí-Baracoa Ophiolitic Belt (eastern Cuba). Contributions to Mineralogy and Petrology 151 (6), 717–736.

Marchesi, C., Garrido, C. J., Bosch, D., Proenza, J. A., Gervilla, F., Monié, P., Rodríguez-Vega, A., 2007. Geochemistry of Cretaceous magmatism in eastern Cuba: recycling of North American continental sediments and implications for subduction polarity in the Greater Antilles Paleo-arc. Journal of Petrology 48, 1813-1840.

Martin, H., 1986. Effect of steeper Archaean geothermal gradient on geochemistry of subduction-zone magmas. Geology 14, 753–756.

Martin, H., 1999. The adakitic magmas: modern analogues of Archaean granitoids. Lithos 46 (3), 411–429.

McCulloch, M.T., Gregory, R.T., Wasserburg, G.J., Taylor, H.P., 1981. Sm–Nd, Rb–Sr, and O18–O16 isotopic systematics in an oceanic crustal section — evidence from the Samail Ophiolite. Journal of Geophysical Research 86 (NB4), 2721–2735.

McDonough, W.F., Sun, S.S., 1995. The composition of the Earth. Chemical Geology 120 (3–4), 223–253.

Millán, G., 1996. Metamorfitas de la asociación ofiolítica de Cuba. In: Iturralde- Vinent, M.A. (Ed.), Ofiolitas y Arcos Volcanicos de Cuba. IGCP Project 364, Miami (USA), pp. 147–153.

Millán, G., Somin, M., 1985. Nuevos aspectos sobre de la estratigrafía del macizo metamórfico de Escambray. Contribución al conocimiento geológico de las metamorfitas del Escambray y Purial. Instituto de Gelogía y Paleontología, La Habana.

Morris, P.A., 1995. Slab melting as an explanation of quaternary volcanism and aseismicity in southwest Japan. Geology 23 (5), 395–398.

O'Connor, J.T., 1965. A classification of quartz-rich igneous rocks based on feldspar ratios. 525B. Professional Paper. U. S. Geological Survey. B79–B84 pp.

Pearce, J.A., Harris, N.B.W., Tindle, A.G., 1984. Trace-element discrimination diagrams for the tectonic interpretation of granitic-rocks. Journal of Petrology 25 (4), 956–983.

Peccerillo, A., Taylor, S.R., 1976. Geochemistry of Eocene calc-alkaline volcanic-rocks from Kastamonu Area, Northern Turkey. Contributions to Mineralogy and Petrology 58 (1), 63–81.

Piepgras, D.J.,Wasserburg, G.J., 1980. Neodymium isotopic variations in seawater. Earth and Planetary Science Letters 50 (1), 128–138.

Proenza, J. A., Díaz-Martínez, R., Iriondo, A., Marchesi, C., Melgarejo, J.C., Gervilla, F., Garrido, C.J., Rodríguez-Vega, A., Lozano-Santacruz, R., Blanco-Moreno, J.A., 2006. Primitive Cretaceous island-arc volcanic rocks in eastern Cuba: the Téneme Formation. Geologica Acta 4, 103–121.

Rapp, R. P., Shimizu, N., Norman, M. D., Applegate, G. S., 1999. Reaction between slab-derived melts and peridotite in the mantle wedge: experimental constraints at 3.8 Gpa. Chemical Geology 160 (4), 335-356

Sajona, F.G., Maury, R.C., Bellon, H., Cotten, J., Defant, M., 1996. High field strength element enrichment of Pliocene–Pleistocene Island arc basalts, Zamboanga Peninsula, western Mindanao (Philippines). Journal of Petrology 37 (3), 693–726.

Sajona, F.G., Maury, R.C., Pubellier, M., Leterrier, J., Bellon, H., Cotten, J., 2000. Magmatic source enrichment by slab-derived melts in a young post-collision setting, central Mindanao (Philippines). Lithos 54 (3–4), 173–206.

Samaniego, P., Martin, H., Monzier, M., Robin, C., Fornari, M., Eissen, J.P., Cotten, J., 2005. Temporal evolution of magmatism in the Northern Volcanic Zone of the Andes: the geology and petrology of Cayambe Volcanic Complex (Ecuador). Journal of Petrology 46 (11), 2225–2252.

Smith, D.R., Leeman, W.P., 1987. Petrogenesis of Mount St-Helens dacitic magmas. Journal of Geophysical Research-Solid Earth and Planets 92 (B10), 10313–10334.

Smithies, R.H., 2000. The Archaean tonalite-trondhjemite-granodiorite (TTG) series is not an analogue of Cenozoic adakite. Earth and Planetary Science Letters 182 (1), 115–125.

Somin, M., Millán, G., 1981. Geology of the Metamorphic Complexes of Cuba (in Russian). Nauka, Moscow. 219 pp.

Somin, M.L., Arakelyants, M.M., and Kolesnikov, E. M., 1992. Age and tectonic significance of high-pressure metamorphic rocks in Cuba. International Geology Review 34, 105–118.

Sorensen, S.S., 1988. Petrology of amphibolite-facies mafic and ultramafic rocks from the Catalina Schist, Southern-California — metasomatism and migmatization in a subduction zonemetamorphic setting. Journal of Metamorphic Geology 6 (4), 405–435.

Sorensen, S.S., Grossman, J.N., 1989. Enrichment of trace-elements in garnet amphibolites from a paleo-subduction zone — Catalina Schist, Southern-California. Geochimica Et Cosmochimica Acta 53 (12), 3155–3177.

Sorensen, S.S., Barton, M.D., 1987. Metasomatism and partial melting in a subduction complex: Catalina Schist, southern California. Geology 15, 115-118.

Staudigel, H., Plank, T., White, W.M., Schmincke, H., 1996. Geochemical fluxes during seafloor alteration of the basaltic upper oceanic crust: DSDP Sites 417 and 418. In: Bebout, G.E., Scholl, S.W., Kirby, S.H., Platt, J.P. (Eds.), Subduction from Top to Bottom. American Geophysical Union, Washington, DC, pp. 19–38.

Stern, C.R., Kilian, R., 1996. Role of the subducted slab, mantle wedge and continental crust in the generation of adakites from the Andean Austral volcanic zone. Contributions to Mineralogy and Petrology 123 (3), 263–281.

Tatsumi, Y., Kogiso, T., 1997. Trace element transport during dehydration processes in the subducted oceanic crust .2. Origin of chemical and physical characteristics in arc magmatism. Earth and Planetary Science Letters 148 (1–2), 207–221

Wasserburg, G.J., Jacobsen, S.B., DePaolo, D.J., McCulloch, M.T., Wen, T., 1981. Precise determination of Sm/Nd ratios, Sm and Nd isotopic abundances in standard solutions. Geochimica Et Cosmochimica Acta 45, 2311–2323.

Workman, R.K., Hart, S.R., 2005. Major and trace element composition of the depleted MORB mantle (DMM). Earth and Planetary Science Letters 231 (1–2), 53–72.

Yogodzinski, G.M., Kay, R.W., Volynets, O.N., Koloskov, A.V., Kay, S.M., 1995. Magnesian Andesite in the Western Aleutian Komandorsky Region — implications for slab melting and processes in the mantle wedge. Geological Society of America Bulletin 107 (5), 505–519.

5- BARIUM-RICH FLUIDS AND MELTS IN THE SUBDUCTION ENVIRONMENT (LA COREA AND SIERRA DEL CONVENTO MÉLANGES, EASTERN CUBA)

I.F. Blanco-Quintero[(1)]; C. Lázaro[(1)]; A. García-Casco[(1,2)]; J.A. Proenza[(3)]; Y. Rojas-Agramonte[(4)].

(1) Departamento de Mineralogía y Petrología, Universidad de Granada, Fuentenueva s/n, 18002-Granada, Spain

(2) Instituto Andaluz de Ciencias de la Tierra (CSIC-UGR), Fuentenueva s/n, 18002-Granada, Spain

(3) Departament de Cristal.lografia, Mineralogia i Dipòsits Minerals, Facultat de Geologia, Universitat de Barcelona, Martí i Franquès s/n, 08028-Barcelona, Spain

(4) Institut für Geowissenschaften, Universität Mainz, D-55099 Mainz, Germany

ABSTRACT

Geochemistry of whole rock samples of muscovite-bearing amphibolite, trondhjemite, pegmatite and quartz-muscovite rocks and their minerals from Sierra del Convento and La Corea mélanges (eastern Cuba) indicates complex circulation of Ba-rich fluids and melts in the subduction environment. Partial melting of fluid-fluxed MORB-derived amphibolite formed trondhjemite magmas that crystallized at depth. Pegmatites are the result of differentiation of trondhjemite melts. Qtz-Ms rocks probably represent primary fluids evolved from subducted sediments. All types of rock have elevated concentrations of large ion lithophile elements, especially in Ba (up to 11810 ppm). Barium enrichment is related to the release of fluids and/or melts from slab sediments. Fluid-rock interaction produced crystallization of phengite in parental amphibolites. Phengite in all types of rock is rich in Ba. Zoning of phengite is characterized by Ba-rich cores and Ba-poor rims, indicating a compatible behaviour of Ba in the studied systems. Zoning in phengite is governed primarily by the celadonite (tschermak) exchange vector ((Mg,Fe)Si-$(Al)_{-2}$), with more moderate contributions of the celsian (BaAl-$(KSi)_{-1}$) and paragonite (NaK_{-1}) exchange vectors. Late remobilisation of Ba at relatively low temperature formed retrograde celsian and cymrite. The compatible behaviour of Ba in the studied rocks strengthens the importance of the stability of phengite for the transfer of LILE elements from the subduction to the volcanic arc environments.

Keywords: Ba-rich fluid, granitoids, phengite, celsian, subduction channel, eastern Cuba, Caribbean plate

INTRODUCTION

Infiltration of fluids/melts derived from subducted slabs trigger partial melting of the mantle wedge and the formation of volcanic arcs. It is widely accepted that these fluids/melts transfer large ion lithophile elements (LILE) from the slab (altered mafic oceanic crust and/or its sedimentary cover) to the melting region of the mantle wedge, as indicated by the trace element signature of arc magmas (e.g., Plank and Langmuir 1993). Barium is a key LILE that has a strong incompatible and mobile behaviour in the subduction environment. High Ba concentrations are found in oceanic sediments deposited in regions of high biological productivity (Dymond et al. 1992; Plank and Langmuir 1998), principally diatom and radiolarian oozes. Hydrothermal fluxes can also produce high barium concentrations in the oceanic environment (Plank and Langmuir, 1998 and references therein). Subduction of these types of rock should eventually transfer large quantities of barium to volcanic arc magmas (Gill 1981; Kushiro 1990; Tatsumi and Kogiso 1997).

The nature of fluids evolved in the subduction environment can be studied in subduction mélanges (e.g., Bebout and Barton 1989; Sorensen et al. 1997; Bebout et al. 2007). Two exceptional melanges occurring in eastern Cuba (La Corea and Sierra del Convento) show abundant evidence for fluid movement and fluid-rock interaction at depth in the subduction environment, including formation of jade and other metasomatic rocks (García-Casco et al. 2009; Cárdenas-Párraga et al. 2010) and fluid-fluxed partial melting of subducted MORB (García-Casco et al. 2008a; Lázaro and Garcia-Casco 2008; Lázaro et al. 2009; Blanco-Quintero et al., 2010a). These mélanges have been interpreted as fossil subduction channels formed after onset of subduction of the Protocaribbean (Atlantic) lithosphere in Aptian times (ca. 120 Ma; García-Casco et al. 2006, 2008a; Lázaro et al. 2009). High-pressure blocks found in these subduction mélanges are mainly composed of amphibolite with N-MORB affinity (Lázaro and Garcia-Casco 2008). An exceptional characteristic is the presence of tonalitic-trondhjemitic bodies, dikes and veins. These rocks formed after fluid-fluxed partial melting of MORB derived amphibolites at peak conditions of 700-750 ºC and 1.5 GPa under a hot geothermal scenario during the infancy of subduction. This makes these rocks important for the study of the nature of infiltrating fluids and the hydrology of the subduction factory. Elemental and isotopic geochemical characteristics of amphibolites and tonalitic-trondhjemitic rocks led Lázaro and Garcia-Casco (2008) to infer a depleted fluid likely evolved from dehydrating serpentinites. However some varieties of MORB-derived amphibolite, associated tonalite-trondhjemite, and vein rocks from these mélanges are rich in Ba and other LILE, suggesting the presence of additional fluids derived from sediment in the subduction environment. In this paper, we study in detail for the first time the mineral and bulk-rock geochemistry of these rocks, and give clues to understand the behaviour of fluids and melts evolved in the subduction environment, with emphasis in the mobility of barium and other LILE.

GEOLOGICAL SETTING

The Cuban orogenic belt formed during the Cretaceous-Tertiary convergence of the Caribbean oceanic plate and the North American margin (Iturralde-Vinent 1998). Cretaceous subduction of the Protocaribbean (i.e., Atlantic) oceanic lithosphere below the Caribbean plate formed an intraoceanic arc system that collided with the

Jurassic-Cretaceous passive margin-like terrane of Caribbeana, the margin of the continental Maya block (Guaniguanico terrane) and the Bahamas platform in latest Cretaceous-Tertiary times (García-Casco et al. 2008b; Iturralde-Vinent et al. 2008). The collision involved tectonic emplacement of oceanic units, including volcanic arc, ophiolites, subduction mélanges (subduction channel), as well as subducted and non-subducted continental margin rocks, and syntectonic basin sequences.

The eastern Cuban block is located to the east of the Cauto-Nipe sinistral fault (Fig. 1a). The most important tectonic units in the northeastern part of the area are the Cretaceous volcanic arc and the Mayarí-Baracoa Ophiolitic Belt. The ophiolite sheets override the Cretaceous volcanic arc units, that are made of several sections with mafic to felsic composition and distinct island arc signatures (tholeiitic, boninitic and calc-alkaline; Proenza et al. 2006). Based on paleontological data, the Cretaceous arc formed during early (Aptian-Albian) to late Cretaceous (Mid Campanian) times (Iturralde-Vinent et al. 2006). The volcanic arc complex of El Purial, located in south eastern part, was metamorphosed to greenschist and blueschist facies conditions (Boiteau et al. 1972; Cobiella et al. 1977; Somin and Millán 1981; Millán et al. 1985), probably during latest Cretaceous times (ca. 70 Ma; Iturralde-Vinent et al. 2006; García-Casco et al. 2006; Lázaro et al. 2009).

The Mayarí-Baracoa Ophiolitic Belt includes mafic and ultramafic rocks with supra-subduction geochemical signatures (Proenza et al., 1999; Proenza et al. 2006; Iturralde-Vinent et al. 2006; Marchesi et al. 2007). The Mayarí-Baracoa Ophiolitic Belt includes two massifs: the Mayarí-Cristal massif to the west and the Moa-Baracoa massif to the east. According to Marchesi et al. (2006) the Mayarí-Baracoa Ophiolitic Belt is represented by highly depleted peridotites and cumulate gabbroic rocks and proposed formation in a back-arc spreading centre environment. An important feature of the Mayarí-Baracoa Ophiolitic Belt peridotites is that they are highly altered (serpentinized) as a consequence of seawater circulation during the oceanic stage in the suprasubduction environment (Proenza et al., 2003).

The largest serpentinite-matrix mélanges are located in the Sierra del Cristal (La Corea) and the Sierra del Convento (Fig. 1a). The La Corea mélange is tectonically below the Mayarí-Cristal Massif (Fig. 1b) while Sierra del Convento mélange overrides El Purial complex (Fig. 1c). These mélanges contain exotic blocks of various origin, size and composition within a serpentinite-matrix. Metamorphic blocks attained high- to medium-pressure and low- to high-temperature (mainly garnet-amphibolite, blueschist and greenschist facies; Somin and Millán 1981; Millán 1996, Garcia-Casco et al. 2006; 2008a; Blanco-Quintero et al. 2010a). They formed in a subduction environment during the Cretaceous (120-75 Ma) subduction of oceanic lithosphere and latest-Cretaceous (70-75 Ma) subduction erosion of the volcanic arc. The most common rock type, however, is MORB-derived amphibolite formed in the earliest stages of oceanic subduction during the Aptian (ca. 120 Ma). The serpentinitic matrix is essentially made of sheared serpentinite, but massive antigoritite is also common as blocks within sheared serpentinite matrix (Blanco-Quintero et al., 2010b).

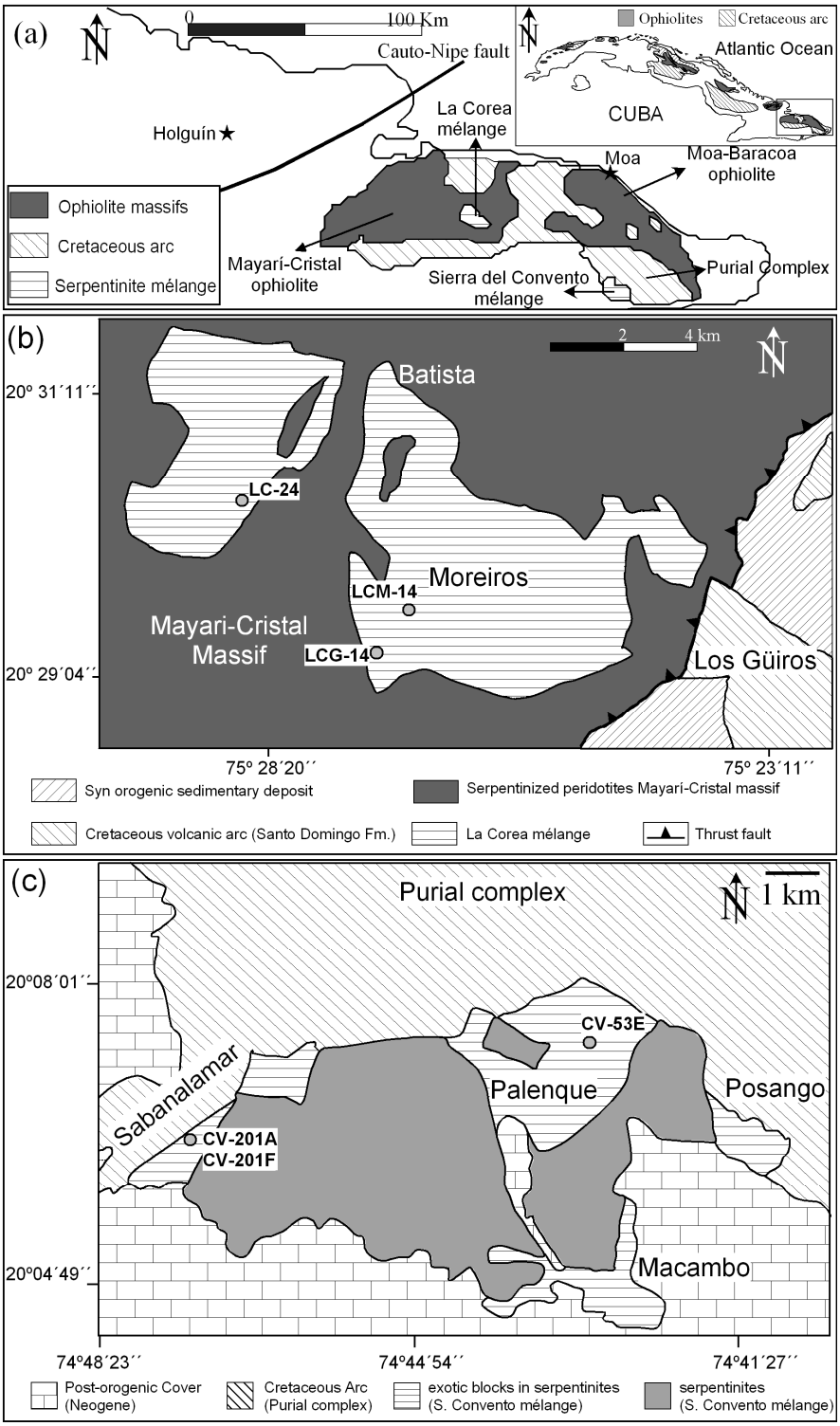

Fig. 1. a) Simplified geological map of northeastern Cuba (after Iturralde-Vinent, 1998) showing the main geological units. b) Geologic maps of the La Corea and c) Sierra del Convento mélanges (after Leyva, 1996) with indication of sample location.

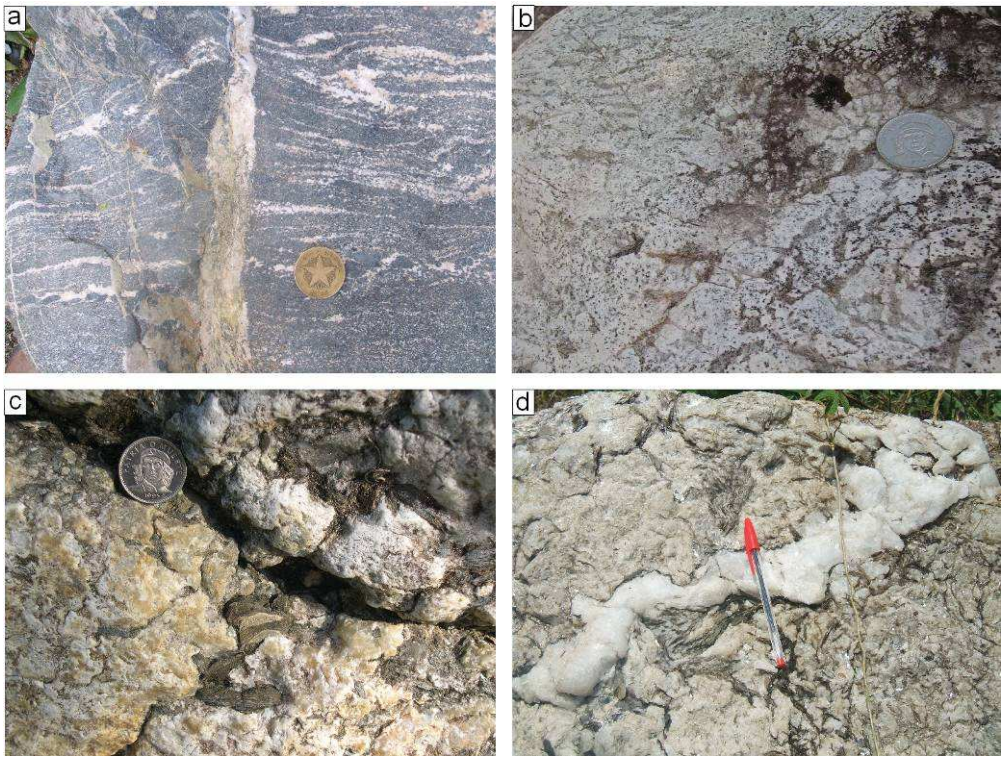

Fig. 2. a) Garnet-amphibolite with different generation of trondhjemite layers (La Corea mélange). b) Trondhjemitic pegmatite body with graphic-like texture (Sierra del Convento mélange). c) Pegmatite block with big pocked of coarse muscovite (Sierra del Convento mélange). d) Hydrothermal Qtz-Ms rock (Sierra del Convento mélange).

Epidote±garnet amphibolites appear as m-size blocks. They are massive to banded and fine to medium grained, within coarse grained varieties. Peak P-T conditions of formation were 700-750 ºC and ca. 1.5 GPa (García-Casco et al. 2006, 2008a; Lázaro et al. 2009). An exceptional characteristic of both mélange complexes is the presence of K-poor leucocratic bodies, dikes and veins of intermediate to acid composition (tonalitic-trondhjemitic) intimately associated with the amphibolites (Fig. 2a). Leucocratic rocks are medium- to coarse-grained, including pegmatitic varieties, that appear as m-sized blocks, concordant layers within amphibolite, and crosscutting veins, indicating syn-metamorphic partial melting of amphibolite. García-Casco (2007), García-Casco et al. (2008a) and Lázaro et al. (2009) estimated melt crystallization at pressures of 1.2-1.4 GPa. SHRIMP, Ar/Ar, and K/Ar data (Adamovich and Chejovich 1964; Somin and Millán 1981; Lázaro et al. 2009) indicates that all these types of rock formed during early stage of formation of mélanges in the subduction environment during the Early Cretaceous (115-120 Ma) and slowly exhumed in the subduction channel environment during the Late Cretaceous until they finally exhumed rapidly during the latest Cretaceous (70-75 Ma) collision stage.

Leucocratic rocks are LILE-poor and show Rb/Sr and Sm/Nd isotopic characteristic indicating derivation from a depleted MORB source (Lázaro and García-Casco 2008). However, the diversity of amphibolite and associated leucocratic rocks in

both mélanges includes Ba-rich rocks not described to date. We studied six samples of Ba-rich rocks (see Figs. 1b and c for location) covering the full compositional spectrum from amphibolite (LCG-14) through trondhjemite (CV-201A) and pegmatite (LCM-14 and LC-24 (Fig. 2b and c). In addition, we studied Qtz-Ms rocks (CV-53E and CV-201F; Fig. 2d) as representative of hydrothermal material not considered by Lázaro and García-Casco (2008). These hydrothermal rocks appear as veins generally within trondhjemites and pegmatites suggesting a close genetic relationship. Less commonly, quartz-muscovite rocks crosscut the amphibolites.

ANALYTICAL TECHNIQUES

Whole-rock major and trace elements analysis (Table 1) were carried out at the University of Granada (Centro de Instrumentación Científica, CIC). Major element and Zr compositions were determined on glass beads, made of 0.6 g of powdered sample diluted in 6 g of $Li_2B_4O_7$, with a PHILIPS Magix Pro (PW-2440) X-ray fluorescence (XRF) equipment. The analyses plotted in the figures were recalculated to an anhydrous 100 wt % basis. Trace elements, except Zr, were determined by ICP-MS after HNO_3 + HF digestion of 0.1000 g of sample powder in a Teflon-lined vessel at ~180 ºC and ~200 p.s.i. for 30 min, evaporation to dryness, and subsequent dissolution in 100 ml of 4 vol.% HNO_3.

Major element composition of minerals (Tables 2-5) was obtained by WDS with a CAMECA SX-100 microprobe (CIC, University of Granada) and a CAMECA SX-50 microprobe (Serveis Cientificotecnics, University of Barcelona). Amphibole composition was normalized following the scheme of Leake et al. (1997) and Fe^{3+} was estimated after the method of Schumacher (in Leake et al. 1997). Garnet composition was normalized to 8 cations and 12 oxygens, and Fe^{3+} was estimated by stoichiometry. Epidote, feldspar and lawsonite were normalized to 12.5, 8 and 8 oxygens, respectively, and assuming $Fe_{total} = Fe^{3+}$. White mica and chlorite were normalized to 22 and 28 oxygens, respectively, and assuming $Fe_{total} = Fe^{2+}$. The atomic concentration of elements per formula units is abbreviated apfu. The Mg number of rocks and minerals (Mg#) is expressed as the atomic ratio $Mg/(Mg+Fe^{2+})$.

Elemental XR images were obtained with the CAMECA SX-100 microprobe of Granada University operated at 20 kV, 150 nA beam current, with step (pixel) size of 3-5 µm and counting time of 30 ms. The images were processed with Imager software (Torres-Roldán and García-Casco unpublished) and consist of the XR signals of Kα lines of the elements (colour coded; expressed in counts/nA/s) corrected for 3.5 µs deadtime. The XR spectra of these images were clipped to show the mineral of interest and set on top of a black and white "Z" image calculated by the sum of the products of the counts by atomic number (Si, Ti, Al, Fe, Mn, Mg, Ca, Na, Ba, K, P, F and Cl) to show the basic textural relations of the scanned areas. The profiles of Figures 9 and 11 show chemical compositions of phengite (normalized to 22 O) and garnet (normalized to 12 O), respectively, calculated from the elemental XR images following the procedure of Bence and Albee (1968) for matrix correction using the composition of an internal standards of phengite and garnet analyzed with the electron microprobe and the α-factor table by Kato (2005).

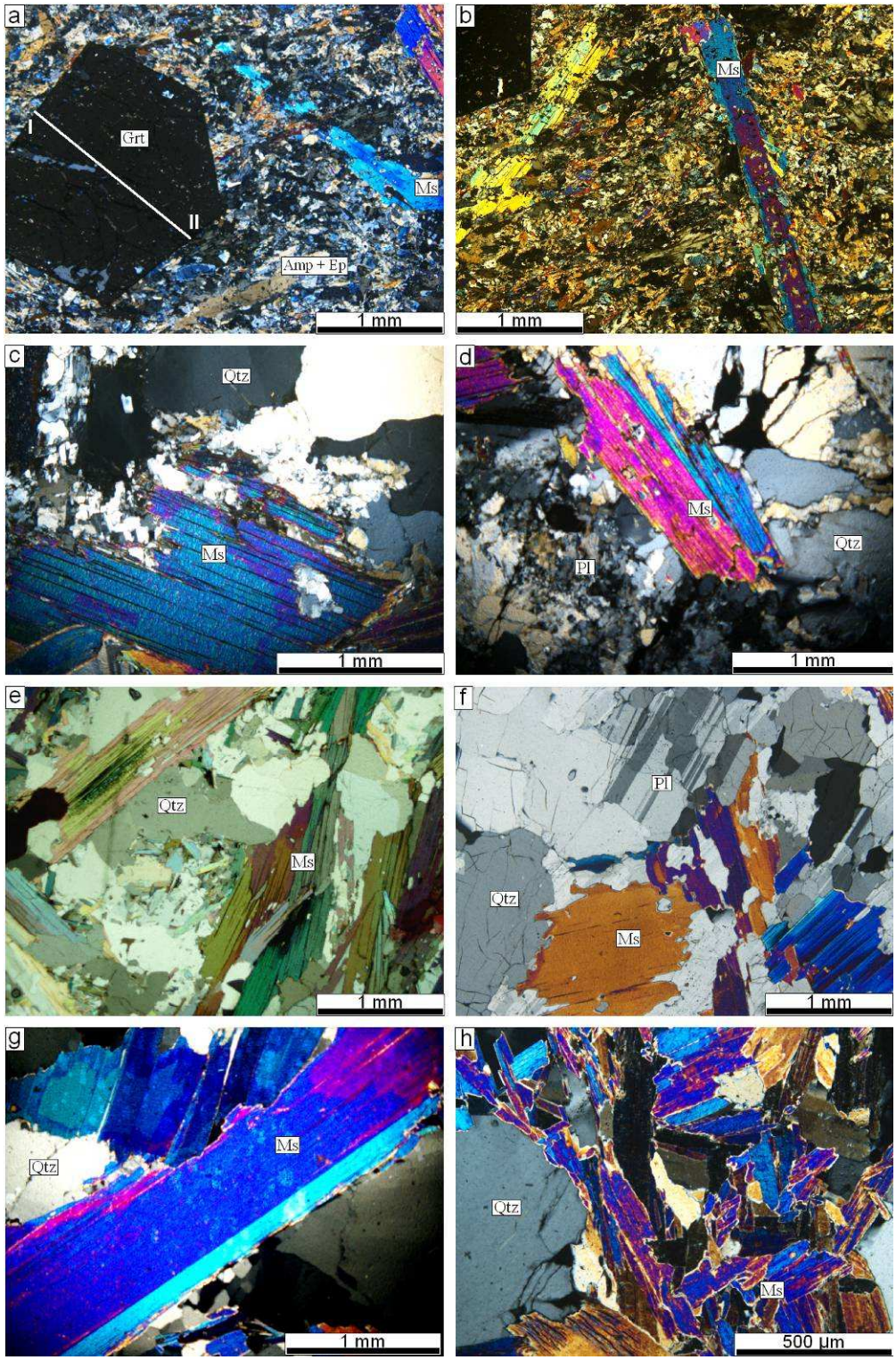
a
I
Grt
II
Ms
Amp + Ep
1 mm
b
Ms
1 mm
c
Qtz
Ms
1 mm
d
Ms
Qtz
Pl
1 mm
e
Qtz
Ms
1 mm
f
Pl
Qtz
Ms
1 mm
g
Ms
Qtz
1 mm
h
Qtz
Ms
500 µm

Fig. 3. a) and b). Photomicrographs of amphibolite LCG-14 showing large crystals of muscovite and garnet porhyroblasts in an epidote-amphibole matrix; the profile along garnet is presented in Fig. 11b. c) and d) Photomicrographs of trondhjemite CV-201A showing magmatic muscovite, quartz and plagioclase. Plagioclase displays a dirty surface due to alteration. e) Photomicrograph of pegmatite LCM-14 from La Corea mélange composed of large (>3 mm) crystals of phengite and quartz, and scarce albitic plagioclase and fine-grained muscovite. f) Photomicrograph of pegmatite LC-24 from La Corea mélange showing primary plagioclase, muscovite and quartz. g) Photomicrograph of Qtz-Ms rock from Sierra del Convento mélange CV-201F showing large (>3 mm) crystals of phengite and quartz. h) Photomicrograph of Qtz-Ms rock from Sierra del Convento mélange CV-201F showing fine-grained muscovite intergrown with quartz and (scarce) albitic plagioclase. Mineral abbreviations after Kretz (1983).

Trace element LA-ICP-MS measurements of minerals (Tables 6-7) were performed at the C.I.C. of Granada University using a 213 nm Mercantek Nd-YAG laser coupled to an Agilent 7500 ICP-MS with a shielded plasma torch. The ablation was carried out in a He atmosphere, using a laser beam fixed at 60 µm diameter. The spot was pre-ablated for 45 s using a laser repetition rate of 10 Hz and 40% output energy. Afterwards, the spot was ablated for 60 s at 10 Hz with laser output energy of 75%. To keep the laser focused during ablation, the sample stage was set to move 5 µm every 20 s. NIST-610 glass (ca. 450 ppb of each element) was employed as an external standard. In each analytical session of a single thick section, the NIST-610 glass was analysed at the beginning and at the end, and also after every six spots to correct for drift. Silicon was used as internal standard. Data reduction was carried out using software written by F. Bea (freely available upon request) in STATA programming language (Statacorp 2005). The precision, calculated on five to seven replicates of the NIST-610 glass measured in every session, was in the range ±3 to ±7% for most elements. Further details on technical methods can be found in Bea (1996) and Bea et al. (2005).

MINERAL ASSEMBLAGES AND TEXTURES

Amphibolite

The peak mineral assemblage of the amphibolite sample LCG-14 consists of pargasite – epidote – garnet – titanite – rutile – quartz – apatite (Figure 3a). Pargasite and epidote define a faint foliation. Garnet forms large porphyroblasts up to 2 mm in length that contain inclusions of epidote, quartz and titanite. The abundance of amphibole and epidote and the lack of peak plagioclase make this amphibolitic rock unusual. Garcia-Casco et al. (2008a) and Blanco-Quintero et al. (2010a) interpreted the lack of peak plagioclase in amphibolite rocks from Sierra del Convento and La Corea mélanges as the result of wet partial melting of the amphibolite at 700-750 ºC and ca. 1.5 GPa.

The studied sample is characterized by large crystals of muscovite up to 4 mm in length that crosscut the foliation of the rock (Fig. 3b). Optically, these crystals appear with patchy to concentric zoning. Inspection of back-scattered electron and XR images reveals xenomorphic Ba-rich cores corroded by phengitic Ba-poor rims (see below). The rims are associated to the retrograde assemblage chlorite - actinolite-magnesiohornblende - albite - titanite that overprints the peak assemblage. The texture, fabric and chemical composition (see below) of the Ba-rich cores, on

the other hand, suggest growth influenced by infiltration of a Ba-rich fluid during near-peak P-T conditions.

Trondhjemite

Trondhjemite sample CV-201A is a non-deformed leucocratic rock consisting of medium-grained magmatic plagioclase and quartz and subordinate Ba-rich muscovite (see below) and epidote (Fig. 3c, d). Plagioclase and quartz represent ca 50 % and 30 % of the modal mineralogy, respectively. Apatite and rutile are present in small concentrations. Magmatic muscovite forms thick tabular crystals (2 mm in length) showing concentric to patchy zoning.

Retrogression affected all types of magmatic crystals. Plagioclase appears altered to albite, clinozoisite, lawsonite, phengite and saussurite. Magmatic epidote shows overgrowths of retrograde clinozoisite that appear as needles. Magmatic muscovite shows retrograde Ba-rich phengite overgrowths, commonly associated to small retrograde crystals of Ba-feldspars (celsian and/or cymrite) when adjacent to plagioclase. This retrograde assemblage indicates high pressure and low temperature during retrogression.

Pegmatites

Pegmatite samples LC-24 and LCM-14 are formed by quartz, albitic plagioclase, and muscovite with magmatic textures, commonly graphic-like (Fig. 3e, f), and minor apatite. The grain size of muscovite in these rocks can exceed several cm in length, and display concentric to patchy zoning. Albite twinning is very common, though Carlsbad twinning is also present in plagioclase. Retrogression is faint, represented by fine-grained albite and phengite.

Quartz-muscovite rocks

Quartz-muscovite samples CV-53E and CV-201F contain grains of muscovite larger than 3 mm in length that display concentric to patchy zoning, and are not oriented (Fig. 3g). Scarce plagioclase crystals are present. Small crystals of retrograde phengite appear in the quartzitic matrix (Fig. 3h). In general, this type of rock contains larger amounts of muscovite than the pegmatites.

WHOLE ROCK GEOCHEMISTRY

Major elements

Amphibolite

Amphibolite has a SiO_2 composition of 48.75 wt.% and Na_2O+K_2O of 2.44 wt % (Table 1) which corresponds to the basaltic composition within the subalkaline series in the TAS diagram of Le Maitre et al (1989; Fig 4a). Its composition is similar to N-MORB, with relatively low Mg# (0.37) and low to moderate Na2O (1.76 wt.%) and K_2O (0.68 wt.%) contents. Nevertheless the K2O content is high relative to typical amphibolite from the Sierra del Convento and La Corea mélanges (range 0.05-0.47 wt %; Lázaro and García-Casco, 2008) and has a medium-K affinity in the K_2O-SiO_2 diagram of Peccerillo and Taylor (1976; Fig. 4b). BaO content is 0.24 wt%, much higher than typical N-MORB (0.002 wt. %; Hofmman

1988; Fig. 4c). The alumina saturation index A/CNK = 0.67, [A/CNK = molar $Al_2O_3/(CaO + Na_2O + K_2O)$] classifies this rock as metaluminous, similar to MORB composition (Fig. 4d), despite of the presence of muscovite.

Trondhjemite

The trondhjemite sample has high SiO_2 (76.16 wt %) and K_2O+Na_2O (6.75 wt %) contents corresponding to subalkaline rhyolitic composition in the TAS diagram (Fig. 4a). The Al_2O_3 and Na_2O contents are high (15.82 and 5.98 wt % respectively), while K_2O is low (0.78 wt. %) and K_2O/Na_2O is very low (0.13), plotting in the low-K tholeiitic series field of Peccerillo and Taylor (1976; Fig. 3b). The FeO and MgO contents are low, with Mg# = 0.17. The BaO content is high (0.50 wt%, Fig. 4c). The rock is peraluminous (Fig. 4d), having A/CNK = 1.29, as would be anticipated by the presence of magmatic muscovite.

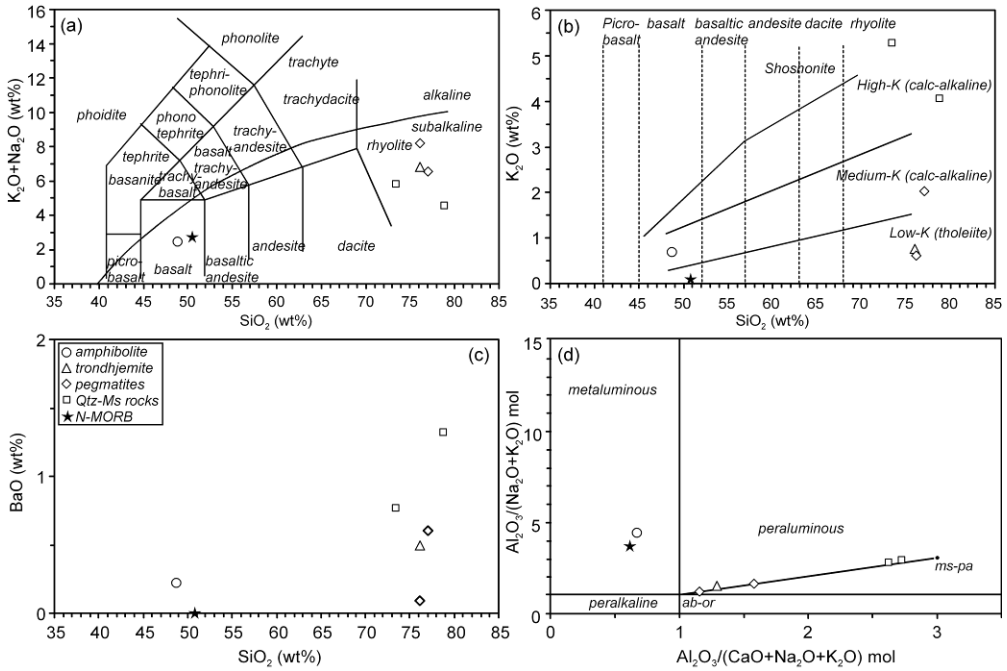

Fig. 4. a) Total alkalis vs. silica diagram of classification of volcanic rocks from Le Maitre et al. (1989). b) K2O vs. SiO2 diagram (Peccerillo and Taylor, 1976). c) BaO vs. SiO2 diagram. d) IAI (inverse agpaitic index) versus ASI (alumina saturation index) diagram with projection of alkali-feldspars and white micas for reference. Symbols as in figure c. The composition of N-MORB is from Hofmman (1988).

Pegmatites

The pegmatites have very high SiO_2 (76.11 and 76.98 wt %) and $Na_2O + K_2O$ (6.51 and 8.20 wt %) contents, which correspond to subalkaline rhyolitic composition in the TAS diagram (Fig. 4a). They have high Na2O (4.48 and 7.58 wt. %), and relatively low FeO (< 0.37 wt. %), MgO (< 0.33 wt. %), Mg# (down to 0.14 in sample LC-24) contents. The K_2O contents are relatively high (0.62 and 2.02 wt. %), plotting in the low to medium-K series of Peccerillo and Taylor (1976: Fig. 4b). The BaO contents (Fig. 4c) varies from 0.09 wt. % (LC-24) to 0.61 wt. % (LCM-14), in

correspondence with larger amounts of white mica in the later. The alumina saturation index indicates peraluminous character (1.15 and 1.58), very similar to the trondhjemite sample (Fig. 4d).

Table 1 Major (wt%)and trace elements composition of studied samples.

Sample	LCG-14	CV-201A	CV-201F	CV-53E	LC-24	LCM-14
Complex	Corea	Convento	Convento	Convento	Corea	Corea
Rock	amph	trondh	Qtz-Ms	Qtz-Ms	pegm	pegm
SiO_2	46.47	75.55	77.11	71.47	76.09	75.78
TiO_2	2.03	0.03	0.13	0.08	0.01	0.03
Al_2O_3	15.23	15.69	14.12	18.26	15.26	15.35
FeO_{tot}	11.36	0.25	0.76	0.70	0.29	0.37
MnO	0.25	0.03	0.01	0.02	0.01	0.01
MgO	6.81	0.05	1.11	1.05	0.05	0.32
CaO	10.64	0.87	0.15	0.19	0.07	0.16
Na_2O	1.68	5.93	0.48	0.48	7.58	4.41
K_2O	0.65	0.77	3.98	5.14	0.62	2.00
P_2O_5	0.21	0.03	0.03	0.01	0.01	0.02
LOI	3.43	0.50	1.83	2.37	0.35	1.04
Total	98.75	99.70	99.71	99.77	100.33	99.49
Mg#	0.37	0.17	0.59	0.60	0.14	0.46
Rb	12.08	12.25	78.80	88.00	10.22	31.46
Cs	0.20	0.10	0.45	0.32	0.03	0.23
Sr	637.88	191.50	24.21	99.61	13.54	92.54
Ba	2014.99	4459.62	11810.00	6882.23	796.68	5425.75
Sc	42.72	0.70	4.56	5.65	0.18	0.55
Ni	94.12	2.77	18.43	23.00	4.54	23.80
Y	35.12	10.67	4.08	5.33	0.67	2.38
Nb	8.46	2.46	8.18	5.60	0.61	3.29
Zr	126.80	17.80	19.30	42.00	9.40	10.50
Pb	9.84	20.01	2.99	5.43	0.96	13.62
U	0.19	0.63	2.56	0.77	0.05	0.38
Th	0.74	0.93	6.44	4.30	0.16	1.15
La	8.92	3.13	10.70	2.96	0.50	2.62
Ce	21.78	4.38	15.05	5.83	1.09	3.95
Pr	3.25	0.65	2.14	0.65	0.13	0.43
Nd	15.56	2.56	8.41	2.79	0.59	1.73
Sm	4.67	0.95	1.95	0.79	0.16	0.53
Eu	1.79	0.63	1.08	0.65	0.06	0.47
Gd	5.50	1.32	1.81	0.83	0.14	0.56
Tb	0.95	0.23	0.23	0.13	0.02	0.08
Dy	6.12	1.53	1.06	0.89	0.12	0.44
Ho	1.31	0.29	0.16	0.18	0.03	0.08
Er	3.59	0.77	0.36	0.53	0.08	0.23
Yb	3.30	0.73	0.29	0.54	0.06	0.20
Lu	0.50	0.11	0.04	0.09	0.01	0.03

Quartz-muscovite rocks

These rocks are similar to pegmatites in terms of SiO_2 (73.38 and 78.78 wt %) and Na_2O+K_2O (4.56 and 5.77 wt %), having (an apparent) subalkaline rhyolitic composition in the TAS diagram (Fig. 4a). However, they have much lower Na_2O (0.49 wt %) and higher FeO (> 0.72 wt %), MgO (> 1.08), Mg# (0.60) and much higher K_2O (4.01-5.28 wt %) as compared to the pegmatites. Correspondingly, they plot in high-K field of Peccerillo and Taylor (1976; Fig. 4b). These rocks have the highest BaO contents of the sample set analyzed (Fig. 4c; up to 1.32 wt % in CV-201F) and are strongly peraluminous (Fig. 4d), having very high A/CNK (2.63-2.73) indicating the prevailing presence of muscovite. The chemical differences between

pegmatites and Qtz-Ms rocks are in correspondence with the abundance of mica and scarcity of plagioclase in the later type of rock as compared to the former.

Trace elements

Amphibolite

The normalized rare earth element (REE) pattern of the amphibolite sample shows enrichments with respect to chondrite C1 (McDonough and Sun, 1995). The pattern has negative slope (Fig 5a), similar to E-MORB. A positive (La/Yb)n value of 1.83 indicates a fractionated REE pattern. It shows no Eu anomaly (Eu/Eu* = 1.07) and only slight HREE depletion with (Gd/Yb)n = 1.19.

This rock shows a flat pattern with similar values for HFSE (Zr, Ti, Y) than N-MORB and enrichment in LILE in a N-MORB normalized trace element diagram (Fig. 6a). The most important deviations from N-MORB composition are enrichment in Ba, Pb and Sr. The elevated Ba/Th (2734.0), Pb/Th (13.4) and Sr/Th (865.5) ratios denote high mobility of Ba, Pb and Sr relative to Th. These enrichments in some mobile LILE are related to the effect of alteration by fluids derived from subducted sediments (Breeding et al. 2004, and see below). Because of the high Ba content of the high-temperature cores of muscovite in this sample (see below), we interpret this stage of alteration occurred at relatively high temperature.

Table 2: Representative analyses of white micas (normalized to 22 O and 4 OH)

Rock	Amph	Amph	Trond	Trond	Trond	Peg	Peg	Qtz-Ms	Qtz-Ms
type	core	rim	Ms	core	rim	core	rim	core	rim
SiO_2	40.90	52.96	44.35	41.30	47.97	42.55	49.02	41.11	48.40
TiO_2	1.20	0.04	0.02	0.14	0.05	0.09	0.11	0.02	0.40
$Al2O_3$	30.26	23.46	38.15	32.11	26.80	34.42	27.47	35.80	28.82
FeO	2.43	3.76	0.04	2.24	4.77	1.67	1.26	1.15	1.72
MnO	0.03	0.02	0.01	0.06	0.36	0.00	0.03	0.03	0.01
MgO	2.15	3.78	0.00	1.31	1.13	1.22	3.32	0.64	3.42
CaO	0.00	0.13	0.01	0.00	0.00	0.00	0.00	0.00	0.00
BaO	8.90	0.25	0.49	8.38	2.64	6.49	1.79	7.33	1.62
Na_2O	0.63	0.04	0.13	0.57	0.11	1.12	0.81	0.89	0.47
K_2O	7.06	10.41	11.18	7.47	9.90	7.76	9.34	7.66	10.19
Total	93.56	94.85	94.37	93.58	93.72	95.32	93.15	94.67	95.09
Si	5.96	7.14	5.96	5.97	6.73	5.93	6.73	5.79	6.55
Ti	0.13	0.00	0.00	0.01	0.01	0.01	0.01	0.00	0.04
Al	5.19	3.73	6.04	5.47	4.43	5.65	4.44	5.94	4.60
Fe^{2+}	0.30	0.42	0.00	0.27	0.56	0.19	0.14	0.14	0.19
Mn	0.00	0.00	0.00	0.01	0.04	0.00	0.00	0.00	0.00
Mg	0.47	0.76	0.00	0.28	0.24	0.25	0.68	0.13	0.69
Ca	0.00	0.02	0.00	0.00	0.00	0.00	0.00	0.00	0.00
Ba	0.51	0.01	0.03	0.47	0.14	0.35	0.10	0.40	0.09
Na	0.18	0.01	0.03	0.16	0.03	0.30	0.22	0.24	0.12
K	1.31	1.79	1.92	1.38	1.77	1.38	1.64	1.38	1.76
Mg#	0.61	0.64	0.07	0.51	0.30	0.57	0.82	0.50	0.78

Trondhjemite

The chondrite-normalized REE pattern of this sample is relatively flat and characterized by moderate REE contents (Fig. 5b). Two positive anomalies in La and Eu are present, which can be correlated to the presence of epidote in this rock (see below). These enrichments yield positive (La/Yb)n (2.91) and Eu anomaly (Eu/Eu* = 1.71).

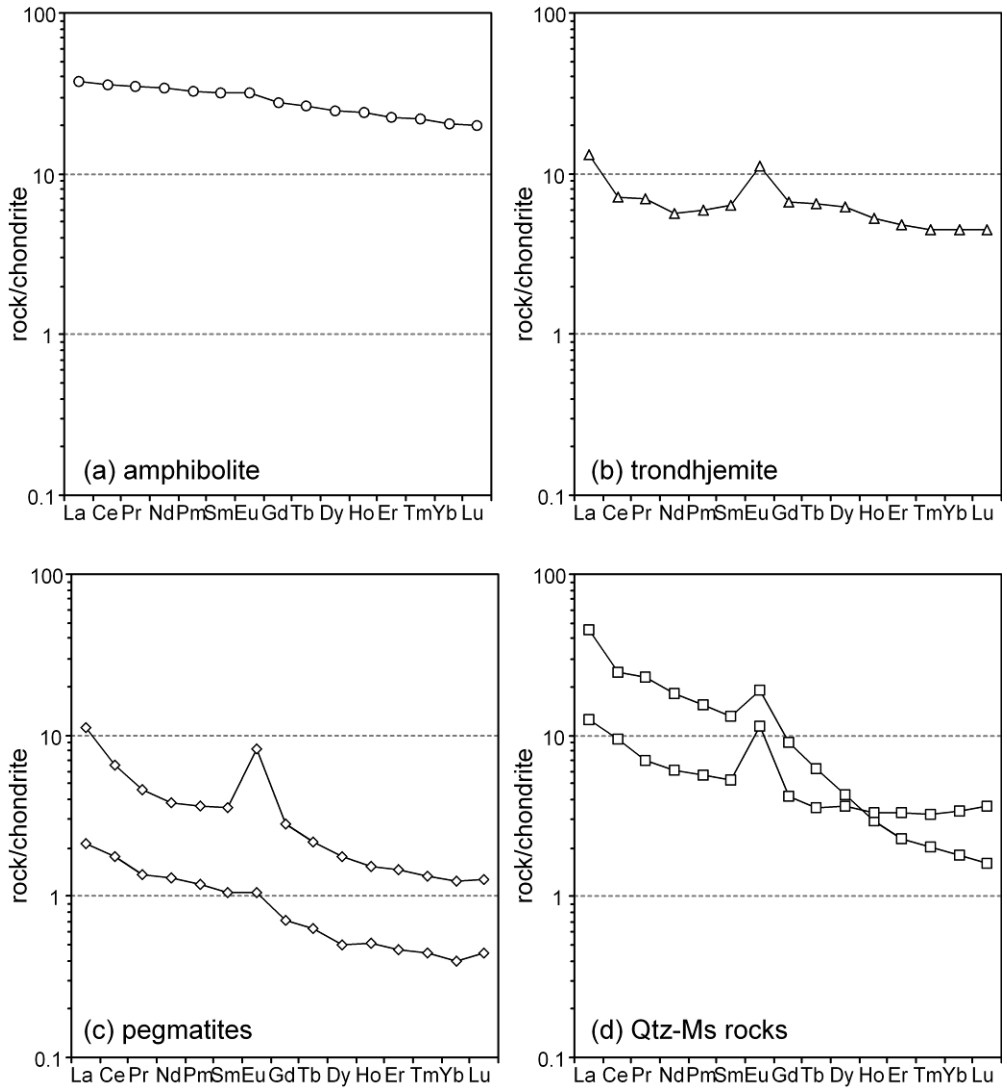

Fig. 5 Chondrite (C1, McDonough and Sun, 1995) normalized REE patterns for: (a) amphibolite, (b) trondhjemite, (c) pegmatites, and (d) Qtz-Ms rocks.

The incompatible trace element pattern normalized to N-MORB composition illustrates enrichment in LILE and depletion in HFSE (Fig. 6b). Strong positive anomalies in Ba and Pb, similar to amphibolite, are notable. The ratios (La/Yb)n (2.91) and Sr/Y (17.95) are very low compared to adakites. The negative Ti anomaly is presumably related to fractionation of rutile in parental amphibolite. Similar to the analyzed amphibolite sample, the elevated Ba/Th (4795.3), Pb/Th (21.5) and Sr/Th (205.9) ratios denote high mobility of Ba, Pb and Sr relative to Th.

Pegmatites

The rare earth element patterns normalized to chondrite C1 show negative slopes (Fig 5c). Notably, HREE contents are sub chondritic in sample LC-24. This feature is also characteristic of K- and Ba- poor melts formed after partial melting of

amphibolite in the Sierra del Convento mélange (Lázaro and García-Casco, 2008). A strong positive Eu anomaly is present in sample LCM-14 (Eu/Eu* = 2.61). The samples show fractioned patterns with HREE depletion as (Gd/Yb)n (1.78 and 2.61) and the (La/Yb)n (5.33 and 8.80) ratios indicate.

The N-MORB normalized trace element patterns are characterized by relatively poor high field strength elements (HFSE) and enrichment in LILE (especially in Ba, Pb, Na) and depletion in Ti (Fig. 6c). These rocks are characterized by high Sr/Y ratio (up to 38.90), similar to that of adakites.

Quartz-muscovite rocks

The chondrite-normalized REE patterns (Fig. 5d) are characterized by negative slopes and enrichment of LREE with respect to HREE [(La/Yb)n = 3.72 and 25.24]. Positive Eu anomalies (Eu/Eu* = 1.75 and 2.45) are distinctive.

Similar to pegmatites, the N-MORB normalized trace element patterns are characterized by relatively poor patterns for the HFSE, enrichment in Ba, Pb and depletion in Ti (Fig. 6d). These rocks display moderate to high Sr/Y (5.93-18.69) ratios.

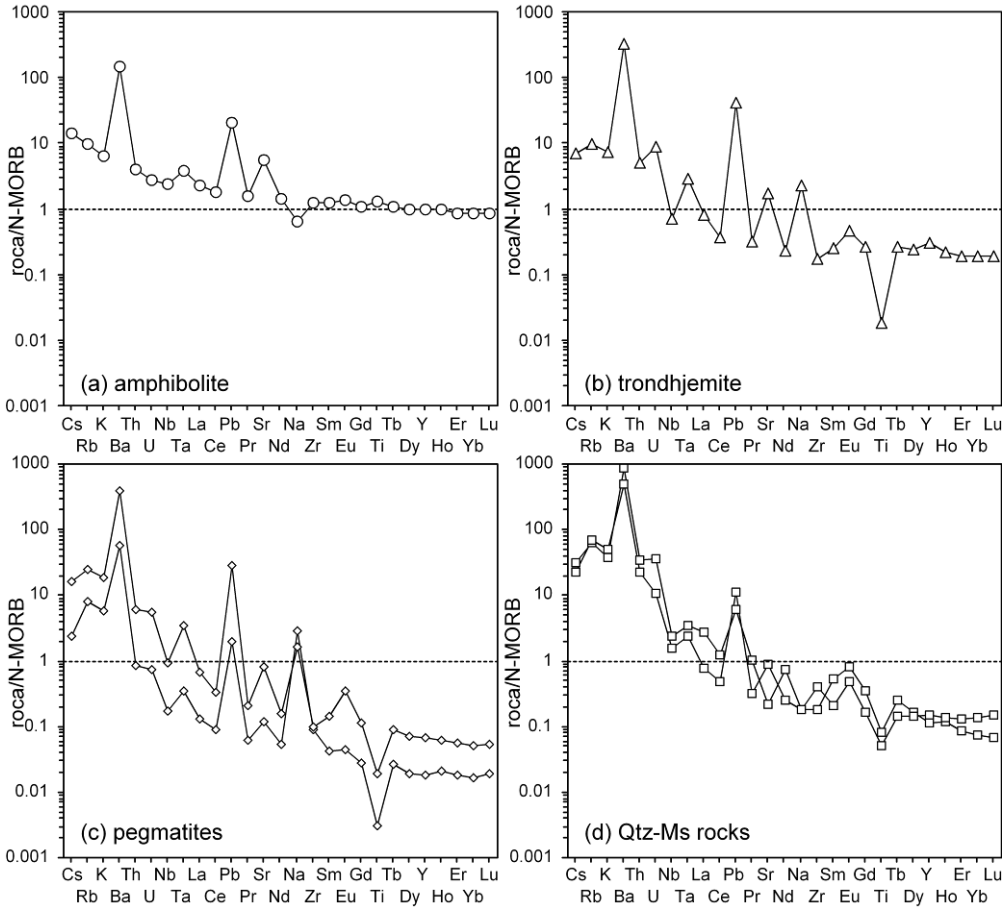

Fig. 6 N-MORB (Hofmann, 1988) normalized spider diagrams for a) amphibolite, b) trondhjemite, c) pegmatites and d) quartz-muscovite rocks.

The similarities in trace element composition between trondhjemite, pegmatites and Qtz-rich rocks support field relationships suggesting a genetic connection. It could be speculated that pegmatites are the result of magmatic differentiation of tonalitic-trondhjemite magmas, while Qtz-Ms rocks may constitute the final hydrothermal products of crystallization of pegmatites. However, evidences given below suggest that Qtz+Ms rocks represent crystallization from a infiltrating primary sediment-derived fluid. Such primary fluid may represent the fluid that triggered partial melting of MORB-derived subducted amphibolite to yield trondhjemitic-pegmatitic rocks.

Tabla 3 Representative analyses of plagioclase and K/Ba-feldspar (normalized to 8 O).

Rock	Amph	Pegm	Pegm	trond	trond	trond	trond	trond	trond	trond	trond
Mineral	Pl	Pl	Pl	Pl	Pl	Kfs	Kfs	Celsian	Celsian	Cymrite	Cymrite
SiO_2	68.91	63.34	68.22	67.52	66.68	63.37	61.11	30.72	30.76	31.55	31.73
TiO_2	0.01	0.00	0.00	0.00	0.00	0.00	0.00	0.05	0.04	0.04	0.03
Al_2O_3	19.54	22.15	19.67	19.51	20.12	18.12	17.98	26.32	26.17	25.39	25.61
FeO_{tot}	0.05	0.00	0.00	0.01	0.01	0.03	0.01	0.08	0.00	0.02	0.00
CaO	0.15	4.38	0.33	0.01	0.76	0.00	0.03	0.05	0.02	0.00	0.03
BaO	0.00	0.00	0.01	0.02	0.09	0.45	3.44	40.50	40.2	37.54	38.48
Na_2O	11.64	9.52	11.71	11.94	11.43	0.04	0.08	0.11	0.1	0.15	0.13
K_2O	0.03	0.05	0.05	0.02	0.03	16.52	15.19	0.20	0.3	0.89	0.70
Sum	100.33	99.44	99.99	99.04	99.11	98.53	97.83	98.03	97.59	95.58	96.71
Si	3.00	2.82	2.98	2.98	2.95	2.99	2.96	1.98	1.99	2.04	2.04
Ti	0.00	0.00	0.00	0.00	0.00	0.00	0.00	0.00	0.00	0.00	0.00
Al	1.00	1.16	1.01	1.02	1.05	1.01	1.03	2.00	1.99	1.94	1.94
Fe^{3+}	0.00	0.00	0.00	0.00	0.00	0.00	0.00	0.00	0.00	0.00	0.00
Ca	0.01	0.21	0.02	0.00	0.04	0.00	0.00	0.00	0.00	0.00	0.00
Ba	0.00	0.00	0.00	0.00	0.00	0.01	0.07	1.02	1.02	0.95	0.97
Na	0.98	0.82	0.99	1.02	0.98	0.00	0.01	0.01	0.01	0.02	0.02
K	0.00	0.00	0.00	0.00	0.00	0.99	0.94	0.02	0.02	0.07	0.06

MINERAL COMPOSITION

White Mica

Major elements

In amphibolite, phengitic mica shows a strong compositional range in terms of Si (5.95 – 6.86 apfu), Mg (0.32 - 0.68), Fe (0.17 - 0.37), Al (4.14 – 5.33), Ti (0.01 - 0.14), Ba (0.08 – 0.57), K (1.31 – 1.85), Na (0.04 – 0.36) and Mg# (0.57 – 0.70) (Table 2; Fig. 7). High Ba contents are recorded in the cores, which stand out clearly in XR images (Fig. 8a, b). These cores appear corroded and overgrown by low-Ba rims (down to 0.21 apfu). High Ba cores are also rich in Na (up to 0.30 apfu) and Ti (up to 0.14 apfu), denoting high temperature of the formation. The contents in Ba is accommodated by the celsian ($[BaAl][KSi]_{-1}$) exchange vector, which makes high-Ba cores to be poor in Si (5.95 – 6.23 apfu) even if the amounts of phengitic component related to the celadonitic (i.e., tschermak) exchange ($[Si(Mg,Fe)][Al]_{-2}$) are moderate to high (Fe+Mg = 0.55 – 0.76 apfu).

Similar complex relations are found in muscovite from the trondhjemite sample CV-201A. High-Ba (0.15 – 0.22 apfu) cores from crystals of magmatic appearance are characterized by Si = 5.97 – 6.12 apfu, Ti < 0.02, Mg = 0.06 - 0.19, Fe = 0.09 - 0.25,

Al = 5.50 – 5.88, K = 1.55 – 1.73, Na = 0.10 – 0.23 and Mg# = 0.32 – 0.46), indicating that muscovite crystallized at high temperature from a silicate liquid. The cores are irregularly corroded and overgrown by low-Ba rims characterized by Si = 6.06 – 6.24 apfu, Mg = 0.14 - 0.22, Fe = 0.20 - 0.26, K = 1.67 – 1.75, Al = 5.32 – 5.63, Ti = 0.01, Ba = 0.09 – 0.15, Na = 0.12 – 0.19 and Mg# = 0.41 – 0.48. These overgrowths yielded subhedral crystals that probably formed above the solidus of the rock. Finally, the rims of magmatic muscovite are overgrown by thin films of Ba-rich muscovite (Fig. 8d), with low Si (5.83 – 6.04 apfu), Mg (0.10 - 0.28), Fe (0.14 - 0.27), K (1.28 – 1.40) and high Al (5.47 – 5.93), Ba (0.31 – 0.47), Na (0.16 – 0.35) and Mg# (0.40 – 0.55). These latest overgrowths formed during subsolidus retrogression of the sample, concomitant with celsian and cyrmrite replacements after plagioclase.

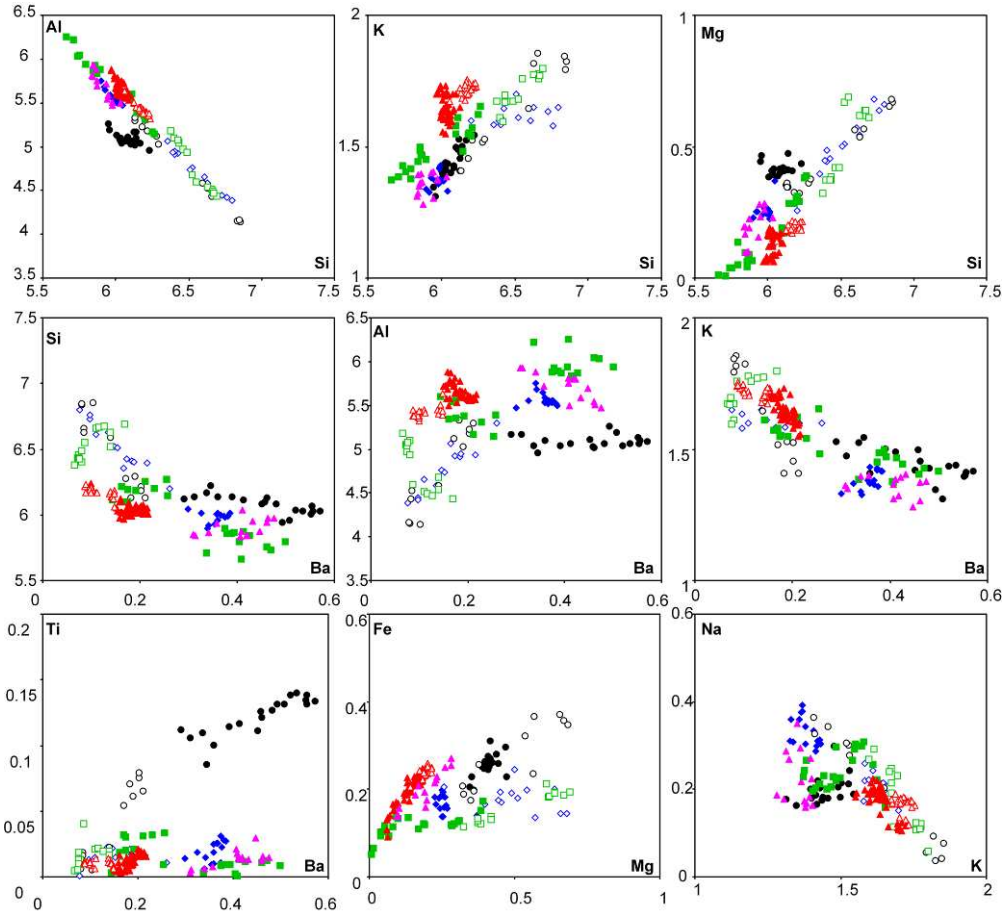

Fig. 7. Composition of white micas from all samples. Circles = amphibolite (black), triangles = trondhjemite (red), diamonds = pegmatite (blue), and squares = Qtz-Ms rocks (green). Solid symbols correspond to the cores of crystals and empty symbol are from the rims, but later retrogression in trondhjemite is indicated by purple triangle.

In the pegmatites, muscovite is also characterized by high-Ba (0.30 – 0.38 apfu) corroded cores and low-Ba overgrowths (Figs. 7 and 8e, f; Table 2). The former have also low Si (5.90 – 6.05 apfu), K (1.33 – 1.43), Mg (0.23 - 0.37), Fe (0.14 –

0.20) and high Al (5.47 – 5.76), Na (0.29 – 0.39), and Mg# (0.55 – 0.73). The Ba-poor rims have high Si (6.15 – 6.80 apfu), K (1.51 – 1.70), Mg (0.26 - 0.68), Mg# (0.56 – 0.82) and low Al (4.39 – 5.45), Ba (0.08 – 0.26), Fe (0.09 - 0.24) and Na (0.15 – 0.36). A representative profile along these micas is presented Fig. 9.

In Qtz-Ms rocks the chemical features of muscovites are similar to that of other rock types. They display corroded Ba-rich cores overgrown by Ba-poor rims (Fig. 8g, h). The core composition is poor in Si (5.66 – 6.27 apfu), Mg (0.01 - 0.39), Fe (0.05 - 0.17), and K (1.37 – 1.65) and rich in Al (5.14 – 6.26), Ba (0.14 – 0.50), Na (0.15 – 0.31) and variable Mg# (0.14 – 0.72). The Ba-poor overgrowths have high Si (6.38 – 6.69 apfu), Mg (0.32 - 0.69), K (1.60 – 1.80), and Mg# (0.74 – 0.78) and low Al (4.43 – 5.18), Fe (0.11 - 0.21), Ba (0.07 – 0.17) and Na (0.06 – 0.29).

The chemical zoning of micas from all types of rock indicates complex fluid/melt evolution during the evolution of these rocks, as discussed below.

Table 4: Representative analyses of epidote (normalized to 12 O and 1 OH) and lawsonite (normalized to 8 O).

Mineral	Ep	Ep	Ep	Ep	Lws	Lws
Rock	Anf	Anf	trond	trond	trond	trond
Type	peak	retro	peak	retro	retro	retro
SiO_2	38.60	38.83	38.47	38.97	37.58	39.18
TiO_2	0.13	0.23	0.03	0.00	0.00	0.00
Al_2O_3	27.70	29.70	32.12	33.18	29.62	30.11
FeO_{tot}	6.64	4.26	1.50	0.15	0.37	0.17
MnO	0.11	0.05	0.40	0.14	0.00	0.00
MgO	0.05	0.08	0.02	0.00	0.00	0.00
CaO	23.68	23.09	23.82	23.73	16.65	16.11
Na_2O	0.01	0.01	0.00	0.00	0.00	0.35
Sum	96.92	96.25	96.36	96.15	84.22	85.92
Si	3.01	3.02	2.98	3.00	2.05	2.10
Ti	0.01	0.01	0.00	0.00	0.00	0.00
Al	2.55	2.72	2.93	3.01	1.91	1.90
Fe^{3+}	0.43	0.28	0.10	0.01	0.02	0.01
Mn	0.01	0.00	0.03	0.01	0.00	0.00
Mg	0.01	0.01	0.00	0.00	0.00	0.00
Ca	1.98	1.92	1.98	1.96	0.97	0.92
Ba	0.00	0.00	0.00	0.00	0.11	0.00
Na	0.00	0.00	0.00	0.00	0.03	0.04
Xps	0.15	0.09	0.03	0.00	0.00	0.00

Trace elements

LA-ICP-MS trace element measurements of the composition of the cores and rims of select white micas of all studied samples are presented in Tables 6 and 7. The compositions normalized to N-MORB (Hofmann, 1988) show similar trends (Fig. 10). In general, the studied muscovite-phengite crystals strongly concentrate Cs, Rb and Ba, as would be expected (e.g. Zack et al. 2001), while are poorer in HFSE relative to their respective whole rock compositions (note that some elements are below the detection limit). In general, the LILE display fractioned patterns while the HFSE have relatively flat patterns, in all aspects resembling the behaviour of the whole rocks. In the amphibolite sample, the cores are richer in all elements except in Pb and Sr, which are prominently enriched in the rims (Fig. 10a). In the trondhjemite and pegmatite samples there is not a clear difference between core and rim in terms of trace elements abundances (Fig. 10 b, c), except for Ba and other

LILE that appear concentrated in the cores. In the Qtz-Ms rock, most LIL elements are concentrated in the cores (Fig. 10d).

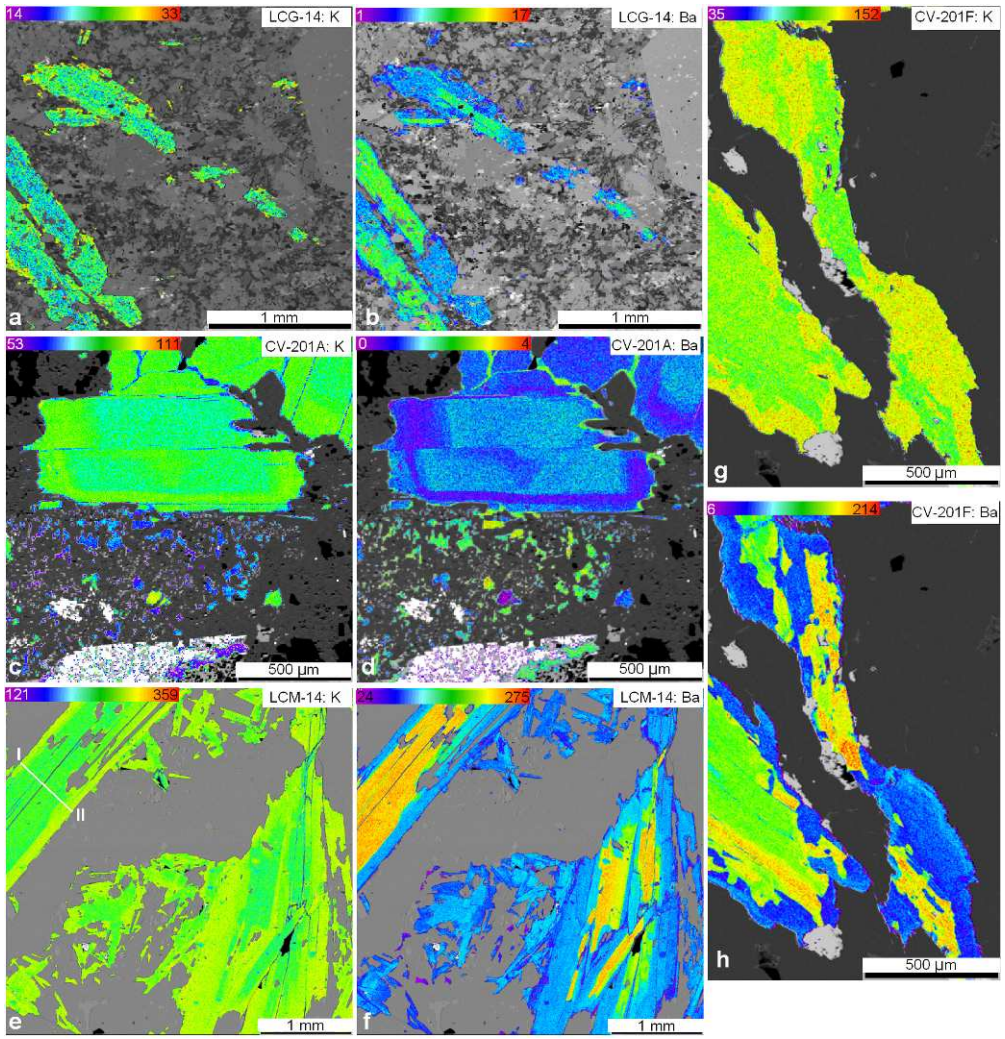

Fig. 8. XR images showing geochemical variation of phengite. a) and b) K (Kα), and Ba (Lα□ images, respectively, from amphibolite sample LCG-14; c) and d) K (Kα) and Ba (Lα) images, respectively, from trondhjemite sample CV-201A; e) and f) K (Kα), and Ba (Lα□ images, respectively, from pegmatite sample LCM-14 (the profile indicated in e is presented in Fig. 9f); g) and h) K (Kα), and Ba (Lα□ images, respectively, from Qtz-Ms rock sample CV-201F. All elemental images are expressed in counts/s (colour scale bar), clipped to show muscovite-phengite chemistry, and set on top of calculated black-and-white images.

Plagioclase

In amphibolite, plagioclase from retrograde pockets within the amphibole-epidote groundmass is albite in composition (Xab = 0.99; Table 3). Magmatic plagioclase from the trondhjemite sample is strongly retrograded to albite. The highest Ca content detected is 0.04 apfu (Table 3).

Fresh magmatic crystals of plagioclase from the pegmatite samples are rich in Ab component (> 0.97), attesting for a near-minimum melt composition of the pegmatitic magma. Sample LCM-14 bears some grains richer in Ca (Xan: 0.14-0.20; Table 3).

Table 5: Representative analyses of amphibole (normalized to 22 O and 2 OH), garnet (normalized to 12 O) and chlorite (normalized to 20 O and 16 OH)

Mineral	Amp	Amp	Grt	Chl	Chl
Type	peak	retro	peak	retro	retro
SiO_2	42.85	53.79	37.78	26.75	26.44
TiO_2	0.61	0.03	0.10	0.06	0.01
Al_2O_3	15.69	2.00	21.29	20.55	18.25
FeO_{tot}	14.73	15.42	27.42	21.18	30.24
MnO	0.09	0.15	2.04	0.13	0.26
MgO	9.13	13.61	2.63	17.94	12.34
CaO	11.05	12.05	9.76	0.02	0.13
Na_2O	2.48	0.58		0.01	0.02
K_2O	0.6	0.07		0.03	0.03
Total	97.23	97.7	101.02	86.67	87.72
Si	6.35	7.82	2.97	5.56	5.73
Ti	0.07	0.00	0.01	0.01	0.00
Al	2.74	0.34	1.98	5.04	4.66
Fe^{3+}	0.05	0.04	0.00	0.00	0.00
Fe^{2+}	1.77	1.83	1.81	3.68	5.47
Mn	0.01	0.02	0.14	0.02	0.05
Mg	2.02	2.95	0.31	5.56	3.98
Ca	1.75	1.88	0.82	0.00	0.03
Na	0.71	0.16		0.00	0.01
K	0.11	0.01		0.01	0.01
Mg#	0.53	0.62	0.15	0.60	0.42

K and Ba minerals

The chemical composition of small disseminated feldspar crystals overprinting plagioclase in trondhjemite sample CV-201A corresponds to orthoclase and celsian (Table 3). Cymrite also appears associated with celsian (Table 3). The coexistence of near-pure orthoclase and celsian compositions indicates solvus relations at very low temperature.

Epidote

Clinozoisite is the most common composition of the epidote group minerals in amphibolite with low pistacite content (Xps = Fe3+/[(Al+Fe3+)] < 0.15; Table 4). Zoning is generally faint or not present. Magmatic crystal of epidote group minerals from trondhjemite have low pistacite contents (<0.12).

Lawsonite

Retrograde crystals of lawsonite are very pure and do not display significant chemical variations (Table 4).

Amphibole

In amphibolite sample, amphibole is calcic ranging in composition from pargasite trough magnesiohornblende to actinolite. Pargasite has (Na+K)A contents in the range 0.53-0.60 apfu, while actinolite-magnesiohornblende has 0.02-0.45 apfu (Fig.

11a, Table 5). The pargasitic compositions correspond to grains formed at the metamorphic peak. They are rich in Na-in-A (max. 0.48 apfu), total Al (max. 2.74), Mg# (max. 0.55) and Ca (max. 1.79), and poor in Si (min. 6.35). The actinolite-magnesiohornblende compositions correspond to retrograde overprints (Fig. 11a). They are poor in Al (even 0.14) and rich in Si (max. 7.90) and Mg# (0.56-0.65).

Table.6 Representative LA-ICP-MS analyses (ppm) of cores of phengite of studied rocks.

Sample	LCM-14	LCM-14	LCM-14	LCG-14	LCG-14	CV-201a	CV-201a	CV-201f	CV-201f	CV-201f
Type	Peg	Peg	Peg	Amph	Amph	trond	trond	Qtz-Ms	Qtz-Ms	Qtz-Ms
Rb	264.69	199.03	83.74	292.50	294.93	166.62	158.92	83.70	135.24	79.79
Cs	6.52	3.91	10.77	0.71	0.59	0.88	0.87	0.41	1.26	0.59
Sr	26.61	22.95	81.14	211.38	195.87	14.71	15.37	59.15	15.39	173.46
Ba	83979.62	61891.90	49765.47	88512.76	104468.64	46163.90	45100.77	86828.49	62598.93	103385.49
Sc	6.75	11.06	3.93	16.28	18.23	6.86	8.02	4.71	25.15	2.39
Ni	0.29	0.07	0.53	23.51	18.45	0.94	0.95	5.35	3.94	6.46
Y	2.41	1.87	1.41	16.68	23.45	1.50	1.52	2.62	1.68	2.69
Nb	17.33	37.96	2.27	19.96	21.22	47.70	41.98	11.00	96.68	7.19
Zr	2.01	6.46	2.58	44.74	43.22	1.31	1.31	0.21	1.49	0.25
Pb	20.08	14.95	46.95	7.03	7.64	12.24	8.24	17.69	12.77	28.64
U	0.01	0.03	0.02	0.05	0.09	0.01	0.01	0.08	0.07	0.26
Th	0.02	0.03	0.03	0.03	0.01	0.00	0.01	0.08	0.04	0.15
La	0.33	0.40	0.32	0.55	0.26	0.54	0.44	0.29	0.24	0.35
Ce	0.07	0.34	0.16	1.17	0.41	0.00	0.01	0.03	0.00	0.08
Pr	0.02	0.02	0.01	0.18	0.13	0.01	0.00	0.02	0.00	0.03
Nd	0.08	0.19	0.14	1.35	0.99	0.03	0.00	0.03	0.00	0.05
Sm	0.09	0.03	0.06	0.89	1.07	0.04	0.09	0.00	0.00	0.02
Eu	0.01	0.00	0.00	0.07	0.25	0.01	0.00	0.00	0.00	0.00
Gd	0.04	0.06	0.00	1.39	2.39	0.00	0.00	0.00	0.00	0.00
Tb	0.02	0.00	0.00	0.28	0.55	0.00	0.00	0.00	0.01	0.00
Dy	0.02	0.01	0.05	2.17	4.02	0.01	0.00	0.00	0.02	0.04
Ho	0.00	0.00	0.01	0.50	0.99	0.00	0.00	0.00	0.00	0.00
Er	0.00	0.03	0.02	1.47	2.16	0.03	0.00	0.00	0.00	0.01
Yb	0.02	0.03	0.02	1.64	1.80	0.03	0.02	0.16	0.01	0.09
Lu	0.01	0.01	0.02	0.23	0.28	0.00	0.00	0.09	0.02	0.04

Garnet

Garnet porphyroblasts from the amphibolite sample are rich in almandine (Xalm = 0.50-0.59) and grossular (0.26-0.35), but poor in pyrope (0.08-0.10) and spessartine (0.04-0.08, Table 5). Zoning is concentric, typical of prograde growth in terms of Sps and Grs components decreasing toward the rim (Fig. 11b). However, the zoning is mild suggesting diffusion reequilibration at near peak conditions. In fact, the distribution of Mg# is mostly constant, attesting for an effective diffusion reequilibration in terms of the Fe-Mg exchange couple.

Chlorite

Retrograde chlorite from amphibolite is heterogeneous in composition (Table 6), with Si = 5.48-5.75 apfu, Al = 4.64-5.12 and Mg# = 0.42-0.60. The compositional variability is due to the effect of primary minerals being retrogressed, with chlorite formed after amphibole being richer in Mg and poorer in Fe (Mg = 5.56 and Fe = 3.68) that chlorite formed after garnet (Mg = 3.99 and Fe = 5.48).

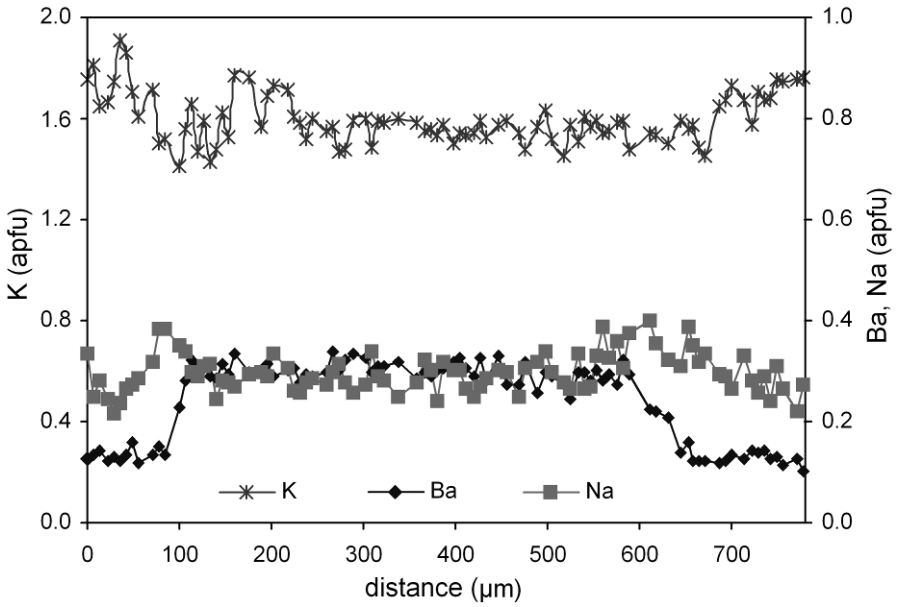

Fig. 9. Profile along phengite of sample LCM-14 (see Fig. 8e for location).

DISCUSSION

Origin of rocks

Fluid-fluxed partial melting of MORB amphibolite in the Sierra del Convento and La Corea mélanges at ca. 1.5 GPa and 700 ºC produced tonalitic-trondhjemitic melts that cooled down in the subduction channel (Garcia-Casco et al. 2008a, Lázaro et al. 2009; Blanco-Quintero et al. 2010a). As indicated by these authors, the implied anomalous high geothermal gradient (>14 ºC/km) in the subducted slab can be explained by onset of subduction combined with subduction of young oceanic lithosphere.

Major and immobile trace elements composition of the amphibolite sample indicate a basaltic MOR affinity (Fig. 12a), even if LILE abundances indicate enrichments relative to N-MORB. These enrichments are interpreted as the consequence of interaction with Ba-rich fluids, probably similar to those represented by the studied Qtz-Ms rocks showing strong enrichment in LREE and LILE (Figs. 5 and 6). Bebout et al. (1999) established that LILE are removed from subducted metasediments by devolatilization, therefore the fluid fluxing of amphibolite probably account for the observed LILE enrichments. This interaction took place in the subduction environment, once the subducting amphibolite attached to the overriding plate and attained peak P-T conditions similar to other amphibolite blocks from both mélanges (i.e., 700-750 ºC, 1.5 GPa; García-Casco et al. 2008a; Lázaro et al, 2009). However, the Ba-poor nature of the retrograde rims of muscovite indicates that Ba-poorer fluids fluxed the rock during retrogression and exhumation in the subduction channel.

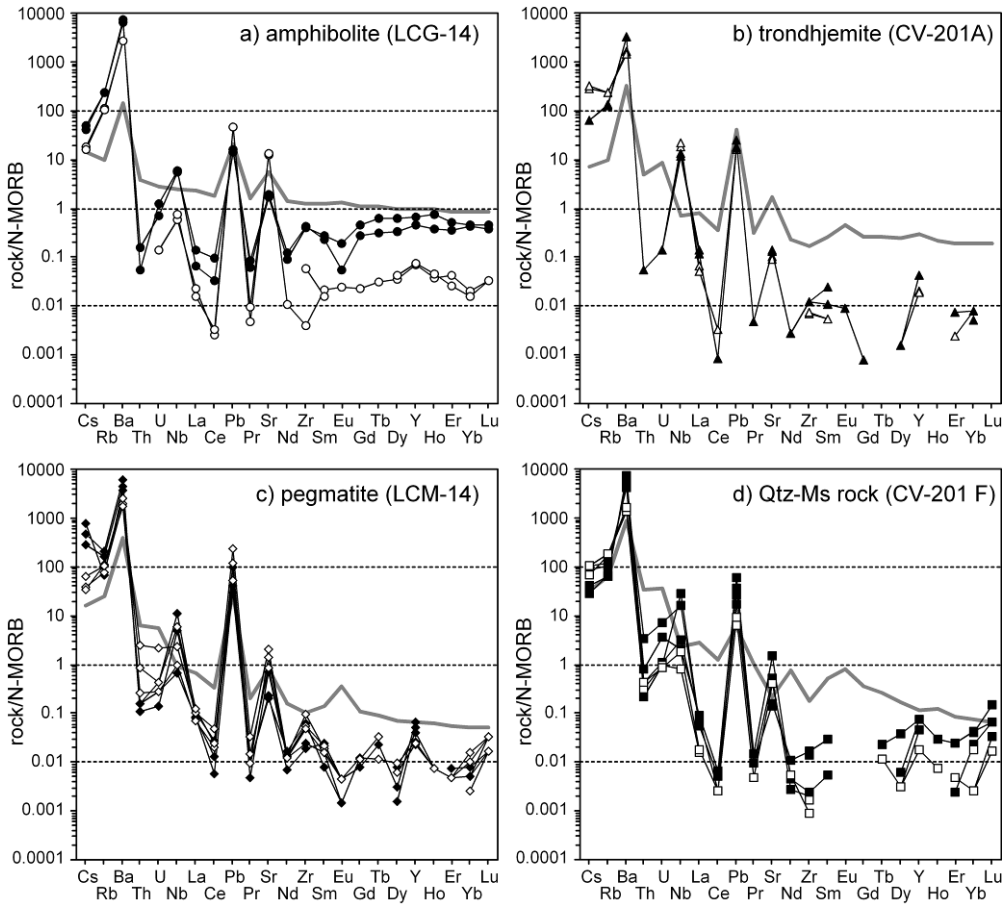

Fig. 10. Spider diagrams normalized to N-MORB (Hofmann, 1988) of phengites from a) amphibolite, b) trondhjemite, c) pegmatite and, d) Qtz-Ms rock. Solid and empty symbols correspond to core and rims, respectively. The compositions of the respective whole rock samples are indicated by thick grey lines.

The trondhjemite sample CV-201A is inferred to have formed after wet partial melting of MORB-derived amphibolite fluxed by K- and LILE-rich fluids derived from subducting sediments. Enrichment in LILE and depletion in Nb and other HFSE (Fig. 12b) strengthen this view. The Ba-rich cores of magmatic muscovite from sample CV-201A indicates a K-, Ba-, and other LILE-rich melt and that enrichment in these elements is certainly not the result of late alteration. Continued crystallization and fractionation of Ba in the cores of muscovite in this sample formed Ba-poorer residual liquids that produced Ba-poor magmatic rims. This indicates a compatible behaviour of Ba in this magmatic system. Local infiltration of fluids during subsolidus conditions allowed the formation of Ba-rich retrograde rims associated with celsian and cymrite, either as a result of Ba remobilisation or the Ba-rich nature of low temperature infiltrating fluid (or both).

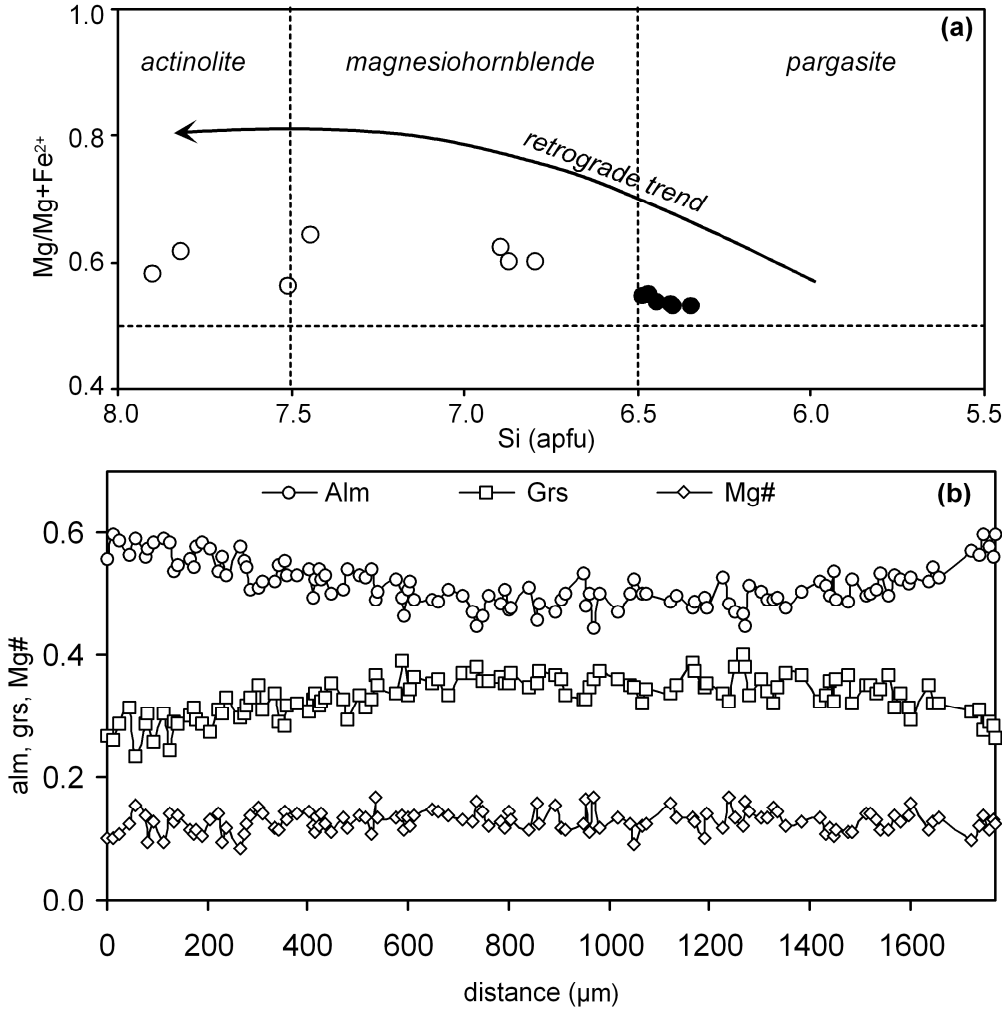

Fig. 11. a) Si versus Mg# composition of calcic amphibole in the classification scheme of Leake et al (1997) with indication of the retrograde trend. The solid symbols correspond to the peak amphibole while the empty symbols correspond to retrograde rims and pockets. b) Profile of garnet from amphibolite (sample LCG-14; see Fig. 3a for location). Note near constant Mg# and inverse relationship between almandine and grossular.

Based on Rb/Sr and Sm/Nd isotopic signature of K- and Ba-poor muscovite-lacking tonalitic-trondhjemitic rocks from the Sierra del Convento mélange, Lázaro and Garcia-Casco (2008) indicated that these rocks formed during partial melting of K-poor amphibolites infiltrated by fluids primarily derived from a depleted source. The most probable source of fluids was subducting serpentinite, and that mild enrichment in LILE resulted from late retrograde alteration during exhumation in the subduction channel. Indeed, the MORB-normalized elemental patterns of trondhjemite CV-201A strongly contrast in terms of Ba (and other LILE and Pb) with the K-poor rocks studied by Lázaro and García-Casco (2008; Figure 12b). Hence, in view of the data presented here, a distinct influence of a sediment-derived fluid component in the fluid that triggered partial melting of amphibolite in the subduction environment must be accepted.

Table.7 Representative LA-ICP-MS analyses (ppm) of rims of phengite of studied rocks.

Sample	LCM-14	LCM-14	LCM-14	LCG-14	LCG-14	CV-201a	CV-201a	CV-201f	CV-201f
Type	Peg	Peg	Peg	Amph	Amph	trond	trond	Qtz-Ms	Qtz-Ms
Rb	97.16	139.53	134.80	136.97	133.20	302.32	293.58	218.36	228.60
Cs	0.54	0.47	0.90	0.25	0.22	3.94	4.57	0.98	1.44
Sr	228.68	156.05	93.90	1453.11	1480.59	11.24	10.29	44.73	46.11
Ba	26763.84	24280.49	34282.62	38319.01	37133.06	22925.54	20240.68	18793.57	22608.26
Sc	5.86	4.59	6.81	11.51	9.86	8.76	8.87	11.88	4.87
Ni	30.73	2.90	3.13	11.19	11.30	0.86	0.56	66.10	92.78
Y	0.95	0.82	0.88	2.47	2.64	0.74	0.66	0.64	0.64
Nb	7.94	3.38	20.23	2.02	2.69	63.90	76.37	2.82	6.30
Zr	9.76	5.75	5.18	0.42	6.17	0.75	0.78	0.17	0.09
Pb	115.53	26.60	59.47	22.06	23.16	7.70	8.79	3.07	4.52
U	0.16	0.02	0.03	0.01	0.00	0.01	0.00	0.07	0.06
Th	0.45	0.05	0.16	0.00	0.00	0.00	0.00	0.06	0.08
La	0.41	0.27	0.47	0.09	0.06	0.25	0.20	0.06	0.07
Ce	0.59	0.24	0.29	0.03	0.04	0.00	0.04	0.00	0.03
Pr	0.07	0.02	0.03	0.02	0.01	0.00	0.00	0.00	0.01
Nd	0.16	0.15	0.14	0.12	0.00	0.00	0.00	0.00	0.06
Sm	0.07	0.08	0.06	0.08	0.06	0.02	0.02	0.00	0.00
Eu	0.01	0.00	0.01	0.03	0.00	0.00	0.00	0.00	0.00
Gd	0.06	0.06	0.00	0.12	0.00	0.00	0.00	0.00	0.00
Tb	0.01	0.03	0.00	0.03	0.00	0.00	0.00	0.00	0.01
Dy	0.06	0.00	0.04	0.22	0.27	0.00	0.01	0.02	0.00
Ho	0.01	0.01	0.01	0.05	0.06	0.00	0.00	0.00	0.01
Er	0.02	0.00	0.02	0.18	0.11	0.00	0.01	0.02	0.00
Yb	0.06	0.01	0.04	0.08	0.06	0.00	0.03	0.01	0.07
Lu	0.02	0.01	0.02	0.02	0.02	0.00	0.00	0.01	0.00

The coarse-grained crystals (>4 mm) of pegmatites indicate crystallization from a H_2O saturated melt. The close spatial relationships between these rocks and K- Ba-rich trondhjemites suggest formation of the former as a result of the magmatic differentiation of the later. Note that Ba in the trondhjemite magma behaves as a compatible element, for it is strongly fractionated in magmatic muscovite, allowing differentiates to be poorer in Ba. This is confirmed by pegmatites, which are poorer in Ba than trondhjemite CV-201A (Fig. 12b). Alternatively, these pegmatitic rocks may represent H_2O-saturated minimum melts formed at the H_2O-saturated solidus of amphibolite fluxed by K- and Ba-rich fluids.

Two possible hypotheses are considered for the origin of Qtz+Ms hydrothermal rocks: 1) they may represent rocks that crystallized from the final hydrothermal fluids which evolved from differentiation of trondhjemitic-pegmatitic melts, or 2) they may constitute the precipitation from primary sediment-derived fluids. Geochemical data cannot discriminate between these hypotheses. However, it should be noted that these rocks are strongly enriched in Ba, as compared to their potential trondhjemitic-pegmatitic sources. The compatible behaviour of Ba in the trondhjemitic-pegmatitic melt system and (apparently) in the hydrothermal system (Ba is similarly concentrated in the cores of hydrothermal muscovite) would argue against the magmatic differentiation hypothesis. Thus, these Ms+Qtz rocks may represent a direct evidence for the circulation of high temperature sediment-derived primary fluids rich in K and Ba in the subduction environment.

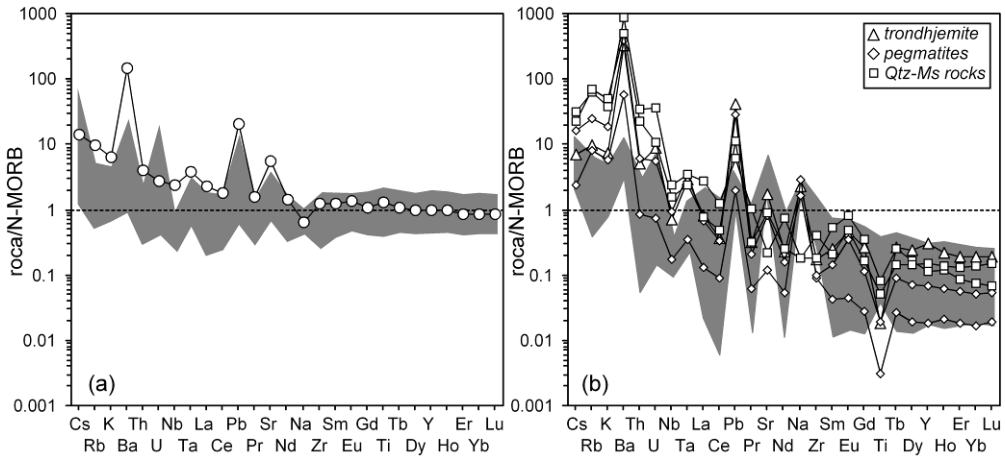

Fig. 12. N-MORB (Hofmman, 1988) normalized spider diagrams of a) amphibolite sample LCG-14, and b) trondhjemite, pegmatites Qtz-Ms rocks. The grey fields represent the composition of a) low-K muscovite-lacking amphibolite rocks and b) low-K muscovite-lacking trondhjemite rocks from Sierra del Convento mélange (data from Lázaro and Garcia-Casco, 2008).

Barium and barium-rich minerals

The presence of Ba in K-minerals is common, for these elements display a similar behaviour in natural systems as a consequence of their similar ionic radii. Because both cations have different charges, however, incorporation of Ba in the structure of K-minerals takes place by means of a coupled cation exchange involving Al and Si, i.e. the celsian coupled substitution $BaAl(SiK)_{-1}$. This exchange vector is inferred from the existence of solid-solution series between the Ba- and K-analogues, intermediate compounds, and Ba end-members with the appropriate stoichiometry, as clearly illustrated by orthoclase and celsian.

Such simple exchange vector scheme is not straight forward in complex mineral solid solutions such as the micas. In these rocks, the chemical changes expected after operation of the celsian exchange are obscured by other substitutions involving octahedral cations (e.g., the celadonite exchange ($(Mg,Fe)Si(Al)_{-2}$) and interlayer cations (e.g, the paragonite exchange NaK_{-1}). In the studied rocks, Ba is enriched in the cores of muscovite crystals having significant Fe+Mg and Na contents, indicating the intervening operation of these exchanges. Because enrichment in Ba implies depletion in Si (and enrichment in Al), and enrichment in Fe+Mg implies enrichment in Si (and depletion in Al), the resulting chemistry of the mica is obscured in terms of tetrahedral cation proportions.

Principal Component Analysis (PCA) was used in an attempt to obtain the relative contribution of the main exchange vectors explaining mica composition in the studied rocks. First, each sample was treated separately. Results indicate similar conclusions. Furthermore, similar conclusions were obtained using the whole data set of analyzed white micas. In all cases the First Principal Component obtained explains more than 90 % of the statistical variance of the data set used. As an example, we give here the results obtained for muscovite from Qtz-Ms rocks. This First Principal Component has the form of the following complex exchange vector:

0.47 Si + 0.35 Mg+Fe + 0.17 K = 0.79 Al + 0.18 Ba + 0.05 Na

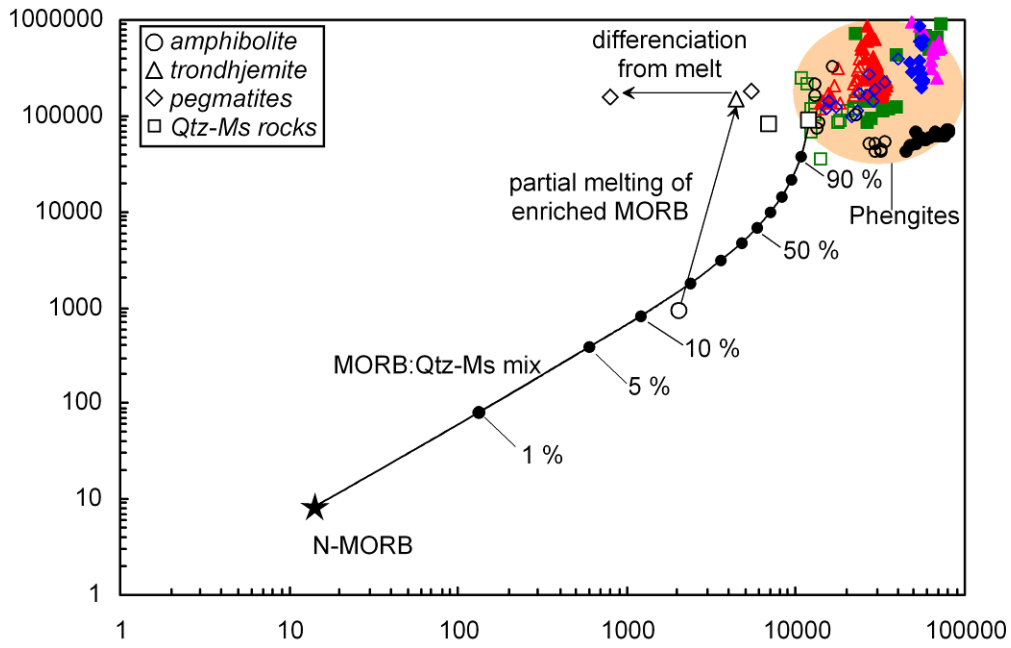

Fig. 13. Ba/TiO2 versus Ba diagram (Sorensen et al. 1997) of studied rocks and phengite showing the mixing curves between N-MORB (Hoffman, 1988) and Qtz-Ms rocks (sample CV-201F), representing a potential sediment-derived slab fluid. Lines representing melting of amphibolite (LCG-14) to form trondhjemite (CV-201A) and differentiation of trondhjemite (CV-201A) to form pegmatite (LC-24) are also showed. Phengite symbols: circles = amphibolite (black), triangles = trondhjemite (red), diamonds = pegmatite (blue), and squares = Qtz-Ms rocks (green), with filled and empty symbols corresponding to the cores and rims of crystals, respectively. Late retrogression of phengite from trondhjemite CV-201A is indicated by purple triangles.

that explains 96.79 % of the chemical variance of muscovite. The mass- (-0.03) and charge-balance (-0.03) of this complex exchange vector are small and can be related to analytical error and/or the lack of consideration of Fe^{3+}, interlayer vacancies, and excess of octahedral occupancy in the calculations. When this vector is decomposed in simple exchange vectors, the results indicate that the celadonite exchange ($(Mg,Fe)Si(^{VI}Al^{VI}Al)_{-1}$) contributes 67.31 % to the total chemical variability of the micas. The celsian exchange $BaAl(SiK)_{-1}$ contributes moderately, 23.07 %, while the paragonite NaK_{-1} exchange contribution is faint (9.62 %). The importance of the celadonite exchange is a relevant conclusion. First, because it allows considering the relatively Si-poor Ba-rich compositions as phengitic, even if the amounts of Si are low, suggesting a relatively high pressure of crystallization at high temperature. Second, because the sluggish kinetics of the celadonitic exchange in the micas did not allow homogenization in crystals formed at high temperature (e.g., Dempster, 1992; García-Casco et al. 1993), explaining the preservation of the strong chemical core-rim zoning that characterize the studied micas.

Celsian and cymrite are common minerals in rocks formed in subduction complexes. Typically, these minerals are related to metasomatic transformations induced by Ba-rich fluids in the subduction channel, including jadeitite deposits (e.g. Harlow 1994; Shi et al., 2010 and references therein). Recently, García-Casco et al. (2009) reported jadeitite deposits in the Sierra del Convento mélange. The presence of

celsian and cymrite-forming fluids in the studied rocks strongly suggest a genetic link between these fluids and jadeitite-forming fluids the studied mélanges

LILE-rich fluids and melts in the slab and implications for mantle wedge processes

According to Lázaro and Garcia-Casco (2008) the tonalitic-trondhjemitic rocks from the Sierra del Convento mélange originated by fluid-induced partial melting of subducted metabasite. These authors stressed that the fluid was evolved from a dehydrating depleted oceanic source. The studied trondhjemitic and pegmatitic rocks have immobile elements (HFSE) contents that are consistent with formation after partial melting of MORB-derived amphibolite, but their substantial enrichment in LILE demonstrates a different nature of the infiltrating fluid. A normal product of subduction of metabasite is the continuous loss of LILE due to dehydration. The higher LILE content of the studied amphibolite sample LCG-14 compared with typical MORB and amphibolite blocks from the Sierra del Convento mélange (Fig. 12a) demonstrates that the former represents subducted MORB that underwent enrichment of LILE from slab fluid components. The presence of white mica in these rocks indicates, on the other hand, that K, Ba and other LILE are fixed during fluid infiltration at high temperature in the subduction channel.

Processes of fluid-amphibolite interaction and melting and differentiation of trondhjemitic rocks explain the chemical variability of studied samples. This is illustrated by means of modelling of mixing between N-MORB and a potential sediment-derived slab fluid using Ba and TiO_2 (Sorensen et al. 1997; Fig.13). The calculations suggest that ca. 15 % of Qtz-Ms fluid component was added to MORB in order to produce their observed Ba enrichment (Fig. 13). The trondhjemite rock, formed by partial melting of MORB-amphibolite, has similar Ba contents but lower TiO_2. These compositions can be explained by the presence of rutile and titanite in residual amphibolite. The process of differentiation of the melts, on the other hand, produced fluid-saturated pegmatites with similar Ba/TiO_2 ratio but lower Ba contents, as a result of the incompatible behaviour of Ba (fractionated in phengite).

Flux of slab-derived fluid and/or melt through the depleted mantle wedge promotes the formation of LILE-rich and HFSE-poor arc magmas (Breeding et al. 2004). The demonstrated circulation of fluids and melts in the Sierra del Convento and La Corea mélanges makes suitable the formation of arc magmas by means of fluid/melt infiltration into the mantle wedge. However, there are no local or regional indications for the transfer of the studied subduction-related fluids and melts to the associated mantle wedge and the volcanic arc. First, the studied rocks do not show geochemical characteristics that can be related to significant interactions with mantle wedge peridotites. In addition, contemporaneous volcanic arc rocks do not show strong enrichment in Ba and Pb and depletion in HREE and other compatible elements. For example, tonalite arc magmas of similar age (110-115 Ma) similar to those from the eastern Cuba mélanges occurring in the volcanic arc Los Ranchos Formation of the Dominican Republic (Escuder-Viruete et al. 2006) show clear differences in terms of trace elements composition (Fig. 14). The magmatic rocks of the eastern Cuba mélanges are poorer in HFSE and enriched in LILE, suggesting contrasted processes of formation. In fact, tonalites from Los Ranchos Fm were formed by melting at the base of thickened early arc crust (Escuder-Viruete et al.

2006), while the eastern Cuba mélange rocks formed almost synchronously by partial melting in the subduction environment.

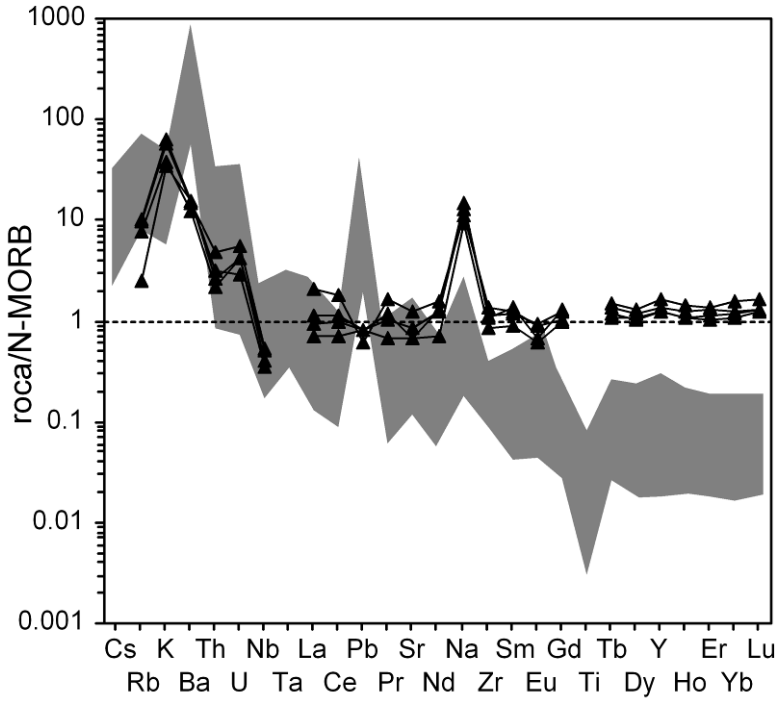

Fig. 14. N-MORB (Hofmman, 1988) normalized diagram comparing the studied leucocratic rocks from eastern Cuba mélanges (grey field; this paper) with volcanic-arc tonalites from Dominican Republic (black triangles; data from Escuder-Viruete et al. 2006).

Phengite is the principal mineral carrying Cs, Rb and Ba in the subduction environment (e.g. Harlow 1995; Sorensen et al. 1997; Zack et al. 2001, Bebout et al. 2007; this paper), and its stability in subducting slabs is a major critical factor in transferring matter to the hanging wall plate (Schmidt 1996; Domanik and Holloway 1996; Hermann 2002). The fact that phengite crystallized at depth in the subduction environment of the Sierra del Convento and La Corea mélanges (ca. 50 km; García-Casco et al. 2008a) implies that LILE were trapped in phengite and were not transported to the mantle wedge. Thus, the fluids/melts of the Sierra del Convento and La Corea mélanges acted as sinks rather than sources for LILE elements, preventing their transfer to the volcanic arc. Colder geothermal gradients prevents partial melting at shallow depths, however, allowing decomposition of phengite at sub-arc depths (100-150 km) and the transfer of LILE to the sub-arc mantle and the volcanic arc. This may explain Ba enrichments in contemporaneous (120-110 Ma) volcanic arc basaltic formations of Hispaniola (e.g. Escuder-Viruete et al. 2010, and references therein). These inferences strengthen the importance of the thermal state of subducting slabs and, hence, the of phengite stability for the transfer of matter from the slab to the hanging wall plate and for the geochemistry of arc magmas.

CONCLUSIONS

Major and trace element composition of phengite-bearing Ba-rich amphibolite, trondhjemite, pegmatite and Qtz+Ms rocks from La Corea and Sierra del Convento mélanges (eastern Cuba) demonstrate the circulation of Ba-rich fluids and melts in the subduction environment. The amphibolite represents subducted MORB material affected by fluid infiltration at high temperature. The trondhjemite was formed by fluid-fluxed melting of amphibolite and represents pristine slab melts that did not react with the upper plate mantle. Crystallization of magmatic phengite rendered Ba a compatible behaviour during crystallization of melt. The pegmatites are interpreted as magmatic products after differentiation of trondhjemitic melts, while Qtz-Ms rocks probably represent material crystallized from a primary sediment-derived fluid. Principal Component Analysis (PCA) indicates that phengite chemistry is primarily governed by the celadonite (tschermak) exchange vector ($(Mg,Fe)Si-(Al)_{-2}$) combined with the celsian ($BaAl-KSi_{-1}$) and paragonite (NaK_{-1}) exchange vectors. The contrasted chemistry of Ba-rich cores and Ba-poor rims of phengite indicates a complex evolution of fluids/melts towards Ba-poor composition, which is explained by the compatible behaviour of Ba in the studied systems. Crystallization of the studied magmatic rocks in the subduction environment made phengite to act as a sink, rather than a source, for Ba (and other LILE, Pb, Sr), preventing the transfer of these elements to the mantle wedge. This strengthens the importance of phengite stability in the subduction environment for control of the flux of material from the slab to the volcanic arc environment.

ACKNOWLEDGMENTS

We appreciate financial support from Spanish MICINN projects CGL2006-08527/BTE and CGL2009-12446. This is a contribution to IGCP-546 “Subduction zones of the Caribbean”. Blanco-Quintero is supported by grant AP2005-5258 from the ‘‘Programa de Formación del Profesorado Universitario’’ of the Spanish Ministry of Education.

REFERENCES

Adamovich A, Chejovich V (1964) Principales características de la geología y de los minerales útiles de la región nordeste de la Provincia de Oriente. Revista Tecnológica 2:14-20

Bea F (1996) Residence of REE, Y, Th and U in granites and crustal protoliths: implications for the chemistry of crustal melts. J Petrol 37:521–552

Bea F, Fershtater GB, Montero P, Smirnov VN, Molina JF (2005) Deformation-driven differentiation of granitic magma: the Stepninsk pluton of the Uralides, Russia. Lithos 81:209–233

Bebout GE, Barton MD (1989) Fluid flow and metasomatism in a subduction zone hydrothermal system: Catalina Schist Terrane, California. Geology 17:976–980

Bebout GE, Ryan JG, Leeman WP, Bebout AE (1999) Fractionation of trace elements during subduction-zone metamorphism: impact of convergent margin thermal evolution. Earth Planet Sci Lett 171:63–81

Bebout GE, Bebout AE, Graham CM (2007) Cycling of B, Li, and LILE (K, Cs, Rb, Ba, Sr) into subduction zones: SIMS evidence from micas in high-P/T metasedimentary rocks. Chem Geol 239:284–304

Bence AE, Albee AL (1968) Empirical correction factors for the electron microanalysis of silicate and oxides. J Geol 76:382–403

Blanco-Quintero IF, García-Casco A, Rojas Agramonte Y, Rodríguez Vega A, Lázaro C, Iturralde-Vinent MA (2010a) Metamorphic evolution of subducted hot oceanic crust, La Corea mélange, Cuba. Am J Sci (in press)

Blanco-Quintero IF, Proenza JA, García-Casco A, Tauler E, Galí S (2010b) Serpentinites and serpentinites within a fossil subdution channel: La Corea melange, eastern Cuba. Geol Acta (in press).

Boiteau A, Michard A, Saliot P (1972). Métamporphisme de haute pression dans le complexe ophiolitique du Purial (Oriente, Cuba). Comptes Rendus de l'Académie des Sciences, Série D 274:2137–2140

Breeding CM, Ague JJ, Bröcker M (2004) Fluid–metasedimentary rock interactions and the chemical composition of arc magmas. Geology 32:1041-1044

Cárdenas-Párraga J, García-Casco A, Núñez-Cambra K, Rodrígez-Vega A, Blanco-Quintero IF, Harlow GE, Lázaro C (2010) Jadeitite jade occurrence from the Sierra del Convento mélange (eastern Cuba). Bol Soc Geol Mex, 62:199-205

Cobiella J, Campos M, Boiteau A, Quintas F (1977) Geología del flanco sur de la Sierra del Purial. Revista La Minería de Cuba 3:54-62

Dempster TJ (1992) Zoning and recrystallization of phengitic micas: implications for metamorphic equilibration. Contrib Mineral Petrol 109:526–537

Domanik KJ, Holloway JR (1996) The stability and composition of phengitic muscovite and associated phases from 5.5 to 11 GPa: Implications for deeply subducted sediments: Geochim Cosmochim Acta 60:4133-4150

Dymond J, Suess E, Lyle M (1992) Barium in deep-sea sediment: a geochemical proxy for paleoproductivity. Paleoceanography 7:163–181

Escuder-Viruete J, Díaz de Neira A, Hernáiz Huerta PP, Monthel J, García Senz J, Joubert M, Lopera E, Ullrich T, Friedman R, Mortensen J, Pérez-Estaún A (2006) Magmatic relationships and ages of Caribbean island-arc tholeiites, boninites and related felsic rocks, Dominican Republic. Lithos 90:161–186

Escuder-Viruete J, Pérez-Estaún A, Weis D, Friedman R (2010) Geochemical characteristics of the Río Verde Complex, Central Hispaniola: Implications for the paleotectonic reconstruction of the Lower Cretaceous Caribbean island-arc. Lithos, 114:168-185

García-Casco A (2007) Magmatic paragonite in trondhjemites from the Sierra del Convento mélange, Cuba. Am Mineral 92:1232–1237

García-Casco A, Sanchez-Navas A, Torres-Roldan RL (1993) Disequilibrium decomposition and breakdown of muscovite in high P-T gneisses, Betic Alpine Belt (Southern Spain). Am Mineral 78:158-177

García-Casco A, Torres-Roldán RL, Iturralde-Vinent MA, Millán G, Núñez Cambra K, Lázaro C, Rodríguez Vega A (2006) High pressure metamorphism of ophiolites in Cuba. Geol Acta 4:63–88

García-Casco A, Lázaro C, Torres-Roldán RL, Núñez Cambra K, Rojas Agramonte Y, Kröner A, Neubauer F, Millán G, Blanco-Quintero I (2008a) Partial melting and counterclockwise P-T path of subducted oceanic crust (Sierra del Convento mélange, Cuba). J Petrol 49:129-161

García-Casco A, Iturralde-Vinent MA, Pindell J (2008b) Latest Cretaceous collision/accretion between the Caribbean Plate and Caribeana: Origin of metamorphic terranes in the Greater Antilles. Int Geol Rev 50:781-809

García-Casco A, Rodríguez Vega A, Cárdenas Párraga J, Iturralde-Vinent MA, Lázaro C, Blanco Quintero I, Rojas-Agramonte Y, Kröner A, Núñez Cambra K, Millán G, Torres-

Roldán RL, Carrasquilla S (2009) A new jadeitite jade locality (Sierra del Convento, Cuba): First report and some petrological and archaeological implications. Contrib Mineral Petrol 158:1-26

Gill J (1981) Orogenic andesite and plate tectonics. Springer, Berlin

Goldschmidt VM (1954). Geochemistry. Oxford University Press

Harlow GE (1994) Jadeitites, albitites and related rocks from the Motagua Fault Zone, Guatemala. J Metamorph Geol 12:49-68

Harlow GE (1995) Crystal chemistry of barian enrichment in micas from metasomatized inclusions in serpentinite, Motagua Fault Zone, Guatemala. Euro J Mineral 7:775–789

Hermann J (2002) Experimental constraints on phase relations in subducted continental crust. Contrib Mineral Petrol 143:219–235

Hofmann AW (1988) Chemical Differentiation of the Earth - the Relationship between Mantle, Continental-Crust, and Oceanic-Crust. Earth Planet Sci Lett 90:297-314

Iturralde-Vinent MA (1998) Sinopsis de la Constitución Geológica de Cuba. Acta Geol Hispanica 33:9-56

Iturralde-Vinent MA, Díaz Otero C, Rodríguez Vega A, Díaz Martínez R (2006) Tectonic implications of paleontologic dating of Cretaceous–Danian sections of Eastern Cuba. Geol Acta 4:89–102

Iturralde-Vinent MA, Díaz Otero C, García-Casco A, Van Hinsbergen DJJ (2008) Paleogene Foredeep Basin Deposits of North-Central Cuba: A Record of Arc-Continent Collision between the Caribbean and North American Plates. Int Geol Rev 50:863–884

Kato T (2005) New accurate Bence-Albee a-factors for oxides and silicates calculated from the PAP correction procedure. Geostandards Geoanalytical Res 29:83–94

Kretz R (1983) Symbols for rock-forming minerals. Am Mineral 68:277–279

Kushiro I (1990) Partial Melting of Mantle Wedge and Evolution of Island-Arc Crust. J Geophys Res 95:15929-15939

Lázaro C, García-Casco A (2008) Geochemical and Sr-Nd isotope signatures of pristine slab melts and their residues (Sierra del Convento mélange, eastern Cuba). Chem Geol 255:120-133

Lázaro C, García-Casco A, Neubauer F, Rojas-Agramonte Y, Kröner A, Iturralde-Vinent MA (2009) Fifty-five-million-year history of oceanic subduction and exhumation at the northern edge of the Caribbean plate (Sierra del Convento mélange, Cuba). J Metamorph Geol 27:19-40.

Le Maitre RW, Bateman P, Dudek A, Keller J, Lameyre Le Bas MJ, Sabine PA, Schmid R, Sorensen H, Streckeisen A, Woolley AR, Zanettin B (1989) A classification of igneous rocks and glossary of terms. Blackwell, Oxford

Leake BE, Woolley AR, Arps CES, Birch WD, Gilbert MC, Grice JD, Hawthorne FC, Kato A, Kisch HJ, Krivovichev VG, Linthout K, Laird J, Mandarino JA, Maresch WV, Nickel EH, Rock NMS, Schumacher JC, Smith DC, Stephenson NCN, Ungaretti L, Whittaker EJW, Touzhi G (1997) Nomenclature of amphiboles: Report of the Subcommittee on Amphiboles of the International Mineralogical Association, Commission on New Minerals and Mineral Names. Am Mineral 82:1019-1037

Leyva RC (1996) Características geológicas, regularidades de distribución y perspectivas de utilización del cuarzo filoniano de la región oriental de Cuba. Unpublished report of the Instituto Superior Minero-Metalúrgico de Moa (Cuba).

Marchesi C, Garrido CJ, Godard M, Proenza JA, Gervilla F, Blanco-Moreno J (2006) Petrogenesis of highly depleted peridotites and gabbroic rocks from the Mayarí-Baracoa Ophiolitic Belt (eastern Cuba). Contrib Mineral Petrol 151:717-736

Marchesi C, Garrido CJ, Bosch D, Proenza JA, Gervilla F, Monié P, Rodríguez-Vega A (2007) Geochemistry of Cretaceous magmatism in eastern Cuba: recycling of North American continental sediments and implications for subduction polarity in the Greater Antilles Paleo-arc. J Petrol 48:1813–1840

McDonough WF, Sun SS (1995) The composition of the Earth. Chemical Geology 120:223-253

Millán G (1996) Metamorfitas de la asociación ofiolítica de Cuba. In: Iturralde-Vinent MA (ed) Ofiolitas y Arcos Volcánicos de Cuba. IGCP Project 364 Special Contribution 1:131–146

Millán G, Somin ML, Díaz C (1985) Nuevos datos sobre la geología del macizo montañoso de la Sierra del Purial, Cuba Oriental. Unpublished report of the Instituto de Geología y Paleontología 2:52–74

Peccerillo A, Taylor SR (1976) Geochemistry of Eocene calc-alkaline volcanic-rocks from Kastamonu Area, Northern Turkey. Contrib Mineral Petrol 58(1):63–81

Plank T, Langmuir CH (1993) Tracing trace elements from sediment input to volcanic output at subduction zones. Nature 362:739-743

Plank T, Langmuir CH (1998) The chemical composition of subducting sediment and its consequences for the crust and mantle. Chem Geol 145(3-4):325-394

Proenza J, Gervilla F, Melgarejo JC, Bodinier JL (1999) Al- and Cr rich chromitites from the Mayarí-Baracoa Ophiolitic Belt (eastern Cuba): consequence of interaction between volatile-rich melts and peridotite in suprasubduction mantle. Econ Geol 94:547–566

Proenza J, Alfonso J, Melgarejo JC, Gervilla F, Tritlla J, Fallick AE (2003) D, O and C isotopes in podiform chromitites as fluid tracers for hydrothermal alteration processes of the Mayarí-Baracoa Ophiolitic Belt, eastern Cuba. J Geochem Explor 78–79:117–122

Proenza JA, Díaz-Martínez R, Iriondo A, Marchesi C, Melgarejo JC, Gervilla F, Garrido CJ, Rodríguez-Vega A, Lozano-Santacruz R, Blanco-Moreno JA (2006) Primitive Cretaceous island-arc volcanic rocks in eastern Cuba: the Téneme Formation. Geol Acta 4:103–121

Schmidt MW (1996) Experimental constraints on recycling of potassium from subducted oceanic crust. Science 272:1927–1930

Shi G, Jiang N, Wang Y, Zhao X, Wang X, Li G, Ng E, Cui W (2010) Ba minerals in clinopyroxene rocks from the Myanmar jadeitite area: implications for Ba recycling in subduction zones. Euro J Mineral 22:199-214

Somin ML, Millán G (1981) Geology of the Metamorphic Complexes of Cuba. Nauka: Moscow, 219 pp. (in Russian)

Sorensen SS, Grossman JN, Perfit MR (1997) Phengite hosted LILE enrichment in eclogite and related rocks: implications for fluid-mediated mass transfer in subduction zones and arc magma genesis. J Petrol 38:3–34

Statacorp. (2005) Stata Statistical Software, Release 9. College Station, TX, StataCorp LP

Tatsumi Y, Kogiso T (1997) Trace element transport during dehydration processes in the subducted oceanic crust .2. Origin of chemical and physical characteristics in arc magmatism. Earth Planet Sci Lett 148(1-2):207-221

Zack T, Rivers T, Foley SF (2001) Cs–Rb–Ba systematics in phengite and amphibole: an assessment of fluid mobility at 2.0 GPa in eclogites from Trescolmen, Central Alps. Contrib Mineral Petrol 140:651–669

6- SERPENTINITES AND SERPENTINITES WITHIN A FOSSIL SUBDUCTION CHANNEL: LA COREA MÉLANGE, EASTERN CUBA.

I.F. Blanco-Quintero[(1)], J.A. Proenza[(2)], A. García-Casco[(1,3)], E. Tauler[(2)], S. Galí[(2)].

(1) Departamento de Mineralogía y Petrología, Universidad de Granada, Fuentenueva s/n, 18002-Granada, Spain Blanco-Quintero Email: blanco@ugr.es

(2) Departament de Cristal.lografia, Mineralogia i Dipòsits Minerals, Facultat de Geologia, Universitat de Barcelona, Martí i Franquès s/n, 08028-Barcelona, Spain

(3) Instituto Andaluz de Ciencias de la Tierra (CSIC-UGR), Fuentenueva s/n, 18002-Granada, Spain

ABSTRACT

A variety of metaultramafic (serpentinite) rocks in La Corea mélange, Sierra de Cristal, Eastern Cuba, show differences in chemical, textural and mineralogical characteristics demonstrating a variety of protoliths. The mélange originated during the Cretaceous as part of the subduction channel associated with the Caribbean island arc. This mélange contains high pressure blocks in a serpentinite matrix and occurs at the base of the large tabular Mayarí-Cristal ophiolite. Two principal groups of serpentinites have been identified in the mélange; a) antigorite serpentinite, mainly composed of antigorite and b) antigorite-lizardite serpentinite, composed of mixtures of antigorite and lizardite and bearing distinctive porphyroblasts of diopsidic clinopyroxene. Antigorite serpentinites are closely related to tectonic blocks of amphibolite (representing subducted MORB) and constitute deep fragments of the serpentinitic subduction channel formed during hydration of the mantle wedge. The composition of the antigorite-lizardite serpentinites and the presence of clinopyroxene porphyroblasts in this type of rock suggest that abyssal lherzolite protoliths transformed into serpentinite before and during incorporation (as tectonic blocks) in the shallow part of the subduction channel. Although the studied rocks have different origins, mineralogical compositions and textures, they display similar PGE compositions, suggesting that these elements experienced no significant redistribution during the metamorphism. Both types of serpentinites were exposed together in the La Corea mélange during the late Cretaceous, during obduction of the overriding Mayarí-Baracoa ophiolitic belt that led to exhumation of the subduction channel (mélange).

Keywords: Serpentinite, Subduction channel, La Corea Mélange, Cuba, Caribbean.

INTRODUCTION

Ophiolite-related ultramafic rocks, commonly strongly serpentinized, appear along the margins of Caribbean Plate, being most abundant in the northern edge, principally on Cuba (Lewis et al., 2006a and references therein). These ultramafic rocks represent fragments of oceanic and sub-arc lithospheric mantle that were altered, completely or partly, to serpentinites by fluids during their evolution and accretion to the Caribbean orogenic belt. In Cuba, these ophiolitic bodies are related to serpentinite-matrix mélanges containing high-pressure (HP) blocks of different origin and composition (e.g., García-Casco et al., 2006, and references therein). These mélanges can be interpreted as the exhumed subduction channel of the Caribbean subduction zone (e.g. Gerya et al., 2002).

Two serpentinite-matrix mélanges have been documented in eastern Cuba, 100 km apart: La Corea and Sierra del Convento mélanges (Fig. 1; Somin and Millán, 1981; García-Casco et al., 2006). The origin and evolution of the HP (garnet-epidote amphibolite and blueschists) blocks from both mélanges has been studied by Garcia-Casco et al. (2006, 2008a), Lazaro and Garcia-Casco (2008), Lazaro et al. (2009) and Blanco-Quintero et al. (in press). However, no detailed petrological and geochemical studies have been performed to characterize mélange serpentinites.

The serpentinitic rocks present in La Corea mélange have mineralogical and geochemical characteristics that indicate varied P-T conditions of formation and variable protoliths. The mélange formed during Cretaceous times in response to SW-dipping subduction beneath the northern Caribbean plate. In this paper we provide new petrological and geochemical data of representative serpentinite samples from the La Corea mélange in order to evaluate its nature, the environments of formation of serpentinites, and the implications for tectonic interactions between the Caribbean and North American plates.

GEOLOGICAL SETTING

The Cuban fold and thrust belt formed during Mesozoic to middle Eocene times in the active Caribbean-North American plate margin. It is now accreted to the southern margin of the North American plate (Fig. 1a). The Cuban orogenic belt includes several imbricated geologic complexes, including fragments of the Caribeana terrane (Cangre, Pinos, Escambray and Asunción metamorphic complexes), the Bahamas platform (Cayo Coco, Remedios, Camajuaní belts), the margin of the Maya block (the Guaniguanico terrane), two different volcanic arc complexes of Cretaceous and Paleogene ages respectively, ophiolite bodies forming the northern and eastern ophiolite belts, and syn- and post-orogenic sedimentary basins (Iturralde-Vinent, 1998; Iturralde-Vinent et al., 2006, 2008; García-Casco et al., 2008b).

The most important tectonic units in northeastern Cuba are the ophiolites and the Cretaceous volcanic arc (Fig. 1b). Systematically the Cretaceous volcanic arc appears tectonically below the ophiolites. The Cretaceous volcanic arc units contain a number of basic to acid volcanic units having distinct island arc tholeiitic, boninitic and calc-alckaline signatures (Iturralde-Vinent et al., 2006; Proenza et al., 2006; Marchesi et al., 2007). The age of these formations has been paleontologically estimated to range from early Cretaceous (Aptian-Albian) to late Cretaceous

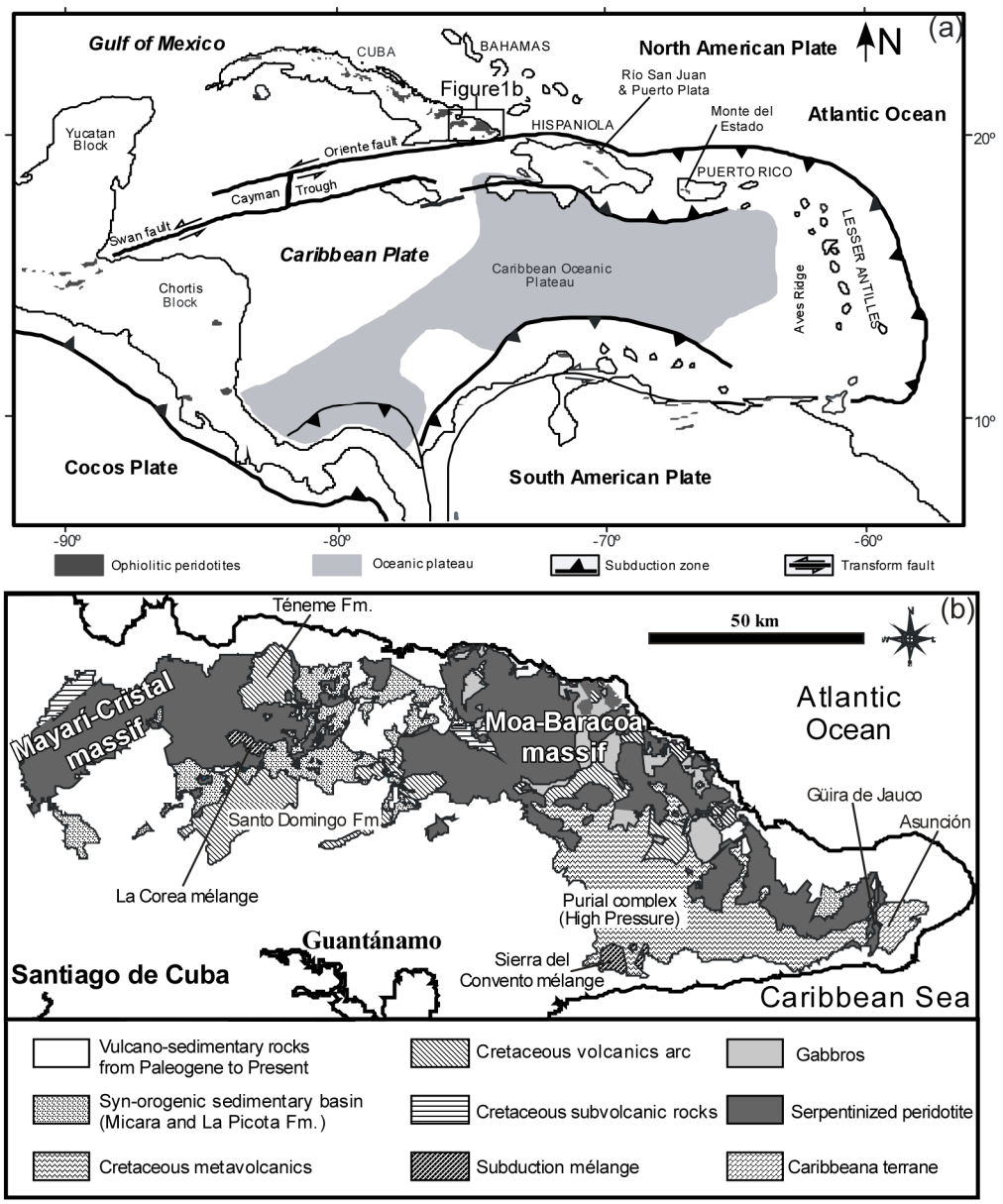

Fig.1 a) Plate tectonic configuration of the Caribbean region, including ophiolitic bodies. b) General geologic map of eastern Cuba showing the main geological units.

(Campanian) times (Iturralde-Vinent, et al., 2006). The Purial volcanic complex, located in the southern part of the region, is metamorphosed to the greenschist and blueschist facies (Boiteau et al., 1972; Cobiella et al., 1977; Somin and Millán, 1981; Millán et al., 1985).

The ophiolite complex is represented by the Mayarí-Baracoa Ophiolitic Belt (MBOB). The MBOB constitutes strongly deformed and faulted mafic-ultramafic thrust sheets overriding the Cretaceous volcanic arc and Maastrichtian-Danian olistostromic formations related to obduction (Iturralde-Vinent et al., 2006). The direction of tectonic transport is NNE (Nuñez-Cambra et al., 2004), as expected for

a SW-dipping subduction zone. The MBOB shows supra-subduction geochemical signatures (Proenza et al., 1999, 2006; Gervilla et al., 2005; Marchesi et al., 2006, 2007), and include the Mayarí-Cristal massif to the west and the Moa-Baracoa massif to the east (Fig. 1b). According to Marchesi et al. (2006) MBOB is composed of highly depleted peridotites and cumulate gabbroic rocks. MBOB peridotites are highly altered (serpentinized) by seawater during the oceanic stage (Proenza et al. 2003). The Moa-Baracoa massif represents MORB-like back-arc lithosphere while Mayarí-Cristal is transitional (MORB to IAT) mantle located closer to the paleo-volcanic arc (Marchesi et al., 2006).

The Mayarí-Cristal massif is > 5 km thick and is made up of harzburgite tectonite hosting minor subconcordant dunite layers and subordinate discordant microgabbro-diabase dykes. Some authors have described a sheeted-dyke complex in the northwestern part of the massif (e.g., Fonseca et al., 1985), but Marchesi et al. (2006) argues that this is a subvolcanic complex made up of massive microgabbros in tectonic contact with harzburgite tectonites. The Mayarí-Cristal harzburgites display porphyroclastic texture. They are Cpx-poor and generally have higher Opx/Ol ratios than the Moa-Baracoa harzburgites (Marchesi et al., 2006). The harzburgite tectonites show a NE–SW oriented foliation dipping NW (Marchesi et al., 2006), and the contact with the dunites is sharp.

The La Corea mélange, containing high pressure exotic blocks, is located in tectonic contact with ultramafic rocks of the Mayarí-Cristal massif (Fig. 1b). The tectonic position of La Corea mélange suggests that this metamorphic complex is overridden by the ophiolites, and that both override the Cretaceous volcanic arc units and the Maastrichtian-Danian olistostromic synorogenic rocks of Micara and La Picota formations. The mélange is made up of exotic blocks of diverse origin and composition (garnet-amphibolite, blueschist and greenschist are dominant) within a serpentinite matrix. Metamorphism of the amphibolites evolved under high- to medium-pressure (ca. 700 ºC, 15 kbar) related to a hot subduction environment from high- to low-temperature following counterclockwise P-T paths related to exhumation in the subduction channel (Blanco-Quintero et al., in press).

The most abundant rock type is a MORB-derived epidote±garnet amphibolite that contains a peak metamorphic assemblage made of pargasite, epidote, titanite, rutile ± quartz ± garnet ± phengite ± plagioclase and accessory apatite (Blanco-Quintero et al., in press). The amphibolite blocks are massive to banded and of m-size. Metaleucocratic rocks (tonalites-trondhjemites) occur as veins and blocks intimately associated with the amphibolites. The tonalites-trondhjemites are medium- to coarse-grained, including pegmatitic varieties, and are composed of quartz, albite-oligoclase, epidote, ± calcic amphibole (pargasite-actinolite) ± muscovite-phengite. These rocks formed after partial melting of subducted MORB amphibolites at 700 ºC, 15 kbar (Blanco-Quintero et al., in press). Other tectonic blocks within the mélange include schists of variable composition and origin. Ultramafic rocks are mainly massive to foliated antigoritite forming the mélange matrix. Occasionally massive antigoritite blocks are included as boudins in strongly foliated antigorite rocks. In addition, blocks of serpentinite with bastite crystals are surrounded by foliated antigoritite. Masses of tremolite-actinolite rocks (composed of > 95 % radial and tabular amphibole) and other metasomatic products of mafic and ultramafic composition are present.

Available isotopic data (Adamovich and Chejovich, 1964; Somin and Millán, 1981) indicates that the subduction channel mélange began to form ca. 110 Ma. Final exhumation of the mélange occurred during the initial thrusting of the ophiolitic and volcanic arc units in the Late Campanian-Maastrichtian (Iturralde-Vinent et al., 2006; Lázaro et al., 2009).

In this study we characterize serpentinite rocks from the La Corea mélange, including antigorite serpentinites (5 samples: LC-G-4, LC-M-17, LC-55, LC-56 and LC-58) and antigorite-lizardite serpentinites (3 samples: LC-66, LC-88 and LC-97).

ANALYTICAL TECNIQUES

Major element compositions were determined on glass beads, made of 0.6 g of powered sample diluted in 6 g of $Li_2B_4O_7$, by a PHILIPS Magix Pro (PW-2440) X-ray fluorescence (XRF) equipment (University of Granada, Centro de Instrumentación Científica, CIC). Precision was better than ±1.5% for a concentration of ≥10 wt% and ±2% for a concentration <10 wt%. The data are listed in Table 7. Platinum-group element concentrations were determined by isotopic dilution using ICP-MS after nickel sulfide fire assay, in the Genalysis Laboratory Services Pty. Ltd. at Maddington (Western Australia) following the method described by Chan and Finch (2001). The detection limits were 1 ppb for Rh, and 2 ppb for Os, Ir, Ru, Pt, Pd. The results are presented in Table 8.

Powder XRD data were collected with a Panalytical X'Pert PRO MPD X-ray diffractometer with monochromatized incident Cu Kα1 radiation at 45 keV and 40 mA, and equipped with a x'Celerator detector of active length of 2.112º at the Serveis Cientificotècnics of the Universitat de Barcelona (Spain). The patterns were obtained by scanning powders from 4°-80° 2θ on samples crushed in an agate mortar to a particle size < 20 mμ. Quantitative mineral phase analyses of samples were obtained by full profile Rietveld refinement using powder diffraction data. The mineral identification software used was TOPAS V3.0.

Mineral compositions were obtained by electron microprobe using a WDS-CAMECA SX 50 at the Serveis Cientificotècnics of the Universitat de Barcelona (Spain). Excitation voltage was 20 kV and beam current 15 nA. Most elements were measured with a counting time of 10 s, except for Ni (30 s). The chemical data for serpentine, clinopyroxene, talc and chlorite compositions were normalized to 14, 6, 22 and 28 oxygens respectively, and $Fe_{total} = Fe^{2+}$. Garnet composition was normalized to 8 cations and 12 oxygens, and Fe^{3+} was estimated by stoichiometry. The atomic concentration of elements per formula units is abbreviated apfu. The Mg number of minerals ($Mg/(Mg+Fe^{2+})$ is expressed as Mg#. Mineral abbreviations are after Kretz (1983).

PETROGRAPHY AND SERPENTINE MINERALS

On the basis of mineral assemblages and textures of metaultramafic rocks, two principal groups of serpentinite have been identified (Figs. 2 and 3): (i) antigorite serpentinite and (ii) antigorite-lizardite serpentinite.

Antigorite serpentinites (group I) consist mainly of antigorite (up to 94 %), with minor talc-magnesite-dolomite (Fig. 2a-d, Fig. 3a). However, some samples (e.g. LC-55) contain abundant talc (Fig. 2c). Kinking of talc crystals, typical of plastic deformation (Escartín et al., 2008), is common. Antigorite grains are partially

replaced by magnesite and minor dolomite (Fig. 2d). Systematically, the relicts of Cr-spinel grains are altered to ferrian chromite and magnetite, and chlorite appears forming rims around altered spinel.

Serpentinites of group I are characterized by non-pseudomorphic textures, typically showing the characteristic interpenetrating needles of antigorite (Fig. 2a, b, d; O'Hanley, 1996).

The antigorite-lizardite serpentinites (group II) contain the mineral assemblage antigorite-lizardite-diopsidic clinopyroxene-chlorite-magnetite-ferrian chromite±brucite. They are characterized by porphyroblastic texture, showing relicts of bastitized clinopyroxene porphyroblasts up to 8 mm in size (Fig. 2e). The dominant serpentine mineral is antigorite (Fig. 2f), but lizardite has been indentified in thin section and by XRD (Figs 2g, 3b). Clinopyroxene porphyroblasts are partly overgrown/replaced by fine-grained clinopyroxene, antigorite, chlorite and magnetite (Fig. 2h). The hedenbergite component of clinopyroxene was oxidized to magnetite, which is mainly associated with serpentine along exfoliation planes and the rims of the grains of clinopyroxene. Primary Cr-spinels were not found; only their alteration products, ferrian chromite and newly formed magnetite, are present. In addition, chlorite forms rims around altered spinel. Andradite garnet is present in veins crosscutting the serpentine matrix. It is colourless and forms granular aggregates.

In general, antigorite-lizardite serpentinites preserve pseudomorphic textures (Wicks and Whittaker, 1977; O'Hanley, 1996): (i) bastites after clinopyroxene and (ii) hourglass textures (Figure 2g). Theses textures can be interpreted as the result of low grade metamorphism (i.e. ocean floor metamorphism).

Serpentine minerals

In order to identify and quantify the amount of serpentine minerals (chrysotile, lizardite and antigorite) and the lattice parameters of these structures, the observed random X-ray powder diffraction profile was simulated using several structural models of antigorite polymorphs (Rietveld method). Commonly, antigorite in serpentinites forms a polysomatic series of sheet silicates of variable structure and composition (e.g. Mellini et al., 1987). The variation of *a* parameter is expressed in terms of *m*, which is the number of SiO_4 tetrahedra seen in a projection along [010] within a full wavelength of the modulated structure.

The calculated XRD profile of group I serpentinite (sample LC-58) agrees well with two serpentine polymorphs (Fig. 3a), one with antigorite polysome m=16 with 16 tetrahedra spanning a wavelength along the *a* axis as proposed by Capitani and Mellini (2006) and the other with antigorite polysome m=17 (Capitani and Mellini, 2004). The structure with m=16 resembles that of the m=17 polysome. In both, a continuous wavy tetrahedra sheet layer (linked to brucite-like layer) reverses polarity through sixfold and eightfold tetrahedra rings. The even number of tetrahedra in m=16, leads to symmetric half-waves, a periodic *b/2* shift involving the eightfold rings, and the doubling of a parameter. The result is a C monoclinic cell.

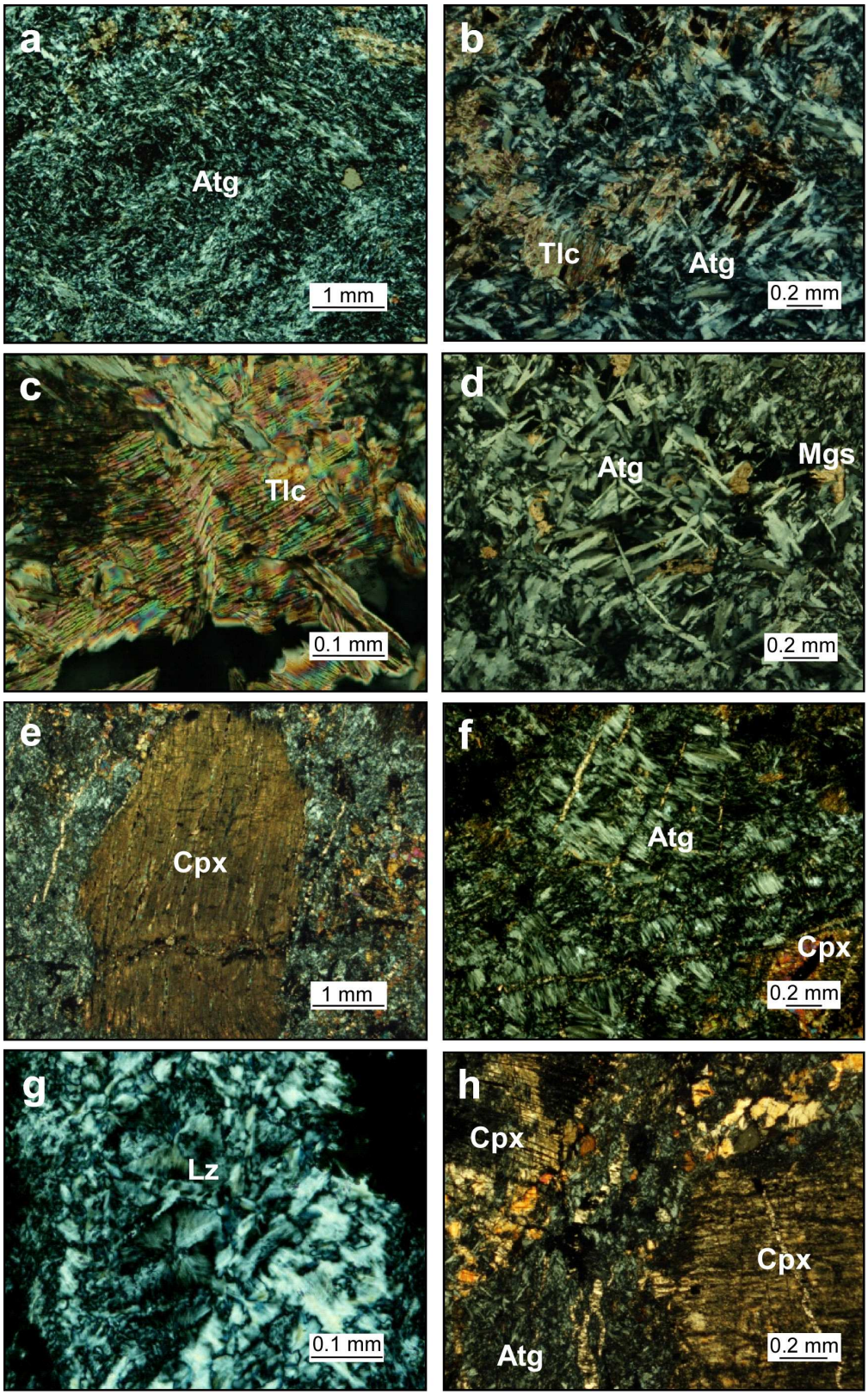
a
Atg
1 mm
b
Tlc
Atg
0.2 mm
c
Tlc
0.1 mm
d
Atg
Mgs
0.2 mm
e
Cpx
1 mm
f
Atg
Cpx
0.2 mm
g
Lz
0.1 mm
h
Cpx
Cpx
Atg
0.2 mm

Fig. 2. Cross-polarized light photographs of antigorite serpentinite (a to d) and antigorite-lizardite serpentinite (e to h). a) Nonpseudomorphic interpenetrating texture typical of antigorite. b) Talc-bearing antigorite serpentinite. Antigorite is partially replaced by talc. c) Kinking of talc in talc-bearing antigorite serpentinites. d) Detail of antigorite interpenetrating texture. Antigorite grains are partially replaced by magnesite and minor dolomite. e) Porphyroclastic texture showing clinopyroxene (diopside). f) Clinopyroxene partly replaced by ribbons of antigorite. Antigorite is a product of recrystallization of lizardite; g) Type-1 lizardite hourglass texture, showing the optical uniformity of lizardite across the mesh cell; h) Porphyroblastic and fine grained diopsidic clinopyroxene.

The antigorite with polysome m=16 yields the best fit for the most abundant in group I serpentinite (93.2 wt %) and the fitted lattice parameters are: a=81.878(5), b=9.264(5), c=7.248(2) Å and β = 91.409(5)º, space group C2/m. The antigorite with m=17 is scarce, 2.5 wt %, and the obtained parameters are: a=43.505(6), b=9.251(1), c=7.263(1) Å and β = 91.32(1)º, space group Pm. Other mineral phases present in the sample are: talc (1.0 wt %), magnesite (1.2 wt %), dolomite (1.6 wt %) and magnetite (0.5 wt %). Mellini et al. (1987) and Li et al. (2004) suggested that m=17 is typical for antigorite formed under greenschist-facies conditions.

In group-II serpentinites (sample LC-88) the calculated profile agrees well with the antigorite polysome m=16 and lizardite 1T (Mellini and Viti, 1994) (Fig. 3b). Antigorite is the most abundant serpentine mineral (48.3 wt %) with lattice parameters a=81.551(6), b=9.247(10), c=7.266(4) Å and β = 91.00(11)º. Lizardite is also abundant (15.7 wt %), with lattice parameters a=5.322(2), c= 7.295 (6) Å and space group P31m. Other phases identified in this sample are: diopside (17.7 wt %), clinochlore (10.3 wt %), magnetite (8.1 wt %) and minor brucite.

In summary, all investigated antigorites of the La Corea mélange presents polysome values with m=16. However, the variability of the refined a parameter in these samples is too low to permit correlation with the metamorphic grade as suggested by Mellini et al. (1987) and Li et al. (2004).

MINERAL CHEMISTRY

Serpentine

Serpentine from antigorite serpentinites have Si ranging 3.94 – 4.04 apfu, Mg = 4.94 – 5.08 apfu, Fe = 0.5 – 0.59 apfu, Cr < 0.05 apfu and Ni < 0.05 apfu (Table 1). In the ternary diagram Mg-Si-Fe (molar proportions, Fig. 4) the analyzed grains of serpentinite confirm with antigorite composition following D'Antonio and Kristensen (2004) classification. The Al contents are relative high (0.21 – 0.30 apfu). High Al and Cr could produce highest stability in temperature for antigorite (Padrón-Navarta et al., 2010). The Mg # ratios are 0.89 – 0.91.

Serpentine from antigorite-lizardite serpentinites have Si = 3.94 – 4.03 apfu, Fe = 0.19 – 0.26 apfu, Mg = 5.34 – 5.41 apfu, Cr < 0.03 apfu and Ni < 0.03 apfu, showing relative high Al = 0.17 – 0.30 apfu (Table 2). In the ternary diagram Mg-Si-Fe (Fig. 4) most point analyses represent antigorite composition, although some points with less Si content indicate lizardite and/or chrysotile composition (D'Antonio and Kristensen, 2004). The Mg# (0.95 – 0.97) is higher than in the antigorite serpentinites. These higher values do not correlate with bulk rock composition, suggesting distinct P-T conditions of growth.

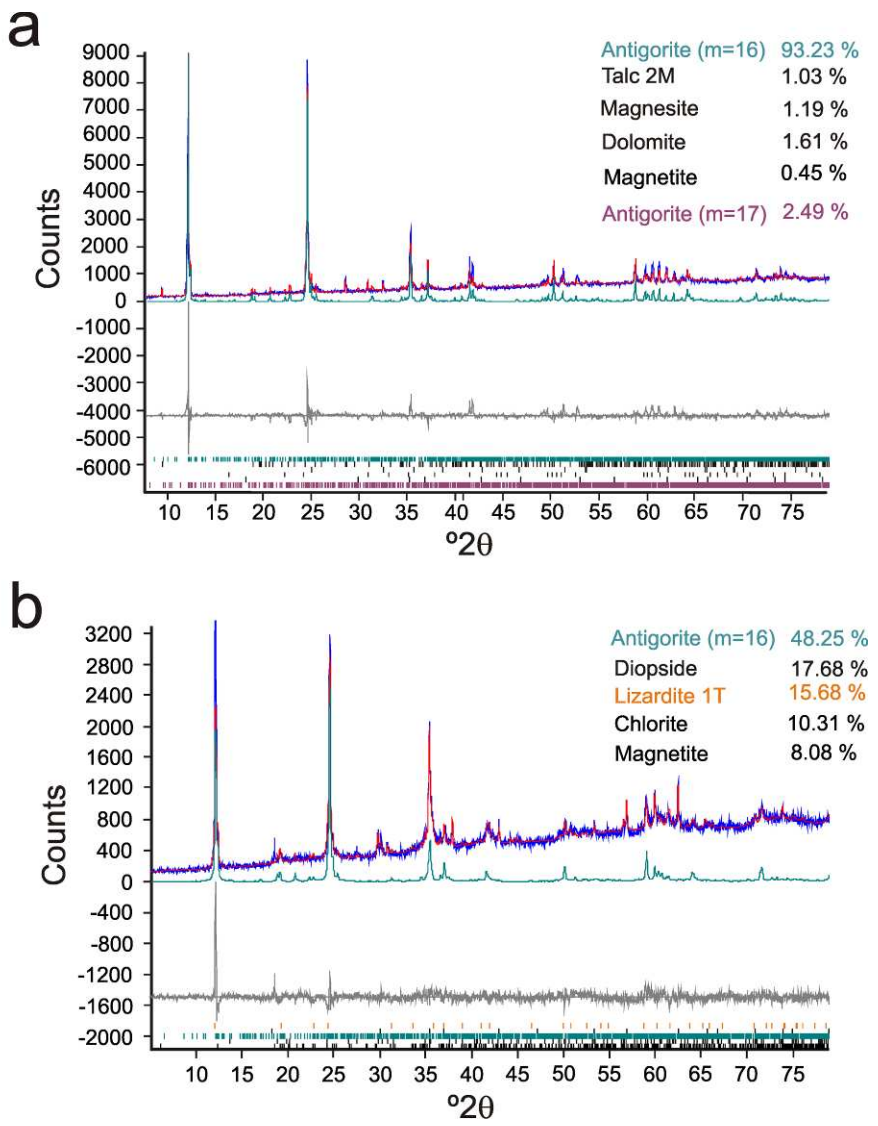

Fig. 3. XRD profile refinements of representative samples of antigorite- (LC-58) and antigorite-lizardite- (LC-88) serpentinites showing experimental (blue), calculated (red), calculated antigorite (turquoise), and difference (grey) profiles. The Bragg positions for all identified mineral phases are indicated at the base of the diagram.

Talc

Talc, present in antigorite serpentinite samples, is almost pure (Table 4), with Si = 8.00 – 8.07 apfu and Mg = 5.60 – 5.73, and low Fe = 0.17 – 0.28 apfu and Al < 0.01 apfu contents (Fig. 5). Mg# is, correspondingly, very high (0.95 – 0.97).

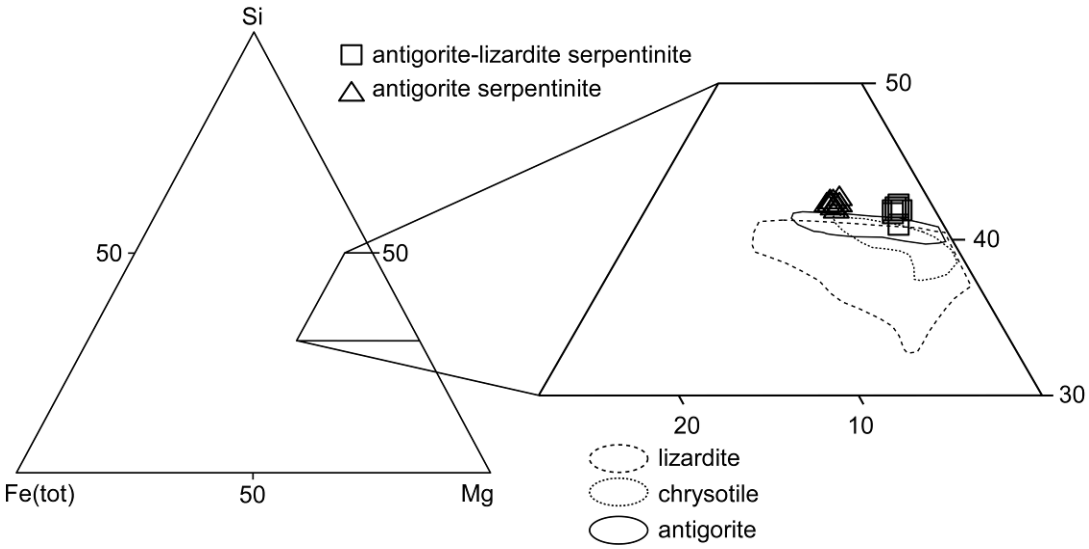

Fig. 4 Ternary atomic Mg-Si-Fe diagram showing the chemical variability of serpentine minerals from La Corea mélange. The fields for lizardite, chrysotile and antigorite were compiled by D`Antonio and Kristensen (2004).

Table.1 Representative analyses of serpentine from antigorite serpentinites (normalized to 10 O and 8 OH).

Sample	LC-58	LC-58	LC-58	LC-58	LC-58	LC-55	LC-55	LC-55	LC-55	LC-55
SiO_2	42.81	43.01	42.46	43.16	42.46	41.84	41.58	42.04	41.54	41.91
TiO_2	0.02	0.04	0.03	0.03	0.03	0.04	0.02	0.03	0.02	0.03
Al_2O_3	1.86	2.31	2.20	2.07	1.88	2.49	2.66	2.47	2.46	2.24
Cr_2O_3	0.26	0.34	0.37	0.17	0.17	0.56	0.58	0.62	0.62	0.53
FeO_{total}	6.39	6.31	6.59	6.78	6.50	7.41	7.08	7.05	7.03	7.05
MnO	0.04	0.03	0.09	0.08	0.04	0.02	0.00	0.05	0.01	0.02
MgO	36.00	35.75	35.64	36.26	36.01	34.86	34.74	35.05	35.54	34.69
NiO	0.15	0.12	0.18	0.15	0.26	0.19	0.25	0.12	0.34	0.13
CaO	0.00	0.01	0.01	0.00	0.00	0.01	0.00	0.01	0.03	0.02
Total	87.53	87.92	87.57	88.70	87.35	87.42	86.91	87.44	87.59	86.62
Si	4.03	4.03	4.01	4.02	4.02	3.98	3.97	3.99	3.94	4.01
Ti	0.00	0.00	0.00	0.00	0.00	0.00	0.00	0.00	0.00	0.00
Al	0.21	0.26	0.24	0.23	0.21	0.28	0.30	0.28	0.27	0.25
Cr	0.02	0.03	0.03	0.01	0.01	0.04	0.04	0.05	0.05	0.04
Fe^{2+}	0.50	0.49	0.52	0.53	0.51	0.59	0.57	0.56	0.56	0.56
Mn	0.00	0.00	0.01	0.01	0.00	0.00	0.00	0.00	0.00	0.00
Mg	5.06	5.00	5.02	5.04	5.08	4.94	4.94	4.96	5.03	4.95
Ni	0.02	0.02	0.03	0.02	0.04	0.03	0.04	0.02	0.05	0.02
Ca	0.00	0.00	0.00	0.00	0.00	0.00	0.00	0.00	0.00	0.00
#Mg	0.91	0.91	0.91	0.91	0.91	0.89	0.90	0.90	0.90	0.90

Chlorite

Chlorite, present in antigorite-lizardite serpentinites, has high Si (5.99 – 6.85 apfu) and Mg (9.71 – 10.27 apfu) contents, and is poor in Al (2.17 – 3.28 apfu) and Fe (0.52 – 0.87 apfu; Table 5). The contents of Cr (0.15 – 0.30 apfu) are not as high as in other serpentinite bodies were chlorite formed by alteration of spinel (Jan and Windley, 1990; Proenza et al., 2004; Abu El Ela and Farahat, 2009). The high Si contents and Mg# (0.92 – 0.95) classify these chlorites as clinochlore (Bailey, 1980). Nevertheless, Al contents are lower than stoichiometric clinochlore (Fig. 5),

probably as a result of intergrowth of serpentinite layers within chlorite (cf. Cressey et al., 2008).

Clinopyroxene

The porphyroblasts of clinopyroxene present in antigorite-lizardite serpentinites are diopside (≈ En_{50} Wo_{49-50} Fs_0; Morimoto et al., 1989; Table 3), with Si contents ranging 1.97 – 1.99 apfu, Mg = 0.96 – 1.03 apfu, Ca = 0.95 – 1.01 apfu, and very low Fe contents (< 0.05 apfu). Correspondingly, Mg# is very high (0.96 – 0.97). Other elements, namely Al and Na, have very low concentration (<0.03 apfu).

Table.2 Representative analyses of serpentine from antigorite-lizardite serpentinites (normalized to 10 O and 8 OH).

Sample	LC-88	LC-88	LC-88	LC-88	LC-66	LC-66	LC-66	LC-66
SiO_2	42.53	42.52	43.66	42.80	43.49	43.09	43.06	42.21
TiO_2	0.06	0.00	0.02	0.03	0.02	0.00	0.04	0.03
Al_2O_3	2.21	2.42	1.54	2.50	2.48	2.40	2.47	2.76
Cr_2O_3	0.31	0.29	0.18	0.25	0.38	0.45	0.35	0.07
FeO_{total}	2.95	2.75	2.83	3.23	2.80	2.50	2.49	3.34
MnO	0.14	0.07	0.10	0.06	0.09	0.14	0.19	0.07
MgO	38.86	38.47	39.23	38.67	39.10	39.41	38.72	38.43
NiO	0.07	0.12	0.20	0.17	0.16	0.12	0.13	0.00
CaO	0.01	0.33	0.00	0.01	0.00	0.02	0.01	0.29
Total	87.14	86.97	87.76	87.72	88.52	88.13	87.46	87.20
Si	3.97	3.97	4.03	3.97	3.98	3.97	3.99	3.94
Ti	0.00	0.00	0.00	0.00	0.00	0.00	0.00	0.00
Al	0.24	0.27	0.17	0.27	0.27	0.26	0.27	0.30
Cr	0.02	0.02	0.01	0.02	0.03	0.03	0.03	0.01
Fe^{2+}	0.23	0.21	0.22	0.25	0.21	0.19	0.19	0.26
Mn	0.01	0.01	0.01	0.00	0.01	0.01	0.01	0.01
Mg	5.40	5.36	5.40	5.34	5.34	5.41	5.35	5.35
Ni	0.01	0.02	0.03	0.02	0.02	0.02	0.02	0.00
Ca	0.00	0.03	0.00	0.00	0.00	0.00	0.00	0.03
#Mg	0.96	0.96	0.96	0.96	0.96	0.97	0.97	0.95

Andradite garnet

Andradite garnet, present in antigorite-lizardite serpentinites, has Si = 2.85 – 2.93 apfu, Ca = 3.04 – 3.09 apfu, and Fe^{3+} = 1.61 – 1.88 apfu, with significant Ti contents (up to 0.32 apfu) and low concentration in Al (< 0.04 apfu), Cr (< 0.04 apfu) and Mg (< 0.06 apfu; Table 6). This type of garnet is deficient in silica as is typical of high Ti-garnets from ultramafic rocks (Müntener and Hermann, 1994 and references therein).

WHOLE ROCK GEOCHEMESTRY

Major element composition

All studied serpentinite samples have large LOI (lost on ignition) values (> 10 wt%; Table 7), indicating that they are almost pure serpentinite, only sample LC-55 has higher LOI content, suggesting alteration. Antigorite serpentinites have MgO = 35.06 – 36.32 wt %, SiO_2 = 36.97 – 42.88 wt %, FeO = 6.78 – 7.39 wt %, Al_2O_3 = 1.49 – 2.51 wt % and CaO = 0.73 – 1.93 wt %. Antigorite-lizardite serpentinites have MgO = 34.72 - 37.48 wt %, SiO_2 = 40.19 – 40.86 wt %, FeO = 6.37 – 7.33 wt %, Al_2O_3 = 2.38 – 2.93 wt % and CaO = 1.12 – 3.72 wt %. The Mg# in both groups is similar (89.41 – 91.00). The higher concentration of CaO in antigorite-lizardite

serpentinites is in correspondence with the presence of clinopyroxene and andradite garnet in these samples while the higher Al_2O_3 is associated with the presence of chlorite.

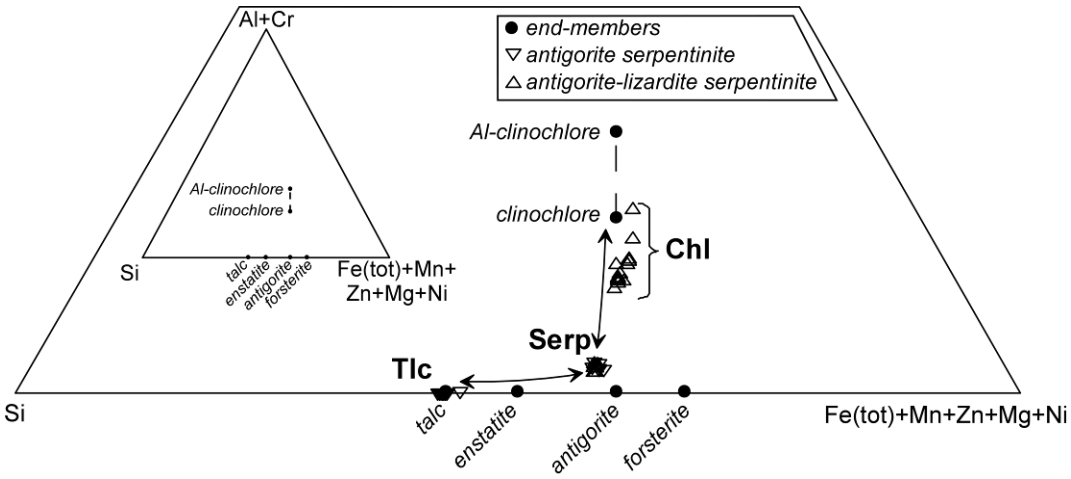

Fig. 5 Atomic Si-(Al+Cr)-(Fe+Mn+Zn+Mg+Ni) diagram showing the composition of chlorite and serpentine from antigorite-lizardite serpentinites and serpentine and talc from antigorite serpentinites. Representative end-members are also projected. Note that chlorites are deficient in Al.

The bulk composition of antigorite serpentinites and antigorite-lizardite serpentinites (Table 7) allow classifying the protoliths as harzburgites and lherzolites using the Ol-Opx-Cpx diagram in mole proportions (Fig. 6), and according to the fields defined by Le Maitre et al. (2002). The diagram represents the projection of bulk compositions (defined by SiO_2, Al_2O_3, FeO_{tot}, MnO, MgO and CaO) in the Fo-En-Di space after projection from the exchange vectors $FeMg_{-1}$ and $FeMn_{-1}$ and the Ca-Tschermak molecule $CaAl_2SiO_6$, as calculated using software CSpace (Torres-Roldán et al., 2000). All antigorite serpentinite samples correspond to harzburgitic protoliths, while the antigorite-lizardite serpentinites suggest lherzolitic-harburgitic composition. A comparison of the whole rock compositions of serpentinites from La Corea mélange with other regionally related ultramafic rocks are presented in Figure 7. These include the Mayari-Baracoa Ophiolite Belt (interpreted as highly refractory peridotites from a arc/back arc environment; Marchesi et al., 2006), Monte del Estado complex in Puerto Rico (interpreted as abyssal peridotite; Lewis et al., 2006b; Marchesi et al., this volume), Central Cuba serpentinites from Zaza zone and Dominican Republic serpentinites from Camú and Septentrional fault zones (interpreted as forearc peridotite; Hattori and Guillot, 2007; Saumur et al., 2010) and Dominican Republic peridotites from Rio San Juan and Puerto Plata complexes (interpreted as abyssal peridotite; Saumur et al., 2010). The antigorite-lizardite serpentinite samples show compositions similar to the lherzolites of the Monte del Estado ultramafic complex and abyssal peridotites from Rio San Juan and Puerto Plata complexes, Dominican Republic. Furthermore, the antigorite serpentinites have composition similar to abyssal peridotites and with Dominican Republic serpentinites from Rio San Juan and Puerto Plata complexes.

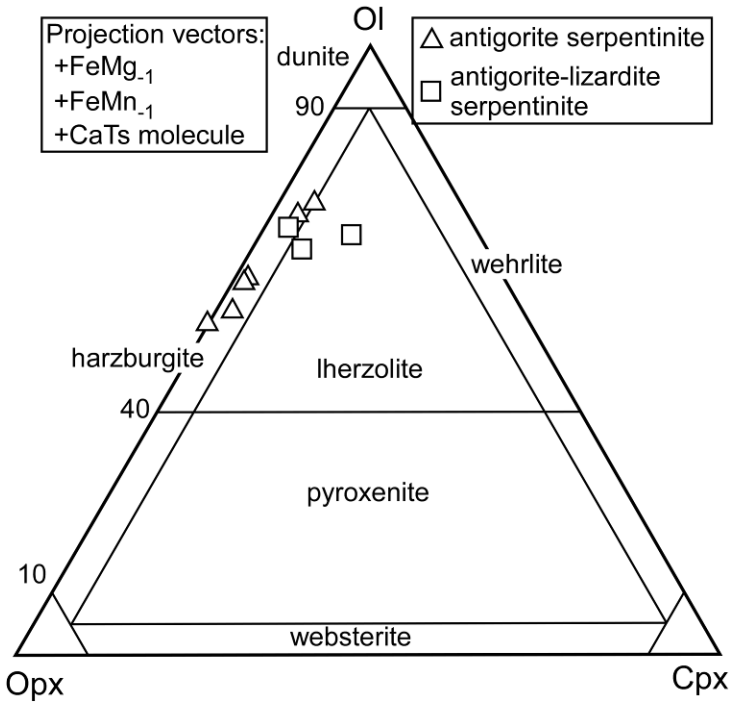

Fig. 6 Calculated molar Ol-Opx-Cpx diagram for serpentinites from La Corea mélange (see text for calculation).

Table.3 Representative analyses of clinopyroxene from antigorite-lizardite serpentinites (normalized to 6 O).

Sample	LC-97	LC-97	LC-97	LC-97	LC-97	LC-97	LC-97	LC-97	LC-97	LC-97
SiO_2	54.13	54.81	54.18	54.43	53.97	53.93	54.44	53.75	54.25	54.08
TiO_2	0.02	0.05	0.00	0.03	0.07	0.04	0.02	0.13	0.06	0.04
Al_2O_3	0.22	0.42	0.16	0.06	0.25	0.27	0.12	0.43	0.61	0.62
Cr_2O_3	0.12	0.09	0.07	0.10	0.20	0.13	0.19	0.14	0.20	0.27
Fe_2O_{3total}	1.33	1.13	1.49	1.51	1.35	1.51	1.38	1.70	1.30	1.35
MnO	0.07	0.02	0.07	0.06	0.06	0.06	0.05	0.15	0.04	0.09
MgO	18.12	18.61	17.83	17.96	18.26	18.09	18.06	18.40	18.27	18.48
CaO	25.17	24.70	25.10	25.41	24.77	24.71	25.23	24.49	24.38	24.39
Na_2O	0.14	0.28	0.21	0.11	0.20	0.18	0.15	0.18	0.27	0.23
K_2O	0.00	0.03	0.00	0.00	0.01	0.00	0.01	0.01	0.00	0.00
Sum	99.32	100.14	99.11	99.67	99.14	98.92	99.65	99.38	99.38	99.55
Si	1.97	1.98	1.98	1.98	1.97	1.97	1.98	1.96	1.97	1.97
Ti	0.00	0.00	0.00	0.00	0.00	0.00	0.00	0.00	0.00	0.00
Al	0.01	0.02	0.01	0.00	0.01	0.01	0.01	0.02	0.03	0.03
Cr	0.00	0.00	0.00	0.00	0.01	0.00	0.01	0.00	0.01	0.01
Fe^{2+}	0.04	0.03	0.04	0.04	0.04	0.04	0.04	0.05	0.04	0.04
Mn	0.00	0.00	0.00	0.00	0.00	0.00	0.00	0.01	0.00	0.00
Mg	0.99	1.00	0.97	0.97	0.99	0.99	0.98	1.00	0.99	1.00
Ca	0.98	0.96	0.98	0.99	0.97	0.97	0.98	0.96	0.95	0.95
Na	0.01	0.02	0.02	0.01	0.01	0.01	0.01	0.01	0.02	0.02
K	0.00	0.00	0.00	0.00	0.00	0.00	0.00	0.00	0.00	0.00
Sum	4.01	4.01	4.00	4.00	4.01	4.00	4.00	4.01	4.00	4.01
Wo	49.97	48.83	50.30	50.41	49.38	49.54	50.11	48.90	48.96	48.69
En	50.03	51.17	49.70	49.59	50.62	50.46	49.89	51.10	51.05	51.31
Fs	0.00	0.00	0.00	0.00	0.00	0.00	0.00	0.00	0.00	0.00

Platinum group elements composition

The studied samples have low total platinum group elements (PGE) concentrations (20-63 ppb, Table 8). The antigorite-lizardite serpentinites show similar values in all samples (35-40 ppb), while the antigorite serpentinites display somewhat larger variations (20-63 ppb). In general, all samples are characterized poorly fractionated IPGE (Os, Ir, Ru) patterns, with relatively flat IPGE segments consistent with the interpretation that they are all mantle residues (Fig. 8a, b). These PGE patterns are very similar to that of the primitive upper mantle (Becker et al., 2006). The composition of the studied samples are also similar to serpentinites of diverse origin (abyssal, forearc) from the Dominican Republic (Saumur et al., 2010).

In the Os versus Ir diagram (Fig. 8c) the samples show chondritic PGE abundances and weak enrichments relative to serpentinized abyssal peridotites (Snow and Reisberg, 1995; Luguet et al., 2003). The iridium contents and Ir/(Pt+Pd) ratios also indicate a mantle peridotite origin for their host protoliths (Fig. 8d). In general, the PGE distribution indicates that the PGE contents of the protoliths have not been significantly affected by metamorphism, in agreement with similar observations by Groves and Keays (1979), Prichard and Tarkian (1988), Angeli et al. (2001) and Proenza et al. (2004).

Table.4 Representative analyses of talc from antigorite serpentinites (normalized to 20 O and 4 OH).

Sample	LC-58	LC-58	LC-58	LC-58	LC-58	LC-58	LC-55	LC-55	LC-55	LC-55
SiO_2	62.40	62.85	62.55	63.61	62.27	61.44	62.49	62.76	61.46	62.63
TiO_2	0.05	0.04	0.00	0.02	0.02	0.04	0.02	0.05	0.05	0.01
Al_2O_3	0.04	0.02	0.04	0.03	0.00	0.01	0.01	0.04	0.00	0.01
FeO_{total}	2.49	2.34	2.20	2.12	2.10	2.33	1.61	2.41	2.60	2.11
MgO	29.54	29.54	29.70	29.88	29.82	28.63	29.61	29.54	29.38	29.57
Total	94.52	94.79	94.49	95.66	94.21	92.45	93.74	94.80	93.49	94.33
Si	8.03	8.05	8.03	8.06	8.02	8.07	8.06	8.04	8.00	8.05
Ti	0.01	0.00	0.00	0.00	0.00	0.00	0.00	0.00	0.01	0.00
Al	0.01	0.00	0.01	0.00	0.00	0.00	0.00	0.01	0.00	0.00
Fe^{2+}	0.27	0.25	0.24	0.23	0.23	0.26	0.17	0.26	0.28	0.23
Mg	5.66	5.64	5.69	5.64	5.73	5.60	5.70	5.64	5.70	5.73
Mg#	0.95	0.96	0.96	0.96	0.96	0.96	0.97	0.96	0.95	0.96

ISOCHEMICAL P-T PROJECTION

Isochemical P-T projections (pseudosections) were calculated for representative bulk-rock compositions of the two groups of serpentinites studied and the results were compared with the observed phase assemblages. The projections were computed with software PerpleX (Connolly, 2005). Thermodynamic data were taken from the internally consisted database of Holland and Powell (1998). Solid solutions considered are from Holland and Powell (1998) for olivine, from Holland and Powell (1996) for orthopyroxene and clinopyroxene, and from Holland et al. (1998) for chlorite. Talc, antigorite and tremolite were treated as ideal binary Fe-Mg solid solutions. Lizardite was not included in the calculations due to the lack of thermodynamic data for this phase. The fluid phase, assumed to be pure H_2O, is considered to be in excess. The antigorite serpentinite sample LC-58 was modeled in the CFMSH (CaO-FeO-MgO-SiO_2-H_2O) system (Fig. 9a). The bulk rock composition of this sample was slightly transformed in order

to account for the Mg and Ca contents present in the carbonate phases (not considered in the calculations).

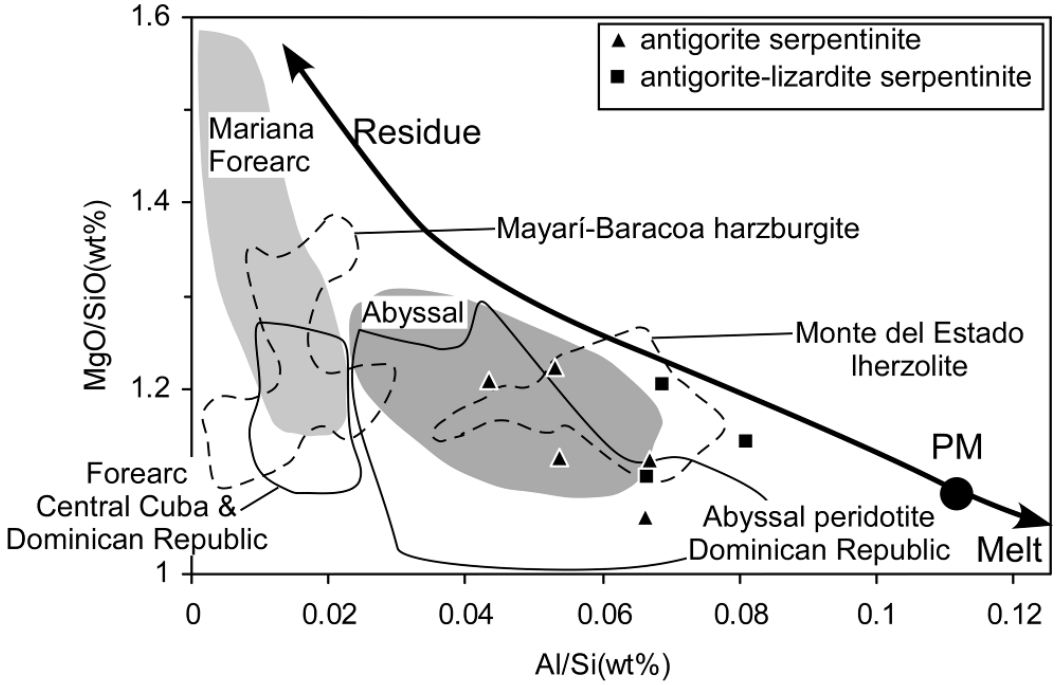

Fig. 7. Weight ratios of Mg/Si versus Al/Si of serpentinite samples from La Corea mélange. Plotted for comparison are the fields of Mayarí-Baracoa harzburgites (Marchesi et al., 2006), Monte del Estado lherzolites (Marchesi et al., this volume), abyssal serpentinites from Dominican Republic (Saumur et al., 2010), and forearc serpentinites from Central Cuba and Dominican Republic (Hattori and Guillot 2007, Saumur et al., 2010). Fields for Mariana forearc and abyssal peridotites complied by Hattori and Guillot (2007). PM is the primitive mantle estimate of McDonough and Sun (1995).

The antigorite-lizardite serpentinite sample LC-97 was modeled in the system CFMASH (CaO-FeO-MgO-Al_2O_3-SiO_2-H_2O) (Fig. 9b). Small proportion of FeO_{total} was extracted to account for the presence of magnetite (not considered in the calculations).Table.5 Representative analyses of chlorite from antigorite-lizardite serpeninites (Normalized to 20 O and 16 OH).

The results of the calculations indicate a wide range of P-T conditions below ca. 500 ºC for the formation of antigorite serpentinites (Fig. 9a). The predicted assemblage for these conditions is made mostly by antigorite, with minor talc, as observed in the studied samples. However, the calculated relations indicate the presence of minor tremolite, not observed in the studied samples. This is likely due to the effect of non-accounted CO_2 component and carbonate (dolomite) phases. Because these rocks are interpreted as the matrix of the subduction channel (i.e., high-T mélange formed above the subduction zone; see below), they should have followed a retrograde trajectory similar to that to the tectonic blocks of subducted oceanic material. For these reason, we have calculated mineral abundances in one point along the P-T trajectory followed by high pressure amphibolite blocks of the La Corea mélange (Blanco-Quintero et al., in

Sample	LC-88	LC-88	LC-88	LC-88	LC-88	LC-88	LC-66	LC-66	LC-66
SiO_2	34.30	34.76	34.43	34.79	34.95	36.06	31.29	32.37	32.93
TiO_2	0.03	0.02	0.01	0.02	0.00	0.00	0.07	0.05	0.01
Al_2O_3	10.57	10.64	10.95	10.57	10.06	9.67	14.55	12.95	12.36
Cr_2O_3	0.96	1.01	1.64	1.62	1.61	1.54	1.97	0.96	0.96
FeO_{total}	3.39	3.23	3.49	3.43	3.30	3.25	5.45	3.54	3.45
MnO	0.08	0.12	0.02	0.07	0.10	0.08	0.07	0.11	0.06
MgO	35.60	35.19	35.21	35.06	35.22	35.78	34.04	34.80	34.99
NiO	0.05	0.14	0.11	0.12	0.14	0.05	0.17	0.23	0.18
CaO	0.09	0.08	0.08	0.08	0.06	0.05	0.01	0.00	0.04
Total	85.07	85.19	85.94	85.76	85.44	86.48	87.62	85.01	84.98
Si	6.64	6.71	6.61	6.69	6.74	6.85	5.99	6.29	6.39
Ti	0.00	0.00	0.00	0.00	0.00	0.00	0.01	0.01	0.00
Al	2.41	2.42	2.48	2.39	2.29	2.17	3.28	2.96	2.83
Cr	0.15	0.15	0.25	0.25	0.25	0.23	0.30	0.15	0.15
Fe^{2+}	0.55	0.52	0.56	0.55	0.53	0.52	0.87	0.58	0.56
Mn	0.01	0.02	0.00	0.01	0.02	0.01	0.01	0.02	0.01
Mg	10.27	10.12	10.07	10.04	10.12	10.14	9.71	10.08	10.12
Ni	0.01	0.04	0.03	0.03	0.04	0.01	0.05	0.07	0.05
Ca	0.02	0.02	0.02	0.02	0.01	0.01	0.00	0.00	0.01
#Mg	0.95	0.95	0.95	0.95	0.95	0.95	0.92	0.95	0.95

Table.6 Representative analyses of garnet from antigorite-lizardite serpentinites (normalized to 12 O).

Sample	LC-66	LC-66	LC-66	LC-66	LC-66	LC-66	LC-66	LC-66	LC-66
SiO_2	33.92	34.25	33.50	33.67	33.80	34.12	33.14	33.70	33.63
TiO_2	3.86	2.79	4.53	4.94	4.09	1.38	4.03	4.63	4.34
Al_2O_3	0.29	0.22	0.30	0.28	0.29	0.44	0.30	0.32	0.26
Cr_2O_3	0.27	0.05	0.08	0.40	0.42	0.54	0.37	0.29	0.34
Fe_2O_{3total}	27.02	27.59	26.17	26.12	26.55	29.21	26.89	25.52	26.36
MnO	0.07	0.04	0.02	0.08	0.13	0.05	0.09	0.06	0.07
MgO	0.33	0.33	0.46	0.41	0.32	0.14	0.36	0.39	0.38
NiO	0.00	0.00	0.00	0.00	0.00	0.00	0.00	0.00	0.17
CaO	33.25	33.27	33.41	33.30	33.45	33.26	33.13	33.77	33.70
Total	99.01	98.54	98.47	99.20	99.05	99.14	98.31	98.68	99.25
Si	2.89	2.93	2.87	2.86	2.88	2.91	2.85	2.87	2.86
Ti	0.25	0.18	0.29	0.32	0.26	0.09	0.26	0.30	0.28
Al	0.03	0.02	0.03	0.03	0.03	0.04	0.03	0.03	0.03
Cr	0.02	0.00	0.01	0.03	0.03	0.04	0.03	0.02	0.02
$Fe^{3+(*)}$	1.68	1.76	1.65	1.58	1.66	1.88	1.73	1.61	1.68
Fe^{2+}	0.06	0.02	0.03	0.09	0.04	0.00	0.01	0.03	0.00
Mn	0.01	0.00	0.00	0.01	0.01	0.00	0.01	0.00	0.01
Mg	0.04	0.04	0.06	0.05	0.04	0.02	0.05	0.05	0.05
Ni	0.00	0.00	0.00	0.00	0.00	0.00	0.00	0.00	0.01
Ca	3.04	3.05	3.06	3.04	3.05	3.04	3.05	3.09	3.07

(*) Calculated by stoichiometry

press). The results indicate that the abundances of antigorite and talc are 93.63 wt % and 3.93 wt %, respectively, similar to estimation from XRD data (see above).

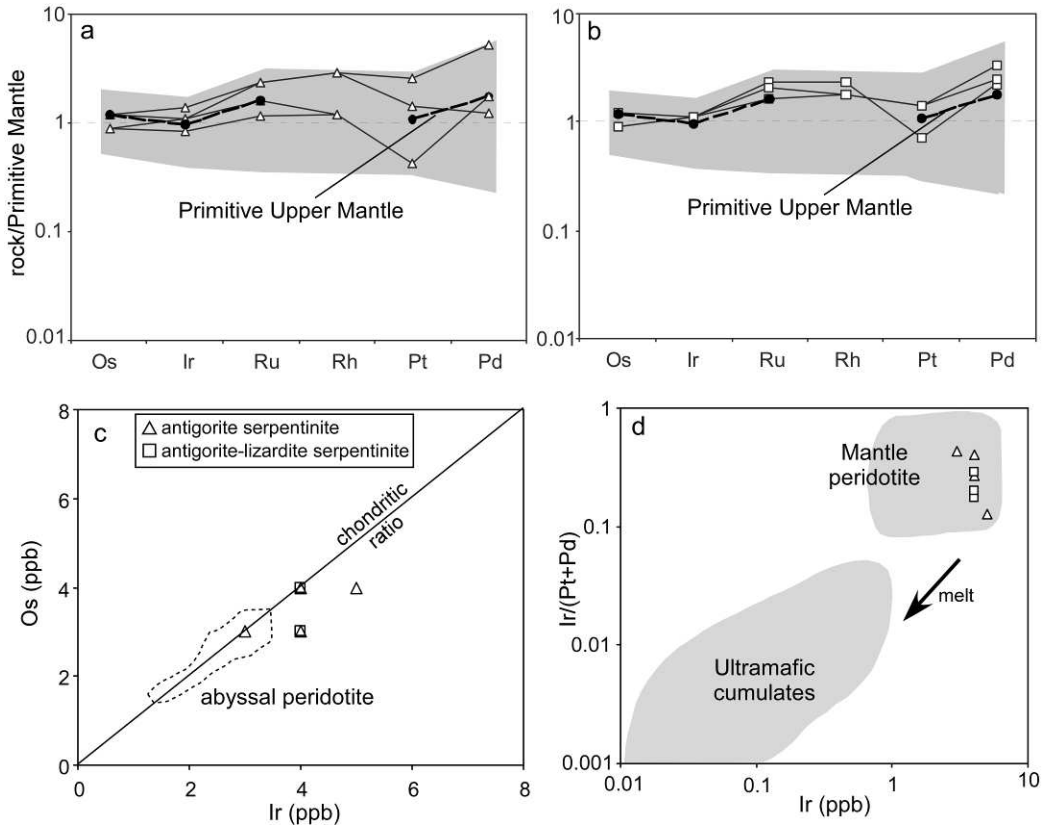

Fig. 8 Primitive mantle (McDonough and Sun, 1995) normalized PGE abundances of a) antigorite serpentinite and b) antigorite-lizardite serpentinite. For reference, the composition of primitive upper mantle (PUM; Becker et al. 2006) and of abyssal and forearc serpentinites from Dominican Republic (Saumur et al., 2010) are plotted (grey fields). c) Ir versus Os diagram for samples from La Corea mélange; the field of abyssal peridotite is after compilation of Agranier et al. (2007); d) Ir versus Ir/(Pt+Pd) diagram for samples from La Corea mélange. It can be appreciated that the samples are similar to mantle peridotite and not ultramafic cumulates. The mantle peridotite and ultramafic cumulate regions (grey fields) are compiled by Hattori and Guillot (2007).

Table.7 Bulk rock chemical composition of serpentinite samples from La Corea. Group A correspond to antigorite serpentinites and group B correspond to antigorite-lizardite serpentinites.

Sample	LC-M-17	LC-G-4	LC55	LC56	LC58	LC66	LC88	LC97
Group	A	A	A	A	A	B	B	B
SiO_2	38.79	40.80	36.97	42.88	41.28	40.19	40.86	40.55
TiO_2	0.04	0.06	0.04	0.09	0.08	0.11	0.07	0.07
Al_2O_3	1.49	2.41	1.73	2.51	1.96	2.44	2.93	2.38
FeO_{tot}	7.03	6.96	6.78	7.39	6.98	6.82	6.37	7.33
MnO	0.11	0.11	0.16	0.10	0.09	0.13	0.13	0.14
MgO	36.32	35.52	35.06	35.31	36.00	37.48	36.17	34.72
CaO	1.20	0.68	1.93	b.d.l.	0.73	1.12	2.30	3.72
P_2O_5	0.01	0.01	0.01	0.01	0.01	0.01	0.01	0.01
LOI	13.52	12.11	17.17	10.88	12.23	11.33	10.77	10.14
Total	98.51	98.66	99.85	99.17	99.36	99.63	99.61	99.06
Mg#	0.84	0.84	0.84	0.83	0.84	0.85	0.85	0.83

Table.8 Whole rock analyses on platinium group elements (PGE) of representative samples from La Corea mélange. Group A correspond to antigorite serpentinites and group B correspond to antigorite-lizardite serpentinites.

Samples	LC-G-4	LC-M-17	LC-55	LC-56	LC-66	LC-88	LC-97
Group	A	A	A	A	B	B	B
Ir	5	3	4	4	4	4	4
Os	4	3	4	3	3	3	4
Pd	21	7	5	7	9	13	10
Pt	18	0	10	3	5	10	10
Rh	5	2	5	2	4	3	3
Ru	10	5	10	7	10	7	9
Suma	63	20	38	26	35	40	40
IPGE	19	11	18	14	17	14	17
PPGE	44	9	20	12	18	26	23
IPGE/PPGE	0.43	1.22	0.90	1.17	0.94	0.54	0.74
Ir/(Pt+Pd)	0.13	0.43	0.27	0.40	0.29	0.17	0.20

IPGE: Os, Ir, Ru. PPGE: Rh, Pt, Pd

The results of calculations for the antigorite-lizardite sample indicates that talc is not stable in the low temperature part of the diagram (< 600 ºC; Fig 9b), as opposed to the calculations for the antigorite serpentinite sample and in agreement with observed assemblages. In addition, brucite, clinopyroxene, and chlorite appear as stable phases in the low temperature field (< 400 ºC), in agreement with the observed assemblages. The predicted stable coexistence of diopsidic clinopyroxene at low temperature suggests that the Cpx porphyroclasts of the studied samples represent former peridotitic porphyroclasts reequilibrated during low-grade metamorphism. Since these rocks constitute tectonic blocks interpreted to have been accreted to the mélange at relatively low temperature (see below), their P-T evolution should have met the retrograde paths of the exhuming rocks of the subduction channel late during the evolution of the latter. In fact, the calculated mineral proportions at conditions appropriate for greenschist facies along the retrograde P-T path of the exotic blocks of La Corea mélange (i.e., 300 ºC and 6 kbar: Atg 66.46 wt %, Cpx 15.20 wt %, Chl 14.65 wt % and Brc 3.70 wt %; Fig. 9b) closely match the proportions obtained after XRD data recalculated for magnetite = 0.

DISCUSSION

The geologic setting of formation of ultramafic complexes is best determined using proxies such as the concentration of Cr, Al and Ti in Cr-spinel (Irvine, 1967; Dick and Bullen, 1984; Arai, 1992). The studied metaultramafic rocks of La Corea mélange do not preserve primary Cr-spinel, which is systematically altered to ferrian chromite or Cr-bearing magnetite. Also, no primary silicates (olivine and pyroxene) have been preserved, since diopsidic clinopyroxene of the antigorite-lizardite rocks is interpreted as metamorphic in equilibrium with antigorite. However, the fact that both types of rock have antigorite as the most abundant phase indicates a moderate temperature of serpentinization. Antigorite is the high temperature stable polymorph of the serpentine group minerals (Evans, 2004), and Ulmer and Trommsdorff (1995) presented experimental results indicating antigorite stability up to 720 ºC and 20 kbar and 620 ºC and 50 kbar. These results are in agreement with formation of antigorite-bearing rocks in the subduction environment for a broad range of P-T conditions. Though the P-T

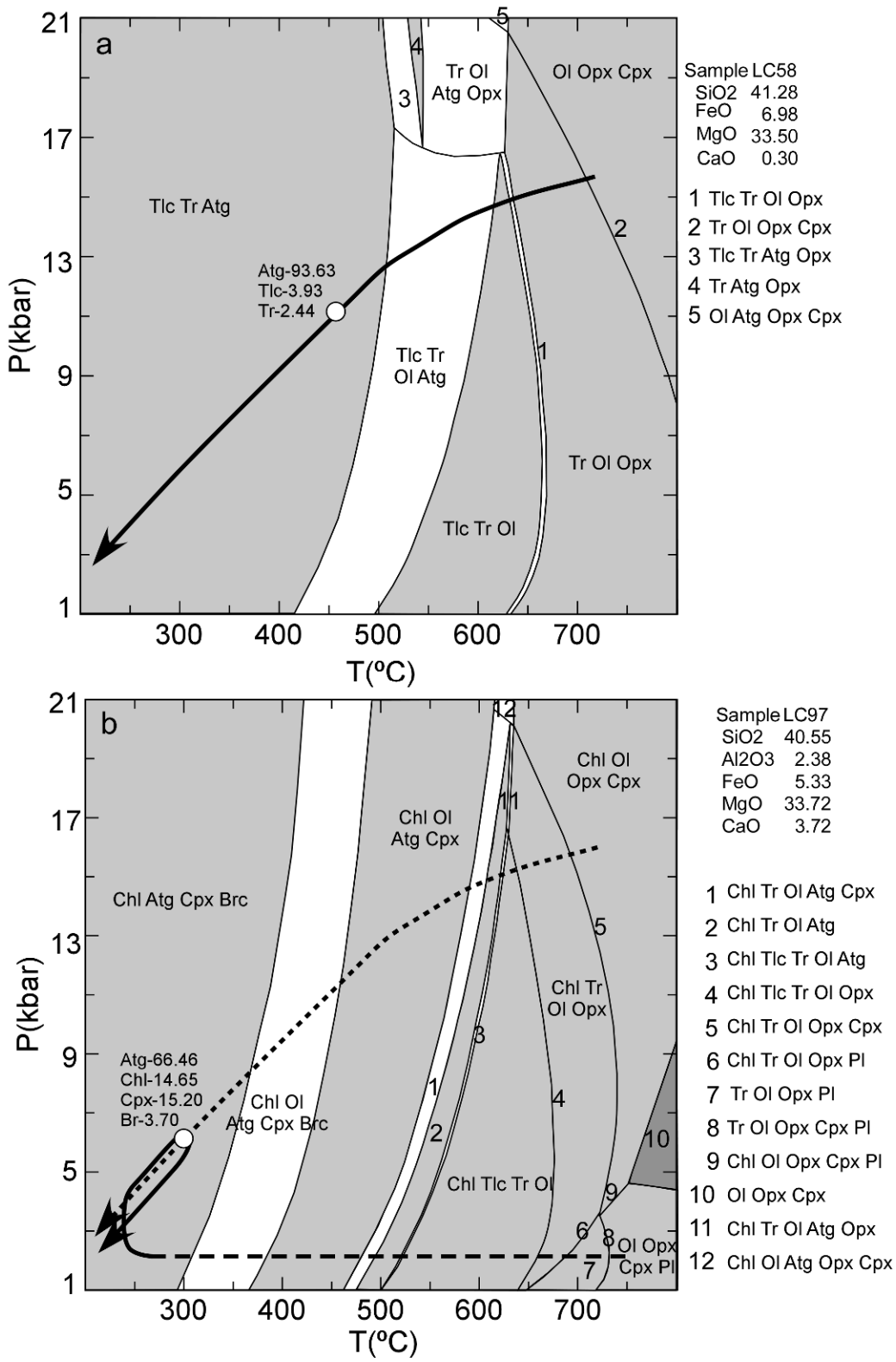
a
Tlc Tr Atg
Tr Ol Atg Opx
Ol Opx Cpx
Tlc Tr Ol Atg
Tr Ol Opx
Tlc Tr Ol
Atg-93.63
Tlc-3.93
Tr-2.44
Sample LC58
SiO2 41.28
FeO 6.98
MgO 33.50
CaO 0.30
1 Tlc Tr Ol Opx
2 Tr Ol Opx Cpx
3 Tlc Tr Atg Opx
4 Tr Atg Opx
5 Ol Atg Opx Cpx
P(kbar)
T(ºC)
b
Chl Atg Cpx Brc
Chl Ol Atg Cpx
Chl Ol Opx Cpx
Chl Tr Ol Opx
Chl Ol Atg Cpx Brc
Chl Tlc Tr Ol
Ol Opx Cpx Pl
Atg-66.46
Chl-14.65
Cpx-15.20
Br-3.70
Sample LC97
SiO2 40.55
Al2O3 2.38
FeO 5.33
MgO 33.72
CaO 3.72
1 Chl Tr Ol Atg Cpx
2 Chl Tr Ol Atg
3 Chl Tlc Tr Ol Atg
4 Chl Tlc Tr Ol Opx
5 Chl Tr Ol Opx Cpx
6 Chl Tr Ol Opx Pl
7 Tr Ol Opx Pl
8 Tr Ol Opx Cpx Pl
9 Chl Ol Opx Cpx Pl
10 Ol Opx Cpx
11 Chl Tr Ol Atg Opx
12 Chl Ol Atg Opx Cpx
P(kbar)
T(ºC)

Fig. 9 Isochemical P-T equilibrium phase diagram for a) antigorite serpentinite (LC58) and b) antigorite-lizardite serpentinite (LC97) calculated with Perplex. Mineral code: Ol (olivine), Atg (antigorite), Tlc (talc), Cpx (clinopyroxene), Opx (orthopyroxene), Chl (chlorite), Tr (tremolite), Brc (brucite). The P-T path in a) is for tectonic blocks of subducted amphibolites incorporated into the subduction channel (Blanco-Quintero et al., in press). The same P-T path is depicted with dotted line in b). In dashed and solid lines in b) represent the inferred P-T paths during ocean-floor evolution of abyssal peridotites and during incorporation into the subduction channel, respectively. The calculated abundance of minerals for the inferred conditions of formation of both types of rocks is indicated.

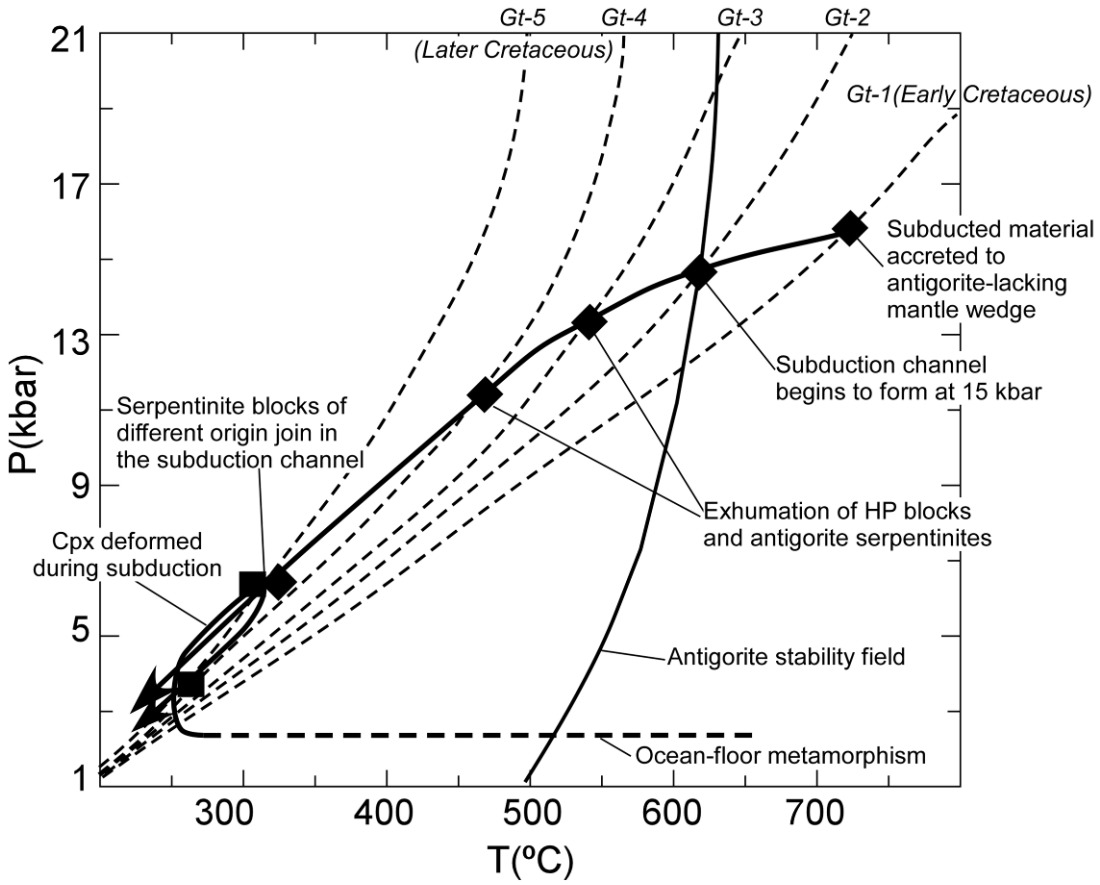

Fig. 10 Schematic P-T diagram showing the model evolution of studied rocks. Dashed lines: evolving isotherms from onset of subduction to mature subduction (not scaled). Diamonds: Points along the inferred path of antigorite serpentinites (from mantle wedge to subduction channel). Square: points along the inferred path of antigorite-lizardite serpentinites (abyssal serpentinite) during and after accretion (from the subduction channel to the mélange). The antigorite stability field corresponds to the calculation of Fig. 9a.

conditions of formation of the serpentinites studied cannot be defined with precision, probable conditions can be deduced taking into account the dynamics of subduction channels and the evolution of high pressure exotic blocks included in the La Corea Mélange.

Dehydration of subducted altered oceanic crust and sediment from the incoming plate evolves large amounts of H_2O-fluid to the upper-plate mantle, for which

models predict the possibility of partial melting at appropriate high temperature or serpentinization at low-medium temperature (e.g., Gerya et al., 2002). Subduction channels, being formed by a serpentinite matrix and HP blocks accreted from the subducting plate and/or detached from the overlying fore-arc lithosphere, may also contain exotic blocks of serpentinite formed in these environments. The strong alteration of spinel and the systematic absence of primary phases (e.g., olivine, orthopyroxene) are indications of elevated fluid fluxes and moderate temperature of formation, as indicated by the pseudosection calculations (Fig. 9). In this context, we interpret antigorite serpentinites as the deep seated serpentinitic matrix of the subduction channel formed after hydration of the boundary layer of the upper plate (harzburgitic) mantle. The bulk-rock major (Fig. 7) and PGE (Fig. 8) chemistry of this type of rock suggests a deep-seated harzburgitic protolith similar to abyssal peridotite. Harzburgites are known in abyssal and mantle wedge environments, but considering field evidence and mineralogy composition we propose that the antigorite serpentinites are derived from the hydrated mantle wedge. This interpretation implies that subduction channel serpentinites do not necessarily resemble residual harzburgites typical of fore-arcs (e.g., Mayarí-Baracoa ophiolitic complex).

The antigorite serpentinites of the subduction channel should have followed a P-T path similar to that of subducted blocks accreted to the upper plate mantle. Exotic blocks of amphibolite were metamorphosed at ca. 15 kbar, 700 ºC, when they were accreted to the upper plate mantle (Blanco-Quintero et al., in press). At these conditions, the calculated pseudosection for antigoritite serpentinites indicates anhydrous peridotite mineral assemblages coexisting with H_2O-fluid (i.e., hydrous peridotite; Fig. 9a). Blanco-Quintero et al. (in press) indicated that these conditions were followed by near-isobaric cooling in the accreted blocks of amphibolite, as expected after refrigeration of the subduction zone due to continued subduction (Gerya et al., 2002). Such isobaric cooling P-T path is also expected for the hydrated peridotite of the upper plate, which would hydrate (i.e., formation of tremolite and talc; Fig. 9a) due to the influx of fluids from the subducting slab. Once antigorite starts forming (ca. 650 ºC, 15 kbar; Fig. 9a), the subduction channel start formation and rocks (both exotic tectonic blocks and hydrated metaharzburgitic matrix) would begin to be exhumed. This is to be expected due to the plastic behavior of serpentinitic rocks (Gerya et al., 2002; Guillot et al., 2009) and implies that the P-T paths of the subduction channel rocks suffer an inflection, with increasing decompression upon cooling (Fig 9a). Further influx of fluids evolved from the subducting plate would allow continued hydration and the formation of almost pure antigoritite in the exhuming matrix of the subduction channel at conditions below 500 ºC and 13 kbar (Fig. 9a).

The lherzolitic bulk rock composition of the antigorite-lizardite serpentinites suggests a different protolith, probably an abyssal peridotite. The presence of abyssal and supra-subduction zone peridotite (protolith) rocks in subduction channels can be explained by three hypotheses. First, basaltic crust produced at slow spreading centers (Atlantic type) is normally thin or even absent, allowing abyssal peridotites to be incorporated in the subduction channel and mixed with metamafic rocks accreted from the incoming plate and hydrated ultramafic rocks of the mantle wedge. Similar rocks are described in mélanges from the Dominican Republic (Gorczyk et al., 2007, Saumur et al., 2010). Second, the

preservation of abyssal-type peridotites in forearc regions has been interpreted as trapped older lithosphere that did not participate in subduction zone melting (Batanova and Sobolev 2000). Finally, it is also possible the inflow of younger abyssal lithosphere along the margins of transform-bounded trench systems, as proposed for the South Sandwich arc (Parkinson et al. 1992; Parkinson and Pearce 1998; Pearce et al. 2000).

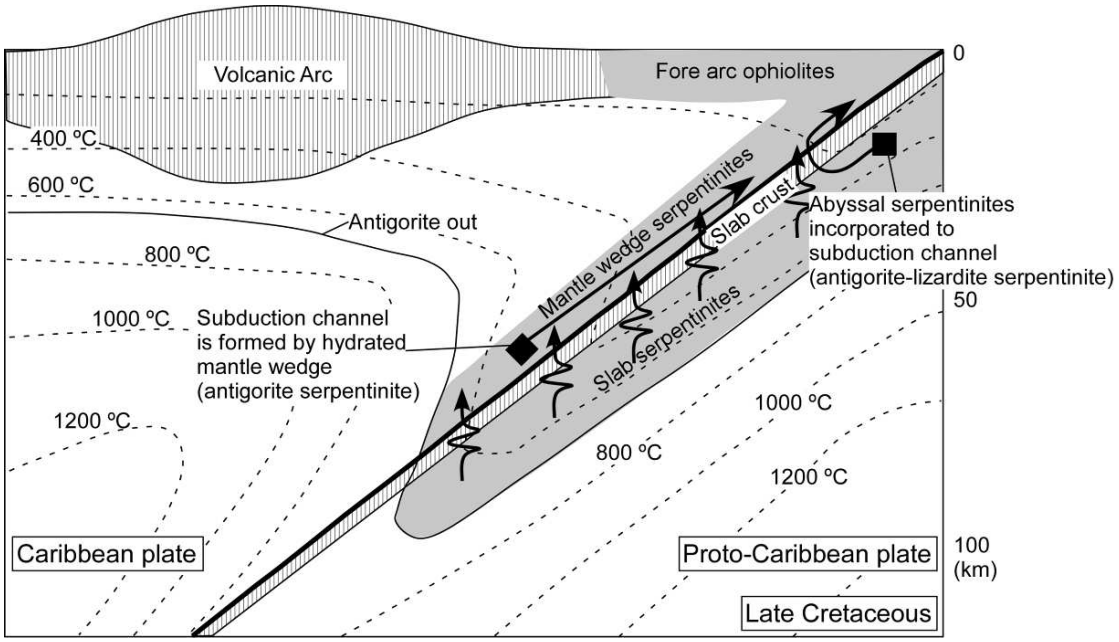

Fig. 11 Schematic cross-section showing the tectonic configuration of the Caribbean region during the Cretaceous and the origin of the studied rocks. The thermal structure of the subduction zone and the stability of serpentinite is after Gerya et al. (2002; Fig. 7a) for a young plate (20 Ma) after 500 km of convergence.

The Proto-Caribbean oceanic lithosphere (Atlantic) was formed as result of breakup and disruption of Pangea during Late Jurassic - Late Cretaceous. Geological and geophysical evidence suggests a slow spreading center in the Proto-Caribbean region during the Mesozoic (e.g., Pindell et al., 2005, 2006) which may have allowed the formation of serpentinite after hydration of abyssal peridotite. Furthermore, chemical similarities among the antigorite-lizardite serpentinites and the Monte del Estado (Puerto Rico) ultramafic rocks (Fig. 7), interpreted as fragments of the Proto-Caribbean lithosphere (Lewis et al., 2006b; Marchesi et al., this volumen), strengthen the view that the former type of rock from La Corea mélange represents fragments of the Proto-Caribbean oceanic lithosphere that escaped deep subduction. This view is consistent with the brucite, lizardite, and andradite-bearing mineral assemblages and textures of this type of rock, which suggest low temperatures of formation (Frost and Beard, 2007) in the oceanic environment and in the shallow subduction environment. Hence, the thermal evolution of this type of rocks should have encountered that of the exhuming subduction channel (mélange) at relatively low temperature and pressure. Using the

P-T path of the exotic blocks of amphibolite, this should have taken place at ca. 300 ºC and 5-6 kbar (Fig. 9b), as indicated above.

An integrated model of evolution of serpentinites is presented in Figures 10 and 11 following the interpretations given above and those of Blanco-Quintero et al. (in press) for the exotic blocks of subducted MORB in the La Corea mélange. At the onset of subduction of young oceanic lithosphere during the early Cretaceous (ca. 120 Ma), the thermal gradient along the subduction interface was very hot. These conditions allowed the breakdown of hydrous phases from subducted hydrous oceanic lithosphere and the formation free fluid that would flux across the mantle wedge. At relatively deep conditions, meta-MORB rocks from the incoming plate (amphibolites) were accreted to hydrous peridotitic mantle wedge. Continued subduction refrigerated the subduction system, allowing formation of hydrated metaperidotitic mantle wedge at similar depth. A serpentinitic subduction channel is formed upon reaction of liberated H_2O with the mantle wedge at conditions within the antigorite stability field (i.e., antigorite serpentinites), allowing henceforth upward flow of the rocks. This general evolution produces counter-clockwise P-T paths of accreted rocks (e.g., Wakabayashi, 1990; Gerya et al., 2002). Similar trajectories has been deduced by Krebs et al. (2008) from contemporaneous (ca. 103 Ma) eclogite blocks in the Rio San Juan complex (Dominican Republic), and amphibolite blocks from the Sierra del Convento mélange (115 Ma; García-Casco et al., 2008a; Lázaro et al., 2009). As the subduction channel flows upward, other blocks join the mélange at shallower depths (i.e., antigorite-lizardite serpentinites). The mélange further exhumes until it is located below the forearc peridotites htat could be represented by the peridotites of the Mayarí-Cristal ophiolite massif. Both the underlying forearc ophiolites and the mélange would be finally exhumed during late Cretaceous obduction, likely caused by the regional arc-platform collision event (García-Casco et al. 2008b).

CONCLUSIONS

Antigorite- and antigorite-lizardite-serpentinites in La Corea mélange (eastern Cuba) document the processes of formation of the subduction channel and accretion of abyssal peridotites. The strong alteration (i.e., serpentinization, Cr-spinel transformation) of harzburgitic and lherzolitic protholiths indicates pervasive fluid flow in all types of rock best explained if the rocks experienced hydration above a subducting plate. Antigorite serpentinites of harzburgitic protolith likely formed at depth after hydration of the mantle wedge (Caribbean lithosphere) by fluids derived from the SW-dipping subducted slab (Proto-Caribbean lithosphere). Antigorite-lizardite serpentinites of lherzolitic composition are best explained as abyssal (meta)peridotites (Proto-Caribbean lithosphere) accreted to the subduction channel developed in the Caribbean-Proto-Caribbean plate interface. Hydration of Caribbean plate mantle wedge allowed the formation and exhumation of a subduction channel during Cretaceous times until final exhumation occurred in late Cretaceous obduction of the supra-subduction zone Mayarí-Baracoa Ophiolite Belt and associated underlying subduction mélanges.

ACKNOWLEDGEMENTS

The authors thank the constructive reviews of Robert J. Stern, Stéphane Guillot and George E. Harlow that substantially improved this paper. We appreciate financial

support from Spanish MEC Spanish projects CGL2006-07384, CGL2006-08527, CGL2009-12446 and CGL2009-10924. This is a contribution to IGCP-546 "Subduction zones of the Caribbean". Blanco-Quintero is supported by grant AP2005-5258 from the ''Programa de Formación del Profesorado Universitario'' of the Spanish Ministry of Education and Science.

REFERENCES

Abu El Ela, F. F., Farahat, E. S., 2009. Neoproterozoic podiform chromitites in serpentinites of the Abu Meriewa–Hagar Dungash district, Eastern Desert, Egypt: Geotectonic implications and metamorphism. Island Arc, doi: 10.1111/j.1440-1738.2009.00689.x.

Adamovich, A., Chejovich, V., 1964. Principales características de la geología y de los minerales útiles de la región nordeste de la Provincia de Oriente. Revista Tecnológica, 2, 14-20.

Agranier A., Lee C.-T. A., Li Z.-X. A., Leeman W. P., 2007. Fluid-mobile element budgets in serpentinized oceanic lithospheric mantle: insights from B, As, Li, Pb, PGEs and Os isotopes in the Feather River Ophiolite, California. Chemical Geology, 245, 230–241.

Angeli, N., Fleet, M.E., Thibault, Y., Candia, M.A.F., 2001. Metamorphism and PGE-Au content of chromitite from the Ipanema mafic/ultramafic Complex, Minas Gerais, Brazil. Mineralogy and Petrology, 71, 173–194.

Arai, S., 1992. Chemistry of chromian spinel in volcanic rocks as a potential guide to magma chemistry. Mineralogical Magazine, 56, 173–784.

Bailey S. W., 1980. Summary of recommendations of AIPEA nomenclature committee. Clay Minerals, 15, 85-93.

Batanova, V.G., Sobolev, A.V., 2000. Compositional heterogeneity in subduction-related mantle peridotites, Troodos massif, Cyprus. Geology, 28, 55–58.

Becker, H., Horan, M.F., Walker, R.J., Gao, S., Lorand, J.P., Rudnick, R.L., 2006. Highly siderophile element compositions of the earth's primitive mantle. Geochimica et Cosmochimica Acta, 70, 4528–4550.

Blanco-Quintero, I., García-Casco, A., Rojas Agramonte, Y., Rodríguez Vega, A., Lázaro, C., Iturralde-Vinent, M. A. Metamorphic evolution of subducted hot oceanic crust, La Corea mélange, Cuba. American Journal of Science. In press.

Boiteau, A., Michard, A., Saliot, P., 1972. Métamporphisme de haute pression dans le complexe ophiolitique du Purial (Oriente, Cuba). Comptes Rendus de l'Académie des Sciences, Série D 274, 2137–2140.

Capitani, G., Mellini, M., 2004.The modulated crystal structure of antigorite: The m = 17 polysome. American Mineralogist, 89, 147-158.

Capitani, G., Mellini, M., 2006. The crystal structure of a second antigorite polysome (m=16), by single-crystal synchrotron diffraction. American Mineralogist, 91, 394-399.

Chan, T.K., Finch, I.J., 2001. Determination of platinum-group elements and gold by inductively coupled plasma mass spectrometry. In: Australian Platinum Conference, Perth, Western Australia.

Cobiella, J., Campos M., Boiteau, A., Quintas, F., 1977. Geología del flanco sur de la Sierra del Purial. Revista La Minería de Cuba, 3, 54-62.

Connolly, J.A.D., 2005. Computation of phase equilibria by linear programming: a tool for geodynamic modeling and its application to subduction zone decarbonation. Earth and Planetary Science Letters, 236, 524–541.

Cressey, G., Cressey, B. A., Wicks, F. J., 2008. The significance of the aluminium content of a lizardite at the nanoscale: the role of clinochlore as an aluminium sink. Mineralogical Magazine, 72, 817–825.

D'Antonio, M.D., Kristensen, M.B., 2004. Hydrothermal alteration of oceanic crust in the West Philippine Sea Basin (Ocean Drilling Program Leg 195, Site 1201): inferences from a mineral chemistry investigation. Mineralogy and Petrology, 83(1–2), doi: 10.1007/s00710-004-0060-6.

Dick, H.J.B., Bullen, T., 1984. Chromian spinel as a petrogenetic indicator in abyssal and alpine-type peridotites and spatially associated lavas. Contributions to Mineralogy and Petrology, 86, 54–76.

Escartín, J., Andreani, M., Hirth, G. Evans, B., 2008. Relationships between the microstructural evolution and the rheology of talc at elevated pressures and temperatures. Earth and Planetary Science Letters, 268, 463–475.

Evans B. W., 2004. The serpentinite multisystem revisited: Chrysotile is metastable. International Geology Review, 46, 479–506.

Fonseca, E., Zelepugin, V.N., Heredia, M., 1985. Structure of the ophiolite association of Cuba. Geotectonic, 19, 321-329.

Frost, B.R., Beard, J. S., 2007. On silica activity and serpentinization. Journal of Petrology, 48, 1351-1368.

García-Casco, A., Torres-Roldán, R.L., Iturralde-Vinent M.A., Millán, G., Núñez Cambra, K., Lázaro, C., and Rodríguez Vega, A., 2006. High pressure metamorphism of ophiolites in Cuba. Geologica Acta, 4, 63–88.

García-Casco, A., Lázaro, C., Torres-Roldán, R. L., Núñez Cambra, K., Rojas Agramonte, Y., Kröner, A., Neubauer, F., Millán, G., Blanco-Quintero, I., 2008a. Partial melting and counterclockwise P-T path of subducted oceanic crust (Sierra del Convento mélange, Cuba). Journal of Petrology, 49, 129-161.

García-Casco, A., Iturralde-Vinent, M.A., Pindell, J., 2008b. Latest Cretaceous collision/accretion between the Caribbean Plate and Caribeana: Origin of metamorphic terranes in the Greater Antilles. International Geology Review, 50, 781-809.

Gervilla, F., Proenza, J.A., Frei, R., González-Jiménez, J.M., Garrido, C.J., Melgarejo, J.C., Meibom, A., Díaz-Martinez, R., Lavaut, W., 2005. Distribution of platinum-group elements and Os isotopes in chromite ores from Mayarí-Baracoa Ophiolitic Belt (eastern Cuba). Contribution to Mineralogy and Petrology, 150, 589–607.

Gerya, T.V., Stoeckhert, B., Perchuk, A.L., 2002. Exhumation of high-pressure metamorphic rocks in a subduction channel—a numerical simulation. Tectonics, 21, 6-1–6-19.

Gorczyk, W., Guillot, S., Gerya, T.V., Hattori, K.H., 2007. Asthenospheric upwelling, oceanic slab retreat and exhumation of UHP mantle rocks: Insights from Greater Antilles. Geophysical Research Letters 34, L21309, doi: 10.1029/2007GL031059.

Groves, D.I., Keays, R.R., 1979. Mobilisation of ore-forming elements during alteration of dunites, Mt Keith-Betheno, Western Australia. The Canadian Mineralogist, 17, 373–389.

Guillot, S. Hattori, K., Agard, P., Schwartz, S., Vidal, O., 2009. Exhumation processes in oceanic and continental subduction contexts: a review. In S. Lallemand and F. Funiciello (eds.) "Subduction Zone Dynamics", 175-204, doi 10.1007/978-3-540-87974-9, Springer-Verlag Berlin Heidelberg.

Hattori, K. H., Guillot S., 2007. Geochemical character of serpentinites associated with high- to ultrahigh-pressure metamorphic rocks in the Alps, Cuba, and the Himalayas: Recycling of elements in subduction zones. Geochemistry, Geophysics, Geosystems, 8, Q09010, doi:10.1029/2007GC001594.

Holland, T.J.B., Powell, R., 1996. Thermodynamics of order–disorder in minerals.2. Symmetric formalism applied to solid solutions. American Mineralogist, 81, 1425–1437.

Holland, T.J.B., Powell, R., 1998. An internally consistent thermodynamic data set for phases of petrological interest: Journal of Metamorphic Geology, 16, 309–343.

Holland, T.J.B., Baker, J., Powell, R., 1998. Mixing properties and activity-composition relationships of chlorites in the system MgO–FeO–Al2O3–SiO2–H2O. European Journal of Mineralogy, 10, 395–406.

Irvine, T.N., 1967. Chromian spinel as a petrogenetic indicator; Part II, Petrologic applications. Canadian Journal of Earth Sciences, 4, 71–103.

Iturralde-Vinent, M. A., 1998. Sinopsis de la Constitución Geológica de Cuba. Acta Geológica Hispánica, 33, 9-56.

Iturralde-Vinent, M.A., Díaz Otero, C., Rodríguez Vega, A., Díaz Martínez, R., 2006. Tectonic implications of paleontologic dating of Cretaceous–Danian sections of Eastern Cuba. Geologica Acta, 4, 89–102.

Iturralde-Vinent, M.A., Díaz Otero, C., García-Casco, A., Van Hinsbergen, D.J.J., 2008. Paleogene Foredeep Basin Deposits of North-Central Cuba: A Record of Arc-Continent Collision between the Caribbean and North American Plates. International Geology Review, 50, 863–884.

Jan, M.Q., Windley, B.F., 1990. Chromian spinel–silicate chemistry in ultramafic rocks of the Jijal Complex, Northwest Pakistan. Journal of Petrology, 31, 667–715.

Krebs, M., Maresch, W.V., Schertl, H.P., Baumann, A., Draper, G., Idleman, B., and Münker, C., 2008. The dynamics of intra-oceanic subduction zones: A direct comparison between fossil petrological evidence (Rio San Juan Complex, Dominican Republic) and numerical simulation: Lithos 103, 106-137.

Kretz, R., 1983. Symbols for rock-forming minerals. American Mineralogist 68, 277–279.

Lázaro, C., García-Casco, A., 2008. Geochemical and Sr-Nd isotope signatures of pristine slab melts and their residues (Sierra del Convento mélange, eastern Cuba: Chemical Geology, 255, 120-133.

Lázaro, C., García-Casco, A., Neubaurer, F., Rojas-Agramonte, Y., Kröner, A., Iturralde-Vinent, M.A., 2009. Fifty-five-million-year history of oceanic subduction and exhumation at the northern edge of the Caribbean plate (Sierra del Convento mélange, Cuba: Journal of Metamorphic Geology, 27, 19-40.

Le Maitre, R. W., Streckeisen, A., Zanettin, B., Le Bas, M. J., Bonin, B., Bateman, P., Bellieni, G., Dudeck, A., Efremova, S., Keller, J., Lameyre, J., Sabine, P.A., Schmid, R., Sorensen, H., Woolley, A. R., 2002. Igneous rocks. A Classification and Glossary of Terms. Recommendations of the International Union of Geological Sciences Subcommission on the Systematics of Igneous Rocks. 2nd Edition. Cambridge. Cambridge University Press, 252 pp.

Lewis, J.F., Draper, G., Proenza, J.A., Espaillat, J., Jimenez, J., 2006a. Ophiolite-Related Ultramafic Rocks (Serpentinites) in the Caribbean Region: A Review of their Occurrence, Composition, Origin, Emplacement and Ni-Laterite Soils Formation. Geologica Acta, 4, 237-263.

Lewis, J.F., Proenza, J.A., Jolly, W.T., Lidiak, E.G., 2006b. Monte del Estado (Puerto Rico) and Loma Caribe (Dominican Republic) peridotites: A look at two different Mesozoic mantle sections within northern Caribbean region. Geophysical Research Abstracts, 8, A-08798.

Li, X.-P., Rahn, M., Bucher, K., 2004. Serpentinites of the Zermatt-Saas ophiolite complex and their texture evolution: Journal of Metamorphic Geology, 22, 159-177.

Luguet, A., Lorand, J.P., Seyler, M., 2003. Sulfide petrology and highly siderophile element geochemistry of abyssal peridotites: a coupled study of samples from the Kane Fracture Zone (45 degrees W23 degrees 20 N, MARK Area, Atlantic Ocean). Geochimica et Cosmochimica Acta, 67 (8), 1553–1570.

Marchesi, C., Garrido, C. J., Godard, M., Proenza, J. A., Gervilla, F., Blanco-Moreno, J., 2006. Petrogenesis of highly depleted peridotites and gabbroic rocks from the Mayarí-Baracoa Ophiolitic Belt (eastern Cuba). Contributions to Mineralogy and Petrology, 151, 717-736.

Marchesi, C., Garrido, C.J., Bosch, D., Proenza, J.A., Gervilla, F., Monié, P., Rodríguez-Vega, A., 2007. Geochemistry of Cretaceous magmatism in eastern Cuba: recycling of North American continental sediments and implications for subduction polarity in the Greater Antilles Paleo-arc. Journal of Petrology, 48, 1813–1840.

Marchesi, C., Jolly, W.T., Lewis, J.F., Garrido, C.J., Proenza, J.A., Lidiak, E.G. Petrogenesis of fertile mantle peridotites from the Monte del Estado massif (southwest Puerto Rico): a preserved section of Proto-Caribbean lithospheric mantle?. Geologica Acta (this volume). Submitted.

McDonough, W. F., Sun, S.-s., 1995. The composition of the Earth. Chemical Geology, 120, 223-254.

Mellini, M., Trommsdorff, V., Compagnoni, R., 1987. Antigorite polysomatism : behaviour during progressive metamorphism. Contributions to Mineralogy and Petrology, 97, 147-155.

Mellini, M., Viti, C., 1994. Crystal structure of lizardite-1T from Elba, Italy. American Mineralogist, 79 1194-1198.

Millán, G., Somin, M.L., Díaz, C., 1985. Nuevos datos sobre la geología del macizo montañoso de la Sierra del Purial, Cuba Oriental. Reporte de Investigación del Instituto de Geología y Paleontología, 2, 52–74.

Morimoto, N., Fabries, J., Ferguson, A.K., Ginzburg, I.V., Ross, M., Seifeit, F.A., Zussman, J., 1989. Nomenclature of pyroxenes. Canadian Mineralogist, 27, 143-156.

Müntener, O., Hermann, J., 1994. Titanian andradite in a metapyroxenite layer from the Malenco ultramafics (Italy) – implications for Ti-mobility and low-oxygen fugacity. Contributions to Mineralogy and Petrology, 116, 156–168.

Nuñez Cambra, K.E., García-Casco, A., Iturralde-Vinent, M.A., Millán, G., 2004. Emplacement of the ophiolite complex in Eastern Cuba. Proceedings of the 32nd International Geological Congress, Florencia. Session: G20.11 Caribbean Plate Tectonics.

O'Hanley, D. S., 1996. Serpentinites Records of Tectonic and Petrological History. Oxford University Press, Oxford, 290 pp.

Padrón-Navarta J. A., Hermann J., Garrido C.J., López Sánchez-Vizcaíno V., Gómez-Pugnaire M. T., 2010. An experimental investigation of antigorite dehydration in natural silica-enriched serpentinite. Contributions to Mineralogy and Petrology, 159, 25-42.

Parkinson, I.J., Pearce, J.A., 1998. Peridotites of the Izu-Bonin-Mariana forearc (ODP Leg 125) evidence for mantle melting and melt–mantle interactions in a suprasubduction zone setting. Journal of Petrology, 39, 1577–1618.

Parkinson, I.J., Pearce, J.A., Thirwall, M.F., Johnson, K.T.M., Ingram, G., 1992. Trace element geochemistry of peridotites from the Izu-Bonin-Mariana forearc, Leg 125. In: Fryer P, Pearce JA, Stokking LB (eds) Proceedings of ODP science results, vol 125. Ocean Drilling Program, College Station, pp 487–506.

Pearce, J.A., Barker, P.F., Edwards, S.J., Parkinson, I.J., Leat, P.T., 2000. Geochemistry and tectonic significance of peridotites from the South Sandwich arc-basin system, south Atlantic. Contributions to Mineralogy and Petrology, 139, 36–53.

Pindell, J.L., Kennan, L., Maresch, W.V., Stanek, K.P., Draper, G., Higgs, R., 2005. Plate-kinematics and crustal dynamics of circum-Caribbean arc–continent interactions: Tectonic controls on basin development in Proto-Caribbean margins. In: Avé Lallemant, H.G., and Sisson, V.B., eds, Caribbean–South American Plate Interactions, Venezuela: Geological Society of America, Special Papers 394, p. 7–52.

Pindell, J. L, Kennan, L., Stanek, K. P., Maresch,W. V., Draper, G., 2006. Foundations of Gulf of Mexico and Caribbean evolution: eight controversies resolved. Geologica Acta, 4, 303-341.

Prichard, H.M., Tarkian, M., 1988. Platinum and palladium minerals from two PGE-rich localities in the Shetland Ophiolite Complex. The Canadian Mineralogist 26, 979–990.

Proenza, J., Gervilla, F., Melgarejo, J.C., Bodinier, J.L., 1999. Al- and Cr rich chromitites from the Mayarí-Baracoa Ophiolitic Belt (eastern Cuba): consequence of interaction between volatile-rich melts and peridotite in suprasubduction mantle. Economic Geology, 94, 547–566.

Proenza, J., Alfonso, J., Melgarejo, J.C., Gervilla, F., Tritlla, J., Fallick, A.E., 2003. D, O and C isotopes in podiform chromitites as fluid tracers for hydrothermal alteration processes of the Mayarí-Baracoa Ophiolitic Belt, eastern Cuba. Journal of Geochemical Exploration, 78–79, 117–122.

Proenza, J.A., Ortega-Guitiérrez, F., Camprubí, A., Tritlla, J., Elías-Herrera, M., Reyes-Salas, M., 2004. Paleozoic serpentinite-enclosed chromitites from Tehuitzingo (Acatlán) Complex, southern Mexico): a petrological and mineralogical study. Journal of. South American Earth Sciences, 16, 649-666.

Proenza, J.A., Díaz-Martínez, R., Iriondo, A., Marchesi, C., Melgarejo, J.C., Gervilla, F., Garrido, C.J., Rodríguez-Vega, A., Lozano-Santacruz, R., Blanco-Moreno, J.A., 2006. Primitive Cretaceous island-arc volcanic rocks in eastern Cuba: the Téneme Formation. Geologica Acta, 4, 103–121.

Saumur, B-M., Hattori, K. H., Guillot, S., 2010. Contrasting origins of serpentinites in a subduction complex, northern Dominican Republic. GSA Bulletin, 122, 292-304.

Snow, J.E., Reisberg, L., 1995. Os isotopic systematics of theMORB mantle: results from altered abyssal peridotites (vol 133, pg 411, 1995). Earth and Planetary Science Letters, 136(3–4): 723–733.

Somin, M.L., Millán, G., 1981. Geology of the Metamorphic Complexes of Cuba. Nauka: Moscow, 219 pp. (in Russian).

Torres-Roldán, R. L., García-Casco, A., García-Sánchez, P. A., 2000. CSpace: An integrated workplace for the graphical and algebraic analysis of phase assemblages on 32-bit Wintel platforms. Computers and Geosciences, 26, 779–793.

Ulmer, P., Trommsdorff, V., 1995. Serpentine stability to mantle depths and subduction-related magmatism. Science, 268, 858–861.

Wakabayashi, J., 1990. Counterclockwise P-T-t paths from amphibolites, Franciscan Complex, California: Relics from the early stages of subduction zone metamorphism. Journal of Geology, 98, 657 – 680.

Wicks, F.J. Whittaker, E.J.W. 1977. Serpentine textures and serpentinization. The Canadian Mineralogy. 15, 459-488.

7- SUBDUCTION OF YOUNG OCEANIC PLATES: A NUMERICAL STUDY WITH APPLICATION TO ABORTED COLD PLUMES (THEORICAL AND NATURAL)

I. F. Blanco-Quintero[(1)], A. García-Casco[(2)], and T. V. Gerya[(3)]

(1) Departamento de Mineralogía y Petrología, Universidad de Granada, Fuentenueva s/n, 18002-Granada, Spain

(2) Departamento de Mineralogía y Petrología, Instituto Andaluz de Ciencias de la Tierra, CSIC-Universidad de Granada, Fuentenueva s/n, 18002-Granada, Spain

(3) Department of Geosciences, Swiss Federal Institute of Technology, 8093 Zurich, Switzerland and Department of Geology, Moscow State University, 119899 Moscow, Russia

*E-mail address: blanco@ugr.es

ABSTRACT

Thermo-mechanical modelling was used to simulate subduction initiation of young (10-30 Ma) oceanic lithosphere. A 2D thermo-mechanical numerical model was developed using the I2VIS code based on conservative finite differences and non-diffusive marker-in-cell techniques. Experiments were carried out varying the age of the lithosphere (10, 12.5, 15, 17.5, 20, 25 and 30 Ma) and rate of convergence (2, 4 and 5 cm/yr) with a wet peridotite in the weak zone. Also a hydrated mantle was used in some experiments in the weak zone, producing premature melting of the weak rock below the serpentinite stability field (wet peridotite). It was found that the age of oceanic lithosphere strongly influences dehydration of subducted oceanic crust and underlying mantle peridotite and partial melting of the slab, which are favored for the younger lithospheres. Partial melting of the subducted slab creates cold plumes that ascend along the slab-mantle interface until they penetrate the upper plate lithosphere and produce volcanic arcs. The rate of convergence has, in turn, strong influence in the slab retreat, for very slow (ca. 2 cm/yr) and younger lithospheres (<20 Ma). The results confirm that the tectonic evolution and volcanism in eastern Cuba (NW Caribbean) during the Cretaceous was the result of onset of subduction of very young lithosphere (i.e. 10 Ma) with convergence rate of 2-4 cm/yr. The serpentinite mélanges present in this region can be considered as fragments of an aborted cold plume frozen at depth.

Keywords: Numerical modelling, young lithosphere, cold plumes

INTRODUCTION

Subduction zones and mid ocean spreading ridges are the most important tectonic features in planet Earth, with more than 55000 km and 60000 km of integrated length, respectively (Lallemand, 1999; Stern, 2002). The fate of lithosphere formed at ridges is to be recycled in the mantle by means of subduction. The geophysical characteristics of subduction zones are varied. The thermal structure and geodynamic conditions of subduction zones depend on factors like plate velocity, direction and angle of convergence, thickness and age of the lithosphere, convection in the overlying mantle wedge, fluids and melts migrating through the subduction zone, and time (e.g., Kirby et al., 1991; Peacock, 1996). All these factors influence in the formation of volcanic arcs, which ultimately contribute to the growing of continental masses.

The addition of aqueous fluids to normal lithospheric mantle produces partial melting at temperatures hundred degrees lower than under dry conditions (e.g., Ulmer, 2001). This addition takes place in convergent margins by means of dehydration of the subducting slab (crust and mantle) caused by increasing pressure and temperature. At the onset of subduction, the fluid released is primarily the result of the expulsion of connate water, but the oceanic crust contains about 6 wt % water in chlorite, lawsonite and amphibole (Iwamori, 1998). This amount is reduced to less than 3 wt % at 50 km depth by metamorphic dehydration reactions (Iwamori, 1998). The fluids released at depth have huge importance for mantle wedge melting and formation of volcanic arcs.

When a young (i.e. hot) oceanic plate subducts, the geothermal gradient involved in the slab-mantle wedge interface is hotter compared to the geothermal gradient generated upon subduction of an old (i.e. cold) plate, making possible the intersection of the wet solidus of basaltic and pelitic rocks at moderate pressure (e.g., 15 kbar; 50 km). Partial melting of the slab at shallow depths has important consequences for the transformation of the mantle wedge and the evolution of volcanic arcs (e.g., Peacock et al., 1994). The addition of the slab melt to the wedge occurs principally by means of cold plumes resulting from Rayleigh-Taylor instabilities (Gerya and Yuen, 2003a), which may have to do with adakite rocks formed as product of slab melting (Defant and Drummond, 1990; Martin, 1999).

Under special circumstances, however, the melt may crystallize at depth, yielding aborted cold plumes. These aborted plumes are of importance because they may be incorporated to developing subduction channels and exhumed, allowing the in-situ characterization of the products slab-derived melts (e.g., Lázaro and García-Casco, 2008). In this paper we study the onset of intra-oceanic subduction using different ages of lithosphere, convergent rates and rocks in the weak zone. To this end, we use a thermomechanical numerical model based on finite differences and marker-in-cell techniques (Gerya and Yuen, 2003b). The model includes spontaneous slab retreat, subducted crust dehydration, aqueous fluid transport and slab and mantle wedge melting. The results, specially those concerning the formation and evolution of cold plumes, are compared with rocks complexes occurring in the northern Caribbean (eastern Cuba), where onset of subduction and partial melting of very young oceanic lithosphere has been recently described in serpentinite mélanges representing fragments of the Cretaceous Antillean subduction channel (García-Casco et al.,

2008; Lázaro and García-Casco, 2008; Lázaro et al., 2009; Blanco-Quintero et al., 2010).

NUMERICAL MODEL DESCRIPTION AND PRINCIPAL EQUATIONS

We developed a 2D thermo-mechanical numerical model of onset of intra-oceanic subduction (Fig. 1) using the I2VIS code based on conservative finite differences and non-diffusive marker-in-cell techniques (Gerya and Yuen, 2003b). The experiments were conducted on Brutus computer cluster of ETH-Zurich. The model dimensions are 4000 km×200 km, distributed over 2001×201 grid nodes. The grid resolution is 2 km×1 km.

The oceanic crust consists of a 3-km layer of basalts and a 5-km layer of gabbroic rocks and the mantle consists of anhydrous peridotite. The lithospheric and asthenospheric mantle is modelled as anhydrous peridotite, extending as a half-space to the lower boundary of the model. This setup is complemented by 3 km of water above and 1 km of air. Sedimentation spontaneously fills the trench after its arc-ward slope reaches certain critical steepness.

Subduction is initiated by a prescribed weak fracture zone between two oceanic plates (Hall et al., 2003). This zone is 30 km wide and 60 km thick. It consists of mantle rocks with wet olivine rheology (Rannalli, 1995) and high pore fluid pressure. In the course of subduction, these mantle rocks are replaced by weak crustal rocks and hydrated mantle, naturally preserving the localizing effect of the initially prescribed fracture zone. However, some experiments were realized using hydrated peridotite in the weak zone (e.g., Regenauer-Lieb et al., 2001; Gerya and Yuen, 2003a; Maresch and Gerya, 2005; Table 1).

The initial temperature varies with the lithosphere age. The isotherm permit to better vizualize the slab and mantle wedge deformation. In the evolution of the model water is expelled from the subducted oceanic crust as a consequence of dehydration reactions and compaction. Because the water transport model does not permit complete hydration of the peridotitic mantle, the mantle solidus is intermediate between the wet and dry peridotite solidus. In reality variable hydration would permit melting over a range of temperatures and water contents (e.g., Grove et al., 2006).

Three principal equations were used in the two dimensional creeping-flow models (momentum, continuity, and thermal equations). The conservation of mass is approximated by the incompressible continuity equation:

$$\frac{\partial v_x}{\partial x} + \frac{\partial v_z}{\partial z} = 0$$

The 2D Stokes equations take the form:

$$\frac{\partial \sigma_{xx}}{\partial x} + \frac{\partial \sigma_{xz}}{\partial z} = \frac{\partial P}{\partial x}$$

$$\frac{\partial \sigma_{zz}}{\partial z} + \frac{\partial \sigma_{xz}}{\partial x} = \frac{\partial P}{\partial z} - g\rho(T,P,C)$$

The density $\rho(T,P,C)$ depends explicitly on the temperature (T), the pressure (P) and the composition (C), and g is the gravitational acceleration.

The Lagrangian temperature equation includes heat effects produced by phase transformations in the crust and mantle and is formulated as (Gerya and Yuen, 2003b):

$$\rho C_P\left(\frac{DT}{Dt}\right) = -\frac{\partial q_x}{\partial x} - \frac{\partial q_z}{\partial z} + H_r + H_a + H_S + H_L,$$

$$q_x = -k(T,C)\frac{\partial T}{\partial x}$$

$$q_z = -k(T,C)\frac{\partial T}{\partial z}$$

$$H_a = T\alpha\frac{DP}{Dt}$$

$$H_S = \sigma_{xx}\dot{\varepsilon}_{xx} + \sigma_{zz}\dot{\varepsilon}_{zz} + 2\sigma_{xz}\dot{\varepsilon}_{xz}$$

where D/Dt is the substantive time derivative; x and z denote, respectively, the horizontal and vertical coordinates; σ_{xx}, σ_{xz}, σ_{zz} are components of the deviatoric stress tensor; $\dot{\varepsilon}_{xx}$, $\dot{\varepsilon}_{xz}$, $\dot{\varepsilon}_{zz}$ are components of the strain rate tensor; P is pressure; T is temperature; qx and qz are heat fluxes; ρ is density; k(T,C) is the thermal conductivity, a function of composition and temperature; Cp is the isobaric heat capacity; Hr, Ha, HS and HL denote, the radioactive, adiabatic, shear and latent heat production, respectively.

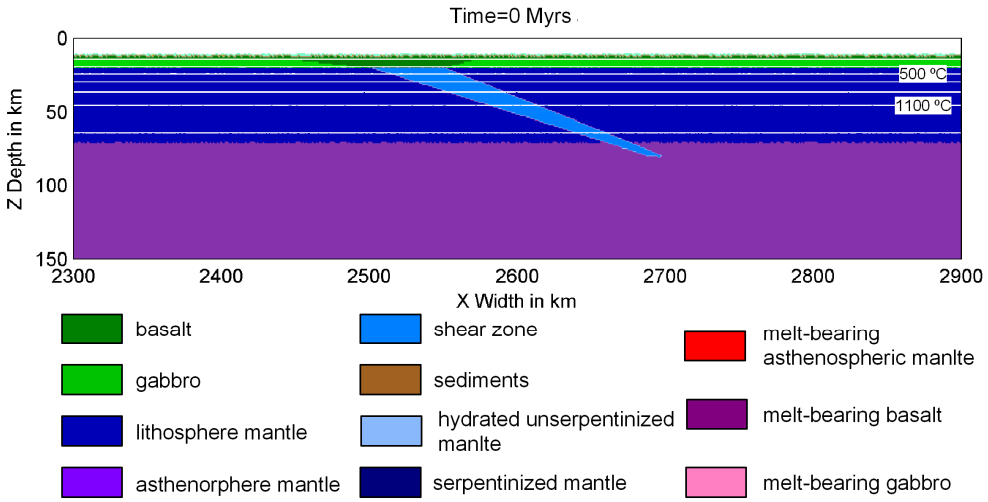

Figure1. Initial configuration of the numerical model (see text for details). White lines are isotherms shown for increments of 200 °C starting from 100 °C. Colors indicate materials (e.g. rock type or melt) which appear in subsequent figures. The resolution of the model: x= 3000 Km and z= 200 Km.

Table 1 Description of numerical experiments.

Model	Slab age	convergent rate (cm/yr)	rock type in weak zone
1	10	2	wet peridotite
2	12.5	2	wet peridotite
3	15	2	wet peridotite
4	17.5	2	wet peridotite
5	20	2	wet peridotite
6	25	2	wet peridotite
7	30	2	wet peridotite
8	10	4	wet peridotite
9	12.5	4	wet peridotite
10	15	4	wet peridotite
11	17.5	4	wet peridotite
12	20	4	wet peridotite
13	25	4	wet peridotite
14	30	4	wet peridotite
15	10	5	wet peridotite
16	12.5	5	wet peridotite
17	15	5	wet peridotite
18	17.5	5	wet peridotite
19	20	5	wet peridotite
20	25	5	wet peridotite
21	30	5	wet peridotite
22	10	5	hydrated mantle
23	12.5	5	hydrated mantle
24	15	5	hydrated mantle
25	17.5	5	hydrated mantle
26	20	5	hydrated mantle
27	25	5	hydrated mantle
28	30	5	hydrated mantle

In the experiments the melt migration is assumed that occur rapidly compared to the deformation of unmelted mantle, so that the velocity of the melt is independent of mantle dynamics (Elliott et al., 1997; Hawkesworth et al., 1997). So, the extracted melt is transported rapidly to the surface forming volcanic arc crust.

RESULTS

The numerical experiments were carried out varying the age of the subducting plate (10, 12.5, 15, 17.5, 20, 25 and 30 Myr), the rate of convergence (2, 4 and 5 cm/yr) and the rock properties of the weak zone (wet pertidotite vs hydrated mantle -serpentinite-) (Table 1).

Figure 2, constructed for a lithosphere of 10 Myr and a convergence rate of 5 cm/yr, summarizes the basic features of the evolution of all types of experiments, including the trenchward displacement and deformation of the overriding plate, the increase in the slab angle, the hydration of the mantle wedge (serpentinization) and development of subduction channels, the generation of molten rocks in the mantle wedge, the development of molten cold plumes and waves along the subduction zone, and the displacement of isotherms (cooling of the subduction zone, heating of the volcanic arc region) with time. The model produces a rapidly retreating trench with formation of a magmatic arc and extensional backarc basin with newly forming

Figure 2. Evolution of the reference model. The model presents a retreating subduction with the formation of a) partial melts in the slab, b) magmatic arc, c) an extensional backarc basin with newly-forming oceanic floor and onset of slab retreat; d) and e) evolution of the subduction zone. The age of the lithosphere is 10 Myr and convergence rate is 5 cm/yr).

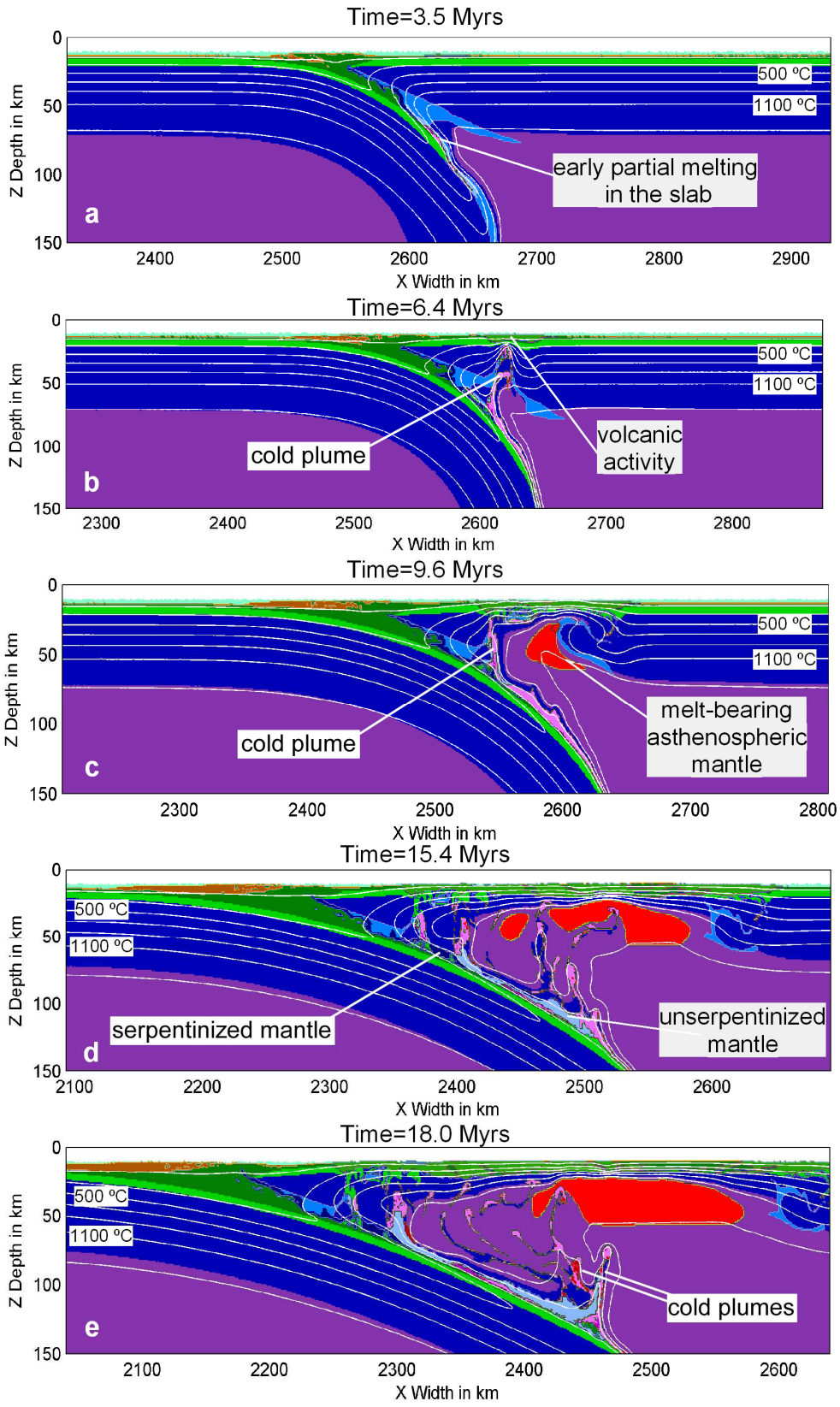
Time=3.5 Myrs
Z Depth in km
X Width in km
500 ºC
1100 ºC
early partial melting in the slab
a
Time=6.4 Myrs
cold plume
volcanic activity
b
Time=9.6 Myrs
cold plume
melt-bearing asthenospheric mantle
c
Time=15.4 Myrs
serpentinized mantle
unserpentinized mantle
d
Time=18.0 Myrs
cold plumes
e

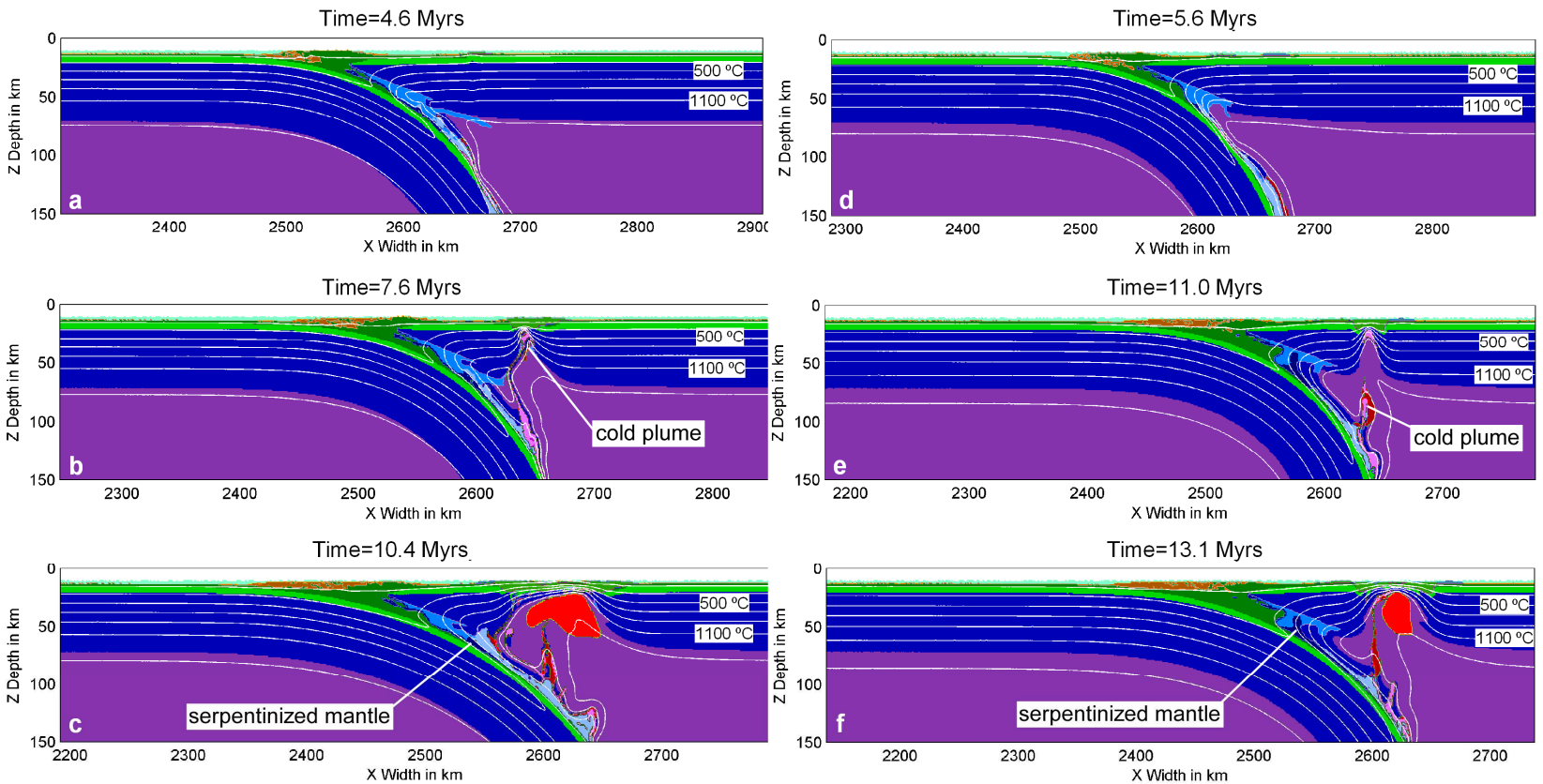

Figure 3. Snapshots from numerical experiments with different lithosphere age; a-c) younger oceanic lithosphere (12.5 Myr) and d-e) oceanic lithosphere of 15 Myr.

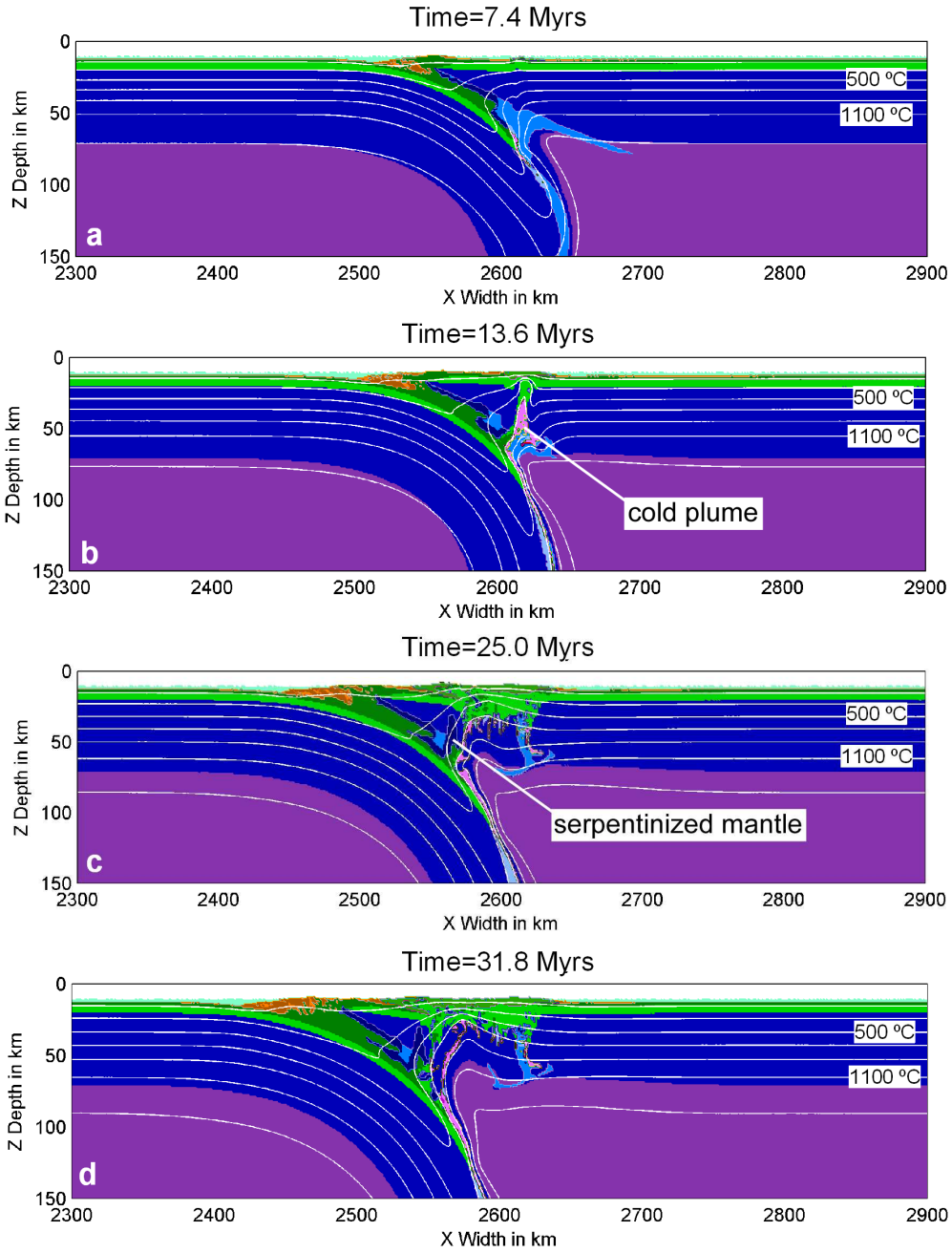

Figure 4. Numerical experiments with small convergence rate (2 cm/yr) and a lithosphere de 10 Myr. In these experiments, partial melting of the slab, formation of cold plumes and volcanic activity are delayed relative to faster convergence rates. No slab retreat and back arc formation is observed.

oceanic floor. When the subducting oceanic plate reaches approximately 50 km depth dehydration and fluid flow leads to hydration and wet melting of the mantle above the slab, in agreement with common views of evolution of subduction zones (Stern, 2002; van Keken et al., 2002). However, this process first produces

upwelling partially molten thermal-chemical plumes (Gerya and Yuen, 2003a) that rise from the slab along the slab-mantle interface until they penetrate the upper plate lithospheric mantle (Fig. 2b-e). These plumes are composed of mixed partially molten components from the subducted crust and the mantle wedge (Gerya and Yuen, 2003a; Gorczyk et al., 2007; Castro et al., 2010).

Rising of cold plumes lead to the growth of a magmatic arc at the surface of the overriding oceanic plate ~6 My after beginning of subduction (Fig. 2b). As the trench retreats the melt-bearing asthenosphere rises forming an intra-arc spreading centre leading to splitting of the arc and development of a remnant arc located trenchward and a back-arc basin (~10 Myr; Fig. 2c). The formation of a spreading center accelerates trench retreat since it breaks apart the overriding plate. The appearance of a melt-bearing mantle region below the spreading centre (cf. broad red region in Fig. 2c-e) is driven by decompression melting.

The age of the subducting lithosphere have strong influence in the evolution of the subduction zone (Fig. 3). For the same convergence rate, subduction of older lithosphere delays slab retreat, early partial melting of the slab and rise of cold plumes. This change in the timing of the events in the order of a few million years is observed even for small variations in the age of the lithosphere (Fig. 3; lithosphere ages of 12.5 Myr and 15 Myr; convergence rate 5 cm/yr). The volcanic activity is consequently affected, especially because the time needed for the dehydration of the slab and development of cold plumes is shortened for younger subducting lithosphere. Also the thermal-chemical plumes are rooted at greater depth in older lithosphere (Fig. 3f).

The rate of convergence between plates also influence in the evolution of the subduction zone. For smaller convergence rates (e.g., ca. 2 cm/yr) slab retreat is not produced (Fig. 4) for very young oceanic lithosphere (<20 Myr). However, probably the most important effect is related to partial melting of the slab and the beginning of volcanic arc activity, which are delayed (Fig 4a, b). Because the slab does not retreat in these models, the arc is constructed in the same vertical emplacement during more of 30 Myr after onset of subduction (Fig. 4d), producing large piles of volcanic rocks. In contrast, for older lithosphere (> 20 Ma) and small convergence rate (2 cm/yr) the model predicts subtle slab retreat, regional dispersion of volcanic arc products, and formation of a backarc spreading center (Fig. 5). In this experiment is important to note the greater depth of the isotherms, yielding slab melt and cold plume formation at greater depth.

In modern slow to very slow-spreading ridges the lithosphere is characterized by a heterogeneous and relatively thin (<5 to 7 km) crust which exposes partially hydrated peridotites (Cannat, 1993; Cannat et al., 1995). In these lithospheres the mafic rocks are partially covered by abyssal sediments far from the ridge (Carlson, 2001). To evaluate the influence of this type of lithosphere, experiments were carry up for a weak zone composed of hydrated peridotite. In these experiments, partial melting of the weak rock below the antigorite stability field (wet peridotite) takes place shortly after onset of subduction (Fig. 6a). However, melt volume is small and is dissipated in the mantle (Fig. 6b). After this early stage, the evolution of the subduction system follows a normal regime as described above. However, the volcanic arc activity occurs later than other experiments (Fig. 6c) and, importantly, a

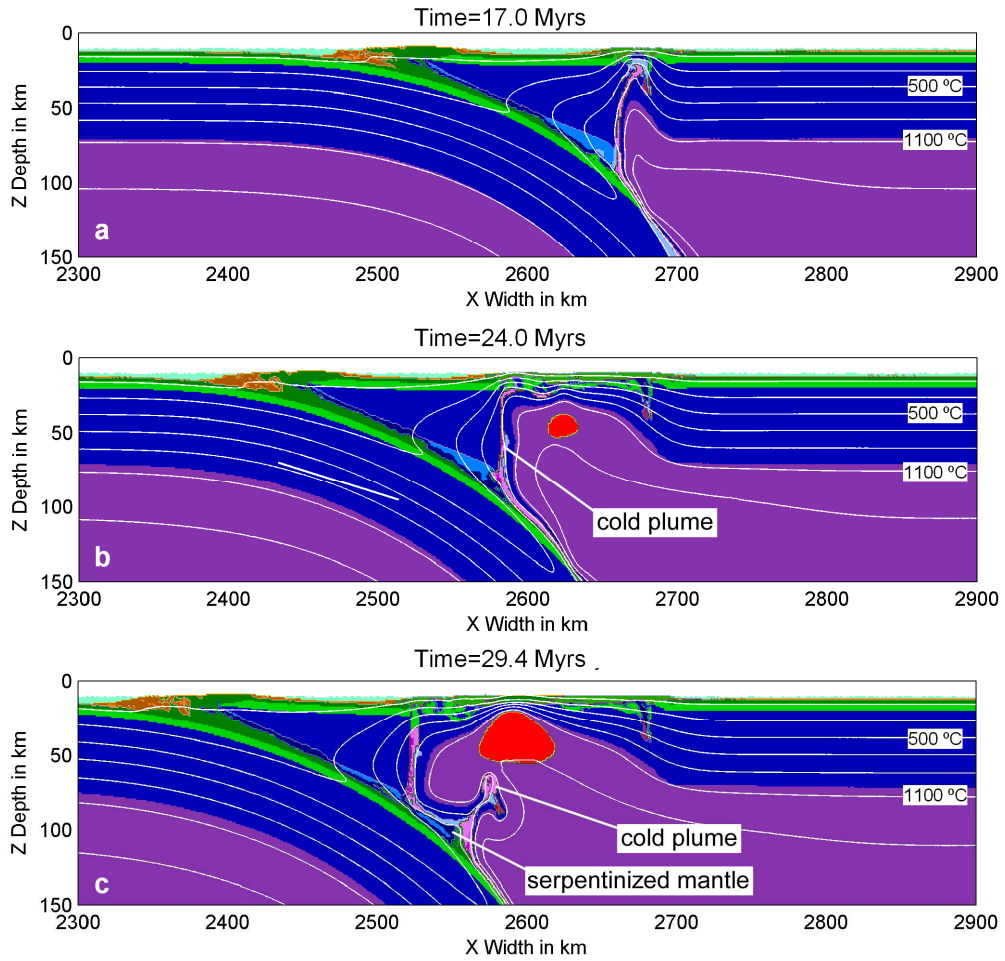

Figure 5. Numerical experiments with small convergence rate (2 cm/yr) and a lithosphere of 25 Myr. Slab retreat and backarc spreading occur relatively late.

large serpentinized mantle (subduction channel) is formed above the slab (Fig. 6d, e) due to large fluid flux from the hydrated peridotite.

Finally, models for very young lithosphere yield small melt fractions in the partially molten slab at moderate depth and relatively low temperature. This setting allow for crystallization of the cold plume at depth. This is illustrated in Fig. 7 for a lithosphere of 10 Myr and a convergence rate of 4 cm/yr. In this experiment, the low proportions of melt produced preclude the rise of the plume through mantle, and the cooling of the system upon continued subduction leads to crystallization of the melt at depth close to the region where the plume nucleated at the slab-mantle wedge interface (50-60 km; Fig. 7). We name this type of plumes crystallized at depth as aborted cold plumes.

DISCUSSION

The subduction of very young oceanic lithosphere and ridges is a normal process of active margins (e.g., Thorkelson and Breitsprecher, 2005). The thermal structure and melting of young subducted slabs was modelled by Peacock et al. (1994), and

Peacock (1996) provided a general conceptual model for melting of young oceanic crust, although in these models melting occurs only for very young crust (< 5 Myr; Peacock, 1996). Subduction of very young oceanic lithosphere has been also linked to the generation of adakites, based on geochemical data (e.g., Defant and Drummond, 1990; Martin, 1999) and numerical models (e.g., Sizova et al., 2010). The data compiled by Drummond and Defant (1990), summarizing adakite occurrences, suggest that melting occurs in slabs as old as 20 Myr.

Our experiments indicate that partial melting occurs in slabs as old as 20-30 Myrs, though it occurs earlier and at shallower depths in younger slabs, determining the evolution of volcanic arcs and back-arc basins. Hydrated partially molten thermal-chemical plumes are responsible for the heterogeneous composition of the mantle wedge and influence the composition of the volcanic arc crust (Gerya and Yuen, 2003a; Gorczyk et al., 2007; Castro et al., 2010).

However, we have also shown that under special circumstances cold plumes may crystallize at depth in the slab-wedge region shortly after onset of subduction. These plumes have no influence on the evolution of the upper plate mantle and arc crust, but this type of aborted cold plumes may offer important information on the partial melting processes attending subduction if exhumed to the Earth's surface. Exhumation of this type of plumes if favored by the fact that they freeze at relatively shallow depth (ca. 50 km) and, importantly, at the slab-wedge interface, where a serpentinitic subduction channel generated with time provides the mechanism for syn-subduction exhumation of accreted material (Gerya et al., 2002). An example of partially melted subducted oceanic material incorporated in a subduction channel is found in the Catalina Schists of the Franciscan belt (Sorensen and Barton, 1987; Sorensen, 1988; Sorensen and Grossman, 1989; Bebout and Barton, 2002). However, a more spectacular example, with larger proportion of melt, has been recently described in the serpentinitic mélanges of eastern Cuba (Sierra del Convento and La Corea mélanges; García-Casco et al., 2008; Lázaro and García-Casco, 2008; Lázaro et al., 2009; Blanco-Quintero et al., 2010).

Comparing a theoretical and a natural aborted cold plume (eastern Cuba).

A belt of Cretaceous-Tertiary volcanic arc rocks occurring all along the entire Caribbean region, from Guatemala, Greater, Lesser, Leeward and Netherland Antilles, northern Venezuela and north and western Colombia (collectively termed "Great Arc of the Caribbean"; Burke, 1988) document a long lasting history of oceanic subduction in this region. Ophiolitic materials of back-arc, arc, fore-arc and abyssal origin are also represented along the belt (for review see Lewis et al., 2006) Associated with these rocks appear serpentinite matrix mélanges with tectonic high-pressure blocks that represent the associated Caribbean subduction channel. Cold, warm and hot subduction has been inferred from petrological studies of these mélanges (e.g., García-Casco et al., 2002; 2006; 2008; Tsujimori et al., 2005, 2006; Krebs et al., 2008; Brueckner et al. 2009; Maresch et al. 2009).

Figure 6. Numerical experiments with the weak zone composed of hydrated peridotite, age of lithosphere of 10 Myr, and convergence rate of 5 cm/yr.

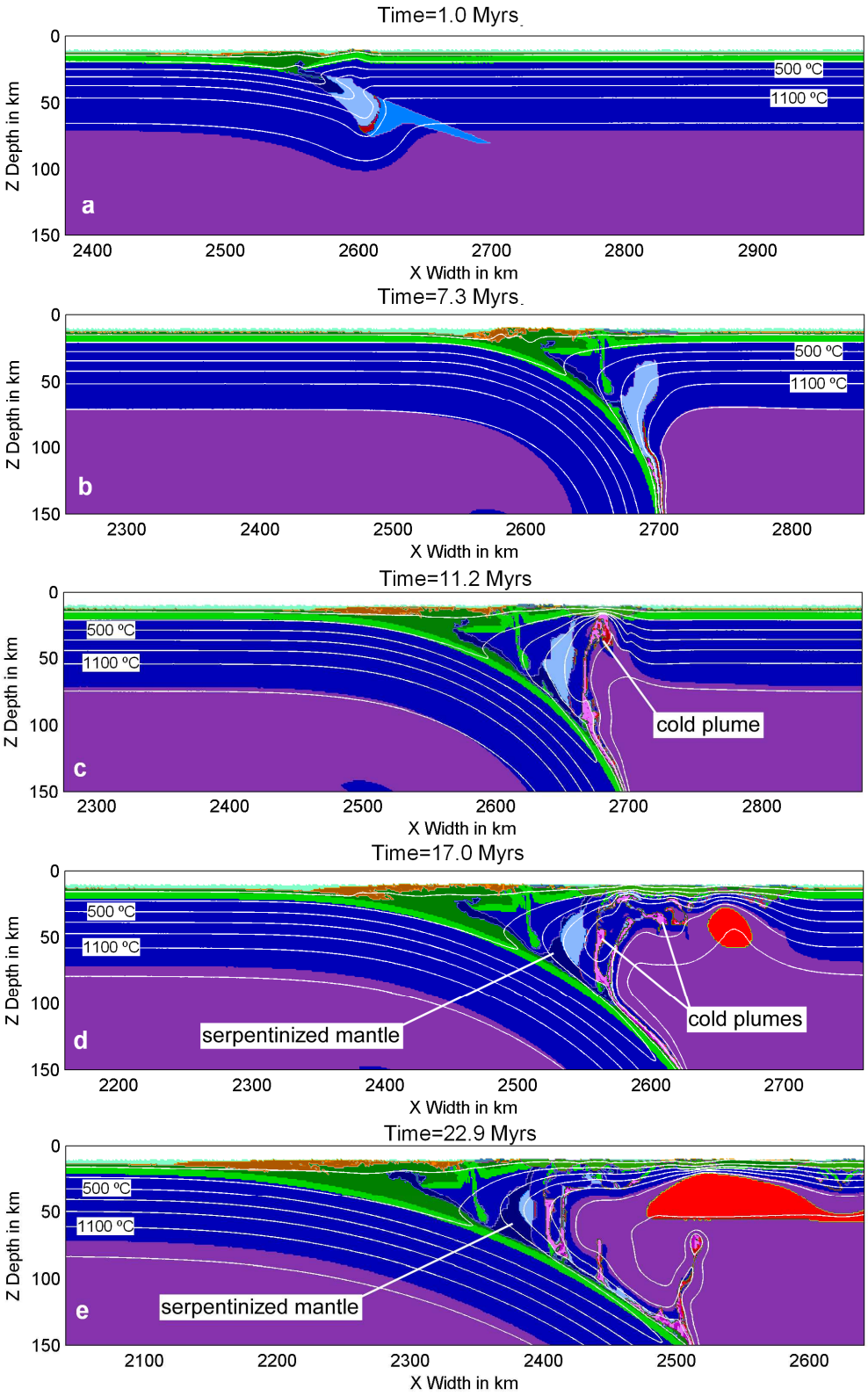
Time=1.0 Myrs
Z Depth in km
X Width in km
500 ºC
1100 ºC
a
Time=7.3 Myrs
b
Time=11.2 Myrs
cold plume
c
Time=17.0 Myrs
serpentinized mantle
cold plumes
d
Time=22.9 Myrs
serpentinized mantle
e

In eastern Cuba, the mélanges (La Corea and Sierra del Convento; Somin and Millán, 1981; García-Casco et al., 2006) bear evidence for hot subduction interpreted as the result of onset of subduction of young oceanic lithosphere (García-Casco et al., 2008; Lázaro and García-Casco, 2008; Lázaro et al., 2009; Blanco-Quintero et al., 2010). These mélanges are characterized by the presence of subducted MORB-derived epidote±garnet amphibolite blocks associated with tonalitic-trondhjemitic-granitic bodies and veins generated after partial melting of the amphibolites and crystallized at depth (ca. 50 km; 15 kbar; 700-750 ºC). The rocks followed counter-clockwise P-T paths documenting subduction shortly after onset of subduction and syn-subduction slow exhumation in a subduction channel.

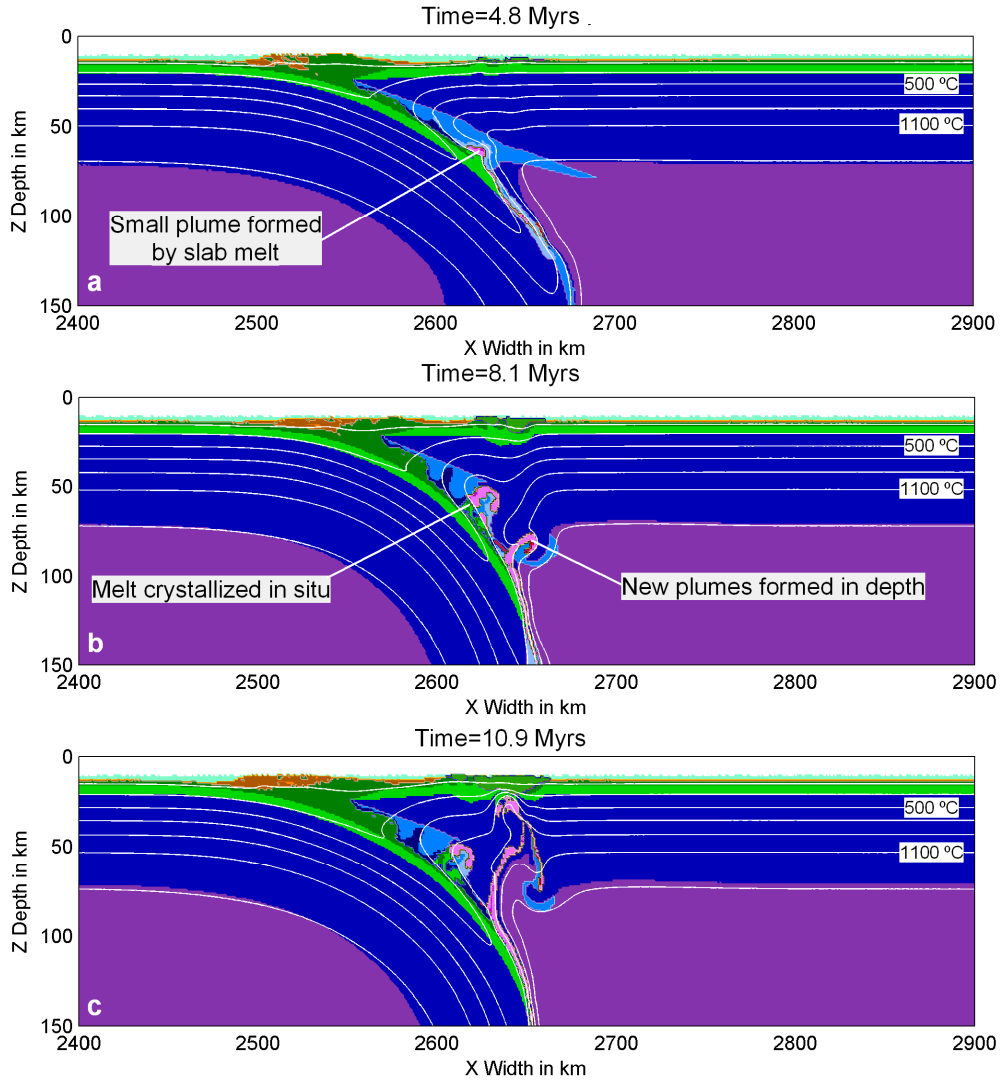

Figure 7. Example of an aborted cold plume due to low melt production. The experiment represents a lithosphere of 10 Myr with a convergence rate of at 4 cm/yr.

Following our results of numerical experiments (i.e., Fig. 7), we consider these blocks of high-grade amphibolite and associated leucocratic igneous rocks as possible fragments of an aborted cold plume incorporated into the Caribbean subduction channel.

Subduction rates for the Caribbean region during the Cretaceous have been estimated in the order of 2-4 cm/yr. (Meschede and Frisch, 1998; Krebs et al., 2008, and references therein). These figures are in agreement with our models, for they allow slab retreat and backarc basin formation, and petrological and geochemical data have shown that Mayarí-Baracoa Ophiolitic Belt of eastern Cuba formed at a back-arc spreading centre (Marchesi et al., 2006). Furthermore, subduction of hot young oceanic lithosphere during the Cretaceous is incorporated in geodynamic models for the region (Pindell and Kennan, 2009), for subduction involved the Proto-Caribbean basin (Atlantic), which was opening at that time due to N America and S A drift, and subduction of a ridge was possible. Subduction of such a young lithosphere is hence possible. Accordingly, we consider the model presented in Fig. 7 involving subduction of very young oceanic lithosphere (10 Myr) at a rate of 4 cm/yr as potentially feasible for eastern Cuba, and the predicted formation of an aborted cold plume as an analogue of the partially melted slab rocks found in eastern Cuba mélanges.

CONCLUSIONS

Thermo-mechanical experiments were used to model intra-oceanic subduction initiation. Experiments were carried out varying the age of the lithosphere from 10 to 30 Ma and convergence rate from 2 to 5 cm/a, influencing slab retreat and back-arc basin and formation and evolution. The volcanic arc crust initially forms as a response of intrusion of cold plumes into the upper plate lithosphere and evolves influenced by decompression melting of rising asthenosphere. Partial melting of subducted material and volcanic arc activity is delayed for very low convergence rates. Experiments for subduction of very young lithosphere (i.e. 10 Ma) at relative low convergence rate 4 cm/a allow formation aborted cold plumes in the slab-mantle interface. These theoretical aborted cold plumes may correspond to Cretaceous partially melted MORB-derived slab material and associated tonalitic-trondhjemitic rocks crystallized at depth in the slab-mantle interface and exhumed in a subduction channel (serpentinite mélanges) in eastern Cuba.

ACKNOWLEDGEMENTS

Blanco-Quintero would like to thanks E. Sizova and Y. Mishin for provision of visualization routines, basic instructions and help during the stay in the ETH. We appreciate financial support from Spanish MCINN project CGL2009-12446 and support from Swiss National Science Foundation research grants 200020_129487, 200020_126832 and Swiss Federal Institute of Technology research grants ETH-06 09-2, ETH-08 07-2 to TVG. This is a contribution to IGCP-546 “Subduction zones of the Caribbean”. Blanco-Quintero is supported by grant AP2005-5258 from the ‘‘Programa de Formación del Profesorado Universitario’’ of the Spanish Ministry of Education and Science.

REFERENCES

Bebout, G.E., Barton, M.D., 2002. Tectonic and metasomatic mixing in a high-T, subduction-zone mélange insights into the geochemical evolution of the slab-mantle interface. Chemical Geology 187, 79-106.

Blanco-Quintero, I.F., García-Casco, A., Rojas-Agramonte, Y., Rodríguez-Vega, A., Lázaro, C., Iturralde-Vinent, M.A., 2010. Metamorphic evolution of subducted hot oceanic crust, La Corea mélange, Cuba. American Journal of Science (in press).

Brueckner H.K., Avé Lallemant H.G., Sisson V.B., Harlow G.E., Hemming S.R., Martens U., Tsujimori T., Sorensen S.S., 2009. Metamorphic reworking of a high pressure–low temperature mélange along the Motagua fault, Guatemala: A record of Neocomian and Maastrichtian transpressional tectonics. Earth and Planetary Science Letters 284, 228–235.

Burke, K., 1988, Tectonic evolution of the Caribbean. Annual Review of Earth and Planetary Sciences 16, 210–230.

Cannat, M., 1993. Emplacement of mantle rocks in the sea-floor at mid-ocean ridges. Journal of Geophysical Research 98, 4163–4172.

Cannat, M., Mevel, C., Maia, M., Deplus, C., Durand, C., Gente, P., Agrinier, P., Belarouchi, A., Dubuisson, G., Humler, E., Reynolds, J., 1995. Thin crust, ultramafic exposures, and rugged faulting patterns at Mid-Atlantic Ridge (22º–24ºN). Geology 23, 49–52.

Carlson, R.L., 2001. Lower crustal water contents, P-wave velocities, and modal mineralogy of oceanic diabase and gabbro, Eos Transactions AGU, 82, 1154.

Castro, A., Gerya, T.V., García-Casco, A., Fernández, C., Diaz-Alvarado, J., Moreno-Ventas, I., Löw. I., 2010. Melting relations of MORB-sediment mélanges in underplated mantle wedge plumes. Implications for the origin of cordilleran-type batholiths. Journal of Petrology 51, 1267-1295.

Defant, M.J., Drummond, M.S., 1990. Derivation of some modern arc magmas by melting of young subducted lithosphere. Nature 347 (6294), 662–665.

Drummond, M.S., Defant, M.J., 1990. A model for trondhjemite-tonalite-dacite genesis and crustal growth via slab melting; archean to modern comparisons. Journal of Geophysical Research 95, 21503–21521.

Elliott, T., Plank, T., Zindler, A., Wjite, W., Bourdon, B.,1997. Element transport from slab to volcanic front at the Mariana arc. Journal of Geophysical Research 102,14991–15019.

García-Casco, A., Torres-Roldán, R.L., Millán, G., Monié, P., Schneider, J., 2002. Oscillatory zoning in eclogitic garnet and amphibole, Northern Serpentinite Melange, Cuba: a record of tectonic instability during subduction?. Journal of Metamorphic Geology 20, 581–598.

García-Casco, A., Torres-Roldán, R.L., Iturralde-Vinent, M.A., Millán, G., Núñez Cambra, K., Lázaro, C., Rodríguez Vega, A., 2006. High pressure metamorphism of ophiolites in Cuba. Geologica Acta 4, 63–88.

García-Casco, A., Lázaro, C., Rojas-Agramonte, Y., Kröner, A., Torres-Roldán, R.L., Núñez, K., Millán, G., Neubauer, F., Blanco-Quintero, I., 2008. Partial melting and counterclockwise P-T path of subducted oceanic crust (Sierra del Convento mélange, Cuba). Journal of Petrology 49, 129-161.

Gerya, T.V., Yuen, D.A., 2003a. Rayleigh–Taylor instabilities from hydration and melting propel cold plumes at subduction zones. Earth and Planetary Science Letters 212, 47–62.

Gerya, T.V., Yuen, D.A., 2003b. Characteristics-based marker-in-cell method with conservative finite-differences schemes for modelling geological flows with strongly variable transport properties. Physics of the Earth and Planetary Interiors 140, 295–320.

Gerya, T.V., Stoeckhert, B., Perchuk, A.L., 2002. Exhumation of high-pressure metamorphic rocks in a subduction channel-a numerical simulation. Tectonics 21, 6–1–6–19.

Gorczyk, W., Gerya, T.V., Connolly, J.A.D., Yuen, D.A., 2007. Growth and mixing dynamics of mantle wedge plumes. Geology 35, 587–590.

Grove, T.L., Chatterjee, N., Parman, S.W., Medard, E., 2006. The influence of H2O on mantle wedge melting. Earth and Planetary Science Letters 249, 74–89.

Hall, C.E., Gurnis, M., Sdrolias, M., Lavier, L.L., Muller, R.D., 2003. Catastrophic initiation of subduction following forced convergence across fracture zones. Earth and Planetary Science Letter 212, 15–30.

Hawkesworth, C.J., Turner, S.P., McDermott, F., Peate, D.W., van Calsteren, P., 1997. U–Th isotopes in arc magmas: implications for element transfer from the subducted crust. Science 276, 551–555.

Iwamori, H., 1998. Transportation of H2O and melting in subduction zones. Earth and Planetary Science Letters 160 (1-2), 65-80.

Kirby, S.H., Durham, W.B., Stern, L.A., 1991. Mantle phase changes and deep-earthquake faulting in subducting lithosphere. Science 252, 216–225.

Krebs, M., Maresch, W.V., Schertl, H.P., Baumann, A., Draper, G., Idleman, B., Münker, C., 2008. The dynamics of intra-oceanic subduction zones: A direct comparison between fossil petrological evidence (Rio San Juan Complex, Dominican Republic) and numerical simulation. Lithos 103, 106-137.

Lallemand, S., 1999. La Subduction Oceanique. Gordon and Breach, Newark, N. J.

Lázaro, C., García-Casco, A., 2008. Geochemical and Sr-Nd isotope signatures of pristine slab melts and their residues (Sierra del Convento mélange, eastern Cuba). Chemical Geology 255, 120-133.

Lázaro, C., García-Casco, A., Neubaurer, F., Rojas-Agramonte, Y., Kröner, A., Iturralde-Vinent, M.A., 2009. Fifty-five-million-year history of oceanic subduction and exhumation at the northern edge of the Caribbean plate (Sierra del Convento mélange, Cuba). Journal of Metamorphic Geology 27, 19-40.

Lewis, J.F., Draper, G., Proenza, J.A., Espaillat, J., Jimenez, J., 2006. Ophiolite-Related Ultramafic Rocks (Serpentinites) in the Caribbean Region: A Review of their Occurrence, Composition, Origin, Emplacement and Ni-Laterite Soils Formation. Geologica Acta, 4, 237-263.

Marchesi, C., Garrido, C.J., Godard, M., Proenza, J.A., Gervilla, F., Blanco-Moreno, J., 2006. Petrogenesis of highly depleted peridotites and gabbroic rocks from the Mayarí-Baracoa Ophiolitic Belt (eastern Cuba). Contributions to Mineralogy and Petrology 151, 717-736.

Maresch, W.V., Gerya, T.V., 2005. Blueschists and blue amphiboles: how much subduction do they need?. International Geology Review 47, 688–702.

Maresch, W. V., Kluge, R., Baumann, A. Pindell, J.L, Krückhans-Lueder, G., Stanek, K., 2009. The occurrence and timing of high-pressure metamorphism on Margarita Island, Venezuela: a constraint on Caribbean-South America interaction. In: James, K.H., Lorente, M.A., Pindell, J.L., eds. The Origin and Evolution of the Caribbean Plate. Geological Society of London, Special Publications, 328, 705–741.

Martin, H., 1999. The adakitic magmas: modern analogues of Archaean granitoids. Lithos 46(3), 411–429.

Meschede, M., Frisch W., 1998. A plate-tectonic model for the Mesozoic and Early Cenozoic history of the Caribbean plate. Tectonophysics 296, 269–291.

Peacock, S.M., 1996. Thermal and petrologic structure of subduction zones. In: Bebout, G.E., School, D., Kirby, S., eds., Subduction: Top to Bottom. American Geophysical Union Geophysical Monograph 96, 119-133.

Peacock, S.M., Rushmer, T., Thompson, A.B., 1994. Partial melting of subducting oceanic crust. Earth and Planetary Science Letters 121, 227– 244.

Pindell, J., Kennan, L., 2009. Tectonic evolution of the Gulf of Mexico, Caribbean and northern South America in the mantle reference frame: an update. In: James, K. H., Lorente, M. A., Pindell, J. L., eds. The Origin and Evolution of the Caribbean Plate. Geological Society of London, Special Publications 328, 1–55.

Ranalli, G., 1995. Rheology of the Earth. Chapman and Hall, London, 413.

Regenauer-Lieb, K., Yuen, D.A., Branlund, J., 2001. The initiation of subduction: Criticality by addition of water?. Science 294, 578–580.

Sizova, E., Gerya, T., Brown, M., Perchuk, L., 2010. Subduction styles in the Precambrian: insight from numerical experiments. Lithos 116, 209–229.

Somin, M., Millán, G., 1981. Geology of the Metamorphic Complexes of Cuba (in russian). Nauka, Moscow.

Sorensen, S.S., 1988. Petrology of amphibolite-facies mafic and ultramafic rocks from the Catalina Schist, Southern California: metasomatism and migmatization in a subduction zone metamorphic setting. Journal of Metamorphic Geology 6, 405-435.

Sorensen, S.S., Barton, M.D., 1987. Metasomatism and partial melting in a subduction complex: Catalina Schist, southern California. Geology 15, 115-118.

Sorensen, S.S., Grossman, J.N., 1989. Enrichment in trace elements in garnet amphibolites from a paleo-subduction zone: Catalina Schist, southern California. Geochimica et Cosmochimica Acta 53, 3155-3177.

Stern, R.J., 2002, Subduction zones. Reviews of Geophysics 40, 1012, doi: 10.1029/2001RG000108.

Thorkelson, D.J., Breitsprecher, K., 2005. Partial melting of slab window margins: genesis of adakitic and non-adakitic magmas. Lithos 79, 25-41.

Tsujimori, T., Liou, J.G., Coleman, R.G., 2005. Coexisting retrograde jadeite and omphacite in a jadeite-bearing lawsonite eclogite from the Motagua fault zone, Guatemala. American Mineralogist 90, 836–842.

Tsujimori, T., Sisson, V.B., Liou, J.G., Harlow, G.E., Sorensen, S.S., 2006. Petrologic characterization of Guatemalan lawsonite–eclogite: direct information on eclogitization of subducted oceanic crust in a cold subduction zone. In: Hacker, B.H., McClelland, W.C., Liou, J.G. (Eds.), Ultrahigh-Pressure Metamorphism: Deep Continental Subduction. Geological Society of America, Special Paper 403, 147–168.

Ulmer, P., 2001. Partial melting in the mantle wedge-the role of H2O in the genesis of mantle-derived 'arc-related' magmas. Physics of the Earth and Planetary Interiors 127, 215–232.

van Keken, P.E., Kiefer, B., and Peacock, S.M., 2002, High-resolution models of subduction zones: Implications for mineral dehydration reactions and the transport of water into the deep mantle. Geochemistry, Geophysics, Geosystems 3, 1056, doi: 10.1029/2001GC000256.

CONCLUSIONS

The La Corea mélange (eastern Cuba) gives the opportunity to study the processes that occur in a subduction environment from onset of subduction to exhumation in a subduction channel. The mélange has a metaharzburgitic antigorite-serpentinite matrix and contains exotic blocks manly composed of amphibolite, blueschist and greenschist. The most common lithology of the blocks is MORB-derived epidote±garnet amphibolite (lacking primary plagioclase) intimately associated with tonalitic-trondhjemitic-granitic rocks formed after partial melting of the former. Metamorphism evolved from high to medium pressure (700 ºC and 15 kbar; >110 Ma), above the wet basaltic solidus and related to subduction and accretion to the upper plate mantle, to medium to low temperature (450 ºC and 8-10 kbar; 83-86 Ma), indicating counterclockwise P-T paths during exhumation in the serpentinitic subduction channel. The geochronologic data indicate very slow (ca. 1 mm/yr) syn-subduction exhumation of the mélange. Occasionally, some blocks experienced large-scale convective circulation in the channel, first described in this work. The melt (mostly peraluminous in composition) crystallized at depth during the isobaric cooling stage (620-680 ºC and 14-15 kbar; 105-110 Ma), before the serpentintic channel started formation.

The geochemistry of the leucocratic rocks indicates adakite affinity, without interaction between the melt and the ultrabasic materials (i.e., mélange matrix). HP blocks of amphibolite and associated trondhjemites, pegmatites and Qtz+Ms rocks locally show enrichment in LILE (specially in K and Ba), indicating interaction with fluids released from the sediments of the subducting slab. In these rocks phengite crystallized at depth, preventing the transfer of K, Ba and other LILE to the mantle wedge and the volcanic arc.

Ultramafic blocks bearing relictic clinopyroxene porphyroblasts appear also in the mélange. The blocks are harzburgitic-lherzolitic in composition and were classified as antigorite-lizardite serpentinites. The protolith of these rocks are best explained as a fragment of the abyssal peridotite (incoming plate) incorporate to the mantle wedge and exhumed in the subduction channel.

Partial melting of a subducted young oceanic lithosphere is an exceptional characteristic rarely observed in exhumed subduction-related complexes, and has significant consequences for the plate tectonic interpretation of the Caribbean region. The counterclockwise paths and the P-T conditions for slab melting are in correspondence with predictions of thermo-mechanical models for onset of subduction of young oceanic lithosphere. These models also confirm that exhumation of HP blocks occurs several tens of Ma after onset of subduction due to sepentinization of the mantle wedge (Caribbean lithosphere) by fluids derived from the SW-dipping subducted slab (Protocaribbean lithosphere). As a result of this process, a subduction channel containing blocks of the subducting plate (crustal and mantle) surrounded by antigorite serpentinite matrix formed. The process included several stages, including onset of subduction (ca. 120 Ma), accretion of subducted MORB to the upper plate hydrous peridotite (115 Ma), isobaric cooling (115-105 Ma), formation of the channel and very slow exhumation (105-70 Ma), and final exhumation (70-65 Ma) as result of collision in the region.

CONCLUSIONES

La mélange de La Corea (Cuba oriental) brinda la oportunidad de estudiar los procesos que ocurren en un ambiente de subducción desde el inicio de la subducción hasta la exhumación en un canal de subducción. La mélange tiene una matriz (metaharzburgítica) de serpentinita antigoritítica y contiene bloques exóticos compuestos principalmente por anfibolitas, esquistos azules y esquistos verdes. La litología más común son bloques anfibolíticos, de composición MORB, con epidota±granate (con ausencia de plagioclasa primaria) íntimamente asociados a rocas tonalíticas-trondhjemíticas-graníticas formadas por la fusión parcial de las anfibolitas. El metamorfismo se desarrolló desde presiones altas a medias (700 ºC y 15 kbar; >110 Ma), por encima del solidus basáltico hidratado y relacionados con la subducción y acreción al manto de la placa superior, hasta temperaturas de medias a bajas (450 ºC y 8-10 kbar; 83-86 Ma), indicando trayectorias P-T antihorarias durante la exhumación en el canal de subducción serpentinítico. Los datos geocronológicos indican una exhumación sin-subducción de la mélange muy lenta (ca. 1 mm/a) en el canal de subducción. Ocasionalmente, algunos bloques indican circulación convectiva en el canal, descrita por primera vez en este trabajo. El fundido (principalmente de composición peraluminoso) cristalizó en profundidad durante un enfriamiento isobárico (620-680 ºC y 14-15 kbar; 105-110 Ma), antes de que comenzara a formarse el canal de subducción.

La geoquímica de las rocas leucocráticas indica afinidad adakítica, sin interacción del fundido con materiales ultrabásicos (la matriz de la mélange). Algunos bloques de anfibolitas de alta presión y las trondhjemitas, pegmatitas y rocas de Qtz+Ms asociadas presentan enriquecimiento en LILE (especialmente K y Ba) indicando alteración del material producido por fluidos derivados de los sedimentos de la corteza oceánica subducida. En estas rocas la fengita cristalizó en profundidad, impidiendo la transferencia del K, Ba y otros LILE al manto superior y al arco volcánico.

Bloques ultramáficos con profidoblastos relictos de clinopiroxeno aparecen también en la mélange. Los bloques son serpentinitas con antigorita-lizardita de composición harzburgítica-lherzolítica . El protolito de estas rocas corresponde a fragmentos de peridotita abisal (placa subducente) incorporados al manto suprasubducción y exhumados en el canal de subducción.

La fusión parcial de una litosfera joven en Cuba oriental es una característica excepcional raramente observada en complejos exhumados relacionados con la subducción, y tiene consecuencias significativas para la interpretación de la tectónica de placas en la región. Las trayectorias antihorarias y las condiciones de P-T para la fusión de la placa subducente están en correspondencia con la predicción de los modelos termo-mecánicos para el inicio de la subducción de una litosfera joven. Estos modelos también confirman que la exhumación de los bloques de alta presión ocurrió algunos millones de años después de iniciada la subducción debido a la serpentinización del manto superior (litosfera del Caribe) por los fluidos derivados de la placa subducente con buzamiento SO (litosfera del Protocaribe). Como resultado de este proceso, se formó un canal de subducción que contenía bloques de la placa subducente (corteza y manto) rodeados de una matriz de serpentinita con antigorita. El proceso incluye varias etapas, incluyendo el inicio de la subducción (ca. 120 Ma), la acreción de las rocas MORB subducidas a la placa superior formada por peridotita hidratada (115 Ma), un enfriamiento isobárico (115-105 Ma), la formación del canal de subducción y una exhumación muy lenta (105-70 Ma), y la exhumación final (70-65 Ma) como resultado de la colisión en la región.

APPENDIX

JOURNAL OF PETROLOGY | VOLUME 49 | NUMBER 1 | PAGES 129–161 | 2008 | doi:10.1093/petrology/egm074

Partial Melting and Counterclockwise *P–T* Path of Subducted Oceanic Crust (Sierra del Convento Mélange, Cuba)

ANTONIO GARCÍA-CASCO[1]*, CONCEPCIÓN LÁZARO[1], YAMIRKA ROJAS-AGRAMONTE[2], ALFRED KRÖNER[2], RAFAEL LUÍS TORRES-ROLDÁN[1], KENYA NÚÑEZ[3], FRANZ NEUBAUER[4], GUILLERMO MILLÁN[3] AND IDAEL BLANCO-QUINTERO[1,5]

[1]DEPARTAMENTO DE MINERALOGÍA Y PETROLOGÍA, UNIVERSIDAD DE GRANADA, AVDA. FUENTENUEVA SN, 18002 GRANADA, SPAIN

[2]INSTITUT FÜR GEOWISSENSCHAFTEN, UNIVERSITÄT MAINZ, 55099 MAINZ, GERMANY

[3]INSTITUTO DE GEOLOGÍA Y PALEONTOLOGÍA, VIA BLANCA Y CARRETERA CENTRAL, SAN MIGUEL DEL PADRÓN, 11000 CIUDAD HABANA, CUBA

[4]FACHBEREICH GEOGRAPHIE, GEOLOGIE UND MINERALOGIE, UNIVERSITÄT SALZBURG, HELLBRUNNER STRASSE 34, A-5020 SALZBURG, AUSTRIA

[5]DEPARTAMENTO DE GEOLOGÍA, INSTITUTO SUPERIOR MINERO-METALÚRGICO, LAS COLORADAS DE MOA, HOLGUÍN, CUBA

RECEIVED FEBRUARY 8, 2007; ACCEPTED OCTOBER 29, 2007
ADVANCE ACCESS PUBLICATION DECEMBER 4, 2007

Partial melting of subducted oceanic crust has been identified in the Sierra del Convento mélange (Cuba). This serpentinite-matrix mélange contains blocks of mid-ocean ridge basalt (MORB)-derived plagioclase-lacking epidote ± garnet amphibolite intimately associated with peraluminous trondhjemitic–tonalitic rocks. Field relations, major element bulk-rock compositions, mineral assemblages, peak metamorphic conditions (c. 750°C, 14–16 kbar), experimental evidence, and theoretical phase relations support formation of the trondhjemitic–tonalitic rocks by wet melting of subducted amphibolites. Phase relations and mass-balance calculations indicate eutectic- and peritectic-like melting reactions characterized by large stoichiometric coefficients of reactant plagioclase and suggest that this phase was completely consumed upon melting. The magmatic assemblages of the trondhjemitic–tonalitic melts, consisting of plagioclase, quartz, epidote, ± paragonite, ± pargasite, and ± kyanite, crystallized at depth (14–15 kbar). The peraluminous composition of the melts is consistent with experimental evidence, explains the presence of magmatic paragonite and (relict) kyanite, and places important constraints on the interpretation of slab-derived magmatic rocks. Calculated P–T *conditions indicate counterclockwise* P–T *paths during exhumation, when retrograde blueschist-facies overprints, composed of combinations of omphacite, glaucophane, actinolite, tremolite, paragonite, lawsonite, albite, (clino)zoisite, chlorite, pumpellyite and phengite, were formed in the amphibolites and trondhjemites. Partial melting of subducted oceanic crust in eastern Cuba is unique in the Caribbean realm and has important consequences for the plate-tectonic interpretation of the region, as it supports a scenario of onset of subduction of a young oceanic lithosphere during the early Cretaceous (c. 120 Ma). The counterclockwise* P–T *paths were caused by ensuing exhumation during continued subduction.*

KEY WORDS: *amphibolite; Cuba; exhumation; partial melting; trondhjemite; subduction*

*Corresponding author. Telephone: +34 958 246613. Fax: +34 958 243368. E-mail: agcasco@ugr.es

INTRODUCTION

Formation and consumption of oceanic lithosphere at ridges and trenches, respectively, are the most important geodynamic processes that cause energy and material recycling (transfer) between the lithosphere and mantle. Subduction consumes lithosphere that sinks into the mantle, but material fractionated into fluids or/and melts formed at various depths in the subducting slab is transferred to the mantle wedge, eventually triggering partial melting of ultramafic material and the formation of volcanic arcs. Because material deeply subducted to sub-arc depths of 100–200 km rarely returns to the surface (Ernst, 1999), deciding whether fluids or melts are formed at sub-arc depths is a matter of geochemical inference, experimental work, and thermal modelling. Fluid fluxing out of the subducting slab is generally considered to be the main control for material transport to, and melting of peridotite in, the mantle wedge (e.g. Schmidt & Poli, 1998; Stern, 2002; Grove *et al.*, 2006, and references therein). However, geochemical data (e.g. Defant & Drummond, 1990; Drummond *et al.*, 1996; Stolz *et al.*, 1996; Elliott *et al.*, 1997), thermal modelling (e.g. Peacock *et al.*, 1994; van Keken *et al.* 2002; Gerya & Yuen, 2003; Peacock, 2003; Kincaid & Griffiths, 2004; Conder, 2005; Abers *et al.*, 2006), and experimental studies (e.g. Johnson & Plank, 1999; Prouteau *et al.*, 200l; Kessel *et al.*, 2005; Hermann *et al*, 2006) have shown that partial melting of subducted sedimentary and/or mafic oceanic crust plays a major role in transferring matter from the slab to the mantle wedge. However, although partial melting of subducted slabs may be a common phenomenon, natural examples of partially molten subduction complexes returned to the Earth's surface are rare.

The amphibolite blocks of the 'Catalina Schist' mélange, California, constitute perhaps the best-known example of exhumed fragments of subducted oceanic crust where partial melting and metasomatic mass-transfer processes took place during subduction and accretion to the upper plate mantle (Sorensen & Barton, 1987; Sorensen, 1988; Sorensen & Grossman, 1989; Bebout & Barton, 2002). The study of these processes in this and other complexes is thus critical to unravel the geochemical evolution of the subduction factory (Bebout, 2007). Here we examine partial melting processes of subducted oceanic mafic crust in the Sierra del Convento serpentinite mélange, eastern Cuba, which represents a subduction channel related to Mesozoic subduction on the northern margin of the Caribbean plate (García-Casco *et al.*, 2006). We present descriptions of field relations, mineral assemblages and textures, and major element compositions of rocks and minerals, as well as P–T estimates for the various stages of evolution of amphibolites and their partial melting trondhjemitic–tonalitic products. These data are used to derive petrogenetic and tectonic models of formation.

GEOLOGICAL OVERVIEW

Geodynamic setting

Cuba forms part of the circum-Caribbean orogenic belt, which extends from Guatemala through the Greater and Lesser Antilles to northern South America (Fig. 1a). The belt encompasses the active volcanic arc of the Lesser Antilles, where the Atlantic lithosphere subducts below the Caribbean plate. However, Cretaceous to Tertiary volcanic-arc rocks all along the belt (Fig. 1a) document a long-lasting history of subduction on this margin of the Caribbean plate. Although the details of the Mesozoic evolution of this plate margin are debated (see Iturralde-Vinent & Lidiak, 2006; Pindell *et al.*, 2005, 2006), geological and geophysical data indicate that the arc probably occupied a position between the Americas, similar to that of the present-day Central American Arc, during the early Cretaceous. This implies that the Caribbean plate formed in the western Pacific and drifted eastwards relative to the Americas during the Mesozoic and Tertiary (Pindell *et al.*, 2005). As a consequence of this drift, the volcanic arc finally collided with the continental margins of North America and South America during the latest Cretaceous–Tertiary.

Eastward drift of the Caribbean plate began in the Aptian (*c.* 120 Ma; Pindell *et al.* 2005), when westward subduction of the Protocaribbean (i.e. Atlantic) also began. Ocean- and continent-derived high-pressure rocks found all along the edges of the Caribbean plate formed during the early Cretaceous to Tertiary and trace the history of subduction in the region (see review by Pindell *et al.*, 2005; also García-Casco *et al.*, 2002, 2006; Harlow *et al.*, 2004; Escuder-Viruete & Pérez-Estaún, 2006; Krebs *et al.*, 2007). In Cuba, metamorphic rocks documenting subduction and accretion of oceanic crust during the Cretaceous are found in serpentinite mélanges associated with ophiolitic tectonic units (collectively termed 'northern ophiolite belt'; Iturralde-Vinent, 1996, 1998) distributed east–west along the >1000 km length of the island (Somin & Millán, 198l; Millán, 1996; García-Casco *et al.*, 2002, 2006; Fig. 1b). Based on an analysis of ages and P–T paths of metamorphic blocks from these mélanges, García-Casco *et al.* (2006) proposed that hot subduction related to Aptian onset of subduction of the Protocaribbean is recorded in the eastern Cuba mélanges. The rocks described in this paper come from one of these mélanges located in the Sierra del Convento (Fig. 1c).

Geological setting

The geology of Eastern Cuba is characterized by large amounts of volcanic arc and ophiolitic materials. The ophiolite bodies (Mayarí–Cristal and Moa–Baracoa; Fig. 1b) were grouped in the 'eastern Cuba ophiolites' by Iturralde-Vinent *et al.* (2006) to emphasize their geological–petrological differences with respect to the

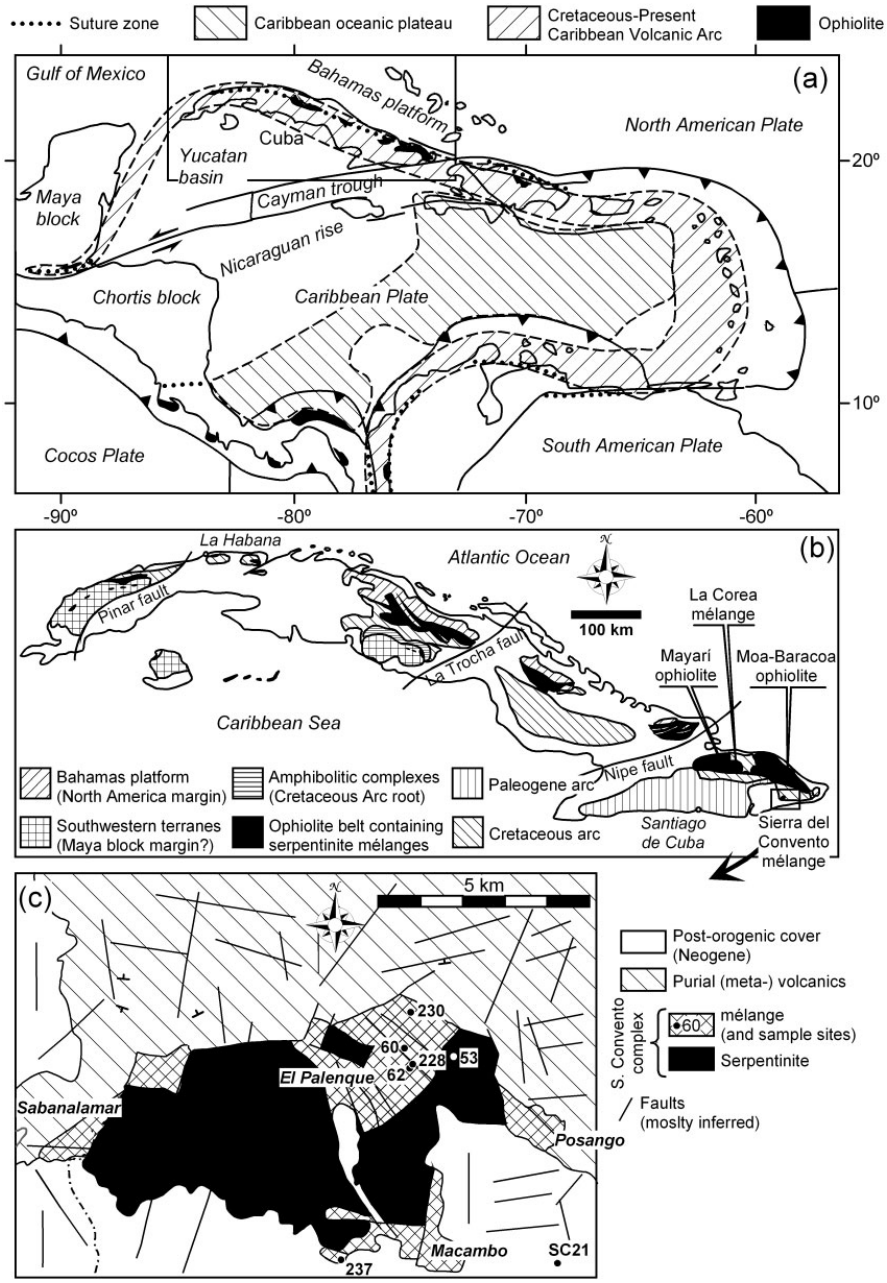

Fig. 1. (a) Plate-tectonic configuration of the Caribbean region, with important geological features including ophiolitic bodies and Cretaceous–Tertiary suture zones. (b) Geological sketch map of Cuba (after Iturralde-Vinent, 1998) showing location of the northern ophiolite belt, other important geological elements mentioned in the text, and the study area. (c) Simplified geological map of the Sierra del Convento mélange (Kulachkov & Leyva, 1990) showing sample localities.

'northern ophiolite belt' of west–central Cuba. The former have geochemical supra-subduction signatures (Proenza *et al.*, 2006; Marchesi *et al.*, 2007) and override Cretaceous volcanic arc complexes along north-directed thrusts. Thrusting occurred during the late Cretaceous to earliest Paleocene (Cobiella *et al.*, 1984; Iturralde-Vinent *et al.*, 2006). This structural arrangement differs from that of west–central Cuba, where the volcanic arc units override the northern ophiolite belt units. Another important difference with respect to west–central Cuba is that the volcanic arc units of eastern Cuba are locally metamorphosed to the blueschist facies (Purial Complex; Boiteau *et al.*, 1972; Somin & Millán, 1981; Cobiella *et al.*, 1984; Millán & Somin, 1985). This type of metamorphism, dated as late Cretaceous (*c.* 75 Ma; Somin *et al.*, 1992; Iturralde-Vinent *et al.*, 2006), documents subduction of the volcanic arc terrane as the result of a complicated plate-tectonic configuration (García-Casco *et al.*, 2006) or subduction erosion processes (J. Pindell, personal communication, 2006). Platform-like Mesozoic sedimentary rocks forming the Asuncion terrane were also metamorphosed under high-P low-T conditions (Millán *et al.*, 1985), but the timing of metamorphism is unknown.

The Sierra del Convento and La Corea mélanges (Fig. 1b) occur at the base of the ophiolite bodies of eastern Cuba, overriding the volcanic arc complexes. The two mélanges are similar and contain subduction-related metamorphic blocks of blueschist and epidote-garnet amphibolite; eclogite is rare or absent. Available K–Ar mineral and whole-rock ages in these mélanges are 125–66 and 116–82 Ma in La Corea and Sierra del Convento, respectively (Somin *et al.*, 1992; Iturralde-Vinent *et al.*, 1996; Millán, 1996, and references therein). These data and our unpublished Ar/Ar and sensitive high-resolution ion microprobe (SHRIMP) zircon ages (ranging from 114 to 83 Ma) from the Sierra del Convento mélange demonstrate that the history of subduction in eastern Cuba can be traced from the early Cretaceous (Aptian) to the late Cretaceous.

The Sierra del Convento mélange

The Sierra del Convento mélange is located in the south of eastern Cuba (Fig. 1b). It is tectonically emplaced on top of the Purial metavolcanic arc complex. The geology of the region is poorly known, and detailed structural and petrologic analysis is lacking. Basic field and petrographic descriptions were provided by Boiteau *et al.* (1972), Somin & Millán (1981), Cobiella *et al.* (1984), Kulachkov & Leyva (1990), Hernández & Canedo (1995), Leyva (1996), and Millán (1996).

The field relationships of the mélange are obscured by intense weathering, tropical vegetation, and recent fracturing related to important post-Eocene activity along the sinistral transcurrent Oriente Fault that connects the Puerto Rico trench with the Cayman trough (Rojas-Agramonte *et al.*, 2005, and references therein). The mélange is made of sheared serpentinite formed by hydration of harzburgite. It lacks exotic bocks in its central and topographically highest portion (maximum height 755 m). Towards its borders, however, exotic blocks occur, forming four submélange bodies of kilometre-scale, namely (Fig. 1c) Posango (to the east), El Palenque (to the north), Sabanalamar (to the west), and Macambo (to the south). Our field observations suggest that these submélange bodies occur at the base of the Sierra del Convento mélange, in contact with the underlying volcanic arc Purial Complex.

These submélange bodies are similar and contain low-grade tectonic blocks of metabasite, metagreywacke, metapelite–semipelite, and pelitic gneiss metamorphosed to the blueschist facies with greenschist-facies overprints. The submélange bodies also contain blocks of metabasites that have been metamorphosed to the epidote–amphibolite facies. These are the 'high-grade' amphibolite blocks described below. Our unpublished trace element analyses of the high-grade blocks show normal mid-ocean ridge basalt (N-MORB) signatures, indicating subducted oceanic lithosphere, as opposed to other low-grade blocks of metabasite, metagreywacke and metapelite–semipelite, which represent metamorphosed volcanic-arc derived rocks of the Purial Complex.

Importantly, the high-grade amphibolite blocks are made of plagioclase-lacking peak mineral assemblages consisting of pargasite, epidote, ± quartz, ± garnet, ± clinopyroxene (the last is rare). The white material seen in the matrix of these rocks (e.g. Fig. 2a and b, except for the leucocratic segregations) is not plagioclase but epidote. Following the common usage and recent recommendations of the IUGS Subcommission on the Systematics of Metamorphic Rocks (Coutinho *et al.*, 2007) the lack of peak metamorphic plagioclase prevents use of the term amphibolite to name these rocks. On the other hand, the abundance of epidote prevents use of the term hornblendite, which would also convey a wrong connotation. Thus, the term amphibolite is used here to name the studied rocks although their mineral assemblages do not conform to its classical use for rocks made of amphibole and plagioclase.

Another prominent petrological feature of the Sierra del Convento mélange is the intimate association of amphibolite with centimetre- to metre-sized layers, pockets and veins of trondhjemite–tonalite (Fig. 2). The nature and origin of these rocks has not been addressed in detail. Somin & Millán (1981) and Millán (1996) suggested that they represent ophiolitic plagiogranite pods formed during differentiation of MOR gabbros, which were later subducted and metamorphosed together with the enclosing mafic rocks. In contrast, Hernández & Canedo (1995) suggested that the leucocratic material is post-metamorphic

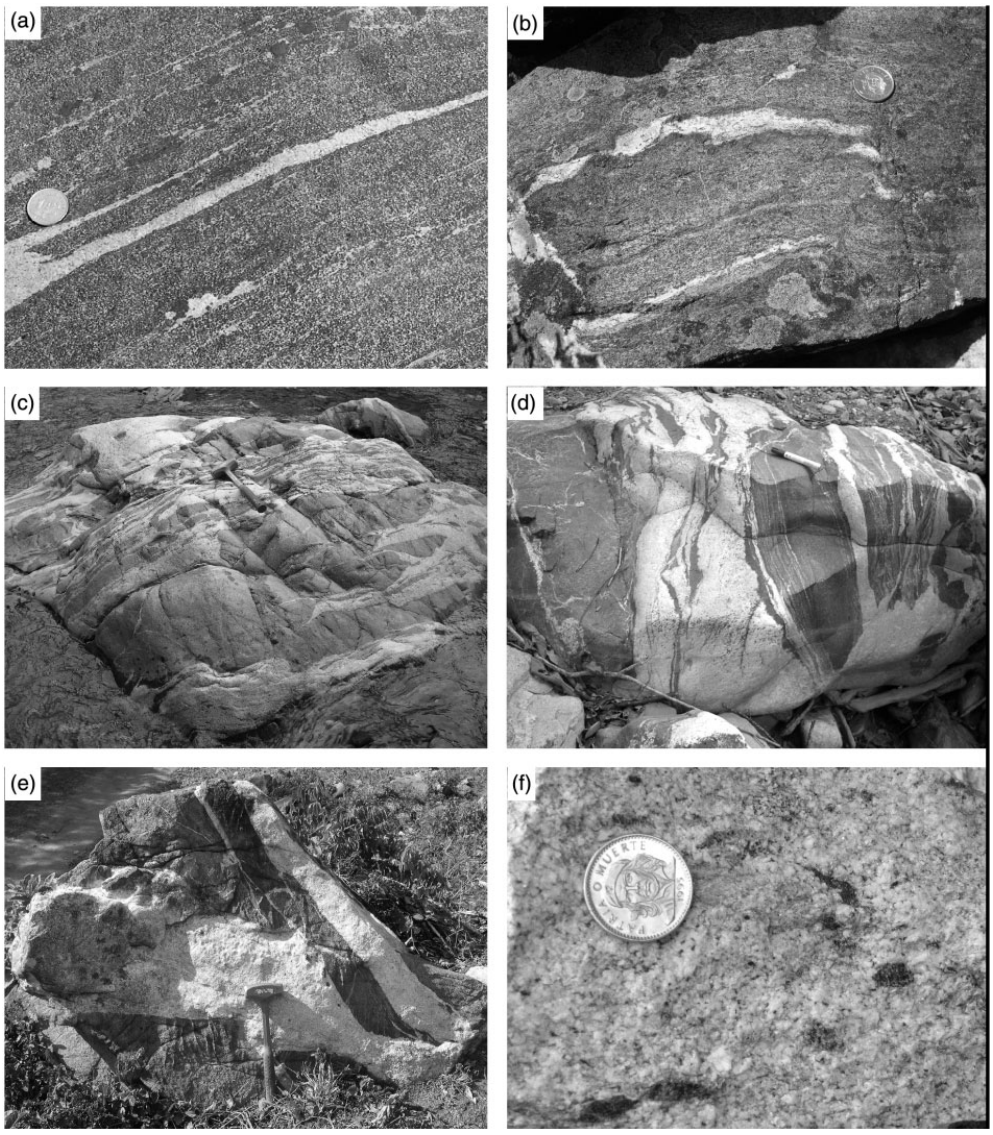

Fig. 2. Field relations of amphibolite blocks and associated tonalite–trondhjemite. (a) Banded amphibolite hosting sheared veins of trondhjemite. (b) Banded structure in migmatitic amphibolite showing hornblendite bands adjacent to trondhjemite segregation. (c) Block of amphibolite invaded by trondhjemite. Intrusion is ductile and contemporaneous with the main foliation of amphibolite. (d) Detail of block of amphibolite invaded by trondhjemite. (e) Brittle intrusion of trondhjemite into amphibolite forming agmatitic structure. (f) Detail of trondhjemite containing small enclaves of amphibolite and hornblendite. Shining crystals of paragonite stand out of the leucocratic groundmass.

and identified it as material of the Cretaceous volcanic arc intruding the mélange. Based on field relations, Kulachkov & Leyva (1990) and Leyva (1996) conceded that there is a genetic relationship between the amphibolites and the leucocratic material but did not indicate the type of relationship. In this paper we concentrate on these high-grade amphibolite blocks and associated trondhjemitic–tonalitic rocks.

FIELD RELATIONSHIPS

The high-grade blocks of amphibolite are of metre to tens of metres size, medium- to coarse-grained, and massive to banded (Fig. 2a-c). In the Macambo region, however, the blocks appear to be larger. In the Palenque region the amphibolites form discrete blocks, commonly metre-sized. This region provides the largest amount of leucocratic material intimately associated with the amphibolites. In the Posango and Sabanalamar regions the blocks are best observed as detrital material forming part of recent alluvial deposits along the Yacabo and Sabanalamar rivers rather than as tectonic blocks within serpentinite.

The tonalitic–trondhjemitic bodies are of centimetre to metre size. They are exclusively associated with the amphibolites and not with other types of exotic blocks within the mélange, and do not appear to crosscut the serpentinite matrix. The structure of the bodies varies from concordant layers to crosscutting veins relative to the metamorphic foliation of the amphibolites. Banded, stromatic, vein-like, and agmatitic structures typical of migmatites are common (Fig. 2a–e).

The banded structure is characterized by the association of mesosome (Ep ± Grt amphibolite) and leucosome (trondhjemite–tonalite) parallel to the main syn-metamorphic foliation. Locally, melanosome material consisting of >90% modal pargasitic amphibole (plus small amounts of epidote, rutile, titanite, and apatite ± quartz) is spatially associated with banded mesosome–leucosome pairs resembling stromatic structure of migmatites (Fig. 2b). The texture of this melanosome is variable, with grain size averaging less than 1 mm in some samples to several centimetres in others. Because of the abundance of pargasite, the melanosome material is termed here hornblendite, following the recent recommendations of the IUGS Subcommission on the Systematics of Metamorphic Rocks (Coutinho *et al.*, 2007). Our unpublished major and trace element and Rb/Sr and Sm/Nd isotope data provide evidence that these hornblendites do not represent true restites but a metasomatic rock formed by interaction (i.e. back-reaction) of the amphibolites and fluids evolved from associated melts.

Stretched, boudinaged and folded veins and pockets of trondhjemite–tonalite indicate that the amphibolites and associated segregations experienced ductile deformation (Fig. 2a–c). However, crosscutting veins and agmatitic (magmatic breccia-like) structures also document brittle behaviour of the amphibolites during melt extraction (Fig. 2d and e). In all types of structures, but most typically in the agmatitic ones, the segregations contain small (generally centimetre-size) nodules of amphibolite with sharp to diffuse boundaries, suggesting disaggregation of amphibolite within the silicic melt (Fig. 2f).

Below we present detailed information on six representative samples of plagioclase-lacking amphibolite and five representative samples of associated trondhjemite–tonalite. Samples CV53b-I and CV62b-I are quartz–epidote amphibolite, CV228d and CV228e are quartz–epidote–garnet amphibolite, CV230b is epidote-garnet amphibolite, and CV237j is epidote–garnet–clinopyroxene amphibolite. Samples CV62b-II, CV228c and SC2l are epidote–amphibole trondhjemite–tonalite, and CV53b-II and CV60a are epidote trondhjemite. The numbers in the sample labels refer to sample sites (see Fig. 1c; sample SC2l is a pebble collected in the bed of the Yacabo River). Closely associated amphibolite–trondhjemite pairs were sampled in sites CV62 and CV228. These samples are used below to examine melting relations.

ANALYTICAL TECHNIQUES

Whole-rock compositions were determined on glass beads by X-ray fluorescence (XRF) using a Philips Magix Pro (PW-2440) spectrometer at the University of Granada (Table 1; trondhjemite sample CV53b-II could not be analysed because of its small size). Loss on ignition (LOI) was determined on pressed powder pellets. Mineral compositions were obtained by wavelength-dispersive spectrometry (WDS) with a Cameca SX-50 microprobe (University of Granada), operated at 20 kV and 20 nA, and synthetic SiO_2, Al_2O_3, $MnTiO_3$, Fe_2O_3, MgO and natural diopside, albite and sanidine as calibration standards, and by energy-dispersive spectrometry (EDS) with a Zeiss DSM 950 scanning microscope, equipped with a Link Isis series 300 Analytical Pentafet system, operated at 20 kV and 1–2 nA beam current, with counting times of 50–100 s, and the same calibration standards. All analyses listed in Tables 3–10 were obtained by WDS. Clinopyroxene and amphibole compositions were normalized following the schemes of Morimoto *et al.* (1988) and Leake *et al.* (1997), respectively. Garnet was normalized to eight cations and 12 oxygens, and Fe^{3+} was estimated by stoichiometry. Epidote, feldspar, lawsonite, and kyanite were normalized to 12·5, eight, eight, and five oxygens, respectively, and $Fe_{total} = Fe^{3+}$. Mica, chlorite, and pumpellyite were normalized to 22, 28, and 24·5, oxygens, respectively, and $Fe_{total} = Fe^{2+}$. Mineral and end-member abbreviations are after Kretz (1983), except for amphibole (Amp), silicate melt (L) and fluid (H_2O), with end-members of phases written entirely in lower case. The atomic concentration of elements per formula units is abbreviated a.p.f.u.

Elemental XR images were obtained with the same Cameca SX-50 microprobe operated at 20 kV and 200–300 nA beam current, with step (pixel) size of 3–10 μm and counting time of 15–100 ms. We found that a high beam current combined with short counting time

Table 1: Chemical composition (wt %) of studied samples

Rock type:	Amphibolite						Trondhjemite			
Sample:	CV53b-I	CV62b-I	CV228d	CV228e	CV230b	CV237j	CV60a	CV228c	CV62b-II	SC21
SiO_2	45·84	46·78	46·26	48·02	43·25	43·94	67·83	60·08	66·32	60·46
TiO_2	1·72	1·26	2·26	2·16	1·94	2·57	0·22	0·19	0·06	0·22
Al_2O_3	16·40	16·98	14·68	14·99	16·70	13·33	18·24	23·65	21·13	22·30
FeO_{tot}	10·71	9·32	13·01	11·65	11·42	14·97	0·84	1·06	0·49	1·68
MnO	0·18	0·17	0·20	0·18	0·39	0·20	0·02	0·02	0·01	0·03
MgO	7·36	7·78	6·98	6·57	7·72	7·56	0·93	0·68	0·17	1·18
CaO	12·33	12·99	11·40	11·51	13·99	12·97	3·54	5·58	3·71	6·01
Na_2O	1·58	1·58	1·61	1·53	1·29	1·85	5·58	7·29	7·55	6·45
K_2O	0·27	0·20	0·26	0·21	0·31	0·05	0·26	0·08	0·15	0·17
P_2O_5	0·15	0·11	0·22	0·21	0·18	0·24	0·08	0·05	0·04	0·05
LOI	1·57	1·80	0·95	1·14	1·18	0·73	1·65	1·15	0·61	1·23
Total	98·11	98·97	97·83	98·17	98·37	98·41	99·19	99·83	100·24	99·78
Mg-no.	0·551	0·598	0·489	0·501	0·547	0·474	0·665	0·533	0·380	0·557

LOI, loss on ignition. Mg-number = $Mg/(Fe^{2+}_{total} + Mg)$.

(milliseconds rather than seconds) avoids the problem of beam damage to silicates (see De Andrade *et al.*, 2006). The images were processed with Imager software (R. L. Torres-Roldán & A. García-Casco, unpublished) and consist of the XR signals of Kα lines of the elements or element ratios (colour-coded; expressed in counts/nA per s), corrected for 3·5 μs deadtime and with voids, polish defects, and all other mineral phases masked out, overlain onto a grey-scale base-layer calculated with the expression $\sum [(\text{counts/nA per s})_i \cdot A_i]$, (where A is atomic number, and i is Si, Ti, Al, Fe, Mn, Mg, Ca, Na, and K), which contains the basic textural information of the scanned areas.

BULK-ROCK COMPOSITION

A detailed assessment of the bulk-rock chemistry of the blocks in the mélange will be presented elsewhere. Here, we briefly comment on some aspects of their major element geochemistry, which help explain key features of their mineral assemblages.

The studied amphibolite samples have subalkaline, low-K (tholeiitic) basaltic composition (Fig. 3a and b). Their SiO_2 content ranges from 43·25 to 48·02 wt %, with lower values in the quartz-free samples. The latter samples trend toward (apparent) picritic composition. Notably, all the samples have relatively low Na_2O contents (1·29–1·85 wt %), so that the samples have a relatively high inverse agpaitic index as compared with MORB (Fig. 3d). The garnet-bearing samples have lower Mg-number [$Mg/(Mg + Fe^{2+}_{total})$] atomic proportions; Table 1).

The composition of the tonalite–trondhjemite samples is varied. In the total alkalis–silica (TAS) diagram they range from andesite through trachyandesite, trachyte and trachydacite to dacite (Fig. 3a). They are rich in Na_2O (5·58–7·55 wt %) and have very low K_2O contents (0·08–0·26 wt %; Fig. 3b, Table 1), resembling rocks of the low-K tholeiite series. The FeO and MgO contents are low, and the Mg-number is relatively high, ranging from 0·38 to 0·67 (Fig. 3c). All the samples are classified as trondhjemite in the O'Connor–Barker (O'Connor, 1965; Barker, 1979) An–Ab–Or classification scheme for granitic rocks (not shown), except for sample SC21, which is classified as tonalite. However, sample SC21 is in fact leucocratic, having a greater amount of epidote (as a result of higher CaO contents). For this reason all the samples are henceforth collectively termed trondhjemites. Importantly, the trondhjemites are Al-saturated (i.e. peraluminous; ASI = 1·023–1·142; Fig. 3d) and plot close to the alkali feldspar–white mica mixing line delineated in Fig. 3d. It should be noted that this line indicates albite–paragonite mixtures in K-poor rocks.

TEXTURES AND MINERAL ASSEMBLAGES

Amphibolites

Peak metamorphic mineral assemblages consist of pargasitic amphibole, epidote, ± garnet, ± quartz, ± diopsidic

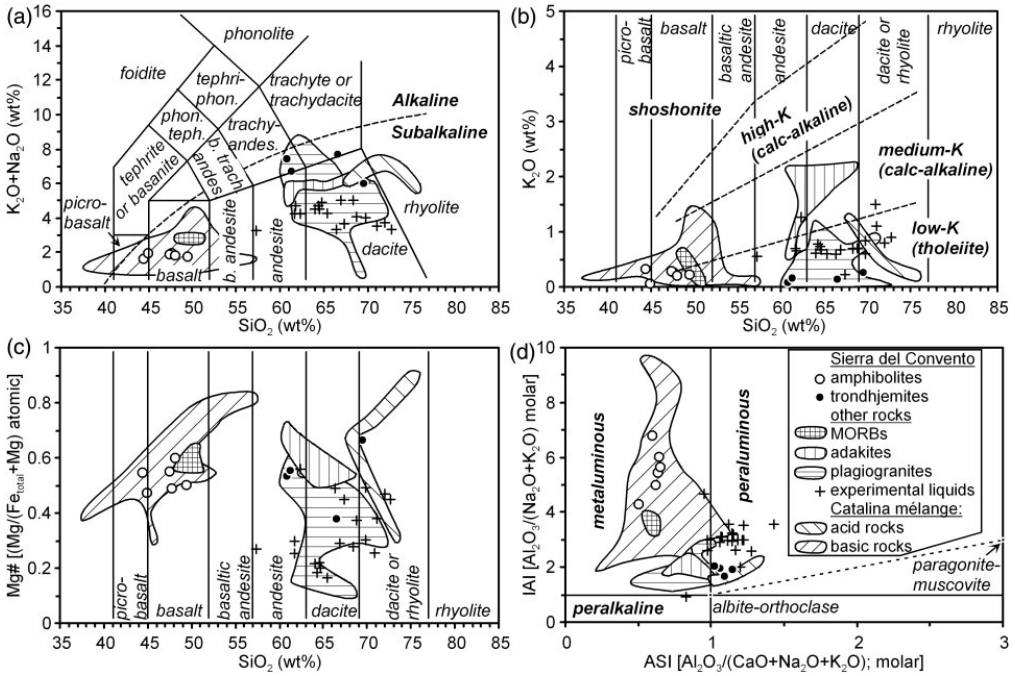

Fig. 3. Bulk composition of studied samples and of other rocks for comparison, including average and altered MORB (Hofmann, 1988; Staudigel *et al.*, 1996; Kelemen *et al.*, 2003), adakites (compiled by Drummond *et al.*, 1996; Martin, 1999; Smithies, 2000), oceanic and ophiolitic plagiogranites (compiled by Koepke *et al.*, 2004), mafic and felsic (pegmatites and leucocratic segregate) rocks from the Catalina Schist (Sorensen & Grossman, 1989), and experimental liquids (glasses) obtained by partial melting of low-K mafic material under H_2O-present conditions at 800–900°C, 2–30 kbar (Nakajima & Arima, 1998; Prouteau *et al.*, 2001; Selbekk & Skjerlie, 2002; Koepke *et al.*, 2004). (a) TAS diagram (Le Maitre *et al.*, 2002). (b) K_2O–SiO_2 diagram. (c) Mg-number–SiO_2 diagram. (d) IAI (inverse agpaitic index)–ASI (alumina saturation index) diagram with indication of the projection of alkali-feldspar and white micas for reference. The TAS-based names of rocks of the low-$K_2O + Na_2O$ series are shown in (b) and (c) for reference. Symbols for (a), (b) and (c) are as in (d).

clinopyroxene (rare), rutile, titanite, and accessory apatite (Fig. 4a–f; Table 2). These assemblages define a crude foliation. Quartz appears as small dispersed grains and millimetre-sized 'pockets' elongated along the foliation, although quartz-lacking samples are also common. Syn- to post-kinematic garnet is abundant but not present in all samples (Fig. 4a–f; Table 2). Its occurrence is influenced by bulk composition, as indicated by the lower Mg-number of garnet-bearing samples (Table 1). If forms large porphyroblasts, 0·5–3 cm in diameter, containing inclusions of amphibole and epidote (Fig. 4a–f). Na-rich diopsidic clinopyroxene has been found in quartz-free samples

Fig. 4. XR images showing key textural and compositional data of amphibolite samples CV228e (a–c) and CV237j (d–f) and trondhjemite samples SC21 (g–i), CV228c (j) and CV60a (k–m). Scale bars represent 1 mm, except in (m), where scale bar represents 0·25 mm. Colour scale bar (counts/nA per s) indicates high (red) and low (purple) concentrations. (a) Mg/(Mg + Fe) image showing pargasite (yellow–orange) and garnet with reverse zoning defined by lower Mg-number at the rims (purple). (b) Al/(Al + Fe + Mn + Mg) image showing epidote (orange–red) with patchy zoning and pargasite (blue) overprinted by retrograde magnesiohornblende–actinolite (purple). (c) Ca/(Ca + Al) image showing retrograde glaucophane (blue) and chlorite (purple) overprinting pargasite (greenish). (d) Mn image showing garnet (blue) with relict core slightly richer in Mn (greenish) and retrograde chlorite (purple). (e) Al/(Al + Fe + Mn + Mg) image showing epidote (red) in the matrix and included in garnet, and peak pargasite (green) and retrograde actinolite (blue–purple). (f) Ca/(Ca + Al) image showing peak diopside (red) and pargasite (green) overprinted by retrograde omphacite (yellow), glaucophane (blue), and chlorite (purple). (g) Ca image showing magmatic oligoclase (yellow–orange) strongly overprinted by retrograde albite (bluish–purple). (h) K image showing magmatic paragonite (green–red) with high-K regions (red) and retrograde paragonite (blue) overprinting magmatic paragonite and plagioclase. (i) Fe image showing magmatic epidote (orange–red) with Fe-rich cores (red) and retrograde (clino)zoisite (blue–purple) overprinting magmatic epidote and plagioclase. (j) Al image showing magmatic pargasite (green–orange) overprinted by tremolite (blue). (k) Ca image showing epidote (orange) and retrograde lawsonite (green) overprinting plagioclase. (l) K image showing magmatic paragonite (blue–purple) overprinted by retrograde phengite (red). (m) Al image showing relict inclusion of kyanite (enclosed in red circle) within magmatic epidote.

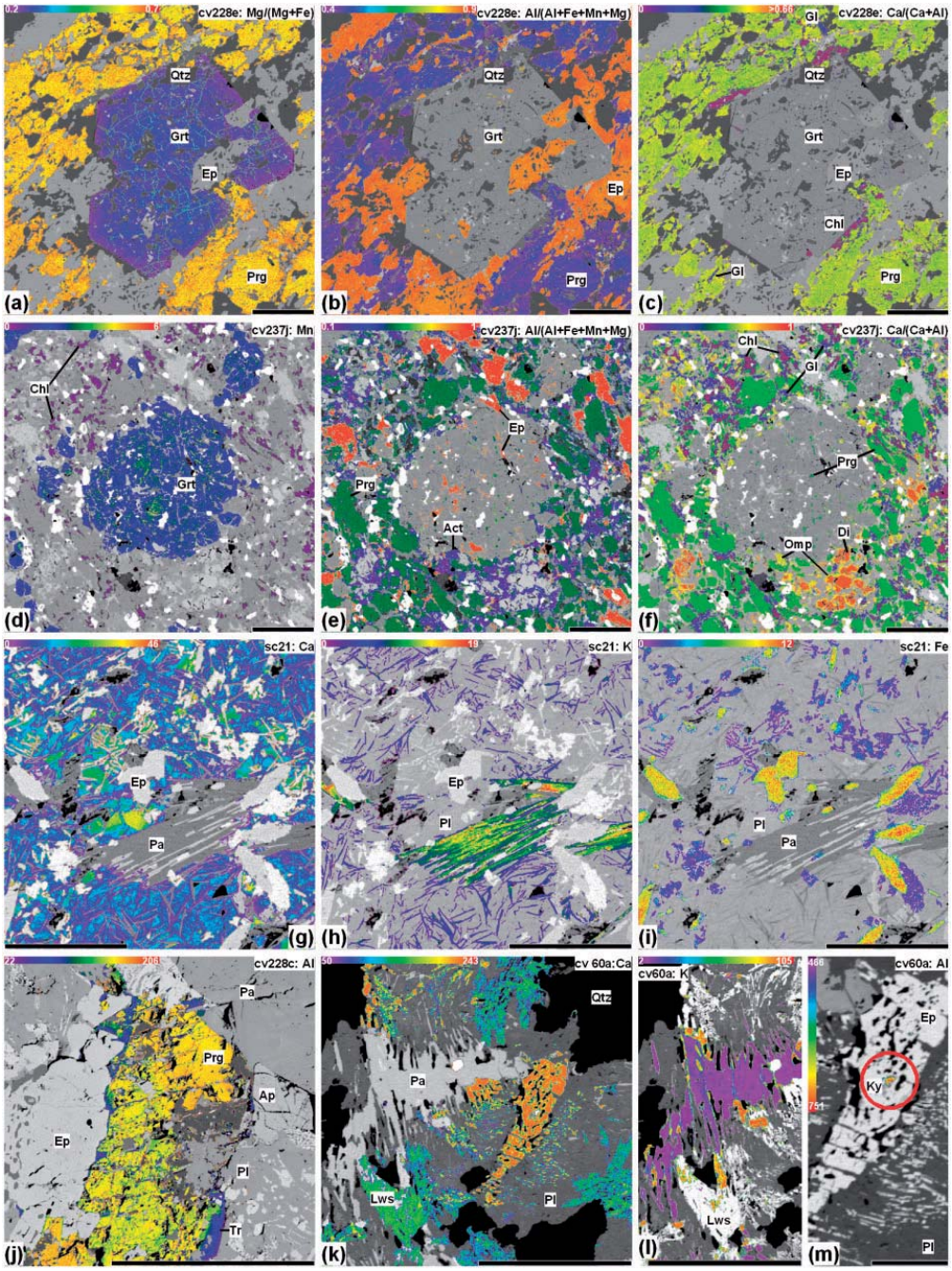
cv228e: Mg/(Mg+Fe)
Qtz
Grt
Ep
Prg
(a)
cv228e: Al/(Al+Fe+Mn+Mg)
Qtz
Grt
Ep
Prg
(b)
cv228e: Ca/(Ca+Al)
Gl
Qtz
Grt
Ep
Chl
Gl
Prg
(c)
cv237j: Mn
Chl
Grt
(d)
cv237j: Al/(Al+Fe+Mn+Mg)
Ep
Prg
Act
(e)
cv237j: Ca/(Ca+Al)
Chl
Gl
Prg
Omp
Di
(f)
sc21: Ca
Ep
Pa
(g)
sc21: K
Ep
Pl
(h)
sc21: Fe
Pl
Pa
(i)
cv228c: Al
Pa
Prg
Ap
Ep
Pl
Tr
(j)
cv 60a:Ca
Qtz
Pa
Lws
Pl
(k)
cv60a: K
Lws
(l)
cv60a: Al
Ep
Ky
Pl
(m)

Table 2: Mineral abundances in the studied samples (visual estimates)

	Peak metamorphic/magmatic												Retrograde									
	Amp	Ep	Grt	Cpx	Qtz	Pl	Pa	Rt	Ttn	Ilm	Ky	Ap	CaAmp	Gl	Omp	Chl	Pmp	Ab	Lws	Pa	Czo	Phe	Kfs
Amphibolites																							
CV53b-I	55	35			10			x	x				x	x		x	x	x			x	x	
CV62b-I	60	30			10			x	x			x	x	x		x	x	x			x	x	
CV228d	60	25	5		10			x	x			x	x	x		x	x	x			x	x	
CV228e	50	35	5		10			x	x			x	x	x		x	x	x			x		
CV230b	60	25	15					x	x			x	x	x		x	x	x			x		
CV237j	50	5	15	15				x	5	x			x	5	x	5	x	x			x		
Trondhjemites																							
CV53b-II					30	60	x?					x				x		x		7	3	x	x
CV62b-II	x	3			20	70	x?					x	x			x		x		5	2	x	
CV228c	3	15			15	55	5		x			x	x			x	x	x	x	3	4		
CV60a		8			30	40	5	x			x	x				x	x	x	5	10	2	x	x?
SC21	5	10			10	60	10	x				x	x			x	x	x		2	1	x	x

x, Present in small amounts.

of the Macambo region. It occurs as medium-grained millimetre-sized grains in the matrix (Fig. 4d–f). Titanite appears as idiomorphic peak metamorphic crystals elongated along the foliation, but it also replaces rutile.

Retrograde overprints consist of combinations of glaucophane, actinolite, albite, (clino)zoisite, chlorite, pumpellyite, and, less abundantly, phengitic mica and omphacite, the latter being observed only in samples containing peak metamorphic diopsidic clinopyroxene (Fig. 4a–f, Table 2). All these retrograde minerals are fine-grained and corrode the peak-metamorphic minerals, but they also are dispersed in the matrix or located in fractures. Retrograde glaucophane is typically aggregated with actinolite, chlorite and albite, and commonly overprints peak amphibole (Fig. 4c and f). Retrograde omphacite replaces peak diopsidic clinopyroxene and is also present in retrograde assemblages consisting of glaucophane + magnesiohornblende–actinolite + albite + epidote, which appear dispersed in the matrix and replacing pargasitic amphibole and garnet (Fig. 4f). Chlorite and pumpellyite replace garnet and pargasite. Scarce phengitic mica appears dispersed in the matrix of some samples. Retrograded crystals of pargasite commonly contain small needles of 'exsolved' rutile or titanite.

Trondhjemitic segregations

The magmatic mineral assemblage of the trondhjemites is composed of medium-grained plagioclase and quartz with subordinate medium-grained paragonite, epidote, ± pargasite, plus accessory apatite, titanite, and rutile (Fig. 4g–m; Table 2). Kyanite is locally present as tiny relict inclusions within magmatic epidote (Fig. 4m). Epidote and pargasite are idiomorphic and medium-grained (1–3 mm in length). Pargasite frequently has a large aspect ratio of 5:1 (Fig. 4j). Paragonite has medium grain size (2–3 mm in length) and idiomorphic habit, and is frequently corroded by plagioclase and fine-grained quartz, ± K-feldspar ± phengite (Fig. 4h and l). Magmatic paragonite has been identified in samples SC2l, CV228c and CV60a, whereas its presence is more uncertain in samples CV62b-II and CV53B-II.

Retrograde mineral assemblages overprint the magmatic assemblages. Magmatic plagioclase appears generally transformed to retrograde albite plus fine-grained (clino)zoisite, paragonite and, locally, lawsonite (Fig. 4g and k; Table 2). Magmatic epidote is overprinted by fine-grained overgrowths of (clino)zoisite + quartz symplectite, which extend outwards from the magmatic epidote crystal and invade nearby plagioclase (Fig. 4i, k, and m). Pargasitic amphibole is partly replaced by magnesiohornblende–tremolite, chlorite, and pumpellyite (Fig. 4j). Glaucophane is not present. Titanite replaces rutile. If present, small laths of retrograde phengitic mica are dispersed in the matrix, associated with retrograde paragonite–chlorite, and replacing magmatic plagioclase and paragonite (Fig. 4l). Very small amounts of retrograde K-feldspar, typically replacing magmatic paragonite, are present in some samples.

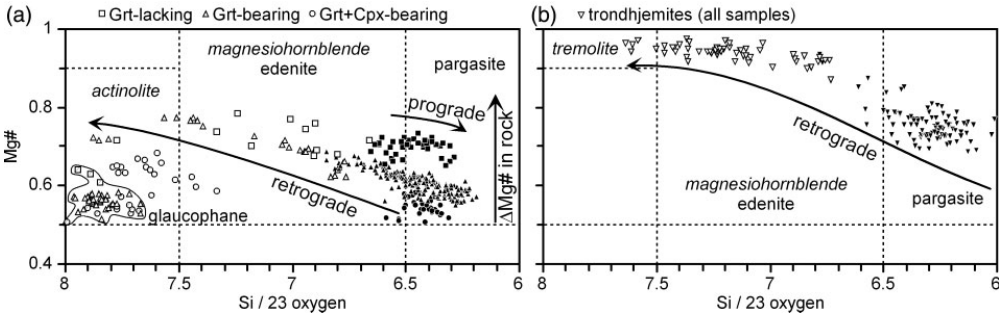

Fig. 5. Composition of amphibole from (a) amphibolites and (b) trondhjemites plotted in the classification scheme of Leake *et al.* (1997). The filled symbols and regular typeface labels correspond to calcic compositions with Sum(*A*) >0·5 (pargasite–edenite), the open symbols and italic labels correspond to calcic compositions with Sum(*A*) <0·5 (magnesiohornblende–actinolite–tremolite), and the hatched symbols (enclosed in field) and regular typeface labels correspond to sodic compositions (glaucophane). For clarity, some analyses with sodic–calcic compositions (magnesiokatophorite and barroisite) have not been differentiated from calcic amphiboles. It should be noted that much of the compositional variation is due to retrograde overprinting.

MINERAL COMPOSITION

Amphibole

Amphibolites

Matrix amphibole is edenitic–pargasitic in composition (Fig. 5a). Zoning is faint (Fig. 4a and c), and appears either as patches or, occasionally, as faint ill-defined concentric bands. Concentric zoning is defined by cores of edenite and outer shells of pargasite, indicating prograde growth (Fig. 6). Peak metamorphic pargasitic compositions are rich in Na-in-A (maximum 0·85 a.p.f.u.), total Al (maximum 2·70 a.p.f.u.), and Ti (maximum 0·3 a.p.f.u.), and poor in Si (minimum 6·19 a.p.f.u.), Na-in-M4 (minimum 0·10 a.p.f.u.), and Mg-number (minimum 0·506; Figs 5a and 6; Table 3). As would be expected for high-variance mineral assemblages, the composition of amphibole is strongly controlled by bulk-rock composition: amphibole with higher Mg-number is present in rocks with higher bulk Mg-number (Fig. 5a). Notably, Na(M4) is relatively high in pre-peak (edenitic) compositions (Fig. 6), in particular in garnet-free samples, where it is up to 0·47 a.p.f.u. and almost reaches magnesiokatophorite compositions. This edenite-to-pargasite prograde zoning correlates with the composition of amphibole inclusions within garnet, which ranges from edenite to pargasite but does not reach peak pargasitic composition as recorded in matrix amphibole.

The outermost rims (50–100 μm in width) of matrix amphibole show zoning from pargasite through edenite–magnesiohornblende to actinolite (Figs 4b and 5a), indicating retrograde growth or overprint. Actinolitic compositions are poor in Na(A) (maximum 0·02 a.p.f.u.), total Al (maximum 0·26 a.p.f.u.), and Ti (maximum 0·001 a.p.f.u.), and rich in Si (minimum 7·88 a.p.f.u.) and Mg-number (minimum 0·78; Fig. 5a; Table 3).

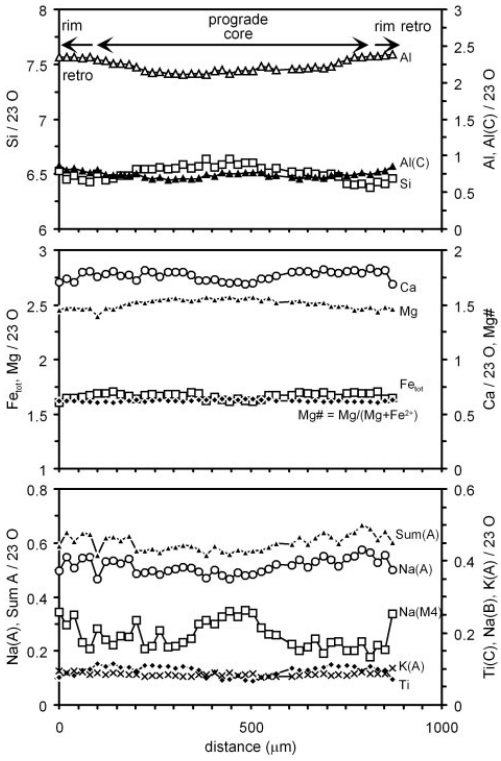

Fig. 6. Profile of amphibole from amphibolite sample CV230b recording a smooth prograde growth zoning [denoted by Si, Al(C), and Ti] from edenite to pargasite, and a retrograde overprint at the rims (edenite). It should be noted that Na(M4) is relatively high in the pre-peak core and the post-peak rim.

Table 3: Representative analyses of calcic amphiboles (normalized to 22 O and 2 OH)

Rock type:	Amphibolite												Trondhjemite					
Sample:	CV228D		CV228E		CV230B		CV237J		CV53B-I		CV62B-I		CV228C		CV62B-II		SC21	
Type:	peak	retro	peak	retro	peak	retro	peak	retro	peak	retro	peak	retro	peak	retro	peak	retro	peak	retro
SiO_2	42·04	46·59	42·64	46·42	42·94	54·45	42·53	53·82	44·58	49·59	44·01	51·13	42·16	54·02	45·44	53·36	42·90	55·22
TiO_2	2·47	0·32	0·78	0·35	0·97	0·01	1·05	0·08	0·68	0·36	0·64	0·24	1·61	0·51	0·57	0·20	1·07	0·06
Al_2O_3	13·72	11·24	14·38	11·02	13·45	1·93	13·31	2·62	13·16	7·50	15·59	8·04	16·72	3·86	15·56	7·38	16·29	4·03
FeO_{total}	15·55	15·31	15·13	14·30	13·57	12·03	16·70	14·61	13·01	12·78	11·47	10·11	10·32	3·95	8·02	3·30	9·68	2·71
MnO	0·22	0·21	0·18	0·18	0·15	0·20	0·05	0·11	0·20	0·22	0·24	0·23	0·22	0·41	0·16	0·13	0·11	0·04
MgO	10·12	10·99	10·25	11·74	11·18	15·77	9·62	14·10	11·96	13·84	12·06	15·43	11·84	21·17	14·02	19·57	12·57	21·69
CaO	10·10	9·07	10·20	9·68	11·49	11·23	11·13	11·00	10·01	10·09	9·93	9·66	10·54	12·01	10·29	11·55	10·50	12·27
BaO	0·08	0·00	0·00	0·23	0·02	0·04	0·01	0·00	0·04	0·00							0·00	0·00
Na_2O	2·79	2·66	3·03	2·90	2·43	0·89	3·09	1·29	3·23	2·43	3·34	2·56	3·73	0·97	3·47	1·73	3·38	1·02
K_2O	0·45	0·37	0·45	0·26	0·46	0·10	0·07	0·04	0·34	0·20	0·40	0·13	0·29	0·10	0·39	0·12	0·26	0·07
H_2O*	2·02	2·04	2·02	2·05	2·02	2·08	2·01	2·08	2·05	2·07	2·08	2·12	2·06	2·16	2·11	2·17	2·06	2·18
Total	99·55	98·80	99·06	99·12	98·67	98·73	99·56	99·75	99·26	99·07	99·76	99·65	99·50	99·17	100·03	99·50	98·83	99·27
Si	6·23	6·83	6·32	6·80	6·39	7·85	6·35	7·77	6·52	7·19	6·35	7·24	6·13	7·51	6·45	7·37	6·23	7·61
Ti	0·28	0·03	0·09	0·04	0·11	0·00	0·12	0·01	0·08	0·04	0·07	0·03	0·18	0·05	0·06	0·02	0·12	0·01
Al	2·40	1·94	2·51	1·90	2·36	0·33	2·34	0·45	2·27	1·28	2·65	1·34	2·87	0·63	2·60	1·20	2·79	0·65
Fe^{3+}	0·31	0·41	0·30	0·30	0·13	0·11	0·16	0·14	0·28	0·26	0·27	0·30	0·08	0·23	0·15	0·07	0·16	0·14
Fe^{2+}	1·61	1·47	1·58	1·45	1·56	1·34	1·93	1·62	1·31	1·29	1·11	0·90	1·17	0·23	0·80	0·31	1·01	0·18
Mn	0·03	0·03	0·02	0·02	0·02	0·02	0·01	0·01	0·02	0·03	0·03	0·03	0·03	0·05	0·02	0·01	0·01	0·00
Mg	2·23	2·40	2·27	2·57	2·48	3·39	2·14	3·04	2·61	2·99	2·59	3·26	2·57	4·39	2·97	4·03	2·72	4·45
Ca	1·60	1·42	1·62	1·52	1·83	1·74	1·78	1·70	1·57	1·57	1·53	1·47	1·64	1·79	1·56	1·71	1·63	1·81
Ba	0·00	0·00	0·00	0·01	0·00	0·00	0·00	0·00	0·00	0·00							0·00	0·00
Na	0·80	0·76	0·87	0·82	0·70	0·25	0·89	0·36	0·91	0·68	0·93	0·70	1·05	0·26	0·96	0·46	0·95	0·27
K	0·08	0·07	0·08	0·05	0·09	0·02	0·01	0·01	0·06	0·04	0·07	0·02	0·05	0·02	0·07	0·02	0·05	0·01
Mg-no.	0·58	0·62	0·59	0·64	0·61	0·72	0·53	0·65	0·66	0·70	0·70	0·78	0·69	0·95	0·79	0·93	0·73	0·96

*Calculated by stoichiometry.

Na(M4) of retrograde edenite and magnesiohornblende reaches 0·49 a.p.f.u. (Fig. 6), and a few analyses attain magnesiokatophorite and barroisite compositions.

The patchy zoning of most matrix crystals reflects a compositional spectrum comprising pargasite–magnesiohornblende–actinolite and indicates that it developed during retrograde adjustment or growth. These retrograde adjustments are clearly developed in single crystals of pargasite containing small needles of exsolved rutile or titanite.

The compositional variability of retrograde glaucophane is relatively large [Si 7·67–7·99, Al 1·46–1·98, Ca 0·04–0·43, Na(M4) 1·54–1·91, Na(A) 0·01–0·17 a.p.f.u., and Mg-number 0·51–0·64; Fig. 5a; Table 4]. This compositional range reflects compositional heterogeneity within single samples as a result of the effects of local effective bulk-composition at reaction sites and the timing of formation during the retrograde path. The first effect is best illustrated by higher Mg-number and lower Mg-number glaucophane grains present in single samples and grown adjacent to matrix amphibole and garnet, respectively.

Trondhjemites

Magmatic amphibole shows no growth zoning. Its composition is pargasitic [Si down to 6·01, Al up to 2·87, Ti up to 0·26, Na(A) up to 0·72, K(A) up to 0·11, Na(M4) ~0·35 a.p.f.u., Mg-number ~0·75; Fig. 5b; Table 3], similar to that of peak metamorphic amphibole from the amphibolites except for having higher Mg-number (Fig. 5b). The composition of these grains is overprinted by patchy retrograde zoning, developed along fractures, exfoliation planes and crystal rims (Fig. 4j). The retrograde composition of amphibole ranges from pargasite through edenite, magnesiohornblende to tremolite (Fig. 5b; Table 3). Notably, Na(M4) first increases along this path (pargasite to edenite), reaching 0·44 a.p.f.u. and approaching

Table 4: Representative analyses of sodic amphiboles (normalized to 22 O and 2 OH)

Sample:	CV228D	CV228E	CV230B	CV237J	CV53B-I	CV62B-I
SiO_2	54·92	55·98	56·54	56·35	57·77	57·10
TiO_2	0·12	0·30	0·09	0·02	0·06	0·16
Al_2O_3	9·73	10·04	11·07	10·67	11·28	10·45
FeO_{total}	15·23	13·74	12·70	13·48	10·92	11·85
MnO	0·13	0·16	0·11	0·02	0·09	0·10
MgO	8·11	8·97	8·60	8·48	9·78	9·98
CaO	1·82	1·76	1·28	1·57	0·30	1·47
BaO	0·00	0·03	0·00	0·00	0·02	
Na_2O	6·52	6·61	6·84	6·66	7·32	6·68
K_2O	0·04	0·02	0·02	0·04	0·00	0·02
H_2O^*	2·10	2·14	2·15	2·14	2·18	2·17
Total	98·71	99·76	99·40	99·42	99·71	99·98
Si	7·84	7·85	7·90	7·90	7·95	7·89
Ti	0·01	0·03	0·01	0·00	0·01	0·02
Al	1·64	1·66	1·82	1·76	1·83	1·70
Fe^{3+}	0·18	0·16	0·08	0·09	0·12	0·16
Fe^{2+}	1·64	1·46	1·41	1·49	1·13	1·21
Mn	0·02	0·02	0·01	0·00	0·01	0·01
Mg	1·73	1·87	1·79	1·77	2·01	2·06
Ca	0·28	0·27	0·19	0·24	0·04	0·22
Ba	0·00	0·00	0·00	0·00	0·00	
Na	1·81	1·80	1·85	1·81	1·95	1·79
K	0·01	0·00	0·00	0·01	0·00	0·00
Mg-no.	0·51	0·56	0·56	0·54	0·64	0·63

*Calculated by stoichiometry.

sodic–calcic (magnesiokatophorite–magnesiotaramite) composition, then decreases almost to zero in the magnesiohornblende–tremolite compositions. This trend suggests a retrograde path with a first step of decreasing temperature at near-constant pressure, followed by decreasing temperature and pressure.

Garnet

Garnets in the amphibolites are relatively rich in almandine ($X_{alm} = 0{\cdot}50$–$0{\cdot}55$) and, to some extent, grossular (0·2–0·3), and poor in pyrope (0·15–0·20) and spessartine (0·02–0·10), comparable with type C (i.e. low-temperature) eclogitic garnet (Fig. 7a; Table 5). As in amphibole, the composition of garnet is influenced by bulk-rock composition; higher Mg-number is observed in garnets from Fe-poorer bulk-rock composition (Fig. 7b).

Garnet zoning is faint. In most samples the cores are near homogeneous. The rims and regions adjacent to fractures show retrograde readjustments denoted by an increase in spessartine and decrease in Mg-number (Figs 4a, d and 7b–d). However, garnet in sample CV230b shows spessartine-poor and high Mg-number rims denoting prograde growth (see García-Casco *et al.*, 2006). Faint prograde zoning and the lack of low-temperature phases included within garnet suggest a relatively late stage of garnet growth during prograde metamorphism (i.e. close to and during peak conditions). Thus, much of the compositional variation of garnet is the result of retrograde readjustments characterized by increase in Mn and decrease in Mg-number (Fig. 7b). Grossular contents may not be significantly affected by retrograde readjustments, but they increase sharply (to $X_{grs} \sim 0{\cdot}6$) in fractures traversing garnet in sample CV237j (Fig. 7e; Table 5).

Epidote

Matrix epidote from amphibolite shows variable Fe^{3+} contents, with pistacite contents ($X_{ps} = Fe^{3+}/[(Al-2)+Fe^{3+})]$ ranging from 0·2 to 0·7, except in sample CV230b, where $X_{ps} = 0{\cdot}1$–$0{\cdot}2$ (Table 6). Zoning is generally patchy, although some grains may show concentric zoning with lower X_{ps} at the rims (Fig. 4b), probably reflecting retrograde readjustments or growth.

In the trondhjemitic segregations magmatic epidote is richer in Fe^{3+} than retrograde grains of (clino)zoisite (X_{ps} up to 0·5 and 0·1, respectively; Fig. 4i and k; Table 6). The exception is sample CV60a, which contains magmatic epidote with low X_{ps} (<0·1; Table 6). Magmatic crystals show patchy zoning, with irregular high-Fe^{3+} areas in the interior, which probably formed at higher temperature. Intermediate compositions of magmatic epidote are interpreted as the result of crystallization upon cooling and/or subsolidus retrograde readjustments.

Clinopyroxene

Peak metamorphic clinopyroxene from sample CV237j is diopsidic in composition (Fig. 8; Table 5), with Mg-number = 0·67–0·74, $Fe^{3+}/(Fe^{3+}+Fe^{2+}) = 0{\cdot}18$–$0{\cdot}37$, Ti up to 0·03 a.p.f.u., and Na = 0·07–0·09 a.p.f.u. ($X_{jd} = 0{\cdot}04$–$0{\cdot}06$). This suggests a relatively high pressure of formation at high temperature. The composition of retrograde omphacite is Ca = 0·51–0·63 a.p.f.u., Mg-number = 0·67–0·82, and $Fe^{3+}/(Fe^{3+}+Fe^{2+}) = 0{\cdot}23$–$0{\cdot}62$, which translates into $X_{jd} = 0{\cdot}32$–$0{\cdot}39$ and $X_{ae} = 0{\cdot}06$–$0{\cdot}14$ (Fig. 8; Table 5).

Plagioclase

Plagioclase in the amphibolites is retrograde and almost pure albite in composition ($X_{ab} > 0{\cdot}92$, with most analyses reaching $X_{ab} > 0{\cdot}99$; Table 7).

The composition of magmatic plagioclase in the trondhjemites is uncertain, as it has been largely retrogressed to albite-rich plagioclase. The magmatic crystals display retrograde patchy zoning that preserves irregular calcic regions dispersed within albite-richer retrograde areas (Fig. 4g). The maximum X_{an} of these relict regions,

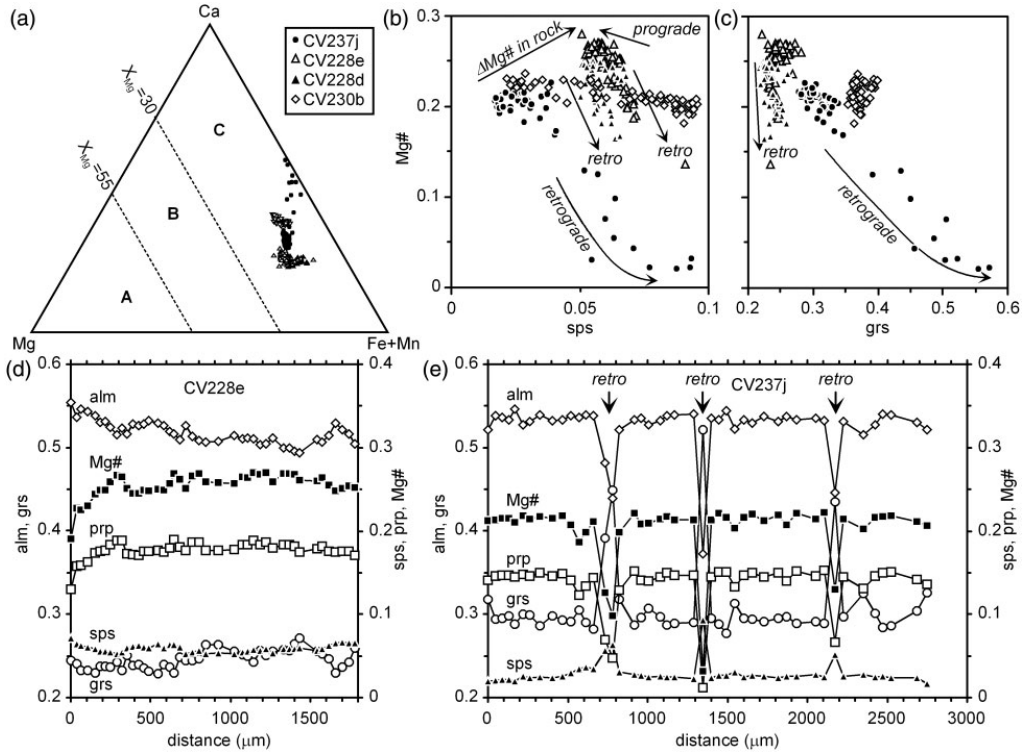

Fig. 7. Composition of garnet from amphibolites. (a) Garnet in the classification scheme of Coleman *et al.* (1965). Mg-number vs (b) spessartine and (c) grossular contents. Rim-to-rim profiles of porphyroblasts from samples (d) CV228e and (e) CV237j. It should be noted the retrograde rims in (d) and the retrograde Ca-rich garnet developed along fractures in (e) indicated by arrows.

identified with the aid of XR images, are 0·29 (CV228c), 0·18 (SC21), 0·18 (CV62b-II), and 0·17 (CV53b-II and CV60a) (Fig. 11b, Table 7). Although these figures do not necessarily represent the original magmatic composition of plagioclase, they suggest that it was sodic andesine to calcic oligoclase.

Paragonite

Magmatic crystals of paragonite from the trondhjemites are rich in the muscovite component (K up to 0·35 a.p.f.u., $X_K = K/(K + Na) = 0·18$; Table 8). These crystals show patchy zoning with relict high-K areas in the interior of the grains with relatively high Ca contents (0·06–0·10 a.p.f.u.) and K-poorer areas distributed irregularly but typically along (001) planes and close to the rims, indicating retrograde readjustments upon cooling (Fig. 4h). The retrograded regions are somewhat richer in the margarite component (Fig. 9). Discrete grains of retrograde paragonite have Ca- and K-poor compositions and are of almost pure paragonite end-member composition (Figs 4h and 9, Table 8). A detailed assessment of the composition of paragonite from sample SC21 has been given by García-Casco (2007).

Phengite

Retrograde phengitic mica in the amphibolites (samples CV53b-I and CV62b-I) is very rich in celadonite content, with Si = 6·89–6·96 a.p.f.u., Mg = 0·77–0·86, Fe^{2+}_{total} = 0·21–0·27, Na = 0·06–0·09, and Mg-number ($Fe = Fe^{2+}_{total}$) = 0·76–0·79 (Fig. 9; Table 8), indicating high pressure during retrogression.

The composition of phengitic mica in the trondhjemites is heterogeneous (Fig. 9; Table 8) and varies from high celadonite content (Si up to 6·97, Fe up to 0·21, Mg up to 0·83 a.p.f.u.) to almost pure muscovite (Si down to 6·05 a.p.f.u.). Mg-number ranges from 0·69 to 0·92 and shows a positive correlation with Si, which is best shown when analysing the chemical variation of phengite in single samples. Ba contents are low (0·06–0·01 a.p.f.u.). The contents of Na (0·27–0·05 a.p.f.u.) and Ti (0·014–0 a.p.f.u.)

Table 5: Representative analyses of garnet (normalized to 12 O) and clinopyroxene (normalized to 6 O)

Phase:	Garnet								Ca-Cpx	Omp
Sample:	CV228D		CV228E		CV230B		CV237J		CV237J	CV237J
Type:	peak	retro	peak	retro	peak	retro	peak	retro	peak	retro
SiO_2	37·31	37·57	37·74	37·44	37·83	37·63	37·90	37·86	50·86	54·60
TiO_2	0·27	0·03	0·20	0·07	0·07	0·07	0·07	0·21	0·30	0·75
Al_2O_3	21·33	21·28	21·48	21·31	21·32	21·56	21·33	20·91	3·35	9·14
FeO_{total}	25·37	27·13	24·74	26·15	21·90	21·95	25·16	16·86	11·18	8·21
MnO	2·56	2·83	2·49	3·12	1·28	1·99	1·11	3·93	0·13	0·05
MgO	4·44	2·97	4·79	3·23	3·62	2·96	3·81	0·19	11·04	6·60
CaO	8·16	7·89	8·79	8·58	13·03	13·46	10·15	19·69	21·69	13·86
Na_2O									1·09	6·66
Total	99·44	99·69	100·23	99·91	99·04	99·62	99·53	99·65	99·62	99·85
Si	2·94	2·99	2·94	2·96	2·97	2·95	2·98	2·98	1·91	1·98
Ti	0·02	0·00	0·01	0·00	0·00	0·00	0·00	0·01	0·01	0·02
Al	1·98	1·99	1·97	1·99	1·98	1·99	1·98	1·94	0·15	0·39
Fe^{3+}	0·10	0·03	0·11	0·08	0·07	0·09	0·05	0·06	0·09	0·08
Fe^{2+}	1·58	1·77	1·50	1·65	1·37	1·35	1·61	1·05	0·27	0·17
Mn	0·17	0·19	0·16	0·21	0·08	0·13	0·07	0·26	0·00	0·00
Mg	0·52	0·35	0·56	0·38	0·42	0·35	0·45	0·02	0·62	0·36
Ca	0·69	0·67	0·73	0·73	1·10	1·13	0·86	1·66	0·87	0·54
Na									0·08	0·47
Mg-no.	0·25	0·17	0·27	0·19	0·24	0·20	0·22	0·02	0·70	0·68

are low to very low, with lower contents in celadonite-rich compositions (Fig. 9; Table 8). These compositional variations are consistent with continuing growth or readjustment during retrogression, with the onset of growth at relatively high temperature being represented by the lower Si and higher Na and Ti compositions.

Chlorite

Retrograde chlorite in the amphibolites has Al = 4·34–5·17 a.p.f.u., Mn = 0·015–0·127 a.p.f.u., and Mg-number ($Fe^{2+} = Fe_{total}$) = 0·50–0·71 (Table 9). Part of this compositional variability is due to the effect of bulk composition, with high Mg-number compositions from high Mg-number samples CV53b-I and CV62b-I and low Mg-number compositions from low Mg-number sample CV237j. The Al- and Mn-richer compositions are found in chlorite from Fe-richer samples bearing garnet. In these samples retrograde chlorite occurs adjacent to garnet and within the amphibolite matrix, and its composition mimics the site of growth, with higher Fe, Al, and Mn contents in the former and higher Mg contents in the latter.

Retrograde chlorite in the trondhjemites is similar to that of the amphibolites (Al = 4·49–5·11 a.p.f.u.), except for being more magnesian (Mg-number = 0·68–0·87; Table 9).

Other minerals

Retrograde pumpellyite in the amphibolite samples has Al = 4·81–4·92 a.p.f.u., Mg = 0·62–0·78 a.p.f.u., Fe^{2+}_{total} = 0·34–0·53 a.p.f.u., and Mg-number ($Fe^{2+} = Fe_{total}$) = 0·56–0·70, whereas in the trondhjemite samples it has Al = 4·47–4·93, Mg = 0·82–1·09 a.p.f.u., Fe^{2+}_{total} = 0·20–0·40 a.p.f.u., and Mg-number ($Fe^{2+} = Fe_{total}$) = 0·70–0·83 (Table 10). This again reflects the effect of bulk-rock composition. Titanite has up to 0·072 Al (per five oxygens). Retrograde K-feldspar from the trondhjemites is almost pure orthoclase in composition, with X_{ab} = 0·004–0·025 and trace amounts of Ba (0·001–0·003 a.p.f.u.; Table 7). Relict magmatic kyanite and retrograde lawsonite from the trondhjemites are almost pure in composition (Table 10).

PEAK METAMORPHIC AND MAGMATIC PHASE RELATIONS

Amphibolites

The peak metamorphic assemblages of the amphibolites are systematized in the ACF and AFN diagrams of Fig. 10. These diagrams are projected from coexisting phases and

Table 6: Representative analyses of epidote (normalized to 12 O and 1 OH)

Rock type:	Amphibolite						Trondhjemite								
Sample:	CV228D	CV228E	CV230B	CV237J	CV53B-I	CV62B-I	CV228C		CV53B-II		CV60A	CV62B-II		SC21	
Type:	peak	peak	peak	peak	peak	peak	peak	retro	peak	retro	peak	peak	retro	peak	retro
SiO_2	37·96	38·11	38·73	38·42	37·93	38·46	38·63	40·21	38·05	38·95	39·31	38·73	39·67	38·89	39·36
TiO_2	0·22	0·22	0·04	0·12	0·14	0·23	0·18		0·10	0·00	0·04	0·17	0·02	0·15	0·01
Al_2O_3	27·05	27·50	31·91	27·25	26·68	26·59	27·87	32·74	28·36	32·59	32·73	28·16	33·46	28·92	33·18
FeO_{total}	8·85	7·88	2·11	7·63	8·38	8·65	6·18	0·91	6·26	1·22	0·96	6·62	0·24	6·12	0·46
MnO	0·17	0·16	0·04	0·09	0·49	0·15	0·10		0·19	0·01	0·01	0·20	0·00	0·15	0·05
MgO	0·10	0·13	0·02	0·01	0·03	0·17	0·18	0·06	0·09	0·01	0·03	0·15	0·03	0·20	0·02
CaO	23·32	23·39	24·29	23·64	23·38	23·05	23·13	24·72	23·81	24·54	23·95	23·07	24·36	23·30	24·01
BaO			0·02	0·04			0·00		0·00	0·00	0·00			0·03	0·03
H_2O^*	1·92	1·92	1·95	1·92	1·91	1·92	1·92	1·99	1·92	1·96	1·96	1·93	1·98	1·95	1·96
Total	99·58	99·31	99·12	99·12	98·94	99·22	98·18	100·63	98·77	99·29	98·99	99·03	99·75	99·70	99·09
Si	2·96	2·97	2·98	3·00	2·98	3·00	3·02	3·03	2·97	2·98	3·01	3·01	3·01	3·00	3·00
Ti	0·01	0·01	0·00	0·01	0·01	0·01	0·01		0·01	0·00	0·00	0·01	0·00	0·01	0·00
Al	2·48	2·53	2·89	2·51	2·47	2·45	2·57	2·90	2·61	2·94	2·95	2·58	2·99	2·63	2·98
Fe^{3+}	0·58	0·51	0·14	0·50	0·55	0·56	0·40	0·06	0·41	0·08	0·06	0·43	0·02	0·39	0·03
Mn	0·01	0·01	0·00	0·01	0·03	0·01	0·01		0·01	0·00	0·00	0·01	0·00	0·01	0·00
Mg	0·01	0·02	0·00	0·00	0·00	0·02	0·02	0·01	0·01	0·00	0·00	0·02	0·00	0·02	0·00
Ca	1·95	1·95	2·00	1·98	1·97	1·93	1·94	1·99	1·99	2·01	1·96	1·92	1·98	1·92	1·96
Ba			0·00	0·00			0·00		0·00	0·00	0·00			0·00	0·00

*Calculated by stoichiometry.

appropriate exchange vectors, which allow condensation of the composition space. To give an indication of the chemistry of the peak metamorphic minerals these phase diagrams also show the projection of relevant end-members of the solid solutions of interest. Because the ACF diagram is constructed after projection from quartz, the lack of quartz in sample CV237j helps explain the apparent reaction relation between the peak metamorphic minerals plotted in Fig. 10c.

The ACF diagrams (Fig. 10a–c) show that epidote is paragenetic with peak pargasitic amphibole ± garnet ± clinopyroxene, indicating epidote-amphibolite facies conditions. These diagrams also help interpret the lack of peak metamorphic plagioclase in the studied samples. This is best illustrated by the quartz–epidote amphibolite samples CV53b-I and CV62b-I (Fig. 10a). The bulk compositions of these samples plot within the tie-lines connecting peak metamorphic epidote and pargasite, implying that no plagioclase was stable in these bulk compositions at peak metamorphic conditions. The same conclusion is reached for the garnet-bearing samples after inspection of the ACF diagram (Fig. 10b and c). However, the lack of peak metamorphic plagioclase in these samples is best appreciated in the AFN diagram projected from epidote (Fig. 10d). In this diagram, the bulk compositions of the epidote–garnet amphibolite samples CV228e and CV228e plot within the tie-lines connecting garnet and pargasite. It should be noted that plagioclase would have been stable only in bulk compositions richer in Na_2O and/or Al_2O_3, such as those of average MORB plotted in Fig. 10d. The relations depicted in the AFN diagram of Fig. 10d strongly suggest that plagioclase consumption in, and alkali subtraction from, a MORB-like amphibolite by means of partial melting and subsequent melt extraction, respectively, are mechanisms that could account for the development of the studied bulk compositions and mineral assemblages.

Trondhjemitic segregations

The magmatic assemblages of the trondhjemites are systematized in the ACF and ACN diagrams of Fig. 11a and b, respectively, projected from coexisting phases and appropriate exchange vectors. It should be noted that the compositions of the trondhjemite samples plot in the respective peraluminous fields of both diagrams. The tie-line crosscutting relations depicted in the ACF diagram (Fig. 11a) do not necessarily represent reaction between magmatic pargasite, epidote, plagioclase and paragonite.

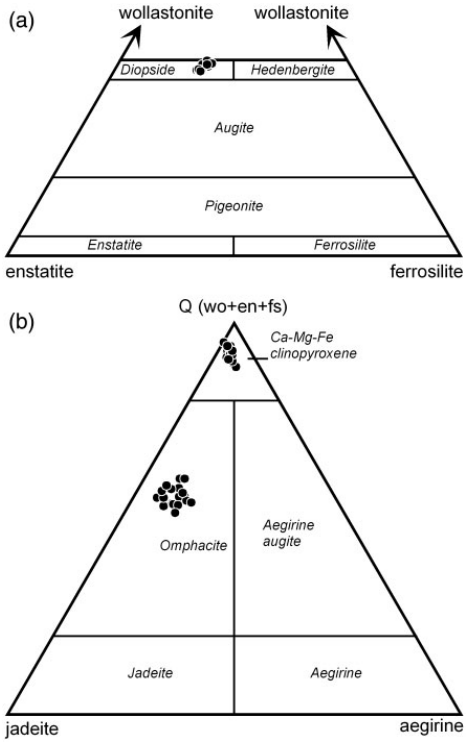

Fig. 8. Composition of clinopyroxene from sample CV237j in the classification scheme of Morimoto *et al.* (1988). (a) Peak calcic clinopyroxene (diopside). (b) Peak diopside and retrograde omphacite.

These apparent reaction relations are best explained as a result of condensation of the composition space by projection from exchange vectors. A better representation of the magmatic assemblages is provided by the ACN diagram projected from pargasite (Fig. 11b). In this diagram no tie-line crosscutting relations exist between the magmatic minerals. Also, it clearly shows that the bulk composition of the trondhjemite magmas is appropriate for crystallization of magmatic paragonite from the melt.

The ACN diagram of Fig. 11b shows variable shapes of the plagioclase–epidote–paragonite tie-triangles. This is a consequence of the variable composition of magmatic plagioclase, which in turn is a result of variable bulk composition of the samples (i.e. magmas). This is indicated by the fact that Na-richer magmatic plagioclase is found in Na-richer samples (CV62b-II). However, as noted above, plagioclase is overprinted by albite, paragonite, and (clino)zoisite, with relict regions having higher Ca contents (Fig. 4g). Although these regions were identified with the aid of XR images, it is probable that they do not retain peak Ca contents. Consequently, the variable shapes of the plagioclase–epidote–paragonite tie-triangles shown in Fig. 11b may be flawed. This has important consequences for thermobarometry, as discussed below.

P–T CONDITIONS AND *P–T* PATHS

Temperatures and pressures were estimated following the optimal *P–T* method of Powell & Holland (1994) using THERMOCALC (Holland & Powell, 1998, version 3.25, dataset 5.5, 12 November 2004). Calculations were performed using different combinations of phases grown during pre-peak, peak, and post-peak conditions, as described below for each sample. An H_2O-fluid was included in all assemblages. All calculations are based on at least four independent reactions. The activities and (1σ) activity uncertainties of each end-member included in the calculations were obtained with software AX (T. Holland & R. Powell, unpublished). As indicated by Powell & Holland (1994), the uncertainties on the calculated P and T are not altered by a proportional change (e.g. doubling) of all the activity uncertainties, as long as the averaging is statistically consistent. The P–T uncertainties (σT and σP) given represent $\pm 1\sigma$ (95% confidence). The correlation between σT and σP for a given calculation is given below as 'corr'. High correlation indicates that with a T (or P) the other value is well constrained. Thus, large σT and σP imply well-constrained P–T data if the former are highly correlated. The σT and σP uncertainties and correlations are appropriately incorporated into the uncertainty ellipses of Fig. 12 calculated following Powell & Holland (1994). To keep the calculated P–T error ellipses small and improve the statistics of the calculations, phase components with very low activities were neglected in the calculations, and some phase components with errant behaviour (outliers) were occasionally rejected [for justification see Powell & Holland (1994)]. The calculations of pre-peak and peak conditions passed the 'sigfit' test for statistical consistency, but some of the calculations of magmatic and retrograde conditions did not pass this test, suggesting equilibrium problems. The test implies that the 'sigfit' values (quoted below for each calculation) should approach unity [for further details see Powell & Holland (1994)].

Amphibolites

For thermobarometry, it is not possible to use the high-variance mineral assemblage amphibole + epidote + quartz of the garnet-free amphibolites because no set of linearly independent reactions can be found. Consequently, P–T calculations were performed only for the lower-variance (garnet-bearing) samples (Fig. 12a–c).

The calculated peak P–T conditions are based on the matrix assemblages Grt + Amp + Ep + Qtz (samples CV228d and CV228e), Grt + Amp + Ep (CV230b),

Table 7: Representative analyses of feldspars (normalized to 8 O)

Phase:	Plagioclase														Kfs
Rock type:	Amphibolite				Trondhjemite										Trondhj.
Sample:	CV230B	CV237J	CV53B-I	CV62B-I	CV228C		CV53B-II		CV60A		CV62B-II		SC21		SC21
Type:	retro	retro	retro	retro	peak	retro	peak	retro	peak	retro	peak	retro	peak	retro	retro
SiO_2	67·90	68·54	67·97	65·84	61·55	67·39	63·58	68·82	63·97	68·71	64·39	68·85	63·48	67·88	64·28
Al_2O_3	19·38	19·57	19·37	20·60	23·41	20·07	22·19	19·30	22·37	19·34	22·41	19·64	22·61	19·84	18·18
FeO_{total}	0·05	0·30	0·14	0·32	0·00	0·03	0·03	0·02	0·00	0·00	0·03	0·01	0·01	0·02	0·02
MnO	0·00	0·00	0·01			0·00					0·00	0·01	0·01	0·00	0·01
CaO	0·02	0·07	0·19	1·09	5·89	0·60	3·53	0·04	3·62	0·01	3·27	0·08	3·77	0·41	0·01
BaO	0·00	0·01	0·00			0·00	0·01	0·01	0·00	0·00			0·02	0·00	0·07
Na_2O	11·77	11·81	11·60	10·76	8·21	11·34	9·76	11·67	9·73	11·80	9·85	11·85	9·49	11·70	0·05
K_2O	0·02	0·01	0·01	0·47	0·04	0·01	0·05	0·03	0·02	0·00	0·05	0·02	0·04	0·03	16·72
Total	99·14	100·31	99·29	99·08	99·10	99·45	99·15	99·89	99·72	99·87	100·00	100·47	99·43	99·89	99·35
Si	2·99	2·99	2·99	2·92	2·75	2·96	2·83	3·01	2·83	3·00	2·84	2·99	2·82	2·97	3·00
Al	1·01	1·00	1·00	1·08	1·23	1·04	1·16	0·99	1·17	1·00	1·16	1·01	1·18	1·02	1·00
Fe^{3+}	0·00	0·01	0·00	0·01	0·00	0·00	0·00	0·00	0·00	0·00	0·00	0·00	0·00	0·00	0·00
Mn	0·00	0·00	0·00			0·00					0·00	0·00	0·00	0·00	0·00
Ca	0·00	0·00	0·01	0·05	0·28	0·03	0·17	0·00	0·17	0·00	0·15	0·00	0·18	0·02	0·00
Ba	0·00	0·00	0·00			0·00	0·00	0·00	0·00	0·00			0·00	0·00	0·00
Na	1·01	1·00	0·99	0·93	0·71	0·97	0·84	0·99	0·83	1·00	0·84	1·00	0·82	0·99	0·00
K	0·00	0·00	0·00	0·03	0·00	0·00	0·00	0·00	0·00	0·00	0·00	0·00	0·00	0·00	1·00

and Grt + Amp + Ep + diopsidic Cpx (CV237j). The assemblages used for *P–T* calculations are shown in the ACF and AFN phase diagrams of Fig. 10 (see also Fig. 14). Pre-peak conditions were calculated using the composition of inclusions within garnet and the assemblages Grt + Amp + Ep + Qtz (sample CV228d) and Grt + Amp + Ep (CV230b). Retrograde conditions were calculated using actinolitic Amp + Gl + Chl + Ep + Grt (retrograded rims) + Qtz + Ab (samples CV228d and CV228e), actinolitic Amp + Gl + Chl + Ep + Grt (retrograded rims) + Ab (CV230b), and actinolitic Amp + Gl + Chl + Ep ± Grt (retrograded rims) + Omp + Ab (CV237j).

The calculated peak conditions are 673 ± 49°C, 14·6 ± 2·2 kbar (corr 0·455, sigfit 1·13), 683 ± 44°C, 15·7 ± 2·1 kbar (0·476, 1·05), and 708 ± 69°C, 13·8 ± 2·2 kbar (−0·251, 0·81) for samples CV228d, CV228d, and CV230b, respectively, suggesting that these blocks underwent similar *P–T* conditions in the range of 675–700°C and 14–16 kbar. However, peak conditions for CV273j are more uncertain. Using the assemblage indicated above with the composition of diopsidic clinopyroxene with the lowest, average, and highest Na contents, the calculated conditions are 859 ± 46°C, 13 ± 2·2 kbar (0·181, 1·04), 811 ± 56°C, 14·4 ± 2·7 kbar (0·134, 1·31) and 768 ± 56°C 15 ± 2·7 kbar (0·107, 1·36), respectively, suggesting higher temperatures and similar to somewhat lower pressures than the above three samples. As discussed below, the results calculated with the highest Na content of diopsidic clinopyroxene are consistent with expected phase relations.

The calculated pre-peak conditions for samples CV228d and CV230b are slightly lower than those for peak conditions, down to 644 ± 42°C, 13·1 ± 1·9 kbar (0·514, 0·88) and 610 ± 62°C, 13·9 ± 2 kbar (−0·218, 0·96), respectively.

The calculated retrograde conditions are 525 ± 28°C, 11·2 ± 1·6 kbar (0·29, 2·35), 520 ± 17°C, 11·2 ± 1 kbar (0·345, 1·49), and 472 ± 21°C, 10 ± 1 kbar (0·473, 1·48) for samples CV228d, CV228d, and CV230b, respectively, suggesting that these blocks underwent similar retrograde *P–T* paths. The retrograde conditions for sample CV237j are 512 ± 33°C, 11·9 ± 1·3 kbar (0·155, 2·64) and 444 ± 29°C, 10·6 ± 1·1 kbar (0·437, 2·19) with or without retrograded garnet, respectively, included in the calculations.

These *P–T* calculations suggest counterclockwise *P–T* paths characterized by pre-peak prograde paths with increasing *P* and *T* within the epidote–amphibolite facies, peak conditions within the epidote–amphibolite facies, and retrogression within the blueschist facies (Fig. 12a–c).

Table 8: Representative analyses of micas (normalized to 20 O and 4 OH)

Phase:	Paragonite									Phengite							
Rock:	Trondhjemite									Amphibolite		Trondhjemite					
Sample:	CV228C		CV53B-II		CV60A		CV62B-II	SC21		CV53B-I	CV62B-I	CV53B-II		CV60A		CV62B-II	
Type:	peak	retro	peak	retro	peak	retro	peak	peak	retro	retro	retro	retro	retro	retro	retro	retro	retro
SiO_2	45·99	45·23	46·14	46·63	45·97	46·18	47·02	46·43	47·46	51·96	52·29	49·84	52·28	46·89	52·27	46·24	52·28
TiO_2	0·07	0·14	0·02	0·00	0·29	0·05	0·21	0·17	0·10	0·07	0·09	0·03	0·01	0·13	0·04	0·08	0·01
Al_2O_3	39·95	40·70	39·58	39·89	39·83	40·57	40·13	39·06	39·70	25·42	25·83	29·22	26·33	36·19	26·32	36·88	26·48
FeO_{total}	0·41	0·27	0·35	0·29	0·27	0·13	0·50	0·39	0·21	2·28	1·92	1·46	1·47	0·38	1·25	0·13	1·22
MnO							0·01	0·02	0·00	0·04	0·00	0·02	0·04			0·00	0·01
MgO	0·14	0·13	0·16	0·27	0·19	0·16	0·21	0·26	0·35	4·05	4·04	2·85	3·88	0·71	4·13	0·63	4·17
CaO	0·77	0·79	0·35	0·36	0·86	0·34	0·49	0·42	0·22	0·03	0·04	0·02	0·00	0·08	0·06	0·05	0·02
BaO			0·12	0·03	0·06	0·06		0·25	0·02	0·29		0·46	0·16	0·21	0·48		
Na_2O	6·73	7·37	6·77	7·22	6·73	7·33	6·64	6·25	7·31	0·24	0·23	0·47	0·26	0·58	0·23	0·59	0·26
K_2O	0·97	0·19	1·36	0·55	1·08	0·55	0·96	2·11	0·67	11·09	10·84	10·74	10·88	10·42	10·66	10·44	10·93
H_2O^*	4·67	4·67	4·65	4·69	4·67	4·70	4·73	4·66	4·74	4·48	4·50	4·48	4·51	4·54	4·51	4·53	4·52
Total	99·70	99·48	99·50	99·95	99·97	100·08	100·90	100·01	100·78	99·94	99·78	99·58	99·83	100·15	99·95	99·58	99·88
Si	5·91	5·81	5·95	5·96	5·90	5·89	5·96	5·98	6·01	6·95	6·96	6·67	6·95	6·19	6·94	6·12	6·93
Ti	0·01	0·01	0·00	0·00	0·03	0·00	0·02	0·02	0·01	0·01	0·01	0·00	0·00	0·01	0·00	0·01	0·00
Al	6·05	6·17	6·01	6·01	6·02	6·10	5·99	5·93	5·93	4·01	4·05	4·61	4·13	5·63	4·12	5·76	4·14
Fe^{3+}																	
Fe^{2+}	0·04	0·03	0·04	0·03	0·03	0·01	0·05	0·04	0·02	0·25	0·21	0·16	0·16	0·04	0·14	0·01	0·14
Mn							0·00	0·00	0·00	0·00	0·00	0·00	0·00			0·00	0·00
Mg	0·03	0·02	0·03	0·05	0·04	0·03	0·04	0·05	0·07	0·81	0·80	0·57	0·77	0·14	0·82	0·12	0·82
Ca	0·11	0·11	0·05	0·05	0·12	0·05	0·07	0·06	0·03	0·00	0·01	0·00	0·00	0·01	0·01	0·01	0·00
Ba			0·01	0·00	0·00	0·00		0·01	0·00	0·02		0·02	0·01	0·01	0·03		
Na	1·68	1·84	1·69	1·79	1·67	1·81	1·63	1·56	1·80	0·06	0·06	0·12	0·07	0·15	0·06	0·15	0·07
K	0·16	0·03	0·22	0·09	0·18	0·09	0·16	0·35	0·11	1·89	1·84	1·83	1·85	1·75	1·81	1·76	1·85
Mg-no.	0·38	0·46	0·44	0·62	0·56	0·70	0·42	0·55	0·74	0·76	0·79	0·78	0·83	0·77	0·85	0·90	0·86

*Calculated by stoichiometry.

Trondhjemitic segregations

As for the amphibolites, P–T calculations were performed using the lower-variance pargasite-bearing assemblages of samples CV228c, SC2l, and CV62b-II (Fig. 12d). The calculated magmatic P–T conditions are based on the assemblages Amp + Ep + high-K Pa + Qtz + high-Ca Pl. The assemblages used for P–T calculations are shown in the ACF and ACN phase diagrams of Fig. 11. Retrograde conditions were calculated using tremolitic Amp + Chl + Ep + low-K Pa + Lws + Qtz + Ab (sample CV228c) and tremolitic Amp + Chl + Ep + low-K Pa + Qtz + Ab (samples SC2l and CV62b-II).

The calculated magmatic conditions are 747 ± 88°C, 14·7 ± 3·2 kbar (0·988, 0·95), 793 ± 96°C, 19·5 ± 4 kbar (0·97, 0·65), and 730 ± 81°C, 16·8 ± 3·6 kbar (0·983, 0·51) for samples CV228c, SC2l and CV62b-II, respectively. The average calculated temperatures (*c.* 750°C) are within error of calculated temperatures for the amphibolites. The pressure for CV228c overlaps with those for the common (Cpx-lacking) amphibolites. However, the pressures for samples SC2l and CV62b-II are higher. This is a consequence of the higher albite contents of plagioclase of these samples (Fig. 11b), and suggests that the equilibrium composition of magmatic plagioclase is probably not recorded in the analyses performed, as indicated above. Indeed, the P–T conditions calculated for SC2l using the composition of plagioclase from sample CV228c (probably closer to the original composition of magmatic plagioclase) are 749 ± 89°C at 15·4 ± 3·3 kbar (0·988, 0·55), similar to those calculated for CV228c and approaching

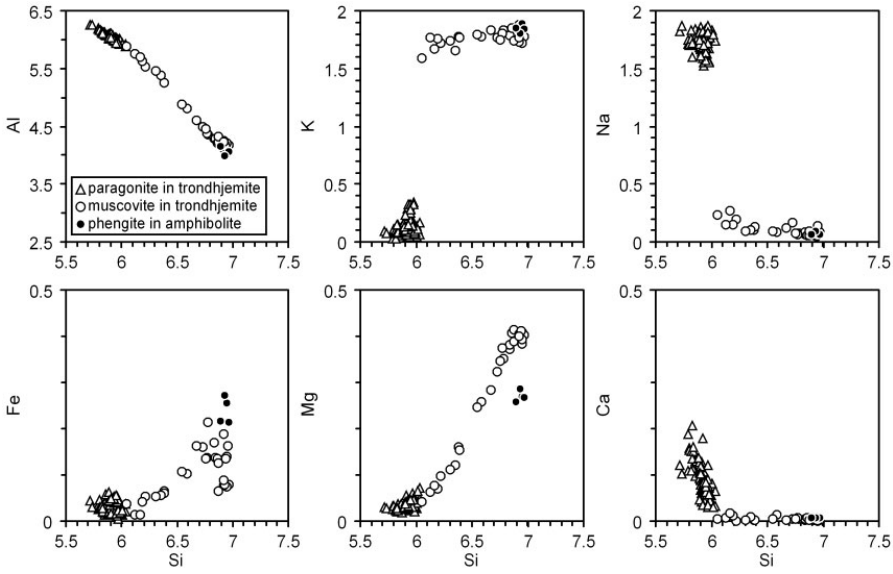

Fig. 9. Composition of micas from amphibolites (phengite) and trondhjemites (paragonite and muscovite–phengite). The high-K analyses of paragonite correspond to magmatic crystals.

Table 9: Representative analyses of chorite (normalized to 20 O and 16 OH)

Rock type:	Amphibolite						Trondhjemite			
Sample:	CV228D	CV228E	CV230B	CV237J	CV53B-I	CV62B-I	CV228C	CV60A	CV62B-II	SC21
SiO_2	25·99	26·36	27·29	26·38	27·85	28·61	29·84	29·38	30·59	29·38
Al_2O_3	20·63	20·61	20·45	18·47	19·10	20·44	19·86	19·77	20·47	20·40
FeO_{total}	22·94	23·02	21·86	27·51	20·08	17·57	14·22	14·62	9·02	12·48
MnO	0·19	0·35	0·26	0·08	0·27	0·26	0·04	0·21	0·18	0·16
MgO	17·73	17·58	17·56	14·80	19·86	21·08	23·71	23·15	27·43	24·83
H_2O^*	11·52	11·56	11·60	11·19	11·66	11·97	12·17	12·05	12·51	12·20
Total	99·01	99·47	99·01	98·43	98·82	99·93	99·84	99·18	100·21	99·44
Si	5·42	5·47	5·64	5·66	5·73	5·73	5·88	5·85	5·87	5·78
Al	5·07	5·04	4·98	4·67	4·63	4·83	4·61	4·64	4·63	4·73
Fe^{2+}	4·00	3·99	3·78	4·93	3·46	2·94	2·34	2·43	1·45	2·05
Mn	0·03	0·06	0·05	0·02	0·05	0·04	0·01	0·03	0·03	0·03
Mg	5·51	5·44	5·41	4·73	6·09	6·30	6·97	6·87	7·84	7·28
Mg-no.	0·58	0·58	0·59	0·49	0·64	0·68	0·75	0·74	0·84	0·78

*Calculated by stoichiometry.

the pressures calculated for peak conditions in the amphibolites. Consequently, these latter P–T conditions for sample SC21 are plotted in Fig. 12d (ellipse with slightly higher peak P).

The conditions calculated for retrogression are 356 ± 18°C, 4·7 ± 1 kbar (0·963, 0·31), 478 ± 43°C, 9·9 ± 2·2 kbar (0·638, 2·15), and 550 ± 21°C, 7·1 ± 0·9 kbar (0·697, 0·79) for samples CV228c, SC21 and CV62b-II, respectively.

Table 10: Representative analyses of pumpellyite (normalized to 28 O and 7 H), lawsonite (normalized to 10 O and 4H), and kyanite (normalized to 5 O)

Phase:	Pumpellyite				Lawsonite		Kyanite	
Rock type:	Amphibolite		Trondhjemite		Trondhjemite		Trondhjemite	
Sample:	CV230B	CV53B-I	CV228C	CV60A	CV228C	CV60A	CV53F	CV60A
Type:	retro	retro	retro	retro	retro	retro	peak	peak
SiO_2	36·86	36·80	38·40	37·70	38·97	38·43	36·06	36·57
TiO_2	0·20	0·07	0·20	0·16	0·05	0·11	0·01	0·04
Al_2O_3	25·27	26·16	25·03	26·16	31·87	32·27	62·48	62·56
FeO_{total}	2·56	2·65	2·30	1·78	0·02	0·04	0·60	0·40
MnO	0·99	0·61	0·59	0·45	0·00	0·00	0·00	0·00
MgO	3·45	3·26	3·96	3·45				
CaO	22·99	23·09	21·16	22·65	18·35	17·53		
BaO		0·00	0·01	0·02	0·00	0·00		
Na_2O		0·19	0·41	0·18				
K_2O		0·00	0·01	0·00				
H_2O^*	6·53	6·58	6·55	6·58	11·54	11·46		
Total	98·85	99·41	98·60	99·14	100·73	99·84	99·14	99·57
Si	5·96	5·91	6·16	6·02	2·03	2·01	0·98	0·99
Ti	0·02	0·01	0·02	0·02	0·00	0·00	0·00	0·00
Al	4·82	4·95	4·73	4·93	1·95	1·99	2·01	2·00
Fe^{3+}	0·00	0·00	0·00	0·00	0·00	0·00	0·01	0·01
Fe^{2+}	0·35	0·36	0·31	0·24				
Mn	0·14	0·08	0·08	0·06	0·00	0·00	0·00	0·00
Mg	0·83	0·78	0·95	0·82				
Ca	3·99	3·98	3·64	3·88	1·02	0·98		
Ba		0·00	0·00	0·00	0·00	0·00		
Na		0·06	0·13	0·06				
K		0·00	0·00	0·00				
Mg-no.	0·71	0·69	0·75	0·78				

*Calculated by stoichiometry (including OH and H_2O).

These conditions are consistent with the retrograde conditions calculated for the amphibolites and indicate cooling at high pressure.

DISCUSSION

A subduction-related migmatitic complex

Field relations in the Sierra del Convento mélange show that the trondhjemitic–tonalitic bodies are closely related to blocks of amphibolite (Fig. 2) and do not crosscut other types of block or the serpentinite matrix of the mélange. This implies that the trondhjemitic–tonalitic melts do not represent exotic intrusions of volcanic-arc magmas and that these melts formed prior to incorporation of the amphibolite blocks into the mélange. On the other hand, the agmatitic structures and veins crosscutting the peak-metamorphic foliation of the amphibolite blocks (Fig. 2d and e) indicate that the melts did not form prior to subduction (i.e. they are not oceanic plagiogranites). The structures show that melt formation and segregation took place during and shortly after ductile deformation at near-peak metamorphic conditions, implying formation by partial melting of amphibolite in the subduction environment.

These inferences are in agreement with the major element composition of the trondhjemites. The peraluminous character of these rocks suggests that they do not represent oceanic plagiogranites or adakitic magmas, which are typically metaluminous (Fig. 3d). The low K_2O contents of the studied rocks also argue against typical adakite magma (Fig. 3b and d). Although less silicic, however, the trondhjemites of the Sierra del Convento mélange are comparable with peraluminous melts of the Catalina Schist formed during partial melting and metasomatism of subducted oceanic crust (Sorensen & Barton, 1987; Sorensen, 1988; Sorensen & Grossman, 1989; Bebout & Barton, 2002; Fig. 3d).

The major element bulk composition of the amphibolites, on the other hand, underlines their residual character attained after extraction of melt. The amphibolites have lower SiO_2 (trending toward apparent picritic compositions) and alkali components, notably Na_2O, and higher molar $Al_2O_3/(Na_2O+K_2O)$ than average MORB (Fig. 3). As discussed below, melting of amphibolite consumed relative large amounts of plagioclase up to its total consumption, a process consistent with these geochemical features if the primary tonalitic–trondhjemitic liquid was extracted after melting (see Fig. 10d). Not surprisingly, the above-mentioned geochemical characteristics are similar to those of residual amphibolite from the Catalina Schist (Fig. 3).

Further evidence for partial melting of amphibolite is given by the calculated peak P–T conditions, which lie above the H_2O-saturated basaltic solidus (Figs 12a, b and 13a). These conditions suggest amphibolite melting at relatively low temperature, below the maximum stability of epidote in the basaltic system (Figs 12a, b and 13). This is in agreement with epidote forming part of the peak metamorphic supersolidus assemblage of the studied amphibolite samples (Fig. 10). In addition, such mineral assemblages and melting conditions indicate that melting occurred under H_2O-present conditions, and that the dry solidus of amphibolite was not intersected (Fig. 12a and b) except perhaps in the Cpx-bearing sample (Fig. 12c).

Wet melting of amphibolite

H_2O-fluid strongly reduces the stability of plagioclase upon melting in the basaltic system, in particular at moderate to high pressure. This effect can be appreciated

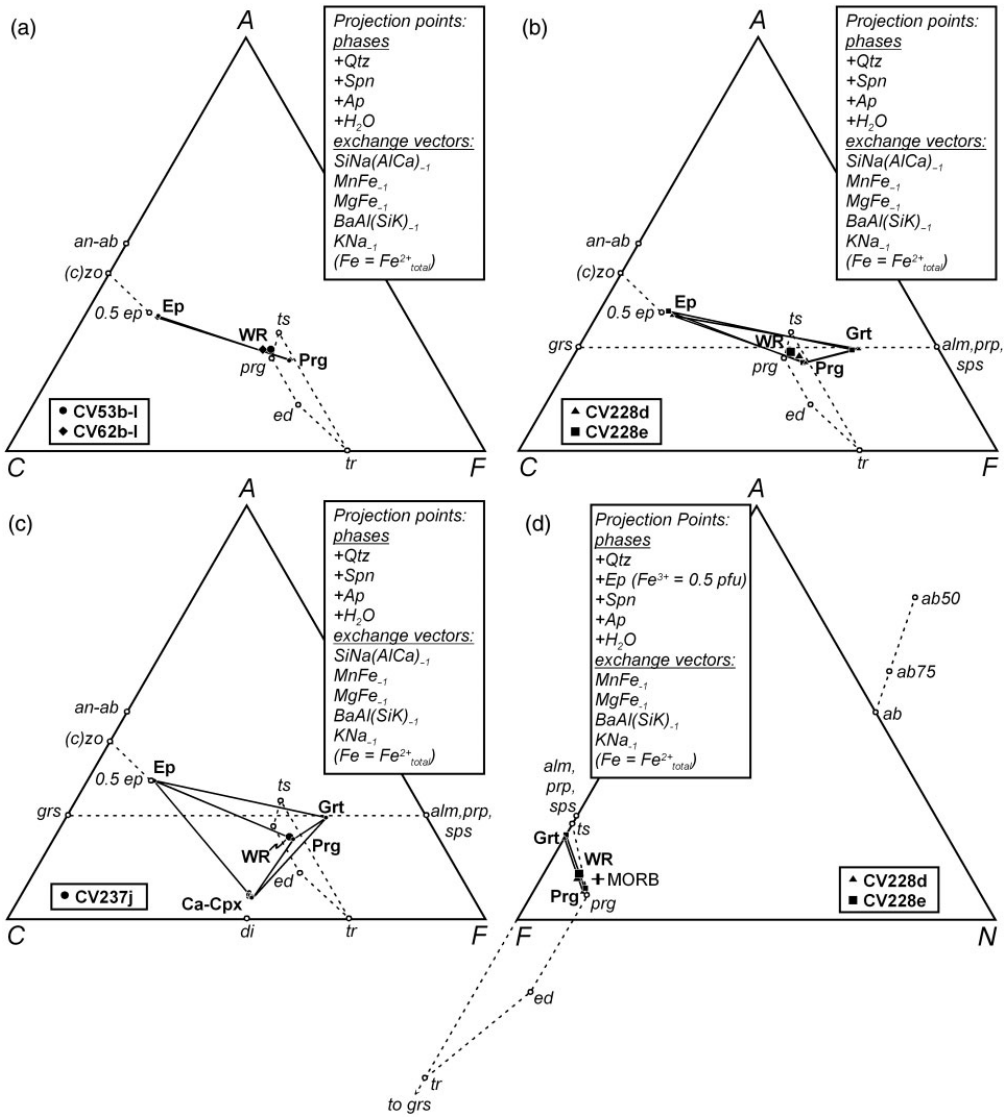

Fig. 10. (a)–(c) ACF and (d) AFN phase diagrams showing peak metamorphic assemblages of amphibolites (continuous tie-lines, labels in bold typeface) and whole-rocks (WR). Average MORB (Hofmann, 1988; Kelemen *et al.*, 2003) has been plotted in (d) for comparison. End-members (labels in italic lower case) of the solid solutions of interest are indicated by open circles joined by dashed lines (0·5 ep: epidote with $Fe^{3+} = 0{\cdot}5$ a.p.f.u.). It should be noted that anorthite and albite end-members are collinear in the ACF diagram. The arrow in (d) indicates projection of grossular at infinity.

in the H_2O-saturated and 5 wt % added H_2O 'experimental pseudosections' compiled by Green (1982) for a standard tholeiitic basaltic composition (Fig. 13). The relations shown in these pseudosections indicate that the stable assemblage appropriate for the calculated peak P–T conditions is Ep + Amp + Cpx + Grt + L ± Qtz, and that the studied amphibolite samples should have contained plagioclase before partial melting.

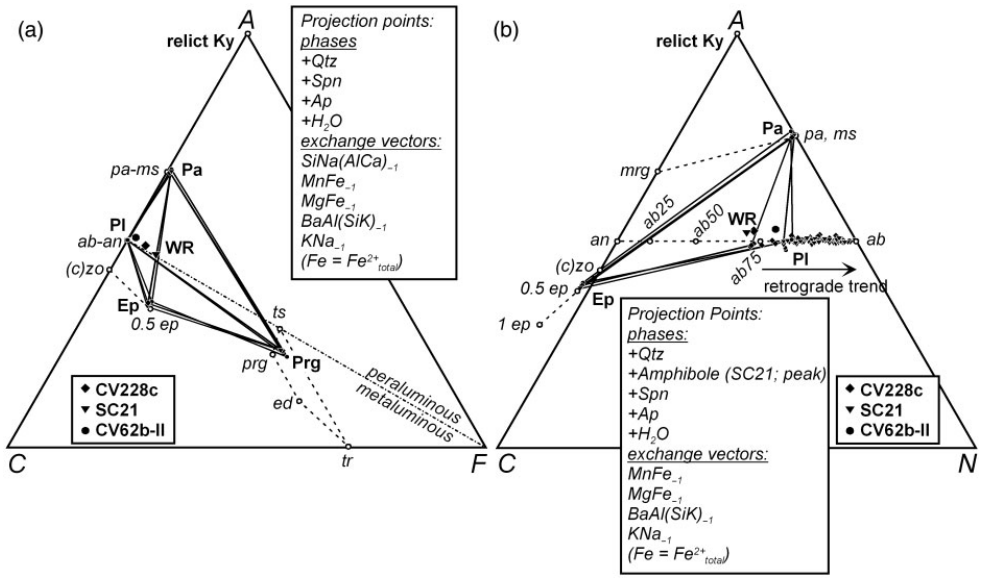

Fig. 11. (a) ACF and (b) ACN phase diagrams showing magmatic assemblages of pargasite-bearing trondhjemites (continuous lines, bold typeface) and whole-rocks (WR). In (b) the retrograde (subsolidus) trend of plagioclase is also shown. End-members (labels in italic lower case) of the solid solutions of interest are indicated by open circles joined by dashed lines (0·5 ep and 1 ep: epidote with $Fe^{3+}=0·5$ and 1·0 a.p.f.u., respectively). It should be noted that the line connecting albite–anorthite in (b) corresponds to the limit of peraluminous vs metaluminous compositions.

The pseudosections of Fig. 13 also suggest that garnet and clinopyroxene are expected after wet melting of amphibolite. As discussed above, the lack of garnet in the higher Mg-number samples can be conceptualized as the result of a bulk composition effect. The lack of clinopyroxene in most samples, however, suggests that this phase is not a necessary product of fluid-present melting of amphibolite. Indeed, whereas experiments indicate that clinopyroxene is a systematic product of melting of rocks of basaltic composition under H_2O-deficient conditions, they also suggest that this phase does not normally form upon wet melting near the solidus (Yoder & Tilley, 1962; Lambert & Wyllie, 1972; Heltz, 1973, 1976; Beard & Lofgren, 1991; Winther & Newton, 1991; Selbekk & Skjerlie, 2002). Consequently, the studied rocks demonstrate that clinopyroxene is not a necessary product of wet melting of amphibolite near the solidus at intermediate pressure, in agreement with proposals by Ellis & Thompson (1986) and Thompson & Ellis (1994).

The calculated conditions for the Cpx-bearing amphibolite sample CV237j (750–850°C, 13–15 kbar) are above the maximum thermal stability of epidote in the water-saturated basaltic system (Figs 12c and 13a). This is not in agreement with textural evidence in this sample, where epidote forms part of the peak assemblage. This conflict is resolved if the peak conditions correspond to those calculated with the maximum Na content of diopsidic clinopyroxene (Fig. 12c) and water availability was more limited (Fig. 13b).

Melting reactions

Establishing the precise nature of the wet-melting reactions undergone by the studied amphibolite samples is hampered by (1) the lack of indication of the composition of peak metamorphic plagioclase present in the samples before melting and (2) the possibility of post-melting processes, such as back-reaction between melt and amphibolite (e.g. Kriegsman, 2001) and/or magmatic differentiation, which would have modified the composition of pristine primary melts. However, the phase relations depicted in the AFM-like diagrams of Fig. 14, combined with the analysis of the respective reaction space, allow us to constrain the nature of the melting reactions for each type of amphibolite. The analysis of reaction space has been performed in the nine-component system SiO_2–TiO_2–Al_2O_3–FeO–MgO–CaO–Na_2O–K_2O–P_2O_5 using the software CSpace (Torres-Roldán *et al.*, 2000). Component H_2O and, consequently, the fluid phase, were excluded from consideration because the H_2O contents of the melts are unknown, although an H_2O-fluid should be considered part of the reactant assemblages. Also, Fe was treated as FeO_{total} and the exchange vector KNa_{-1} was

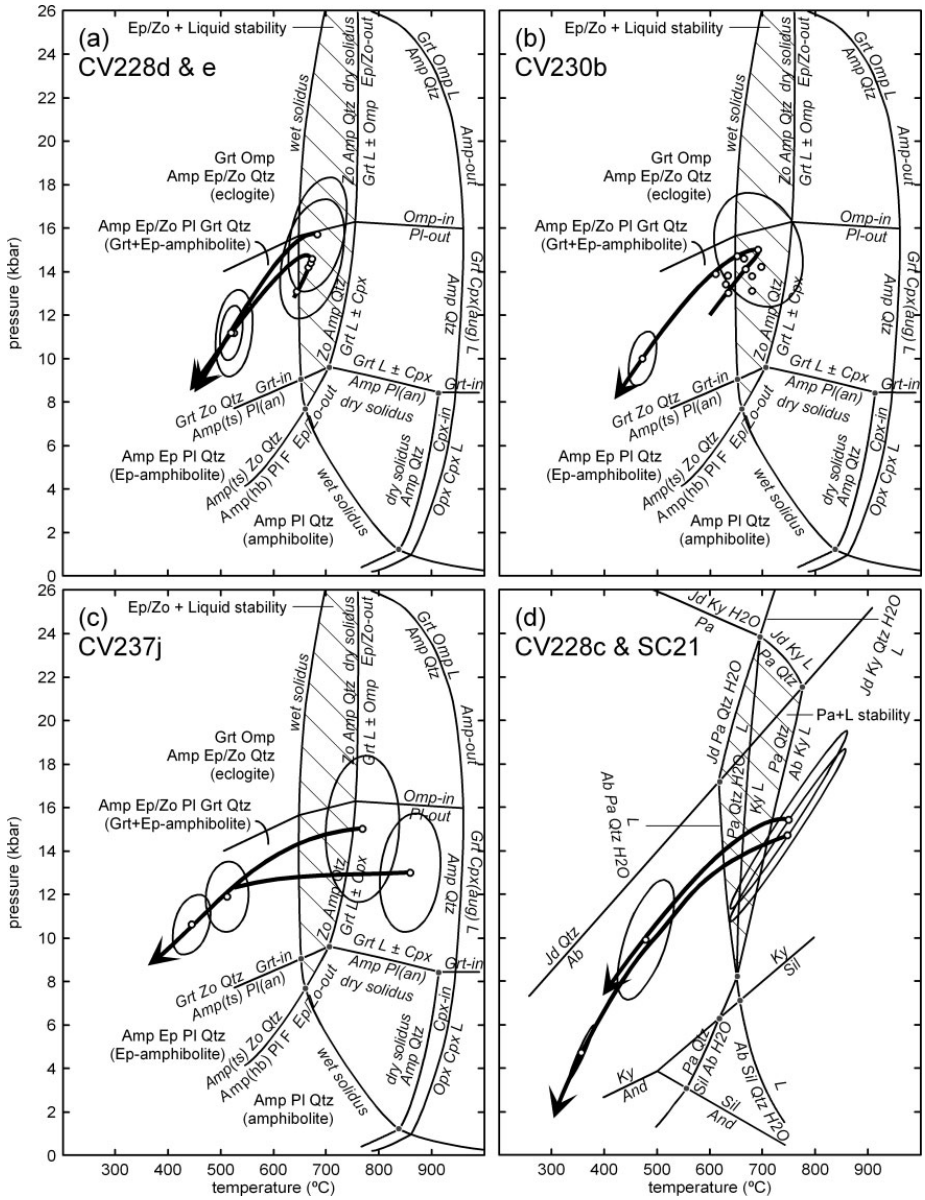

Fig. 12. *P–T* diagrams showing conditions calculated with THERMOCALC and paths for (a)–(c) Grt-bearing amphibolites and (d) Amp-bearing trondhjemites. Error ellipses: ±1 σ. For reference, the grid for the basaltic system (Vielzeuf & Schmidt, 2001) is included in (a)–(c), and a grid for a simple trondhjemitic (NASH) system (Spear, 1993; García-Casco, 2007) is included in (d). The hatched regions in (a)–(c) and (d) represent the stabilities of epidote + liquid and paragonite + liquid, respectively. The two peak *P–T* conditions for the Cpx-bearing sample CV237j shown in (c) correspond to results using low Na (higher *T*) and high Na (lower *T*) contents of peak diopsidic clinopyroxene.

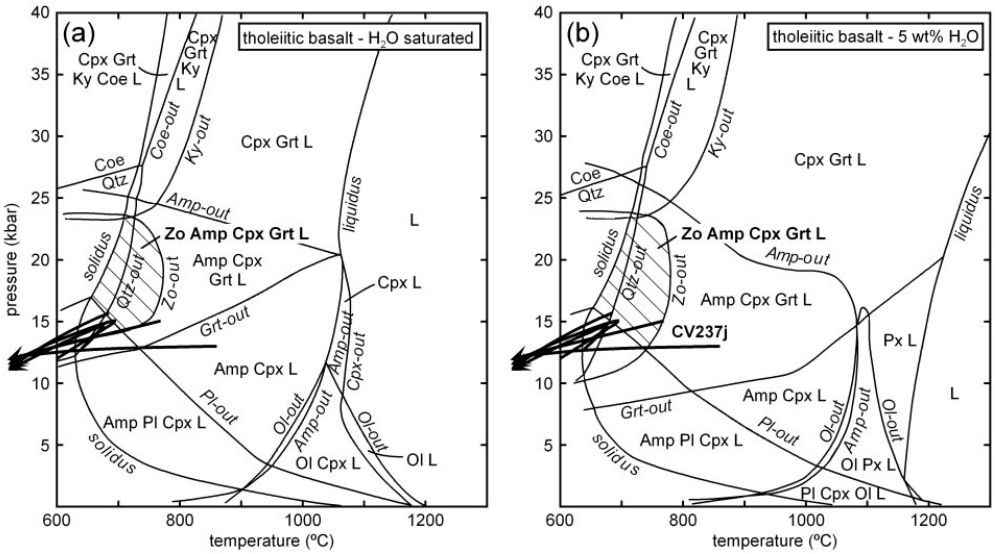

Fig. 13. Experimental pseudosections for the tholeiitic basaltic system constructed by Green (1982) for (a) water-saturated and (b) 5 wt % added H_2O conditions, and *P–T* paths calculated for the studied amphibolites. The hatched regions represent the stability fields of epidote + liquid above the stability limit of plagioclase, consistent with the mineral assemblages and calculated peak *P–T* conditions of the studied amphibolites. As shown in (b), the calculated *P–T* conditions and peak assemblage of the clinopyroxene-bearing sample CV237j suggest limited availability of H_2O.

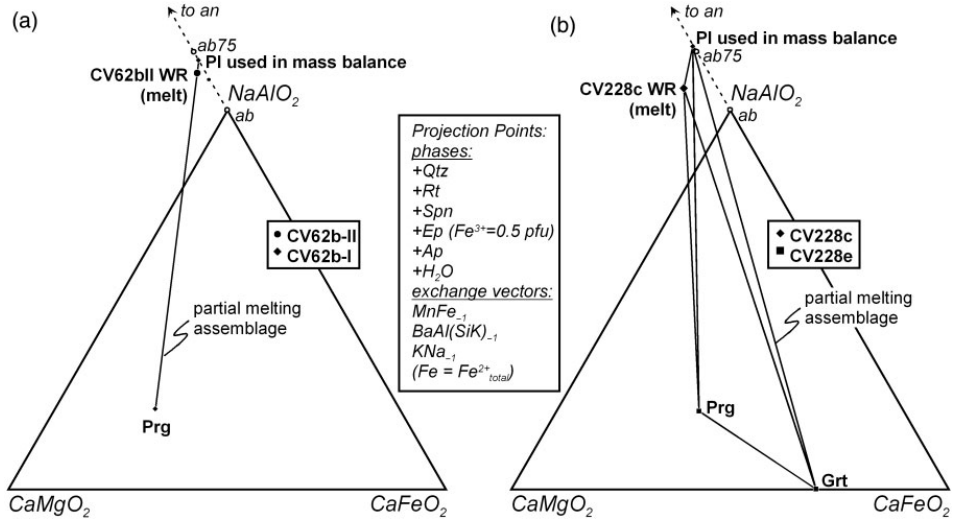

Fig. 14. AFM-like phase diagrams for sample sites (a) CV62 and (b) CV228. The continuous tie-lines and triangles represent the partial melting assemblages amphibole ± garnet + plagioclase + melt (see text for justification of plagioclase composition and mass-balance calculations using these assemblages). The arrows indicate projection of anorthite component at infinity.

included in the calculation because of the lack of K-bearing phases during partial melting. With these and other constraints related to system degeneracy discussed below, the reaction space for each case discussed in the following paragraphs is uni-dimensional, and the resulting single reaction represents a mass balance that can be potentially identified as a melting reaction. All the reactions are expressed in oxy-equivalent units.

Garnet-lacking amphibolites

The mineral assemblage of the garnet-lacking amphibolite samples is represented in the AFM-like diagram of Fig. 14a by no more than peak pargasite (note that the phase relations are projected from epidote). This allows deduction of the composition of coexisting plagioclase before melting, provided that the composition of the melt is known. As an example, Fig. 14a shows the relations for sample site CV62b. If (1) trondhjemite vein CV62b-II represents the primary melt evolved from adjacent amphibolite CV62b-I, and (2) plagioclase was totally consumed upon melting, the composition of peak metamorphic plagioclase is constrained to be collinear with peak pargasite and melt, implying a degenerate relation (Fig. 14a). The corresponding calculated composition of plagioclase is $X_{ab} = 0{\cdot}78$ and the associated reaction is

$$82{\cdot}3\ \mathrm{Pl}(X_{ab} = 0{\cdot}78) + 14{\cdot}1\ \mathrm{Qtz} + 4{\cdot}1\ \mathrm{Ep} + 1{\cdot}9\ \mathrm{Rt} + 1{\cdot}2\ \mathrm{Amp} + 0{\cdot}1\ \mathrm{Ap}(+\mathrm{H_2O}) = 100\ \mathrm{L(CV62b-II)} + 4{\cdot}5\ \mathrm{Spn}.$$

It should be noted that large relative amounts of reactant plagioclase contribute to melt formation. This is a consequence of melt and plagioclase being similar in composition, as clearly shown in the AFM diagram of Fig. 14a, where both phases plot close to one each other.

The melting reaction deduced above is near-eutectic (i.e. $\mathrm{Pl} + \mathrm{Qtz} + \mathrm{Amp} + \mathrm{Ep} = \mathrm{L}$). This general form remains unchanged even if the primary melt has a different composition from that of trondhjemite vein CV62b-II. Mass-balance constraints imply collinearity between amphibole, primary melt and plagioclase, and large relative amounts of reactant plagioclase in the associated degenerate reaction for any other tonalitic–trondhjemitic primary melt composition rich in plagioclase component. Consequently, we consider that the eutectic melting reaction $\mathrm{Pl} + \mathrm{Qtz} + \mathrm{Amp} + \mathrm{Ep} = \mathrm{L}$ is a good approximation to the wet-melting process undergone by the garnet-lacking amphibolites.

Garnet-bearing amphibolites

As an example, we discuss the relations for sample site CV228, where amphibolite CV228e is closely associated with trondhjemite segregate CV228c (Fig. 14b). The latter sample is taken as a preliminary guess for the primary melt. Fixing the composition of the primary melt does not uniquely constrain the composition of plagioclase coexisting with the mineral assemblage of amphibolite CV228e. Three reactions are possible depending on the composition of plagioclase. Plagioclase with $X_{ab} = 0{\cdot}69$ is collinear with amphibole and melt, implying a degenerate reaction involving no garnet (i.e. $\mathrm{Pl} + \mathrm{Qtz} + \mathrm{Amp} + \mathrm{Ep} = \mathrm{L}$, as above). For plagioclase with $X_{ab} > 0{\cdot}69$ the melt plots to the left of the tie-line pargasite–plagioclase in the AFM-like diagram, as shown in Fig. 14b for plagioclase with $X_{ab} = 0{\cdot}72$. This type of topology implies a peritectic AFM reaction of the form $\mathrm{Amp} + \mathrm{Pl} + \mathrm{Ep} + \mathrm{Qtz} = \mathrm{L} + \mathrm{Grt}$. For plagioclase with $X_{ab} < 0{\cdot}69$ the melt plots to the right of the tie-line pargasite–plagioclase and within the tie-triangle pargasite–garnet–plagioclase in the AFM-like diagram, implying an AFM melting reaction of the form $\mathrm{Amp} + \mathrm{Pl} + \mathrm{Grt} + \mathrm{Qtz} = \mathrm{L} + \mathrm{Ep}$. The corresponding mass-balance reactions calculated for $X_{ab} = 0{\cdot}72$, $X_{ab} = 0{\cdot}69$ and $X_{ab} = 0{\cdot}66$, respectively, are

$$84{\cdot}2\ \mathrm{Pl}(X_{ab} = 0{\cdot}72) + 11{\cdot}5\ \mathrm{Ep} + 8{\cdot}1\ \mathrm{Amp} + 4{\cdot}5\ \mathrm{Qtz} + 3{\cdot}6\ \mathrm{Rt} + 0{\cdot}1\ \mathrm{Ap}(+\mathrm{H_2O}) = 100\ \mathrm{L} + 8{\cdot}8\ \mathrm{Spn} + 4{\cdot}4\ \mathrm{Grt}$$

$$87{\cdot}3\ \mathrm{Pl}(X_{ab} = 0{\cdot}69) + 0{\cdot}7\ \mathrm{Ep} + 5{\cdot}9\ \mathrm{Amp} + 4{\cdot}7\ \mathrm{Qtz} + 1{\cdot}6\ \mathrm{Rt} + 0{\cdot}1\ \mathrm{Ap}(+\mathrm{H_2O}) = 100\ \mathrm{L} + 3{\cdot}6\ \mathrm{Spn}$$

$$92{\cdot}9\ \mathrm{Pl}(X_{ab} = 0{\cdot}66) + 4{\cdot}7\ \mathrm{Amp} + 2{\cdot}6\ \mathrm{Grt} + 4\ \mathrm{Qtz} + 0{\cdot}6\ \mathrm{Rt} + 0{\cdot}01\ \mathrm{Ap}(+\mathrm{H_2O}) = 100\ \mathrm{L} + 1{\cdot}3\ \mathrm{Spn} + 5{\cdot}8\ \mathrm{Ep}.$$

For the same reasons as indicated above, these reactions involve large relative amounts of reactant plagioclase and suggest total consumption of this phase upon melt formation.

Similar reactions would be deduced if trondhjemite CV228c does not represent a pristine primary melt. For other tonalitic–trondhjemitic primary melt compositions rich in plagioclase component it is possible to evaluate the melting relations fixing the composition of plagioclase. Our results indicate reactions with the same general forms as those deduced above (i.e. $\mathrm{Pl} + \mathrm{Qtz} + \mathrm{Amp} + \mathrm{Ep} = \mathrm{L} + \mathrm{Grt}$, $\mathrm{Pl} + \mathrm{Qtz} + \mathrm{Amp} + \mathrm{Ep} = \mathrm{L}$, and $\mathrm{Pl} + \mathrm{Qtz} + \mathrm{Amp} + \mathrm{Grt} = \mathrm{L} + \mathrm{Ep}$). Therefore, melting of the studied garnet-bearing amphibolites should conform to one of these reactions.

The degenerate eutectic-like reaction $\mathrm{Pl} + \mathrm{Qtz} + \mathrm{Amp} + \mathrm{Ep} = \mathrm{L}$ involving no garnet is considered unlikely because there is no fundamental reason for a general collinear relation between plagioclase, amphibole and melt in garnet-bearing assemblages. The other two reactions are peritectic. We favour reaction $\mathrm{Pl} + \mathrm{Qtz} + \mathrm{Amp} + \mathrm{Ep} = \mathrm{L} + \mathrm{Grt}$ (Fig. 14b) because garnet is idiomorphic in sample CV228e (Fig. 4a), a feature that conflicts with reactant garnet as predicted by reaction $\mathrm{Amp} + \mathrm{Pl} + \mathrm{Grt} = \mathrm{L} + \mathrm{Ep}$. Furthermore, the latter reaction has epidote in the product, a result that is inconsistent with theory and

experiments (e.g. Ellis & Thompson, 1986; Thompson & Ellis, 1994; Quirion & Jenkins, 1998).

A variety of melting reactions are possible for the garnet + clinopyroxene-bearing amphibolite sample CV237j. The number of possible reactions is larger in this case because the presence of quartz in the pre-melting assemblage of this quartz-lacking sample is uncertain. Garnet, clinopyroxene, amphibole and epidote may appear either as reactants or products in these reactions, depending on the composition of plagioclase and melt and the presence or absence of quartz. However, in all the possible reactions the amount of plagioclase involved is large, in agreement with the behaviour of this phase in other types of amphibolite studied.

Thus, it is concluded that the amount of plagioclase present in amphibolite prior to melting is a major control on the extent of wet melting. This inference applies to amphibolite with different mineral assemblages undergoing different melting reactions. Because of the relatively high pressure of melting (*c.* 15 kbar) the amount of plagioclase present in the pre-melting assemblages is inferred to have been small and, consequently, low melt fractions should have been produced. Low melt fractions are consistent with the Fe + Mg-poor nature of the studied trondhjemitic rocks. These inferences strongly suggest that plagioclase was completely consumed in the amphibolites upon melting and that the trondhjemites are (near-) primary melts.

Peraluminosity of primary slab melts

The studied rocks confirm that melts formed upon partial melting of metabasite at intermediate pressure under fluid-present conditions are peraluminous (see Ellis & Thompson, 1986; Thompson & Ellis, 1994) and that this type of melt can form in a subducting slab. However, peraluminosity is not a typical characteristic of magmas thought to have formed upon partial melting of subducted slabs (e.g. Cenozoic adakites, Archaean tonalite–trondhjemite complexes; Defant & Drummond, 1990; Martin, 1999). This observation should be taken into consideration when the origin of slab-derived magmas is addressed.

Experimental work on melting of natural and synthetic metabasites has shown that peraluminous melts form at low-temperature conditions close to the wet basaltic solidus, and metaluminous melts form under conditions that deviate from the wet basaltic solidus, typically at >850°C (Yoder & Tilley, 1962; Holloway & Burnham, 1972; Heltz, 1976; Ellis & Thompson, 1986; Beard & Lofgren, 1989; Rapp *et al.*, 1991; Winther & Newton, 1991; Gaetani *et al.*, 1993; Thompson & Ellis, 1994; Kawamoto, 1996; Springer & Seck, 1997; Nakajima & Arima, 1998; Prouteau *et al.*, 2001; Selbekk & Skjerlie, 2002; Koepke *et al.*, 2004). Under conditions close to the solidus, amphibole is abundant and plagioclase is scarce or not present in the residua, small melt fractions are formed, and the resulting melt is acid, in all aspects similar to characteristic amphibolite–trondhjemite associations of the Sierra del Convento mélange. Under conditions that deviate from the solidus, amphibole is scarce or not present, large melt fractions are formed, and the resulting melt is relatively basic (andesitic). It follows that metaluminous slab magmas, if formed by melting of mafic rocks close to the wet solidus, are not pristine slab melts. Metaluminosity of such magmas should be identified, instead, as a consequence of post-melting processes such as interaction with the mantle wedge and/or the base of the crust (see Kepezhinskas *et al.*, 1995; Stern & Kilian, 1996; Martin, 1999; Prouteau *et al.*, 2001; Yogodzinski *et al.*, 2001).

Magmatic paragonite and kyanite

Magmatic paragonite is expected in peraluminous melts that crystallized at moderate to high pressure. As shown in Fig. 12d, magmatic paragonite is stable in the model NASH system above 8 kbar. Similar relations are predicted in the more complex NCASH system (García-Casco, 2007). Using a NCASH pseudosection approach, García-Casco (2007) calculated that paragonite is stable above the solidus of sample SC21 in the range 680–730°C at *c.* 14 kbar. This is consistent with the high K content of magmatic paragonite (Fig. 9), which indicates crystallization at high temperature (García-Casco, 2007). Crystallization of trondhjemitic melt at depth within the stability field of paragonite is also consistent with the occurrence of magmatic epidote in the studied rocks (Fig. 4i and k), a feature that is normally taken as an indication of moderate to high pressure of crystallization of magmatic rocks (Schmidt & Poli, 2004, and references therein). The model phase relations calculated by García-Casco (2007) show that magmatic epidote is not stable at <13 kbar in bulk composition SC21, in agreement with the calculated crystallization pressure of 14–16 kbar (Fig. 12d).

The presence of kyanite relicts within magmatic epidote in some samples (Fig. 4m) also points to crystallization at high pressure. The NCASH pseudosection for sample SC21 shows stable kyanite + epidote above the solidus at >720°C, 14–15 kbar and total consumption of kyanite upon reaction with melt to produce paragonite and more epidote during near-isobaric cooling (García-Casco, 2007). These relations explain the relict nature of kyanite within epidote in the studied rocks.

The consistency between natural mineral assemblages and theoretical phase relations allows the conclusion that paragonite is an expected product of crystallization of peraluminous trondhjemitic melt at intermediate to high pressure. Therefore, relatively low pressure (<8 kbar) of crystallization explains the lack of paragonite in natural peraluminous trondhjemites (e.g. Johnson *et al.*, 1997).

Tectonic implications

Recent thermal models incorporating appropriate temperature dependence of mantle rheology suggest that melting of subducted oceanic crust may occur at shallower depths and be more general over a range of plate velocities and ages, subduction angles, and other geophysical variables (i.e. not restricted to special cases of subduction) than previously assumed based on the relatively cool slabs calculated in earlier models (e.g. van Keken *et al.*, 2002; Gerya & Yuen, 2003; Conder, 2005; Abers *et al.*, 2006). Following these recent results, melting in the Sierra del Convento could be interpreted as the result of normal subduction. Thermal models, however, also point towards special subduction environments where melting is possible at relatively shallow depths, including the edge of a slab (e.g. Kincaid & Griffiths, 2004), subhorizontal subduction (e.g. Manea *et al.*, 2005), subduction retreat (e.g. Kincaid & Griffiths, 2003, 2004), onset of subduction (e.g. Gerya *et al.*, 2002), or subduction of a very young slab or a ridge (e.g. Okudaira & Yoshitake, 2004; Uehara & Aoya, 2005). Though it is difficult to decipher the precise subduction environment of formation of the studied rocks, regional arguments favour a scenario of onset of subduction of young oceanic lithosphere.

Regional geological data for the Caribbean realm point to initiation of subduction during the Aptian (*c.* 120 Ma; Pindell *et al.*, 2005, 2006). Pindell *et al.* have developed a tectonic model for the evolution of the Caribbean realm that incorporates the birth of a SW-dipping subduction system during the Aptian that consumed oceanic lithosphere of the Protocaribbean (Atlantic) basin, which was opening at that time, and, consequently, subduction of a hot, young oceanic lithosphere and/or a ridge was possible. Indirect evidence for the existence of a (near-orthogonal) subducting Protocaribbean ridge during the Cretaceous is given by geochemical studies of magmatic rocks from the overriding Caribbean plate (e.g. Jolly & Lidiak, 2006; Escuder-Viruete *et al.*, 2007; see also discussion by Pindell *et al.*, 2005, 2006). Thus, because age data indicate that the earliest stage of subduction in eastern Cuba is Aptian (*c.* 120 Ma; see García-Casco *et al.*, 2006), the studied rocks probably formed in a scenario of onset of subduction of young lithosphere (Fig. 15).

After a thorough consideration of *P–T–t* data and thermal models, Krebs *et al.* (2007) recently developed a similar scenario of onset of Aptian subduction of young (*c.* 20 Ma) Protocaribbean lithosphere for eclogite blocks of the Río San Juan mélange (Dominican Republic). The descriptions and interpretations of those workers suggest that the Río San Juan and the Sierra del Convento mélanges are geologically correlated. The Río San Juan mélange contains eclogites formed during the early Cretaceous (103·6 ± 2·7 Ma) and blueschist formed during the late Cretaceous. The eclogites attained similar peak temperature (*c.* 750°C) to the Sierra del Convento amphibolites, although the former attained substantially higher peak pressure (*c.* 23 kbar) and did not apparently undergo partial melting. These differences in the earliest products of subduction point to strike-parallel variations in the thermal structure (i.e. age) of the subducting Protocaribbean during the early Cretaceous. Plate-tectonic reconstructions locate eastern Cuba to the NNW of Hispaniola by Aptian times (Pindell *et al.*, 2005), implying that the subducting slab was hotter (i.e. younger) to the NNW (relative to Hispaniola) and, consequently, that the ridge should have been located close to eastern Cuba by Aptian times.

This scenario for the onset of subduction explains the observed counterclockwise *P–T* paths of the Sierra del Convento amphibolite blocks. Onset of subduction produces a transient geothermal gradient at the slab–mantle interface, which cools upon continued subduction (Gerya *et al.*, 2002). Our calculated *P–T* paths suggest that, after accretion to the overriding plate, the blocks of amphibolite and associated trondhjemites were refrigerated at depth, in agreement with the expected effects of continued subduction (Fig. 12). At this stage in the Sierra del Convento mélange the trondhjemite magmas formed by partial melting of amphibolite, cooled and crystallized. The subduction models of Gerya *et al.* (2002) show that continued subduction leads to the formation of a serpentinitic layer (subduction channel) by hydration of the overriding mantle some Ma after the onset of subduction. Gerya *et al.* also indicated that formation of such a serpentinite layer allows formation of serpentinite mélanges and the onset of exhumation of early accreted blocks along the subduction channel. In the Sierra del Convento mélange this stage is recorded by the blueschist-facies overprints developed as the amphibolite and trondhjemite blocks followed counterclockwise *P–T* paths (Fig. 15).

As subduction proceeds, more material normally of lower grade can be accreted to the subduction channel (Gerya *et al.*, 2002). Blocks of blueschist not studied here record this stage in the Sierra del Convento. A similar picture evolves for the Río San Juan mélange (Krebs *et al.*, 2007). Thus, both mélanges constitute fragments of a subduction channel documenting a long-lasting history of subduction, accretion, mélange formation, and uplift, and both give direct evidence for Aptian onset of subduction of the Protocaribbean (Fig. 15).

CONCLUSIONS

The Sierra del Convento mélange (eastern Cuba) contains high-grade tectonic blocks of plagioclase-lacking epidote ± garnet amphibolite and associated tonalite–trondhjemite, which formed during subduction of oceanic lithosphere. Field relations, major element bulk-rock

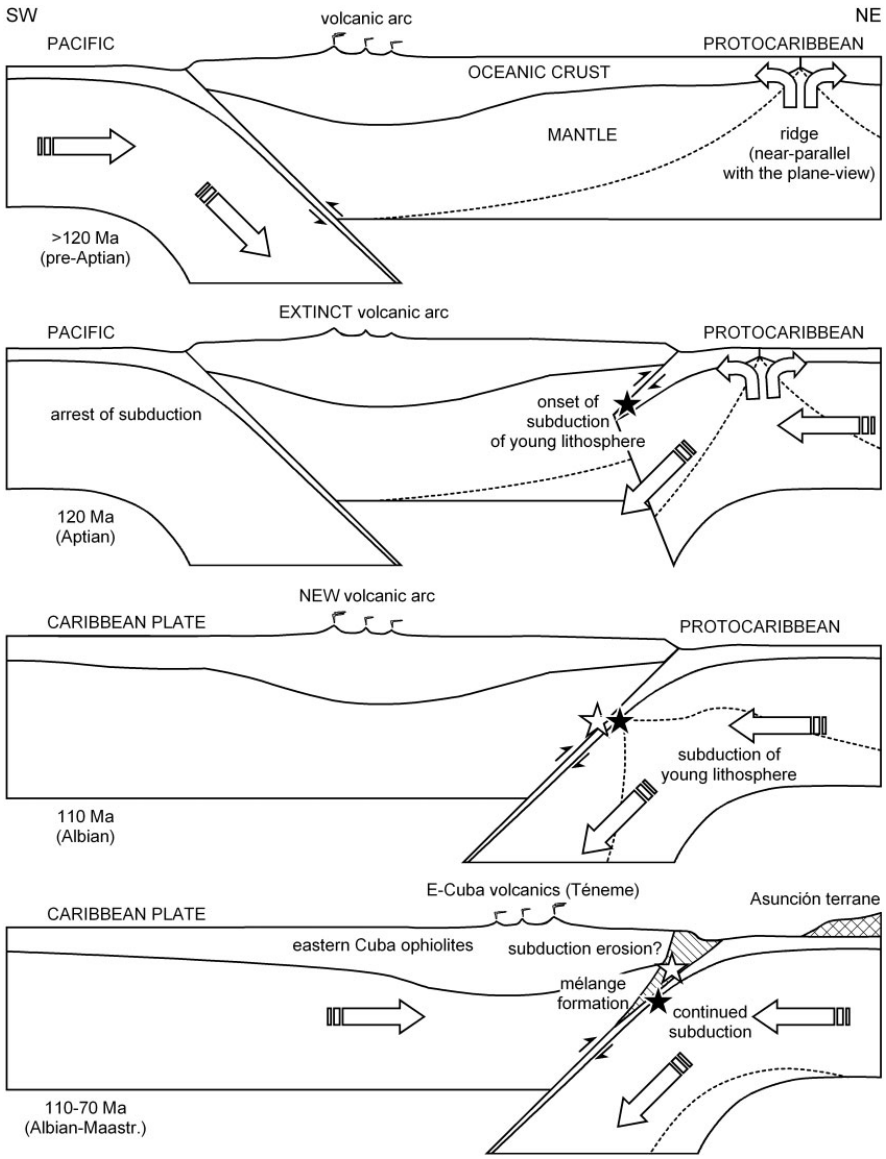

Fig. 15. Schematic representation of the tectonic evolution of eastern Cuba (see Pindell *et al.*, 2005). The filled and open stars indicate amphibolite in the course of Aptian onset of subduction of young lithosphere and late Cretaceous accretion–exhumation of the tectonic blocks, respectively. The Sierra del Convento mélange formed in the subduction channel (hatched). Subduction of volcanic-arc material (Purial Complex) suggests subduction erosion during the late Cretaceous.

compositions, textures, peak metamorphic, magmatic and retrograde mineral assemblages, and P–T conditions, and the agreement between the observed mineral assemblages and those predicted by experimental and theoretical studies indicate that tonalite–trondhjemite formed by partial melting of amphibolite in the subduction environment and that both shared a common P–T history during exhumation. Thus, these tectonic blocks represent a rare

example of oceanic subduction-related migmatites that have returned to the Earth's surface. Regional arguments suggest a scenario of onset of subduction of young oceanic lithosphere (during the Aptian). Partial melting at *c.* 15 kbar, 750°C was characterized by low melt fractions, was fluid-assisted, occurred close to the metabasite solidus, consumed large relative amounts of plagioclase in the amphibolites, and formed plagioclase-lacking residual amphibolite and peraluminous, K-poor, high Mg-number leucocratic tonalitic–trondhjemitic melts that segregated into veins, layers and agmatitic structures. Shortly after melt formation amphibolite + melt blocks were accreted to the overriding plate, where they began to cool as subduction proceeded, allowing the partial melts to crystallize at depth. This favoured the formation of magmatic paragonite, kyanite, epidote, plagioclase, pargasite, and quartz during crystallization of the melts. Later, syn-subduction exhumation in the mélange caused counter-clockwise P–T paths, forming retrograde blueschist-facies assemblages in all types of rock. Blueschist-facies conditions prevailed during the ensuing history of subduction, when other blocks were incorporated into the mélange, attesting to a long-lasting history of accretion, mélange formation and uplift.

ACKNOWLEDGEMENTS

The authors thank Walter Maresch, an anonymous reviewer, and editor Ron Frost for their perceptive comments and suggestions, which substantially improved this paper. Walter Maresch is also thanked for providing a preprint manuscript by Krebs and co-workers on the Río San Juan mélange. Manuel Iturralde-Vinent kindly reviewed an early version. This is a contribution to IGCP-546 'Subduction zones of the Caribbean' and is Mainz Geocycles contribution 318. We appreciate financial support from MEC project CGL2006-08527/BTE.

REFERENCES

Abers, G. A., van Keken, P. E., Kneller, E. A., Ferris, A. & Stachnik, J. C. (2006). The thermal structure of subduction zones constrained by seismic imaging: Implications for slab dehydration and wedge flow. *Earth and Planetary Science Letters* **241**, 387–397.

Barker, F. (1979). Trondhjemites: Definition, environment and hypotheses of origin. In: Barker, F. (ed.) *Trondhjemites, Dacites and Related Rocks*. Amsterdam: Elsevier, pp. 1–12.

Beard, J. S. & Lofgren, G. E. (1989). Effect of water on the composition of melts of greenstone and amphibolites. *Science* **244**, 195–197.

Beard, J. S. & Lofgren, G. E. (1991). Dehydration melting and water-saturated melting of basaltic and andesitic greenstones and amphibolites at 1, 3, and 6·9 kb. *Journal of Petrology* **32**, 365–401.

Bebout, G. E. (2007). Metamorphic chemical geodynamics of subduction zones. *Earth and Planetary Science Letters* **260**, 373–393.

Bebout, G. E. & Barton, M. D. (2002). Tectonic and metasomatic mixing in a high-T, subduction-zone mélange—insights into the geochemical evolution of the slab–mantle interface. *Chemical Geology* **187**, 79–106.

Boiteau, A., Michard, A. & Saliot, P. (1972). Métamorphisme de haute pression dans le complexe ophiolitique du Purial (Oriente, Cuba). *Comptes Rendus de l'Académie des Sciences, Série D* **274**, 2137–2140.

Cobiella, J., Quintas, F., Campos, M. & Hernández, M. (1984). *Geología de la Región Central y Suroriental de la Provincia de Guantánamo. Santiago de Cuba*. Santiago de Cuba: Editorial Oriente, 125 pp.

Coleman, R. G., Lee, D. E., Beatty, L. B. & Brannock, W. W. (1965). Eclogites and eclogites: their differences and similarities. *Geological Society of America Bulletin* **76**, 483–508.

Conder, J. A. (2005). A case for hot slab surface temperatures in numerical viscous flow models of subduction zones with an improved fault zone parameterization. *Physics of the Earth and Planetary Interiors* **149**, 155–164.

Coutinho, J. M. V., Kräutner, H. G., Sassi, F., Schmid, R. & Sen, S. (2007). A systematic nomenclature for metamorphic rocks: 8. Amphibolite and granulite. *Recommendations by the IUGS Subcommission on the Systematics of Metamorphic Rocks. Web version of 01.02.2007* (http://www.bgs.ac.uk/SCMR/docs/papers/paper.8.pdf).

De Andrade, V., Vidal, O., Lewin, E., O'Brien, P. & Aagard, P. (2006). Quantification of electron microprobe compositional maps of rock thin sections: an optimized method and examples. *Journal of Metamorphic Geology* **24**, 655–668.

Defant, M. J. & Drummond, M. S. (1990). Derivation of some modern arc magmas by melting of young subducted lithosphere. *Nature* **347**, 662–665.

Drummond, M. S., Defant, M. J. & Kepezhinskas, P. K. (1996). Petrogenesis of slab-derived trondhjemite–tonalite–dacite/adakite magmas. *Transactions of the Royal Society of Edinburgh: Earth Sciences* **87**, 205–215.

Elliott, T., Plank, T., Zindler, A., White, W. & Bourdon, B. (1997). Element transport from slab to volcanic front at the Mariana arc. *Journal of Geophysical Research* **102** (B7), 14991–15019.

Ellis, D. J. & Thompson, A. B. (1986). Subsolidus and partial melting reactions in the quartz-excess $CaO + MgO + Al_2O_3 + SiO_2 + H_2O$ system under water-excess and water-deficient conditions to 10 kb: Some implications for the origin of peraluminous melts from mafic rocks. *Journal of Petrology* **27**, 91–121.

Ernst, W. G. (1999). Metamorphism, partial preservation, and exhumation of ultrahigh-pressure belts. *The Island Arc* **8**, 125–153.

Escuder-Viruete, J. & Pérez-Estaún, A. (2006). Subduction-related P–T path for eclogites and garnet glaucophanites from the Samaná Peninsula basement complex, northern Hispaniola. *International Journal of Earth Sciences* **95**, 995–1017.

Escuder-Viruete, J. Contreras, F., Stein, G., Urien, P., Joubert, M., Pérez-Estaún, A., Friedman, R. & Ullrich, T. (2007). Magmatic relationships and ages between adakites, magnesian andesites and Nb-enriched basalt–andesites from Hispaniola: Record of a major change in the Caribbean island arc magma sources. *Lithos* **99**, 151–177.

Gaetani, G. A., Grove, T. L. & Bryan, W. B. (1993). The influence of water on the petrogenesis of subduction-related igneous rocks. *Nature* **365**, 332–335.

García-Casco, A. (2007). Magmatic paragonite in trondhjemites from the Sierra del Convento mélange, Cuba. *American Mineralogist* **92**, 1232–1237.

García-Casco, A., Torres-Roldán, R. L., Millán, G., Monié, P. & Schneider, J. (2002). Oscillatory zoning in eclogitic garnet and amphibole, Northern Serpentinite Mélange, Cuba: a record of tectonic instability during subduction? *Journal of Metamorphic Geology* **20**, 581–598.

García-Casco, A., Torres-Roldán, R. L., Iturralde-Vinent, M. A., Millán, G., Núñez Cambra, K., Lázaro, C. &

Rodríguez Vega, A. (2006). High pressure metamorphism of ophiolites in Cuba. *Geologica Acta* **4**, 63–88.

Gerya, T. V. & Yuen, D. A. (2003). Rayleigh–Taylor instabilities from hydration and melting propel 'cold plumes' at subduction zones. *Earth and Planetary Science Letters* **212**, 47–62.

Gerya, T. V., Stoeckhert, B. & Perchuk, A. L. (2002). Exhumation of high-pressure metamorphic rocks in a subduction channel—a numerical simulation. *Tectonics* **21**, 6-1–6-19.

Green, T. H. (1982). Anatexis of mafic crust and high pressure crystallization of andesite. In: Thorpe, R. S. (ed.) *Andesites*. Chichester: John Wiley, pp. 465–487.

Grove, T. L., Chatterjee, N., Parman, S. W. & Médard, E. (2006). The influence of H_2O on mantle wedge melting. *Earth and Planetary Science Letters* **249**, 74–89.

Harlow, G. E., Hemming, S. R., Avé Lallemant, H. G., Sisson, V. B. & Sorensen, S. S. (2004). Two high-pressure–low-temperature serpentinite-matrix mélange belts, Motagua fault zone, Guatemala: A record of Aptian and Maastrichtian collisions. *Geology* **32**, 17–20.

Heltz, R. T. (1973). Phase relations of basalt in their melting ranges at $P_{H2O} = 5$ kb as a function of oxygen fugacity. Part I. Mafic phases. *Journal of Petrology* **14**, 249–302.

Heltz, R. T. (1976). Phase relations of basalt in their melting ranges at $P_{H2O} = 5$ kb. Part II. Melt compositions. *Journal of Petrology* **17**, 139–193.

Hermann, J., Spandler, C., Hack, A. & Korsakov, A. V. (2006). Aqueous fluids and hydrous melts in high-pressure and ultra-high pressure rocks: Implications for element transfer in subduction zones. *Lithos* **92**, 399–417.

Hernández, M. & Canedo, Z. (1995). Geoquímica de las ofiolitas meridionales de Cuba oriental. *Revista Minería y Geología* **3**, 3–9.

Hofmann, A. W. (1988). Chemical differentiation of the Earth: the relationship between mantle, continental crust, and oceanic crust. *Earth and Planetary Science Letters* **90**, 297–314.

Holland, T. J. B. & Powell, R. (1998). An internally consistent thermodynamic data set for phases of petrological interest. *Journal of Metamorphic Geology* **16**, 309–343.

Holloway, J. R. & Burnham, C. W. (1972). Melting relations of basalt with equilibrium water pressure less than total pressure. *Journal of Petrology* **13**, 1–29.

Iturralde-Vinent, M. A. (1996). Introduction to Cuban Geology and Geophysics. In: Iturralde-Vinent, M. A. (ed.) *Ofiolitas y Arcos Volcánicos de Cuba. IGCP Project 364 Special Contribution* **1**, 3–35.

Iturralde-Vinent, M. A. (1998). Sinopsis de la constitución Geológica de Cuba. *Acta Geologica Hispanica* **33**, 9–56.

Iturralde-Vinent, M. A. & Lidiak, E.G. (2006). Caribbean tectonic, magmatic, metamorphic and stratigraphic events. Implications for plate tectonics. *Geologica Acta* **4**, 1–5.

Iturralde-Vinent, M. A., Millán, G., Korkas, L., Nagy, E. & Pajón, J. (1996). Geological interpretation of the Cuban K–Ar data base. In: Iturralde-Vinent, M. A. (ed.). *Ofiolitas y Arcos Volcánicos de Cuba. IGCP Project 364 Special Contribution* **1**, 48–69.

Iturralde-Vinent, M. A., Díaz Otero, C., Rodríguez Vega, A. & Díaz Martínez, R. (2006). Tectonic implications of paleontologic dating of Cretaceous–Danian sections of Eastern Cuba. *Geologica Acta* **4**, 89–102.

Johnson, K., Barnes, C. G. & Miller, C. A. (1997). Petrology, geochemistry, and genesis of high-Al tonalite and trondhjemites of the Cornucopia Stock, Blue Mountains, northeastern Oregon. *Journal of Petrology* **38**, 1585–1611.

Johnson, M. C. & Plank, T. (1999). Dehydration and melting experiments constrain the fate of subducted sediments. *Geochemistry, Geophysics, Geosystems* **1**, paper number 1999GC000014.

Jolly, W. T. & Lidiak, E. G. (2006). Role of crustal melting in petrogenesis of the Cretaceous Water Island Formation (Virgin Islands, northeast Antilles Island arc). *Geologica Acta* **4**, 7–33.

Kawamoto, T. (1996). Experimental constraints on differentiation and H_2O abundance of calc-alkaline magmas. *Earth and Planetary Science Letters* **144**, 577–589.

Kelemen, P. B., Hanghoj, K. & Greene, A. R. (2003). One view of the geochemistry of subduction-related magmatic arcs with an emphasis on primitive andesite and lower crust. In: Rudnick, R. L. (ed.) *The Crust*. [*Treatise on Geochemistry, Volume 3* (eds H. D. Holland & K. K. Turekian).] Oxford: Elsevier–Pergamon, pp. 593–659.

Kepezhinskas, P. K., Defant, M. J. & Drummond, M. S. (1995). Na metasomatism in the island-arc mantle by slab melt–peridotite interaction: evidence from mantle xenoliths in the north Kamchatka arc. *Journal of Petrology* **36**, 1505–1527.

Kessel, R., Ulmer, P., Pettke, T., Schmidt, M. W. & Thompson, A. B. (2005). The water–basalt system at 4 to 6 GPa: Phase relations and second critical endpoint in a K-free eclogite at 700 to 1400°C. *Earth and Planetary Science Letters* **237**, 873–892.

Kincaid, C. & Griffiths, R. W. (2003). Laboratory models of the thermal evolution of the mantle during rollback subduction. *Nature* **425**, 58–62.

Kincaid, C. & Griffiths, R. W. (2004). Variability in flow and temperatures within mantle subduction zones. *Geochemistry, Geophysics, Geosystems* **5**, Q06002, doi:10.1029/2003GC000666.

Koepke, J., Feig, S. T., Snow, J. & Freise, M. (2004). Petrogenesis of oceanic plagiogranites by partial melting of gabbros: an experimental study. *Contributions to Mineralogy and Petrology* **146**, 414–432.

Krebs, M., Maresch, W.V., Schertl, H.-P., Baumann, A., Draper, G., Idleman, B., Münker, C. & Trapp, E. (2007). The dynamics of intra-oceanic subduction zones: A direct comparison between fossil petrological evidence (Rio San Juan Complex, Dominican Republic) and numerical simulation. *Lithos* (in press).

Kretz, R. (1983). Symbols for rock-forming minerals. *American Mineralogist* **68**, 277–279.

Kriegsman, L. M. (2001). Partial melting, partial melt extraction and partial back reaction in anatectic migmatites. *Lithos* **56**, 75–96.

Kulachkov, L. V. & Leyva, R. C. (1990). Informe sobre los resultados de los trabajos de reconocimiento geológico para cuarzo filoniano en la parte oriental de Cuba. Unpublished report of the Instituto Superior Minero-Metalúrgico de Moa (Cuba).

Lambert, I. B. & Wyllie, P. J. (1972). Melting of gabbro (quartz-eclogite) with excess water to 35 kilobars, with geological applications. *Journal of Geology* **80**, 693–708.

Leake, B. E., Woolley, A. R., Arps, C. E. S. *et al.* (1997). Nomenclature of amphiboles: Report of the Subcommittee on Amphiboles of the International Mineralogical Association, Commission on New Minerals and Mineral Names. *American Mineralogist* **82**, 1019–1037.

Le Maitre, R. W., Streckeisen, A. & Zanettin, B. *et al.* (eds) *Igneous Rocks: A Classification and Glossary of Terms*, 2nd edn. Cambridge: Cambridge University Press, 236 p.

Leyva, R. C. (1996). Características geológicas, regularidades de distribución y perspectivas de utilización del cuarzo filoniano de la región oriental de Cuba. Unpublished report of the Instituto Superior Minero-Metalúrgico de Moa (Cuba), 90 pp.

Manea, V. C., Manea, M., Kostoglodov, V. & Sewell, G. (2005). Thermo-mechanical model of the mantle wedge in Central Mexican subduction zone and a blob tracing approach for the magma transport. *Physics of the Earth and Planetary Interiors* **149**, 165–186.

Marchesi, C., Garrido, C. J., Bosch, D., Proenza, J. A., Gervilla, F., Monié, P. & Rodríguez-Vega, A. (2007). Geochemistry of Cretaceous magmatism in eastern Cuba: recycling of North

American continental sediments and implications for subduction polarity in the Greater Antilles Paleo-arc. *Journal of Petrology* **48**, 1813–1840.

Martin, H. (1999). Adakitic magmas: modern analogues of Archaean granitoids. *Lithos* **46**, 411–429.

Millán, G. (1996). Metamorfitas de la asociación ofiolítica de Cuba. In: Iturralde-Vinent, M. A. (ed.). *Ofiolitas y Arcos Volcánicos de Cuba. IGCP Project 364 Special Contribution* **1**, 131–146.

Millán, G. & Somin, M. L. (1985). Contribución al conocimiento geológico de las metamorfitas del Escambray y Purial. *Reportes de Investigación de la Academia de Ciencias de Cuba* **2**, 1–74.

Millán, G., Somin, M. L. & Díaz, C. (1985). Nuevos datos sobre la geología del macizo montañoso de la Sierra del Purial, Cuba Oriental. *Reporte de Investigación del Instituto de Geología y Paleontología* **2**, 52–74.

Morimoto, N., Fabries, J., Ferguson, A. K., Ginzburg, I. V., Ross, M., Seifert, F. A., Zussman, J., Aoki, K. & Gottardi, G. (1988). Nomenclature of pyroxenes: Report of the Subcommittee on Pyroxenes of the International Mineralogical Association, Commission on New Minerals and Mineral Names. *American Mineralogist* **73**, 1123–1133.

Nakajima, K. & Arima, M. (1998). Melting experiments on hydrous low-K tholeiite: Implications for the genesis of tonalitic crust in the Izu–Bonin–Mariana arc. *The Island Arc* **7**, 359–373.

O'Connor, J. T. (1965). A classification of quartz-rich igneous rocks based on feldspar ratios. *US Geological Survey Professional Papers* **525B**, B79–B84.

Okudaira, T. & Yoshitake, Y. (2004). Thermal consequences of the formation of a slab window beneath the Mid-Cretaceous southwest Japan arc: A 2-D numerical analysis. *The Island Arc* **13**, 520–532.

Peacock, S. M. (2003). Thermal structure and metamorphic evolution of subducting slabs. In: Eiler, J. (ed.). *Inside the Subduction Factory. Geophysical Monograph, American Geophysical Union* **138**, 7–22.

Peacock, S. M., Rushmer, T. & Thompson, A. B. (1994). Partial melting of subducting oceanic crust. *Earth and Planetary Science Letters* **121**, 227–244.

Pindell, J. L, Kennan, L., Maresch, W. V., Stanek, K. P., Draper, G. & Higgs, R. (2005). Plate-kinematics and crustal dynamics of circum-Caribbean arc–continent interactions: Tectonic controls on basin development in Proto-Caribbean margins. In: Avé Lallemant, H. G. & Sisson, V. B. (eds) *Caribbean–South American Plate Interactions, Venezuela. Geological Society of America, Special Papers* **394**, 7–52.

Pindell, J. L., Kennan, L., Stanek, K. P., Maresch, W. V. & Draper, G. (2006). Foundations of Gulf of Mexico and Caribbean evolution: eight controversies resolved. *Geologica Acta* **4**, 303–341.

Powell, R. & Holland, T. J. B. (1994). Optimal geothermometry and geobarometry. *American Mineralogist* **79**, 120–133.

Proenza, J. A., Díaz-Martínez, R., Iriondo, A., Marchesi, C., Melgarejo, J. C., Gervilla, F., Garrido, C. J., Rodríguez-Vega, A., Lozano-Santacruz, R. & Blanco-Moreno, J. A. (2006). Primitive Cretaceous island-arc volcanic rocks in eastern Cuba: the Téneme Formation. *Geologica Acta* **4**, 103–121.

Prouteau, G., Scaillet, B., Pichavant, M. & Maury, R. C. (2001). Evidence for mantle metasomatism by hydrous silicic melts derived from subducted oceanic crust. *Nature* **410**, 197–200.

Quirion, D. M. & Jenkins, D. M. (1998). Dehydration and partial melting of tremolitic amphibole coexisting with zoisite, quartz, anorthite, diopside and water in the system H_2O–CaO–MgO–Al_2O_3–SiO_2. *Contributions to Mineralogy and Petrology* **130**, 379–389.

Rapp, R. P., Watson, E. B. & Miller, C. F. (1991). Partial melting of amphibolite/eclogite and the origin of Archean trondhjemites and tonalites. *Precambrian Research* **51**, 1–25.

Rojas-Agramonte, Y., Neubauer, F., Handler, R., García-Delgado, D. E., Friedl, G. & Delgado-Damas, R. (2005). Variation of paleostress patterns along the Oriente Transform Fault, Cuba: Significance for Neogene–Quaternary tectonics of the Caribbean realm. *Tectonophysics* **396**, 161–180.

Schmidt, M. W. & Poli, S. (1998). Experimentally based water budgets for dehydrating slabs and consequences for arc magma generation. *Earth and Planetary Science Letters* **163**, 361–379.

Schmidt, M. W. & Poli, S. (2004). Magmatic epidote. In: Liebscher, A. & Franz, G. (eds) *Epidotes. Mineralogical Society of America, Reviews in Mineralogy and Geochemistry* **56**, 399–430.

Selbekk, R. S. & Skjerlie, K. P. (2002). Petrogenesis of the anorthosite dyke swarm of Tromsø, North Norway: Experimental evidence for hydrous anatexis of an alkaline mafic complex. *Journal of Petrology* **43**, 943–962.

Smithies, R. H. (2000). The Archaean tonalite–trondhjemite–granodiorite (TTG) series is not an analogue of Cenozoic adakite. *Earth and Planetary Science Letters* **182**, 115–125.

Somin, M. L. & Millán, G. (1981). *Geology of the Metamorphic Complexes of Cuba*. Nauka: Moscow, 219 pp. (in Russian).

Somin, M. L., Arakelyants, M. M. & Kolesnikov, E. M. (1992). Age and tectonic significance of high-pressure metamorphic rocks in Cuba. *International Geology Review* **34**, 105–118.

Sorensen, S. S. (1988). Petrology of amphibolite-facies mafic and ultramafic rocks from the Catalina Schist, Southern California: metasomatism and migmatization in a subduction zone metamorphic setting. *Journal of Metamorphic Geology* **6**, 405–435.

Sorensen, S. S. & Barton, M. D. (1987). Metasomatism and partial melting in a subduction complex: Catalina Schist, southern California. *Geology* **15**, 115–118.

Sorensen, S. S. & Grossman, J. N. (1989). Enrichment in trace elements in garnet amphibolites from a paleo-subduction zone: Catalina Schist, southern California. *Geochimica et Cosmochimica Acta* **53**, 3155–3177.

Spear, F. S. (1993). *Metamorphic Phase Equilibria and Pressure–Temperature–Time Paths. Mineralogical Society of America, Monograph* **1**, 799 p.

Springer, W. & Seck, H. A. (1997). Partial fusion of basic granulites at 5 to 15 kbar: implications for the origin of TTG magmas. *Contributions to Mineralogy and Petrology* **127**, 30–45.

Staudigel, H., Plank, T., White, B. & Schmincke, H. U. (1996). Geochemical fluxes during seafloor alteration of the upper oceanic crust: DSDP sites 417–418. In: Bebout, G. E., Scholl, D. W., Kirby, S. H. & Platt, J. P. (eds) *Subduction Top to Bottom. Geophysical Monograph, American Geophysical Union* **96**, 19–38.

Stern, C. R. & Kilian, R. (1996). Role of the subducted slab, mantle wedge and continental crust in the generation of adakites from the Andean Austral Volcanic Zone. *Contributions to Mineralogy and Petrology* **123**, 263–281.

Stern, R. J. (2002). Subduction zones. *Reviews of Geophysics* **40**, article number 1012, doi:10.1029/2001RG000108.

Stolz, A. J., Jochum, K. P., Spettel, B. & Hofman, A. W. (1996). Fluid- and melt-related enrichment in the subarc mantle: evidence from Nb/Ta variations in island-arc basalts. *Geology* **24**, 587–590.

Thompson, A. B. & Ellis, D. (1994). $CaO + MgO + Al_2O_3 + SiO_2 + H_2O$ to 35 kb: Amphibole, talc, and zoisite dehydration and melting reactions in the silica-excess part of the system and their possible significance in subduction zones, amphibole melting, and magma fractionation. *American Journal of Science* **294**, 1229–1289.

Torres-Roldán, R. L., García-Casco, A. & García-Sánchez, P. A. (2000). CSpace: An integrated workplace for the graphical and algebraic analysis of phase assemblages on 32-bit Wintel platforms. *Computers and Geosciences* **26**, 779–793.

Uehara, S. & Aoya, M. (2005). Thermal model for approach of a spreading ridge to subduction zones and its implications for high-*P*/high-*T* metamorphism: Importance of subduction versus ridge approach ratio. *Tectonics* **24**, TC4007, doi:10.1029/2004TC001715.

van Keken, P. E., Kiefer, B. & Peacock, S. M. (2002). High-resolution models of subduction zones: Implications for mineral dehydration reactions and the transport of water into the deep mantle. *Geochemistry, Geophysics, Geosystems* **3**, 1056, doi:10.1029/2001GC000256.

Vielzeuf, D. & Schmidt, M. W. (2001). Melting reactions in hydrous systems revisited: applications to metapelites, metagreywackes and metabasalts. *Contributions to Mineralogy and Petrology* **141**, 251–267.

Winther, K. T. & Newton, R. C. (1991). Experimental melting of hydrous low-K tholeiite: evidence on the origin of Archaean cratons. *Bulletin of the Geological Society of Denmark* **39**, 213–228.

Yoder, H. S., Jr & Tilley, C. E. (1962). Origin of basalt magmas; an experimental study of natural and synthetic rock systems. *Journal of Petrology* **3**, 342–532.

Yogodzinski, G. M., Lees, J. M., Churikova, T. G., Dorendorf, F., Wörner, G. & Volynets, O. N. (2001). Geochemical evidence for the melting of subducting oceanic lithosphere at plate edges. *Nature* **409**, 500–504.

Contrib Mineral Petrol (2009) 158:1–16
DOI 10.1007/s00410-008-0367-0

ORIGINAL PAPER

A new jadeitite jade locality (Sierra del Convento, Cuba): first report and some petrological and archeological implications

Antonio García-Casco · A. Rodríguez Vega · J. Cárdenas Párraga · M. A. Iturralde-Vinent · C. Lázaro · I. Blanco Quintero · Y. Rojas Agramonte · A. Kröner · K. Núñez Cambra · G. Millán · R. L. Torres-Roldán · S. Carrasquilla

Received: 19 July 2008 / Accepted: 24 November 2008 / Published online: 12 December 2008

Abstract A new jadeitite jade locality has been discovered in the serpentinite-matrix subduction mélange of the Sierra del Convento (eastern Cuba) in a context associated with tectonic blocks of garnet-epidote amphibolite, tonalitic–trondhjemitic epidote gneiss, and blueschist. The mineral assemblages of jadeitite jade and jadeite rocks are varied and include combinations of jadeite, omphacite, albite, paragonite, analcime, clinozoisite-epidote, apatite, phlogopite, phengite, chlorite, glaucophane, titanite, rutile, zircon, and quartz formed during various stages in their P–T evolution. Field relationships are obscure, but some samples made almost exclusively of jadeite show evidence of crystallization from fluid in veins. In one of these samples studied in detail jadeite shows complex textural and chemical characteristics (including oscillatory zoning) that denote growth in a changing chemical medium. It is proposed that interaction of an Al–Na rich fluid with ultramafic rocks produced Al–Na–Mg–Ca fluids of varying composition. Episodic infiltration of these fluids, as a result of episodic opening of the veins, developed oscillatory zoning by direct precipitation from fluid and after reaction of fluid with pre-existing jadeite. The latest infiltrating fluids were richer in Mg–Ca, favouring the formation of omphacite and Mg–Ca rich jadeite in open voids and the replacement of earlier jadeite by fine-grained omphacite + jadeite at 550–560°C. This new occurrence of jadeite in Cuba opens important perspectives for archeological studies of pre-Columbian jade artifacts in the Caribbean region.

Keywords Jadeitite jade · High pressure · Fluids · Subduction · Caribbean · Eastern Cuba

Communicated by H. Keppler.

A. García-Casco (✉)
Departamento de Mineralogía y Petrología, Universidad de Granada, and Instituto Andaluz de Ciencias de la Tierra, CSIC-Universidad de Granada, Avda Fuentenueva sn, 18002 Granada, Spain
e-mail: agcasco@ugr.es

A. Rodríguez Vega · Y. Rojas Agramonte
Departamento de Geología, Instituto Superior Minero-Metalúrgico, Las Coloradas s/n., Moa 83329, Holguín, Cuba

J. Cárdenas Párraga · C. Lázaro · I. Blanco Quintero · R. L. Torres-Roldán · S. Carrasquilla
Departamento de Mineralogía y Petrología, Universidad de Granada, Avda Fuentenueva sn, 18002 Granada, Spain

M. A. Iturralde-Vinent
Museo Nacional de Historia Natural, Obispo no. 61, Plaza de Armas, 10100 La Habana, Cuba

Y. Rojas Agramonte · A. Kröner
Institut für Geowissenschaften, Universität Mainz, 55099 Mainz, Germany

K. Núñez Cambra · G. Millán
Instituto de Geología y Paleontología, Via Blanca y Carretera Central, San Miguel del Padrón, 11000 Ciudad Habana, Cuba

Introduction

Jade is a gemological term embracing actinolite–tremolite amphibolitite rocks (termed nephrite jade) and jadeite pyroxenite rocks or jadeitite (jadeite jade). Nephrite jade is a metasomatic rock that forms in a variety of petrologic–geologic settings, including the replacement of dolomitic marble by Si-rich fluids associated with magmatic rocks in contact aureoles and the replacement of meta-ultramafic rocks (serpentinite) by Ca-rich fluids in (tectonic) interfaces between serpentinite and Si-rich rocks such as

plagiogranite, graywacke, argillite or chert (Harlow and Sorensen 2005). Jadeite jade, in turn, is found almost exclusively associated with serpentinite, generally within serpentinite-matrix tectonic mélanges containing exotic blocks formed in high-pressure subduction environments (Harlow and Sorensen 2005). The temperature of crystallization of jadeite jade is generally relatively low (250–550°C), as documented by in situ jadeitite deposits where antigoritite forms the wall rock of jade bodies. Harlow and Sorensen (2005) noted the scarcity of jadeitite in high-pressure complexes, citing only 12 localities in Myanmar, Guatemala, Russia, Kazakhstan, Japan, California, Italian Alps, and Turkey. Sorensen et al. (2006) cited only eight "well documented, primary, hard-rock occurrences" of jade. Recently, new jadeitite localities have been documented in Iran (Oberhänsli et al. 2007) and Dominican Republic (Schertl et al. 2007a, b; Baese et al. 2007). Harlow and Sorensen (2005) indicated that, in spite of probable fairly common formation of jadeitite in subduction environments, complex sequences of tectonic of events/conditions should concur in order to exhume serpentinite-matrix mélanges bearing jadeitite.

Metasomatism of blocks of trondhjemite, plagiogranite, (meta)granitoid, leucogabbro, eclogite, metapelite, and metagraywacke has been classically considered the main jadeitite-forming process (see review by Harlow and Sorensen 2005 for complete list of references). However, these authors have noted a number of problems with this interpretation, including the common lack of protoliths and protolith replacement textures, severe mass-balance problems, and the common occurrence of idiomorphic oscillatory zoning of jadeite. After reviewing worldwide jadeitite occurrences (Harlow and Sorensen 2005, see also Sorensen et al. 2006) emphasized that jadeite precipitates directly from fluids evolved at depth. This conclusion makes this type of rock of interest for the direct characterization of fluids and fluid-assisted processes in the subduction environment, including processes of mass transfer from the downgoing slab to the upper plate which may ultimately lead to the formation of arc magmas.

Jadeitite and jadeite-bearing rocks are scarce in the Caribbean region. Rare river pebbles of jadeitite of unknown in situ location were found in the Cretaceous subduction complex of Escambray, central Cuba, by Millán and Somin (1981). This "old" finding has reached only limited audience due to editorial and language problems. However, only a brief petrographic description was made available by Millán and Somin (1981), who indicate radial aggregates of jadeite and isolated grains of clinozoisite, lawsonite and albite. Rare relictic presumably magmatic clinopyroxene partly replaced by fine-grained jadeite led these authors to suggest formation of jadeitite by replacement of basic intrusive bodies, implying metasomatic origin. A variety of jadeitite and jadeite-bearing rocks have been recently discovered in the Cretaceous subduction mélange of Río San Juan, Dominican Republic (Schertl et al. 2007a, b; Baese et al. 2007; Krebs et al. 2008). The available information suggests complex processes including direct precipitation from fluid. The high-pressure Escambray complex and Rio San Juan mélange may be geologically correlated to Cretaceous high pressure complexes of central Guatemala (Motagua Valley region), where jadeitite is abundant and varied in terms of P–T conditions of formation (Harlow 1994; Harlow et al. 2003).

In this paper, we document for the first time the occurrence of jadeite jade in eastern Cuba. The new locality is in the subduction mélange of Sierra del Convento (Fig. 1), which correlates with the Rio San Juan mélange (García-Casco et al. 2008; Lázaro et al. 2008). These mélanges and the Escambray complex may have formed in the same subduction zone, but the latter mostly records late Cretaceous subduction-accretion of margin-like sediments (García-Casco et al. 2008) while the former record mid-late subduction of oceanic material. Our goal is not to offer a full description of the variety of jadeitite and related rocks in the mélange, but to give notice of the finding and to provide some insight into the origin of jadeitite and jadeitite-forming fluids. This is relevant because the Sierra del Convento mélange shows abundant evidence for fluid circulation in the subduction environment. In particular, fluid infiltration triggered metasomatism and partial melting of subducted ocean crust (García-Casco et al. 2008; Lázaro and García-Casco 2008), a process hardly ever seen in other worldwide occurrences of oceanic subduction complexes exhumed to the Earth's surface (e.g., Sorensen and Barton 1987; Sorensen 1988). Partial melts crystallized in the subduction environment (García-Casco 2007; García-Casco et al. 2008) and evolved fluids that formed pegmatitic and hydrothermal rocks that may have had to do with jadeite formation. Also, the mélange contains a high quantity of pure rock crystal quartz in hydrothermal veins and blocks prospected for electronic applications (Kulachkov and Leyva 1990; Leyva 1996).

The new finding, together with other old and recent findings of jadeitite in the Caribbean region, opens new archeological perspectives for the source of pre-Columbian jade artifacts found in the Antilles (e.g., Harlow et al. 2006, Fig. 1a).

Geologic and petrologic settings

The Sierra del Convento mélange represents an oceanic subduction channel related to subduction of Proto-Caribbean lithosphere below the Caribbean plate during the Cretaceous (García-Casco et al. 2006, 2008; García-Casco 2007; Lázaro

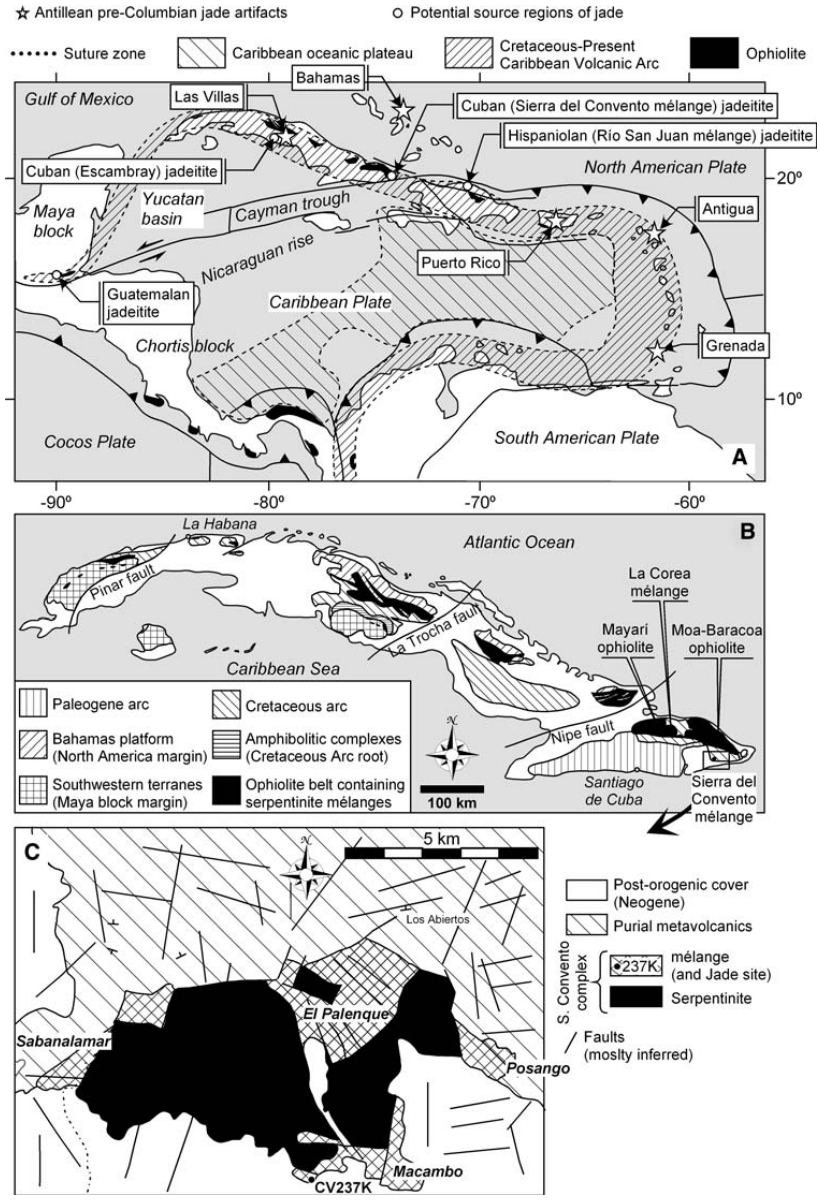

Fig. 1 **a** Plate tectonic scheme of the Caribbean region, with important geological features including ophiolitic bodies and location of geological jadeitite source regions (Millán and Somin 1981; Harlow 1994; Harlow and Sorensen 2005; Schertl et al. 2007a; Schertl et al. 2007b; Baese et al. 2007, this paper) and of archeological locations of Antillean jade artifacts (Calvache 1944; Soto González 1981; Keegan 1991; Aarons 1990; Rodriguez 1991; Harlow et al. 2006; García Padilla et al. 2006; Wilson 2007). **b** Geological sketch map of Cuba (after Iturralde-Vinent 1998) showing location of the study area. **c** Geologic map of the Sierra del Convento mélange (Kulachkov and Leyva 1990) showing jade locality

and García-Casco 2008, and Lázaro et al. 2008 for details of the following descriptions and for references on the geology of the region). The mélange is formed by a serpentinite matrix, which contains a variety of tectonic blocks metamorphosed to high pressure and low to high temperature, including blueschists, pelitic gneisses, tonalitic–trondhjemitic gneisses, and epidote-garnet plagioclase-lacking amphibolites. The formation of the mélange began in the early Cretaceous (ca. 120 Ma) and proceeded until the complex was emplaced on top of the Cretaceous volcanic arc complex of El Purial during the latest Cretaceous.

The most typical type of tectonic block in the mélange is MORB-derived plagioclase-lacking epidote ± garnet ± clinopyroxene amphibolite. This type of rock is typically closely associated with cm- to dm-sized trondhjemitic to tonalitic segregations forming concordant layers parallel to

the main syn-metamorphic foliation of the amphibolites and cross-cutting bodies and veins. The segregations have high SiO_2 (60.08–67.83 wt%) and Na_2O (5.58–7.55 wt%) contents and low K_2O (0.08–0.26 wt%), FeO (0.49–1.68 wt%) and MgO (0.17–1.18 wt%) contents, and are peraluminous (alumina saturation index = 1.023–1.142). They are made of magmatic quartz, oligoclase, epidote, paragonite, and (minor) pargasite. Locally, the segregations are pegmatitic and made of quartz, albitic plagioclase, epidote and white micas. Petrological and geochemical evidence support that the segregations formed due to H_2O fluxed melting of subducted tholeiitic rocks (amphibolites) at 700–750°C and 14–16 kbar. These conditions indicate very hot subduction likely caused by the onset of subduction of a young oceanic lithosphere at ca. 120 Ma. Metasomatic alteration of amphibolite at high temperature formed amphibolitite pods (made almost exclusively of pargasite, plus minor amounts of epidote, titanite, and rutile). Pods of talc rock indicate metasomatic alteration of ultramafic material. During exhumation, amphibolite blocks and associated trondhjemite–tonalite and pegmatitic rocks attained low-T high-P blueschist facies conditions, with development of retrograde glaucophane and lawsonite. At this stage, new blocks of blueschist were incorporated into the exhuming subduction channel (mélange), including subducted fragments of the volcanic arc Purial complex. The origin of rock crystal quartz described by Kulachkov and Leyva (1990) and Leyva (1996) is uncertain.

Jade samples have been discovered in the Macambo region of the mélange (Fig. 1c). They have appeared as loose blocks of dm–m size laid on the ground made of weathered peridotite and serpentinite. Blocks of a variety of rocks, including jadeite–epidote–paragonite–phengite-bearing gneiss, trondhjemite, plagioclase-lacking epidote ± garnet amphibolite, pargasite amphibolitite, (clino)zoisitite, albite-rich rock, talc-bearing schist, tremolite–actinolite schist, and glaucophane ± lawsonite schist appear associated with jadeitite blocks. Original (in situ) field relations of jadeitite with enclosing serpentinite matrix have not been discovered. Work is in progress to identify this important aspect.

Jadeitite rocks vary from grayish/bluish green massive almost pure jadeitite to heterogeneous impure jadeitite that may show color and compositional banding. Commonly, the latter contain cm-sized pods of deep green jade (Fig. 2a). Occasionally, the rocks appear sheared. Grain size varies from less than 0.1 to ca. 0.5 mm. The mineral assemblages and textures are varied, attesting to a variety of crystallization and (metasomatic) replacement processes. Some samples contain a number of minerals formed at various stages of evolution including jadeite, omphacite, albite, paragonite, analcime, clinozoisite-epidote, apatite, phlogopite, phengite, chlorite, glaucophane, titanite, rutile, and zircon. Quartz has been detected in one sample coexisting with jadeite and albite. In this sample jadeite and quartz form bands, whereas albite forms fine reaction bands along the jadeite–quartz contacts. This texture attests to a relatively high temperature and pressure of formation of jadeite + quartz and late retrograde growth of albite after the reaction Jd + Qtz = Ab (Holland 1979).

Other samples, however, are simpler and made almost exclusively of medium-grained jadeite. This type of sample likely represents direct crystallization of jadeite from fluid in open veins. In this paper, we will focus on one of such type of sample (CV237k). It was taken as loose material from sample site CV237 of García-Casco et al. (2008) and Lázaro and García-Casco (2008). This location (Fig. 1c) is characterized by tectonic blocks of epidote-garnet amphibolite and associated epidote-bearing tonalite–trondhjemite within a serpentinite matrix.

Analytical and computation techniques

Mineral composition (Table 1) was determined by WDS with a CAMECA SX–100 microprobe at the University of Granada operated at 15 keV and 15 nA, beam size of 5 μm, and using albite (Na), periclase (Mg), SiO_2 (Si), Al_2O_3 (Al), sanidine (K), Fe_2O_3 (Fe), $MnTiO_3$ (Mn), vanadinite (Cl), diopside (Ca), TiO_2 (Ti), SO_4Ba (Ba), CaF_2 (F), Cr_2O_3 (Cr), and NiO (Ni) as calibration standards.

Back-scattered electron (BSE) and elemental (Si, Ti, Al, Fe, Mn, Mg, Ca, Ba, Na, and K) XR images were obtained with the same microprobe operated at 15 keV and 150 nA, a focused beam, step (pixel) size of 3 μm, and counting time of 30 ms/pixel. These images were processed with *DWImager* software (Torres-Roldán and García-Casco unpublished) in order to obtain quantitative images of pyroxene composition performed according to the procedure of Bence and Albee (1968) for matrix correction using an internal standard of jadeite analyzed with the microprobe (Table 1), the α-factor table by Kato (2005), see also http://www.nendai.nagoya-u.ac.jp/gsd/a-factor/), and after correction for 3.5 μs deadtime. The images of Figs. 4, 5 show these pixel-sized pyroxene analyses expressed in atoms per 6 oxygen formula unit (color code). In the images of Fig. 4 the voids, polish defects, and all other mineral phases are masked out, and the resulting images are overlain onto a gray-scale BSE image with the same spatial resolution that contains the basic textural information of the scanned area.

Fe^{3+} in clinopyroxene was calculated after normalization to 4 cations and 6 oxygens (Morimoto et al. 1988). Mineral and end-member abbreviations are after Kretz (1983) with end-members (components) of phases written entirely in the lower case. The atomic concentration of

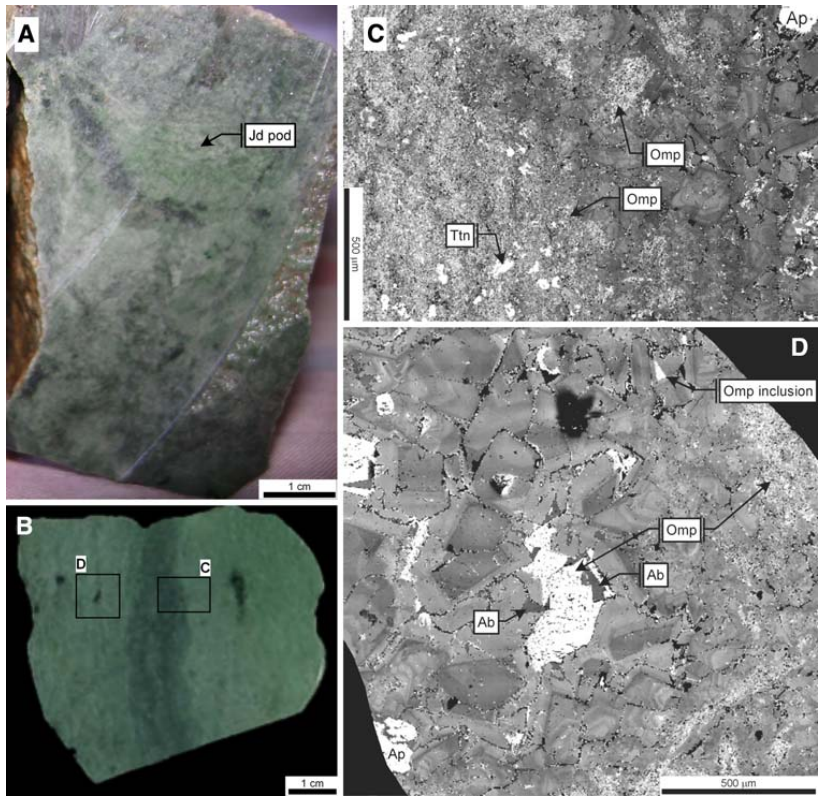

Fig. 2 **a** Sample of heterogeneous jadeitite from the Sierra del Convento with pod of green jade. **b** Studied sample of banded green jade CV237k. *Lighter* and *darker areas* correspond to jadeite- and omphacite-rich regions, respectively. The *boxes* indicate the areas scanned in **c** and **d**. **c** BSE image of the band of jadeite–omphacite rock (*brighter left region*) and jadeitite (*darker right region*). **d** BSE image of jadeitite with nodular region rich in omphacite. Jadeitite is made of blocky jadeite with oscillatory zoning, negative crystals of omphacite in voids and inclusions within blocky jadeitite. The band of jadeite–omphacite rock is formed by fine-grained aggregates of omphacite (*lighter*) and jadeite (*intermediate*) that overprint blocky jadeite (*darker*). Albite and titanite are associated with omphacite

elements per formula units is abbreviated apfu. Tetrahedral and ternary composition diagrams were performed using software *CSpace* (Torres-Roldán et al. 2000). T–X phase diagrams were calculated with *THERMOCALC* (Holland and Powell 1998, version 3.30, dataset 5.5, 12 Nov 04) using the clinopyroxene solution model in the system jadeite–diopside–hedenbergite–acmite of Green et al. (2007).

Textures and mineral assemblages

The mineral assemblage and texture of jadeitite sample CV237k are heterogeneous at the scale of the hand specimen (Fig. 2b). Most of the sample is made of almost pure light green jadeitite that contains darker mm- to cm-sized nodular areas rich in omphacite (Fig. 2d). A dark green band rich in omphacite and with diffuse limits crosscuts and overprints jadeitite (Fig. 2c). This type of rock is termed here jadeite–omphacite rock.

Jadeitite is made essentially of idiomorphic blocky crystals of jadeite of 0.25–0.5 mm in size that display oscillatory zoning (Fig. 2c, d). Omphacite, albite, titanite, and apatite are minor constituents. In the nodular regions omphacite has a similar grain size as blocky jadeite. Omphacite clearly occupies interstitial positions in these nodules and has a xenomorphic or faceted habit resembling negative crystals (Fig. 2d). Omphacite also appears as fine-grained inclusions within jadeite displaying faceted habit (Fig. 2d). These textures are interpreted as indicating a late stage of crystallization in open cavities. Albite crystals are interstitial, fine-grained and xenomorphic, generally associated with omphacite. Apatite is found as rounded crystals dispersed in the matrix, apparently crystallized at the time of jadeite growth. Titanite is scarce and very fine-grained, associated with omphacite or dispersed in grain contacts of jadeite crystals. Textures of albite and titanite indicate late stage of growth.

The jadeitite–omphacite band is made of jadeite and omphacite as major constituents, though omphacite tends to occur in larger amounts than jadeite. Both phases appear as fine to very fine-grained intergrown aggregates of xenomorphic crystals (Fig. 2c, d). Titanite is relatively abundant and associated with omphacite aggregates

Table 1 Representative analyses of jadeite and omphacite from sample CV237k. Mineral formulas and quadrilateral (q), jadeite and acmite end-members calculated following Morimoto et al. (1988)

	Jadeite			Omphacite	
	Max jd	Standard	Min jd	Max jd	Min jd
SiO_2	58.64	58.04	57.57	55.96	55.71
TiO_2	0.20	0.00	0.03	0.08	0.05
Al_2O_3	22.96	19.69	17.86	11.51	8.79
Cr_2O_3	0.00	0.00	0.01	0.00	0.01
FeO_{total}	1.26	2.34	2.39	4.01	4.04
MnO	0.05	0.08	0.06	0.09	0.13
MgO	0.51	2.31	3.65	7.30	9.39
NiO	0.01	0.01	0.01	0.03	0.01
CaO	0.92	3.79	5.48	10.97	14.16
BaO	0.03	0.00	0.00	0.00	0.00
Na_2O	14.21	12.56	11.61	8.13	6.50
K_2O	0.02	0.01	0.02	0.05	0.02
Sum	98.82	98.83	98.71	98.13	98.81
Si	2.01	2.02	2.01	2.01	2.00
Ti	0.01	0.00	0.00	0.00	0.00
Al	0.93	0.81	0.73	0.49	0.37
Cr	0.00	0.00	0.00	0.00	0.00
Fe^{3+}	0.00	0.01	0.03	0.06	0.08
Fe^{2+}	0.04	0.06	0.04	0.06	0.04
Mn	0.00	0.00	0.00	0.00	0.00
Mg	0.03	0.12	0.19	0.39	0.50
Ni	0.00	0.00	0.00	0.00	0.00
Ca	0.03	0.14	0.21	0.42	0.54
Ba	0.00	0.00	0.00	0.00	0.00
Na	0.95	0.85	0.79	0.57	0.45
K	0.00	0.00	0.00	0.00	0.00
$Mg/(Mg + Fe^{2+})$	0.42	0.67	0.83	0.87	0.92
$Fe^{3+}/(Fe^{3+} + Fe^{2+})$	0.00	0.12	0.43	0.51	0.64
$Fe^{3+}/(Fe^{3+} + Al)$	0.00	0.01	0.04	0.11	0.17
q	4.85	15.91	21.69	43.52	54.66
jd	95.15	83.23	75.26	50.19	37.48
acm	0.00	0.86	3.05	6.29	7.86

(Fig. 2c). These aggregates invade the regions of jadeitite and preserve relicts of oscillatory zoned blocky jadeite crystals, suggesting replacement of the latter.

Pyroxene composition

Jadeite is heterogeneous in composition. The amounts of Na and Al range from 0.79 to 0.95 and 0.74 to 0.93 apfu, respectively (Fig. 3). These elements are inversely correlated with Mg and Ca, which range from 0.025 to 0.19 and 0.034 to 0.21 apfu, respectively (Fig. 3). Total iron is low, ranging from 0.036 to 0.080 apfu, and calculated Fe^{3+} and Fe^{2+} range from 0 to 0.047 and 0.023 to 0.073 apfu, respectively (Fig. 3). These relations indicate jadeite–diopside solid solution with minor contribution of hedenbergite and acmite components. The jadeite, quadrilateral pyroxene (wollastonite + clinoestatite + clinoferrosilite) and acmite components range from 75.3 to 95.1, 4.9 to 21.7, and 0 to 4.8 mole %, respectively.

The compositional variations of jadeite are due to a complex growth history that includes distinctive idiomorphic oscillatory zoning of blocky jadeite. Two types of blocky jadeite crystals are distinguished. The earliest grains are relatively small (due to cataclasis, see below), have Na–Al poor compositions and show several idiomorphic oscillatory bands in terms of Al, Na, Ca, Fe and Mg (Figs. 3, 4a–e, 5). This type of grain shows cores poorer in jadeite component that trend towards Na–Al richer at the rims. The amplitude of the peak maxima and minima of oscillations decreases towards the rims (Fig. 5). It merits to mention the close behavior of Ca and Mg atoms along the oscillations, otherwise seen in the quantified XR maps by almost indistinguishable images of both elements (Fig. 4c, d).

Grains with oscillatory zoning are rimmed by distinctive overgrowths of almost pure jadeite composition. These rims may show coherent overgrowth over previous chemical bands, but they commonly crosscut previous oscillatory structure. This relation clearly indicates cataclasis of the earlier grains with oscillatory zoning followed by new growth of Na–Al rich, almost pure jadeite. The idiomorphic shape of oscillatory bands and cataclasis of grains suggest crystallization in a cavity formed (and deformed) along a fault.

A second type of blocky jadeite is made of larger crystals that show relatively homogeneous composition rich in Na–Al and little or no oscillatory zoning (Figs. 3, 4a–e). The composition of this type of grain is similar to that of the rims of almost pure jadeite composition that overgrow the smaller grains with oscillatory zoning. This relation and the lack of evidence of cataclasis of this type of grain indicate that it grew later than the grains with oscillatory zoning. Furthermore, idiomorphic shapes are consistent with crystallization in a void, probably as the cavity opened during fault movement.

The last event of jadeite growth recorded in jadeitite is characterized by Na–Al-poor overgrowths on all types of grains. This stage is characterized by sharp increases in Ca, Mg, and Fe in the rims that overgrow both types of blocky crystals (with oscillatory zoning and with homogeneous high Na–Al composition; Fig. 4a–e). The composition of these overgrowths is similar to that of the earliest interiors of the grains with oscillatory zoning, but they reach somewhat higher Ca- and Mg contents (Fig. 3). Importantly, these outer bands of Ca- and Mg-richer jadeite are in contact with omphacite located in the nodular regions

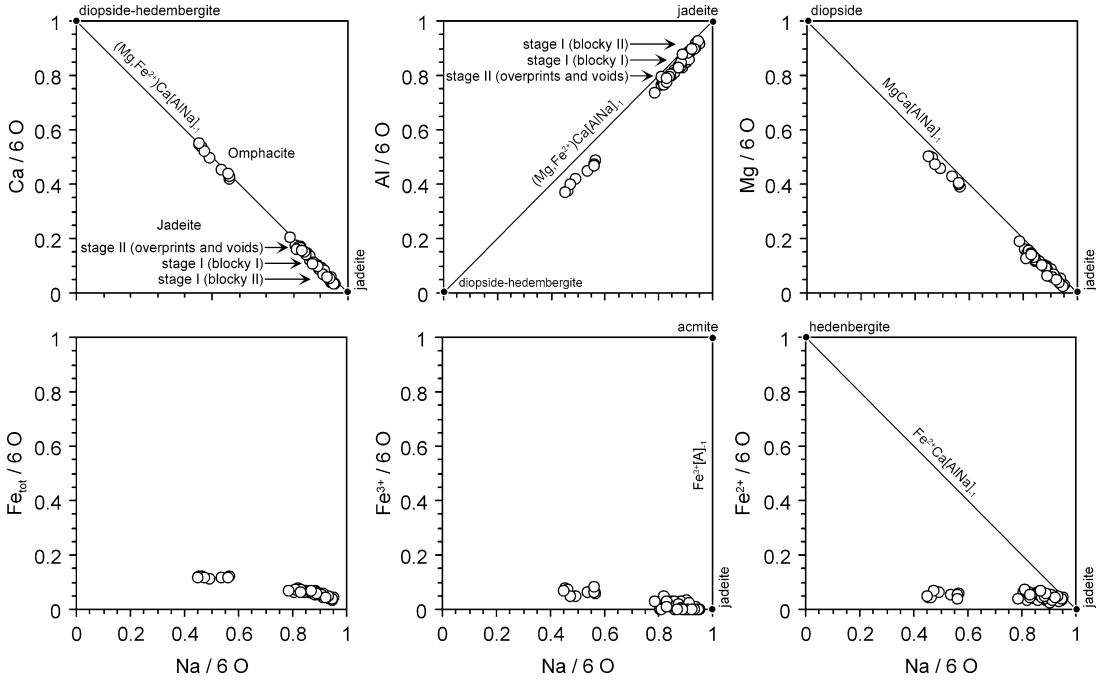

Fig. 3 Composition of jadeite and omphacite from sample CV237k, with indication of significant end-members, exchange vectors and the typical composition of the types of jadeite grains distinguished

(voids) defined by idiomorphic faces of jadeite. In fact, the association of Ca–Mg rich overgrowths of jadeite plus omphacite grew synchronously in voids. This is shown in Fig. 4a–f by a hatched area, where it can be appreciated that the Ca–Mg rich jadeite grew in the walls of the voids defined by idiomorphic Na–Al blocky jadeite, and omphacite grew in the interior of the void, forming a geode-like structure.

Omphacite from these voids does not show oscillatory zoning. In turn, the grains display irregular patchy zoning with no discernible chronological pattern. The compositional range is 0.37–0.49 Al, 0.11–0.12 Fe_{total}, 0.05–0.08 Fe^{3+}, 0.04–0.07 Fe^{2+}, 0.39–0.51 Mg, 0.42–0.55 Ca, and 0.45–0.57 Na apfu (Fig. 3). As in jadeite, total iron is low in omphacite, indicating jadeite–diopside solid solution with minor contribution of hedenbergite and acmite components, but the $Fe^{3+}/(Fe^{3+}+Fe^{2+})$ ratio is generally greater (0.41–0.69). The jadeite, quadrilateral pyroxene (wollastonite–clinoestatite–clinoferrosilite) and acmite components range from 37.5 to 50.2, 43.5 to 55.0, and 4.9 to 8.4 mole %, respectively.

In the regions of fine-grained aggregates of jadeite–omphacite (jadeite–omphacite rock), jadeite and omphacite are similar in composition to those of jadeite (rich in Ca and Mg) and omphacite from the voids within jadeitite. Relict grains of blocky jadeite, locally with oscillatory zoning and high Na–Al rims, are discernible. These relations indicate that the jadeite + omphacite rock band grew by replacement of earlier jadeite from jadeitite, and that this event occurred while jadeite + omphacite were forming in voids by direct precipitation from fluid.

All the textural and chemical relations described so far suggest a complex growth-replacement story in a vein that was probably driven by crystallization in a changing chemical medium. This, in turn, suggests that the composition of infiltrating fluids changed in the course of vein formation.

Phase relations in the diopside–hedenbergite–jadeite–acmite system

Except for albite, titanite and apatite, present in minor amounts, the phase relations in the studied sample can be described in the system diopside–hedenbergite–jadeite–acmite (Fig. 6a). It is long known that two solvi relations occur in this system at low temperature, namely calcic pyroxene–omphacite and omphacite–jadeite. The diagram of Fig. 6a contains the phase relations calculated by Green et al. (2007) in the hedenbergite-free system

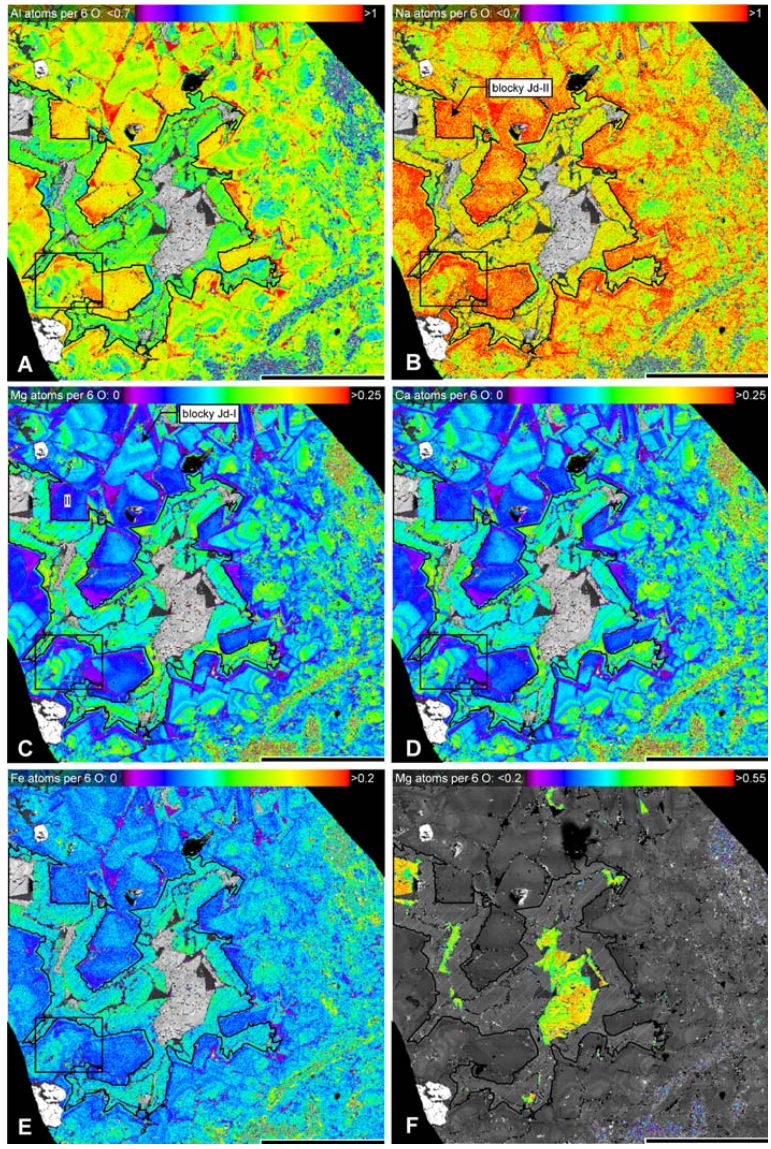

Fig. 4 Images of quantified elemental XR signals of the area shown in Fig. 2d expressed as atoms per six oxygen (*color scale*) showing compositional features and zoning of jadeite and omphacite. Voids, polish defects, and all other mineral phases are masked out and the resulting images are overlain onto a gray-scale BSE image with the same spatial resolution that contains the basic textural information of the scanned area. **a** Al, **b** Na, **c** Mg, **d** Ca, and **e** in jadeite, and **f** Mg in omphacite. Scale bar = 0.5 mm. The spatial resolution in *X* and *Y* directions is 3 μm/pixel. The two types of blocky jadeite are indicated. The hatchet region indicates Ca–Mg rich jadeite and omphacite precipitated in a void. The *box* indicates location of detail shown in Fig. 5. See text for details

diopside–jadeite–acmite at 500°C. Note that the acmite component acts as a dilutent with the effect of shrinking the solvi surfaces at fixed temperature. The textural and chemical relations involving earlier blocky jadeite from jadeitite indicate formation at conditions that deviate from the omphacite–jadeite solvus, whereas the late stage association of Ca-rich jadeite and omphacite suggest a physicochemical relation as described by the omphacite–jadeite solvus.

The distribution of mineral composition in Fig. 6a shows (1) the low content of hedenbergite and acmite components, particularly in jadeite, and (2) a compositional trend of both phases that approaches a line in this system. This trend points from jadeite towards a complex end-member in the di–acm–hd subsystem. Three model end-members are considered 0.9di·0.05hd·0.05acm, 0.8di·0.1hd·0.1acm, and 0.7di·0.15hd·0.15acm (Fig. 6a). The nature of the linear trend is best seen, however, in the triangular diagrams. Using the end-members of Morimoto et al. (1988) the data distribute along lines of acmite/(acmite + quadrilateral components) ratios ranging from 0.05 to 0.15 (Fig. 6b). The

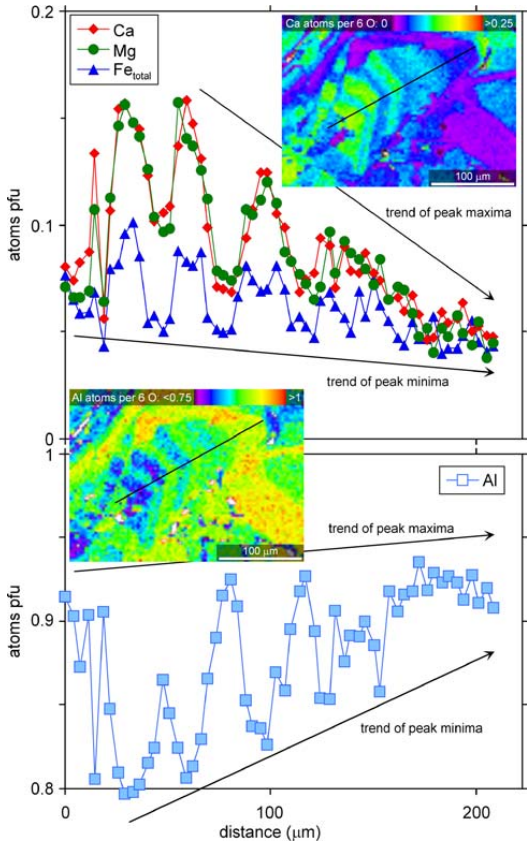

Fig. 5 Detail of grain of jadeite with oscillatory zoning (Fig. 4 for location). The images shows quantified Ca-Kα XR and Al-Kα XR signals and the compositional profile extracted from the quantified image with a resolution of 3 µm/point (total number of points plotted: 58). Note that the amplitude of the oscillations attenuates towards the rim of the crystal and that the peak maxima and minima trend towards end-member jadeite

distribution of compositions of the analyzed pyroxenes roughly conforms to the phase relations calculated by Green et al. (2007), but some analyses of jadeite with higher Mg–Ca contents plot within the "forbidden" omphacite–jadeite solvus region. Because the phase relations offered by Green et al. (2007) in the diopside–jadeite–acmite system did not take into account the effect of hedenbergite component, the compositions of pyroxene have been projected from hedenbergite component into the diopside–jadeite–acmite subsystem in Fig. 6c. The projection shows better agreement of the composition of jadeite with the calculated phase relations, but a few analyses of omphacite plot in the calculated "forbidden" region. These inconsistencies are due to the non-accounted effect of hedenbergite in the calculated phase relations and/or a different temperature of formation of pyroxenes of sample CV237k.

To solve these problems, we have calculated T–X relations in the system diopside–hedenbergite–jadeite–acmite. The calculations were performed along the pseudobinary joins indicated in Fig. 6a and representing acm/(Q + acm) = 0.05, 0.10 and 0.15. Of these, only the first two joins (0.9di·0.05hd·0.05acm—jadeite and 0.8di·0.1hd·0.1acm—jadeite) are shown in Fig. 7b, c, respectively, together with the relations calculated by Green et al. (2007) in the binary diopside–jadeite (Fig. 7a), for comparison. Using jadeite of the latest overgrowths (with maximum Mg–Fe–Ca contents) as probable composition coexisting in equilibrium with omphacite (with maximum Al–Na) in the voids, no agreement between observed compositions and predicted phase relations is observed in the binary diopside–jadeite, as would be expected due to the non-accounted effect of Fe^{2+} and Fe^{3+} in the model. Good fits, however, are obtained in the pseudobinary systems for acm/(Q + acm) = 0.05 and 0.1 (Fig. 7b, c, respectively). The predicted temperature of formation of late jadeite–omphacite is ca. 550–560°C.

Discussion

Formation of oscillatory zoning in blocky jadeite

As shown above, omphacite is texturally late and related to jadeite compositions with high Mg–Fe–Ca contents in the two types of rock identified (jadeitite and fine-grained jadeite–omphacite rock band). This implies that the composition of earlier blocky jadeite with oscillatory zoning and rich in Na–Al can hardly be related to formation on the solvus surface along a cooling path. These compositions must have formed in the one-phase region of jadeite solid solution at high temperature. Similar relations (i.e., jadeitite containing jadeite and omphacite formed at lower temperature than jadeitite with only jadeite) have been described by Oberhänsli et al. (2007). Changes in temperature, pressure and/or system composition can explain the formation of oscillatory zoning in jadeite within the one-phase jadeite region.

Sample CV237k formed in an opening fracture filled with fluid. This scenario is indicated by events of cataclasis of jadeite, with disruption of previous oscillatory zoning and development of new overgrowths. Cataclasis is expected to create porosity and to drive episodic fluid infiltration. In this context, development of oscillatory zoning strongly suggests recurrent infiltration of fluid with diverse chemical composition (Sorensen et al. 2006). For simplicity, we consider this scenario in an isothermal–isobaric medium.

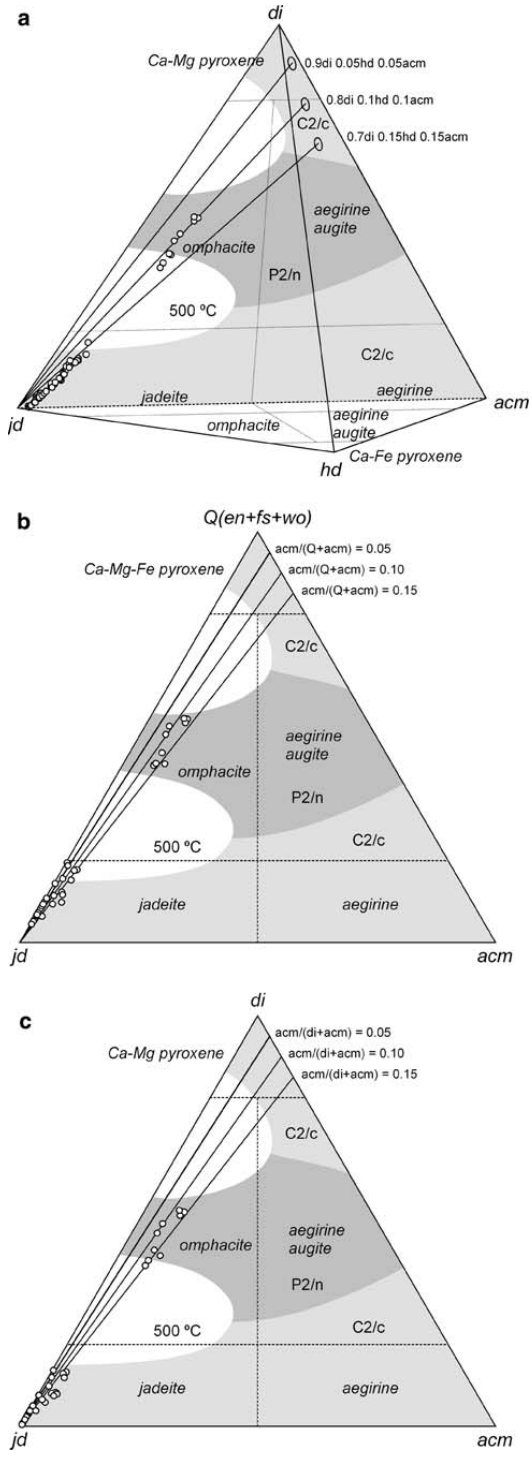

Fig. 6 **a** Composition of jadeite and omphacite in the jadeite–diopside–hedenbergite–acmite tetrahedra. Note the near-linear alignment of data points. *Solid lines* represent pseudobinary sections of the system relevant for calculation of phase relations (Fig. 7b, c). The jadeite–diopside–acmite and jadeite–hedembergite–acmite base triangles show the compositional boundaries of pyroxene in the classification scheme of Morimoto et al. (1988 names in *italics*). The jadeite–diopside–acmite triangle shows the phase relations of pyroxene (denoted by space groups C2/c and P/2n) calculated by Green et al. (2007) at 500°C in this system. **b** The same data in the classification scheme of Morimoto et al. (1988) and the phase relations of pyroxene calculated by Green et al. (2007) at 500°C in the system jd–di–acm. Note that jadeite with higher *Q* component plots in the omphacite–jadeite solvus (forbidden) region as a consequence of the lack of consideration of hedenbergite in the calculated phase relations and/or different temperature of formation. **c** Same as in **b** but projecting the data analyses of clinopyroxene from hedenbergite. In this diagram omphacite with lower diopside component plots in the solvus region. *Solid lines* in **b** and **c** indicate varying acmite/(Q + acmite) and acmite/(diopside + acmite) ratios, respectively

The composition of the infiltrating fluid considered is saturated in SiO_2, Al_2O_3, Na_2O, and CaO and poor in FeO and MgO, as suggested by pegmatitic material found in the mélange made of quartz, albitic plagioclase, paragonite, and epidote (see below). This fluid is indicated in the ternary diopside–jadeite–H_2O diagram of Fig. 8b as point 1, which is assumed to be subsaturated with respect to jadeite–omphacite–diopside. This diagram is qualitative with respect to the saturation surface of the fluid, though the solid–solid relations depicted are based on the calculated anhydrous phase relations in the pseudobinary 0.9di·0.05hd·0.05acm—jadeite system (Fig. 8a). Interaction of this fluid with ultramafic rocks (represented by point 2 in Fig. 8b) would make the composition of the original fluid to change towards saturation. Once saturation is reached (point 3, Fig. 8b) the fluid precipitates jadeite (point 4). Formation of jadeite with different composition should take place upon subsequent infiltration of fluid with composition different than 1. This process may help explaining formation of zoning in jadeite, though no intrinsic reason exists that can explain a systematic recurrence in the composition of infiltrating fluid, suggesting that additional processes occurred during formation of jadeite.

New infiltrating fluid of different composition should not be in equilibrium with previously formed jadeite, promoting jadeite–fluid interaction. This is exemplified in Fig. 8b by a fluid that did not attain saturation after interaction with ultramafic rocks (point 5). Once within the vein this fluid should react with previously formed jadeite, driving its composition towards saturation (point 6). At this stage, the fluid precipitates jadeite richer in Al–Na (point 7). Thus, we envisage formation of an oscillatory pair made of Mg–Fe–Ca-richer and Al–Na-richer bands as a single response to a discrete event of fluid infiltration characterized by saturation at a first stage, followed by subsaturation. This is

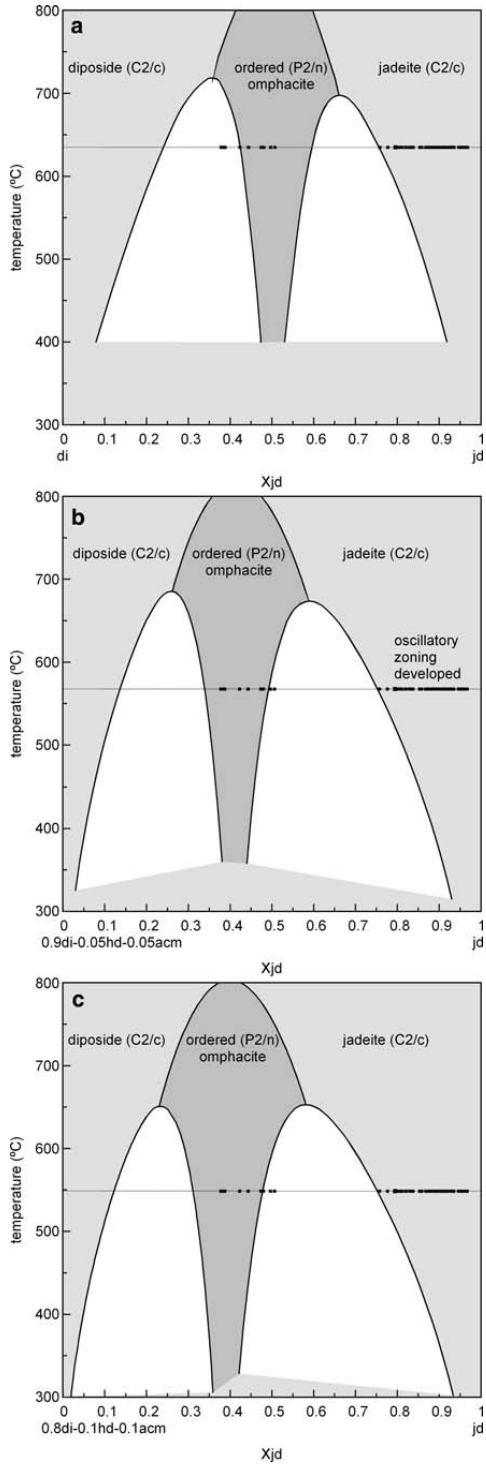

Fig. 7 Phase relations of pyroxene as a function of temperature. ▶ **a** Calculated by Green et al. (2007) in the simple binary system di–jd. **b**, **c** Calculated using *THERMOCALC* in the jd–di–hd–acm system along the pseudobinary joins 0.9di·0.05hd·0.05acm-jd and 0.8di·0.1hd·0.1acm-jd, respectively. The compositional ranges of analyzed jadeite and omphacite are plotted in all diagrams for comparison. The different locations of the data in the temperature scale are based on the analysis of jadeite with minimum jadeite content, assumed to have formed at the solvus surface in equilibrium with omphacite

conceptualized as due to the decreasing capability of a single batch of infiltrating fluid to react with the developing selvage in the ultramafic wall rock. In this model, a sequence of infiltration events should drive the composition of the sequential pairs of oscillatory bands towards Al–Na richer compositions. This is consistent with the observed decrease in amplitude of the oscillations and the overall trend towards Na–Al rich compositions from core to rim (Fig. 5) indicating progressively lower contents in Mg of infiltrating fluid.

Though the entire process can be isothermal–isobaric, a decrease in temperature can also help explaining a decrease in the extent fluid-ultramafic rock interaction and, hence, the development of Al–Na richer bands. This is shown schematically in the T–X diagram of Fig. 8a. At lower temperature the saturation surface of fluid should shift towards the H_2O apex of Fig. 8b and, hence, the phase region of fluid should shrink in composition space. However, the basic relations shown in Fig. 8b would be maintained. Similarly, changes in pressure should affect the location of the fluid saturation surface in P–T–X space. Evidence given below suggests, however, that the process occurred at constant lithostatic pressure.

Formation of Al–Na rich blocky jadeite

At an intermediate stage the vein underwent cataclasis, and Na–Al rich idiomorphic blocky jadeite formed. In the model devised here, this event is explained as the latest stage of formation of oscillatory zoning. However, it was characterized by infiltration of a large batch of fluid triggered by a significant increase in porosity of the vein due to cataclasis. Reaction of Al-rich fluid with pre-existing jadeite did not change the fluid composition significantly because of the relatively large amount of fluid, and just a thin rim of Na–Al poor jadeite formed (otherwise consistent with previous trend of the oscillatory grains).

Formation of omphacite and associated Ca–Mg rich jadeite

The final event of vein formation was characterized by fluids saturated in omphacite. This indicates a distinct temperature or the infiltration of a fluid with contrasted composition, as indicated in Fig. 8b by fluid of composition 8. Omphacite

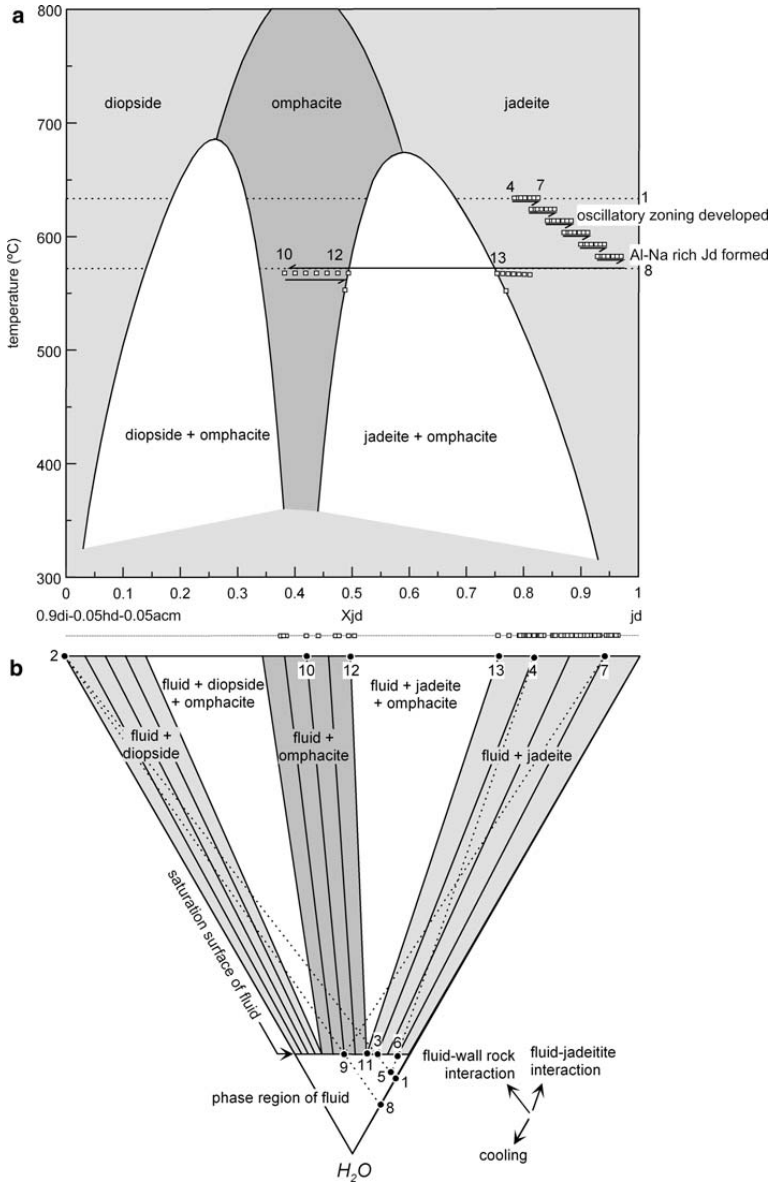

Fig. 8 Model of formation of jadeite and omphacite from the studied sample in the model ternary system calcic pyroxene-jadeite-fluid. **a** T-Xjd diagram projected from fluid (Fig. 7b). **b** Ternary system at 560°C constructed from **a**. The saturation surface of fluid is schematic. See text for details

saturation in this type of fluid can be reached upon reaction with ultramafic rock (point 9 in Fig. 8b). At this point the fluid precipitates omphacite relatively poor in Al–Na (point 10). Note that jadeite is not formed at this stage. However, this new fluid would not be in equilibrium with previously formed blocky jadeite of jadeitite (e.g., point 7), promoting reaction and change in composition. Fluid-jadeite reaction drives the composition of fluid along the fluid saturation surface towards Al–Na richer compositions until the fluid attains point 11, where it reaches a composition in equilibrium with both omphacite (point 12) and jadeite (point 13). At this stage all three phases are in equilibrium, and precipitation of Ca–Mg rich jadeite together with Na–Al rich omphacite is promoted, as in the voids of jadeitite. However, the reaction path drives the extensive replacement of previously formed Al–Na rich jadeite by omphacite, as is observed in the fine-grained jadeite–omphacite band. In this band relict jadeite with oscillatory zoning is still present,

omphacite is dominant, and new jadeite bears Al–Na poorer compositions, as predicted in the model. The fluid left after reaction precipitated omphacite and jadeite in the voids. Subsequent readjustments formed patchy zoning in omphacite.

Similar views of changing composition of infiltrating fluids were presented by Sorensen et al. (2006). The samples studied by these authors show a systematic trend in terms of jadeite zoning, with early jadeite being richer in Na–Al and late jadeite rich in Ca and Mg. The sample studied here records this trend in the late overgrowths rich in Ca and Mg, but it also records an earlier trend of decreasing Ca and Mg that apparently contradicts the general patterns of jadeitite formation inferred by Sorensen et al. (2006). In our view, this is simply the result of the complex dynamics of fluid flux in subduction environments, which are characterized by discrete pulses as clearly demonstrated by the sample studied here and the heterogeneous elemental and isotopic composition of fluids that formed jadeitite documented by Sorensen et al. (2006).

Origin of jadeitite-forming fluids in the Sierra del Convento mélange

The Sierra del Convento mélange provides ample evidence for fluid movement in the subduction environment. Here, we discuss the P-T-t history of the amphibolite blocks and associated trondhjemitic-pegmatitic rocks, as deduced by García-Casco et al. (2006), García-Casco (2007), García-Casco et al. (2008), Lázaro and García-Casco (2008) and Lázaro et al. (2008) to place constraints for the origin of jadeitite forming fluids.

Upon onset of subduction of young oceanic lithosphere during Aptian times (ca. 120 Ma), epidote ± garnet amphibolite formed from subducted MORB at ca. 700–750°C and 14–16 kbar. Shortly after onset of subduction, blocks of amphibolite were accreted to the upper plate mantle. At these conditions, eclogite is not formed (e.g., Vielzeuf and Schmidt 2001). Shortly after accretion, fluid infiltration occurred in the upper plate ultramafic material and accreted tectonic blocks of amphibolite at high temperature, promoting wet (fluxed) melting of amphibolite and the formation of peraluminous tonalitic–trondhjemitic melts. Melts formed were rich in H_2O-fluid, as indicated by crystallization of magmatic paragonite and other hydrous minerals. Continued subduction refrigerated the upper plate material and, as a consequence, the blocks followed isobaric cooling P–T paths and the associated tonalitic–trondhjemitic melts crossed their solidi and crystallized at depth. García-Casco (2007) calculated solidus conditions of ca. 680°C, 14 kbar. At these conditions residual melts saturated in H_2O and fluids formed pegmatitic/hydrothermal segregations made of quartz, albitic plagioclase, paragonite, and epidote. The composition of residual fluids should be saturated in SiO_2, Al_2O_3, Na_2O, and CaO. Following the P–T data of Lázaro et al. (2008), the residual fluids would have been released at ca. 15 kbar and 600–650°C. This temperature is similar to the high-T stage of formation of oscillatory zoning in blocky jadeite from the studied sample (Fig. 8a).

As discussed above, aluminous quartz-feldspathic fluid extracted out of the mother trondhjemitic–pegmatitic rocks may have produced jadeitite after infiltration within, and reaction with, the surrounding ultramafic material of the upper plate. This is in agreement with experiments at 600°C and 22 kbar by Schneider and Eggler (1986) showing that fluids in equilibrium with jadeite–peridotite assemblages have solutes dominated by quartz–feldspathic components, with high Si and Na contents and substantial Al, though are peralkaline rather than peraluminous in composition (Manning 2004). Metasomatic rocks (amphibolitite, zoisitite, talc-bearing rocks) indicating significant pervasive fluid-rock interaction are abundant in the mélange. However, the fluid may have also escaped along fractures, perhaps favored by some sort of seismic pumping effect responsible for episodic fluid infiltration, as indicated by the studied rock sample. Fluid channeling in a cooling medium allowed the fluids to cold down progressively, reaching conditions of ca. 550°C for the formation of omphacite–jadeite in voids and the replacement of early blocky jadeite by omphacite in the studied sample. Following the P–T data of Lázaro et al. (2008), this temperature condition would have been reached during the isobaric cooling stage at ca. 15 kbar. To be noted is that these conditions are consistent (within error) with the presence of quartz–jadeite samples in the Sierra del Convento mélange, for the reaction Jd + Qtz = Ab is located at ca. 15 kbar at 550°C (Holland 1979).

There is no age available for the formation of jadeitite in the Sierra del Convento mélange. Lázaro et al. (2008) document zircons from a trondhjemite with a mean $^{206}Pb/^{238}U$ SHRIMP age of 112.8 ± 1.1 Ma, interpreted as the onset of isobaric cooling of the trondhjemitic liquids at ca. 15 kbar. These authors calculated ca. 106.8 Ma for the end of the isobaric cooling stage at 550°C 15 kbar. Thus, an early Cretaceous age (100–110 Ma) is expected for jadeitite if the original fluids evolved from the tonalitic–trondhjemitic rocks of the mélange.

After the isobaric cooling stage, the rocks experienced exhumation within the subduction channel in a syn-subduction scenario (Lázaro et al. 2008). This event took place mostly within the blueschist facies during several tens of My (107–70 Ma). Formation of retrograde blueschist assemblages in jadeitite samples (including albite in jadeite + quartz samples) indicates that jadeitite jade rocks were already formed by this time.

Thus, taking all the lines of evidence together, we consider that jadeite-forming fluids in the Sierra del Convento mélange originally evolved from partial melts in the subduction environment at high temperature. The inferred >550°C conditions of formation of the studied jadeitite sample, higher than those normally recorded in other jadeitite localities (Harlow and Sorensen 2005; Oberhänsli et al. 2007), strengthen this view.

Sorensen et al. (2006) suggested that devolatilization of spilitized mafic rocks metamorphosed to high pressure conditions (blueschists) might yield fluids that could crystallize jadeitite, but indicated that fluid in equilibrium with an "igneous" or "mantle" source also formed jadeitite. Isotopic data of jadeitite from the Sierra del Convento are not available, but the amphibolites and associated tonalitic–trondhjemitic rocks have Sm/Nd and Rb/Sr isotopic signatures consistent with the mantle array (Lázaro and García-Casco 2008). If jadeitite-forming fluids are related to these rocks, a fluid in equilibrium with an "igneous" or "mantle" source can be anticipated. To our knowledge, other world wide occurrences of jadeite do not show association with partial melting of the subducted oceanic crust. But, certainly, fluids evolved upon cooling of hydrated melts at great depth are potential parental sources of jadeitite-forming fluids.

Archeological implications

Pre-Columbian artifacts of jade or "probable" jade have been documented in the Antilles (Fig. 1a), including Cuba (Calvache 1944; Soto González 1981, citing René Herrera Fritot), Bahamas (Johnson 1980; Aarons 1990; M. J. Berman, personal communication 2008), Puerto Rico (Rodriguez 1991; García Padilla et al. 2006; Wilson 2007), Antigua (Harlow et al. 2006), and Grenada (Keegan 1991). Until recently, the Motagua Valley of Guatemala was the only known source region of jadeitite for these artifacts in Mesoamerica and the Caribbean (e.g., Harlow 1994; Harlow and Sorensen 2005; Harlow et al. 2006). However, old (but bibliographically "hidden") discoveries of jadeitite in the Escambray complex of Cuba (Millán and Somin 1981), and recent discoveries in the Río San Juan mélange, Dominican Republic (Schertl et al. 2007a, b; Baese et al. 2007) and the Sierra del Convento mélange, Cuba (this paper) open new perspectives for archeological and historical studies concerning trade in the ancient Antilles.

Jadeitite and related source rocks of archeological jade are quite varied, as demonstrated in the Motagua Valley of Guatemala (Harlow 1994; Harlow et al. 2003), making the recognition of source regions in terms of mineralogy and mineral assemblages uncertain. For example, Harlow et al. (2006) indicated mineralogical similarities among Antiguan jade artifacts and Guatemalan jadeitites and implied possible extended trade between Mesoamerica and the Antilles. These authors, however, acknowledge other possibilities related to unknown or uncertain sources of Antillean jade. In fact, the rare occurrence of quartz in Antiguan jade and some Guatemalan samples (in addition to phengite, lawsonite and glaucophane) indicated by Harlow et al. (2006) cannot be taken as diagnostic because similar quartz-bearing jadeitite are present in the Rio San Juan and Sierra del Convento mélanges. Thus, if Dominican and Cuban jadeitite are demonstrated to be similar to Antillean pre-Columbian jade artifacts, a local (Caribbean) rather than an exotic (Guatemalan) source is more probable, and the statement of existence of extended trade between Mesoamerica and the Antilles (e.g., Saladoid, La Hueca and Taino cultures, c. V B.C.—IX A.D., III B.C.—XV A.D., and XII–XVI A.D., respectively) based on jade artifacts should be questioned.

Conclusions

Jadeite jade has been discovered for the first time in eastern Cuba. It occurs as loose blocks within the Sierra del Convento mélange. The mélange contains a variety of high-pressure blocks formed during the Cretaceous in the subduction environment of the Proto-Caribbean (Atlantic) lithosphere. Fluids evolved in this environment, likely upon crystallization of trondhjemitic liquids formed upon partial melting of subducted oceanic crust, percolated ultramafic material of the upper plate and deposited jadeitite in veins. The diversity in the chemical composition of jadeite, including distinctive oscillatory zoning, indicates crystallization from chemically diversified fluids during recurrent episodes of infiltration. Fluid-ultramafic rock interaction is the main cause of diversification of fluids. However, fluid-jadeite interaction within the vein is an important process in the development of oscillatory zoning in jadeite and the formation of late jadeite and omphacite. This new jade locality suggests a local (Caribbean) rather than an exotic (Guatemalan) source for Antillean pre-Columbian jade artifacts.

Acknowledgments We thank two anonymous reviewers for perceptive comments and Dr. Mary Jane Berman for discussion on Caribbean archeological artifacts and for providing an unpublished report on Bahamian jade artifacts by K. R. Johnson. Y. Rojas-Agramonte acknowledges a Humboldt-Foundation Georg Forster Fellowship and a post-doctoral fellowship of the Geocycles Cluster of Mainz University. This is Mainz Geocycles contribution no. 498 and a contribution to IGCP-546 'Subduction zones of the Caribbean'. Research for this paper has received financial support from the Spanish Ministerio de Educación y Ciencia project CGL2006-08527/BTE.

References

Aarons GA (1990) The Lucayans: the people whom Columbus discovered in the Bahamas. "Five Hundred" Magazine 2:6–7. http://www.millersville.edu/~columbus/data/ant/AARONS01.ANT

Baese R, Schertl HP, Maresch WV (2007) Mineralogy and petrology of Hispaniolan jadeitites: first results. In: Martens U, García-Casco A (eds) High-pressure belts of Central Guatemala: the Motagua suture and the Chuacús Complex. IGCP 546 Special Contribution, 1. http://www.ugr.es/~agcasco/igcp546/≫Activities≫Guatemala 2007≫Abstracts

Bence AE, Albee AL (1968) Empirical correction factors for the electron microanalysis of silicate and oxides. J Geol 76:382–403

Calvache A (1944) Historia y Desarrollo de la Minería en Cuba. Ed. Neptuno, La Habana, p 100

García-Casco A (2007) Magmatic paragonite in trondhjemites from the Sierra del Convento mélange, Cuba. Am Mineral 92:1232–1237. doi:10.2138/am.2007.2598

García-Casco A, Torres-Roldán RL, Iturralde-Vinent MA, Millán G, Núñez Cambra K, Lázaro C, Rodríguez Vega A (2006) High pressure metamorphism of ophiolites in Cuba. Geol Acta 4:63–88

García-Casco A, Lázaro C, Rojas-Agramonte Y, Kröner A, Torres Roldán RL, Núñez K, Millán G, Neubaurer F, Blanco-Quintero I (2008a) Partial melting and counterclockwise P-T path of subducted oceanic crust (Sierra del Convento, E Cuba). J Petrol 49:129–161. doi:10.1093/petrology/egm074

García-Casco A, Iturralde-Vinent MA, Pindell J (2008b) Latest Cretaceous collision/accretion between the Caribbean Plate and Caribbean: origin of metamorphic terranes in the Greater Antilles. Int Geol Rev 50:781–809. doi:10.2747/0020-6814.50.9.781

García Padilla A, Escalona de Motta G, Ramos Escobar JL, Marichal Lugo F, Méndez Bonilla I, González Rivera V, Chanlatte Baik L, Narganes Storde Y, Ortiz Meléndez L, Marrero JE, Auerbach D, Muñoz Arjona G Santiago Gracia Ch, de Jesús Ortega V, de Mater O'Neill M (2006) Indigenous cultures of Puerto Rico. Museum of history, anthropology and art and University of Puerto Rico at Rio Piedras. http://www.universia.pr/culturaindigena/index_ing.html (revision: MMO, Tuesday, July 25, 2006, 3:36:29 PM)

Green ECR, Holland TJB, Powell R (2007) An order-disorder model for omphacitic pyroxenes in the system jadeite-diopside-hedenbergite-acmite, with applications to eclogite rocks. Am Mineral 92:1181–1189. doi:10.2138/am.2007.2401

Harlow GE (1994) Jadeitites, albitites and related rocks from the Motagua Fault Zone, Guatemala. J Metamorph Geol 12:49–68. doi:10.1111/j.1525-1314.1994.tb00003.x

Harlow GE, Sorensen SS (2005) Jade (nephrite and jadeitite) and serpentinite: metasomatic connections. Int Geol Rev 47:113–146. doi:10.2747/0020-6814.47.2.113

Harlow GE, Sisson VB, Avé Lallemant HG, Sorensen SS (2003) High-pressure, metasomatic rocks along the Motagua Fault Zone, Guatemala. Ofioliti 28:115–120

Harlow GE, Murphy AR, Hozjan DJ, De Mille CN, Levinson AA (2006) Pre-Columbian jadeite axes from Antigua, West Indies: description and possible sources. Can Mineral 44:305–321. doi:10.2113/gscanmin.44.2.305

Holland TJB (1979) Experimental determination of the reaction paragonite = jadeite + kyanite + H2O, and internally consistent thermodynamic data for part of the system Na2O-Al2O3–SiO2–H2O, with applications to eclogites and blueschists. Contrib Mineral Petrol 68:293–301. doi:10.1007/BF00371551

Holland TJB, Powell R (1998) An internally consistent thermodynamic data set for phases of petrological interest. J Metamorph Geol 16:309–343. doi:10.1111/j.1525-1314.1998.00140.x

Iturralde-Vinent MA (1998) Sinopsis de la constitución Geológica de Cuba. Acta Geol Hispanica 33:9–56

Johnson KR (1980) Results of test to determine the mineralogy of an artifact from San Salvador, Bahamas. Bahamas. Archaeology Project Reports and Papers. College Center of the Finger Lakes, Bahamian Field Station, San Salvador, Bahamas, pp. 1–7 (unpublished)

Kato T (2005) New accurate Bence-Albee α-factors for oxides and silicates calculated from the PAP correction procedure. Geostandards Geoanalytical Res 29:83–94. doi:10.1111/j.1751-908X.2005.tb00657.x

Keegan WF (compilator 1991) Archaeology at pearls, Grenada: the 1990 field season. Miscellaneous Project Report Number 47, Florida Museum of Natural History, Gainesville, May 1991. http://www.flmnh.ufl.edu/Caribarch/grenada.htm

Krebs M, Maresch WV, Schertl HP, Münker C, Baumann A, Draper G, Idleman B, Trapp E (2008) The dynamics of intra-oceanic subduction zones: a direct comparison between fossil petrological evidence (Rio San Juan Complex, Dominican Republic) and numerical simulation. Lithos 103:106–137. doi:10.1016/j.lithos.2007.09.003

Kretz R (1983) Symbols for rock-forming minerals. Am Mineral 68:277–279

Kulachkov LV, Leyva RC (1990) Informe sobre los resultados de los trabajos de reconocimiento geológico para cuarzo filoniano en la parte oriental de Cuba. Unpublished report of the Instituto Superior Minero-Metalúrgico de Moa

Lázaro C, García-Casco A (2008) Geochemical and Sr-Nd isotope signatures of pristine slab melts and their residues (Sierra del Convento mélange, eastern Cuba). Chem Geol 255:120–133. doi:10.1016/j.chemgeo.2008.06.017

Lázaro C, García-Casco A, Neubaurer F, Rojas-Agramonte Y, Kröner A, Iturralde-Vinent MA (2008) 55-million-year history of oceanic subduction and exhumation in the northern edge of the Caribbean plate (Sierra del Convento mélange, Cuba). J Metamorph Geol. doi:10.1111/j.1525-1314.2008.00800.x

Leyva RC (1996) Características geológicas, regularidades de distribución y perspectivas de utilización del cuarzo filoniano de la región oriental de Cuba. Unpublished report of the Instituto Superior Minero-Metalúrgico de Moa, p 90

Manning CE (2004) The chemistry of subduction-zone fluids. Earth Planet Sci Lett 223:1–16. doi:10.1016/j.epsl.2004.04.030

Millán G, Somin M (1981) Litología, estratigrafía, tectónica y metamorfismo del Macizo del Escambray. Editorial Academia, La Habana, p 104

Morimoto N, Fabries J, Ferguson AK, Ginzburg IV, Ross M, Seifert FA, Zussman J, Aoki K, Gottardi G (1988) Nomenclature of pyroxenes. Am Mineral 73:1123–1133

Oberhänsli R, Bousquet R, Moinzadeh H, Moazzen M, Arvin M (2007) The field of stability of blue jadeite: a new occurrence of jadeitite at Sorkhan, Iran, as a case study. Can Min 45:1501–1509. doi:10.3749/canmin.45.6.1501

Rodriguez M (1991) Early trade networks in the Caribbean. In: Cummins A, King P (eds) Proc. Fourteenth Congress of the International Association for Caribbean Archaeology, Barbados, pp 306–314

Schertl HP, Maresch WV, Krebs M, Draper G (2007a) The Rio San Juan serpentinite complex and its jadeitites (Dominican Republic). In: Martens U, García-Casco A (eds) High-pressure belts of Central Guatemala: the Motagua suture and the Chuacús Complex. IGCP 546 Special Contribution, 1. http://www.ugr.es/~agcasco/igcp546/≫Activities≫Guatemala2007≫Abstracts

Schertl HP, Krebs M, Maresch WV, Draper G (2007b) Jadeitite from Hispaniola: a link between Guatemala and Antigua? 20th Colloquium on Latin American Earth Sciences, Kiel, Germany, Abstract Volume, 167–168

Schneider ME, Eggler DH (1986) Fluids in equilibrium with peridotite minerals: implications for mantle metasomatism. Geochim Cosmochim Acta 50:711–724. doi:10.1016/0016-7037(86)90347-9

Sorensen SS (1988) Petrology of amphibolite-facies mafic and ultramafic rocks from the Catalina Schists, Southern California: metasomatism and migmatization in a subduction zone metamorphic setting. J Metamorph Geol 6:405–435. doi:10.1111/j.1525-1314.1988.tb00431.x

Sorensen SS, Barton MD (1987) Metasomatism and partial melting in a subduction complex: Catalina schist, southern. Calif Geol 15:115–118

Sorensen S, Harlow GE, Rumble DIII (2006) The origin of jadeitite-forming subduction-zone fluids: CL-guided SIMS oxygen-isotope and trace-element evidence. Am Mineral 91:979–996. doi:10.2138/am.2006.1949

Soto González LD (1981) Apuntes sobre la historia de la minería cubana. Editorial Oriente, Santiago de Cuba, p 121

Torres-Roldán RL, García-Casco A, García-Sánchez PA (2000) CSpace: An integrated workplace for the graphical and algebraic analysis of phase assemblages on 32-bit Wintel platforms. Comput Geosci 26:779–793. doi:10.1016/S0098-3004(00)00006-6

Vielzeuf D, Schmidt MW (2001) Melting reactions in hydrous systems revisited: applications to metapelites, metagreywackes and metabasalts. Contrib Mineral Petrol 141:251–267

Wilson SM (2007) The archaeology of the Caribbean. Series: Cambridge World Archaeology. Cambridge University Press, Cambridge, p 222